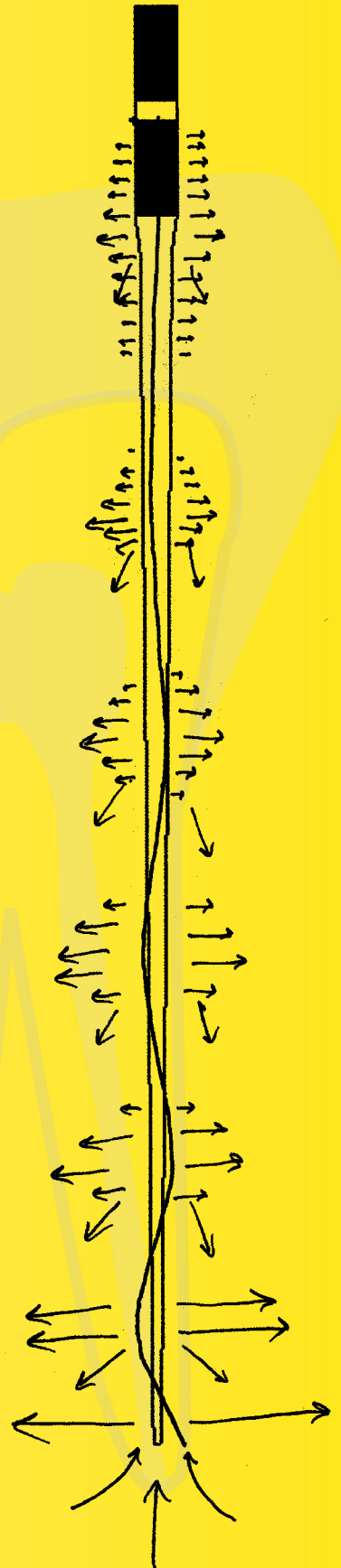


# ROOT CANAL CLEANING

THROUGH  
CAVITATION AND MICROSTREAMING

BRAM VERHAAGEN



# ROOT CANAL CLEANING

through

Cavitation and Microstreaming

Bram Verhaagen

## **Samenstelling promotiecommissie:**

Prof. dr. ir. L. van Wijngaarden (voorzitter)	Universiteit Twente, TNW
Prof. dr. rer. nat. D. Lohse (promotor)	Universiteit Twente, TNW
Dr. A.M. Versluis (assistent promotor)	Universiteit Twente, TNW
Dr. L.W.M. van der Sluis (assistent promotor)	Université Paul Sabatier, Toulouse, France
Prof. A.D. Walmsley	University of Birmingham, UK
Prof. dr. P.R. Wesselink	Academisch Centrum voor Tandheelkunde, Amsterdam
Prof. dr. ir. G.J.M. Krijnen	Universiteit Twente, EWI
Prof. dr. ir. R.G.H. Lammertink	Universiteit Twente, TNW



PHYSICS OF FLUIDS

**MIRA**

INSTITUTE FOR BIOMEDICAL TECHNOLOGY AND TECHNICAL MEDICINE

**UNIVERSITY OF TWENTE.**



The work in this thesis was carried out at the Physics of Fluids group of the Faculty of Science and Technology, and the MIRA Institute for Biomedical Engineering and Technical Medicine, both at the University of Twente. This research was financially supported by the Dutch Technology Foundation STW (07498).

### *Nederlandse titel:*

Wortelkanaalreiniging met behulp van cavitatie en microstromingen

### *Publisher:*

Bram Verhaagen, Physics of Fluids group, University of Twente,  
P.O.Box 217, 7500AE Enschede, The Netherlands  
<http://pof.tnw.utwente.nl>  
[b.verhaagen@alumnus.utwente.nl](mailto:b.verhaagen@alumnus.utwente.nl)

*Cover design:* Bram Verhaagen

*Printed by:* Gildeprint Drukkerijen - Enschede

*Supplementary movie material can be found online at:*

[http://stilton.tnw.utwente.nl/rootcanalcleaning/Gallery\\_of\\_Irrigant\\_Motion](http://stilton.tnw.utwente.nl/rootcanalcleaning/Gallery_of_Irrigant_Motion)

© Bram Verhaagen, Enschede, The Netherlands, 2012.

No part of this work may be reproduced by print, photocopy or any other means without the permission in writing from the publisher.

ISBN: 978-90-365-3413-0

DOI: <http://dx.doi.org/10.3990/1.9789036534130>

# ROOT CANAL CLEANING THROUGH CAVITATION AND MICROSTREAMING

PROEFSCHRIFT

ter verkrijging van  
de graad van doctor aan de Universiteit Twente,  
op gezag van de rector magnificus,  
Prof. dr. H. Brinksma,  
volgens besluit van het College voor Promoties  
in het openbaar te verdedigen  
op vrijdag 28 september 2012 om 16.45 uur

door

Bram Verhaagen  
geboren op 6 augustus 1985  
te Hengelo (Ov)

Dit proefschrift is goedgekeurd door de promotor:

Prof. dr. rer. nat. Detlef Lohse

en de assistent-promotoren:

Dr. Michel Versluis en Dr. Luc van der Sluis

# Contents

<b>1</b>	<b>Introduction</b>	<b>1</b>
<b>I</b>	<b>Needle irrigation</b>	<b>21</b>
<hr/>		
<b>2</b>	<b>Role of the confinement of a root canal on jet impingement during endodontic irrigation</b>	<b>23</b>
<b>3</b>	<b>Irrigant flow in the root canal: experimental validation of an unsteady Computational Fluid Dynamics model using high-speed imaging</b>	<b>49</b>
<b>II</b>	<b>Passive Ultrasonic Irrigation</b>	<b>69</b>
<hr/>		
<b>4</b>	<b>Oscillation characteristics of endodontic files</b>	<b>71</b>
<b>5</b>	<b>Measurement and visualization of the occurrence of contact during Passive Ultrasonic Irrigation</b>	<b>99</b>
<b>6</b>	<b>Acoustic streaming induced by an ultrasonically oscillating endodontic file</b>	<b>121</b>
<b>7</b>	<b>Influence of the oscillation direction of an ultrasonic file on the cleaning efficacy of passive ultrasonic irrigation</b>	<b>161</b>
<b>8</b>	<b>The influence of the ultrasonic intensity on the cleaning efficacy of passive ultrasonic irrigation</b>	<b>171</b>
<b>9</b>	<b>Evaluation of a sonic device designed to activate irrigant in the root canal</b>	<b>181</b>

<b>10 An evaluation of the effect of pulsed ultrasound on the cleaning efficacy of passive ultrasonic irrigation</b>	<b>191</b>
<b>11 Irrigant flow beyond the insertion depth of an ultrasonically oscillating file in straight and curved root canals: visualization and cleaning efficacy</b>	<b>203</b>
<b>12 Sonochemical and high-speed optical characterization of cavitation generated by an ultrasonically oscillating file in root canal models</b>	<b>215</b>
<b>III Laser-Activated Irrigation</b>	<b>247</b>
<hr/>	
<b>13 Laser-activated irrigation within root canals: cleaning efficacy and flow visualization</b>	<b>249</b>
<b>IV Cleaning efficacy</b>	<b>261</b>
<hr/>	
<b>14 Irrigant transport into dental microchannels</b>	<b>263</b>
<b>15 Removal of a hydrogel with Passive Ultrasonic Irrigation</b>	<b>287</b>
<b>16 Localized removal of layers of metal, polymer or biomaterial by ultrasound cavitation microbubbles</b>	<b>303</b>
<b>V Backmatter</b>	<b>335</b>
<hr/>	
<b>17 General discussion and outlook</b>	<b>337</b>
<b>Summary</b>	<b>345</b>
<b>Samenvatting</b>	<b>349</b>
<b>List of publications and presentations</b>	<b>353</b>
<b>Dankwoord</b>	<b>357</b>
<b>About the author</b>	<b>359</b>

# 1

## Introduction \*

Whereas before the 17<sup>th</sup> century a tooth simply would be extracted in the case of pain, tremendous advantage has been made since then to preserve teeth rather than extracting them. A root canal treatment is a tool that has been proven to be successful in preserving a tooth, nowadays making use of advanced equipment and techniques that should make the trip to the dentist as pleasant and brief as possible. Nevertheless, to many, root canal treatments are synonymous with pain, even though the treatment relieves rather than causes pain. (The author has to note here an absence of experience as a patient.) In this thesis I will try to show that, at least from a fluid dynamics researcher's point-of-view, root canal treatments can actually be very interesting. The role of fluid dynamics in root canal treatments may not be apparent at first, but in this thesis it will be shown that it plays a crucial role for successful treatment of a tooth.

This introduction will cover the basics of root canal treatments, in order to familiarize the reader with the dental aspects of this thesis. The chapter will cover the root canal geometry and its treatment at the dentist, including common antimicrobial fluids, irrigation techniques and biofilms.

---

\*This chapter is partly based on the book chapter: "Root canal irrigation", L.W.M. van der Sluis, M. Versluis, C. Boutsoukis, B. Verhaagen, L.-M. Jiang and R. Macedo. In: *The root canal biofilm*, L. Chávez de Paz, A. Kishen and C. Sedgley, Springer Series on Biofilms, Springer, to be published



## 1.1 Endodontics

### 1.1.1 Tooth anatomy

A tooth can roughly be divided into crown and root(s); the latter can number from 1 (incisors) to 3 or more (molars). The roots contain a hollow space called the *root canal*, which is filled with pulp tissue (nerves, undifferentiated cells, connective tissue and blood vessels) that supply the tooth with nutrients [1]. The root canal system is geometrically very complex, as the root canal can be curved and have side canals, apical ramifications and isthmuses [2]. Figure 1.1a shows an example of a clinically encountered root canal geometry. The wall of the root canal is furthermore made of dentin and is a porous structure, as it contains microchannels (*tubules*) with a diameter of 0.5 to 3.2  $\mu\text{m}$  with a density of  $10^3 - 10^4$  tubules/ $\text{mm}^2$  [3]. More details on the complex geometry of root canals can be found in Chapter 14.

In this thesis, the root canal system has been simplified to a straight, unbranched frustum of a cone (Figure 1.1b), in order to have a standardized root canal model that allows for understanding the influence of the geometry on a flow inside the root canal.

### 1.1.2 Pulpitis and apical periodontitis

The pulp tissue inside the root canal can become infected (*pulpitis*) with bacteria or their products when the pulp is exposed, for example due to caries or dental trauma

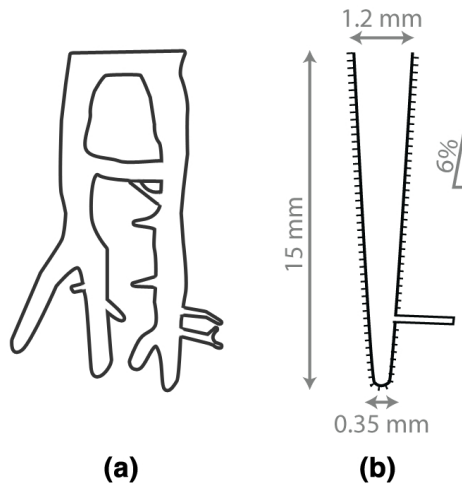


**Figure 1.1:** sketches of a root canal geometry as could be encountered clinically (a) and the simplified model as used in this thesis (b), with dimensions and optional side canal indicated.

or when the tubules are exposed to air. This infection inside the root canal can trigger an inflammatory reaction and can spread to the tip (*apex*) of the root canal, where it can cause an inflammation of the periapical tissue surrounding the apex (*apical periodontitis*) [1]. The body's immune system can attack this infection, but not its source inside the tooth because the blood circulation has been cut off. The inflammation is therefore sustained and causes major discomfort (pain) to the patient. Furthermore, over time it can cause major damage to the tissue and the bone (bone resorption) around the tooth. Beside the oral health, *apical periodontitis* is also suspected to affect the overall health of a patient [4].

### 1.1.3 Endodontic treatment

As the body's immune system is unable to attack the source of the inflammation inside the root canal, a root canal or *endodontic* treatment is necessary. The goal of a root canal treatment is to remove the source of the inflammation and to prevent a reinfection. Broadly speaking, the treatment consists of four steps, outlined below. [5]

#### Diagnosis

The presence of *apical periodontitis* can be diagnosed using clinical tests (e.g. sensitivity to heat/cold) and an X-ray photograph (Figure 1.2); the lesion will show up as a dark region surrounding the apex of the tooth.

#### Access cavity and canal instrumentation

A cavity needs to be created in the crown of the tooth, in order to gain access to the root canals. Pulp tissue remnants are then removed from the pulp chamber, before the entrance to the root canals can be found. The length and curvature of the root canal is probed with very thin hand files.

Using miniature files, the root canals are roughly cleaned and shaped. However, a *smear layer* is created on the root canal wall during this procedure, which is a mixture of microbes, dentin debris and organic material, and should be removed during the treatment.

#### Canal disinfection

Disinfection, the subject of this thesis, is arguably the most important step of a root canal treatment, as it has a major impact on the likeliness of a reinflammation. Disinfection is performed by *irrigation*, which can be defined as the procedure to introduce a liquid or *irrigant* in the root canal system before, during and after instrumentation of

the root canal. The aims of this procedure are the chemical dissolution and mechanical detachment of pulp tissue, dentin debris and smear layer and bacteria and their products (hereafter named *biomaterial*) from the root canal wall and their removal out of the root canal system.

The objectives of irrigation, with respect to the flow of irrigant, are:

- to create a flow of the irrigant in the entire root canal system and subsequently to the canal orifice, in order to bring the irrigant in close contact with the biomaterial, carry away the biomaterial and provide lubrication for the instruments,
- to ensure adequate (re)placement and mixing of the irrigant, in order to maintain a high concentration of irrigant and compensate for its rapid inactivation,
- to apply force on the root canal wall (wall shear stress), in order to detach/disrupt the biomaterial, and
- to restrict the flow within the constraints of the root canal and prevent irrigant extrusion towards the periapical tissues.

During the irrigation procedure (called *syringe* or *needle irrigation*), two phases can be distinguished: the flow phase, during which the irrigant is delivered and flows in and out of the root canal, and a rest phase, during which the irrigant is at rest in the root canal. Irrigant *activation* systems can introduce an additional activation phase,

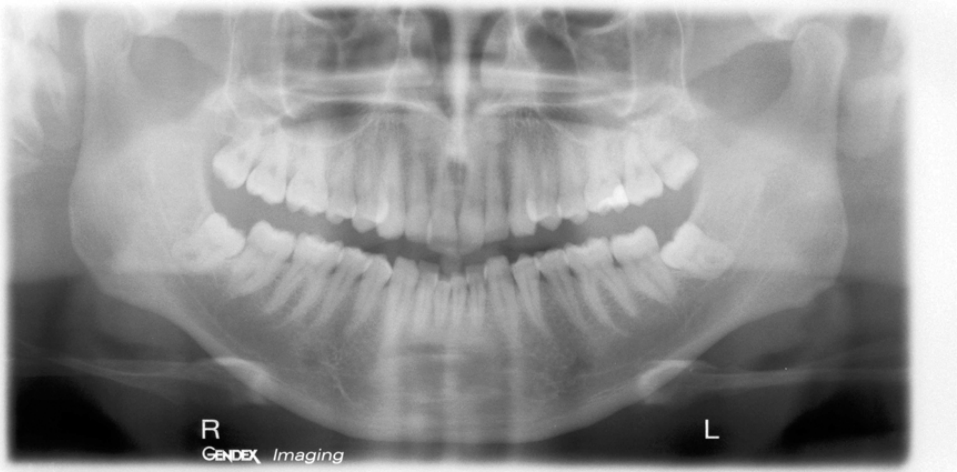


**Figure 1.2:** X-ray of the full mouth (orthopantomogram) of the author, fortunately showing no lesion at the tooth apices. Image courtesy of P. Verbeek.

during which the irrigant is agitated. The flow phase and the activation phase influence the chemical activity through convection and diffusion of the irrigant. During the rest phase, the chemical activity will probably mostly occur through diffusion, which is typically slow.

There are many techniques for irrigation on the market, including combinations of needle irrigation for delivery of the irrigant in the root canal and various ways to agitate the irrigant. Four of those systems are studied in this thesis and will be introduced below; explanatory sketches can be found in Figure 1.3.

**Needle Irrigation** Throughout a root canal treatment fresh irrigant is delivered frequently with a needle positioned in the apical third of the root canal, close to working length (Figure 1.3a). A dentist can exert a pressure of a few bar on the barrel of the syringe to which the needle is attached, resulting in flow rates of the order of 0.1 mL/s [6]. In combination with a 30G needle this results in a velocity of the order of 10 m/s and corresponding Reynolds number<sup>†</sup> of the order of  $10^3$ . The flow pattern depends primarily on the type of needle used, while flow rate, needle insertion depth, precise horizontal positioning (lateral displacements from the central axis of the root canal), root canal size and taper have a limited influence [7–10].

Conventional irrigation with a syringe and needle remains widely accepted [11]. However, motivation to improve irrigation efficacy and safety led to the development other systems [12–15], three of which are described below. A non-instrumentation technique would be the ideal irrigation technique, preventing the instrumentation of the root canal with its related disadvantages [14]. Unfortunately, such a system is not yet available.

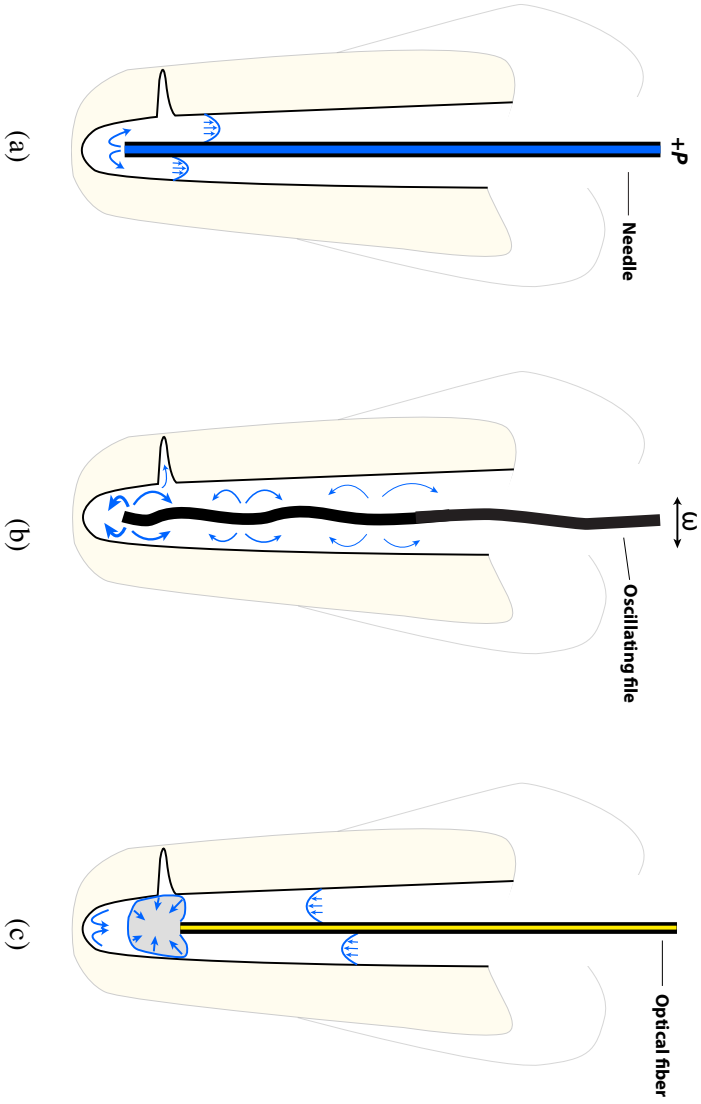
**Ultrasonic irrigation** Ultrasound has a wide-spread use in science and industry. A well-known application is fetal and cardiac imaging (‘echo’) [16], possibly enhanced by microbubbles [17, 18] delivering drugs [19], but ultrasound can also be used for modification of materials (e.g., cutting and welding of plastics, breaking of kidney stones) [20], chemical synthesis (sonochemistry) [20, 21] and bubble sorting [22], to name just a few. Ultrasound is also known to enhance healing of, among others, bone, dental pulp and dentin [23], and can penetrate the dental hard tissue [24], opening up possibilities for ultrasonic imaging of the root canal.

A large part of this thesis deals with the use of ultrasound for cleaning, or ultrasonic cleaning. A common application of ultrasonic cleaning is the ultrasound bath, in which lab equipment and jewelry can be cleaned [20]. In dentistry, ultrasound was introduced by Richman in 1957 [25] and is nowadays used frequently for clean-

---

<sup>†</sup>Reynolds number  $Re = \rho UD/\mu$  = ratio of inertial to viscous contributions, and is often used to characterize a flow.  $U$  is velocity,  $D$  a typical length and  $\rho$  and  $\mu$  the density and viscosity of the liquid.

**Figure 1.3:** Sketch of the use of needle irrigation (a), passive ultrasonic irrigation (b) and laser-activated irrigation (c) inside a root canal.



ing of the tooth' outer surface by scalers [26, 27]. For cleaning of the inside of the tooth during endodontic irrigation, ultrasound is applied through a miniature file that is driven at ultrasonic frequencies (see Part II of this thesis), similar to the work by Williams and Nyborg, who used a thin, oscillating capillary or tungsten wire [28, 29] to remove biomaterial from a surface. Initially, these files were used for instrumentation of the root canal and were supposed to make contact with the root canal walls. In 1980 Weller *et al.* [12] proposed to avoid contact with the wall and use the induced streaming to clean the root canal, thereby introducing the technique *Passive Ultrasonic Irrigation* (see Figure 1.3b; more details can be found in a recent review by Van der Sluis *et al.* [30]).

Nowadays there are several commercial ultrasonic irrigation devices on the market (a.o. by EMS, Nyon, Switzerland; and Satelec Acteon, Merignac, France), that allow for variation of the size and type of the files and the driving power. Irrigant is supplied intermittently before ultrasonic activation, or during activation through the hand piece to the corona of the tooth, or, in some of the latest systems, through the file (or needle) (VPro Streamclean, Vista Dental, Racine, WI, USA; Vibringe, Vibringe B.V., Amsterdam, The Netherlands [sonic frequencies]).

During the high-amplitude oscillation of the file during ultrasonic irrigation, *cavitation* may be induced. Cavitation is defined as the growth and collapse of bubbles within a liquid [31–33]. Cavitation on or very close to endodontic files has been observed in a number of studies [34–37], but its contribution to cleaning in endodontics is not yet clear [34]. Earlier studies have ruled out cavitation as a significant contribution to root canal cleaning [34, 35]. However, recent articles with newer ultrasound systems show otherwise [38].

In order to create a vapor bubble, the stress within the liquid has to be larger than the tensile strength of the liquid, which is of the order of  $10^7$  Pa for pure water [39]. However, in non-pure water (tap water, distilled water), there are often tiny pockets (*nuclei*) with entrapped gas on surfaces of walls or particles [40], from which it is much easier to grow bubbles (a process called *heterogeneous cavitation*), as only the vapor pressure of  $10^3$  Pa has to be overcome. The typical velocity  $u$  necessary to generate this pressure  $\Delta P$  in a liquid of density  $\rho$  can be estimated from the Bernoulli relation:

$$\Delta P = \frac{1}{2} \rho u^2. \quad (1.1)$$

In water, the velocity threshold is around 15 m/s.

Bubbles grow during the negative phase of a pressure wave, and collapse when the pressure becomes positive. Near a solid hard wall, bubbles tend to collapse in the direction of the wall. Alternatively, during bubble collapse next to a soft wall (like a biofilm covering a wall), the soft material might be pulled from the wall toward the bubble [41]. High-velocity jets (hundreds of meter per second) and shock waves are reported to accompany the bubble collapse [31, 42]. The bubble collapse can

also trigger a couple of consecutive bubble growths and collapses, until it is damped out. The violent bubble collapse is called *transient cavitation* and is associated with surface erosion [43, 44], surface cleaning [20, 45] and other mechanical effects of ultrasonic cleaning. Severe cavitation damage to ship propellers was in fact the phenomenon that led Lord Rayleigh to start investigating bubble dynamics [46].

Bubbles don't necessarily need to collapse. Gas-filled bubbles may be stable for a relatively long time and oscillate together with the oscillating pressure field induced by the oscillating file. This stable cavitation can enhance the streaming and consequently the cleaning locally, through unsteady oscillations of the bubble shape [31, 47]. Assistance in cleaning by a stable cavitation bubble was described already in 1958 by Jackson & Nyborg [48].

**Sonic irrigation** There are also commercial devices for sonic activation, which make use of lower driving frequencies (in the audible range, below 20 kHz). One such system, the EndoActivator (Advanced Endodontics, Santa Barbara, CA, USA), is discussed in Chapter 9.

**Laser-activated irrigation** Another technique, relying primarily on cavitation, is Laser-Activated Irrigation (LAI), which employs laser energy to agitate the irrigant. These lasers are typically of the type Er:YAG or Er,Cr:YSGG, with a wavelength in the infrared region (2796-2940 nm) which is absorbed well in water [49]. The dynamics of LAI have been studied using high-speed imaging ([50] and Chapter 13) showing the generation and implosion of a large vapor bubble at the tip of the file (Figure 1.3c), generated by the absorption of laser energy and fast heating of the irrigant. Laser-activated irrigation is a passive technique, not relying on direct ablation of the biomaterial.

## Obturation

The final step of a root canal treatment is filling or *obturation*. Typically, Gutta-Percha is used as filling material, which is melted and compacted into the root canal space (figure 1.4). In order to adhere well to the root canal wall, a sealer is applied beforehand.

Occasionally, in the case of a two-appointment visit, the root canal is first filled with an antimicrobial paster for the time between the two visits and which is removed at the second visit when the final filling takes place.

## Outcome of the treatment

Even though root canal treatments are a routine procedure for dentists, it has been proven difficult (if not impossible) to clean the root canal system completely with the



**Figure 1.4:** an X-ray image of a tooth with two canals that have been obturated (by the author)

conventional cleaning techniques. In The Netherlands, where each day ca. 2000 root canal treatments are performed, an estimated total of 40% of the treatments are unsuccessful [51] and a reinflammation can occur within a few weeks, months or years. This demonstrates the need for a better understanding of the cleaning mechanisms of the various irrigation systems and their chemical and mechanical interaction with the biomaterial that needs to be removed from the root canal system.

## 1.2 Irrigants

The ideal irrigant for root canal irrigation should [52]:

- have a broad antimicrobial spectrum and high efficacy against bacteria organized in biofilms,
- dissolve pulp tissue remnants,
- inactivate endotoxins,
- prevent the formation of a smear layer during instrumentation or dissolve it once it has formed, and
- be biocompatible (i.e., non-toxic, cause no allergy, etc.).

The most frequently used irrigants are NaOCl, EDTA and CHX [11]. *Sodium hypochlorite* (NaOCl, or simply bleach), used in concentrations of 0.5-10%, has the highest antimicrobial effectiveness and tissue dissolving capabilities [53]. However, NaOCl can also cause major tissue damage and severe pain when it is extruded to the periapical tissue surrounding the tooth [54]. *Ethylenediaminetetraacetic acid* (EDTA) is frequently used to remove the smear layer from the root canal wall, but its antimicrobial potential appears to be limited [55]. *Chlorhexidine* (CHX) does have antimicrobial potential, but has no tissue dissolving capacity.

The chemical effect of these irrigants will be significantly influenced by its concentration, the contact surface between the substrate and the irrigant, exposure time,



	Density [kg/m <sup>3</sup> ]	Surface tension [mN/m]	Viscosity [mPas]
Demi-water	1.010 ± 0.002	72.9 ± 0.0	1.14 ± 0.03
NaOCl 2.5%	1.065 ± 0.002	74.3 ± 0.1	1.37 ± 0.03
NaOCl 5%	1.105 ± 0.002	76.6 ± 0.0	1.65 ± 0.03
NaOCl 10%	1.229 ± 0.002	80.0 ± 0.0	2.58 ± 0.03
Carbonated water (Spa Barisart)	1.000 ± 0.002	73.5 ± 0.0	1.02 ± 0.03

**Table 1.1:** Fluidic properties of distilled water, carbonated water and various concentrations of NaOCl, all at 21°C

type of reactant, pH, temperature, interaction with other chemicals, and volume [52, 56]. The contact surface between the biomaterial and the irrigant is important in endodontics because the ratio volume of irrigant to contact surface is quite small for a human root canal (typical volume of 10  $\mu\text{L}$ , typical surface area of 50  $\text{mm}^2$ ). As described above, the typical anatomical structure of the root canal system contains many areas which are difficult to reach, limiting convection and diffusion of the irrigant.

The flow of irrigant is affected by its physical properties, mainly density, viscosity and surface tension. The fluidic properties of NaOCl have been measured and compared to those of water [57]. The results can be found in Table 1.1, showing that the properties of NaOCl are very similar to those of water; the influence on Passive Ultrasonic Irrigation has been reported in the article by Van der Sluis *et al.* [57].

### 1.2.1 Mixing

The irrigant is consumed during its reaction with biomaterial and therefore needs to be mixed with fresh irrigant [58]. During an endodontic treatment the root canal is flushed with fresh irrigant regularly. Mixing is further enhanced by the activation systems, which can be considered *active micromixers*, employing both convection and diffusion for mixing [59]. In microfluidics, mixing in the microchannels is typically slow because turbulence is very hard to achieve [60]. Mixing can take place nonetheless through ‘chaotic convection’, which folds and stretches the interface between fresh and consumed irrigant; the interfacial area increases then exponentially [61].

Flows with convection and diffusion are often characterized with the non-dimensional Péclet number  $Pe$ , which is the ratio of convection (local velocity  $U$ , typical length scale  $L$ ) over diffusion (diffusion coefficient  $D$ ):

$$Pe = \frac{UL}{D} \quad (1.2)$$

However, for reacting flows like the irrigant inside the root canal, the typical reaction time  $\tau$  should also be taken into account. Therefore we define a non-dimensional number, the Damköhler number  $Da$ , which is defined as the ratio of typical irrigant transport time to reaction time. The transport time can be determined from the local flow velocity  $U$  and vorticity  $\Omega$  scaled with a typical length  $L$ . For areas with low velocity, diffusion (with coefficient  $D$ ) may also play a role.

The Damköhler number is then given by

$$Da = \frac{L}{(U + \Omega L + \frac{D}{L})\tau} \quad (1.3)$$

At a Damköhler number  $Da \leq 1$ , the mixing is optimal, meaning that the consumed irrigant is replaced in time by fresh irrigant. At  $Da > 1$  however, the reaction is slowed down because of a lack of fresh irrigant. The velocity and vorticity of the irrigant can both be obtained from experiment; the diffusion coefficient depends on the irrigant used. The reaction time  $\tau$  depends on the irrigant and the biomaterial, but is generally not known. Studies on the half-time of the amount of active chlorine reacting with proteins or a dental biofilm report time scales of the order of one minute [53, 62, 63]; on a smaller scale of  $O(100 \mu\text{m})$  we estimate here a reaction time  $\tau = 10$  seconds.

## 1.3 Biofilms

### 1.3.1 Composition

The bacteria that cause apical periodontitis are typically not in planktonic state, but agglomerate in a structure called *biofilm*. The bacteria produce an extracellular polymeric matrix (EPS) to protect themselves against mechanical attacks. Only approx.

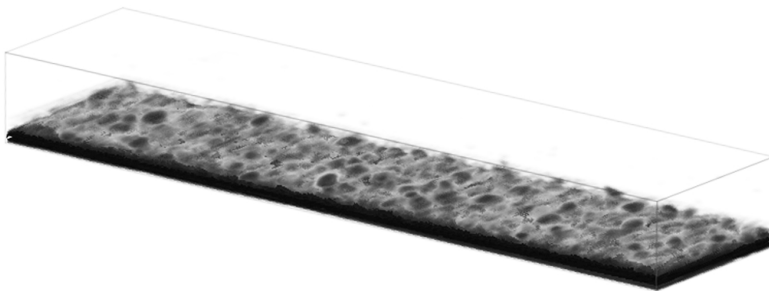


**Figure 1.5:** 3D ultrasound scan of an *S. mutans* biofilm. The width of the scanned section is 1 mm; the biofilm structures protrude up to 100  $\mu\text{m}$ . Image courtesy of dr. L-M Jiang (ACTA).

4% of the biofilm consists of the bacteria themselves. Small channels run throughout the biofilm in order to supply the bacteria with nutrients [64].

A number of articles have shown that biofilms are stratified, having typically two to three layers of different composition and mechanical properties [65]. The outermost layer is quite soft and easy to remove and consists of many different species, whereas the layer closest to the wall is hard and difficult to remove (the shear stress necessary for its removal can be two orders of magnitude higher than that of the outermost layer) and consists of a few dominant, aged bacterial species.

The composition of biofilms varies widely from patient to patient and even from tooth to tooth [66], with as many as 400 different species detected within one root canal, one specie being more abundant than others [67]. There are only a few bacterial types that have been observed frequently, being *Streptococcus mutans* and *Enterococcus faecalis*. However, those types cannot be directly related to the occurrence of apical periodontitis, and other bacterial types may be present equally frequent but may be more difficult to culture. Because of the varying compositions between biofilms, it is also very difficult to define a ‘standard biofilm’, to be cultured in the lab, and consequently not much is known about their mechanical properties and attachment strength to the dentinal wall. A dual-species biofilm of *S. mutans* and *E. faecalis* has been cultured at the Academic Center for Dentistry in Amsterdam to study biofilm removal by irrigation techniques, because they have shown to be relatively easy to culture and attach well to substrates.

### 1.3.2 Viscoelastic properties

The biofilm is a viscoelastic material, showing both elastic and viscous behavior when a stress is applied. Its viscoelastic properties are determined by the composition of the EPS-matrix. The specific constitution of EPS strongly depends on the type of microbial species and, moreover, on environmental conditions during growth such as nutrition [64]. For example, metal ions like  $\text{Ca}^{2+}$  can be incorporated in the EPS, causing cross-links of the negative binding sides of polysaccharides and reinforcing the matrix [68].

Compression experiments [69] revealed that a biofilm in response to pressure can go through a phase of elastic behavior until a breakpoint (yield strength) is reached, after which the biofilm behaves as a viscous fluid [70]. In the elastic regime of viscoelastic materials, they absorb stress energy through deformation, and transient stress events might be resisted by reversible transformation. During higher stress (induced, for example, by steady flow from a needle) viscoelastic materials will flow, which is just one of the survival strategies of biofilms under mechanical attack.

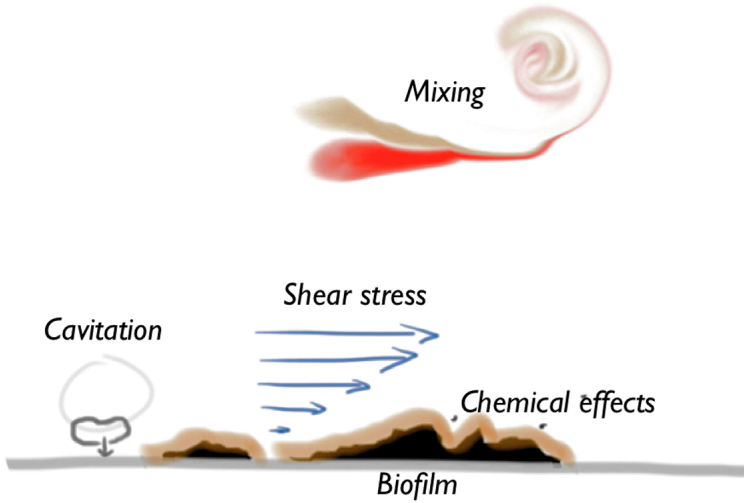


**Figure 1.6:** Mechanisms for removal of a biofilm from a substrate, encompassing chemical (dissolution and mixing) and mechanical (shear stress and cavitation) effects.

### 1.3.3 Removal mechanisms

At even higher stresses, the response of the biofilm can be non-linear, leading to plastic deformation (cohesive failure) at very high stresses, when the stress exerted onto the biofilm is larger than the local tensile strength [64]. From a 3D numerical study on the effect of fluid flow on a biofilm, it was concluded that for high matrix stability, only exposed structures at the surface of the biofilm are detached. Low matrix stabilities might lead to the detachment of large portions from the top of the biofilm. This detachment of portions of a biofilm is a process called *sloughing* [71]. A smooth basal biofilm surface structure has been observed to remain after detachment [72], demonstrating the stratification of the biofilm. This basal layer can detach when the exerted stress exceeds the attachment strength of the biofilm to the substrate [64].

Chemically, the irrigant has to penetrate the EPS matrix before it can affect the bacteria inside. Disruption or poration of this matrix is imperative to induce an antimicrobial effect. Irrigants like NaOCl or chelators have the possibility to affect, disrupt or penetrate the EPS [73]. Mass transfer into a biofilm occurs through both convection and diffusion processes [74] and can be characterized with the surface-averaged relative effective diffusion coefficient ( $D_{rs}$ ). The  $D_{rs}$  profiles decrease from the top of the biofilm toward the bottom, and differ for biofilms of different ages. Different biofilms show similar  $D_{rs}$  profiles near the top of the biofilm, but different profiles near the bottom of the various biofilms [75], demonstrating the stratification of the biofilm.

Biofilms can also decide on their own to detach, in order to reattach and grow at another location. The biofilm is induced to do so when the local conditions are unfavorable, for example due to overcrowding in the center of the biofilm or changing environmental conditions. A disturbance of the biofilm or its environment might therefore be enough already to have the biofilm detach by itself. [64]

It has been pointed out that the fight against bacteria is a fight which can only be won for a short period of time [64]. Biofilms have been around for around 3.5 billion years and have invented many strategies to overcome chemical and mechanical attacks. A biofilm may be removed locally, but planktonic bacteria and parts of biofilm detached elsewhere will cause a regrowth. Any system, especially one geometrically as complex as a root canal system, will never be completely sterile. Root canal cleaning strategies should therefore be based on reducing the number of bacteria as much as possible and sealing off the remaining bacteria, to shield them from nutrients and prevent them from regrowing.

## 1.4 Aim of this thesis

Summarizing this introduction, a biofilm inside the root canal causes major dental problems, but its removal is challenging, due to the complexity of the root canal system and the defense strategies of biofilms. Root canal disinfection strategies are typically a combination of chemical and (fluid) mechanical effects, however the exact cleaning mechanisms are not yet fully known. This thesis therefore addresses the dynamics of irrigant flow inside the confinement of the root canal and the interaction of the flow with biomaterial, giving insight into the working mechanisms of various activation systems and the mixing of irrigant and shear stresses induced. This project is a collaboration between the Physics of Fluids group at the University of Twente and the Academic Center for Dentistry in Amsterdam, combining knowledge and expertise from both fluid physics and dentistry.

## 1.5 Guide through the chapters

This thesis is divided into four parts, each covering a different aspect of root canal irrigation.

**Part I** describes the flow from a needle during needle irrigation inside a root canal. High-speed experimental investigations (**chapter 2**) have given some insight into the role of the confinement on the flow inside a root canal. The experimentally obtained results have also been used to validate a numerical model of needle irrigation (**chapter 3**), which has been used subsequently to study the influence of clinically important parameters like needle type [7], needle insertion depth [10] and root canal size [9] and taper [8], as published elsewhere.

**Part II** focuses on Passive Ultrasonic Irrigation, starting with the oscillation characteristics of endodontic files (**chapter 4**) and an evaluation in a clinical setting of the likeliness and implications of touching the root canal wall (**chapter 5**). The oscillation characteristics are then coupled to a two-dimensional theoretical description of the induced acoustic streaming, validated with experiments and numerical simulations (**chapter 6**). The cleaning efficacy of the induced flow is evaluated in an extracted tooth model, focusing on the direction of oscillation of the file (**chapter 7**), the oscillation intensity (**chapter 8**), sonic frequencies (**chapter 9**), pulsed activation (**chapter 10**) and the area beyond the tip of the file (**chapter 11**), all supported by high-speed visualizations. Finally, sonochemical measurements and visualizations of cavitation occurring during Passive Ultrasonic Irrigation are reported (**chapter 12**).

In **Part III** cavitation is generated by a laser in Laser Activated Irrigation, of which the cleaning efficacy is evaluated and visualized with high-speed imaging (**chapter 12**).

Finally, in **Part IV**, the cleaning *mechanisms* of needle irrigation and Passive Ultrasonic Irrigation are investigated. The penetration of irrigant into side canals, and specifically tubules, through diffusion and convection is evaluated using a combined theoretical, numerical and experimental approach (**chapter 14**). The removal of a biofilm from a substrate is evaluated by mimicking the viscoelastic behavior of a biofilm with a hydrogel, whose behavior under an external flow is evaluated visually (**chapter 15**). Finally, with a novel system employing cavitation from micromachined pits, the removal of biofilm, hydrogel, cells and even deposited metals like gold and platinum due to cavitation is demonstrated (**chapter 16**).

This thesis will end in **Part V** with a discussion of the obtained results and insights of the various irrigation techniques and their cleaning mechanisms and efficacy, followed by an outlook for future work (**chapter 17**).

## References

- [1] S. Cohen and K. M. Hargreaves, *Pathways of the pulp*, 9th edition (Mosby Elsevier) (2006).
- [2] Q. D. De Deus and B. Horizonte, “Frequency, location, and direction of the lateral, secondary, and accessory canals”, *Journal of Endodontics* **1**, 361–366 (1975).
- [3] D. H. Pashley, S. M. Thompson, and F. P. Stewart, “Dentin permeability: Effects of temperature on hydraulic conductance”, *Journal of Dental Research* **62**, 956–959 (1983).
- [4] M. K. Wu and P. R. Wesselink, “Lokale en eventuele systemische gevolgen van endodontische infecties”, *Nederlands Tijdschrift voor Tandheelkunde* **112**, 416–419 (2005).
- [5] M. Torabinejad and R. E. Walton, *Endodontics - principles and practice*, 4th edition (Saunders Elsevier) (2009).

- [6] C. Boutsoukakis, T. Lambrianidis, E. Kastrinakis, and P. Bekiaroglou, "Measurement of pressure and flow rates during irrigation of a root canal ex vivo with three endodontic needles", *International Endodontic Journal* **40**, 504–13 (2007).
- [7] C. Boutsoukakis, B. Verhaagen, M. Versluis, E. Kastrinakis, P. R. Wesselink, and L. W. M. van der Sluis, "Evaluation of irrigant flow in the root canal using different needle types by an unsteady computational fluid dynamics model", *Journal of Endodontics* **36**, 875–879 (2010).
- [8] C. Boutsoukakis, C. Gogos, B. Verhaagen, M. Versluis, E. Kastrinakis, and L. W. M. van der Sluis, "The effect of root canal taper on the irrigant flow: evaluation using an unsteady computational fluid dynamics model", *International Endodontic Journal* **43**, 909–916 (2010).
- [9] C. Boutsoukakis, C. Gogos, B. Verhaagen, M. Versluis, E. Kastrinakis, and L. W. M. van der Sluis, "The effect of apical preparation size on irrigant flow in root canals evaluated using an unsteady computational fluid dynamics model", *International Endodontic Journal* **43**, 874–881 (2010).
- [10] C. Boutsoukakis, T. Lambrianidis, B. Verhaagen, M. Versluis, E. Kastrinakis, P. R. Wesselink, and L. W. M. van der Sluis, "The effect of needle-insertion depth on the irrigant flow in the root canal: evaluation by an unsteady computational fluid dynamics model", *Journal of Endodontics* **36**, 1664–1668 (2010).
- [11] J. Dutner, P. Mines, and A. Anderson, "Irrigation trends among american association of endodontists members: A web-based survey", *Journal of Endodontics* **38**, 37–40 (2012).
- [12] R. N. Weller, J. M. Brady, and W. E. Bernier, "Efficacy of ultrasonic cleaning", *Journal of Endodontics* **6**, 740–743 (1980).
- [13] P. J. Lumley, A. D. Walmsley, and W. R. E. Laird, "Streaming patterns produced around endosonic files", *International Endodontic Journal* **24**, 290–297 (1991).
- [14] A. Lussi, U. Nussbächer, and J. Grosrey, "A novel noninstrumented technique for cleansing the root canal system", *Journal of Endodontics* **19**, 549–553 (1993).
- [15] L.-M. Jiang, B. Lak, L. M. Eijssvogels, P. R. Wesselink, and L. W. M. Van der sluis, "Comparison of the cleaning efficacy of different final irrigation techniques", *Journal of Endodontics* **38**, 838–841 (2012).
- [16] T. L. Szabo, *Diagnostic ultrasound imaging: inside out*, 1st edition (Elsevier Academic Press, Oxford, UK) (2004).
- [17] N. De Jong, M. Emmer, A. Van Wamel, and M. Versluis, "Ultrasonic characterization of ultrasound contrast agents", *Medical and Biological Engineering and Computing* **47**, 861–873 (2009).
- [18] C. Chlon, C. Guédon, B. Verhaagen, W. T. Shi, C. S. Hall, J. Lub, and M. R. Böhmer, "Effect of molecular weight, crystallinity, and hydrophobicity on the acoustic activation of polymer-shelled ultrasound contrast agents", *Biomacromolecules* **10**, 1025–1031 (2009).
- [19] D. Lensen, E. C. Gelderblom, D. M. Vriezema, P. Marmottant, N. Verdonschot, M. Versluis, N. De Jong, and J. C. M. van Hest, "Biodegradable polymeric microcapsules for sequential ultrasound-triggered drug release", *Soft Matter* **7**, 5417–5422 (2011).
- [20] T. J. Mason and D. Peters, *Practical sonochemistry: power ultrasound uses and applications*, Chemical Science series (Horwood) (2002).

- [21] D. Fernandez Rivas, A. Prosperetti, A. G. Zijlstra, D. Lohse, and H. J. G. E. Gardeniers, “Efficient sonochemistry through microbubbles generated with micromachined surfaces”, *Angewandte Chemie International Edition* **49**, 9699–9701 (2010).
- [22] T. J. Segers, M. Versluis, and *et al.*, “Acoustic bubble sorting: contrast enrichment by primary radiation forces”, *Lab on a Chip to be submitted* (2012).
- [23] J. Man, R. M. Shelton, P. R. Cooper, and B. A. Scheven, “Low-intensity low-frequency ultrasound promotes proliferation and differentiation of odontoblast-like cells”, *Journal of Endodontics* **38**, 608–613 (2012).
- [24] S. Ghorayeb, C. A. Bertoncini, and M. K. Hinders, “Ultrasonography in dentistry”, *IEEE Transactions on Ultrasonics, Ferroelectrics and Frequency Control* **55**, 1256–1266 (2008).
- [25] M. Richman, “The use of ultrasonics in root canal therapy and root resection”, *Journal of Dental Medicine* **12**, 12–18 (1957).
- [26] A. D. Walmsley, “Ultrasound and root canal treatment: the need for scientific evaluation”, *International Endodontic Journal* **20**, 105–111 (1987).
- [27] W. R. E. Laird and A. D. Walmsley, “Ultrasound in dentistry. part 1 - biophysical interactions”, *Journal of Dentistry* **19**, 14–17 (1991).
- [28] A. R. Williams and W. L. Nyborg, “Microsonation using a transversely oscillating capillary”, *Ultrasonics* **8**, 36–38 (1970).
- [29] A. R. Williams and J. S. Slade, “Ultrasonic dispersal of aggregates of *sarcina lutea*”, *Ultrasonics* **8**, 85–87 (1971).
- [30] L. W. M. Van der Sluis, M. Versluis, M. K. Wu, and P. R. Wesselink, “Passive ultrasonic irrigation of the root canal: a review of the literature”, *International Endodontic Journal* **40**, 415–426 (2007).
- [31] C. E. Brennen, *Cavitation and bubble dynamics* (Oxford University Press) (1995).
- [32] M. Brenner, S. Hilgenfeldt, and D. Lohse, “Single-bubble sonoluminescence”, *Reviews of Modern Physics* **74**, 425–484 (2002).
- [33] A. Prosperetti, “Bubbles”, *Physics of Fluids* **16**, 1852–1865 (2004).
- [34] M. Ahmad, T. R. Pitt Ford, L. A. Crum, and A. J. Walton, “Ultrasonic debridement of root canals: Acoustic cavitation and its relevance”, *Journal of Endodontics* **14**, 486–493 (1988).
- [35] P. J. Lumley, A. D. Walmsley, and W. R. E. Laird, “An investigation into cavitation activity occurring in endosonic instrumentation”, *Journal of Dentistry* **16**, 120–122 (1988).
- [36] B. Felver, D. V. King, S. C. Lea, G. J. Price, and A. D. Walmsley, “Cavitation occurrence around ultrasonic dental scalers”, *Ultrasonic Sonochemistry* **16**, 692–697 (2009).
- [37] L.-M. Jiang, B. Verhaagen, M. Versluis, C. Zangrillo, D. Cuckovic, and L. W. M. Van der Sluis, “An evaluation of the effect of pulsed ultrasound on the cleaning efficacy of passive ultrasonic irrigation”, *Journal of Endodontics* **36**, 1887–1891 (2010), *see also Chapter 10 of this thesis*.



- [38] T. Joyce Tiong and G. J. Price, "Ultrasound promoted reaction of rhodamine b with sodium hypochlorite using sonochemical and dental ultrasonic instruments", *Ultrasonic Sonochemistry* **19**, 358–364 (2012).
- [39] S. A. Sedgewick and D. H. Trevena, "An estimate of the ultimate tensile strength of water", *Journal of Physics D: Applied Physics* **9**, L203–205 (1976).
- [40] A. Zijlstra, "Acoustic surface cavitation", Ph.D. thesis, University of Twente (2011).
- [41] E.-A. Brujan, K. Nahen, P. Schmidt, and A. Vogel, "Dynamics of laser-induced cavitation bubbles near an elastic boundary", *Journal of Fluid Mechanics* **433**, 251–281 (2001).
- [42] M. Versluis, B. Schmitz, A. Von der Heydt, and D. Lohse, "How snapping shrimp snap: through cavitating bubbles", *Science* **289**, 2114–2117 (2000).
- [43] D. Krefting, R. Mettin, and W. Lauterborn, "High-speed observation of acoustic cavitation erosion in multibubble systems", *Ultrasonics sonochemistry* **11**, 119–123 (2004).
- [44] W. J. C. Terwisga, P. A. Fitzsimmons, L. Zirru, and E. J. Foeth, "Cavitation erosion – a review of physical mechanisms and erosion risk models", in *Proceedings of the 7th International Symposium on Cavitation CAV2009* (2009).
- [45] L. Junge, C.-D. Ohl, B. Wolfrum, M. Arora, and R. Iking, "Cell detachment method using shock-wave-induced cavitation", *Ultrasound in Medicine and Biology* **29**, 1769–1776 (2003).
- [46] D. Lohse, "Bubble puzzles", *Physics Today* **56**, 36–41 (2003).
- [47] P. Marmottant, M. Versluis, N. De Jong, S. Hilgenfeldt, and D. Lohse, "High-speed imaging of an ultrasound-driven bubble in contact with a wall: "narcissus" effect and resolved acoustic streaming.", *Experiments in FLuids* **41**, 147–153 (2006).
- [48] F. J. Jackson and W. L. Nyborg, "Small scale acoustic streaming near a locally excited membrane", *Journal of the Acoustical Society of America* **30**, 614–619 (1958).
- [49] C. W. Robertson and D. Williams, "Lambert absorption coefficients of water in the infrared", *Journal of the Optical Society of America* **61**, 1316–1320 (1971).
- [50] S. D. de Groot, B. Verhaagen, M. Versluis, M. K. Wu, P. R. Wesselink, and L. W. M. van der Sluis, "Laser activated irrigation within root canals: cleaning efficacy and flow visualization", *International Endodontic Journal* **42**, 1077–1083 (2009), *see also Chapter 13 of this thesis*.
- [51] M. J. De Cleen, A. H. Schuurs, P. R. Wesselink, and M. K. Wu, "Periapical status and prevalence of endodontic treatment in an adult dutch population", *International Endodontic Journal* **26**, 112–119 (1993).
- [52] M. Zehnder, "Root canal irrigants", *Journal of Endodontics* **32**, 389–398 (2006).
- [53] W. R. Moorer and P. R. Wesselink, "Factors promoting the tissue dissolving capability of sodium hypochlorite", *International Endodontic Journal* **15**, 187–196 (1982).
- [54] M. Hülsmann, T. Rödiger, and S. Nordmeyer, "Complications during root canal irrigation", *Endodontic Topics* **16**, 27–63 (2009).

- [55] L. E. Chavez de Paz, G. Bergenholtz, and Svensäter, “The effects of antimicrobials on endodontic biofilm bacteria”, *Journal of Endodontics* **36**, 70–77 (2010).
- [56] R. G. Macedo, P. R. Wesselink, F. Zaccaro, D. Fanali, and L. W. M. Van der Sluis, “Reaction rate of naocl in contact with bovine dentine: effect of activation, exposure time, concentration and ph”, *International Endodontic Journal* **43**, 1108–1115 (2010).
- [57] L. W. M. van der Sluis, M. P. J. M. Vogels, B. Verhaagen, R. Macedo, and P. R. Wesselink, “Study on the influence of refreshment/activation cycles and irrigants on mechanical cleaning efficiency during ultrasonic activation of the irrigant”, *Journal of Endodontics* **36**, 737–740 (2010).
- [58] P. V. Danckwerts, “The effect of incomplete mixing on homogeneous reactions”, *Chemical Engineering Science* **8**, 93–102 (1958).
- [59] E. G. Kastrinakis and S. G. Nychas, “Mixing at high schmidt numbers in the near wake of a circular cylinder”, *Chemical Engineering Science* **53**, 3977–3989 (1998).
- [60] T. M. Squires and S. R. Quake, “Microfluidics: Fluid physics at the nanoliter scale”, *Reviews of Modern Physics* **77**, 977–1026 (2005).
- [61] A. Sarkar, A. Narváez, and J. Harting, “Quantification of the performance of chaotic micromixers on the basis of finite time lyapunov exponent”, *Microfluidics and Nanofluidics* (2012).
- [62] R. W. R. Baker, “Studies on the reaction between sodium hypochlorite and proteins”, *Biochemical Journal* **41**, 337–342 (1947).
- [63] N. T. Sena, B. P. F. A. Gomes, M. E. Vianna, V. B. Berber, A. A. Zaia, C. C. R. Ferraz, and F. J. Souza-Filho, “In vitro antimicrobial activity of sodium hypochlorite and chlorhexidine against selected single-species biofilms”, *International Endodontic Journal* **39**, 878–885 (2006).
- [64] H.-C. Flemming, J. Wingender, and U. Szewzyk, *Biofilm highlights*, Springer Series on Biofilms, 1st edition (Springer) (2011).
- [65] A. Rochex, A. Massé, R. Escudie, J. J. Godon, and N. Bernet, “Influence of abrasion on biofilm detachment: evidence for stratification of the biofilm”, *Journal of Industrial Microbiology and Biotechnology* **36**, 467–470 (2009).
- [66] L. E. Chavez de Paz, “Redefining the persistent infection in root canals: possible role of biofilm communities”, *Journal of Endodontics* **33**, 652–62 (2007).
- [67] A. R. Özok, I. F. Persoon, S. M. Huse, B. J. F. Keijser, P. R. Wesselink, W. Crielaard, and E. Zaura, “Ecology of the microbiome of the infected root canal system: a comparison between apical and coronal root segments”, *International Endodontic Journal* **45**, 530–541 (2012).
- [68] S. V. Van der Waal and L. W. M. Van der sluis, “Potential of calcium to scaffold an endodontic biofilm, thus protecting the micro-organisms from disinfection”, *Medical Hypotheses* **in press** (2012).
- [69] V. Körstgens, H.-C. Flemming, J. Wingender, and W. Borchard, “Uniaxial compression measurement device for investigation of the mechanical stability of biofilms”, *Journal of Microbiological Methods* **46**, 9–17 (2001).
- [70] A. W. Cense, “A spray based method for biofilm removal”, Ph.D. thesis, Technical University of Eindhoven (2005).

- [71] C. Picioreanu, M. C. M. van Loosdrecht, and J. J. Heijnen, “Two-dimensional model of biofilm detachment caused by internal stress from liquid flow”, *Biotechnology and Bioengineering* **72**, 205–218 (2001).
- [72] M. Böl, R. B. Möhle, M. Haesner, T. R. Neu, H. Horn, and R. Krull, “3d finite element model of biofilm detachment using real biofilm structures from clsm data”, *Biotechnology and Bioengineering* **103**, 177–186 (2009).
- [73] E. R. Brindle, D. A. Miller, and P. S. Stewart, “Hydrodynamic deformation and removal of staphylococcus epidermidis biofilms treated with urea, chlorhexidine, iron chloride, or dispersinb”, *Biotechnology and Bioengineering* **108**, 1–10 (2011).
- [74] D. De Beer, P. Stoodley, and Z. Lewandowski, “Liquid flow in heterogeneous biofilms”, *Biotechnology and Bioengineering* **44**, 636–641 (1994).
- [75] R. S. Renslow, P. D. Majors, J. S. McLean, J. K. Fredrickson, B. Ahmed, and H. Beyenal, “In situ effective diffusion coefficient profiles in live biofilms using pulsed-field gradient nuclear magnetic resonance”, *Biotechnology and Bioengineering* **106**, 928–937 (2010).

**Part I**

**Needle irrigation**



# 2

## Role of the confinement of a root canal on jet impingement during endodontic irrigation \*

**Abstract:** Irrigation of a root canal with two different types of needles can be modeled as an impinging axisymmetric or non-axisymmetric jet. These jets are investigated experimentally with high-speed Particle Imaging Velocimetry, inside and outside the confinement (concave surface) of a root canal, and compared to theoretical predictions for these jets. The efficacy of irrigation fluid refreshment with respect to the typical reaction time of the antimicrobial fluid with a biofilm is characterized with a non-dimensional Damköhler number. The pressure that these jets induce on a wall or at the apex of the root canal is also measured. The axisymmetric jet is found to be stable and its velocity agrees with the theoretical prediction for this type of jet, however, a confinement causes instabilities to the jet. The confinement of the root canal has a pronounced influence on the flow, for both the axisymmetric and non-axisymmetric jet, by reducing the velocities by one order of magnitude and increasing the pressure at the apex. The non-axisymmetric jet inside the confinement shows a cascade of eddies with decreasing velocities, which at the apex does not provide adequate irrigation fluid refreshment.

---

\*Published as: B. Verhaagen, C. Boutsoukis, G.L. Heijnen, L.W.M. van der Sluis and M. Versluis, "Role of the confinement of a root canal on jet impingement during endodontic irrigation", *Experiments in Fluids*, accepted

## 2.1 Introduction

A root canal treatment is a dental therapeutic procedure, which is necessary when bacteria cause an inflammation of the bone around the tip of the tooth. During a treatment, the root canal is irrigated and disinfected with an antibacterial solution (the ‘irrigant’) using a syringe and a needle [1]. This irrigant needs to be refreshed frequently for optimal reaction with the bacteria. However, the flow created by a syringe and needle has been shown to be marginally effective in entirely cleaning the root canal system [2], due to the flow of irrigant not being able to penetrate deeply into the remote areas (side canals, isthmuses, apical delta) of the geometrically complex root canal system [3, 4]. It is therefore of interest to study the fluid flow and resulting dynamics of the irrigation technique, to understand irrigant refreshment mechanisms and to improve the success rate of a root canal treatment.

Previous studies on the flow behavior of root canal irrigation typically evaluated the effect post-treatment, because the root canal wall is opaque and the root has to be disassembled for evaluation [4–6]. Other studies have used transparent, artificial roots, but those have their limitations, mainly in mimicking the root canal geometry accurately [5, 7]. Furthermore, the sub-millimeter dimensions of the root canal in combination with velocities of the order of 1 m/s require high-speed equipment to capture the full details of the flow at the microsecond time scale.

Recently, Computational Fluid Dynamics (CFD) was introduced [8–10] to simulate the real-time flow of irrigant from different types of needles inside a root canal. The simulations showed that the needle types that are typically used in endodontics can be divided into two categories, based on the flow pattern that they create [11]. On the one hand, there is the beveled, notched and flat-ended needle, which have an open end and create an axisymmetric jet aimed at the apex, at which point the flow has to return coronally between the needle and the root canal wall. The side-vented and double-side-vented needles, on the other hand, have a closed end and an opening on one or two sides, and create a non-axisymmetric jet that flows around the tip of the needle, driving a cascade of eddies towards the apex. Which one is more suitable for irrigation is not known at present.

A high pressure can cause extrusion of the irrigant into the periapical tissue [12]. Therefore it is important to know the pressure that develops at the apex. The influence of the confinement on the pressure developed for a confined jet appears to be unexplored yet in literature; also, the pressure at the apex of a root canal has never been measured or calculated before, except in the above mentioned CFD studies. However, it is also not known what the maximum allowed pressure is before extrusion of the irrigant to the surrounding tissue occurs.

Here we model irrigation with a needle in a root canal as an axisymmetric or non-axisymmetric microjet into a concave surface. It is a simplification of the complex geometry of real root canals [13] but should give us more insight into the effect of a

concave surface or confinement on the flow. Cornaro *et al.* [14] have done experiments of a jet of air in air onto concave and convex surfaces, for various jet-to-surface spacings and surface curvatures. Their results show that the flow that returns from the concave surface can influence the incoming jet, causing instabilities of the jet beyond a distance of one jet diameter from the surface. In the present case of a jet in a root canal, the surface curvature is high (needle diameter / concave surface diameter ratio of 1 typically), therefore strong instabilities of the jet are expected. On the other hand, Gau *et al.* [15] have shown recently that free microjets are typically more stable than their large-scale counterparts, because the frequency of the instabilities that lead to jet breakdown is too high for the flow to sustain. In the present study we have a combination of both, the irrigation with a needle being modeled as a microjet inside a concave surface.

The aims of this study are to investigate experimentally both mixing and apical pressure inside a simple root canal geometry, based on the CFD model by Boutsioukis *et al.* [8]. The mixing is determined by measuring the velocities in axisymmetric and non-axisymmetric jets, at different jet Reynolds numbers and distances between the needle tip and the root canal apex, using high-speed Particle Imaging Velocimetry. Using these velocities, the mixing rate is evaluated by comparing them to reaction times between irrigant and bacteria or biofilm, as obtained from literature. The pressure induced at the apex of the root canal is measured with a miniature pressure sensor; both the velocities and the pressures will then be validated with theoretical and numerical predictions. The influence of the confinement on the flow and the pressure is investigated by comparing the velocities and pressures developed by these jets in impingement on a plate and inside the confinement of a simple root canal model.

### 2.1.1 Theoretical description of the flow

Liquid jets have been studied in literature in great detail [16–19]; we will repeat the main results here for validation of our experimental results.

#### Impinging axisymmetric jet

The flow from an open-ended needle towards a wall can be described by an impinging axisymmetric jet, which is a combination of a free jet and a stagnation flow (figure 2.1) [19]; the radial outflow along the wall is described by the wall jet [17]. Gravity is neglected. The analytical solution for a three-dimensional, axisymmetric laminar free jet is given by Schlichting & Gersten [16] using a boundary layer approach. Here we repeat the final results for the velocity field  $v(y, r = 0)$  along the center axis and the width  $b(y)$  (full width at half maximum) of the jet [20]:

$$\frac{v(y)}{v_0} = 0.0938Re \frac{2R}{y} \quad (2.1)$$



$$b(y) = \frac{4.67}{Re}y \quad (2.2)$$

where  $v_0 = Q/(\pi R^2)$  is the average velocity of the flow (with flow rate  $Q$ ) at the needle orifice of diameter  $R$ . The typical jet Reynolds number  $Re = (v_0 2R)/\nu$  (with  $\nu$  the dynamic viscosity of the fluid) for endodontic needles and flow rates [21] is of order  $10^3$ .

Equation 2.1 suggests that the axial velocity in the center of the jet decreases with increasing distance from the jet, due to the divergence of the axisymmetric jet.

The presence of a wall changes the flow significantly within a distance of typically  $d_{stag} = 0.2R$  from the wall, although the presence of a wall is also known to affect the free jet velocities [19] at distances larger than  $d_{stag}$ . The impingement area bounded by  $d_{stag}$  can be described with stagnation flow, of which the velocity potential  $\phi$  is directly related to the inflow velocity from the free jet. The stagnation pressure can be obtained from the Bernoulli pressure relation [22]

$$p + u^2 + v^2 = f(\phi) \quad (2.3)$$

which implies that the total pressure is conserved on stream surfaces. The stagnation pressure should therefore scale as  $P \sim v^2$ .

### Impinging non-axisymmetric jet

In the case of a side-vented needle, the flow leaves the needle obliquely at an angle  $\theta$ . Due to symmetry-breaking, the flow can be characterized as a non-axisymmetric jet (figure 2.1). Taylor [23] discussed the case of an oblique impact of a jet onto a surface and suggested that, for a two-dimensional jet with oblique angle  $\theta$  with respect to the surface, the flow would split in a backward and forward component upon impact, with fractions of  $\cos^2 \frac{1}{2}\theta$  and  $\sin^2 \frac{1}{2}\theta$ , respectively.

### Non-dimensional mixing-reaction parameter

The induced flow causes mixing of fresh irrigant with irrigant that has been consumed during its reaction with bacteria. The efficacy of this mixing of irrigant with respect to the reaction rate of the irrigant with bacteria (agglomerated in a biofilm) on the root canal wall can be characterized with the Damköhler number, which is defined as

$$Da = \frac{\text{typical transport time}}{\text{reaction time}} \quad (2.4)$$

The transport time can be determined from the local velocity  $\mathbf{u}$  together with a typical length scale  $L$ . However, also the vorticity  $\Omega$  should be taken into account, in combination with the velocity (e.g., when the velocity is zero, the contribution of

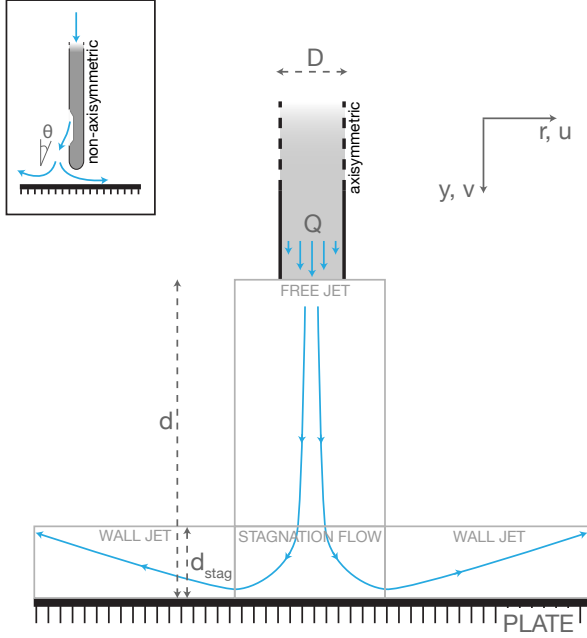


**Figure 2.1:** Schematic overview of the problem of an impinging axisymmetric and non-axisymmetric (inset) jet.

the vorticity should also be zero, as it would give no refreshment of irrigant). The Damköhler number with vorticity included is defined here as:

$$Da = \frac{L}{\tau(\mathbf{u} + \Omega L)} \quad (2.5)$$

$Da$  should be around unity (or less) for optimal reaction versus refreshment. The reaction time  $\tau$  of NaOCl (a commonly used irrigant) with endodontic biofilms (aggregations of bacteria) is, however, not exactly known. Studies on the half-time of the amount of active chlorine reacting with milliliter volumes of proteins, tissue or a dental biofilm report time scales of the order of one minute [24–26]; on a smaller scale ( $O(100 \mu\text{m})$ , typical length scale of velocity gradients and biofilm heights) we assume here a reaction time  $\tau = 10$  seconds.

Flow rate (mL/min)	1.2	4.0	8.4	12.0	15.6	
Corresponding Reynolds number	127	424	891	1273	1655	
Distance $d$ from jet orifice to plate/apex (mm)	0.2	1.0	2.0	3.0	4.0	5.0
Corresponding normalized distance (jet diameter $D$ )	$1D$	$5D$	$10D$	$15D$	$20D$	$25D$

**Table 2.1:** *Experimental parameters: flow rates and distances between needle orifice and apex or plate.*

## 2.2 Experimental setup

### 2.2.1 Visualization setup

The flow from an open-ended needle (NaviTip 30G, Ultradent Products Inc., South Jordan, UT, USA) or a side-vented needle (30G Irrigation Probe, KerrHawe SA, Bioggio, Switzerland) was recorded using a high-speed camera (HPV-1, Shimadzu Corp., Kyoto, Japan), capable of recording 100 frames at speeds up to  $10^6$  frames/sec (figure 2.2). The typical flow velocity of 1 m/s inside the root canal and its small dimensions of typically  $100 \mu\text{m}$  requires high-speed imaging if one wants to visualize the dynamic activity of irrigation techniques [27]:

$$\text{recording speed} = \frac{10u}{L} \quad (2.6)$$

where  $u$  is the velocity (typically 1 m/s) and  $L$  a length scale (typically  $100 \mu\text{m}$ ). The recording speed therefore has to be higher than 10 Kfps to capture the dynamic behavior of irrigation techniques.

The camera was attached to a microscope (BX-FM, Olympus Corp, Tokyo, Japan) for  $1.25\times$  to  $20\times$  magnification. Illumination was provided for bright field imaging by a high intensity continuous cold-light source (ILP-1, Olympus Corp, Tokyo, Japan).

The flow through the needles was driven by a syringe pump (NE-1010, New Era Pump Systems, Wantagh, NY, USA) at five different flow rates in the range  $10^0 - 10^1$  mL/min. The corresponding Reynolds numbers span two orders of magnitude,  $10^2 - 10^3$ ; see table 2.1. The flow was allowed to start up for three seconds before the start of a measurement.

Monodisperse hollow glass spheres (Sphericul, Potters Industries, South Yorkshire, UK) with a mean diameter of  $10 \mu\text{m}$  and a mean density of  $1.1 \cdot 10^3 \text{ kg/m}^3$  were added to distilled water as tracer particles for micro-Particle Imaging Velocimetry ( $\mu\text{PIV}$ ). For  $\mu\text{PIV}$ , tracer particles should have a density equal to that of water (*neutrally buoyant*) and a diameter much smaller than the typical length scale, in order to be able to neglect pressure gradients over its surface and the influence of particles on the flow. These requirements are fulfilled when the Stokes number  $St \ll 1$

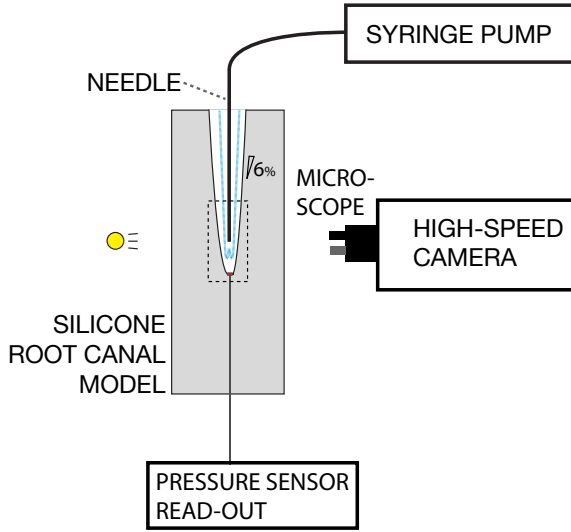


**Figure 2.2:** Schematic drawing (not to scale) of the setup used to study the flow velocities and pressure in a silicon root canal model. Velocity measurements are performed in the dashed area.

[28]:

$$St = \frac{\text{particle response time}}{\text{typical flow time}} = \frac{\tau_p u}{L} \quad (2.7)$$

where the particle response time  $\tau_p$  is given by:

$$\tau_p = \frac{2}{9} d_p^2 \frac{\rho_f - \rho_p}{\mu} \quad (2.8)$$

which depends on the particle size  $d_p$  and density  $\rho_p$  and fluid density  $\rho_f$  and viscosity  $\mu$ . For the current system,  $St < 1$  even for the highest velocities; these particles were furthermore experimentally verified to be suitable tracers for this type of flow.

Traditional PIV techniques rely on two consecutive photos illuminated with a laser sheet and light-scattering particles to visualize a thin plane in the volume of interest. However, in  $\mu$ PIV such a laser sheet would have a thickness of the same order as the volume of interest. Therefore here the total volume is illuminated and the depth of focus of the microscope objective is used to image only a thin plane. The depth of measurement  $\delta_z$  of a  $\mu$ PIV system is then defined as twice the distance from the focal plane where the particles become sufficiently unfocused that they don't

contribute to the velocity field any more, and is given by [29]:

$$\delta_z = \frac{3n\lambda_0}{NA^2} + \frac{1 - \sqrt{\phi}}{\sqrt{\phi}} \frac{d_p}{\tan \theta} + d_p. \quad (2.9)$$

The first term is related to diffraction and depends on the refractive index  $n$  of the fluid in front of the objective, the wavelength  $\lambda_0$  of the light being used for illumination, and the numerical aperture  $NA$ . The second term is related to geometrical optics, being the measurement cone with half-angle  $\theta = \tan^{-1} \left( \frac{NA}{n} \right)$  and the particle diameter  $d_p$ ;  $\phi$  is the fraction of the intensity of a particle beyond which it does not contribute to the velocity measurement any more. For an objective with  $NA = 0.25$ , imaging  $10 \mu\text{m}$  particles scattering white light through air, the depth of measurement is approximately  $100 \mu\text{m}$ , which indicates that the captured particle movement was limited to a plane with thickness of approximately  $1/5^{\text{th}}$  of the root canal diameter and 10 times the particle diameter.

The flow direction and velocity magnitude is obtained from the recordings of particle motion by calculating the cross-correlation between (parts of) two consecutive frames. Sub-pixel accuracy can be obtained by fitting a Gaussian curve to the 2D cross-correlation. The accuracy can be increased further using image processing techniques and data validation strategies. From the obtained velocity components  $u$  and  $v$ , the vorticity  $\omega$  can be obtained:

$$\omega = \frac{\partial v}{\partial x} - \frac{\partial u}{\partial y}. \quad (2.10)$$

This equation can be discretized and applied explicitly to the PIV velocity data.

Each recording consisted of 100 frames, which allowed for *ensemble averaging* [28]. A cross-correlation is made for each pair of frames, and these cross-correlations are added. This results in a higher peak in the final cross-correlations, which is equivalent to a higher signal-to-noise ratio. However, ensemble averaging reduces the spatial resolution and is therefore only suitable for steady flows. Variations in the flow were not observed within those 100 frames, therefore it was assumed that ensemble averaging did not cause a loss of temporal detail.

The flow from the needles was studied both inside a large water tank of dimensions  $50 \times 10 \times 50 \text{ mm}$  and inside a transparent model of a root canal. The transparent model was created by solidifying Poly-DiMethyl-Siloxane (PDMS) (Sylgard 184, Silicone Elastomer Kit, Dow Corning, Coventry, UK) around a D-size finger spreader (Dentsply Mailefer, Bellaigues, Switzerland), creating a conical root canal model of length  $18 \text{ mm}$ , apical diameter of  $0.45 \text{ mm}$  and a taper of  $6\%$  [9].

The silicon model was positioned in front of the microscope; the needle under investigation was positioned inside the model using a micrometric translation

stage (9067M, New Focus, San Jose, CA, USA and M-044.00, Physik Instrumente, Karlsruhe, Germany) capable of adjusting its position in three directions and tilting around two axes, attempting accurate centering of the needle inside the model. The distance  $d$  of the needle tip to the apex was varied from 0.2 to 5 mm, which corresponds to 1 to 25 times the jet diameter (see table 2.1). Although the two needles both were of gauge 30, microscopic examination revealed that the inner diameters were 220 and 196  $\mu\text{m}$  for the open-ended and side-vented needle, respectively.

### PIV error estimation

The accuracy of PIV depends on many factors, both in the measurement equipment and in the analysis. The error in the analysis can be estimated by taking an image representative for the experiments that need to be analyzed, and displacing this image over a certain number of pixels. The PIV analysis should result in velocities equal to the displacements applied to the image. The script used in this thesis showed that the applied displacements could indeed be recovered, within an error of approximately 5%, which can be attributed to noise. This error analysis also pointed out that the result of the PIV analysis is very sensitive to the amount of details in the image, as low-contrast areas in the image will result in a zero velocity.

### 2.2.2 Pressure measurements

A miniature fiber-optic pressure sensor (FOP-M260, FISO Technologies Inc., Quebec, Canada) with a sensor diameter of 260  $\mu\text{m}$  was used for measuring the pressure at the apex or the plate. The pressure sensor was fitted inside a 25G needle, which was positioned at the apex of the transparent silicon root canal model or inside a hole of diameter 0.6 mm inside an aluminum plate. The needle under investigation was positioned carefully above the sensor, which measured at a rate of 5000 Hz. The influence of misalignment was observed to be small. The pressure measurements revealed that the flow needed a few seconds to reach a steady state with a constant pressure at the apex; the average of this constant pressure was used as the final value. The standard deviation during the steady state was taken as a measure of the fluctuations in the flow, after subtraction of the background noise level being the average of the first second of recorded pressure data.

The sensitivity characteristics of the pressure sensor were obtained by performing a hardware convolution. The axisymmetric jet was translated in a straight line across the surface of the pressure sensor in steps of 25  $\mu\text{m}$  while recording its pressure. The sensitivity of the sensor was found to be non-homogeneous across the sensor area (figure 2.3), which can affect the sensor readout when there are pressure gradients over the sensor surface. However, it is not known how exactly the sensor determines the single value for the pressure from its total sensor area, therefore it is not possible

to calculate a correction factor for the measured pressure.

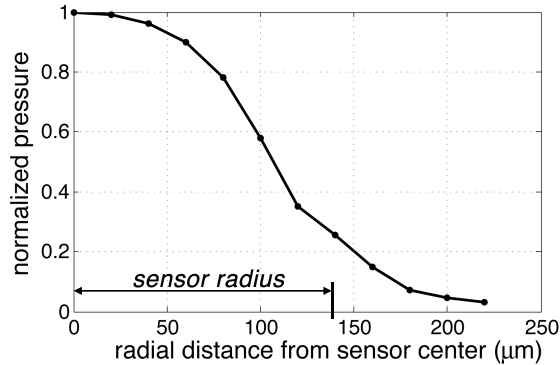


**Figure 2.3:** Sensor sensitivity characteristics as a function of radial distance from the sensor center, measured by moving a jet of orifice radius  $100\ \mu\text{m}$  across the sensor area. The sensor measures a pressure even when the jet is outside the sensor area due to the spreading of the jet.

## 2.3 Results

### 2.3.1 Flow patterns

The streamlines representing the measured flow patterns for the two types of jets are shown in figures 2.5 and 2.6. The global features of the measured velocity patterns match those predicted by the CFD model (figure 2.4), showing two distinct velocity patterns: a straight, divergent jet (axisymmetric jet) and a cascade of eddies (non-axisymmetric jet). The measured velocities are of the same order of magnitude as calculated by the theory and CFD model, although the maximum velocity values are not always observed.

#### Impinging axisymmetric jet

The axisymmetric jet is observed to diverge slowly upon exiting the needle orifice; there is entrainment of the surrounding fluid, but no instabilities or break up of the jet is observed. Near the flat plate, the jet is spread out radially. Figure 2.7 shows the measured velocity profiles as a function of distance from the jet orifice, demonstrating the spreading of the jet. The velocity decrease has a slope very similar to the predicted  $1/x$  slope for a free jet, although there is some deviation due to the presence of the plate. At a distance of  $1D$  from the plate (figure 2.8), the stagnation flow region starts and the velocity rapidly decreases. The width of the jet increases with distance from

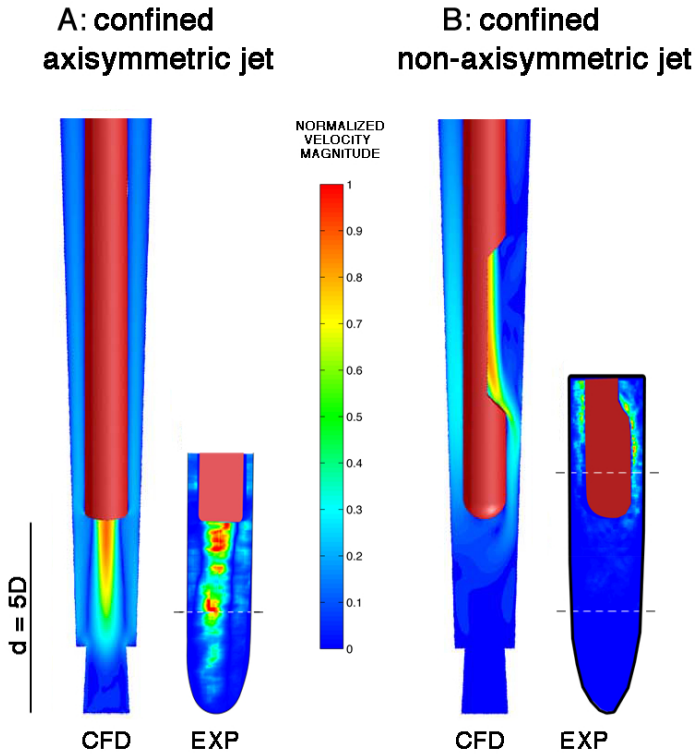


**Figure 2.4:** Comparison of the normalized flow velocity magnitude between CFD model and experiments, for both the axisymmetric (A) and non-axisymmetric (B) jets. In the experimental results, the horizontal lines indicate separate measurements. CFD images adapted from [11].



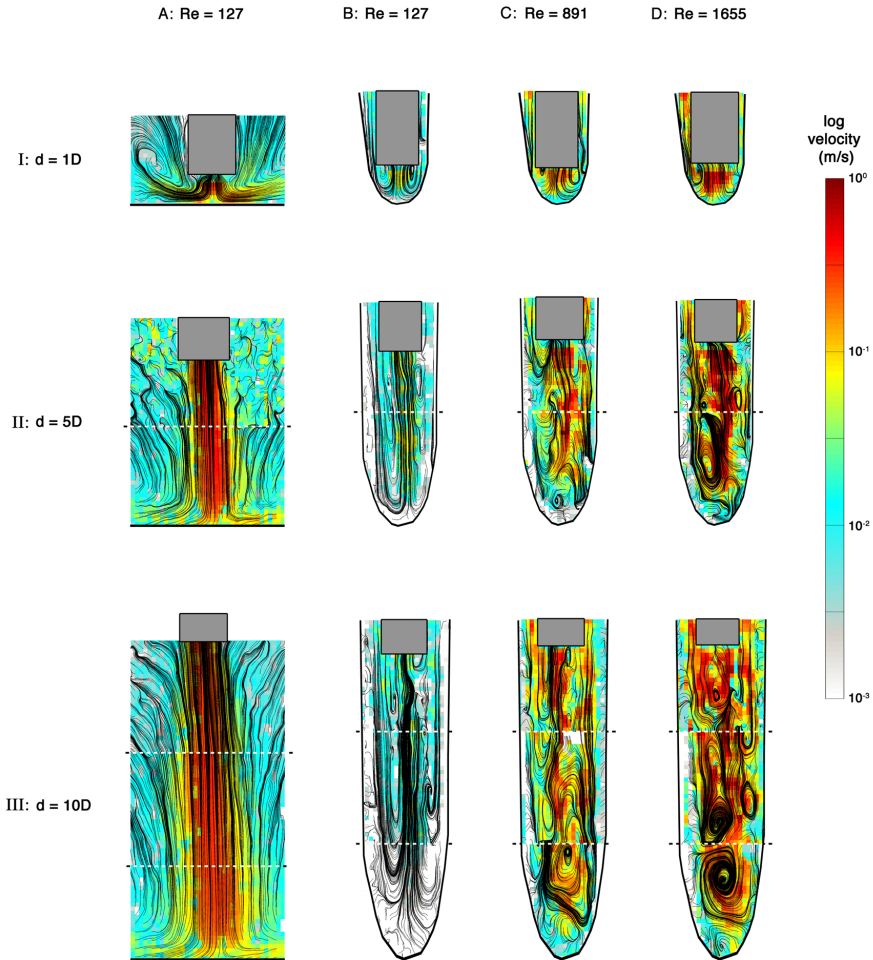


**Figure 2.5:** Streamlines of the flow in the case of an impinging (column A) or confined (columns B-D) axisymmetric jet, for three different distances between jet orifice and wall/apex (rows I-III), and three different flow rates (confined jet only, columns B-D). The horizontal lines indicate separate measurements

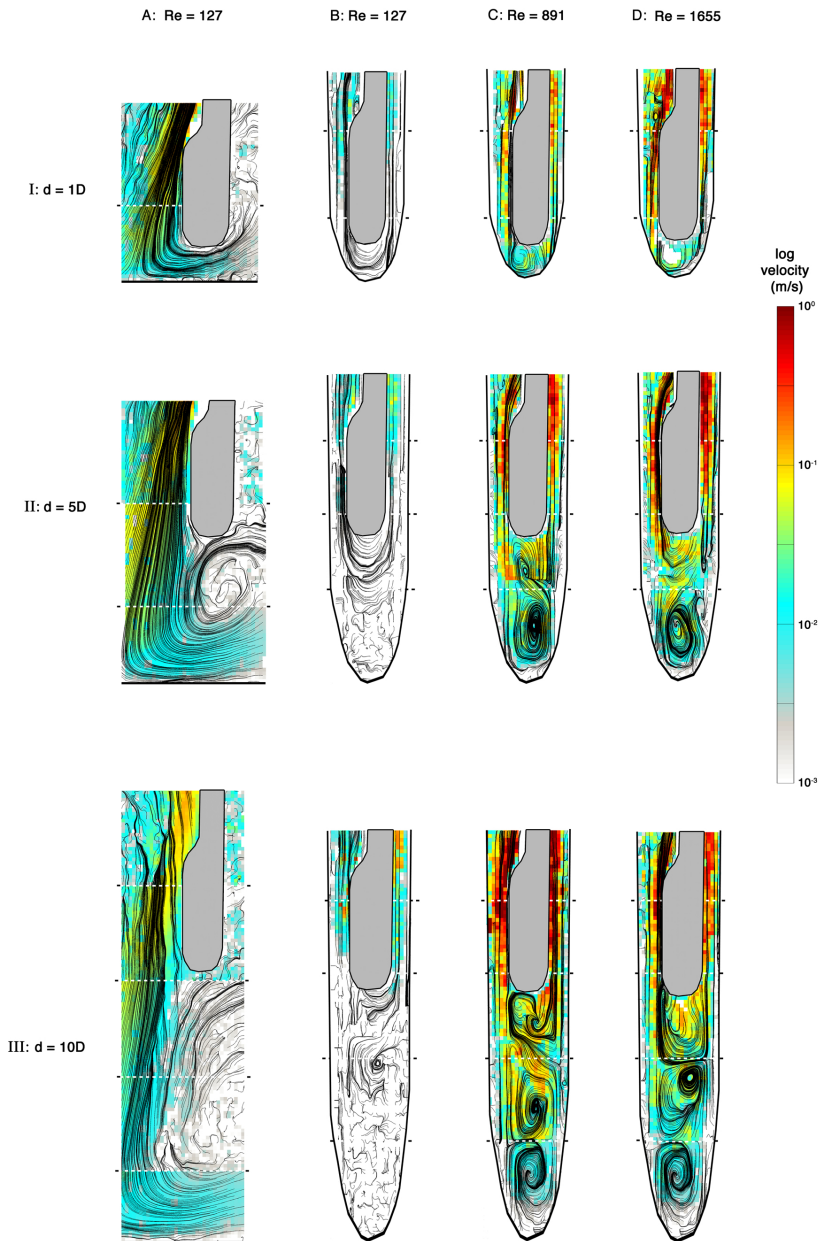


**Figure 2.6:** Streamlines of the flow in the case of an impinging (column A) or confined (columns B-D) non-axisymmetric jet, for three different distances between jet orifice and wall/apex (rows I-III), and three different flow rates (confined jet only, columns B-D). The horizontal lines indicate separate measurements.

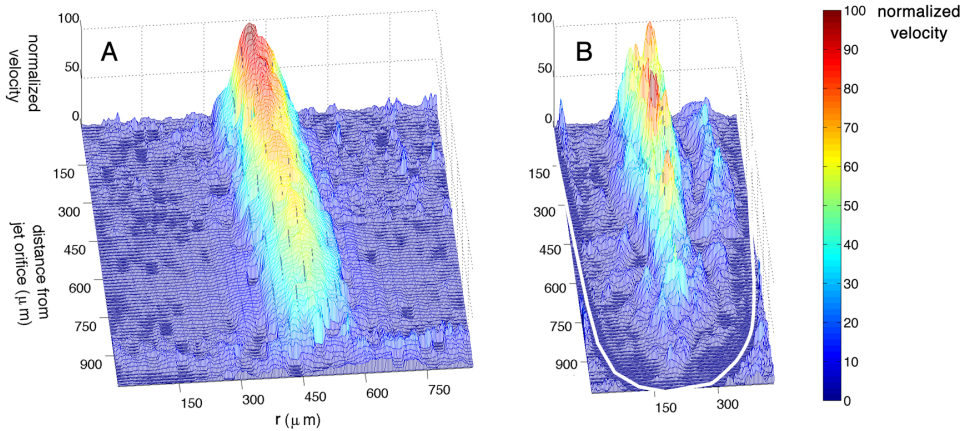


**Figure 2.7:** Velocity magnitude for the axisymmetric jet, both unconfined (A) and confined (B).

the jet orifice, although the data points do not perfectly align to a straight line due to a limited resolution. A linear fit through the data has a slope very similar to the theoretically predicted linear slope of  $\frac{4.67}{Re}$ , see figure 2.9.

### Confined axisymmetric jet

Inside the confinement of the root canal, the impinging jet is directed toward the apex, where it has to reverse direction and flow coronally along the wall of the confinement. The reverse flow is observed to interact with the incoming flow, leading to instabilities in the jet when the distance from jet orifice to apex is larger than  $1D$  and for Reynolds numbers of 891 and higher. At the highest Reynolds number  $Re = 1655$  and a distance of  $10D$  the jet can no longer be recognized as such in the apical area, and there the jet is considered to have broken up.

The velocities inside the confined axisymmetric jet are typically one order of magnitude less than in the unconfined jet, but the velocities outside the jet are typically higher than for the case of the unconfined jet (fig. 2.7), suggesting an increased radial outflow from the jet.

The jet profile as a function of the distance from the jet orifice is plotted in figure 2.7; figures 2.8 and 2.9 show (blue lines) the maximum velocity at each distance and the width of the jet, respectively. Due to the instabilities induced by the returning flow there is some spreading in the velocity of the jet, however overall the decrease in the maximum velocity appears to follow a  $\frac{1}{x}$  relationship, similar to the unconfined jet. The influence of the bottom wall is more pronounced than for the unconfined impinging jet. The width of the jet is decreasing with distance from the orifice, having

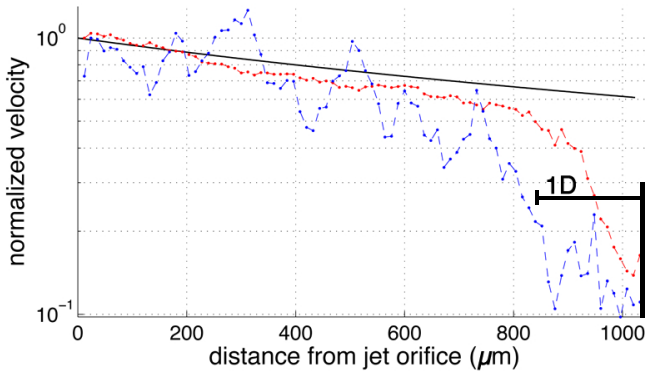


**Figure 2.8:** Centerline velocity  $\log(v)$  of the axisymmetric jet; theoretical prediction (—) and experimental result for the unconfined (●) and confined jet (●). The wall, and a distance of one jet orifice diameter away from it, is indicated at  $x = 1000 \mu\text{m}$ .

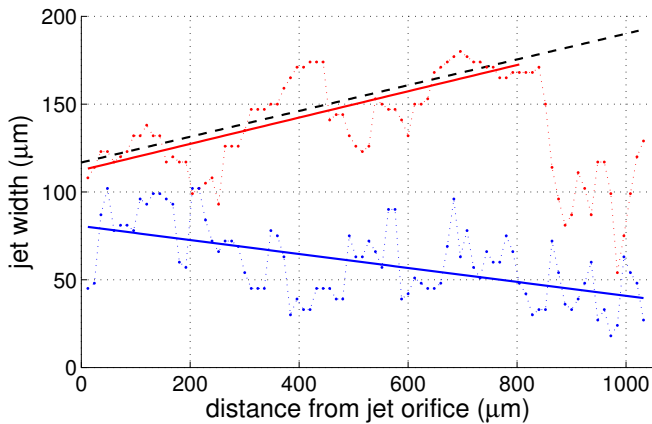


**Figure 2.9:** Width of the axisymmetric jet; theoretical prediction (--) and experimental result for the unconfined (●) and confined jet (●) with their linear fits (—).

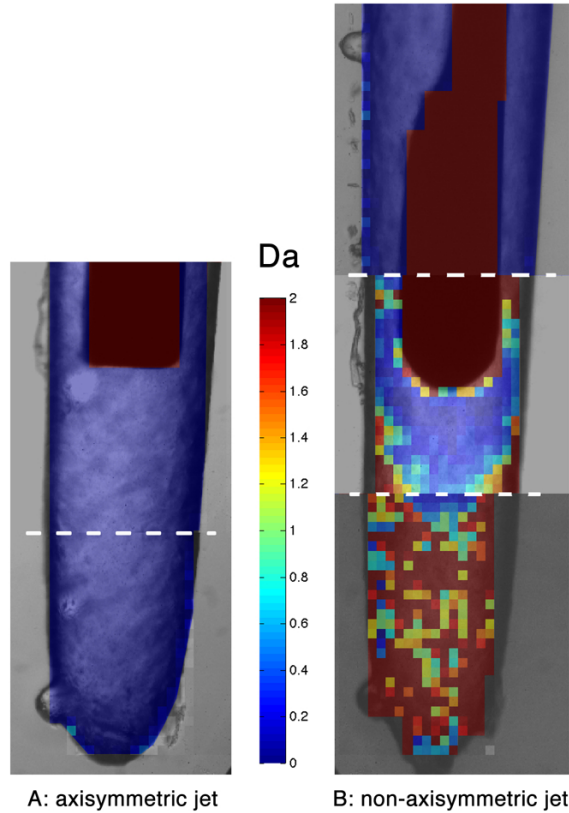


**Figure 2.10:** Damköhler values for the confined axisymmetric (A) and non-axisymmetric (B) jet, indicating whether or not there is adequate replacement ( $Da \leq 1$ ) of the irrigant compared to the reaction time with a biofilm.

a slope of  $\frac{-2.53}{Re}$ , probably due to the taper of the root canal.

There is good agreement with the CFD model (fig. 2.4) in (normalized, in-plane) velocity magnitudes. The Damköhler number (fig. 2.10,  $Re = 127$ ) predicts that the velocity is high enough everywhere to ensure adequate irrigant replacement ( $Da \leq 1$ ).

### Impinging non-axisymmetric jet

For the side-vented needle, the fluid leaves the needle orifice under an angle of  $19^\circ$  and impinges onto the plate obliquely. The fluid flows around the tip of the needle; if the distance between needle tip and wall is larger than  $1D$ , one vortex is formed due to recirculating flow. An estimate from the measurements shows that approx. 15% of the flow goes backward (around the needle); the other 85% should then go forward.

### Confined non-axisymmetric jet

Due to the confinement of the root canal, the angle under which the fluid leaves the side-vented needle is reduced to  $14^\circ$ . The fluid first flows along the needle toward the apex, then around the tip of the needle before flowing upward along the needle towards the coronal opening of the root canal. At distances  $d > 5D$  and Reynolds number of 891, the flow around the tip of the needle drives an eddy with a size of approximately 1 mm in the space lateral to the needle tip. For Reynolds number 1655, this eddy then drives another eddy at the apex of size 0.5 mm. The velocities inside these consecutive eddies decrease by approximately one order of magnitude. Also for this jet the velocities of the non-axisymmetric jet inside the root canal are typically an order of magnitude less than the unconfined jet.

Comparison of the velocity magnitudes with the CFD model show again a good agreement. A more detailed comparison of the velocity vectors showed only minor differences, like a small vortex just below the needle tip for Reynolds numbers larger than 424, which is not observed in the experiments. The angle under which the flow exits the needle in the CFD model is  $15^\circ$ .

For the confined non-axisymmetric jet, the Damköhler number, also shown in figure 2.10 for the lowest flow rate with  $Re = 127$ , predicts that only around the needle the flow is fast enough to adequately replace the irrigant; toward the apex the velocity and/or vorticity is not high enough.

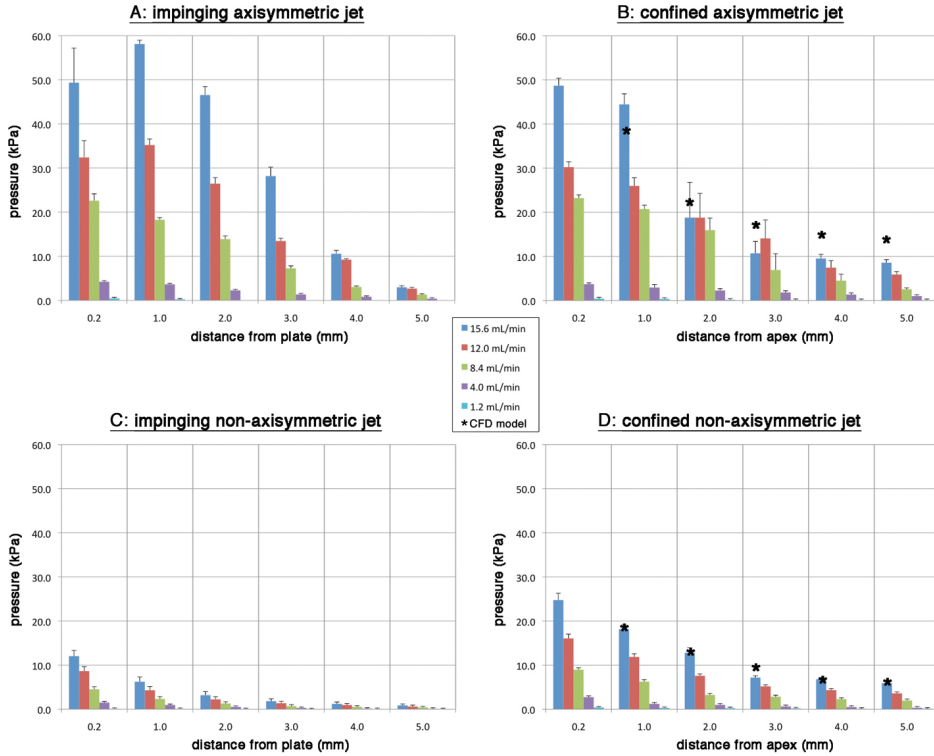
#### 2.3.2 Apical pressure

Figure 2.11 shows the pressures measured at the flat plate and the apex for the two different jets, with the errorbars indicating the fluctuation in the pressure signal (defined as the standard deviation of the signal). For both needles the pressure is of order  $10^3$  Pa and generally increases with flow rate and decreases with distance to the plate or the apex. Within this range of distances, the non-axisymmetric jet typically leads to pressures that are almost one order of magnitude lower than the axisymmetric jet, also inside the confinement of the root canal. The confinement causes the pressure to increase at the apex for the non-axisymmetric jet, but not for the axisymmetric jet.

The pressures measured for the confined non-axisymmetric jet agree very well with the values obtained with the CFD model of the side-vented needle (indicated with asterisks). Also for the axisymmetric jet the agreement is good.

The instabilities observed for the confined axisymmetric jet can be observed from the errorbars of the corresponding pressure in figure 2.11: the fluctuations in the pressure signal are largest around distances of 2 and 3 mm ( $10D$  and  $15D$ , respectively) from the apex and high flow rates.

The decrease in pressure as a function of distance to the apex or wall (normalized at  $d = 5D$ ) is plotted in figure 2.12, showing the pressures obtained from measure-



**Figure 2.11:** Measured pressure for the two different jets and with/without confinement, for five flow rates and six distances between jet orifice and wall or apex. The ‘errorbars’ indicate the standard deviation in the pressure signal, giving a measure for pressure fluctuations. The asterisks indicate the value obtained from the CFD model.

ments, CFD simulations [8] and theory (axisymmetric jet). It can be observed that inside the confinement there is a slower decrease in pressure with distance from the apex, for both the axisymmetric and the non-axisymmetric jet, suggesting a pressure build-up as the flow cannot escape due to the confinement. The theoretical prediction shown is based on the Bernoulli theorem: the velocity in the center of the free jet is used to calculate  $P \propto v^2 \propto y^{-2}$ . Figure 2.13 shows the square root of the pressure plotted as a function of the jet Reynolds number. It shows the validity of this assumption, as all lines appear to be linear, both for the axisymmetric jet and the non-axisymmetric jet.

At short distances from the plate, the measured pressure for the unconfined axisymmetric jet is higher than that predicted by the CFD model or the Bernoulli pressure. In addition, the pressure decrease does not follow a  $y^{-2}$  decrease. This could be due to the measured non-homogenous sensitivity across the sensor area of the pressure sensor (figure 2.3). But this is only relevant for the impinging axisymmetric jet, with a diameter at the needle orifice smaller than the sensor diameter. For the unstable axisymmetric jet inside the confinement and for the non-axisymmetric jet, the pressure variations across the sensor area are expected to be small, therefore the pressure sensor is expected to give the correct value in those cases.

## 2.4 Discussion

### 2.4.1 Influence of the confinement of the root canal

The influence of the confinement of the root canal on the flow patterns is clear from figures 2.5 and 2.6. Qualitatively, for the axisymmetric jet, the confinement causes the impinged flow to recirculate and interact with the incoming flow, causing the jet to break up. For the non-axisymmetric jet, the flow around the needle tip drives a cascade of eddies with a rapid decrease of the velocities. Quantitatively, the velocity magnitudes decrease by approximately one order of magnitude for both jets. This could be related to a pressure build-up in the apical area, forcing the fluid to be spread out toward the wall and along the file to the coronal opening of the confinement of the root canal. Indeed, the absolute pressure of the non-axisymmetric jet tends to increase due to the confinement, as the jet cannot spread out. For the axisymmetric jet the influence of the confinement is less pronounced, but from the observation that the decrease in pressure as a function of distance to the plate or apex is slower when the confinement is included, it can be deduced that the confinement causes pressure build-up as the flow cannot leave the impingement area easily.



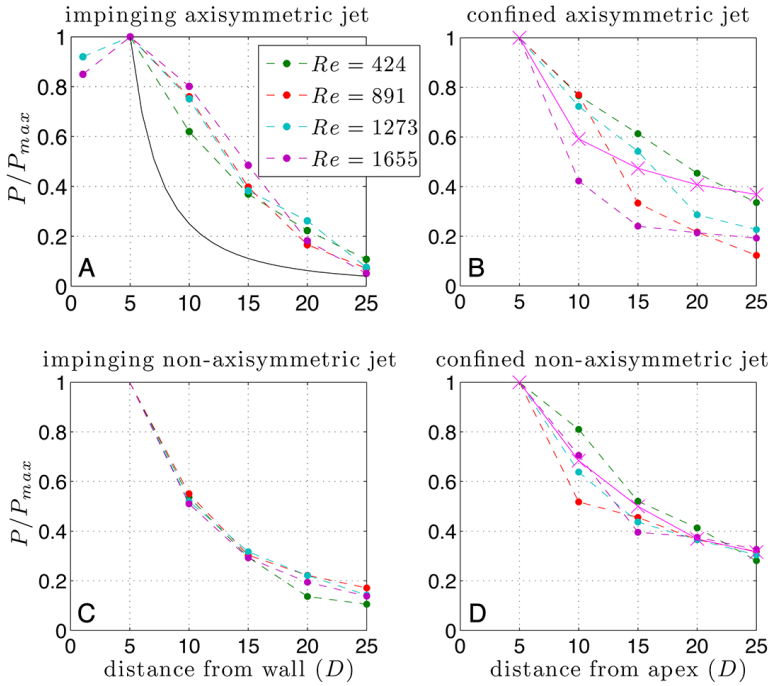


**Figure 2.12:** Measured pressure, normalized at  $d = 5D$ , as a function of distance from the wall, for the two different jets and with/without confinement. Four different Reynolds are plotted with dashed lines:  $Re = 424$  (-●-),  $891$  (-●-),  $1273$  (-●-) and  $1655$  (-●-). The result from the CFD model for  $Re = 1655$  is represented with a solid line (-×-). The black line in the panel A (—) is the pressure as calculated from the Bernoulli theorem, i.e.  $P \propto u^2$ , where  $u$  is the velocity at the center of the jet.

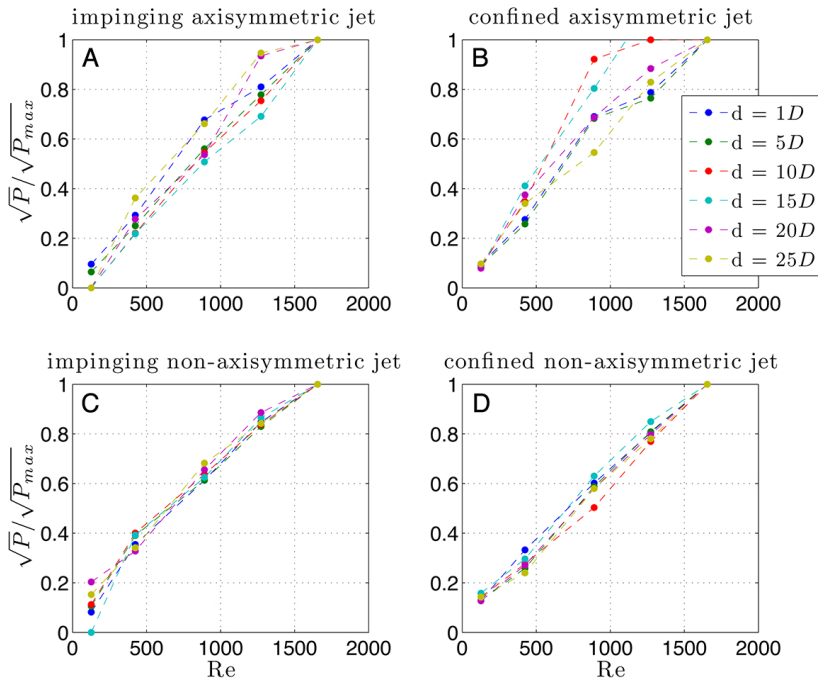


**Figure 2.13:** Measured pressure, normalized at  $Re = 1655$ , as a function of Reynolds number, for the two different jets and with/without confinement. Six different distances between jet orifice and wall/apex have been plotted:  $d = 1D$  (-●-),  $5D$  (-●-),  $10D$  (-●-),  $15D$  (-●-),  $20D$  (-●-) and  $25D$  (-●-).

## 2.4.2 Comparison of measured flow to the CFD model

Overall, the agreement between the measured flow pattern, velocity magnitudes and pressures and those predicted by the CFD model [21] is good. There are some differences, which we will try to explain here. First, the confined axisymmetric jet shows jet break up that are not predicted by the CFD model; this is likely due to the fact that the needles in the CFD model are perfectly aligned, whereas small misalignments or root canal geometry imperfections could have destabilized the flow in the experiments. Also, measurements have been done in a relatively large depth of focus whereas the flow is essentially three-dimensional; particles being out of focus and moving out of focus could affect the measured flow pattern. The depth of focus also gives an explanation for the the measured velocity magnitudes to have a lower maximum value than predicted by theory and CFD model, as only very few particles will obtain the maximum value and these will be averaged out in time and in focal depth; clearly a limitation of the experimental method.

## 2.4.3 Comparison to previous studies

A recent article by Gau *et al.* [15] discussed the differences between a microjet and a macrojet and concluded that there are significant differences in the jet breakdown point and the onset of turbulence. Due to the small scale of the microjet, instabilities in the microjet do not grow as easily as in a macrojet, resulting in a jet which retains its original, non-turbulent structure for a long distance, thereby penetrating deeper than a macrojet would do. In our experiments with an unconfined impinging axisymmetric jet, we have visualized the flow up to a distance of  $10D$  and not observed breakup of the jet. This agrees well with the quoted article, where a distance of more than  $50D$  at  $Re = 167$  was necessary before breakdown would occur.

Instabilities did occur inside the confinement of the root canal. The confined axisymmetric jet is very similar to the study by Cornaro *et al.* [14], who discussed a jet impinging onto concave and convex surfaces. At relatively small radius of curvature for the concave surfaces, high Reynolds numbers and large distances between nozzle and surface, the recirculating flow interacted with the incoming flow, causing instabilities and eventual breakup of the impinging jet. We see the same behavior in our experiments, for Reynolds numbers larger than 127 and distances larger than  $1D$ .

The impinging non-axisymmetric jet resembles an oblique jet, for which Taylor [23] predicted the fractions of the flow going backward and forward. In our case,  $\theta = 19^\circ$ , therefore the backward component should be of the order of 37%, but a rough estimation gave a value of only 15%. The theoretical value, however, is based on a two-dimensional model, whereas the present experiments are essentially three-dimensional.

The confined non-axisymmetric jet is very similar to the flow studied by Taneda and by Kent [30, 31], who investigated the flow in a V-shaped cavity driven by a circular cylinder. The cascade of eddies that Kent observed in his system are of the type that Moffatt described for a flow near a sharp corner [32], termed Moffatt-eddies. A similar cascade of eddies was observed in the present study, consisting of two primary eddies and corner eddies, of which the location and strength varies. According to Shankar & Deshpande [33], a cascade of eddies in a lid or shear driven cavity is due to viscous effects; the size and relative velocities between eddies can be determined from the eigenvalues of the stream functions that govern the flow. For a three-dimensional, cylindrical cavity the first eigenvalue is  $\mu_1 = 2.586 + 1.123i$ , which results in a spacing between (and size of) the eddies of  $\frac{\pi}{\text{Im}(\mu_1)} = 2.8$  times the cavity diameter. The radius of the cavity (root canal model) used in this study just below the needle tip is  $300 \mu\text{m}$ , giving a theoretical distance between eddy centers of  $0.84 \text{ mm}$ . Experiments show a distance between primary eddy centers of  $0.5 - 1 \text{ mm}$ , which is a satisfactory agreement. The root canal is furthermore of a conical shape, which typically leads to smaller eddies towards the apex of the cone. However, for a corner angle of  $3.4^\circ$ , which corresponds to a root canal with taper  $6\%$ , the change in eddy size is smaller than  $1\%$ , according to Moffatt [32], suggesting that all eddies should be of similar size.

For a lid or shear-driven cylindrical cavity, the velocity decrease from eddy to eddy is a constant that is given by

$$e^{-\pi \frac{\text{Re}(\mu_1)}{\text{Im}(\mu_1)}} = 1386. \quad (2.11)$$

Thus, the velocity is predicted to decrease rapidly, with three orders of magnitude between eddies. However, in the present experimental study and in the CFD model, the decrease in velocity from eddy to eddy is only 5 to 10 times. The discrepancy with the theory is likely due to the large longitudinal component of the flow, whereas in the theoretical model of lid- or shear driven cavity flow, the driving flow is purely horizontal and eddies are induced solely through viscous effects.

#### 2.4.4 Damköhler number

In this study it was shown that, for the lowest flow rates, the non-axisymmetric jet could not refresh the irrigant in the apical part of the root canal model adequately, slowing down the cleaning process. This is in agreement with the observation by Boutsoukis *et al.* [11] and references therein, that irrigant flow was only effective up to  $1 \text{ mm}$  in front of a side-vented needle. Higher flow rates will make the refreshment more effective in the apical area, however, the root canal geometry is much more complex in natural teeth than in the present model. Oval extensions, isthmuses, apical ramifications, lateral and accessory canals provide locations difficult to reach with

irrigant flow and consequently will have inadequate refreshment. This geometrical complexity is not covered with the root canal model used in this study.

Furthermore, with the higher pressure for the axisymmetric jet than for the non-axisymmetric jet, there is a risk of extruding the irrigant through the apical foramen of the root canal to the periapical tissue surrounding the tooth, where it can result in tissue damage and patient discomfort. In this respect, the side-vented needle is safer to use because of its lower apical pressure. However, at present it is not known what the maximum allowed apical pressure is before extrusion occurs.

### 2.4.5 Recommendations

In this study, high-speed PIV has been a valuable tool for studying the flow at the short time scales and small length scales that are present in root canal irrigation. The results can be made more accurate with a smaller focal depth of the microscope, which could also give a full 3D velocity field [34], or with a higher number of measurements to reduce statistical errors. To better understand the role of the confinement, different shapes and sizes of the confinement should be studied. For practical, endodontic purposes this has already been evaluated with the previously mentioned CFD model [35, 36], although those studies also do not take into account the full complex geometry of a real root canal.

## 2.5 Conclusions

High-speed PIV recordings have revealed the flow pattern and velocity magnitudes for an axisymmetric and a non-axisymmetric microjet. The axisymmetric jet is found to be stable and agree with the theoretical prediction for this type of jet, however, a confinement causes instabilities to the jet. The confinement of the root canal has a pronounced influence on the flow, for both the axisymmetric and non-axisymmetric jet, by reducing the velocities in the jets by one order of magnitude and increasing the pressure at the apex. The non-axisymmetric jet inside the confinement shows a cascade of eddies with decreasing velocities, which, according to the calculated Damköhler numbers, does not provide adequate irrigation fluid refreshment at the apex with respect to the reaction of the irrigant with a biofilm.

## References

- [1] M. Haapasalo, U. Endal, H. Zandi, and J. M. Coil, "Eradication of endodontic infection by instrumentation and irrigation solutions", *Endodontic Topics* **10**, 77–102 (2005).
- [2] P. Nair, "Pathogenesis of apical periodontitis and the causes of endodontic failures", *Critical Review of Oral Biology & Medicine* **15** (2004).

- [3] F. Paqué, C. Boessler, and M. Zehnder, “Accumulated hard tissue debris levels in mesial roots of mandibular molars after sequential irrigation steps”, *International Endodontic Journal* **44**, 148–153 (2011).
- [4] J. M. Adcock, S. J. Sidow, S. W. Looney, Y. Liu, K. McNally, K. Lindsey, and F. R. Tay, “Histologic evaluation of canal and isthmus debridement efficacies of two different irrigant delivery techniques in a closed system”, *Journal of Endodontics* **37**, 544–548 (2011).
- [5] F. H. Kahn, P. A. Rosenberg, and J. Gliksberg, “An in vitro evaluation of the irrigating characteristics of ultrasonic and subsonic handpieces and irrigating needles and probes”, *Journal of Endodontics* **21**, 277–280 (1995).
- [6] M. Amato, I. Vanoni-Heineken, H. Hecker, and R. Weiger, “Curved versus straight root canals: the benefit of activated irrigation techniques on dentin debris removal”, *Oral Surgery, Oral Medicine, Oral Pathology, Oral Radiology and Endodontology* **111**, 529–534 (2011).
- [7] J. B. Moser and M. A. Heuer, “Forces and efficacy in endodontic irrigation systems”, *Oral Surgery, Oral Medicine, Oral Pathology, Oral Radiology and Endodontology* **53**, 425–428 (1982).
- [8] C. Boutsioukis, T. Lambrianidis, and E. Kastrinakis, “Irrigant flow within a prepared root canal using various flow rates: a computational fluid dynamics study”, *International Endodontic Journal* **42**, 144–155 (2009).
- [9] C. Boutsioukis, B. Verhaagen, M. Versluis, E. Kastrinakis, and L. W. M. Van der Sluis, “Irrigant flow in the root canal: experimental validation of an unsteady computational fluid dynamics model using high-speed imaging”, *International Endodontic Journal* **43**, 393–403 (2010), *see also Chapter 3 of this thesis*.
- [10] Y. Gao, M. Haapasalo, Y. Shen, H. Wu, B. Li, N. D. Ruse, and X. Zhou, “Development and validation of a three-dimensional computational fluid dynamics model of root canal irrigation”, *Journal of Endodontics* **35**, 1282–1287 (2009).
- [11] C. Boutsioukis, B. Verhaagen, M. Versluis, E. Kastrinakis, P. R. Wesselink, and L. W. M. Van der Sluis, “Evaluation of irrigant flow in the root canal using different needle types by an unsteady computational fluid dynamics model”, *Journal of Endodontics* **36**, 875–879 (2010).
- [12] M. Hülsmann, T. Rödiger, and S. Nordmeyer, “Complications during root canal irrigation”, *Endodontic Topics* **16**, 27–63 (2009).
- [13] S. Cohen and K. M. Hargreaves, *Pathways of the pulp*, 9th edition (Mosby Elsevier) (2006).
- [14] C. Cornaro, A. S. Fleischer, and R. J. Goldstein, “Flow visualization of a round jet impinging on cylindrical surfaces”, *Experimental Thermal and Fluid Science* **20**, 66–78 (1999).
- [15] C. Gau, C. H. Shen, and Z. B. Wang, “Peculiar phenomenon of micro-free-jet flow”, *Physics of Fluids* **21** (2009).
- [16] H. Schlichting and K. Gersten, *Boundary-layer theory*, 8th edition (Springer, Berlin) (2000).
- [17] M. B. Glauert, “The wall jet”, *Journal of Fluid Mechanics* **1**, 625–643 (1956).
- [18] M. D. Deshpande and Vaishnav, “Submerged laminar jet impingement on a plane”, *Journal of Fluid Mechanics* **114**, 213–236 (1982).

- [19] D. J. Phares, G. T. Smedley, and R. C. Flagan, "The inviscid impingement of a jet with arbitrary velocity profile", *Physics of Fluids* **12**, 2046–2055 (2000).
- [20] D. J. Phares, G. T. Smedley, and R. C. Flagan, "The wall shear stress produced by the normal impingement of a jet on a flat surface", *Journal of Fluid Mechanics* **418**, 351–375 (2000).
- [21] C. Boutsoukias, T. Lambrianidis, E. Kastrinakis, and P. Bekiaroglou, "Measurement of pressure and flow rates during irrigation of a root canal ex vivo with three endodontic needles", *International Endodontic Journal* **40**, 504–513 (2007).
- [22] A. Rubel, "Computations of jet impingement on a flat surface", *AIAA Journal* **182**, 168–175 (1980).
- [23] G. Taylor, "Oblique impact on a plane surface", *Philosophical Transactions of the Royal Society of London. Series A, Mathematical and Physical Sciences* **260**, 96–100 (1966).
- [24] R. Baker, "Studies on the reaction between sodium hypochlorite and proteins", *Biochemistry* **41**, 337–342 (1947).
- [25] W. R. Moorer and P. R. Wesselink, "Factors promoting the tissue dissolving capability of sodium hypochlorite", *International Endodontic Journal* **15**, 187–196 (1982).
- [26] N. Sena, B. P. Gomes, M. E. Vianna, V. B. Berber, A. A. Zaia, C. C. R. Ferraz, and F. J. Souza-Filho, "In vitro antimicrobial activity of sodium hypochlorite and chlorhexidine against selected single-species biofilms", *International Endodontic Journal* **39**, 878–885 (2006).
- [27] M. Versluis, "High-speed imaging in fluids", *Experiments in Fluids* **submitted** (2012).
- [28] M. Raffel, C. E. Willert, S. T. Wereley, and J. Kompenhans, *Particle imaging velocimetry - a practical guide*, 2nd edition (Springer, Berlin, Germany) (2007).
- [29] C. Meinhart, S. Wereley, and M. Gray, "Volume illumination for two-dimensional particle image velocimetry", *Measurement Science and Technology* **11**, 809–814 (2000).
- [30] S. Taneda, "Visualization of separating Stokes flows", *Journal of the Physical Society of Japan* **46**, 1935–1942 (1979).
- [31] E. F. Kent, "Flow visualization experiments in a v-shaped channel bounded by a cylindrical surface", *Journal of the Physical Society of Japan* **68**, 1887–1890 (1999).
- [32] H. K. Moffatt, "Viscous and resistive eddies near a sharp corner", *Journal of Fluid Mechanics* **18**, 1–18 (1964).
- [33] P. N. Shankar and M. D. Deshpande, "Fluid mechanics in the driven cavity", *Annual Review of Fluid Mechanics* **32**, 93–136 (2000).
- [34] Y. Won, E. N. Wang, K. E. Goodson, and T. W. Wenny, "3-d visualization of flow in microscale jet impingement systems", *International Journal of Thermal Sciences* **50**, 325–331 (2011).
- [35] C. Boutsoukias, C. Gogos, B. Verhaagen, M. Versluis, E. Kastrinakis, and L. W. M. Van der Sluis, "The effect of apical preparation size on irrigant flow in root canals evaluated using an unsteady computational fluid dynamics model", *International Endodontic Journal* **43**, 874–881 (2010).
- [36] C. Boutsoukias, C. Gogos, B. Verhaagen, M. Versluis, E. Kastrinakis, and L. W. M. Van der Sluis, "The effect of root canal taper on the irrigant flow: evaluation using an unsteady computational fluid dynamics model", *International Endodontic Journal* **43**, 909–916 (2010).

# 3

## Irrigant flow in the root canal: experimental validation of an unsteady Computational Fluid Dynamics model using high-speed imaging \* †

**Abstract:** The results of a Computational Fluid Dynamics (CFD) simulation of the irrigant flow from a needle and a syringe are compared in this chapter with experimental high-speed visualizations and theoretical calculations of the same system. A CFD model was created to simulate irrigant flow from a side-vented needle inside a prepared root canal. Calculations were carried out for four different positions of the needle inside a prepared root canal. An identical root canal model was made from poly-dimethyl-siloxane (PDMS). High-speed micro Particle Image Velocimetry ( $\mu$ PIV) was used to obtain the velocity field inside the root canal experimentally. Comparison between CFD computations and experiments revealed good agreement in the velocity magnitude and vortex location and size., even though the flow was unsteady. The CFD model can therefore be considered validated.

---

\*Published as: C. Boutsoukis, B. Verhaagen, M. Versluis, E. Kastrinakis and L.W.M. van der Sluis, "Irrigant flow in the root canal: experimental validation of an unsteady Computational Fluid Dynamics model using high-speed imaging", *International Endodontic Journal* **43**, pp. 393-403 (2010)

†The experimental validation of the CFD model in this chapter is part of the present thesis. The numerical model is due to Christos Boutsoukis.



### 3.1 Introduction

Irrigation of root canals with antibacterial solutions is considered an essential part of chemo-mechanical preparation [1]. Irrigation with a syringe and needle remains the most commonly used irrigation procedure [2, 3]. However, there is a general uncertainty about the efficiency of this procedure in the narrow, most apical part of the root canal [4–6]. It has been argued that the limiting factor of the irrigation procedure is the difficulty to flush the apical root canal with large volumes of fresh irrigant [7].

To study this problem, attempts to evaluate the irrigant flow within the root canal have been attempted, based on macroscopic observations [8–10]. However, these studies of the fluid dynamics were limited because such a macroscopic approach can provide only a general description of the irrigant flow.

Computational fluid dynamics (CFD) represents a powerful tool to investigate flow patterns and physical and chemical phenomena by mathematical modelling and computer simulation [11, 12]. Despite the fact that CFD was originally developed for industrial and engineering purposes, applications in the biomedical field have also attracted considerable attention [13], aided by the increasing power of computers [14]. CFD simulations can provide details on the velocity field in areas where experimental measurements are difficult to perform. Furthermore, important properties such as shear stress and pressure can easily be obtained, in contrast to experiments, especially in microscale flow problems. Recently, a CFD model was implemented for the evaluation of irrigant flow in the root canal [15]. However, this model has not been validated yet through comparison to experimental data, a procedure that is considered essential for any model [16]. A similar model has also been introduced [17], but its validation lacked detail on the actual fluid dynamics.

Particle image velocimetry (PIV) is a well-established non-intrusive technique for the measurement of a velocity field. The displacement of small tracer particles added to a fluid is recorded by high-speed imaging and analysed using statistical correlation methods to extract the velocity distribution in the examined plane [18]. MicroPIV is a modification of PIV to access the small scales of microfluidic devices. High-speed imaging experiments have been performed in the past to visualize and analyse the action of endodontic irrigation systems inside simulated root canals [19, 20]. However, this method has not been applied yet to the study of needle irrigation in root canals.

The aim of this study was twofold: (i) to compare the results of a CFD simulation of the irrigant flow within a prepared root canal, during final irrigation with a syringe and needle, to high-speed visualizations, theoretical calculations and the results of a previous study [21]; (ii) to evaluate the effect of off-centre positioning of the needle inside the root canal, as it is likely to occur during the experimental part of this study and also under clinical conditions.

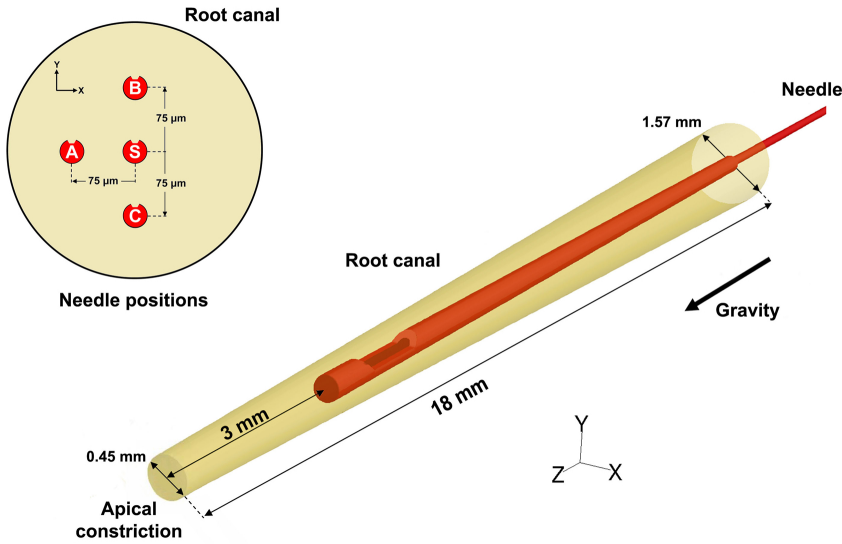


**Figure 3.1:** Geometrical characteristics of the computational fluid dynamics root canal model used. Off-center positions studied are depicted in the upper left circle.

## 3.2 Materials and methods

### 3.2.1 CFD setup

The root canal was simulated as a geometrical frustum of a cone (the portion of a cone which lies between two parallel planes cutting the solid). The apical constriction and apical foramen were not simulated because they were not within the focus of this study. The apical terminus of the root canal was simulated as an impermeable wall. The length of the root canal model was 18 mm, the diameter was 1.57 mm at the canal orifice and 0.45 mm (ISO size 45) at the most apical point (6.2% taper) (Fig. 3.1). This shape is consistent with the root canal model used in the experimental setup.

The needle was modelled using the 30G KerrHawe Irrigation Probe (KerrHawe SA, Bioggio, Switzerland) as a reference, similarly to a previous study (Boutsioukis et al. 2009). The external and internal diameter and the length were defined as  $D_{ext} = 320 \mu\text{m}$ ,  $D_{int} = 196 \mu\text{m}$ ,  $L = 31 \text{ mm}$ , respectively. The needle was fixed and centred within the canal, 3 mm short of the working length (Fig. 3.1 case S). This setup allows for the evaluation of irrigant flow apically to the needle tip, the most challenging area for irrigation. Three additional cases were modelled to study the effect of off-centre positioning of the needle with respect to the longitudinal axis of the root canal. The needle was assumed to be displaced  $75 \mu\text{m}$  away from the

longitudinal axis towards the negative x, positive y or negative y direction (Fig. 3.1 cases A, B and C respectively). In all cases, the needle remained parallel to the longitudinal axis of the root canal.

The pre-processor software Gambit 2.4 (Fluent Inc., Lebanon, NH, USA) was used to build the 3-D geometry and the mesh. No symmetry assumption was made for the flow domain. A hexahedral mesh was constructed and refined near the walls and in the areas where high gradients of velocity were anticipated, such as near the needle outlet. A grid-independency check was performed to determine the minimum number of computational cells required for a grid-independent flow simulation and ensure reasonable use of computational resources. The final mesh consisted of 587 417 cells (mean cell volume  $2.6487 \cdot 10^{-5} \text{ mm}^3$ ). A similar mesh was used for all cases studied.

No-slip boundary conditions were applied to the walls of the root canal and that of the needle, under the hypothesis of rigid, smooth and impermeable walls. The fluid flowed into the simulated domain through the needle inlet and out of the domain through the root canal orifice, where atmospheric pressure was imposed. The canal and the needle were assumed to be completely filled with irrigant. A velocity inlet boundary condition was selected for the inlet of the needle. A flat velocity profile with a constant axial velocity of 8.6 m/s was imposed at the inlet, which is consistent with a clinically realistic irrigant flow rate of 0.26 mL/s through a 30G needle [21]. The irrigant was distilled water, and it was modelled as an incompressible Newtonian fluid with a density  $\rho = 0.998 \text{ g/cm}^3$  and a viscosity  $\mu = 1.0 \cdot 10^{-3} \text{ Pa s}$  (Lide 2005). Gravity was included in the flow field in the direction of the positive z axis.

The commercial CFD code FLUENT 6.3 (Fluent Inc.) was used to set up and solve the problem and to analyse the results. The uncoupled NavierStokes equations which describe the time-dependent, three-dimensional, incompressible flow were solved by an implicit iterative solver. The numerical solution method uses a finite volume approach. An unsteady isothermal flow was assumed; steady-state solutions were obtained first, then used as initial conditions for the unsteady simulations, to avoid transient effects. No turbulence model was used, as the flow under these conditions (Reynolds number  $Re = 1678$  inside the needle lumen) was expected to be laminar [15]. All transport equations were discretized to be at least second-order accurate. A time-step of  $10^{-6} \text{ s}$  was used throughout the calculations, which were carried out for a real flow time of 50 ms for each of the four cases. The convergence criterion of the maximum scaled residuals was set at  $10^{-4}$ . Pressure, velocity and vorticity in selected areas of the flow domain were also monitored to ensure adequate convergence in every time-step. Computations were carried out in a computer cluster (45 dual core AMD Opteron 270 processors) running 64-bit SUSE Linux 10.1 (kernel version 2.6.16). The instantaneous and time-averaged velocity field for selected time-points (case S) were extracted and compared to results obtained in the

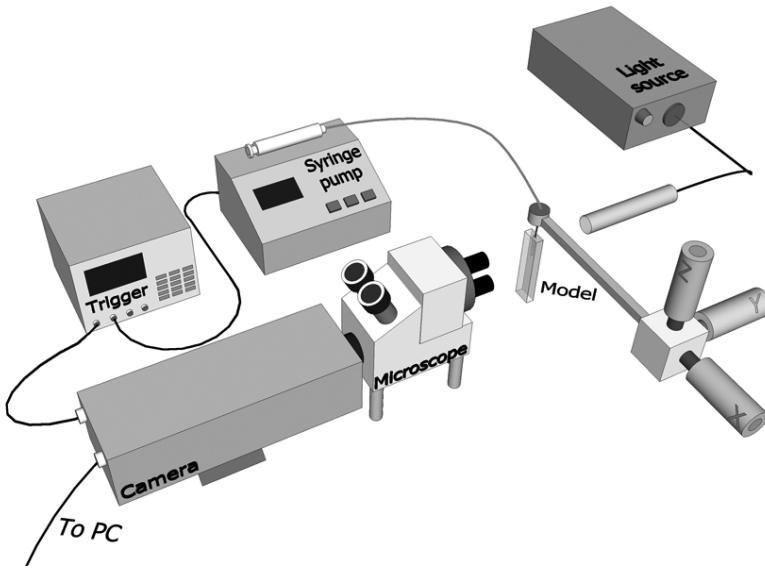


**Figure 3.2:** Schematic diagram of the experimental high-speed visualization setup.

experimental section of this study. The time-averaged velocity field for cases A, B and C was also extracted and compared to each other and to case S. Additional assessment of the validity of the CFD model was attempted through comparison of the theoretical velocity profile inside the needle lumen [22] to the CFD results, 1 mm coronally to the needle outlet, assuming a fully developed laminar flow there. The time-averaged pressure at the needle inlet was also extracted and compared to the results of a previous study [21].

### 3.2.2 Experimental setup

A transparent root canal model was fabricated using poly-dimethyl-siloxane (PDMS) (Sylgard 184, Silicone Elastomer kit; Dow Corning, Coventry, UK). The polymer was mixed at a base:curing agent ratio of 15 : 1. To obtain specific dimensions of the root canal, a modified D-size finger spreader (Dentsply Maillefer, Ballaigues, Switzerland) was used. This instrument has a tip diameter of 0.31 and a 6.2% taper, determined under stereoscopic microscope. A 2.2-mm section from the tip of the spreader was carefully removed to increase the tip diameter to 0.45 mm. The PDMS root canal had a total length of 18 mm. These dimensions match the root canal as simulated in the CFD model.

For the high-speed imaging, a high-speed camera (Shimadzu HPV-1; Shimadzu Corp., Kyoto, Japan), capable of recording up to  $10^6$  frames/s, was attached to an

optical microscope (BX-FM; Olympus Corp., Tokyo, Japan) (Fig. 3.2). Immediately before use, the model was rinsed thoroughly with 95% ethanol and left to dry, and then fitted in front of the microscope. A side-vented endodontic needle (30G KerrHawe Irrigation Probe, KerrHawe SA, Bioggio, Switzerland) was attached to a Luer-Lock T-connector, which was mounted on a micrometric translation stage (9067M; New Focus, San Jose, CA, USA and M-044.00; Physik Instrumente, Karlsruhe, Germany) capable of adjusting its position in three directions and tilting around two axes. This setup ensured accurate and stable positioning of the needle inside the model. In addition, a rubber stop was applied to indicate the desired depth of penetration of the needle. The needle was placed 3 mm from the apical terminus of the canal and at the best centre position possible.

Two different views of the needle were studied: side view, with the needle outlet at right angle to the lens, and front view, with the outlet oriented towards the objective lens. An  $1.25\times$  objective lens (PlanApoN  $1.25\times$ ; Olympus Corp.) was used to assist positioning of the needle with accuracy, while a  $10\times$  objective lens (MPlanN  $10\times$ ; Olympus Corp.) was used for image recording. The microscope was focused at the centre plane of the canal, guided by the major perimeter of the needle. The depth of focus of the objective was calculated to be approximately  $120\ \mu\text{m}$  [23] which indicates that the particle movement captured was limited to a shallow plane with thickness of approximately one-fifth of the root canal diameter and 10 times the particle diameter. This depth was considered a sufficient experimental approximation to the infinitely shallow plane used by the CFD software to report velocity distribution. Light was provided for bright-field imaging by a high-intensity continuous cold-light source (ILP-1; Olympus Corp.).

The T-connector was further connected through a thick-walled Teflon tubing to a 20-mL disposable syringe with a Luer-Lock connector (Plastipak; Becton Dickinson, Oxford, UK). A programmable precision syringe pump (NE-1010; New Era Pump Systems, Wantagh, NY, USA) was used to deliver irrigant at the precise rate of 0.26 mL/s, to maintain irrigation consistency. Distilled water at room temperature was used as an irrigant. Hollow-glass spherical particles (mean diameter  $11\ \mu\text{m}$ , mean density  $1.1 \cdot 10^3\ \text{kg/m}^3$ ) (Spherical; Potters Industries, Barnsley, UK) were added to the irrigant at a concentration of 10 mg/mL to allow visualization of the flow inside the simulated root canal. The syringe was filled prior to each experiment with special care taken to avoid insertion of air into the system. The fluid was stirred continuously by a custom-made magnetic stirrer to avoid precipitation of particles. Between successive recordings, the needle, connecting tube, T-connector and model were flushed with distilled water to prevent particle accumulation.

The camera was triggered 4 s after the start of the syringe pump, using a pulse and delay generator (BNC-565; Berkeley Nucleonics, San Rafael, CA, USA). Images were recorded at a speed up to 250 000 frames/s at three different parts of the

experimental root canal model for both the front view and the side view (Figs 3.3 and 3.4, positions IIII). The exposure time was set to one-eighth of the interframe time, which corresponded to 500 ns for the highest frame rate. Recordings were transferred to MATLAB (The Mathworks, Natick, MA, USA) and were analysed using in-house built PIV code. Several frames from a single recording were ensemble-averaged before being analysed. The resulting velocity fields in the two orthogonal planes (side view and front view) were compared to the CFD results regarding velocity direction and magnitude.

### 3.3 Results

#### 3.3.1 Validation of the CFD model

The flow field within the canal revealed an unsteady behaviour, as determined by both the CFD simulation (Fig. 3.5, Movie 1) and the PIV experiments. The normalized standard deviation of the time-averaged velocity magnitude, which is a measure of the unsteadiness of the flow, was calculated in the range 0.001 - 10 times the local time-averaged velocity, with very few points reaching a value of 500.

Comparison of the velocity magnitude and vectors (Figs 3.3 and 3.4) in the z-y plane (side view) and z-x plane (front view) between CFD calculations and experiments revealed a close agreement in terms of velocity magnitude and vortex location and size. The direction of the vortices near the boundary of adjacent positions was also in good agreement (Fig. 3.4IIII), even though the results for each positions were based on separate recordings. The main characteristic bands occurred in regions where the velocity was high. The vector images resulting from both the CFD and the experiments (Fig. 3.4) showed a number of Moffatt vortices (Moffatt 1964), which were driven by the flow from the needle outlet around the tip.

To test the inflow conditions, the theoretical and the CFD velocity profile inside the needle lumen were compared (Fig. 3.6). The two profiles were almost identical with differences smaller than 1%.

The time-averaged pressure at the inlet of the needle for the period  $t = 050$  ms as calculated by the CFD model was  $244.0 \pm 0.5$  kPa. The average intrabarrel pressure recorded close to the needle inlet for the same irrigant flow rate during a previous study [21] was  $232.2 \pm 23.6$  kPa.

#### 3.3.2 Effect of off-centre positioning of the needle

Comparison of the velocity magnitude in the z-y plane (side view) and z-x plane (front view) as calculated by the CFD model for cases A, B and C showed that small displacements from the central position may have a limited effect on the flow field (Fig. 3.7). Some differences in magnitude were found near the apical terminus of the

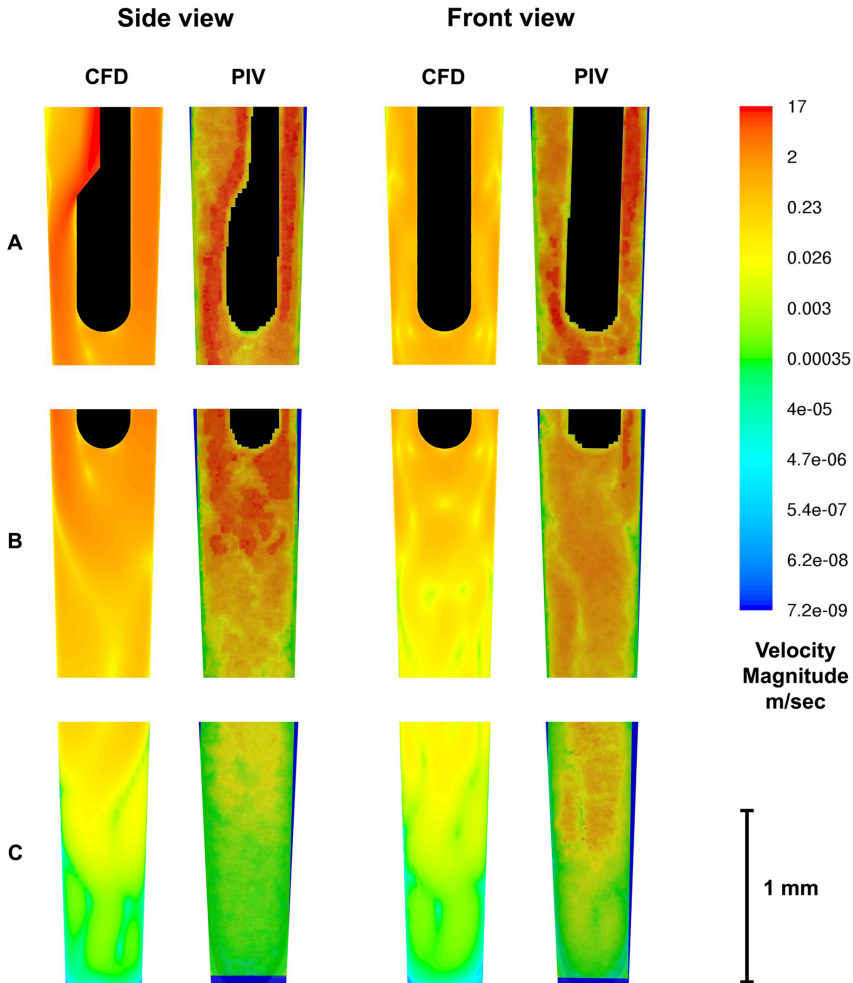


**Figure 3.3:** Contours of velocity magnitude along the  $z$ - $y$  (sideview) and  $z$ - $x$  (front view) plane of the domain for case S. Lower velocity regions, like the center of vortices, show up as lighter areas. A good agreement between computational fluid dynamics and particle image velocimetry (PIV) results is evident in most of the domain studied. PIV results close to the wall of the root canal (dark blue stripes) are not considered accurate due to inherent limitations of the PIV method. The needle wall is coloured black.

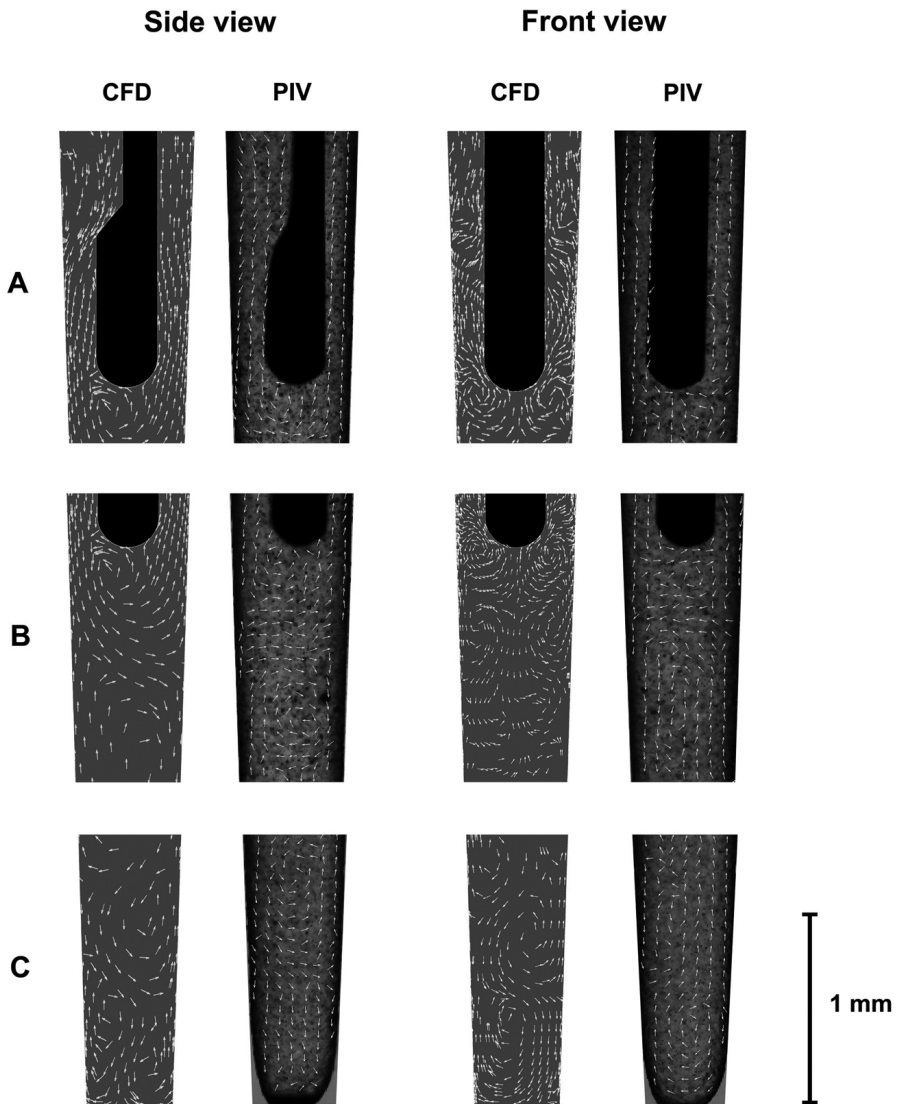


**Figure 3.4:** Velocity vectors along the  $z$ - $y$  (side-view) and  $z$ - $x$  (front view) plane of the domain for case S. Only the direction and not the magnitude of the velocity is depicted. A good agreement between computational fluid dynamics and particle image velocimetry (PIV) results regarding the direction of velocity is shown. The needle wall is coloured black.



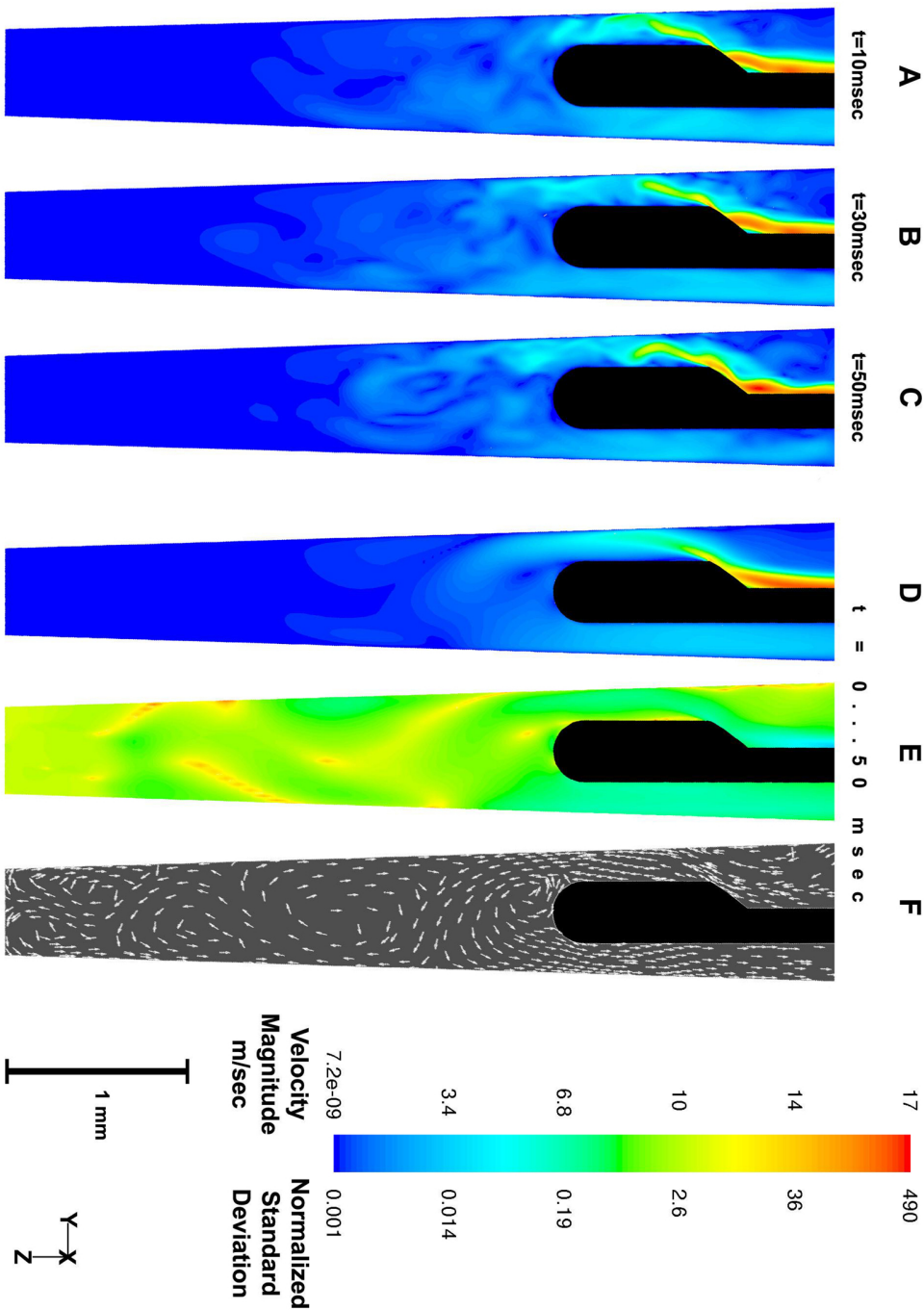


**Figure 3.5:** Overview of the results of the CFD calculations for case S. (a-c) Contours of instantaneous velocity magnitude at  $t = 10, 30$  and  $50$  ms respectively. (d) Time-averaged velocity magnitude (e). Standard deviation of the time-averaged velocity magnitude normalized with the time-averaged velocity magnitude (f). Time-averaged velocity vectors. The needle wall is coloured black. (Case S, z-y plane).

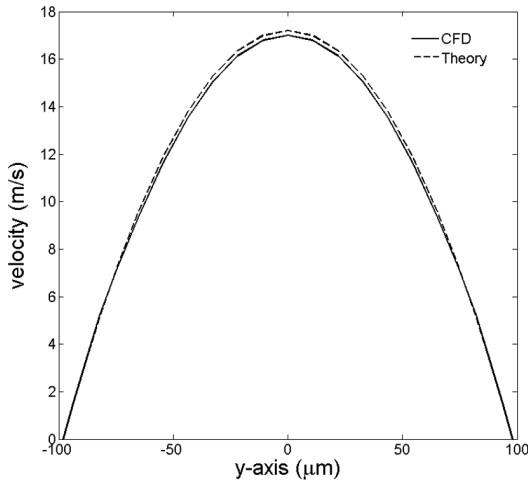


**Figure 3.6:** Comparison of the theoretical velocity profile inside the needle lumen to the CFD results, 1 mm coronally to the needle outlet, assuming a fully-developed laminar flow at that point. The two profiles are almost identical with differences smaller than 1%.

canal, where the increase in velocities was up to two orders of magnitude compared to case S.

Comparison of the velocity vectors in the z-y plane (side view) and z-x plane (front view) for different needle positions (Fig. 3.8) revealed that the flow pattern in the z-y plane was not greatly affected by off-centre positioning of the needle. Most of the vortices formed in case S also appeared in cases A, B and C in almost identical positions. In the z-x plane, the symmetry that was observed close to the needle tip in cases S, B and C was absent in case A. This resulted in a flow pattern similar to the one observed during the experiments, where the needle was slightly displaced from the centre of the canal (Fig. 3.4, Front view, PIV, I).

### 3.3.3 Discussion

In this chapter, irrigant flow inside a root canal was evaluated by a previously published CFD model that was modified, and a microPIV setup. Comparison of the detailed flow field resulting from CFD and PIV was performed to assess the validity of the CFD model. A simple root canal geometry resembling the prepared root canal of a maxillary central incisor was used, to facilitate manufacturing of an accurate PDMS model for the experiments. The geometrical complexity of a CFD model is only limited by the intentions of the researcher and the computational resources available, in contrast to the manufacturing of root canals in resin blocks or PDMS. Clinically realistic CFD models of arteries and respiratory tracts have already been constructed using MRI scans [14, 24, 25]. An additional advantage of CFD modelling is the ability to create strictly standardized root canals regardless of the desired complexity, and evaluate the isolated effect of different parameters on the flow. However,

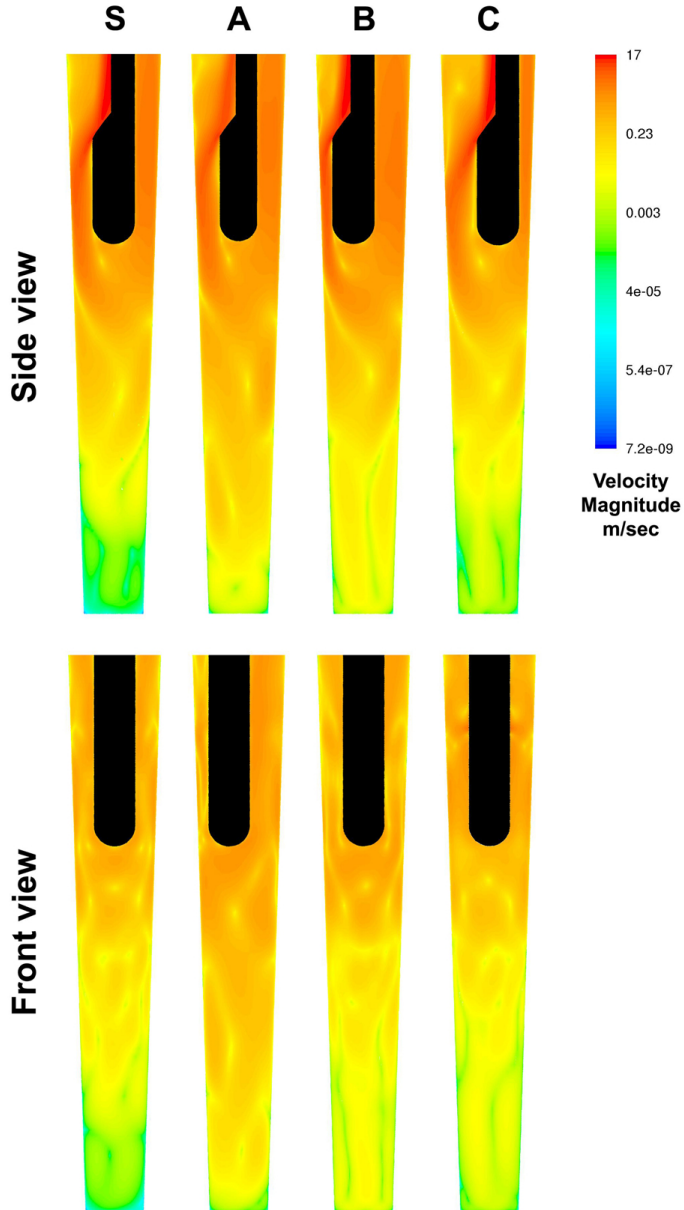


**Figure 3.7:** Time-averaged velocity magnitude along the  $z$ - $y$  (side-view) and  $z$ - $x$  (front view) plane of the domain for cases S, A, B and C, according to CFD calculations. Small displacements from the central position had a limited effect on the velocity magnitude. The needle wall is coloured black.

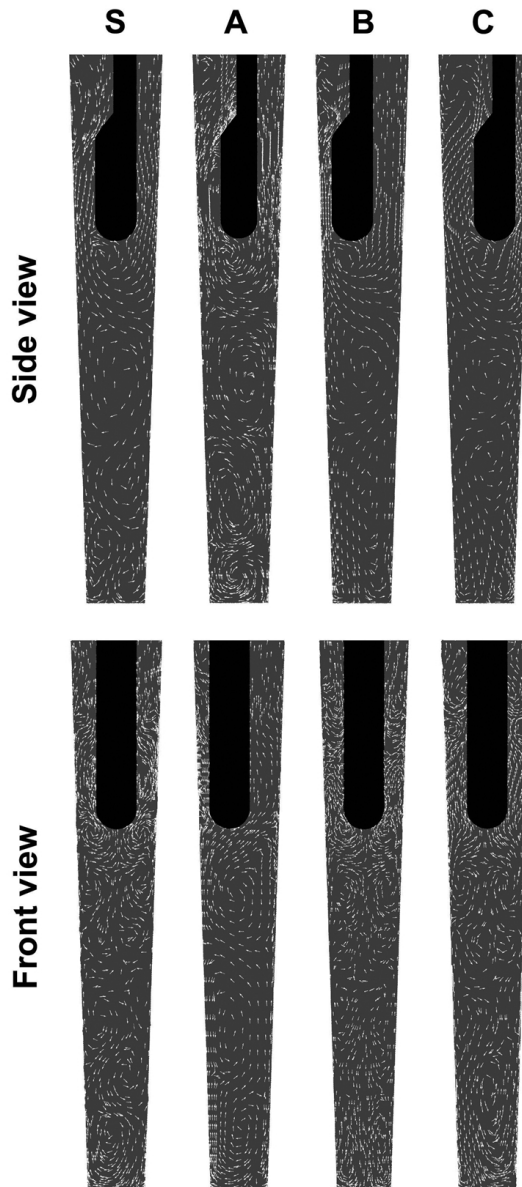


**Figure 3.8:** Velocity vectors along the  $z$ - $y$  (side-view) and  $z$ - $x$  (front view) plane of the domain for cases  $S$ ,  $A$ ,  $B$  and  $C$ , according to CFD calculations. Only the direction and not the magnitude of the velocity is depicted. The flow pattern in the  $z$ - $y$  plane is not affected by off-center positioning of the needle. The symmetry observed in the  $z$ - $x$  plane close to the needle tip in cases  $S$ ,  $B$  and  $C$  is absent in case  $A$ . The needle wall is coloured black.

only one parameter should be modified and evaluated in each set of CFD simulations and the overall complexity of the model should be gradually increased during this procedure. In this way, a clear correlation between each change in the geometry and the resulting change in the flow can be established.

In the current CFD model, no assumption was made about the symmetry of the flow inside the root canal, in contrast to an earlier study [15]. It can be speculated that this assumption is valid for low velocities, but there is an increasing possibility of symmetry-breaking downstream of a sudden expansion of the flow domain such as the area of the root canal near the needle outlet as the velocity of the fluid increases, even for a steady flow rate [26, 27]. This modification is considered to increase the accuracy and validity of the model.

In addition, the flow was simulated in an unsteady, time-dependent manner, which more closely resembles real conditions. In both the computational and experimental elements of this study it was confirmed that the flow of the irrigant under the conditions described is unsteady (Fig. 3.5, Movie 1). The flow parameters were averaged over a time period of 50 ms to distinguish the most stable characteristics of the flow, which are relevant for replacement of irrigant, thereby probably omitting transient flow characteristics. This modification is also considered to increase the accuracy and validity of the model. Nevertheless, significantly more computational resources were required to make these modifications possible, which were not available during the previous study [15]. Comparison of the previous study with the time-averaged velocities from the current unsteady simulation revealed small differences.

The internal diameter of the needle used has been reported to be  $168\ \mu\text{m}$  [28]. However, the presence of irregularities on the internal surface has also been reported to hinder accurate measurements of the internal diameter and increase the uncertainty [28]. In this study, the methodology described by Boutsoukis et al. (2007b) was combined with measurement of the pressure drop across the needle for known flow rates (data not shown), according to the methodology of another study [21], to determine the internal needle diameter as accurately as possible. Results of these preliminary experiments showed that the internal diameter should be adjusted to  $196\ \mu\text{m}$  in the CFD model. Close agreement of the CFD results on pressure drop along the needle with a previous experimental study [21] and with the preliminary experiments conducted revealed that the determined internal diameter was correct.

The release of neutrally buoyant tracer particles within the flow is a procedure that aids enhanced visualization of the flow pattern. Such particles are expected to follow the path of the fluid with accuracy [11, 18]. A conventional PIV setup makes use of a laser sheet to illuminate fluorescent tracer particles to visualize and analyse the flow. In the present microPIV setup, an objective with a small depth of focus and a continuous light source were used instead of a laser sheet. The main advantage of this setup was that the recording speed was not restricted by the amount of light

emitted from fluorescent particles. Therefore, recordings could be made both at high recording speeds and for a prolonged time (100 frames). A prolonged recording time allowed for ensemble averaging, which reduces the noise in the individual PIV recordings [18].

Nevertheless, according to the CFD results, velocities up to 17 m/s appeared near the needle outlet but such high velocities were rarely identified in the PIV results. It is possible that only a few particles acquired such high velocities and because of ensemble averaging performed by the PIV code, calculated velocities appeared lower. Manual tracking of individual particles revealed that velocities at least up to 13 m/s were indeed present in the experiments. Moreover, measured velocities close to the wall appeared to be lower than the computed velocities. This can be attributed to an inherent limitation of PIV, which uses an interrogation area to calculate the velocity, instead of a single point [18]. In the immediate vicinity of the wall, the interrogation area is partly comprised of the flow domain and partly of the wall. Therefore, averaging over this area is expected to reduce the average velocity [29].

The assumption of smooth walls of both the root canal and the needle in the CFD model is inconsistent with real dentine anatomy and to the findings of a previous study [28]. Wall roughness is expected to have a limited effect on pressure drop as long as the flow remains laminar [30], but it may induce vorticity or even turbulence in the flow [31]. Scanning electron microscopy examination of the PDMS model used in the experiments revealed that its surface presented irregularities 36  $\mu\text{m}$  wide (data not shown), which were in the order of magnitude of the dentinal tubule orifices. However, no turbulence was noticed during the experiments with these models. Furthermore, the surface of PDMS is naturally hydrophobic [32]. Yet, PDMS is the most widely used material in the construction of microfluidic devices. During a pilot study, oxygen plasma was used to modify the surface of PDMS models and increase its hydrophilicity, as suggested in the literature [32]. However, no measureable difference was noted in the flow as a result of this treatment and it was therefore excluded from the main experimental protocol.

Both in the CFD model and in the experiments, distilled water was used as irrigant. NaOCl solutions used during routine endodontic treatment have physical properties very similar to those of water [33, 34], and should therefore exhibit the same flow characteristics. Furthermore, significant experimental disadvantages, such as oxidation of metal parts and crystal precipitation were noted during a previous study during which NaOCl was used [21]. In addition, NaOCl might affect the surface of the PDMS model.

In spite of the precise alignment of the needle inside the PDMS model, the possibility of small displacements from the central position could not be excluded. Such displacements are also expected during a clinical irrigation procedure. Therefore, the effect of such small displacements on the flow inside the root canal model was stud-

ied by the additional CFD cases (A, B and C). Off-centre positioning may affect the overall flow pattern. Positioning the needle closer to canal wall generally resulted in slightly increased velocities apically to the needle tip, most noticeably near the apical terminus of the canal (Fig. 3.7). The more limited space available laterally to the needle in these cases possibly resulted in this increase in velocities. However, it is doubtful whether these differences can have a significant effect on clinically relevant parameters such as irrigant replacement, shear stress on the canal wall and irrigant pressure at the apical foramen.

The agreement between CFD and PIV results regarding velocity vectors in the front view was not exact (Fig. 3.4). This could be attributable to small displacements of the needle from the central position during experiments. Moreover, the highest velocities and most consistent flow pattern occurred in the z-y plane, which makes the experimental results in the z-x plane more dependent on the focal position of the microscope. A detailed description of the flow and its relevance to root canal debridement and disinfection was not included in this study, as the aim was to assess the validity of the CFD model. A validated CFD model can be used to predict the flow not only in the domain used for validation but also in similar and more complicated flow domains, which is an additional advantage over experimental methods. The absence of turbulence that was verified in both CFD and experimental sections of this study (Reynolds number of ca. 1500) provides further confidence about the validity of the CFD model. This CFD model will be used in subsequent studies to evaluate the effect of various factors on the fluid dynamics during root canal irrigation.

### 3.4 Conclusions

High-speed imaging experiments together with PIV analysis of the flow inside a simulated root canal have shown a good agreement with the velocity field as calculated by a CFD model, even though the flow was unsteady. Therefore, the CFD model is able to predict reliably the flow in similar domains. Small lateral displacements of the needle inside the canal had a limited effect on the flow.

### References

- [1] M. Haapasalo, U. Endal, H. Zandi, and J. Coil, "Eradication of endodontic infection by instrumentation and irrigation solutions", *Endodontic Topics* **10**, 77–102 (2005).
- [2] J. Ingle, V. Himel, and C. Hawrish, "Endodontic cavity preparation", *Endodontics* 405–570 (2002).
- [3] O. Peters, "Current challenges and concepts in the preparation of root canal systems: A review", *Journal of Endodontics* **30**, 559–567 (2004).

- [4] E. Senia, F. Marshall, and S. Rosen, "The solvent action of sodium hypochlorite on pulp tissue of extracted teeth", *Oral Surgery, Oral Medicine, Oral Pathology* **31**, 96–103 (1971).
- [5] J. VandeVisse and J. Brilliant, "Effect of irrigation on the production of extruded material at the root apex during instrumentation", *Journal of Endodontics* **1**, 243–246 (1975).
- [6] Z. Ram, "Effectiveness of root canal irrigation", *Oral Surgery, Oral Medicine, Oral Pathology* **44**, 306–312 (1977).
- [7] A. Druttman and C. Stock, "An in vitro comparison of ultrasonic and conventional methods of irrigant replacement.", *International Endodontic Journal* **22**, 174–178 (1989).
- [8] F. Kahn, P. Rosenberg, and J. Gliksberg, "An in vitro evaluation of the irrigating characteristics of ultrasonic and subsonic handpieces and irrigating needles and probes.", *Journal of Endodontics* **21**, 277–280 (1995).
- [9] O. Peters and C. Peters, *Pathways of the Pulp*, chapter Cleaning and shaping of the root canal system, 9th edition (Mosby, St. Louis, USA) (2005).
- [10] M. Zehnder, "Root canal irrigants", *Journal of Endodontics* **32**, 389–398 (2006).
- [11] J. Tilton, "Fluid and particle dynamics", *Perry's Chemical Engineer's Handbook* 6.1–50 (1999).
- [12] A. Arvand, M. Hormes, and H. Reul, "A validated computational fluid dynamics model to estimate hemolysis in a rotary blood pump", *Artificial Organs* **29**, 531–540 (2005).
- [13] A. Yoganathan, K. Chandran, and F. Sotiropoulos, "Flow in prosthetic heart valves: State-of-the-art and future directions", *Annals of Biomedical Engineering* **33**, 1689–1694 (2005).
- [14] D. Steinman, "Image-based computational fluid dynamics modeling in realistic arterial geometries", *Annals of Biomedical Engineering* **30**, 483–497 (2002).
- [15] C. Boutsoukis, T. Lambrianidis, and E. Kastrinakis, "Irrigant flow within a prepared root canal using various flow rates: A computational fluid dynamics study", *International Endodontic Journal* **42**, 144–155 (2009).
- [16] W. Oberkampf and T. Trucano, "Verification and validation in computational fluid dynamics", *Progress in Aerospace Sciences* **38**, 209–272 (2002).
- [17] Y. Gao, M. Haapasalo, Y. Shen, H. Wu, B. Li, N. Ruse, and X. Zhou, "Development and validation of a three-dimensional computational fluid dynamics model of root canal irrigation", *Journal of Endodontics* **35**, 1282–1287 (2009).
- [18] M. Raffel, C. Willert, and J. Kompenhans, *Particle Image Velocimetry*, 2nd edition (Springer, Berlin, Germany) (1998).
- [19] S. D. De Groot, B. Verhaagen, M. Versluis, M.-K. Wu, P. R. Wesselink, and L. van der Sluis, "Laser-activated irrigation of the root canal: cleaning efficacy and flow visualization", *International Endodontic Journal* **42**, 1077–1083 (2009), *See also chapter 13 of this thesis.*
- [20] L.-M. Jiang, B. Verhaagen, M. Versluis, and L. van der Sluis, "Evaluation of a sonic device designed to activate irrigant in the root canal", *Journal of Endodontics* **36**, 143–146 (2010), *See also chapter 9 of this thesis.*



- [21] C. Boutsoukis, T. Lambrianidis, E. Kastrinakis, and P. Bekiaroglou, "Measurement of pressure and flow rates during irrigation of a root canal ex vivo with three endodontic needles", *International Endodontic Journal* **40**, 504–513 (2007).
- [22] P. Kundu and I. M. Cohen, *Fluid Mechanics*, 3rd edition (Elsevier Academic Press, San Diego, CA, USA) (2004).
- [23] C. Meinhart, S. Wereley, and M. Gray, "Volume illumination for two-dimensional particle image velocimetry", *Measurement Science and Technology* **11**, 809–814 (2000).
- [24] C. Xu, S. Sin, J. McDonough, J. Udupa, A. Guez, R. Arens, and D. Wootton, "Computational fluid dynamics modeling of the upper airway of children with obstructive sleep apnea syndrome in steady flow", *Journal of Biomechanics* **39**, 2043–2054 (2006).
- [25] C. Wang, K. Pekkan, D. De Zélicourt, M. Horner, A. Parihar, A. Kulkarni, and A. Yoganathan, "Progress in the cfd modeling of flow instabilities in anatomical total cavopulmonary connections", *Annals of Biomedical Engineering* **35**, 1840–1856 (2007).
- [26] S. Sherwin and H. Blackburn, "Three-dimensional instabilities and transition of steady and pulsatile axisymmetric stenotic flows", *Journal of Fluid Mechanics* **533**, 297–327 (2005).
- [27] T. Mullin, J. Seddon, M. Mantle, and A. Sederman, "Bifurcation phenomena in the flow through a sudden expansion in a circular pipe", *Physics of Fluids* **21** (2009).
- [28] C. Boutsoukis, T. Lambrianidis, and L. Vasiliadis, "Clinical relevance of standardization of endodontic irrigation needle dimensions according to the iso 9626:1991 and 9626:1991/amd 1:2001 specification", *International Endodontic Journal* **40**, 700–706 (2007).
- [29] G. Usera, A. Vernet, and J. Ferré, "Considerations and improvements of the analysing algorithms used for time resolved piv of wall bounded flows", in *Proceedings of the 12th International Symposium on Applications of Laser Techniques to Fluid Mechanics* (Lisbon, Portugal) (2004).
- [30] W. McCabe, J. Smith, and P. Harriott, *Unit Operations of Chemical Engineering*, 7th edition (McGraw-Hill, New York, NY, USA) (2004).
- [31] T. Azuma and T. Hoshino, "Radial flow of a thin liquid film - (5th report, influence of wall roughness on laminar-turbulent transition).", *Bulletin of the JSME* **28**, 1682–1689 (1985).
- [32] D. Bodas and C. Khan-Malek, "Formation of more stable hydrophilic surfaces of pdms by plasma and chemical treatments", *Microelectronic Engineering* **83**, 1277–1279 (2006).
- [33] D. Guerisoli, R. Silva, and J. Pecora, "Evaluation of some physico-chemical properties of different concentrations of sodium hypochlorite solutions", *Brazilian Endodontic Journal* **3**, 21–23 (1998).
- [34] D. Lide, *CRC Handbook of Chemistry and Physics*, 86th edition (CRC Press, Boca Raton, FL, USA) (2005).

## Appendices

### 3.A Supplementary material

*(Online at [http://stilton.tnw.utwente.nl/rootcanalcleaning/Gallery\\_of\\_Irrigant\\_Motion](http://stilton.tnw.utwente.nl/rootcanalcleaning/Gallery_of_Irrigant_Motion))*

Movie 1. Contours of instantaneous velocity magnitude (m/s) along the z-y plane (side view) of the domain for case S ( $t = 0 - 50$  ms), according to CFD calculations. Unsteady behavior of the flow is evident. The needle wall is colored white.



## **Part II**

# **Passive Ultrasonic Irrigation**



# 4

## Oscillation characteristics of endodontic files \*

**Abstract:** The oscillation characteristics of ultrasonically driven endodontic files is investigated, numerically and experimentally. Numerical analysis of the oscillation characteristics of the file, modeled as a tapered, driven rod, shows a sinusoidal wave pattern with an increase in amplitude and decrease in wavelength toward the free end of the file. Measurements of the file oscillation with a scanning laser vibrometer show good agreement with the numerical simulation. The numerical model of endodontic file oscillation can be used to study the oscillation of various file types and the acoustic streaming they induce during passive ultrasonic irrigation.

---

\*Published as: B. Verhaagen, S.C. Lea, G.J. de Bruin, L.W.M. van der Sluis, A.D. Walmsley, M. Versluis, "Oscillation characteristics of endodontic files: numerical model and its validation", *IEEE - Transactions on Ultrasonics, Ferroelectrics and Frequency Control* **in press**

## 4.1 Introduction

A crucial step during a root canal treatment is irrigation, where an antimicrobial fluid is injected into the root canal to eradicate all bacteria from the root canal system. However, the root canal system is geometrically very complex, and bacteria form a strong biofilm, both making it difficult to clean the root canal system completely using the common technique employing a syringe and needle [1, 2].

Agitation of the fluid using an ultrasonically vibrating miniature file has shown a significant improvement in the cleaning efficacy over conventional needle irrigation [3, 4]. This technique has been named ‘Passive Ultrasonic Irrigation’ (PUI), where ‘passive’ implicates an indirect way of cleaning, without contact between file and biofilm. Ultrasound is a well-established technique for cleaning [5], however in the context of root canal irrigation the exact cleaning mechanism, being streaming, cavitation or chemical effects, and their relation to the vibrating file, are not yet fully understood. We therefore study the oscillation characteristics of the vibrating files, both experimentally and numerically, in order to get a better understanding of the file-fluid interaction.

The oscillation of the file generates acoustic streaming of the fluid, of which the velocity  $v$  is related to the displacement amplitude  $y$  of the file by: [6]

$$v \propto \frac{\omega y^2}{R} \quad (4.1)$$

where  $\omega = 2\pi f$  is the oscillation frequency and  $R$  the file radius. The induced streaming will mix fresh irrigant with irrigant that is consumed during the reaction with bacteria, and it exerts a shear stress on the biofilm on the wall. Transient cavitation bubbles, formed at a high oscillation amplitude of the file, can locally enhance the cleaning efficacy of PUI [7]. Ultrasound is also known to enhance chemical reactions during endodontic treatments [8, 9].

The oscillation pattern of dental scalars (for periodontal applications) and some endodontic files have been studied before [10–12], using a fast, non-intrusive optical method (vibrometry) for measuring the oscillation amplitude. While these studies have given valuable information on the oscillation characteristics of these files, a simple, validated model of the oscillation characteristics is still lacking. Such a model could be used for optimization of the file oscillation and induced streaming and to minimize the risk of file fracture.

The vibrating file will be modeled here as a cylinder (or beam, rod) driven at one end, which is well-studied in literature [13, 14], often in the context of oscillating cantilevers in (non-contact) Atomic Force Microscopy [15, 16], but typically those structures are non-tapered. The taper however has a significant influence on the oscillation pattern, but prevents an exact analytical solution [17, 18]. In the numerical model that we will present here, the taper has been included in order to capture and

predict the oscillation amplitudes and characteristics of dental instruments that are in clinical use today. This model is then validated experimentally with a vibrometry system for various endodontic file types. Parameters included here are: file length and diameter, surrounding medium (water or air), confinement of the root canal and driving frequency and amplitude. We also look at the influence of a rubber stopper on the file, the motion perpendicular to the main direction of oscillation and the start-up behaviour of the file, in order to complement the full picture of file oscillations.

## 4.2 Theoretical aspects: On the behaviour of a driven, tapered rod

### 4.2.1 Equation of motion and boundary conditions

The files as used in endodontics will be treated as a solid, non-uniform rod of length  $L$  with decreasing diameter  $r = r_0 - \delta x$  along the length of the rod, with  $x$  the distance from the driven, thick end of the bar and  $\delta$  the taper (see Fig. 4.1). The oscillatory motion of a rod is similar to that of a string, but in the case of a rod the bending and shear moments and damping have to be taken into account [19].

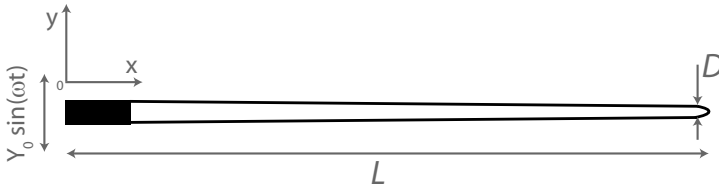


**Figure 4.1:** Definition of the problem of a driven file.

The rod is driven laterally at the thick end by a periodic force of frequency  $\omega = 2\pi f$ ; the amplitude at the driven end is  $y(x=0, t) = Y_0 \sin(\omega t)$ . The driving amplitude  $Y_0$  can be obtained from experiment. The thin end of the file ( $x = L$ ) is allowed to oscillate freely.

As the bar has a non-uniform diameter along the file, both its cross-section  $S = \pi r^2$  and its radius of gyration  $\kappa = \frac{r}{2}$  change with distance along the file:

$$S(x) = \pi(r_0 - \delta x)^2 \quad (4.2)$$

$$\kappa^2(x) = \frac{1}{4}(r_0 - \delta x)^2. \quad (4.3)$$

The one-dimensional equation of motion for the file, without damping, is given by: [19]

$$\frac{1}{S(x)} \frac{\partial^2}{\partial x^2} \left( S(x) \kappa^2(x) \frac{\partial^2 y(x, t)}{\partial x^2} \right) = -\frac{\rho}{Q} \frac{\partial^2 y(x, t)}{\partial t^2} \quad (4.4)$$



where  $\rho$  (density) and  $Q$  (Young's modulus) are material properties.

Four boundary conditions are needed, two at  $x = 0$  (driven end) and two at  $x = L$  (free end). At  $x = 0$  the amplitude is equal to the driving amplitude and the first spatial derivative of the amplitude is 0, because the bar is considered 'clamped' at its attachment point.

$$y(x = 0, t) = Y_0 \quad (4.5)$$

$$\left. \frac{\partial y(x, t)}{\partial x} \right|_{x=0} = 0. \quad (4.6)$$

At the free end (the tip), both the second and third spatial derivatives equal 0, because there can be no moment or shear stress.

$$\left. \frac{\partial^2 y(x, t)}{\partial x^2} \right|_{x=L} = 0 \quad (4.7)$$

$$\left. \frac{\partial}{\partial x} \left( S(x) \kappa^2(x) \frac{\partial^2 y(x, t)}{\partial x^2} \right) \right|_{x=L} = 0. \quad (4.8)$$

which for a sharp edge at  $x = L$  simplifies to

$$\left. \frac{\partial^3 y(x, t)}{\partial x^3} \right|_{x=L} = 0 \quad (4.9)$$

Solving (4.4) with the given boundary conditions gives the oscillation amplitude for a driven rod at each location  $x$ . If the rod is not tapered, there is an analytical solution, given by: [19]

$$\begin{aligned} \frac{1}{A} y(x) = & \cos(\mu x) + \frac{1}{2} \left( 1 + \frac{\sin(\mu L) \sinh(\mu L)}{1 + \cos(\mu L) \cosh(\mu L)} \right) (\cosh(\mu x) - \cos(\mu x)) \\ & - \frac{1}{2} \frac{\cos(\mu L) \sinh(\mu L) + \sin(\mu L) \cosh(\mu L)}{1 + \cos(\mu L) \cosh(\mu L)} (\sinh(\mu x) - \sin(\mu x)). \end{aligned} \quad (4.10)$$

with

$$\mu^4 = \frac{\rho \omega^2}{Q \kappa^2} \quad (4.11)$$

The presence of a taper makes the cross-section  $S(x)$  non-uniform along  $x$ ; an approximate analytical solution to equation 4.4 can be obtained using a Rayleigh-Ritz technique [18], however, as further on described, real endodontic files also have a cylindrical section near its driving end. Therefore not only the cross-section but also the taper is non-uniform, which makes finding an analytical solution to (4.4) a tedious task. Here we therefore solve the equation of motion numerically. Details on the fully explicit discretization are given in Appendix A. The numerical solution is verified with the analytical solution (14.4) for a non-tapered, driven rod.

### 4.2.2 Eigenfrequency

The files should be driven at a resonance mode in order to obtain the highest oscillation amplitude. The fundamental eigenfrequency of a non-tapered rod is given by: [20]

$$f_0 = \frac{K_n}{2\pi} \sqrt{\frac{Q\kappa^2}{\rho L^4}} \quad (4.12)$$

with  $K_n$  a constant where  $n$  refers to the mode of vibration. For the first 5 modes,  $K_n = 3.52, 22.0, 61.7, 121, 200$ .

With this equation the eigenfrequency of a circular, stainless steel rod of constant diameter  $150 \mu\text{m}$  and length  $25 \text{ mm}$  can be calculated to be  $170.8 \text{ Hz}$ . This rod is a basic model for real endodontic files, for which the eigenfrequency needs to be determined numerically by applying a quadratic displacement  $y_0(x) \propto x^2$  as initial condition and allowing the file to oscillate freely (without driving). Tracking the displacement of the tip of the file allows for an estimation of the eigenfrequency of the file.

### 4.2.3 Damping

The oscillation of the file is damped due to material damping and interaction with the surrounding fluid. The damping force on the file due to the surrounding fluid is the sum of three forces: drag, added mass and history (or Basset) force [21]. These terms may have a significant influence on the file oscillation in water; however, in air the contribution from the damping forces can be neglected.

The drag force is calculated from:

$$D_{drag} = C_D \frac{1}{2} \rho \left( \frac{\partial y}{\partial t} \right)^2 A \quad (4.13)$$

The drag is calculated at every point along the cylinder, as the radius and velocity are position-dependent.  $A = A(x)$  is the front-facing area,  $C_D$  is the drag coefficient which is dependent on the cross-sectional shape and the Reynolds number. The Reynolds number is defined as the ratio of inertial to viscous forces:

$$Re = \frac{\rho v 2R}{\mu_f} \quad (4.14)$$

(with  $\mu_f$  the viscosity of the fluid) and is typically  $O(10^2)$  for ultrasonically oscillating endodontic files.

The added mass force is related to the acceleration of the file:

$$D_{added\ mass} = C_{MP} \rho \frac{\partial^2 y}{\partial t^2} V \quad (4.15)$$

$V = V(x)$  is the local volume of the file and changes with distance along the file.  $C_M$  is the added mass coefficient and depends on the cylinder diameter and the oscillation frequency [21].

The history force takes into account the details of the flow around the file and how that flow affects the drag. This term therefore requires knowledge of the complete flow field around the file, which is not known at this stage. However, for the Reynolds numbers of  $O(10^2)$  in the present study, the contribution of the history force will only be small [22].

With these three damping terms, the one-dimensional equation of motion (4.4) becomes non-linear and cannot be solved any more with the current explicit discretization technique. Nevertheless, the presented model without damping can be used to study file oscillation characteristics in air, and comparison with experiments in a liquid can reveal the influence of the damping terms.

#### 4.2.4 Structural properties of real endodontic files

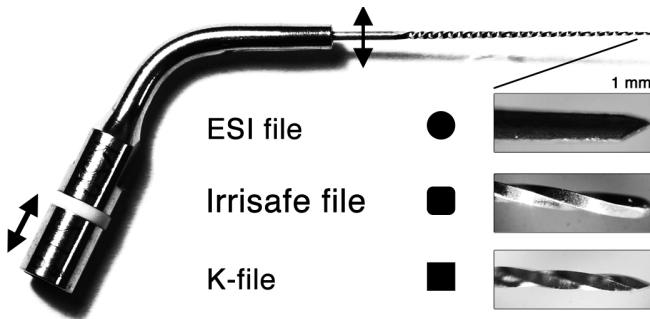
The cross-section of the file determines the surface area  $S$  and radius of gyration  $\kappa$ . The radius of gyration is used in predicting buckling behaviour: a material will buckle easiest in the direction of lowest radius of gyration; a cylinder is the strongest shape because it has the same radius of gyration in every direction [20].

The radius of gyration can be calculated from:

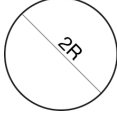
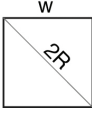
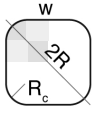
$$\kappa = \sqrt{\frac{I}{S}} \quad (4.16)$$

where  $I$  is the area moment of inertia, a measure of the spreading of the area around the central axis:

$$I = \int_S y^2 dS. \quad (4.17)$$



**Figure 4.2:** Photograph of a K-file, with microscopic photos (inserts) of the 1 mm from the tip for the ESI015 file, Irrisafe file and K-file.

	Geometry	Cross-sectional area $S$	Radius of gyration $\kappa$
ESI file	 radius $R$	$\pi R^2$	$\sqrt{\frac{\int_0^R \int_0^\pi r^2 r d\theta dr}{\pi R^2}} = \frac{R}{2}$
K-file	 sides $w = \frac{2R}{\sqrt{2}}$	$w^2$	$\sqrt{4 \frac{\int_{-w/2}^{w/2} \int_{-w/2}^{w/2} x^2 dx dy}{w^2}} = \frac{w}{\sqrt{12}}$
Irrisafe	 sides $w = \frac{2R}{\sqrt{2}}$ corner radius $R_c = \frac{w}{4}$	$w^2 - (4R_c^2 - \pi R_c^2)$ $\approx 0.95w^2$	$\sqrt{\frac{(\frac{w}{4})^4 (20 + \frac{\pi}{4})}{0.95w^2}}^{(1)}$

**Table 4.1:** Structural properties of real endodontic files with specified diameter  $D = 2R$

$y$  is here the distance from the centre of the object in the direction of interest. Table 4.1 gives the cross-sectional area and radius of gyration for three typical endodontic files: ESI files (circular cross-section), K-files (square cross-section) and Irrisafe files (square cross-section with rounded corners).

The K-files and Irrisafe files have a square cross-section that is twisted along the length of the file, creating flutes with a spacing of  $\theta$  (in mm/90°), see Fig 4.2. Rotation around the axis (with angle  $\beta$ ) results in a change in area moment of inertia (and consequently the resistance to buckling):

$$I^* = I + I_{xy} \sin 2\beta \tag{4.19}$$

<sup>(1)</sup> In order to calculate the radius of gyration of the Irrisafe file, the cross-section has to be split up into multiple sections and the parallel axis theorem for the area moment of inertia has to be used:

$$I_{total} = \sum_{k=I}^{IV} I_k = I_{cm} + d^2 A \tag{4.18}$$

where  $k$  indicates the separate regions,  $I_{cm}$  the area moment of inertia of the region about an axis passing through its center of mass, and  $d$  the distance from the original axis. The rounded-square cross-section can be split up into three squares with sides  $\frac{w}{4}$  and a quarter of a circle with radius  $R_c$  (indicated with shaded areas), resulting in the equation for the radius of gyration as given in Table 4.1.

where  $I_{xy}$  is the product moment of inertia, defined as:

$$I_{xy} = \int_A xy dA \quad (4.20)$$

However, for symmetric cross-sectional shapes like a circle or a square, the product moment of inertia is zero, therefore a rotation around the axis does not cause a change in area moment of inertia. The damping, however, does change for the files with (rounded) square cross-section, as the drag is related to the area facing the direction of oscillation.

### Material properties

The exact material properties of the endodontic files are not known, therefore literature values for the density and Young's modulus have been used in the simulations. The K-files and Endosonore files are made of stainless steel, having a density of  $\rho = 7750 \text{ kg/m}^3$  and Young's modulus of  $Q = 200 \cdot 10^9 \text{ N/m}^2$ . The ESI file is made of a nickel-titanium alloy (NiTi, also known as Nitinol [23]), creating a flexible file, with density  $\rho = 6400 \text{ kg/m}^3$  and Young's modulus of  $Q = 120 \cdot 10^9 \text{ N/m}^2$  (Austenitic phase).

### Geometrical notes

The endodontic files have a taper of typically 2%, up to 16 mm from the tip; the remainder of the file  $L_C$  is cylindrical (with diameter  $D_C$ ) and non-tapered. Modeling these geometrical characteristics in detail is necessary because they affect the numerical result significantly.

## 4.3 Experimental setup

The oscillation characteristics of 10 endodontic files were measured using a scanning laser vibrometer (OFV056, Polytec, Waldbronn, Germany), sampling at 1.5 MHz and averaging three measurements at each of the 50 points along a file. These points were chosen such as to have maximum reflection, which in the case of files with square cross-section only occurred when the flute faced the vibrometer. At the tip of the file, it was difficult to get a good reflection as the file diameter there is of the same size as the vibrometers spot size (100  $\mu\text{m}$  in diameter).

The files were driven by commercial endodontic devices. The K-files and IR-RIsafe files were driven with a Suprasson P-Max device (Satelec Acteon, Merignac, France) at power setting 'Green 5', 'Yellow 5' or 'Blue 5' (listed with increasing power); the ESI and Endosonore files were driven with a miniPiezon device (EMS, Nyon, Switzerland) at power setting 1 or 2. The vibrometer was synchronized to

the driving signal; the driving frequency was calculated by the vibrometer system software with a resolution of 125 Hz.

For the part of the study where the influence of the driving frequency was studied, three customized hand pieces (same piezo elements, but different masses added) with resonant frequency at 20, 30 or 40 kHz were used, driven with a sine wave of the appropriate frequency which was generated by an arbitrary waveform generator (33220A, Agilent, Santa Clara, California, United States) and amplified with an audio amplifier (TA-FB740R, Sony, Tokyo, Japan). The exact resonance frequency of the combined piezo-file system was obtained by finding the frequency at which the current to the hand piece was minimum, a technique (feedback loop) that is also used in the commercial devices.

The files were attached to the piezo with a chuck with a bend of  $120^\circ$ . Measurements were performed in air, in a water tank (dimensions  $100 \times 100 \times 100$  mm) filled with tap water, and inside root canal models. These root canal models were made by solidifying silicon (Polydimethylsiloxane, Sylgard 184, Dow-Corning, Midland, Michigan, United States) around a C- or D-sized hand spreader, creating a 17 mm long root canal with a taper of 6% and an apical diameter of  $300 \mu\text{m}$  ('30/0.06') or  $350 \mu\text{m}$  ('35/0.06'), respectively [24]. The files were inserted up to 3 mm from the apex of those canals.

Measurements of the oscillation amplitude were performed in the direction of driving; for two files the oscillation amplitude in the perpendicular direction was also measured. Also, the motion of the hand piece and chuck relative to the file have been measured. The transient start-up of the file has been studied by measuring the oscillation amplitude of the tip during the first 20 ms.

Finally, the influence of a rubber stopper has been measured by placing a rubber stopper at 15 mm from the tip. These rubber stoppers are used in clinical practice to indicate the length of the root canal on a file. A rubber stopper is a disc with a diameter of 3.3 mm, a thickness of 1.7 mm and a mass of 15 mg.

The geometrical file properties that are necessary for the numerical model, were obtained from pictures taken with a digital camera (D300, Nikon, Tokyo, Japan) and are listed in Table 4.2. The convention for the endodontic file names are as follows: the first number behind the letter (denoting the file type) indicates the diameter of the file at the tip, in tens of micrometer; the second number indicates the length of the file, in millimeter. Example: the 'K15/25' file is a K-type file with a tip diameter of  $150 \mu\text{m}$  and a length of 25 mm.

	$L$ (mm) $\pm 0.05$	$D$ ( $\mu\text{m}$ ) $\pm 5$	$\delta$ $\pm 0.1$	$L_c$ (mm) $\pm 0.1$	$D_c$ ( $\mu\text{m}$ ) $\pm 5$	$\theta$ (mm/90°) $\pm 0.05$	Cross-section	Material
K10/21	21.0	100	2.00%	6.0	500	0.5	square	stainless steel
K10/25	25.0	100	2.00%	6.0	500	0.5	square	stainless steel
K15/25	25.0	150	2.19%	9.0	500	0.5	square	stainless steel
K25/21	21.0	230	2.24%	4.5	600	0.5	square	stainless steel
IRR20/21	21.0	200	0.3.%	4.0	300	0.8	rounded square	stainless steel
IRR20/25	25.0	200	0.3.%	8.0	600	0.8	rounded square	stainless steel
IRR25/21	21.0	250	0.0.%	6.0	600	0.8	rounded square	stainless steel
Endosonore #020	25.0	250	2.25%	6.0	720	0.5	square	stainless steel
ET25L	25.0	250	3.00%	2.0	1000	-	circular	stainless steel
ESI015	25.0	160	2.00%	2.0	840	-	circular	NiTi

**Table 4.2:** Geometrical properties of endodontic files

## 4.4 Results

### 4.4.1 Typical oscillation pattern

Both the experiments and the numerical simulation show that the oscillation pattern of an endodontic file is typically a standing wave of two or three wavelengths, see Fig. 4.3. As most files are tapered toward the tip, the amplitude of the antinodes increases toward the tip, and the wavelength simultaneously decreases. Without taper (Irrisafe files), the antinode amplitude and wavelength do not change along the file.

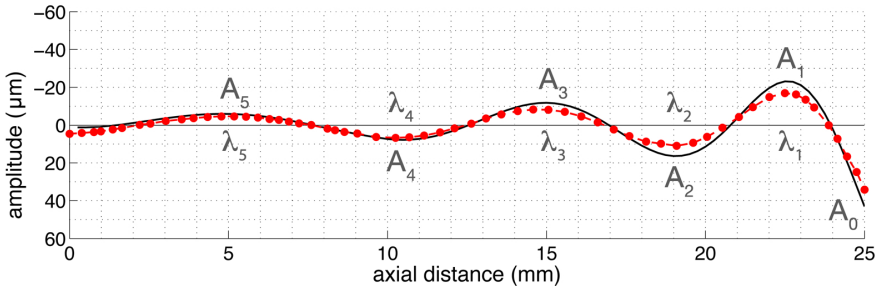


**Figure 4.3:** Wave pattern of a K15/21 file, as determined by simulation (—) and experiment (-●-●-). The oscillation pattern typically consists of a number of nodes and antinodes (of amplitude  $A_n$  and (half-)wavelength  $\lambda$ ).

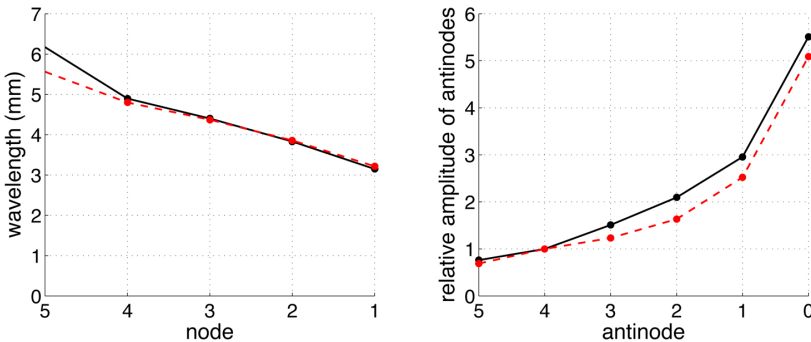


**Figure 4.4:** Wave pattern characteristics of a K15/21 file, showing (left) the decrease of wavelength (with slope  $\Delta\lambda$ ) toward the file tip, and (right) the increase in antinode amplitude (with exponential factor  $\alpha_A$ , plot normalized to  $A_5$ ) toward the file tip. Both numerical (-●-●-) and experimental (-●-●-) results are shown.

The files can be characterized with six parameters, which will be used in the remainder of this paper to characterize the oscillation pattern of different files, settings



and conditions. The first two parameters are the amplitude of the first antinode away from the tip,  $A_1$ , and the decrease of the amplitude with distance from the file tip, which is observed (Fig. 4.4, right) to follow an exponential trend with exponent  $\alpha_A$ :

$$A_n = A_1 e^{\alpha_A n} \quad (4.21)$$

where  $n$  is counted from the tip.

The second set of parameters is based on the (half) wavelength  $\lambda$ , which is the distance between two consecutive nodes. The oscillation pattern of a file can be characterized by  $\lambda_1$ , which is the distance between the first and second antinode from the tip, and the change in wavelength with distance from the tip, which is observed (Fig. 4.4, left) to increase linearly:

$$\lambda_n = \lambda_1 + n\Delta\lambda. \quad (4.22)$$

This equation is a linear fit based on the observation that the reduction in wavelength appears to be linear. Considering the limited number of points (4 or 5), a higher-order fit was deemed inappropriate.

The final parameter is the number of nodes on the file and the driving frequency of the file, as obtained from the driving signal in the ultrasound device.

Both the vibrometer and the simulation showed no phase difference along the length of the file during the steady oscillation of the file.

### Comparison between numerical and theoretical oscillation pattern

A comparison between the numerical model and the theoretical prediction for the wave pattern can only be done when the taper and the cylindrical section at the beginning of the file are excluded. Fig. 4.5 shows the result for a cylindrical rod of length 25 mm and diameter 150  $\mu\text{m}$  and shows differences less than 0.01% between the two, which is considered a very good agreement. Around the nodes, a small misalignment between the two solutions causes differences around 1%.

### Comparison between numerical and experimental oscillation pattern

A comparison of the measurement and numerical simulation of a K15/21 file oscillating in air (Fig. 4.3) shows an agreement within 10% between the two methods, both in amplitude and location of nodes. Other files give similar results, however, the numerical result is sensitive to inaccuracies in geometrical properties, material properties and driving conditions. In order to estimate the influence of each of these factors, a parametric study has been performed by varying these factors within 10% of their estimated value. The results of this parametric study is shown in Fig. 4.6. The amplitude can change up to 200% when varying the material or driving properties, which is probably due to a mismatch between the driving frequency and the

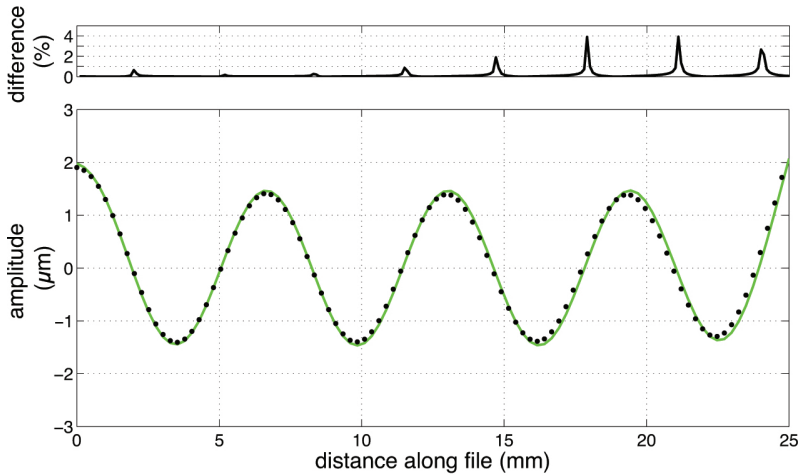


**Figure 4.5:** Comparison between numerical (-●-●-) and theoretical (—) solution for a 25 mm long, 150  $\mu\text{m}$  diameter cylindrical rod. The difference between the two solutions is plotted in the top panel.

resonance frequency of the simulated file. The first wavelength  $\lambda_1$ , however, changes only within 8%.

Besides this inaccuracy in the numerical model, there is a spreading in amplitude within the three measurements made by the vibrometer, which is typically 10%. The location of the nodes is estimated to be accurate within 1%.

The driving amplitude  $Y_0$  was measured to be on the order of 1  $\mu\text{m}$ . The driving point  $x = 0$  is not necessarily a node, as it is not exactly known how the file is fixed inside the chuck; the actual point of driving can be somewhere inside the chuck. For the files where  $x = 0$  is close to an antinode, the driving amplitude was only of the order of hundred nanometer.

### Differences between endodontic files

Each endodontic file has a specific oscillation characteristic, which is shown in Table 4.3, as obtained from vibrometer measurements. The K-files and ESI015 file all have an increase of antinode amplitude and a decrease of their wavelength toward the file tip in common, which is due to their taper. The Irrisafe files, however, have almost no taper and therefore an almost constant wavelength and antinode amplitude.

For the present set of files it can be observed that thicker files tend to oscillate with a higher amplitude and have larger wavelengths, although the increase in wavelength ( $\Delta\lambda$ ) is not necessarily affected. Longer files generally result in more nodes and lower amplitudes.

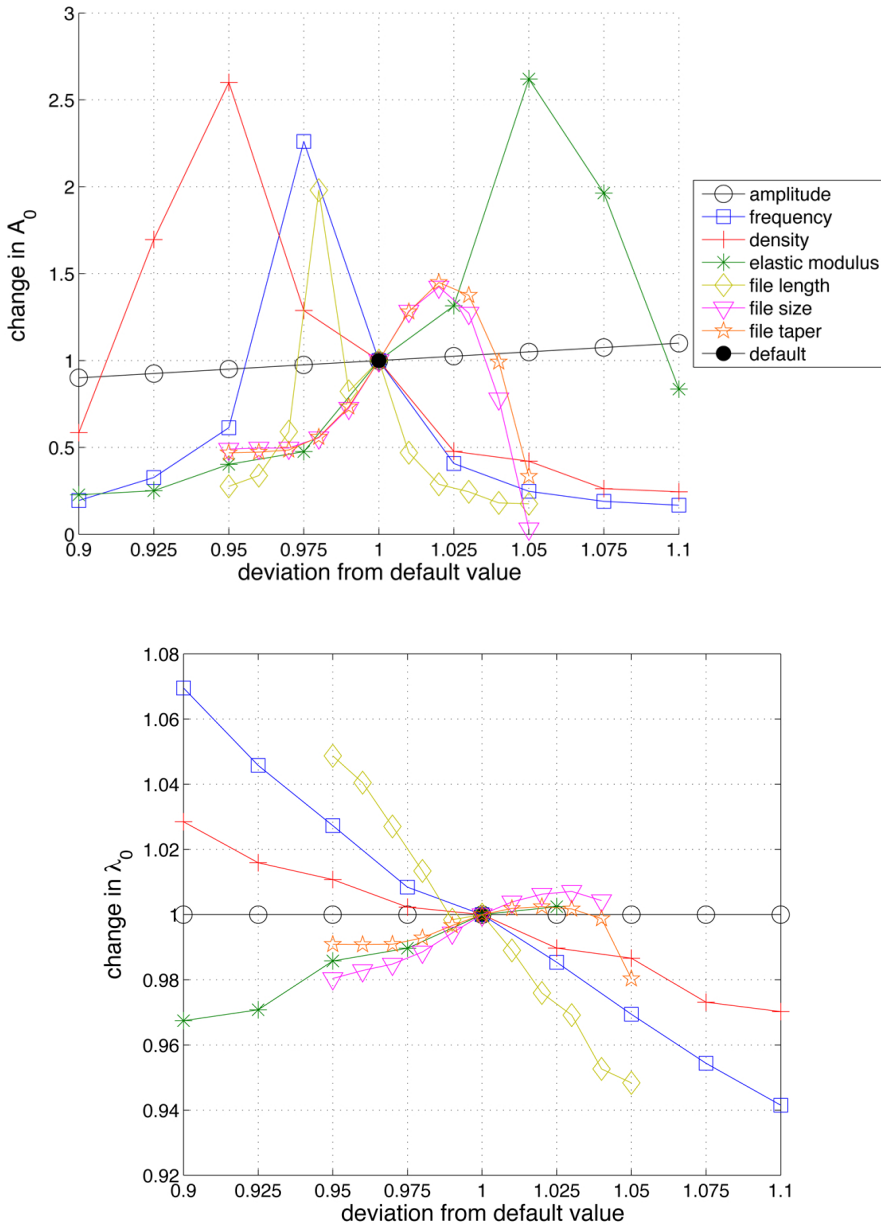


**Figure 4.6:** Parametric study of the numerical solution of a K15/21 file. All parameters were varied within 10% of their default value; the change in tip amplitude (left) and first wavelength (right) with respect to the default result is plotted. Note the different scale on the y-axis in the left panel.

	# of nodes	$A_1(\mu m)$	$\alpha_A$	$\lambda_1(mm)$	$\Delta\lambda$	$f(kHz)$
K10/21	6	38.08	-0.38	2.42	0.48	30.50
K10/25	7	31.44	-0.38	2.29	0.63	30.54
K15/25	6	40.19	-0.32	2.85	0.50	30.38
K25/21	5	14.72	-0.28	3.44	0.49	30.25
IRR20/21	6	14.00	-0.03	2.88	0.15	30.38
IRR20/25	6	11.01	-0.07	2.72	0.18	30.50
IRR25/21	5	30.06	-0.06	3.06	0.25	30.38
Endosonore*	5	2.44	-0.26	3.83	1.01	29.42
ET25L	4	9.14	-0.33	4.45	0.72	33.13
ESI015*	7	5.84	-0.26	2.35	0.44	29.17

**Table 4.3:** Oscillation pattern characteristics for different endodontic files, as determined experimentally in water, at power setting ‘Yellow 5’ (or ‘1’ = \*).

The ESI015 file was found to have two different oscillation frequencies, 24 and 29 kHz. At start-up, the feedback mechanism of the ultrasound device locked into one of these two frequencies.

The Endosonore020 file was observed to have a large frequency component at 88 kHz, i.e. three times the driving frequency of 29 kHz. This component could actually be two times higher than the fundamental component, suggesting a complex oscillatory motion of the file.

### Influence of the driving frequency and amplitude

An increase in driving frequency from 20 kHz to 30 kHz or 40 kHz resulted in a shorter wavelength, according to the vibrometer measurements (Table 4.4) and agreeing with numerical simulations. A significant reduction in oscillation amplitude was also observed at 20 and 40 kHz with respect to 30 kHz. This could be due to the frequency response of the piezo elements and the attached file, because the numerical simulation actually predicted higher oscillation amplitudes at 20 and 40 kHz for the same driving amplitude.

Changing the driving power showed a linear relation between driving amplitude and overall oscillation amplitude. For the commercial devices, the driving frequency typically decreased with approximately 0.01 %/mW with increasing power.

### Influence of damping

The influence of damping on the oscillation pattern can be observed in Table 4.5, where the measured oscillation characteristics in air and water are listed. The damping forces due to water (drag force, added mass force and history force together)

	# of nodes	$A_1(\mu m)$	$\alpha_A$	$\lambda_1(mm)$	$\Delta\lambda$	$f(kHz)$
<i>frequency</i>						
20 kHz	5	8.31	-0.32	3.30	0.36	18.94
30 kHz	6	9.27	-0.24	2.61	0.45	27.06
40 kHz	7	2.90	-0.21	2.24	0.36	35.19
<i>amplitude</i>						
30mW	6	7.24	-0.25	2.61	0.45	27.06
50mW	6	9.27	-0.24	2.61	0.45	27.06
70mW	6	11.00	-0.25	2.60	0.45	27.06

**Table 4.4:** Oscillation pattern characteristics for an ESI015 file driven at different frequencies (at 50mW) and amplitudes (at 30 kHz), as determined experimentally.

changes the oscillation pattern by increasing the wavelength on the file with approximately 5%. The driving frequency typically decreases with approximately 1% when the file oscillated in water, however, the numerical simulation predicted that this would change the wavelength by less than 1%, showing that the increase in wavelength is primarily due to damping. The reduction in driving frequency suggests an increase in driving power by the commercial device as it tries to compensate for the load due to the water. This can also be observed from the oscillation amplitude, which is not reduced significantly in water, and is occasionally even increased.

### Influence of the confinement

Files oscillating in the confinement of a root canal have oscillation characteristics (Table 4.5) that are between those in air and in water, reflecting the fact that 33% to 44% of the file is outside of the root canal. From these results it cannot be deduced how large the contribution of the presence of the wall is, because the results for the two different confinements (sizes ‘C’ and ‘D’) are not significantly different. However, the wall does not appear to introduce a large damping to the file oscillation, as the oscillation characteristics inside the confinements are close to those in water.

The influence of PDMS in front of the oscillating file on the vibrometer result was checked by placing a slab of PDMS of thickness 6 mm in front of an unconfined file, oscillating in water. No difference was observed with respect to the same file oscillating freely in water (data not shown).

### Influence of a rubber stopper

When a rubber stopper was placed on the file, no significant change in oscillation pattern was observed (Table 4.6). It should be noted that the rubber was found to have been placed at a node of the file oscillation pattern.

	# of nodes	$A_2(\mu m)$	$\alpha_A$	$\lambda_1(mm)$	$\Delta\lambda$	$f(kHz)$
Air	6	18.23	-0.33	2.98	0.51	30.38
Water	6	28.37	-0.27	2.89	0.50	30.34
Root canal size 'C'	6	24.31	-0.30	2.94	0.51	30.38
Root canal size 'D'	6	27.86	-0.28	2.93	0.50	30.38

**Table 4.5:** Oscillation pattern characteristics for a K15/25 file in different media and confinements, as determined experimentally, at power setting 'Blue 5'. Note that  $A_2$  is used instead of  $A_1$ , because of non-representative fluctuations in the amplitude  $A_1$

Stopper	# of nodes	$A_1(\mu m)$	$\alpha_A$	$\lambda_1(mm)$	$\Delta\lambda$	$f(kHz)$
no	6	25.76	-0.31	2.73	0.54	24.18
yes	6	27.78	-0.30	2.73	0.58	24.23

**Table 4.6:** Oscillation pattern characteristics for an ESI015 file driven at power 1, with and without rubber stopper placed at a distance of 15 mm from the tip.

### Oscillation direction

In the direction perpendicular to the main direction of oscillation, the oscillation pattern was observed to have the same number and position of nodes and antinodes (Table 4.7) as in the main direction of oscillation. The oscillation amplitude was up to 25% of the amplitude of the main direction of oscillation.

### Start-up characteristics

For the commercial device (MiniPiezon, EMS) it took 8 to 10 seconds before the maximum oscillation amplitude of the file tip was obtained. During this start-up time the frequency and amplitude were observed to vary, contrary to the file being driven by our own equipment, where the frequency was observed to be constant and the amplitude increased linearly, within approximately 3 ms until full oscillation amplitude was obtained. During this start-up time, there was a phase difference between the driving signal and the oscillation amplitude during the first millisecond. In the simulation, there also is a phase difference between the file tip and the driving signal, but that disappeared already after 0.2 ms.

	# of nodes	$A_1(\mu m)$	$\alpha_A$	$\lambda_1(mm)$	$\Delta\lambda$	$f(kHz)$
main oscillation direction	6	28.07	-0.33	2.98	0.51	30.38
perpendicular direction	6	7.78	-0.26	2.83	0.52	30.38

**Table 4.7:** Oscillation pattern characteristics for a K15/25 file driven at power 'Blue 5', measured in the main direction of oscillation and perpendicular to it.

**Table 4.8:** Eigenfrequencies of several files, as determined from the simulated free oscillation of the file tip in air.

File type	Eigenfrequency (Hz)
K10/21	1511
K10/25	1282
K15/25	1160
K25/21	1541
IRR20/21	549
IRR20/25	549
IRR25/21	504
Endosonore #020	1236
ET25L	1907
ESI015	1123

A frequency analysis of the first 20 ms after start-up (Fig. 4.7) shows that the frequency spectra for experiment and simulation are similar except for stronger peaks at the harmonic frequencies in the experimental signal.

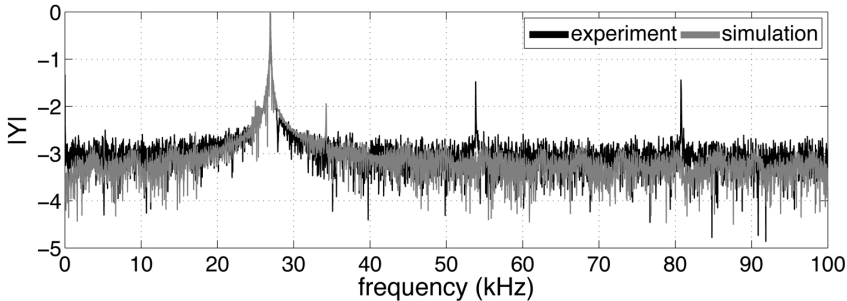


**Figure 4.7:** Power spectrum (in decibel) of the oscillation amplitude of the tip during the first 20 millisecond after start-up, for both experiment (black) and simulation (grey).

### Eigenfrequency

The eigenfrequency of each specific file as determined from the numerical simulation is listed in Table 4.8, with an error of 1%. For a cylindrical stainless steel file of diameter 150  $\mu\text{m}$  length 25 mm and no taper, the eigenfrequency is 170.9 Hz, according to the numerical model, agreeing well with the theoretically predicted value of 170.8 Hz. Note that the driving frequency is more than 20 times the file's eigenfrequency.

## 4.5 Discussion

The sinusoidal oscillation pattern as measured with the laser vibrometer matches the numerically predicted oscillation pattern very well, when the geometrical, material and driving properties are known accurately. Inaccuracies in these properties cause the file in the simulation to be driven above or under resonance, which may affect the oscillation amplitude significantly, although the location of nodes and antinodes remains unaffected. The numerical model also matches well with the theoretical prediction for the oscillation characteristics and eigenfrequency of a non-tapered cylindrical rod and can therefore be considered validated.

At present, the tools necessary to measure the (hyper)elastic modulus of the stainless steel or NiTi-alloy files were not available. Furthermore, determination of the material density is complicated by the very small volume of those files. Measuring the material properties and also the geometrical properties of the files will make the numerical model more accurate.

The numerical model can also be made more accurate by including material damping and the fact that, due to the displacement of the file, the length in the model becomes shorter. This reduction is typically less than 0.01% but can become more important for larger amplitudes. The numerical model could also be expanded by including the perpendicular motion of the file, which has shown to be up to 25% of the main direction of oscillation. However, without the phase information between the two oscillation directions, the full two-dimensional oscillation (e.g., circular, ‘figure 8’) cannot be determined. This bidirectional oscillation has already been reported in earlier investigations of oscillations of dental files [25] and could actually be useful in clinical practice because the anatomic complexity of the root canal necessitates cleaning in all directions [26]. The bidirectional oscillation could be attributed to lift induced by the surrounding fluid, different resonance modes of the piezo or due to file imperfections. File imperfections are actually likely to occur because in clinical setting the files are known to bent easily. A preliminary scan with the vibrometer system of a bent file has shown that a bend in the file can influence the oscillation pattern significantly. Also, in clinical settings file fracture is known to occur, due to high bending in combination with file imperfections. A preliminary investigation has shown that the location of file fracture can be predicted well with the numerical model presented here.

From the obtained oscillation patterns it cannot readily be determined which file is more effective in generating fluid streaming for cleaning of the root canal, because the fluid-structure coupling is not only dependent on oscillation amplitude but also involves the front-facing area of the file and damping. A recent study has however shown an increase in root canal cleaning efficacy with higher oscillation amplitudes [27]. Studying the fluid-structure interaction in more detail would require a more sophisticated, three-dimensional finite element solver.



Some clinical implications can already be deduced from the results from this study. Primarily, the presence of the confinement of the root canal did not have a large affect on the file oscillation with respect to the oscillation in water, although the fact that a large part of the file is outside the root canal was visible in the results. Considering the acoustics inside the root canal confinement, standing waves can be ruled out, as the acoustic wavelength at 30 kHz in water is 5 cm. However, in the present experiments, the wall of the root canal is made of silicone, which changes the acoustic coupling between the oscillating file and the wall. Silicone has a different acoustic reflection coefficient than dentin, leading to a different reflection coefficient of the generated sound waves. The reflection coefficient can be determined from the acoustic impedances  $Z = \rho c$  (with  $\rho$  the material density and  $c$  the speed of sound in that material), which for water at 20° C is 1.5 MRayls, for silicone (PDMS) is 1.1 MRayls and for dentin is 8.8 MRayls. The reflection coefficients for each interface is given by:

$$R = \left( \frac{Z_2 - Z_1}{Z_2 + Z_1} \right)^2. \quad (4.23)$$

For water-dentin, this reflection coefficient is 0.50; for water-silicone it is 0.02. Therefore, inside the silicone root canals, the acoustic coupling with the reflected ultrasound is neglected. The wall does have an influence on the fluidic streaming induced by the file, independent of the material of the wall, as long as the wall doesn't deform at the scale of the induced microstreaming ( $O(100 \mu\text{m})$  [6]). A pilot experiment with a temporal resolution of 4  $\mu\text{s}$  and an optical resolution of 3  $\mu\text{m}$  showed no deformation of the silicon wall, therefore the silicon root canal model is considered a good substitute for a dentinal root canal. More accurate measurements of file oscillations inside different root canal confinements could elucidate the role of the confinement in more detail.

The presence of a rubber stopper is also of clinical relevance. In this study it was shown that the presence of the rubber stopper does not alter the file oscillation significantly, even though it has a mass of approximately 1/4th of a file. The stopper was placed at a node of the oscillation pattern of the file, and the feedback system of the ultrasound device was likely to have compensated for the presence of the additional weight introduced by the rubber stopper. When placed at antinodes, the rubber stopper may have a larger influence on the file oscillation.

The observation that the oscillation amplitude of the file in water is not reduced (and sometimes is even increased) compared to oscillation in air is a result of the feedback system of commercial ultrasound devices, which measures the load on the file and adjusts the power output, thereby compensating for the increase in load due to the water. However, the load on the file also changes the resonance frequency of the file. At start-up, the feedback system of the commercial ultrasound devices look for

the optimal driving frequency in the range 24-32 kHz, and therefore by monitoring the driving frequency one can deduce the presence of a load on the file.

The feedback system was found to need approximately 10 ms to find this optimal driving frequency. During this start-up time the file tip exhibits instationary behaviour, which are transients induced by the frequency scanning. This can be deduced from the observation that file driven by equipment without feedback system needed only 3 ms to reach full amplitude and did not show in stationary behaviour. *Ex vivo* experiments have shown that the instationary start-up phase of commercial devices may be beneficial for the induced fluid flow [28].

The endodontic files are attached to the piezo element with a chuck, into which the file is screwed (EMS ultrasound devices) or attached inside (Satelec ultrasound devices). The attachment of the file to the chuck and of the chuck to the piezo element may introduce additional movement if the attachment is not firm enough [25]. However, a pilot measurement with the vibrometer system showed no significant phase difference between the piezo element and the chuck, or the chuck and the file (for the EMS system).

The hand piece and the file are known to heat up during use [29]; their temperature can increase with up to 50° C. This, however, should not lead to a significant change in file length and consequently the oscillation characteristics, as the heat expansion coefficient of stainless steel or NiTi suggest that a temperature rise of 300 °C is necessary to increase the length of the file with only 0.1 mm. Furthermore, the heat will be dissipated to the surrounding water.

In clinical practice, contact of the file with the wall of the root canal is likely to occur. Preliminary measurements have shown that this contact leads to a rich behaviour of the file, including traveling waves and secondary frequencies. Understanding this behaviour and measuring the amount of contact occurring clinically is the subject of an ongoing study.

## 4.6 Conclusions

Using a combination of experimental and numerical techniques, the oscillation characteristics of ultrasonically driven endodontic files have been analyzed, showing a good agreement between numerical model and experimental results and theoretical predictions. The numerical model can therefore be considered validated and can in the future be used to predict the oscillation characteristics of new file designs.

The presence of a liquid changes the oscillation characteristics due to damping; on the other hand, the confinement of an artificial root canal or the presence of a rubber stopper did not affect the file oscillation significantly. The feedback system of commercial endodontic ultrasound devices compensates for the damping by the liquid and assures that the file can oscillate optimally during clinical use.

The oscillation pattern is typically a sinusoidal wave of 3 periods, although the amplitude and wavelength characteristics differ between files. Such an oscillation pattern could induce streaming between antinodes and nodes and therefore knowing the oscillation pattern and amplitudes is important for understanding the file behavior and induced streaming that is associated with cleaning of the root canal system by the current and new endodontic file designs.

## References

- [1] O. Peters, "Current challenges and concepts in the preparation of root canal systems: a review", *Journal of Endodontics* **30**, 559–567 (2004).
- [2] P. Nair, "Pathogenesis of apical periodontitis and the causes of endodontic failures", *Critical Review Of Oral Biology & Medicine* **15**, 348–381 (2004).
- [3] S. J. Lee, M. K. Wu, and P. R. Wesselink, "The effectiveness of syringe irrigation and ultrasonics to remove debris from simulated irregularities within prepared root canal walls", *International Endodontic Journal* **37**, 672–678 (2004).
- [4] L. W. M. Van der Sluis, M. Versluis, M. K. Wu, and P. R. Wesselink, "Passive ultrasonic irrigation of the root canal: a review of the literature", *International Endodontic Journal* **40**, 415–426 (2007).
- [5] T. J. Mason and D. Peters, *Practical sonochemistry: power ultrasound uses and applications*, Chemical Science series (Horwood) (2002).
- [6] M. Ahmad, T. R. Pitt Ford, and L. A. Crum, "Ultrasonic debridement of root canals: acoustic streaming and its possible role", *Journal of Endodontics* **13**, 490–499 (1987).
- [7] M. Ahmad, T. R. Pitt Ford, L. A. Crum, and A. J. Walton, "Ultrasonic debridement of root canals: acoustic cavitation and its relevance", *Journal of Endodontics* **14**, 486–493 (1988).
- [8] R. G. Macedo, P. R. Wesselink, F. Zaccaro, D. Fanali, and L. W. M. Van der sluis, "Reaction rate of naocl in contact with bovine dentine: effect of activation, exposure time, concentration and ph", *International Endodontic Journal* **43**, 1108–1115 (2010).
- [9] T. Joyce Tiong and G. J. Price, "Ultrasound promoted reaction of rhodamine b with sodium hypochlorite using sonochemical and dental ultrasonic instruments", *Ultrasonics Sonochemistry* **19**, 358–364 (2012).
- [10] M. Ahmad, R. A. Roy, A. Ghani Kamarudin, and M. Safar, "The vibratory pattern of ultrasonic files driven piezoelectrically", *International Endodontic Journal* **26**, 120–124 (1993).
- [11] S. C. Lea, G. Landini, and A. D. Walmsley, "Vibration characteristics of ultrasonic scalers assessed with scanning laser vibrometry", *Journal of Dentistry* **30**, 147–151 (2002).
- [12] S. C. Lea, A. D. Walmsley, P. J. Lumley, and G. Landini, "A new insight into the oscillation characteristics of endosonic files used in dentistry", *Physics in Medicine and Biology* **49**, 2095–2102 (2004).
- [13] A. R. Williams and W. L. Nyborg, "Microsonation using a transversely oscillating capillary", *Ultrasonics* **8**, 36–38 (1970).

- [14] L. Meirovitch, *Fundamentals of Vibrations*, 1st edition (McGraw-Hill) (2001).
- [15] U. Rabe, K. Janser, and W. Arnold, “Vibrations of free and surface-coupled atomic force microscope cantilevers: Theory and experiment”, *Review of Scientific Instruments* **67**, 3281–3293 (1996).
- [16] F. J. Giessibl, “Advances in atomic force microscopy”, *Reviews of Modern Physics* **75**, 949–983 (2003).
- [17] R. P. Goel, “Transverse vibrations of tapered beams”, *Journal of Sound and Vibration* **47**, 1–7 (1976).
- [18] G. W. Gatecliff and E. R. Lardy, “Forced vibration of a cantilever valve of uniform thickness and non-uniform width”, *International Compressor Engineering Conference* **50** (1972).
- [19] P. Morse, *Vibration and Sound*, 2<sup>nd</sup> edition (McGraw-Hill) (1948).
- [20] W. C. Young and R. G. Budynas, *Roark’s formula’s for stress and strain*, 7th edition (McGraw-Hill) (2002).
- [21] T. Sarpkaya, “Force on a circular cylinder in viscous oscillatory flow at low keulegan-carpenter numbers”, *Journal of Fluid Mechanics* **165**, 61–71 (1986).
- [22] E. Michaelides, “Hydrodynamic force and heat/mass transfer from particles, bubbles, and drops—the freeman scholar lecture”, *Journal of Fluids Engineering* **125**, 209–238 (2003).
- [23] S. Thompson, “An overview of nickel-titanium alloys used in dentistry”, *International Endodontic Journal* **33**, 297–310 (2000).
- [24] C. Boutsioukis, B. Verhaagen, M. Versluis, E. Kastrinakis, and L. W. M. Van der Sluis, “Irrigant flow in the root canal: experimental validation of an unsteady computational fluid dynamics model using high-speed imaging”, *International Endodontic Journal* **43**, 393–403 (2010), *see also Chapter 3 of this thesis*.
- [25] S. C. Lea, A. D. Walmsley, and P. J. Lumley, “Analyzing endosonic root canal file oscillations: an in vitro evaluation”, *Journal of Endodontics* **36**, 880–883 (2010).
- [26] L.-M. Jiang, B. Verhaagen, M. Versluis, and L. W. M. Van der Sluis, “Influence of the oscillation direction of an ultrasonic file on the cleaning efficacy of passive ultrasonic irrigation”, *Journal of Endodontics* **36**, 1372–1376 (2010), *see also Chapter 7 of this thesis*.
- [27] L.-M. Jiang, B. Verhaagen, M. Versluis, J. Langeijk, P. R. Wesselink, and L. W. M. Van der Sluis, “The influence of the ultrasonic intensity on the cleaning efficacy of passive ultrasonic irrigation”, *Journal of Endodontics* **37** (2011), *see also Chapter 8 of this thesis*.
- [28] L.-M. Jiang, B. Verhaagen, M. Versluis, C. Zangrillo, D. Cuckovic, and L. W. M. Van der Sluis, “An evaluation of the effect of pulsed ultrasound on the cleaning efficacy of passive ultrasonic irrigation”, *Journal of Endodontics* **36**, 1887–1891 (2010), *see also Chapter 10 of this thesis*.
- [29] S. C. Lea, G. Landini, and A. D. Walmsley, “Thermal imaging of ultrasonic scalar tips during tooth instrumentation”, *Journal of Clinical Periodontology* **31**, 370–375 (2004).
- [30] M. Ahmad, “An analysis of breakage of ultrasonic files during root canal instrumentation”, *Endodontics & Dental Traumatology* **5**, 78–82 (1989).

- [31] M. Ahmad and R. A. Roy, "Some observations on the breakage of ultrasonic files driven piezo-electrically", *Endodontics & Dental Traumatology* **10**, 71–76 (1994).

## Appendices

### 4.A Discretization of the equation of motion

A central difference explicit discretization scheme is used for the discretization of the 4<sup>th</sup> order spatial derivative and the 2<sup>nd</sup> order time derivative of the equation of motion of the endodontic file (4.4). The discretization on the spatial domain  $j = 0..J$  is given by:

$$\begin{aligned}
 Y_j^{n+1} - 2Y_j^n + Y_j^{n-1} = & \\
 & \frac{S_{j-1}\kappa_{j-1}^2}{MS_j} v^2 (Y_{j-2}^n - 2Y_{j-1}^n + Y_j^n) \\
 & - \frac{2\kappa_j^2}{M} v^2 (Y_{j-1}^n - 2Y_j^n + Y_{j+1}^n) \\
 & + \frac{S_{j+1}\kappa_{j+1}^2}{MS_j} v^2 (Y_j^n - 2Y_{j+1}^n + Y_{j+2}^n)
 \end{aligned} \quad (4.24)$$

where  $M = -\frac{\rho}{Q}$  and  $v = \frac{\Delta t}{\Delta x^2}$ . Neumann analysis showed that the numerical scheme for a non-tapered beam is stable for

$$v \leq \frac{1}{2} \sqrt{\frac{M}{\kappa^2}}. \quad (4.25)$$

The taper for endodontic files is typically small (typically less than 6%) and therefore it is assumed that, for a tapered beam, the stability criterium is approximately the same as(4.25).

The discretized boundary conditions at  $j = 0$  (corresponding to  $x = 0$ ) are given by:

$$Y_0^n = Y_0 \sin(\omega t) \quad (4.26)$$

$$Y_1^n = Y_0^n. \quad (4.27)$$

At  $j = J$  (corresponding to  $x = L$ ) the discretized boundary conditions are given by:

$$Y_{J+1}^n = 2Y_J^n - Y_{J-1}^n \quad (4.28)$$

$$Y_{J+2}^n = 3Y_J^n - 2Y_{J-1}^n. \quad (4.29)$$

The cross-sectional area  $S(j)$  and radius of gyration  $\kappa$  are evaluated at each  $j$ ; the file diameter is assumed constant over a length  $dx$ . The driving amplitude  $Y_0^n$  is apodized linearly for the first millisecond, to avoid transient behaviour.

## 4.B File fracture

File fracture can occur during passive ultrasonic irrigation of the root canal. The origin of the fracturing is not yet fully elucidated, but could be related to high bending during oscillation or due to cavitation. In two studies by Ahmad *et al.* [30, 31], where she studied the fracture of a ultrasonic files, she found that the fracture location was close to a node. Thin files broke more easily and the fracture was of the brittle type; the contribution of cavitation was deemed to be insignificant. However, files and ultrasonic equipment have changed in the more than 20 years since that study was performed.

In order to predict the location of fracture from the numerical simulations, the bending moment needs to be considered [19]. The bending moment  $M$  can be calculated from the second derivative of the file oscillation pattern:

$$M(x,t) \propto \frac{\partial^2 y(x,t)}{\partial x^2} \quad (4.30)$$

### 4.B.1 Measurements of file fracture occurrences

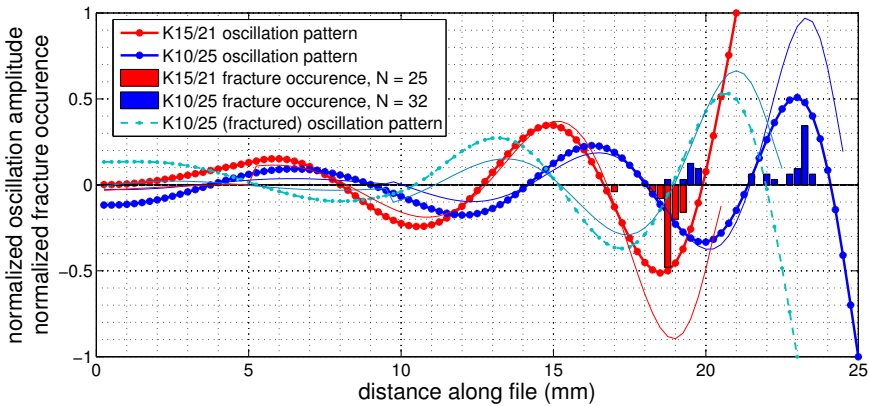
By measuring the remaining length of files of two specific types (K10/25 and K15/21, Satelec, Merignac, France) that had been used during a period of four years and had fractured. All files have been oscillating freely in water or air, without the constraints of the root canal space. The measurement error in the length determination is  $\pm 0.1$  mm.

Figure 4.8 shows the number of fracture occurrences at a specific length for those two files, plotted next to the file oscillation pattern as calculated with the numerical model described in this chapter. It can be observed that most of the files fracture near (but not at) their first antinode ( $A_1$ ) away from the tip, which results in a loss of approximately 2 mm of length. These fracture locations coincide well with the maximum bending moment (thin lines).

For the K10/25 file it can furthermore be observed that the second peak of fracture occurrences is near the second antinode ( $A_2$ ) of the intact file, suggesting that a second fracture of the file is related to weaknesses of the file induced during the oscillation of the intact file. A numerical simulation of a broken file (light blue) verified that the new antinode  $A_{1,fractured}$  and maximum bending moment are located at a different position than the second peak in fracture occurrences.

### 4.B.2 Observations of file fractures

Visualization of the file fracture was performed using a high-speed camera (APX-RS, Photron, Tokyo, Japan) recording at 30,000 fps the oscillation of the two files submerged in water or air. Magnification of  $5\times$  was provided by a microscope (BX-FM,



**Figure 4.8:** Normalized oscillation pattern (thick lines) and fracture occurrences (bar plots) for the K10/25 and K15/21 files. The thin lines represent (normalized) bending moments.

Olympus, Japan) and illumination was provided in bright-field mode (ILP1, Olympus, Japan). The power setting on the endodontic ultrasound device (P-Max, Satelec) was set to ‘Red 5’.

In water, it took 82.15 sec for the K10/25 file to break, at a distance of 1.85 mm from the tip. In air, it took 0.37 sec for the file to break, at a distance of 1.70 mm from the tip. In water, a cloud of cavitation bubbles (see chapter 12 of this thesis) could be identified at the tip of the file and also at the first antinode  $A_1$ , where cavitation occurred over a length of approximately 1 mm (figure 4.9a). At some point a crack started to be visible at a location between the first node and the first antinode from the tip (figure 4.9b,c), after which the file oscillation was significantly affected. In water, cavitation concentrated to the area around and inside the crack. This crack grew for approx. 50 oscillation cycles before detaching from the bulk of the file (figure 4.9d).

Often the fracture occurred at a location where the file is widest in the image (figure 4.9e), corresponding to a diagonal cross-section of the file with respect to the direction of oscillation.

### 4.B.3 Hypothesis for the cause of fracture

The fact that fracture occurred in air in a similar way as in water already suggests that cavitation may not be the main cause of file fracture. The high-speed visualizations confirm this suggestion, as at the site of fracture only little cavitation occurs as compared to other locations on the file. These results agree with the findings by Ahmad *et al.* (1994) [31], who showed that cavitation caused some pitting on the file surface, but not enough to be likely to contribute to fracture.

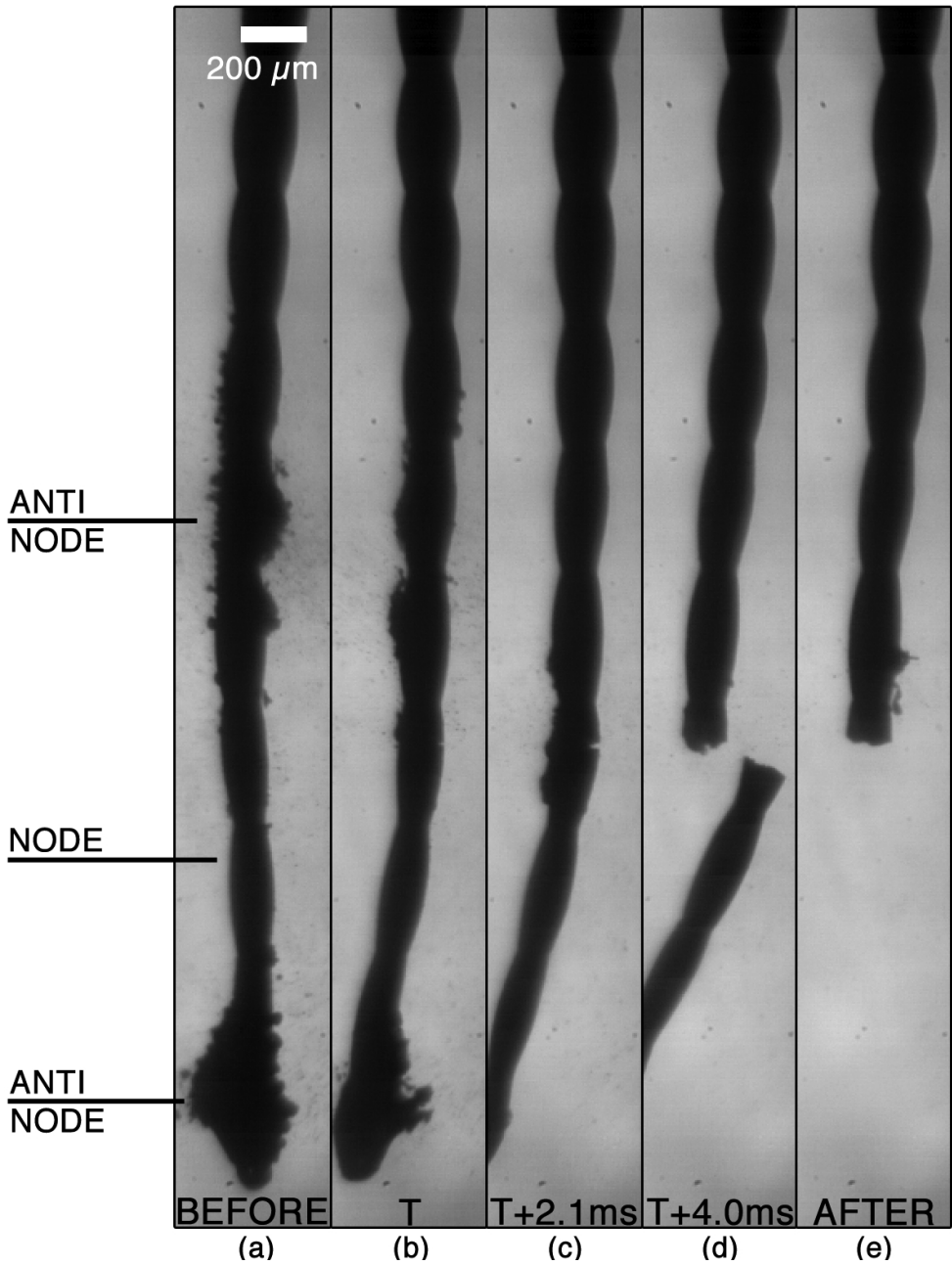


Figure 4.9: Fracture visualization for a K10/25 file.



The bending of the file is then a more likely cause of fracturing. The file may experience fatigue due to its continuously changing bending, which shows primarily at the points of high bending moment, near the first antinode. This bending moment is distributed along the cross-section of the file; at points where the cross-section of the file with respect to the direction of oscillation is diagonal (every 0.5 mm), the bending moment will be highest and fracture is most likely to occur. The twisting of the files, however, is not the same for files of the same type, which contributes to the spreading in the fracture locations as observed in figure 4.8. The spreading in fracture locations is also due to file imperfections and a difference in node/antinode locations of ca. 0.5 mm between water and air.

As the files are never perfect (due to material imperfections or macroscopic bending), the motion of the file will be slightly unsteady, causing occasionally a higher than average amplitude of the file oscillation. In water these transients will be damped, contrary to air. This would explain why the file is observed to break sooner and more often in air than in water, as observed in our experiments, by Ahmad *et al.* (1994) [31] and by clinicians. In the study by Ahmad *et al.* it was also observed that files that came purposely in contact with a wall never fractured, supporting the hypothesis that transients are the main cause of file fracture.

### **Recommendations**

Improved resistance to file fracture could possibly be obtained by reducing the bending of the file, which corresponds to a longer wavelength of the file oscillation pattern if the same oscillation amplitude is required. A longer wavelength can be obtained by using a different driving frequency or material properties.

Alternatively, if the transient motion of the file would be the main cause of file fracture, transients, induced by file imperfections and wall contact, should be avoided. However, as is shown in the next chapter, file contact with the wall is very likely to occur.

A more systematic study of file fracture locations and times, combined with a more thorough theoretical analysis of file bending and plastic deformation, should be undertaken to elucidate the main mechanism of file fracture.

# 5

## Measurement and visualization of the occurrence of contact during Passive Ultrasonic Irrigation \*

**Abstract:** the occurrence of contact of a file with the root canal wall during Passive Ultrasonic Irrigation is inevitable considering the small dimensions and complex geometry (e.g., curvature in the axial direction) of the root canal system. Until today, it has never been evaluated how much contact will occur, and its resulting effect during clinical use of the PUI technique. In this chapter we measured the amount of contact occurring during use of PUI inside two metal root canal models of different apical size, performed by 15 trained and 15 untrained postgraduate students from two different dental schools. Most of the contact was found to take place at the coronal section of the root canal, with decreasing contact for larger canals. At the apical section of the smallest root canal, the file was found to make contact on average 20% of the time. However, the file oscillation was affected by 94% of the time. High-speed visualizations and numerical simulations of the file oscillation show that the file bounces back and forth against the wall at audible frequencies (near 5 kHz), but meanwhile can still perform its 30 kHz oscillation. No damping of the file oscillation amplitude is observed for the range of contact strengths measured. The secondary frequencies lead to interference with the 30 kHz oscillation, but acoustic streaming and cavitation will still be induced, and therefore contact does not violate the requirements for PUI to be passive. Vibrometer analysis shows furthermore that traveling waves arise on the file during contact.

---

\*To be submitted to *International Endodontic Journal* as: C. Boutsoukis, B. Verhaagen, A.D. Walmsley, M. Versluis and L.W.M. van der Sluis, "Measurement and visualization of the occurrence of contact during Passive Ultrasonic Irrigation"

## 5.1 Introduction

Irrigation of root canals with antimicrobial solutions is considered an essential part of an endodontic treatment [1], relying both on the mechanical cleaning action and the chemical ability of irrigants to kill bacteria, disrupt biofilm and dissolve tissue[2]. During the past decade irrigant activation methods, such as Passive Ultrasonic Irrigation (PUI), have been widely adopted [3], in order to augment debridement and elimination of microorganisms achieved by conventional positive-pressure irrigation with a syringe and a needle [4].

The aim of PUI is to agitate the irrigant inside the root canal system, without intentional contact between the ultrasonic file and the root canal wall [5]. This objective is highlighted by the term passive as opposed to earlier active ultrasonic preparation techniques that combined instrumentation and irrigation [4]. Therefore, the operating principle of PUI is based on the interaction between file and fluid and between fluid and debris, tissue remnants, microorganisms or dentin. However, the occurrence of direct contact between the ultrasonic file and the root canal wall is very probable considering the small dimensions (sub-millimeter) and complex geometry of the root canal system [6]. As an analogue for the likelihood of making contact inside a root canal, one can consider the popular game of Wacky Wire, where one has to pull a ring around a wire without making contact. For passive ultrasonic irrigation, this game is inverted, scaled down 20 times and performed blindly. One can then understand the difficulty in avoiding contact with the walls of the root canal during PUI.

This aspect has only been evaluated during ultrasonic instrumentation of root canals with respect to the removal of dentine by a K-file [7, 8], but in these cases a force is deliberately applied to ensure contact, in contrast to PUI. Previous experiments evaluating the interaction between file and fluid during PUI have not eliminated the influence of contact as contact with the root canal was not avoided [9, 10]. Furthermore, contact of a plastic file with the wall has been suggested as one of the reasons of ineffectiveness of sonic cleaning of the root canal [11]. Contact is also suggested to reduce the cleaning efficacy of PUI due to damping of the file motion [12, 13], and could furthermore lead to uncontrolled removal of dentin [14]. However, to date, the occurrence of contact during PUI or its effect on file oscillation and irrigant streaming has not been fully evaluated.

The aims of the present study were to:

- quantify *in vitro* the amount of contact occurring during PUI and to evaluate the effect of root canal size, file insertion depth, ultrasonic power, root canal level and previous training on PUI, and
- investigate the effect of contact on the file oscillation using experimental high-speed visualizations, laser vibrometer measurements and numerical simulations.

Two time scales are considered here, one being the time scale of the file oscillation (which is a measure for changes to the file oscillation and for potential cutting into the wall) and one being the time scale of the operator (the dentist). The latter will answer the question whether there are times during PUI in which the file is located in the center of the root canal without any contact, at which PUI can truly be called *passive*.

## 5.2 Materials & Methods

### 5.2.1 Measurement of the amount of contact *in vitro*

#### Device for electrical measurement

For the recording of the amount of contact occurring during PUI, two straight metal root canal models were manufactured (see Figure 5.1). For each one, a frustum of a cone was cut in a block of hardened steel, resulting in root canals with an apical size of 0.35 mm (ISO size 35) or 0.50 mm (ISO size 50), a taper of 0.06 mm/mm (6%) and a length of 15 mm. Each metal block was subsequently separated into three sections, coronal, middle and apical. Each section of the root canal was 5 mm high. A cylindrical opening (diameter 4.25 mm, height 5 mm) was cut in one additional section and was positioned on top of the coronal section to simulate the presence of a pulp chamber. All four sections were reassembled to form a complete root canal and

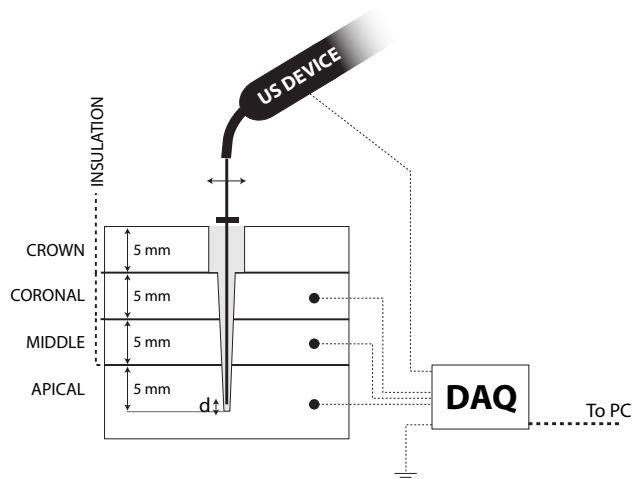


**Figure 5.1:** sketch of the metal root canal model and its connections as used for contact measurement *in vitro*. DAQ stands for Data Acquisition Device. The drawing is not to scale.

secured in place by plastic bolts. Plastic insulation layers of 0.2 mm were placed between adjacent sections, electrically isolating each section of the artificial root canal from the other sections.

Each of the three sections (coronal, middle, apical) was connected to a high-speed data acquisition device (USB 6356, National Instruments, Austin, TX, USA) capable of simultaneously recording the voltage at each root canal level at a rate of 300.000 samples per second.

A commercial dental ultrasound device (Suprasson P-Max Newtron; Satelec Acteon) was used for PUI. This device supplied the ultrasonic file with an electrical signal through the hand piece, which was also recorded by the data acquisition device. During PUI, contact between the file and one of the root canal sections resulted in the measurement of the same voltage at the file and at the root canal section, as recorded by the data acquisition device.

### Measurement protocol

To test the hypothesis that previous training and regular application of PUI may have an effect on the amount of contact, measurements were done in two Endodontology departments, being the Academic Center for Dentistry Amsterdam, The Netherlands (ACTA, group 1) and the Dental School of the Aristotle University of Thessaloniki, Greece (AUTH. group 2). Postgraduate students in ACTA are taught and employ PUI during root canal treatment on a regular basis, while no such recommendation is given to the postgraduate students in AUTH.

Postgraduate students or endodontists that had completed their training up to 5 years before the experiment in one of the departments were included in the present study. Fifteen training/trained endodontists in each of the two departments volunteered to perform a series of PUI procedures *in vitro*. Participants were kept blinded to the purpose of the study and the variables recorded during each cycle, and were assured that all data would be treated with confidentiality. The participant's profile (years of experience in dentistry, years of experience in endodontics, weekly workload in endodontics, practice limited to endodontics or not, and regular application of PUI or not) was also recorded.

Participants were asked to perform a series of typical passive ultrasonic activation cycles in the metal root canals just as they would do clinically during endodontic treatment. Silicon oil (Brookfield, Middleboro, MA, USA) that had an equal density but a viscosity 5 times that of water, was used as irrigant, because of its non-conductive and non-corrosive properties.

Activation was performed for 20 seconds using a size 20, length 25 mm Irrisafe file (Satelec Acteon, Merignac, France) positioned at  $d = 1$  mm or 3 mm short of working length, in size 35 .06 taper and size 50 .06 taper root canals, and at either low or high power ('Green 4' or 'Yellow 4'). The insertion depth was marked by a

rubber stop on the file. All experiments were performed in triplicate. No feedback on their performance was provided during or after the experiments.

### Data analysis

Voltage measurements recorded by the data acquisition device were subsequently analyzed in MatLab (The Mathworks, Natick, MA, USA) both for the time scale of the file oscillation and for the time scale of the operator.

The signal from each root canal section was compared to the original signal in the hand piece; the total percentage of time during which the two signals differed by less than 5% (noise level) was noted as *contact*. This value indicated the amount of contact on the time scale of the file oscillation.

The signal from each root canal section was also filtered by calculating the Root-Mean-Square (RMS) value for each set of 1000 data points, which allowed contact on the time scale of the operator to be calculated. The percentage of time for which this filtered signal was below a threshold level (half of the supplied voltage), was noted as *time the file is not affected by contact*, or *non-contact-affected (NCA) time*. This value indicated the time that the file spends far enough from the wall so that it cannot make contact during its oscillation. As the dentists were not asked specifically to avoid contact with the wall, this variable does not indicate the ability of a dentist to keep the file centered. Rather, this value is a result of random motion by the hand of the dentist and gives an idea of the amount of contact on the time scale of the dentist.

### Statistical analysis

The effect of dental school (ACTA, AUTH), root canal section (coronal, middle, apical), ultrasonic power (low, high), root canal size (size 35 or 50) and file insertion depth (1 mm, 3 mm) on the two variables were analyzed by two separate 5-way mixed design ANOVAs. The Shapiro-Wilk test was used to determine whether the residuals of the ANOVAs followed a normal distribution. Sphericity of the within-subjects data was evaluated by Mauchys test and equality of error variances of the between-subjects data was assessed by Levenes test. In cases that the data violated the sphericity assumption, the Greenhouse-Geisser correction was applied to the degrees of freedom. The null hypothesis was that dental school, root canal section, ultrasonic power, root canal size and file insertion depth have no significant effect on the amount of contact between the ultrasonically oscillating file and the wall of the artificial root canals, or on the fraction of time that the file is not near the wall. Planned contrasts between successive root canal sections were employed for pair-wise comparisons. Correlation between participant characteristics and the two variables was evaluated by Pearsons correlation coefficient  $r$  and point-biserial correlation, where appropriate. The level of significance was set to  $p < 0.05$ . Bonferroni correction for

multiple comparisons was applied to the level of significance when appropriate. Statistical analysis was performed using SPSS 15.0 for Windows (SPSS Inc, Chicago, IL, USA).

## 5.2.2 File oscillation characteristics

### Vibrometer measurements

The oscillation characteristics of the file in contact with a hard surface were measured using a laser scanning vibrometer [15]. A K-file (size 15, length 21 mm; Satelec Acteon), driven at ‘high’ (‘Yellow 4’) power setting by a commercial dental ultrasound device (Suprasson P-Max Newtron; Satelec Acteon), was positioned inside a water bath of 1 L in front of the laser scanning vibrometer (OFV-056; Polytec, Waldbronn, Germany). The file was made to oscillate in the scanning plane of the vibrometer. A dental excavator was brought in contact using a translation stage (9067M, New Focus, San Jose, CA, USA) from the back of the file at different positions along the file with such force that the excavator touched the file but did not bend it. Measurements were conducted while the excavator was positioned at the following distances  $d_c$  from the tip of the file:

- No contact
- At the tip ( $d_c = 0$  mm)
- At the first antinode from the tip ( $d_c = 3$  mm)
- Halfway the flutes ( $d_c = 7.5$  mm)
- At the start of the flutes ( $d_c = 15$  mm)
- At the driving end of the file ( $d_c = 21$  mm)

Contact was verified audibly.

Approximately 50 measurement points were set up along the file at which the vibrometer measured the oscillation amplitude and phase at a sampling rate of 1.5 MHz.

### High-speed imaging

A high-speed camera was used to visualize the file oscillations on the time scale of the file oscillations itself. A high-speed camera (HPV-1; Shimadzu Corp, Kyoto, Japan), recording at a speed of 250.000 frames/s, was attached to a microscope (BX-FM; Olympus, Tokyo, Japan) with 10 $\times$  magnification. Illumination was provided in bright-field mode by a continuous-wave cold light source (ILP-1; Olympus). A K-file

(size 15, length 21 mm; Satelec Acteon) driven by a commercial dental ultrasound device (Suprasson P-Max Newtron; Satelec Acteon) was used at ‘low’ (‘Green 4’) or ‘high’ (‘Yellow 4’) power setting. The file was placed near a hard plastic wall inside a water bath of dimension  $75 \times 62 \times 117$  mm, under an angle of approximately 5 degrees with respect to the wall. The file was then translated in steps of  $50 \mu\text{m}$  toward the wall, thereby increasing the contact strength. Calibration with a balance (TP-3002, Denver Instruments, Gttingen, Germany; accuracy 0.01g) showed that the contact strength (defined here as weight) for this configuration increased at a rate of  $6 \text{ mg}/\mu\text{m}$ .

The frequency of oscillation was obtained by tracking the oscillation of the file tip in the high-speed recording.

### Numerical simulation

The oscillation of the file was simulated using a previously described and validated numerical model (Chapter 4)[15]. Briefly, the one-dimensional equation of motion for a tapered beam was explicitly discretized, on a grid with a resolution of 0.25 mm and a time step of 10 ns. In order to simulate the presence of the wall, the oscillation amplitude  $Y$  at the point of contact  $d_c$  was required to be positive for all times  $n$ : [16]

$$Y_{d_c}^n \geq 0 \quad (5.1)$$

The frequency of oscillation was obtained by tracking the oscillation of the file tip in the high-speed recording.

The numerical model assumed the file to be oscillating in air, in the absence of viscous damping forces. Instabilities may therefore be overestimated compared to when the file is oscillating in an irrigant.

## 5.3 Results

### 5.3.1 Contact occurring inside a root canal

An overview of the results is given in Figure 5.2. Overall, the range of values for the actual contact was 0.04-91.64% of the activation time. At the narrowest section (apical) of the smallest root canal (size 35) and at a distance of 1 mm from working length, the average amount of contact was 20%. Supplementary Material movie 1 shows a reconstruction of the contact occurring during the 20 seconds of PUI, based on one randomly chosen measurement.

There was a significant main effect for all four within-subjects factors (*root canal section, ultrasonic power, root canal size and file insertion depth*). Contact was significantly increased at the low power setting as compared to the high power setting ( $p < 0.001$ ), in size 35 root canals as compared to size 50 ( $p < 0.001$ ) and when



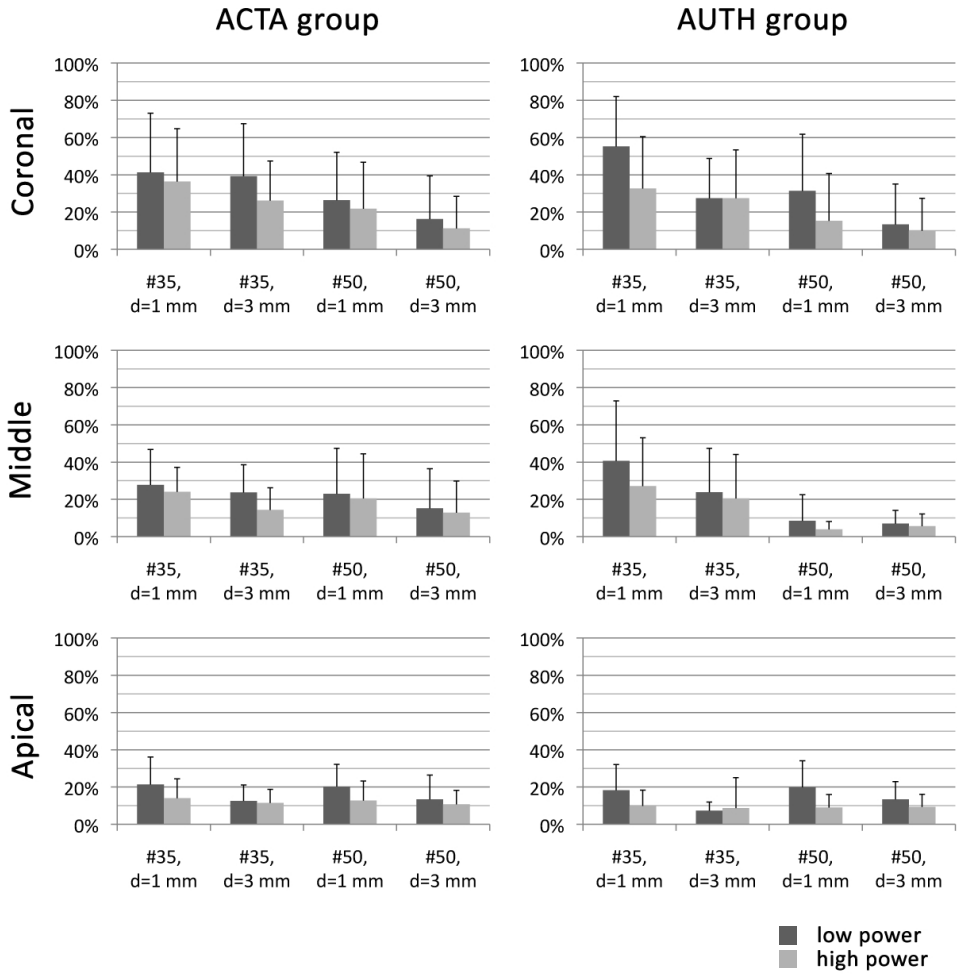


Figure 5.2: Average and standard deviation of the measured contact.

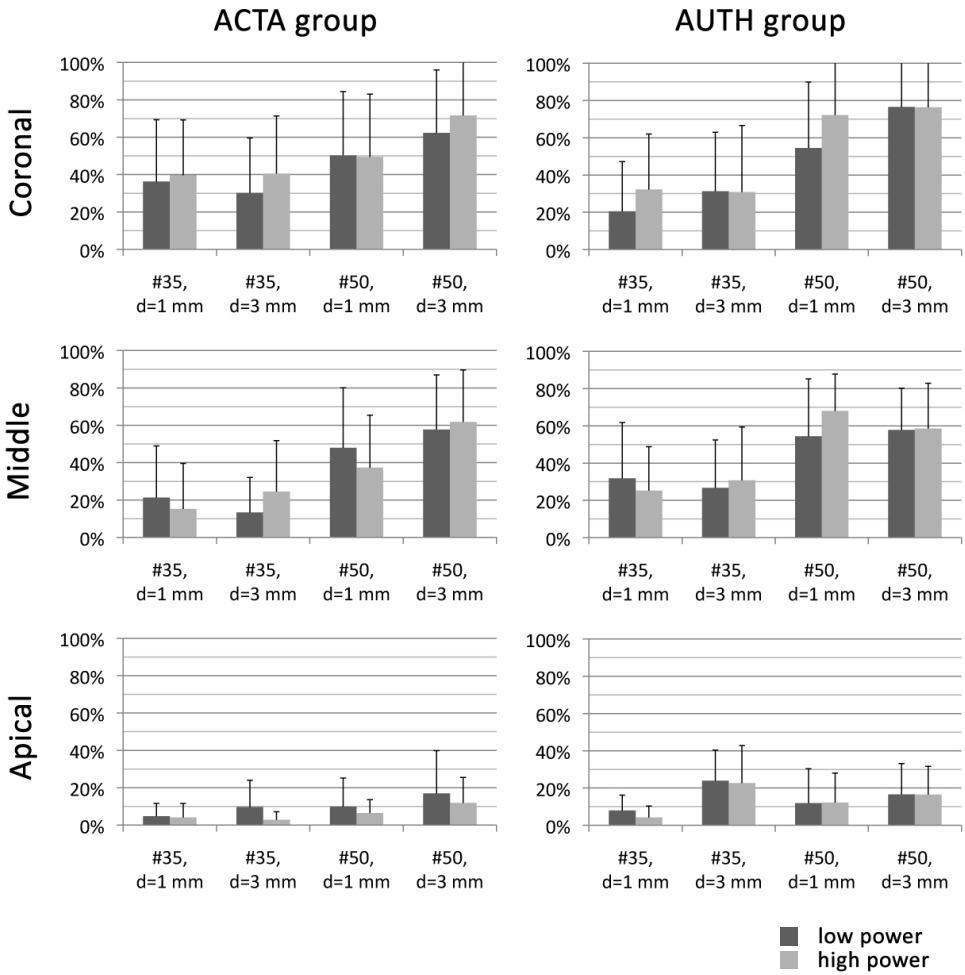


Figure 5.3: Average and standard deviation of the NCA contact.

the file was positioned at 1 mm short of working length as compared to 3 mm ( $p < 0.001$ ). Moreover, the three *root canal sections* showed a significant main difference ( $p < 0.001$ ). Planned contrasts revealed that the amount of contact was significantly more in the coronal third as compared to the middle third ( $p = 0.001$ ) and in the middle third as compared to the apical third ( $p = 0.014$ ). The main effect of the between-subjects factor dental school was non-significant ( $p = 0.534$ ).

Furthermore, there was a statistically significant interaction between *root canal section* and *root canal size* ( $p < 0.001$ ). While in size 35 root canals the amount of contact decreased from the middle towards the apical section, in size 50 root canals it showed an increase.

In addition, a statistically significant interaction between *root canal section*, *root canal size* and *dental school* was identified ( $p = 0.022$ ). Planned contrasts revealed that among the dentists from ACTA, the amount of contact showed a similar gradual decrease from the middle towards the apical section for both size 35 and 50 root canals, while among the dentists from AUTH the amount of contact showed a decrease from the middle towards the apical section for size 35 root canals, but an increase for size 50 root canals ( $p = 0.003$ ). All other interactions were non-significant.

No significant correlations were identified between the participant characteristics (years of experience in dentistry, years of experience in endodontics, weekly workload in endodontics, practice limited to endodontics or not, and regular application of PUI or not) and the amount of contact.

### 5.3.2 Non-contact-affected (NCA) time

An overview of the results is shown in Figure 5.3. Overall, the range of values for the NCA time was 0.15-100%. In the narrowest case, at the apical section of the smallest root canal (size 35) and at a distance of 1 mm from working length, the average fraction of time was 6%.

There was a significant main effect for *root canal section*, *root canal size* and *file insertion depth*. The NCA time significantly increased in size 50 root canals as compared to size 35 ( $p < 0.001$ ) and when the file was positioned at 3 mm short of working length as compared to 1 mm ( $p = 0.004$ ). Moreover, the main effect of *root canal section* was also statistically significant ( $p < 0.001$ ). Planned contrasts revealed that the NCA time significantly decreased in the middle third as compared to the coronal third ( $p = 0.010$ ) and in the apical third as compared to the middle third ( $p < 0.001$ ). The main effects of *ultrasonic power* and the between-subjects factor *dental school* were not significant ( $p = 0.278$  and  $p = 0.150$  respectively).

Furthermore, there was a statistically significant interaction between *root canal section* and *ultrasonic power* ( $p = 0.012$ ), indicating that the effect of root canal section differed according to the ultrasonic power. Planned contrasts showed that the NCA time in the coronal third was higher for high power as compared to low power, but in

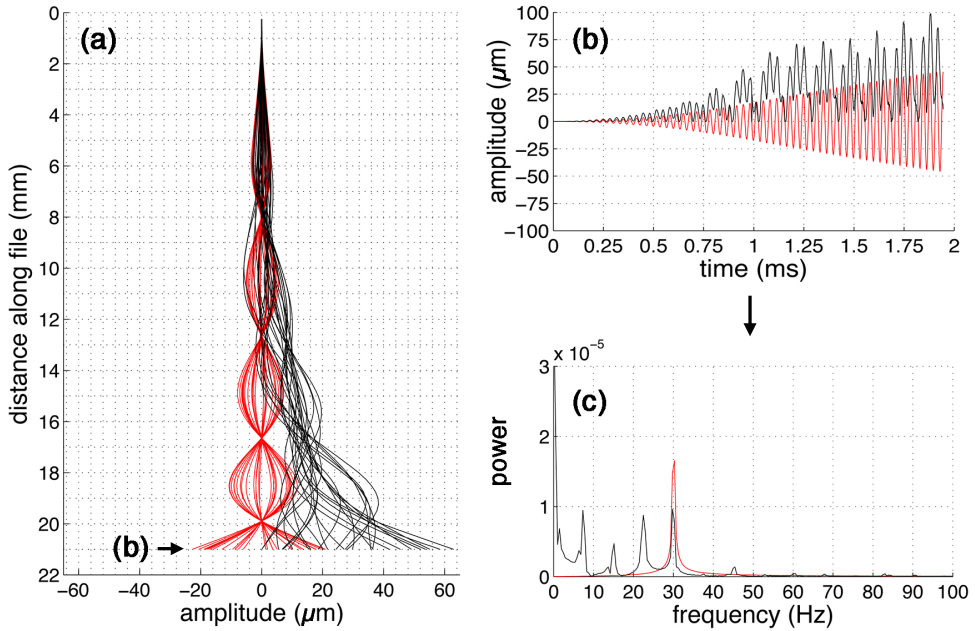


**Figure 5.4:** Oscillation pattern (a) for a K15/21 file, without (red) and with (black) contact at the tip. The oscillation amplitude of the tip (b) is used to calculate the frequency spectrum (c). The file was driven at a frequency of 30 kHz and an amplitude of 0.1 μm and assumed to oscillate in air. The time interval between lines in (a) is 6 μs.

the apical third this difference was reversed.

In addition, a statistically significant interaction between *root canal section* and *root canal size* was identified ( $p < 0.001$ ). When comparing the NCA time in the middle third of the root canal to the NCA time in the apical third, the decline is significantly greater in size 50 root canals as compared to size 35. Another significant interaction was identified between *insertion depth*, *ultrasonic power* and *dental school* ( $p = 0.031$ ). The increase in the NCA time was more pronounced between 1 and 3 mm insertion depth when the high power was used by the participants from ACTA, but this increase was more evident when participants from AUTH used the low power.

Similarly, a significant interaction was identified between *insertion depth*, *root canal size* and *dental school* ( $p = 0.007$ ). There was a similar increase in the NCA time between 1 mm and 3 mm insertion depth for both size 35 and size 50 root canals used by participants from AUTH, while for participants from ACTA there was also an increase between 1 mm and 3 mm insertion depth in size 50 root canals but not in

size 35.

Finally, a statistically significant interaction between *root canal section*, *root canal size* and *file insertion depth* was also identified ( $p=0.024$ ). Planned contrasts revealed that the NCA time was similarly decreased between the coronal and the apical third for both insertion depths in size 50 root canals, whether the decrease was more evident when the file was inserted to 1 mm short of working length as compared to 3 mm in size 35 root canals ( $p=0.013$ ).

All other interactions were non-significant. No significant correlations were identified between the participant characteristics and the NCA time.

### 5.3.3 File oscillation characteristics

The high-speed visualization and the numerical model showed that, when the file is near the wall, the file still oscillates with a frequency of 30 kHz, but occasionally hits the wall and is then displaced away from the wall (see Supplementary Material movie 2). The file then tends to move back to the wall because of the persistent load exerted by the operator, causing a low-frequency secondary oscillation of the whole file on top of the driving frequency of 30 kHz.

A Fourier analysis of the motion of the file tip in the numerical simulation (Figure 5.4) and in the high-speed recording (Figure 5.5) showed a main peak at approximately 30 kHz when the file oscillates unconstrained; when the file is allowed to make contact, another peak around 6 kHz shows up (besides an increase for all frequencies). Figure 5.6 shows an example of the frequency analysis of a signal from the apex of the metal root canal. An increase of amplitude for all frequencies, but most noticeably for frequencies around 4-5 kHz, can be observed.

The numerical simulation showed a continuing increase in amplitude of the secondary frequency and also instabilities along the file that were not observed in the

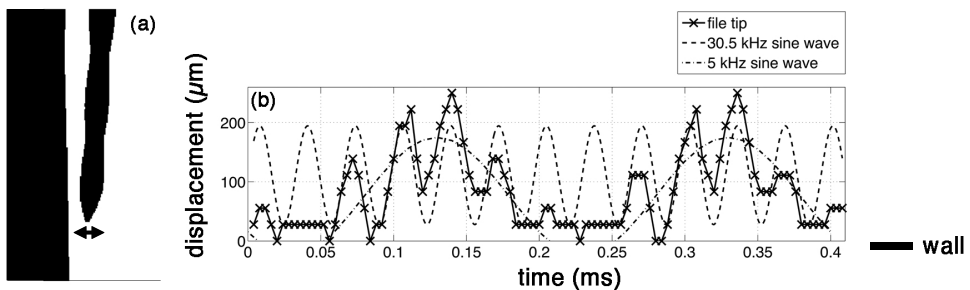


**Figure 5.5:** Analysis of a high-speed recording of an oscillating file in contact (shown in (a)). The oscillation amplitude is tracked (b) and appears to be a superposition of a 5 kHz and a 30.5 kHz sine wave (both shown for reference).

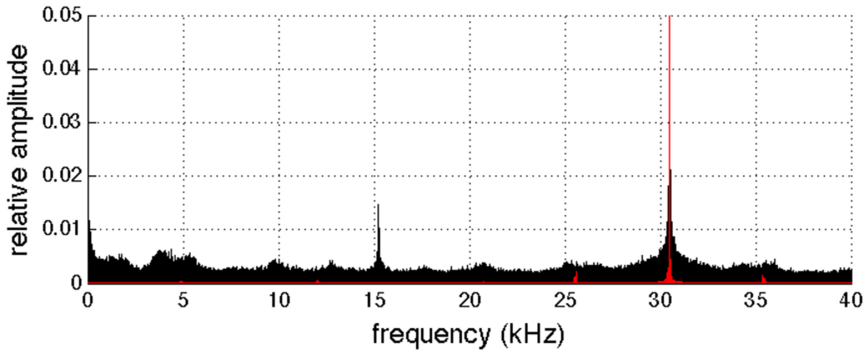


**Figure 5.6:** *Frequency analysis of one measurement with the metal root canal model, showing an increase in amplitude for all frequencies for the signal at the apex (black), where most contact is expected, compared to the hand piece voltage (red). Especially around 4 kHz there is a significant increase in amplitude.*

high-speed recordings. These effects became increasingly apparent when the simulation was allowed to continue for tens of cycles (of the fundamental frequency).

Interference of the 30 kHz oscillation with a secondary frequency leads occasionally to higher amplitudes and velocities, a process known as beating or constructive interference. (In the remainder of this article we avoid the use of the word beating, to avoid mistaking it for the bouncing against the wall.) This can be observed in Figures 5.4 and 5.5 and Supplementary Material movie 2.

In the absence of a wall, a cloud of cavitation bubbles was observed at the tip of the file at power setting ‘high’; no cavitation was visible at power setting ‘low’. When the file was allowed to make contact, cavitation did occur at power setting ‘low’ and increased for power setting ‘high’. The bubble cloud was most pronounced between the file and the wall when there was constructive interference of the two oscillation frequencies.

The RMS amplitude (Figure 5.7), as calculated from the high-speed recordings, showed that an increase in contact strength did not reduce the oscillation amplitude of the file tip significantly, for both low and high driving power.

The measurements with the vibrometer showed that contact at an antinode of the unconstrained file induced traveling waves along the file (Figure 5.8). This was verified (data not shown here) with high-speed recordings and also observed in the numerical simulations of file oscillation. Traveling waves were not present when contact was made at a node of the unconstrained file oscillation.

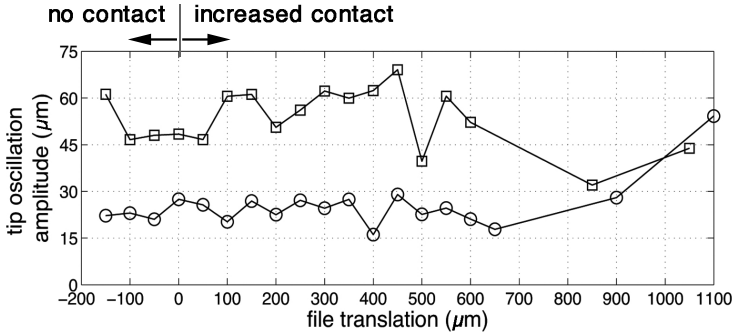


**Figure 5.7:** Oscillation amplitude of a file in contact with a wall, as determined from the high-speed recordings. The file translation on the horizontal axis corresponds to an increased contact force, up to 6 g at 1000  $\mu\text{m}$ . The file was driven at low (circles) or high (squares) power.

## 5.4 Discussion

In this study it was found that none of the 30 participants managed to avoid contact with the wall during the 20 seconds of passive ultrasonic irrigation, although sometimes the amount of contact was close to zero. In the narrowest section (apical) of the smallest root canal (size 35) and at a distance of 1 mm from working length, the file was affected by contact during, on average, 94% of the time. In other words, during only 6% of the time was the file kept far away enough from the wall in order not to make contact. The time that the file was actually in contact with a wall, however, was only 20%. This can be attributed to the secondary frequency of oscillation that was observed after its collisions with the root canal wall, which makes the file oscillate away from the wall for half a period of the secondary frequency. During this period, the contact value is zero, but the file oscillation is nevertheless affected by the contact and therefore the NCA time is zero as well. Note that the contact time and the NCA time represent different measures of the contact (or non-contact). Due to time-averaging, the NCA time is not simply the inverse of the contact time.

With more space available around the file tip (a larger root canal and/or a larger distance away from working length), the amount of contact decreased and the NCA time increased, suggesting that it becomes easier to keep the file away from the wall.

Surprisingly, most of the actual contact occurred at the coronal section of the root canal, which is always wider than the apical section. However, also the NCA time was highest at the coronal section. This can be explained by considering that the files were probably inserted under an angle with respect to the central axis of the root canal. At the apex there may be a lot of contact as the NCA time is low, but due to the secondary frequency, the file bounces away from the walls during a large

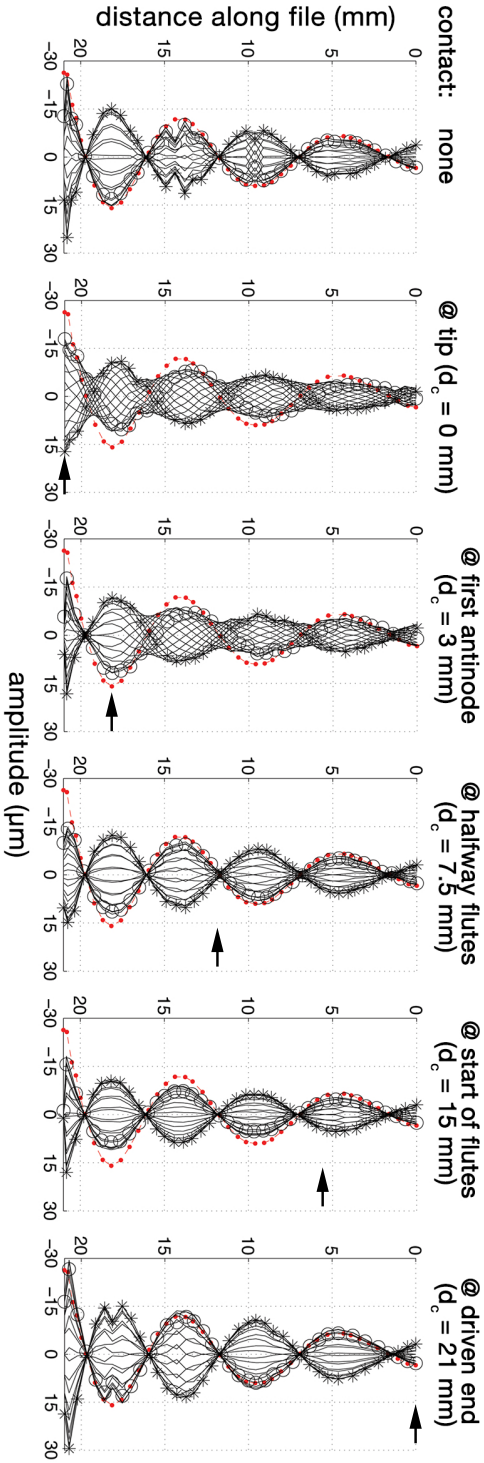


**Figure 5.8:** Oscillation patterns for a file in contact at different locations along the file (indicated above each plot and with a circle on the right) as measured with the vibrometer system. Each line represents a  $20^\circ$  phase shift; the lines for  $0^\circ$  and  $180^\circ$  are indicated with a circle and an asterisks respectively. The dashed line indicates the non-contact result.



period of time, which results in a low contact value. At the coronal section, the file is meanwhile often being rested against the wall and not bouncing back and forth as much as at the apical section.

None of the individual characteristics of the participants had a significant influence on the amount of contact or the NCA time in the root canal. Other characteristics, not recorded in this study, may be important, or the dynamics that govern the file oscillation may be more important than movements induced by the dentist. No specific guidelines were given to carefully avoid contact of the file with the root canal wall. Thus, the trained participants (ACTA group) were expected to follow the taught protocol and try to avoid contact, while the non-trained participants (AUTH group) would probably apply PUI according to their best clinical judgement. It can be argued that comparison between the two groups may have been biased. However, the purpose of this comparison was to investigate the difference between a trained and a non-trained group of clinicians, rather than the ability of the two groups to follow a specific PUI protocol, therefore not balancing the groups was an inherent requirement. Even so, lack of significant differences between the two groups indicated that previous training and regular application of PUI did not affect the performance of the participants, therefore the relevant hypothesis was disproved. It is possible that even the non-trained participants (AUTH group) had some previous information on the purpose and method of PUI, which is widely discussed in congresses and in the current literature, but this was expected to be the case for any group of dentists following an endodontic training program, thus, the comparison was considered valid.

Interestingly, a higher power setting, which was shown in a previous study to increase the oscillation amplitude [17], resulted in less contact. This counterintuitive result can be understood from the secondary frequency induced during contact. The secondary frequency can be attributed to conservation of momentum, as during the inelastic collision with the wall, the momentum of the oscillating file is converted to a displacement away from the wall. At a higher power setting, the momentum of the file will be larger and therefore the displacement after collision with the wall will be larger. This leads to a lower secondary frequency and therefore a lower contact value.

The high-speed visualizations and vibrometer measurements have shown that contact did not necessarily reduce the oscillation amplitude, at least for contact forces smaller than 6 g, thereby disproving earlier suggestions [12, 13]. The feedback system of the commercial endodontic device probably compensates for the increase in load, as was also concluded elsewhere [15, 18]. As the file can still oscillate freely during several cycles when it is away from the wall, the interaction between the file and the fluid, a requirement for passive ultrasonic irrigation, is still there. Acoustic streaming and cavitation are therefore likely to remain present. The cleaning mechanisms of passive ultrasonic irrigation should therefore not be affected, even though contact is nearly always present during ultrasonic irrigation of the root canal. Thus

passive ultrasonic irrigation may still be called *passive*. Alternatively, the term ‘ultrasonic activated irrigation’ may be adopted to avoid confusion.

The secondary frequency that is introduced due to contact can by itself introduce additional streaming, but it can also affect the 30 kHz oscillations. Constructive interference of the two frequencies leads to an increased file displacement amplitude and velocity; destructive interference leads to the opposite. Transients may be induced in the flow, which may actually be beneficial for the induced acoustic streaming and mixing, and increase the likeliness of cavitation. Transient file behavior has already been shown in a previous study to be beneficial for dentin debris removal [9].

The vibrometer measurements did not show a secondary frequency, however a vibrometer measures only relative displacement. The vibrometer did however show the occurrence of traveling waves. Traveling waves on solids have been shown to be able to induce a streaming along the surface [19, 20], in this case in the apical and coronal direction. The high-speed visualization and numerical simulation showed that these traveling waves do indeed occur.

Damage to the dentin wall due to contact by cutting files is related to repeated hitting of the wall by the file [14]. Based on the findings of the present study, the rate of damage should be associated with the secondary frequency of a few kHz rather than the 30 kHz driving frequency, as the file only hits the wall once per cycle of the secondary frequency. A lower secondary frequency is therefore desirable, which can be obtained by avoiding (strong) pushing against the wall by the dentist or using a file with a lower stiffness and/or non-cutting cross-section [21]. A high power setting was also associated with a lower secondary frequency and less contact, however, the momentum of each collision with the wall is then also higher than at low power setting, and reduced damage cannot be ensured.

The fact that there is an audible sound when the oscillating file is in contact with a wall, already suggests that there is a low-frequency component. The high-speed visualization has shown that that is indeed the case. Sound can therefore be a first, but not exclusive, indicator for contact. There may be other sources of sound, and very strong contact may dampen the file oscillation and associated sound completely.

Unfortunately, the strength with which the endodontists pushed the file against the wall could not be determined with the current experimental setup. As Figure 5.6 shows, there is not a single but a multitude of secondary frequencies associated with contact. Furthermore, the motion of the file may become chaotic when there are multiple points of contact inside a root canal, and when traveling waves are included, prohibiting calibration of the contact. The fact that the feedback system of an endodontic device compensates its driving voltage for the presence of load, could also not be used for calibration, due to a lack of knowledge on the exact feedback mechanism. With the present set of data, therefore only general comments could be made on the contact strength.

The contact strength is likely to be involved in the secondary frequencies that are generated. The high-speed recording and numerical simulation showed secondary frequencies of 5 and 7 kHz respectively, whereas the secondary frequency obtained from the electrical signal at the apex was typically smaller than 5 kHz. These differences are likely due to the force with which the file is pushed against the wall, and due to the stiffness of the file. When a large force is applied to the file, it will oscillate back to the wall sooner than with a small force. Indeed, a pilot experiment showed that the amount of contact increased as the file was pushed with higher force against a wall. This change in frequency can also be demonstrated by holding the oscillating file against the table; a higher force results in an audibly different tone.

Different files were used in the contact measurements (Irrisafe file, size 20, length 25 mm) and in the visualization (K-file, size 15, length 21 mm), which may affect the secondary frequency as well. The secondary frequency is likely to be dependent on the stiffness of a file, determined by the file geometry and material. A stiff file will tend to move back to the wall quicker than a more flexible file. A pilot simulation with the numerical model described above confirmed this prediction. The stiffness of a file can be estimated from the eigenfrequency of the file, which have been determined numerically for several endodontic files in Chapter 4 [15]. For typical K-files, used in the oscillation characteristics measurements, the eigenfrequency has a value between 1.1 and 1.6 kHz; for the Irrisafe file used in the electrical contact model the eigenfrequency is around 0.5 kHz. The measured secondary frequencies are however approximately 10 times higher than the eigenfrequencies, suggesting that the driving of the file and the presence of a wall have a significant influence on the secondary frequency. Nevertheless, the relative stiffness of endodontic files as observed from the eigenfrequencies can give a relative prediction for the secondary frequency.

Similarly, the viscosity of the irrigant may affect the secondary frequency, by increasing the damping on the file oscillation. In the *in vitro* experiments silicon oil, with a viscosity 5 times that of water, was used as irrigant. Thus, the secondary frequency may have been increased, and the amount of contact underpredicted. This, however, should not affect the inter-study results of the *in vitro* measurements.

It must be kept in mind that the simplified geometry of the root canals used in the present study followed a “best-case scenario”. Clinically, it is expected that more extensive contact would occur, due to more complex root canal geometries. Future studies should analyze the influence of the root canal geometry on the occurrence of contact, and should also evaluate the effect that contact has on cleaning.

## 5.5 Conclusion

Contact of the ultrasonic file with a wall during PUI occurred in most of the cases studied and during a large fraction of time. The amount of contact was reduced in

larger root canals, when a higher power was used, when the file was positioned further away from working length and from coronal towards apical third of the root canal. Previous training and regular application of PUI did not have a significant effect.

High-speed visualizations, vibrometer measurements and numerical simulations showed the occurrence of traveling waves during contact, as well as the generation of a secondary, audible frequency on top of the 30 kHz driving frequency. Due to this secondary frequency, the oscillation amplitude is not reduced, and acoustic streaming and cavitation can still take place. As the working mechanisms of PUI are therefore not affected, PUI may still be called *passive*.

## References

- [1] M. Haapasalo, U. Endal, H. Zandi, and J. M. Coil, "Eradication of endodontic infection by instrumentation and irrigation solutions", *Endodontic Topics* **10**, 77–102 (2005).
- [2] K. Gulabivala, B. Patel, G. Evans, and Y.-L. Ng, "Effects of mechanical and chemical procedures on root canal surfaces", *Endodontic Topics* **10**, 103–122 (2005).
- [3] J. Dutner, P. Mines, and A. Anderson, "Irrigation trends among american association of endodontists members: A web-based survey", *Journal of Endodontics* **38**, 37–40 (2012).
- [4] L. W. M. van der Sluis, M. Versluis, M. K. Wu, and P. R. Wesselink, "Passive ultrasonic irrigation of the root canal: a review of the literature", *International Endodontic Journal* **40**, 415–426 (2007).
- [5] R. N. Weller, J. M. Brady, and W. E. Bernier, "Efficacy of ultrasonic cleaning", *Journal of Endodontics* **6**, 740–743 (1980).
- [6] F. Vertucci, "Root canal morphology and its relationship to endodontic procedures", *Endodontic Topics* **10**, 3–29 (2005).
- [7] P. Briggs and K. Gulabivala, "The dentine-removing characteristics of an ultrasonically energized Kfile", *International Endodontic Journal* 259–268 (1989).
- [8] J. Regan, M. Sherriff, and N. Meredith, "A survey of interfacial forces used during endosonic instrumentation of root canals", *International Endodontic Journal* **34**, 54–62 (2001).
- [9] L. Jiang, B. Verhaagen, M. Versluis, C. Zangrillo, D. Cuckovic, and L. W. M. van der Sluis, "An evaluation of the effect of pulsed ultrasound on the cleaning efficacy of passive ultrasonic irrigation", *Journal of Endodontics* **36**, 1887–1891 (2010), *see also Chapter 10 of this thesis*.
- [10] L. Jiang, B. Verhaagen, M. Versluis, and L. van der Sluis, "Influence of the Oscillation Direction of an Ultrasonic File on the Cleaning Efficacy of Passive Ultrasonic Irrigation", *Journal of Endodontics* **36**, 1372–1376 (2010), *see also Chapter 7 of this thesis*.
- [11] L. Jiang, B. Verhaagen, M. Versluis, and L. van der Sluis, "Evaluation of a sonic device designed to activate irrigant in the root canal", *Journal of Endodontics* **36**, 143–146 (2010), *see also Chapter 9 of this thesis*.
- [12] M. Ahmad, T. R. Pitt Ford, and L. A. Crum, "Ultrasonic Debridement of Root Canals: An Insight into the Mechanisms Involved", *Journal of Endodontics* **13**, 93–101 (1987).

- [13] A. D. Walmsley and A. R. Williams, “Effects of constraint on the oscillatory pattern of endosonic files”, *Journal of Endodontics* **15**, 189–194 (1989).
- [14] S. C. Lea, B. Felver, G. Landini, and A. D. Walmsley, “Ultrasonic scaler oscillations and tooth-surface defects”, *Journal of Dental Research* **88**, 229–234 (2009).
- [15] B. Verhaagen, S. C. Lea, L. W. M. van der Sluis, A. D. Walmsley, and M. Versluis, “Oscillation characteristics of endodontic files: numerical model and its validation”, *IEEE - Transactions on Ultrasonics, Ferroelectrics and Frequency Control* accepted (2012), *see also Chapter 4 of this thesis*.
- [16] F. Avanzini and M. van Walstijn, “Modelling the Mechanical Response of the Reed-Mouthpiece-Lip System of a Clarinet. Part I. A One-Dimensional Distributed Model”, *Acta Acustica* **90**, 537–547 (2004).
- [17] L.-M. Jiang, B. Verhaagen, M. Versluis, J. Langedijk, P. R. Wesselink, and L. W. M. Van der Sluis, “The influence of the ultrasonic intensity on the cleaning efficacy of passive ultrasonic irrigation”, *Journal of Endodontics* **37**, 688–692 (2011), *see also Chapter 8 of this thesis*.
- [18] D. Parmar, M. Mann, A. D. Walmsley, and S. C. Lea, “Cutting characteristics of ultrasonic surgical instruments”, *Clinical Oral Implants Research* **22**, 1385–1390 (2011).
- [19] C. Bradley and R. White, “Acoustically driven flow in flexural plate wave devices: theory and experiment”, *IEEE Ultrasonics Symposium Proceedings* **1**, 593–597 (1994).
- [20] C. J. Cunningham and E. S. Senia, “A 3-Dimensional study of canal curvatures in the mesial roots of mandibular molars”, *Journal of Endodontics* **18**, 294–300 (1992).
- [21] L. W. M. Van der Sluis, M. K. Wu, and P. R. Wesselink, “A comparison between a smooth wire and a k-file in removing artificially placed dentine debris from root canals in resin blocks during ultrasonic irrigation”, *International Endodontic Journal* **38**, 593–596 (2005).

## Appendices

### 5.A Physical model for the secondary frequency

A physical model is constructed to investigate the origin of the secondary frequency, see Figure 5.9. The tip of the file is considered to be a spring with constant  $k = m\omega_0^2$  (with  $m$  and  $\omega_0$  the mass and eigenfrequency of the file, respectively), which is being forced toward the wall with the operators force  $F_{dent}$ . The equation of motion for the file tip, relating the operator force and the spring force to the file displacement  $y$ , is then given by:

$$m\ddot{y} = F_{dent} + ky \quad (5.2)$$

The double dot indicates the second derivative to time. The two boundary conditions consist of the requirement that the file amplitude is initially zero and the velocity is

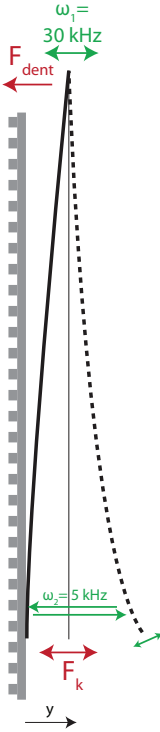


**Figure 5.9:** Sketch of the force balance and oscillations of the file (black) when in contact with a wall (gray), showing the forces (red) and oscillations (green) on the file.

given by the oscillatory velocity  $A\omega_1 \cos(\omega_1 t_c)$  at the time of collision  $t_c$ , associated with the driving frequency of  $\omega_1 = 2\pi 30$  kHz. The solution for each displacement after collision (i.e. half a period of the secondary frequency) is given by:

$$y(t) = \frac{\epsilon A \omega_1 \cos(\omega_1 t_c)}{\omega_0} \sin(\omega_0 t) + \frac{F_{dent}}{k} \cos(\omega_0 t) - \frac{F_{dent}}{k} \quad (5.3)$$

This equation is a superposition of two sinusoidal waves with a frequency that is the eigenfrequency of the file, and two different amplitudes. The resulting secondary frequency is twice the eigenfrequency (i.e. only half the oscillation is finished when the next collision comes). This equation can be used recursively to simulate multiple collisions with the wall. The secondary frequency  $\omega_2$  can then be obtained from the resulting motion. The collision may not be elastic, due to the otherwise neglected deformation of the file, which can be incorporated by taking  $\epsilon < 1$ . Fluidic damping is neglected.

The resulting displacement as a function of time is shown in Figure 5.10 and looks typically very similar to the graphs shown earlier in this article. Using a measured file weight of 30 mg and eigenfrequency of 1.2 kHz and estimating the operator force to be 5 g results in a secondary frequency of 2.5 kHz. This secondary frequency is slightly lower than that observed experimentally, but can be increased by changing  $\epsilon$ .

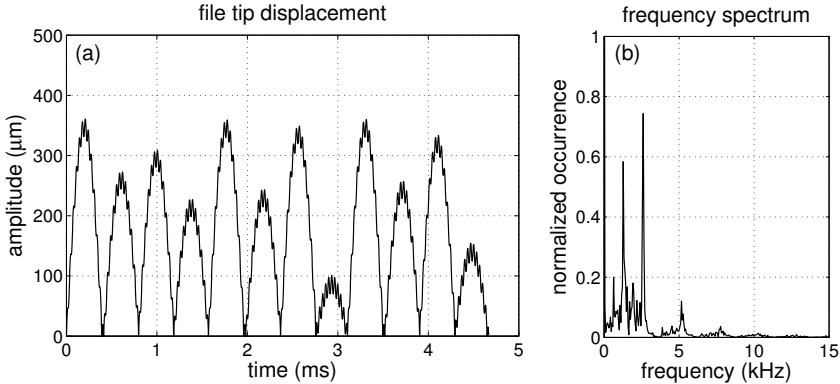


**Figure 5.10:** File displacement (a) and corresponding frequency spectrum (b) for a file in contact with a wall, as calculated with the physical model.

The model furthermore predicts an increase in secondary frequency with increasing file stiffness and operator force, and decreasing secondary frequency with increasing driving frequency and amplitude, agreeing with the earlier observations from the measurements and the simulations.

## 5.B Supplementary material

(Online at [http://stilton.tnw.utwente.nl/rootcanalcleaning/Gallery\\_of\\_Irrigant\\_Motion](http://stilton.tnw.utwente.nl/rootcanalcleaning/Gallery_of_Irrigant_Motion))

Movie 1. Reconstruction of the contact occurring during the 20 seconds of PUI, based on one randomly chosen measurement. Contact is represented in red at the relevant section.

Movie 2. High-speed visualization of a file oscillating against a wall. Interference of the two frequencies can be observed, as well as cavitation between the file and the wall. Recording speed is 250 Kfps; the diameter of the file is 200  $\mu\text{m}$ .

# 6

## Acoustic streaming induced by an ultrasonically oscillating endodontic file \*

**Abstract:** In this chapter we investigate the induced acoustic streaming, pressure and shear stress in a two-dimensional cross-section of the root canal, using a combination of theoretical and numerical predictions and high-speed experimental validations. The endodontic file is modeled as a cylinder oscillating inside a larger, concentric cylinder representing the confinement of the root canal. The induced flow consists of an oscillatory and a steady component, each with different flow characteristics. Of specific interest are the influence of the oscillation characteristics of the inner cylinder on the flow characteristics and the presence of a wall or confinement. The theory of acoustic streaming describes very well the flow induced by an ultrasonically oscillating endodontic file, consisting of an oscillatory component, dominant near the file, and a steady component, further away from the file. Measurement of the steady pressure with a hydrophone and the instantaneous local pressure field from bubble oscillations, also agree well with the theoretical and numerical predictions. The oscillatory component of both the pressure and shear stress is two or three orders of magnitude higher than the steady component. Furthermore, the presence of a confinement affects the formation of steady jets and increases the oscillatory velocities and associated pressure and shear stress. Previous work considering only the steady component of the flow therefore underestimated the hydrodynamic effect induced by ultrasonic files in confinement.

---

\*To be submitted to *Journal of the Acoustical Society of America* as: B. Verhaagen, C. Boutsioukis, L.W.M. van der Sluis and M. Versluis, "Acoustic streaming induced by an ultrasonically oscillating endodontic file"



## 6.1 Introduction

During a root canal treatment an antimicrobial fluid is injected into the infected root canal in order to disinfect the root canal system [1]. However, the complex geometry of the root canal system limits the effectiveness of the flow of irrigant when using a needle and syringe, resulting in an incomplete disinfection of the root canal [2, 3].

Passive Ultrasonic Irrigation (PUI) was introduced in endodontics in 1970 [4, 5] as a method to enhance the cleaning efficacy. An ultrasonically oscillating miniature file agitates the fluid by inducing microstreaming, more commonly known as *acoustic streaming*, which is a well-studied problem in the literature of the past century [6, 7]. The acoustic streaming is believed to improve cleaning by enhancing mixing of the antimicrobial fluid (irrigant) and by exerting a shear stress on the bacteria, dentine debris and smear layer on the root canal wall. Concurrently, cavitation (formation and collapse of vapor bubbles) can be generated, enhancing the cleaning efficacy. [8, 9]

The exact working mechanisms of PUI were not fully elucidated for 20 years until the articles by Ahmad and coworkers [10–13]. They attributed the improvement in cleaning to the induced streaming and not to cavitation, which they reasoned to have a limited occurrence because of the small dimensions of the root canal. Two equations have been derived, one for the induced flow velocity ( $U = \frac{\omega y^2}{R}$ ) and one for the shear stress ( $\tau = \frac{\mu \omega y^2}{\delta R}$ ). These have been used frequently in the endodontic literature to explain PUI cleaning efficacy findings [13–16].

However, only the velocities and pressures of the steady component of the flow were considered, whereas acoustic streaming is known to consist of an oscillatory component as well, which may contribute to the cleaning process. The aim of the present study is therefore to investigate both components of the flow by evaluating the two-dimensional in-plane velocity field. Characteristics of the velocity field, e.g. the directivity or angle dependance, and the associated pressures on the wall of the root canal confinement will elucidate the contribution of both velocity components in the cleaning by acoustic streaming. The typical frequency of 30 kHz as used in endodontics requires high-speed experiments and Computational Fluid Dynamics simulations on the time scale of the file oscillations, which is of the order of microseconds.

## 6.2 Theoretical description of acoustic streaming around an endodontic file

Acoustic streaming was introduced by Lord Rayleigh in 1884 [17] to describe the transport phenomena occurring in a Kundt's tube. Schlichting [18] extended this theory to the case of an oscillating cylinder, which was mathematically and numerically elaborated by Nyborg [19], Westervelt [20] and Holtmark [21] and later by Riley and

co-workers [7, 22, 23] to include high Reynolds numbers [24] and the confinement of an outer cylinder [25, 26].

The ultrasonically driven file will be modeled as a cylinder of radius  $R$ , oscillating with an amplitude of  $y(z, t) = A(z) \sin(\omega t)$  and frequency  $\omega = 2\pi f$ , with  $z$  the direction along the length of the file. The oscillation characteristics  $A(z)$  of various endodontic files have been described in previous articles [27–29], where a sinusoidal oscillation pattern of typically 3 wavelengths was shown, with amplitudes of 10–100  $\mu\text{m}$ . With a driving frequency in commercial endodontic system of 30 kHz, the associated oscillation velocity is  $U_{z,t} = U_{z,0} \cos(\omega t)$  with  $U_{z,0} = \omega A(z) = O(1)$  m/s at the antinodes. The Reynolds number  $Re_o$  based on this oscillatory motion is of the order of  $10^2$ . In this article we limit ourselves to a two-dimensional description of the flow, therefore the  $z$  subscript will be omitted from here on.

Oscillating cylinders can generate acoustic streaming, which is a superposition of an oscillating, non-viscous velocity field and a steady streaming velocity field induced by the viscous boundary layer around the cylinder. The steady streaming has its own associated Reynolds number,  $Re_s$ . In the literature it is assumed that the two components of the acoustic streaming are fully decoupled [22]. Furthermore, there is a one-way coupling only, i.e. the file oscillation induces streaming, but the streaming is assumed not to affect the file oscillation.

The theoretical analysis of acoustic streaming is based on an approximation of the Navier-Stokes equation in the boundary layer of the oscillating cylinder. A solution to the resulting boundary layer equations can be obtained using a Taylor expansion in  $\varepsilon = \frac{U_0}{\omega R} = \frac{A}{R}$ . The time-average of the solution can be shown to be non-zero, leading to a steady streaming which persists even outside the boundary layer. For  $Re_o \gg 1$  it is necessary to take into account the higher order terms  $\varepsilon^2$  as well, giving rise to a second boundary layer [24]. The theoretical analysis is explained in more detail below.

For acoustic streaming to occur, the following conditions must be met:

1. the fluid is assumed to be incompressible (small Mach number,  $U_0/c \ll 1$ , with  $c$  the speed of sound in the fluid)
2. the boundary layer must remain attached (no boundary layer separation)
3. small amplitude of oscillation ( $\varepsilon \ll 1$ )
4. sound waves unimportant ( $\frac{\omega R}{c} \ll 1$ )

For passive ultrasonic irrigation, requirements 1 and 4 are fulfilled. The boundary remains attached because the endodontic file oscillates too fast for vortices to be created. The frequency of vortex shedding can be estimated from the Strouhal number:

$$St = \frac{f_{St} R}{U_0} = 0.2 \quad (6.1)$$

which gives a vortex shedding frequency  $f_{St}$  of approximately 10 kHz. Therefore requirement 2 is also fulfilled.

Requirement 3 is not fulfilled due to the high oscillation amplitude of the endodontic file, which confirms that  $\varepsilon^2$  terms must also be taken into account. The new requirement  $\varepsilon^2 \ll 1$  is fulfilled for typical oscillation amplitudes of endodontic files.

In the remainder of this section the velocities, pressure and wall shear stress will be derived, for cylinders with a circular cross-section oscillating in an unbounded fluid. We also consider the influence of the presence of a flat wall or the confinement of the root canal, the latter will be modeled as a cylinder of radius  $R_{rc}$  concentric with the file at rest and with a ratio of radii  $\alpha = \frac{R_{rc}}{R}$ .

## 6.2.1 Velocities

### Oscillatory component of the flow

#### *Free field*

The oscillatory component of the acoustic streaming around an oscillating cylinder can be described with potential flow. The oscillating cylinder is represented by a dipole (or doublet) with sinusoidal strength  $m = m_0 \sin(\omega t)$ . The real component of the complex potential of the flow, in cartesian coordinates, is given by:

$$\phi = \frac{m_0 \sin(\omega t)x}{x^2 + y^2}. \quad (6.2)$$

The coordinate system has its axis fixed at the center of the cylinder; the cylinder oscillates in the  $x$ -direction.

The oscillatory velocities  $u_o$  and  $v_o$  in the  $x$  and  $y$  direction, respectively, can be calculated from the velocity potential:

$$u_o = \frac{\partial \phi}{\partial x} = \frac{m_0 \sin(\omega t)}{x^2 + y^2} - 2 \frac{m_0 \sin(\omega t)x^2}{(x^2 + y^2)^2} \quad (6.3a)$$

$$v_o = \frac{\partial \phi}{\partial y} = -2 \frac{m_0 \sin(\omega t)xy}{(x^2 + y^2)^2} \quad (6.3b)$$

The radial velocity along the direction of oscillation therefore decreases quadratically with the distance to the file. The streamlines of the instantaneous velocity field are shown in Figure 6.1a.

The strength  $m_0$  of the dipole can be obtained from the no-slip boundary condition at the surface of the file, requiring the fluid velocity at  $x = R$  to be equal to the velocity of the oscillating file:

$$u_o(x = R) = \left. \frac{m_0}{x^2} \right|_{x=R} = A\omega \quad (6.4)$$

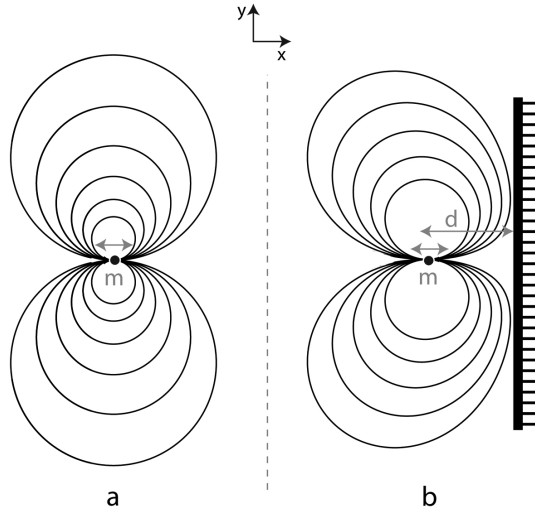


**Figure 6.1:** Streamlines of the potential flow induced by an oscillating cylinder, in the unbounded fluid (a) and in close proximity to a wall (b). The strength  $m$  of the dipole and its distance  $d$  to the wall are oscillating in time:  $m = m_0 \sin(\omega t)$  and  $d = d_0 - A \cos(\omega t)$ .

giving

$$m_0 = A\omega R^2 \quad (6.5)$$

The dipole is a point source and does not take into account finite-size effects; the potential flow solution should therefore only be used in the far field:  $x > R$ .

#### *Presence of a wall*

When the file oscillates at a distance  $x = d$  next to a wall, a mirror-dipole with a phase difference of  $\pi$  is introduced at a distance  $x = -d$  from the wall. Note that the coordinate system is now fixed in the wall. The velocity potential  $\phi_w$  is the sum of the two dipoles:

$$\phi_w = \frac{m_0 \sin(\omega t)(x+d)}{(x+d)^2 + y^2} + \frac{-m_0 \sin(\omega t)(x-d)}{(x-d)^2 + y^2}. \quad (6.6)$$

However,  $d$  is also a function of time as the file oscillates toward the wall:  $d = d_0 - A \cos(\omega t)$ . The velocity components  $u_o$  and  $v_o$  can be derived from the new velocity potential, Equation 6.6. Due to the presence of the wall, the velocity field becomes asymmetric (see Figure 6.1b) and the flow has to diverge more because of the wall. Furthermore, the radial velocities between the cylinder and the wall on the  $x$ -axis ( $y = 0$ ) decrease with respect to the unbounded case. This leads to increased velocities elsewhere, if the dipole strength is assumed to be unaffected by the wall.

*Presence of a confinement*

Continuing from the argument for a single wall, the confinement imposed by a larger, concentric cylinder ( $\alpha > 1$ ) can be modeled using an array of mirror sources at specific locations around the center dipole representing the oscillating cylinder. The strength of the dipole is unaffected, as the oscillation amplitude was found previously to remain unaffected inside the confinement [29]. Therefore the confinement reduces the velocity in the direction of oscillation even further, leading to a further divergence of the flow and to stronger recirculation velocities.

**Boundary layer and steady component of the flow***Inner boundary layer*

The boundary layer around the oscillating cylinder has a thickness of:

$$\delta_1 = \sqrt{\frac{\nu}{\omega}} = \sqrt{\frac{10^{-6}}{2\pi 30 \cdot 10^{-3}}} \quad (6.7)$$

which is typically of the order of 1  $\mu\text{m}$  for endodontic files. The boundary layer moves together with the oscillating file, however, the time-average of the flow in the inner boundary layer is not zero, leading to steady streaming outside the boundary layer that coexists with the oscillating flow field.

*Outer boundary layer*

For Reynolds numbers  $Re_o \gg 1$  there is a second boundary layer outside the first boundary layer, due to a contribution of higher order terms  $\varepsilon^2$  in the velocity field solution approximation that cannot be neglected. A sketch of the double boundary layer system is indicated in Figure 6.2. The steady velocity from the inner boundary layer decays to zero in this outer boundary layer. The thickness of the outer boundary layer is given by: [24]

$$\delta_2 = \frac{2R}{U_0} \sqrt{\frac{\omega \nu}{12}} (1 + \sigma_1 \theta_1^2 + \sigma_2 \theta_1^4 + \dots) \quad (6.8)$$

with  $\theta_1 = \theta - \frac{\pi}{4}$  ( $\theta$  = angle around cylinder with respect to the oscillation direction), and  $\sigma_n$  a constant ( $\sigma_1 = \frac{112}{51}$ ,  $\sigma_2 = 3.93$ ). Note that the outer boundary layer is non-uniform around the cylinder, with maxima in the direction of oscillation. For endodontic files the thickness of the outer boundary layer is of the order of  $10^2 \mu\text{m}$ .

The velocity solution shows that there is a net flow inside the outer boundary layer toward the poles of the cylinder in the direction of oscillation. [24] In order to balance this flow, there is an entrainment of flow toward the equator of the cylinder (perpendicular to the direction of oscillation).

*Steady streaming, or 'jet'*

The outer boundary layers interact and form *jets* at the poles in the direction of oscillation (Figure 6.2). Details of the interaction itself are complex, but the initial velocity of the induced jet  $u_s$  can be obtained from the steady component of the flow [30]:

$$u_s = \frac{U_0}{\omega} \frac{\partial U_0}{\partial x} \left( E(x) - \frac{3}{4} \right) \quad (6.9)$$

where  $E(x)$  is a function that decreases from  $\frac{3}{4}$  near  $x = 0$  to zero for large  $x$  and determines therefore the start of the jet. The shape of  $E(x)$  is unknown and is dictated by the movement of the cylinder in this region.  $U_0 = \omega A$  is the amplitude of the oscillation velocity; its derivative to  $x$  is taken as the variation of  $U_0$  along the cylinder surface:

$$\frac{\partial U_0}{\partial x} \approx \frac{U_0}{R} \quad (6.10)$$

The role of the radius of the cylinder in the jet velocity can be understood from the fact that the jet is generated by viscous effects in the boundary layer and the interaction of the steady flow component at the poles. For a large cylinder, the region of boundary layers interaction is smaller compared to the cylinder radius.

The final jet velocity is then:

$$u_s = -\frac{3}{4} \frac{\omega A^2}{R} = -\frac{3}{4} U_0 \frac{A}{R} \quad (6.11)$$

and is proportional to the oscillation velocity times the ratio of amplitude to file diameter. The very same expression has been introduced by Ahmad *et al.* [10], except for the prefactor.

Experimental validation by Davidson & Riley [31] of the acoustic streaming theory showed that, beyond a distance of one cylinder diameter, the jet can be described as a two-dimensional jet, for which it is known [18] that the center velocity decreases with  $x^{-1/3}$ . The steady Reynolds number  $Re_s$  can be defined using the initial velocity of the jet (Equation 6.11) and its initial width, which is of order  $R$ . For steady Reynolds number of the order of  $10^3$ , in the upper range of oscillation amplitudes for endodontic files, the jet can be unsteady or even turbulent [32].

*Presence of a wall*

The induced jet will impinge onto a wall that is present near the oscillating cylinder. The wall, in turn, will affect the entire jet profile, through a rapid decrease in velocity in the impingement region and an increase in velocity near the jet orifice [32, 33].

When the cylinder is placed very close to the wall, within the thickness of the outer boundary layer, the outer boundary layer may be severely affected so that the

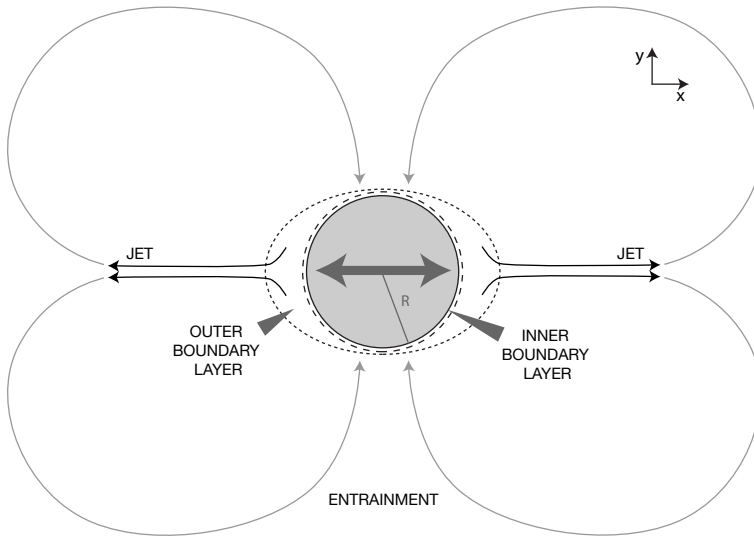


**Figure 6.2:** Double boundary layer and jet (with recirculation) generated by an oscillating cylinder.

jet obtains a lower velocity, or there is no jet formation at all.

#### *Presence of a confinement*

The effect of a second, larger cylindrical concentric with the oscillating cylinder has been studied by Duck & Smith and Haddon & Riley [25, 26]. The inner boundary layer is dominated by local viscous effects and is therefore unaffected by the presence of the outer cylinder [26]. The fluidic jet, on the other hand, is significantly influenced by the presence of the outer cylinder. The jet impinges onto the outer cylinder, similar to jet impingement on a concave surface [32], and is then forced to flow along the outer cylinder to become the entrained flow toward the equator of the cylinder. For small values of  $\alpha$ , when the outer cylinder approaches the domain of the outer boundary layer, the recirculating flow may interfere with the outer boundary layer, thereby also influencing the formation of the jet. When  $\alpha < 2$ , the outer boundary layer (in an unbounded fluid) extends up to the outer cylinder and consequently may be severely affected so that there is no formation of a jet.

The influence of the outer cylinder is reported to decrease as  $\alpha^{-1/3}$ , according to Duck & Smith [25].

## 6.2.2 Pressure

### Oscillatory component

The pressure  $P_o$  increase due to the oscillatory component can be calculated from the unsteady Bernoulli equation and Equation 6.2:

$$P_o = -\rho \frac{\partial \phi}{\partial t} - \frac{1}{2} \rho w^2 = -\rho \frac{m_0 \omega \cos(\omega t) x}{x^2 + y^2} - \frac{1}{2} \rho w^2 \quad (6.12)$$

where  $w = \sqrt{u^2 + v^2}$  is the magnitude of the velocity. The time derivative of the velocity potential is a cosine, whereas the velocity potential itself is a sine, which means that the pressure has a phase difference of  $\pi/2$  with respect to the oscillation velocity. Its physical origin can be understood from a Lagrangian analysis of the flow. During deceleration of the cylinder, the cylinder will appear to be moving away from a fluid element, which therefore feels a negative pressure.

The presence of a wall or confinement can be taken into account by using the velocity potential  $\phi_w$ , Equation 6.6. The velocities at the wall are zero, leaving only the first term determining the pressure [34]. A smaller distance between the file and the wall leads to higher pressures on the wall. Figure 6.3 shows the pressure increase at the wall during three cycles, for two different distances between the file and the wall.

### Steady component

The pressure inside the steady jet can be estimated from the steady Bernoulli equation and Equation 6.11:

$$P_s = \frac{1}{2} \rho u_s^2. \quad (6.13)$$

The presence of a wall or confinement changes the velocities inside the jet and consequently also the pressure inside the jet. On the wall there is an impingement area with a maximum pressure given by the stagnation pressure, which can be calculated with Equation 6.13 and the maximum velocity inside the jet [33]. The location of maximum pressure in the impingement area is at the center of the jet. For a cylindrical confinement the curvature of the impingement area has to be taken into account for the pressure distribution.

## 6.2.3 Shear stress

### Oscillatory component

The potential flow theory that governs the oscillatory component of the flow assumes no viscous dissipation anywhere, not even at the wall. The shear stress at the wall



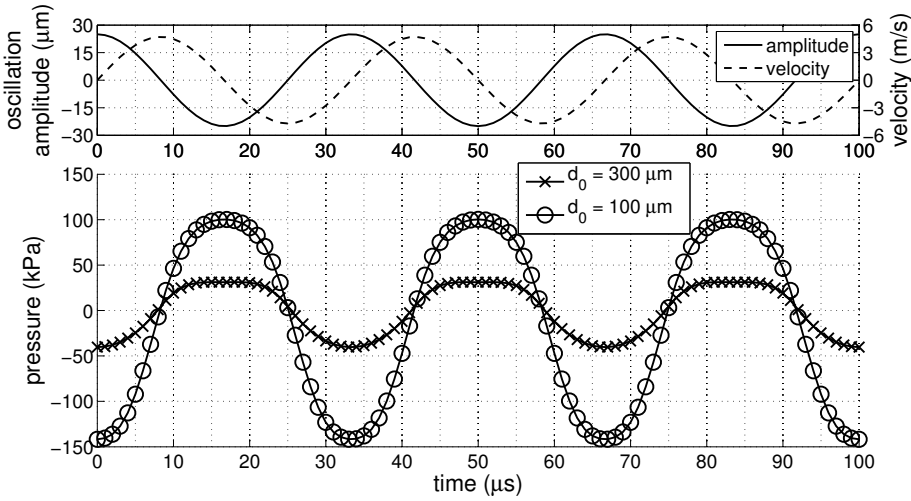


**Figure 6.3:** Oscillatory component of the pressure at the wall next to an oscillating file, for distances of  $d_0 = 300 \mu\text{m}$  (crosses) or  $100 \mu\text{m}$  (circles) between the file center ( $R = 100 \mu\text{m}$ ) and the wall. Positive oscillation amplitude (solid line in the top panel) is defined as a displacement toward the wall. Its derivative (velocity) is plotted with a dashed line.

can nevertheless be approximated by calculating the derivative in the  $x$ -direction of the velocity  $v$  parallel to the wall, and evaluating close to the wall:

$$\tau_o(x, t) = \rho v \left. \frac{\partial v}{\partial x} \right|_{x \rightarrow 0} \quad (6.14)$$

The shear stress is highest off-center, where the change in velocity parallel to the wall is highest. The location of maximum shear stress changes during one oscillation, due to the translation of the dipole.

### Steady component

The maximum value of the shear stress due to a fully-developed two-dimensional impinging jet can be approximated with:

$$\tau_{s,max} \approx \rho v \frac{u_s}{\delta_w} \quad (6.15)$$

where  $\delta_w$  is the boundary layer on the wall, given by the Blasius solution [35]:

$$\delta_w = 4.91 \sqrt{\frac{\mu x}{\rho u_s}}. \quad (6.16)$$

Inserting the equation for  $u_s$  (Equation 6.11) into Equation 6.15 results in the same equation as used by Ahmad *et al.* [10]:

$$\tau = \frac{\mu \omega y^2}{\delta R} \quad (6.17)$$

The shear stress is highest at an off-axis location, which for short distances between the file and the wall lies between 1 and 2 times the radius of the jet. For a jet induced by a cylinder oscillating inside a bigger cylinder, the distribution of wall shear stress as a function of the angle is given by Duck & Smith [25]. Its maximum depends on the ratio of cylinder radii and Reynolds number  $R_s$ , but is typically around an angle of  $15^\circ$  with respect to the direction of oscillation.

## 6.3 Materials & Methods

### 6.3.1 Experimental setup

#### High-speed particle imaging velocimetry

The streaming around an endodontic file was recorded using a high-speed camera (HPV-1, Shimadzu Corp., Kyoto, Japan), capable of recording 100 frames at speeds up to  $10^6$  frames/sec. The camera was attached to a microscope (BX-FM, Olympus Corp, Tokyo, Japan) for  $1.25\times$  to  $20\times$  magnification. Light was provided for bright field imaging by a high-intensity continuous cold-light source (ILP-1, Olympus Corp, Tokyo, Japan). An endodontic file with circular or square cross-section (ESI015 or Endosonore #15, respectively, diameter 0.15 mm, length 25 mm; EMS, Nyon, Switzerland) was positioned in front of the microscope, on the optical axis of the microscope, so that the cross-section of the file was visible. The file with a square cross-section was rotated in such a way that it was oscillating along one of its diagonals. The microscope was focused on the tip of the file and had a measurement depth of  $100\ \mu\text{m}$ . The file was fixed in a chuck with a  $120^\circ$  bend, which was in turn attached to a piezo element inside a hand piece, driven at 30 kHz by the power module from a commercial endodontic device (miniPiezon, EMS). The power to the hand piece was varied between 0.5 and 2.5W; the corresponding file oscillation amplitude was measured from the high-speed recordings.

The file was immersed in a large water tank of dimensions  $75\times 64\times 60$  mm ( $\alpha \approx 300$ ), filled with demineralized water. Monodisperse hollow glass spheres of diameter  $10\ \mu\text{m}$  (Sphericul, Potters Industries, South Yorkshire, UK; mean density of  $1.1 \cdot 10^3$  kg/m<sup>3</sup>, Stokes number  $O(1)$  for the highest velocities occurring) were added to the water. The flow was analyzed from the high-speed recordings using an in-house developed particle tracking algorithm. The obtained particle trajectories were separated

into a steady and an oscillatory component with a running average filter with Gaussian window and the standard deviation of 10 samples, respectively. The resulting velocities were stored as a function of the distance to the file and the angle with respect to the oscillation direction.

Measurements were performed three times for each file and power setting. Due to the large variations in velocities, recordings were made at two recording speeds: at 250 Kfps, for the oscillatory component, and at 63 Kfps, for the steady component. The influence of the confinement of the root canal was studied with an aluminum flat plate of thickness 2 mm with a hole of diameter 0.6 mm, positioned around the tip of the file.

### Measurement of the steady pressure

The pressure of the steady jet induced in the direction of oscillation of a file with a square cross-section (K10/21, diameter 0.15 mm, length 21 mm; Satelec Acteon, Merignac, France) was measured using a miniature fiber-optic pressure sensor with a sensor diameter of 260  $\mu\text{m}$  (FOP-M260, FISO Technologies Inc., Quebec, Canada). The sensor was aligned perpendicular to the file at a distance of 0.5, 1, 2 or 3 mm from the file tip; its height and angle with respect to the tip of the file was optimized manually. The file was driven with a commercial device (Suprasson P-Max, Satelec Acteon) at power setting ‘Yellow 1, 4 or 7’, ‘Blue 1, 4 or 7’ or ‘Red 1, 4 or 7’ (low to high). The file was allowed to oscillate freely inside a large water bath and the resulting pressure with respect to ambient pressure was recorded.

The pressure sensor equipment measured at a rate of 5000 samples/second; the noise in the signal was measured to be 0.01 kPa. The sensor diameter is approximately equal to the diameter of the steady jet and is known to have a non-uniform sensitivity across its measuring surface [32], introducing an additional error in the measured pressure.

### 6.3.2 Numerical model

The two-dimensional flow around a file (circular cross-section, radius = 100  $\mu\text{m}$ ) oscillating inside a root canal (radius = 300  $\mu\text{m}$ ,  $\alpha = 3$ ) or a large rectangular container (dimensions 1.4 $\times$ 2.0 mm,  $\alpha = 8.25$ ) was simulated. In the root canal (‘confined’ case) the file was positioned at the center; in the rectangular container (‘wall-bounded’ case) the center of the file was positioned at  $(x,y) = (0,0)$ , with walls at  $x = 0.3$  mm (right),  $x = -1.1$  mm (left),  $y = 1.0$  mm (top),  $y = -1.0$  mm (bottom), i.e. a distance of  $d_0 = 300$   $\mu\text{m}$  between the file center and the nearest wall. The preprocessor Gambit 2.4 (ANSYS Inc., Canonsburg, Pennsylvania, USA) was used to create the 2-D geometry and the structured hexahedral mesh of 1792 or 11718 cells, for the confined and wall-bounded case, respectively.

Grid-independence of the results was verified prior to the main simulations. In both cases a fully enclosed flow domain was studied (no inlet or outlet). The area between the walls and the file was assumed to be filled with 1% NaOCl solution, which was modeled as an incompressible Newtonian fluid with a density of  $1040 \text{ kg/m}^3$  and viscosity  $0.986 \cdot 10^{-3} \text{ Pa s}$ . No-slip boundary conditions were imposed on all walls. An isothermal flow was assumed.

The commercial CFD code FLUENT 13.0 (ANSYS Inc.), which applies finite-volume discretization, was used for the numerical simulations. Built-in Dynamic Mesh capability combined with the Arbitrary Lagrange-Euler (ALE) formulation were employed to solve the time-dependent Navier-Stokes equations on a moving grid. File oscillation velocity along the  $x$ -axis was explicitly defined by a User-Defined Function (one-way Fluid-Structure Interaction) according to the equation  $u = \omega A \cos(\omega t)$ . The amplitude  $A$  was set to  $25 \text{ }\mu\text{m}$  and the frequency  $f = \omega/2\pi$  at 30 KHz, as in the experiments. No oscillation was specified along the  $y$ -axis. Initial conditions were  $u, v = 0$  for the irrigant and  $x = 0$  for the moving file. Second-order accuracy in space and first order in time were ensured. The convergence criterion was set to  $10^{-6}$  of the maximum scaled residuals. A time-step of  $1.66 \cdot 10^{-7} \text{ s}$  was used, which equals 1/200 of the oscillation period, to fully resolve the file oscillation and resulting irrigant flow.

During preliminary simulations it was noticed that transient start-up effects had disappeared after the first two periods, so the main simulations were continued for 10 full periods ( $t = 33.3 \cdot 10^{-5} \text{ s}$ ). The velocities between the file and the wall, as well as the pressure and shear stress on the wall, were extracted at 8 time steps during the last oscillation period. Time-averaged results were calculated by averaging during the last five periods. Computations were carried out on a Dell OptiPlex 990 workstation (Dell corp., Round Rock, Texas, USA) with a quad-core Intel i7 processor (Intel, Santa Clara, CA, USA) and 4 GB of RAM, running 64-bit Windows 7 (Microsoft corp., Redmond, WA, USA).

## 6.4 Results

### 6.4.1 Velocity

#### Unconfined cylinder with circular cross-section

The high-speed recordings of the ultrasonically oscillating endodontic file in a large water tank showed that acoustic streaming indeed takes place for endodontic files (see Supplementary Material movie 1). The suspended particles were observed to move in radially toward the equator of the oscillating cylinder, before being entrained in the jets that had developed in the direction of oscillations. These jets were formed within 3 ms (or 100 oscillations), during which the file is also known to start-up

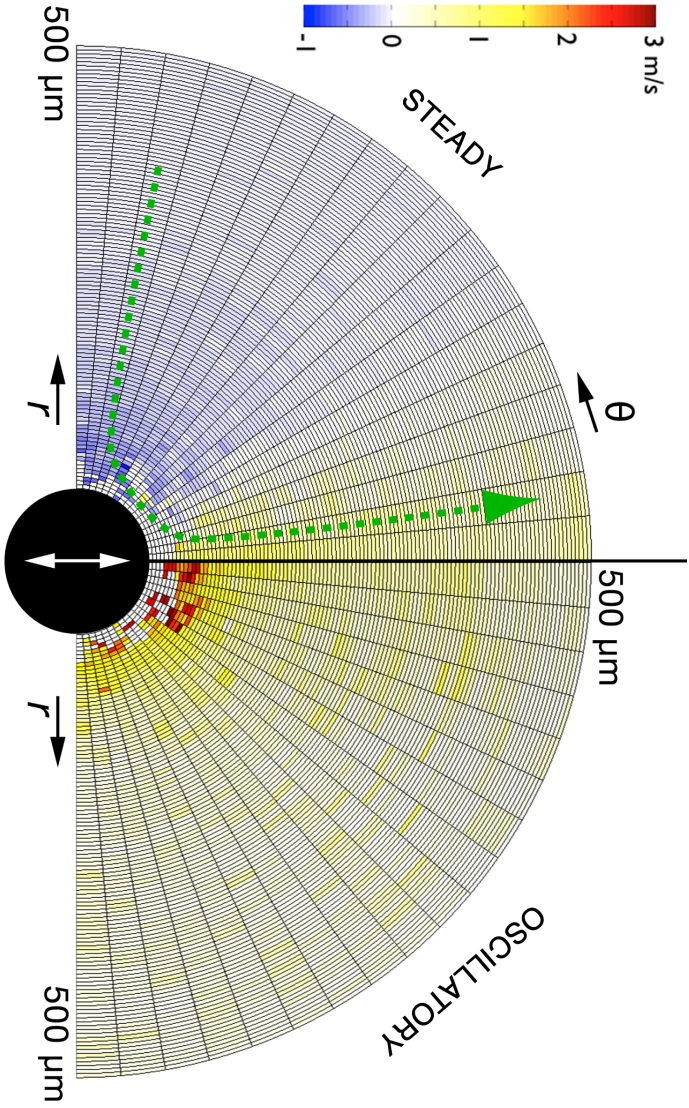


**Figure 6.4:** Steady (left) and oscillatory (right) components of the measured radial flow velocities around an oscillating endodontic file. A typical steady particle trajectory is indicated with a green arrow.

before obtaining its full oscillation amplitude [29]. Within a radial distance of approximately  $100 \mu\text{m}$  of the cylinder the particles were observed to oscillate together with the cylinder simultaneous with the steady streaming; the amplitude of oscillation decreased with increasing distance from the cylinder.

Decomposition of the particle trajectories resulted in their steady and oscillatory component as a function of radial distance from the file and angle with respect to the direction of oscillation. Because of symmetry, the velocity results in each quadrant around the cylinder can be grouped, which is shown in Figure 6.4 for an endodontic file with circular cross-section. The left quadrant shows that there is a steady jet that covers an angle of  $\frac{1}{9}\pi$ ; the remainder is governed by the inflow, with increasing (negative) radial velocity toward the cylinder. The right quadrant demonstrates that the oscillatory component is most pronounced close to the file. The oscillatory component also has an angle dependence, as the radial velocity is highest in the direction of oscillation and decreases toward an angle of  $\frac{1}{2}\pi$ , which is in qualitative agreement with the theoretical solution for an oscillating dipole.

Figure 6.5 shows the decrease in radial velocities with distance from the center of the oscillating file, obtained by averaging over an angle of  $\theta = 0$  to  $\frac{1}{9}\pi$  (oscillatory and steady jet components) or  $\theta = \frac{2}{9}\pi$  to  $\frac{1}{4}\pi$  (steady inflow component). Near the cylinder, the oscillatory component is almost one order of magnitude higher than the steady component, however the oscillatory component decreases rapidly with distance. Its slope within the first 300 micrometer appears to follow the theoretically predicted  $x^{-2}$  slope well. Further away from the file, the oscillatory velocities below 1 m/s were difficult to determine as noise in the recorded images contributes significantly to the oscillatory component.

The steady jet velocity had a magnitude of  $O(1)$  m/s, which is of the same order of magnitude but more than two times lower than the theoretical prediction. The steady velocity decreased slowly, although faster than the  $x^{-1/3}$  decrease predicted for a 2D jet, possibly due to the jet having a component in the  $z$ -direction as well. The steady inflow velocity toward the oscillating cylinder was observed to increase with  $x^{4/3}$  as it approached the cylinder.

The CFD model confirmed the presence of steady jets coexisting with the oscillatory flow, both for the confined and the wall-bounded case, and arising within 3 oscillations. Figure 6.6 shows the velocity vectors at one instant of time and the average over 5 cycles of the CFD simulation; Supplementary Material movies 2 and 3 show the velocities at 68 time steps of one full cycle. Similar to the experiments, the maximum velocity of the jet was  $1/5^{\text{th}}$  of the theoretically predicted velocity for the wall-bounded case, both toward and away from the wall (Figure 6.7). The jet velocity toward the wall decreased rapidly, following a  $x^{-7}$  power law; the jet away from the wall in the wall-bounded case appeared to follow a  $x^{-3}$  law rather than the predicted  $x^{-1/3}$  law. This discrepancy may be related to the presence of the wall, which, due to

the small distance between the file and the wall, affects the entire jet profile.

In the experiments, increasing the electrical power to the driving piezo element resulted in an increase in oscillation amplitude, which in turn resulted to an increase in jet velocity, balanced by an increase in inflow velocities. This behavior is demonstrated in Figure 6.8, where for four file oscillation amplitudes a histogram of the measured velocities is shown. At large oscillation amplitudes, an increase in high jet velocities and low inflow velocities can be observed, which both appear to follow the quadratic increase expected from theory (Equation 6.11). However, the maximum jet velocities are approximately  $1/4^{\text{th}}$  of the magnitudes predicted by the theory.

For the oscillatory component of the flow (Figure 6.8b), no increase in maximum velocities was observed with increasing oscillation amplitude, whereas a linear increase is expected (Equations 6.3 and 6.5). A possible explanation is the noise level of approximately 1 m/s for the oscillatory component. Furthermore, the highest velocities are only obtained locally, very close to the file, where there is only a small number of particles to be tracked, and they reside there only for a brief time.

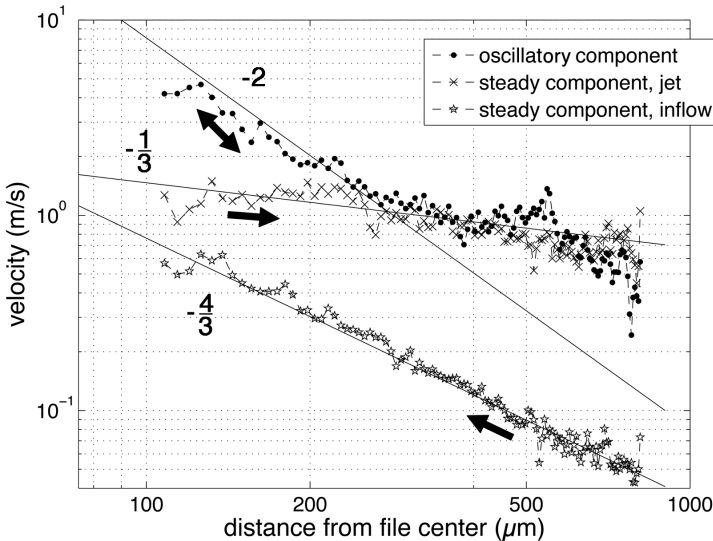


**Figure 6.5:** Measured velocities as a function of distance from the center of the oscillating endodontic file. The start of the  $x$ -axis is at  $x = 75 \mu\text{m}$ , which is the edge of the file in its center position; the velocities close to the file are severely affected by the displacement of the file during its oscillation. The solid lines have a slope based on theory ( $x^{-2}$  for the oscillatory component and  $x^{-1/3}$  for the steady jet) or estimation ( $x^{-4/3}$  for the steady inflow); their offsets are fitted to the measurement data. The black arrows indicate the direction of particle motion.

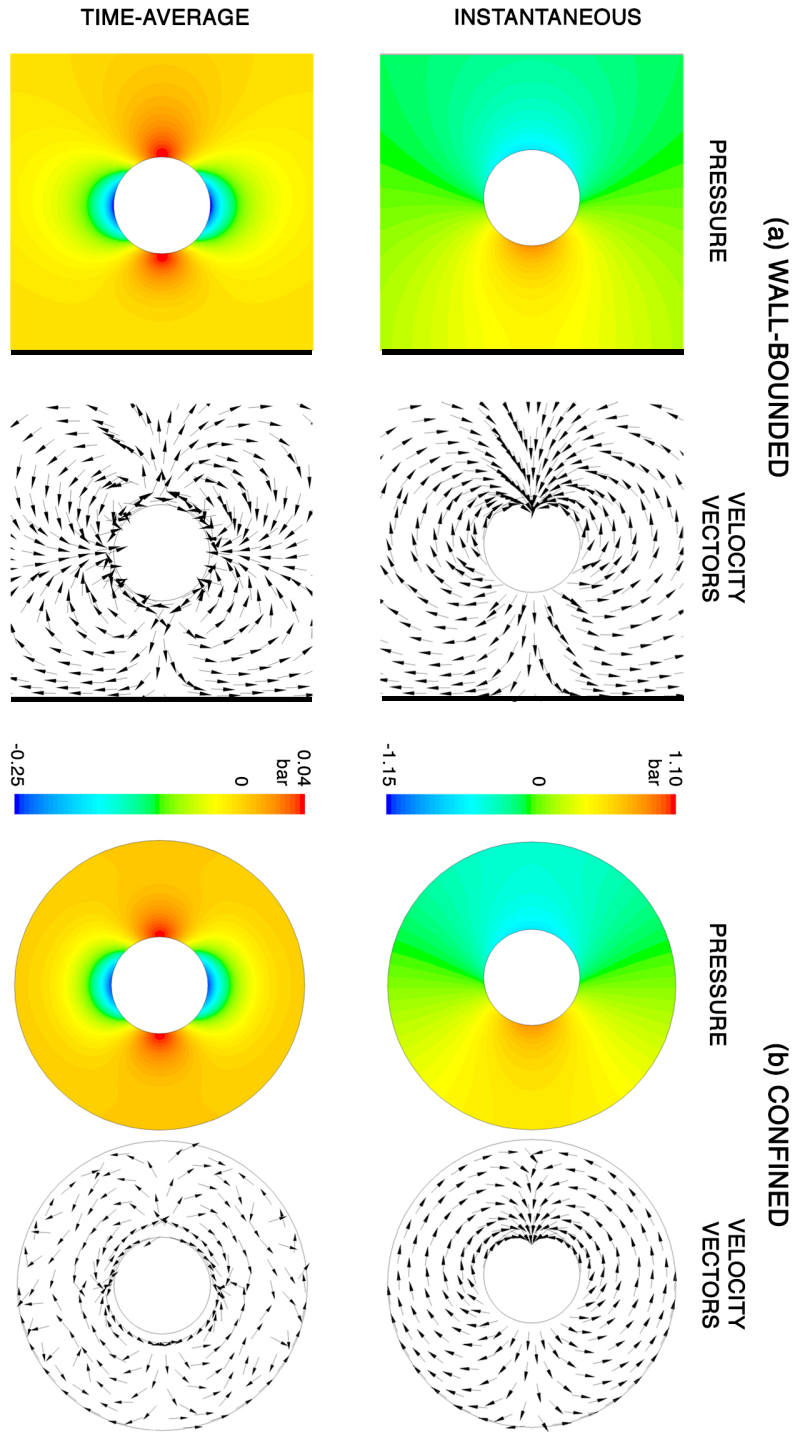


**Figure 6.6:** Velocity vectors and pressure magnitudes for an wall-bounded (a) and confined (b) oscillating cylinder of radius  $100 \mu\text{m}$  as calculated by the CFD model. The results at one instant of time is shown in the top row; the bottom row shows the time-average.



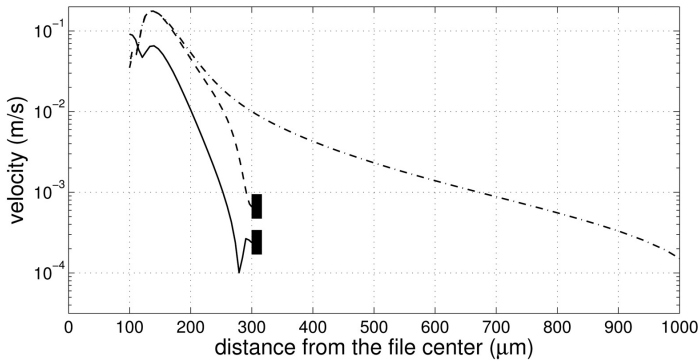


**Figure 6.7:** *Steady velocity versus distance from the file center, from the numerical model. The solid line represents the confined case; the dashed lines are for the wall-bounded case, for the direction toward and away from the wall. The wall is located at a distance of  $d_0 = 300 \mu\text{m}$  and is indicated with black bars on the relevant lines.*

### Confined cylinder with circular cross-section

Figure 6.8 also shows (in red) the velocity distribution when the endodontic file oscillated inside the confinement of the root canal. Due to the limited space between the file and the wall of the confinement, the steady jets cannot develop fully, leading to a significant reduction in highest steady velocities. The numerical model agreed with this observation, with the jet velocity decreasing by a factor of 2 inside the confinement. The inflow toward the file appears to be unaffected by the confinement. The oscillatory velocity in the direction of oscillation does appear to be reduced, confirming the theoretical prediction for the influence of a confinement on the oscillatory radial velocity.

### Unconfined cylinder with square cross-section

A cylinder with a square cross-section was observed to generate a cloud of cavitation bubbles at the edges, which was more pronounced at higher oscillation amplitudes. The collapse of this bubble cloud lead to additional, high-velocity, unsteady streaming close to the file. Jets were still formed in the direction of oscillation, but the bubble cloud dynamics created additional steady streaming, making the total angle of the jet  $\frac{1}{4}\pi$ . The velocities in the jet, when scaled by the change in oscillation velocity with respect to the circular cylinder, increased with approximately 33%.

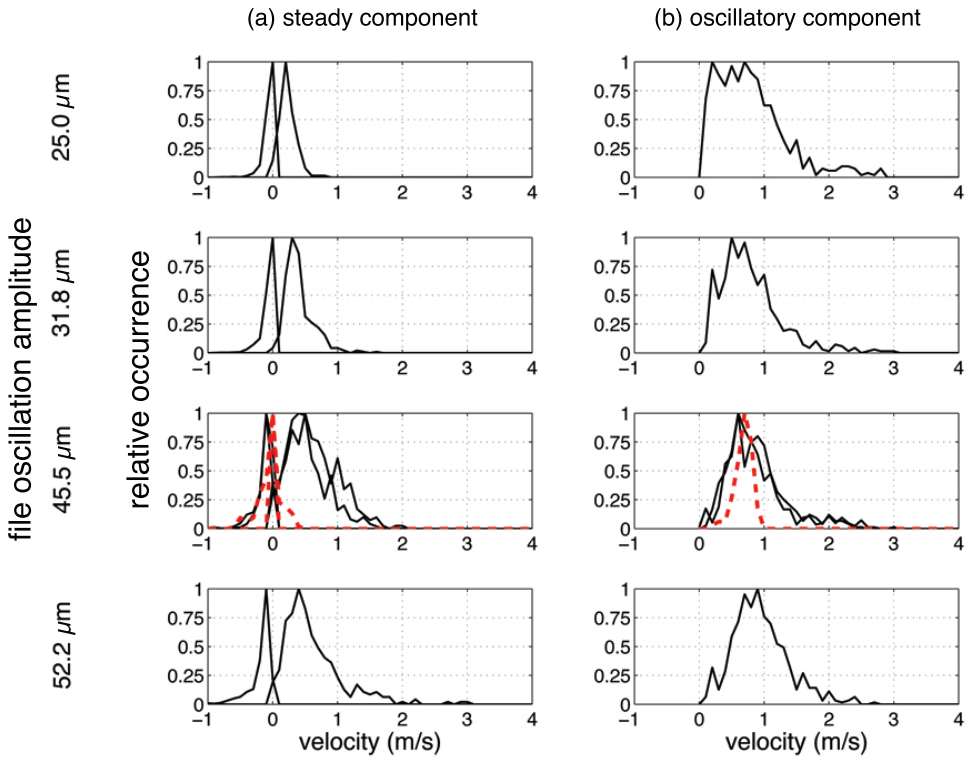


**Figure 6.8:** Histograms of particle velocities, separated into their steady (a) and oscillatory (b) component, as a function of oscillation amplitude of the endodontic file. The black solid lines represent measurements of the file oscillating unconfined, whereas the red dashed lines indicate measurements done within the confinement of the root canal.

## 6.4.2 Pressure

### Around the file

The pressure sensor positioned near the oscillating file measured pressures of the order of a few kPa in the direction of oscillation, where the jets were expected; in other directions no pressure could be measured above the noise level. This agrees with the earlier observed directivity of the induced steady flow field. Increasing the power setting caused a more or less linear increase in measured pressure, up to a power setting of ‘Blue 7’, where the pressure in the jet at a distance of 0.5 mm from the file was 2.9 kPa. For even higher power settings (‘Red 1, 4 or 7’) the pressure actually decreased, sometimes after an initially high pressure, which can be attributed to the occurrence of cavitation on the file that may have interfered with the jet development.

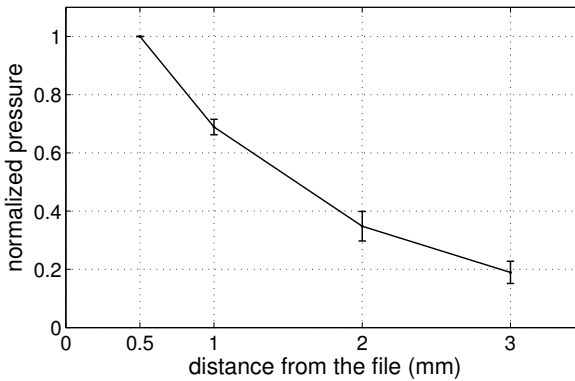
The measured pressure of 2.9 kPa at power setting ‘Blue 7’ corresponds to a velocity of  $\sqrt{0.5\rho/P} = 2.7$  m/s, according to the steady Bernoulli equation. Assuming that the relation between jet velocity and oscillation amplitude for a file with square cross-section is the same as for a circular cross-section (equation 6.11), the oscillation amplitude is estimated to have been 31  $\mu\text{m}$ , which is the same order of magnitude but approximately 2 times lower than the amplitude reported in literature [29]. Again the jet velocity prediction (Equation 6.11,  $u_s \propto A^2$ ) appears to be overestimated by a factor 4.

Figure 6.9 shows the normalized measured pressure as a function of distance, which is observed to decrease with increasing distance from the oscillating file. The decrease is faster than the theoretically predicted decrease rate of  $x^{-1/3}$  for the velocity and consequently  $x^{-2/3}$  for the pressure, which can be attributed to misalignment and the jet not being completely 2D.

### On the wall

In Figure 6.6 the instantaneous and time-averaged pressure fields around the wall-bounded and confined cylinder are shown, as calculated from theory and with the numerical model.

Both the theoretical solution and the numerical model predicted a pressure magnitude along the flat wall of the order of 10 kPa for the oscillatory component of the streaming (see Figure 6.10). The pressure is observed to become negative during the deceleration of the file, confirming the theoretical prediction. The pressure magnitudes from the numerical model are a factor of 2 higher than those predicted from the theory, but are in the same order of magnitude and show good agreement in shape along the flat wall. Inside the confinement, the pressures increased with up to 25%, mostly during the negative pressure phase. In both cases, the maximum pressure occurs on the axis of oscillation ( $y=0$ ).



**Figure 6.9:** Normalized measured pressure as a function of distance for the steady jet.

The steady component of the pressure is two orders of magnitude smaller than the oscillatory component (see Figure 6.10), according to both the numerical model and the theoretical prediction, although the exact magnitude in the numerical model was three times lower than predicted (Figure 6.12). Inside the confinement the steady pressure was observed to increase compared to the wall-bounded case, even though it was found earlier that the radial velocity along the direction of oscillation decreases within the confinement.

### Bubble behavior

The radial motion of a stable bubble, observed to oscillate between a file with square cross-section (K10/25, Satelec Acteon, Merignac, France) and flat wall, was tracked during one recording (200  $\mu\text{s}$ , or 6 oscillations). This bubble had an equilibrium radius of approximately 3  $\mu\text{m}$ . This bubble was observed to grow only during one half of the cycle (when the file was approaching the wall) and grew already during the deceleration phase of the file oscillation, confirming the  $\pi/2$  phase difference between the file velocity and the generated pressure.

The radius of the bubble was estimated from the pixel area occupied by the bubble in the recorded images. The bubble radius during one recording (6 cycles) is plotted interleaved in Figure 6.11, together with the theoretically predicted radius, for which the driving pressure is calculated from the measured file oscillation amplitude (75  $\mu\text{m}$ ) and distance to the wall (200  $\mu\text{m}$ ), and multiplied with a correction factor of 1.73 to obtain the correct bubble radius. This correction matches well with the earlier observation of 33% velocity increase (and  $P \propto u^2$ ) for a file with a square instead of circular cross-section, especially considering the complex acoustic field for such a file and in the presence of a cavitation cloud and a wall.

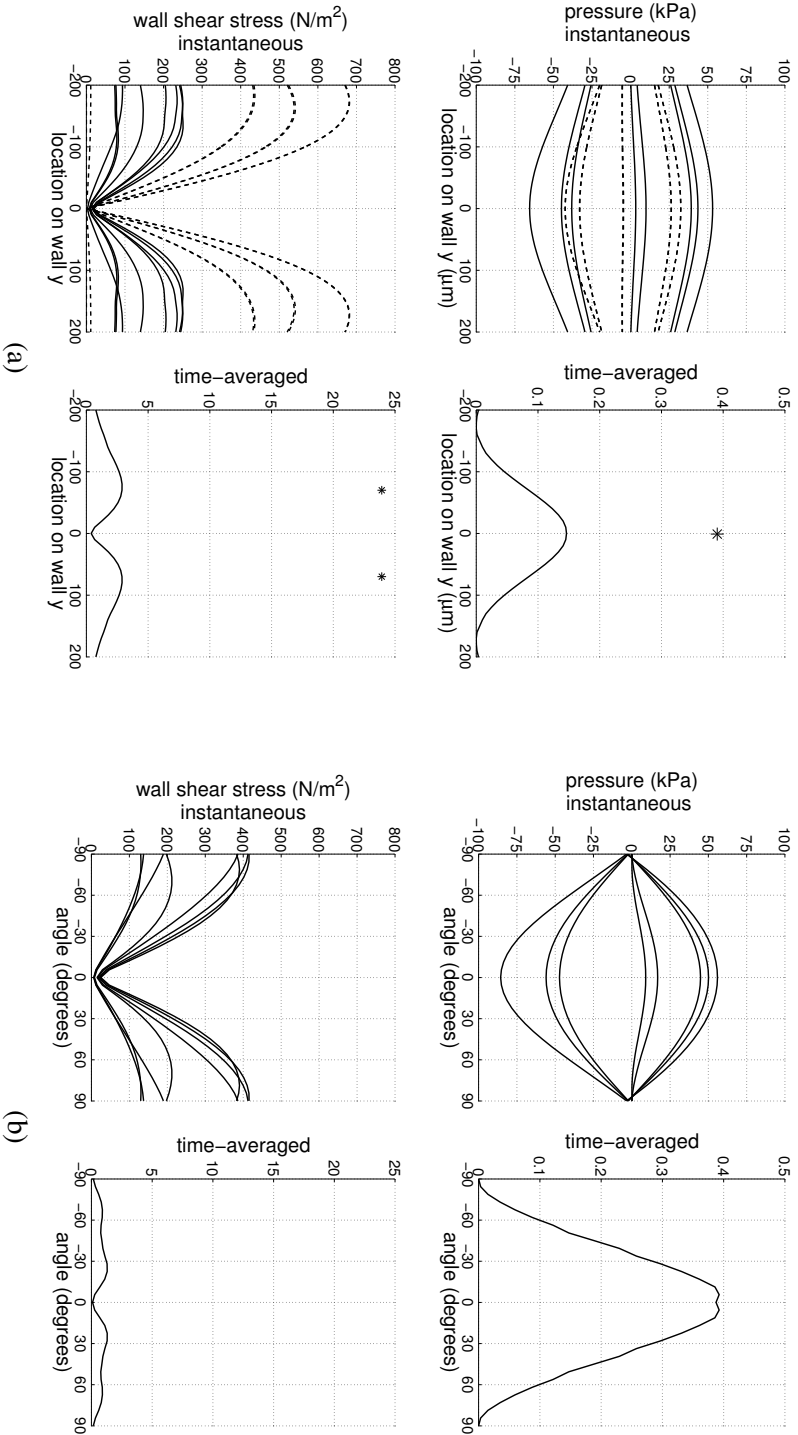


**Figure 6.10:** Pressure (top row) and wall shear stress (bottom row) on a wall when  $d_0 = 300 \mu\text{m}$ . Both the instantaneous (8 time points spaced  $4.15 \mu\text{s}$  apart) and the average over 5 cycles of the numerical simulation are plotted, for both the wall-bounded (a) and confined (b) case. The theoretical predictions (dashed lines and asterix) are also indicated. Note the different scales on the y-axes for the instantaneous and time-averaged graphs.

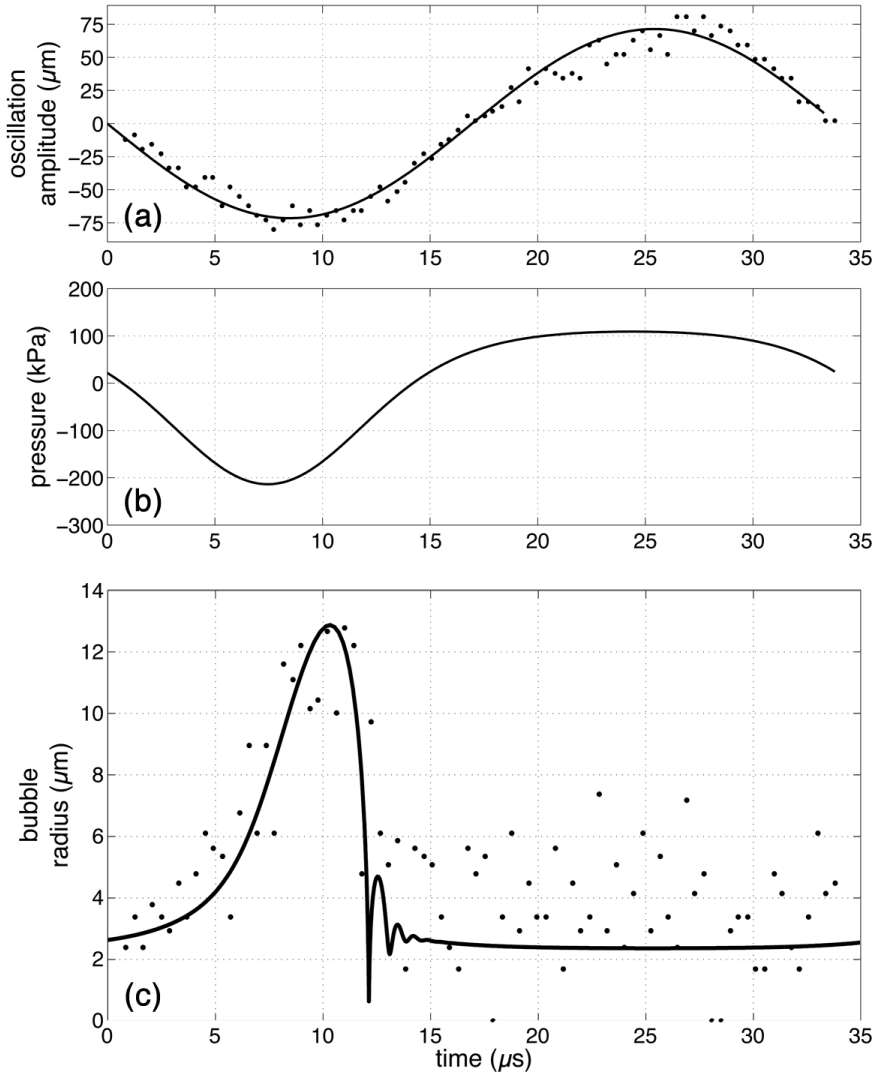


**Figure 6.11:** (a) File oscillation amplitude as obtained from high-speed recordings, plotted interleaved from six cycles (dots) and approximated with a sine of frequency 29.5 kHz (solid line). (b) Pressure on a nearby wall ( $d_0 = 200 \mu\text{m}$ ) according to the theoretical description of acoustic streaming, including both oscillatory and steady component, with a correction factor of 1.67. (c) Bubble radius, as measured in the high-speed recording (dots) and from solving the Rayleigh-Plesset equation (solid line). Negative file oscillation displacement means closer to the wall.

The behavior of a bubble during a certain pressure field can be calculated using an Rayleigh-Plesset type equation [36]:

$$\left(1 - \frac{\dot{R}_b}{c}\right) \rho R_b \ddot{R}_b + \frac{3}{2} \dot{R}_b^2 \rho \left(1 - \frac{\dot{R}_b}{3c}\right) = \left(1 + \frac{\dot{R}_b}{c}\right) [p_g - P_0 - P(t)] \quad (6.18)$$

$$+ \frac{R_b}{c} \dot{p}_g - 4\nu \frac{\dot{R}_b}{R_b} - \frac{2\sigma}{R_b} \quad (6.19)$$

with  $R_b$  the bubble radius,  $\dot{R}_b$  and  $\ddot{R}_b$  its first and second time derivatives,  $c$ ,  $\rho$ ,  $\eta$  and  $\sigma$  the speed of sound, density, viscosity and surface tension of the liquid, respectively. The effect of thermal damping has been included by multiplying the viscosity  $\nu$  of the liquid by 10 [37].

The gas pressure  $p_g$  is given by:

$$p_g = \left(P_0 + \frac{2\sigma}{R_{b,0}}\right) \frac{(R_{b,0}^3 - h^3)^\gamma}{(R_b(t)^3 - h^3)^\gamma} \quad (6.20)$$

with  $h$  the van der Waals hard-core radius (assumed to be negligible) and  $\gamma$  the polytropic constant for the gas inside the bubble when the heat exchange during bubble collapse goes adiabatically; for air the polytropic constant is  $\frac{7}{5}$ .

The pressure  $P_0$  is the sum of the ambient pressure of  $1 \cdot 10^5$  Pa and the pressure induced by the steady jet (Equation 6.13). Secondary Bjerknes forces due to the presence of a wall were not taken into account.

Equation 6.19 was solved in MatLab using the ode45 solver, see Figure 6.11. There is also a good agreement in timing of bubble growth and collapse and phase difference with the driving pressure. The rebounds predicted by the Rayleigh-Plesset-type equation solution could not be observed directly in the recording, but the measured radius after the initial collapse correlates well with the predicted rebounds.

During the second half of the acoustic cycle the measured bubble radius is often above the equilibrium radius of  $3 \mu\text{m}$ , possibly due to reflections and the collapse of the cavitation cloud around the file, which generate additional pressure gradients.

### 6.4.3 Wall shear stress

According to the CFD model, the wall shear stress along the flat wall or confinement is of the order of  $10^2$  N/m<sup>2</sup> for the oscillatory component and of order 1 N/m<sup>2</sup> for the steady component, i.e. two orders of magnitude difference. These values are smaller but of the same order of magnitude as those predicted by the theory. Inside the confinement, the oscillatory component of the shear stress increases with a factor of almost 2, whereas the steady component decreases by a factor of 2. The maximum values for the shear stress occur off-axis. For the oscillatory component this location

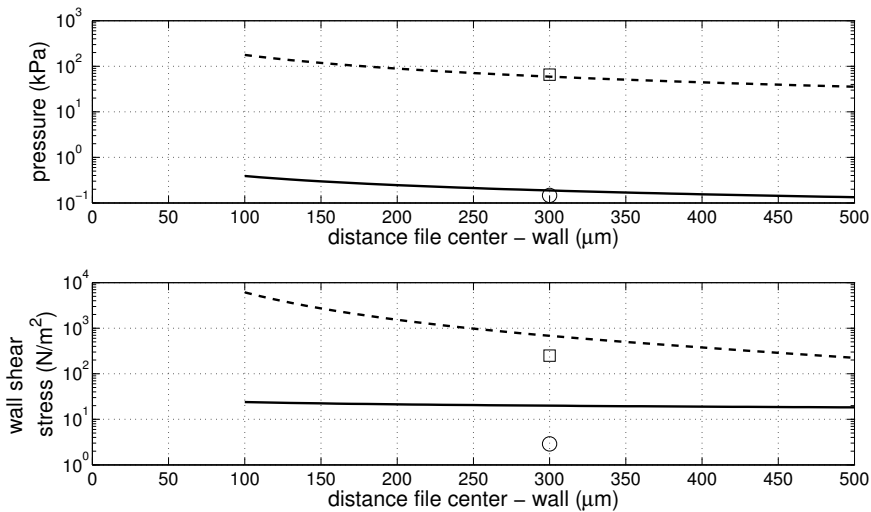


**Figure 6.12:** Pressure (top) and shear stress (bottom) as a function of distance between the file and a wall. The solid lines represent the steady component, the dashed lines indicate the oscillatory component. The results from the numerical model are indicated with squares (oscillatory component) and circles (steady component).

changes with time, but is typically between one and two times the jet diameter of  $R$ ; for the steady component the maximum occurs at  $x = 80 \mu\text{m} = 0.80R$  (corresponding to a solid angle of  $14.9^\circ$ ) for the wall-bounded case, and at  $22.5^\circ$  for the confined case.

#### 6.4.4 Influence of the distance between file and wall

In Figure 6.12 the distance between the file center and the wall is varied and the resulting pressure and wall shear stress is calculated from the theory. The results from the numerical model at one distance are also indicated. The steady component of the pressure and the wall shear stress decreases slowly, as they are derived from the slowly decreasing jet velocity. The oscillatory component of the shear stress decreases much faster and at some point may actually cross the line for the steady component. The oscillatory component of the pressure doesn't decrease as fast, as according to theory (Equation 6.12) the pressure decreased with  $d$ .



## 6.5 Discussion

The theory of acoustic streaming appears to describe well the flow induced by an ultrasonically oscillating endodontic file. The presence of an oscillatory component, dominant near the file, and a steady component, further away from the file, has been confirmed experimentally and numerically. The oscillatory component of both the pressure and the shear stress is two or three orders of magnitude higher than its steady counterpart. Furthermore, the formation of steady jets is affected by the presence of a confinement; meanwhile the oscillatory velocities and associated pressure and shear stress are increased. Previous work considering only the steady component of the flow therefore underestimated the hydrodynamic effects induced by ultrasonic files.

The oscillatory and the steady components have different contributions to cleaning. Cleaning in principle consists of the chemical attack of organic material by the irrigant, and mechanical removal of dentin debris and also the biofilm and the smear layer on the root canal wall. For the chemical mechanism, the steady component of the flow is doing the actual transport and mixing of the antimicrobial irrigant, but its velocity magnitude has been found to be much lower than the oscillatory velocity magnitude. Nevertheless, the steady velocity decreases slowly and may therefore be able to deliver irrigant into remote locations, although the flow is highly direction-dependent.

For the mechanical component, the wall shear stress and pressure are important. Compared to the wall shear stress reported for needle irrigation [38], the oscillatory component of the wall shear stress induced by the acoustic streaming is of the same order of magnitude. Nevertheless, PUI has been found repeatedly to be more efficient than needle irrigation in removing dentin debris [16, 39–41], biofilms [42] and in dissolving tissue [43], suggesting that the wall shear stress may not be the key factor for cleaning. The oscillating pressure at the wall, together with stable or transient cavitation, both of which are not present for needle irrigation, may be contributing significantly to the cleaning. Also, the oscillation of the pressure and the wall shear stress may induce fatigue in the viscoelastic material to be removed due to repeated loading, thereby enhances biofilm failure.

In order to increase the oscillatory component of the pressure and shear stress for cleaning, the strength  $m_0$  of the dipole should be increased, which, according to Equation 6.5, is linearly related to the oscillation amplitude and frequency, and quadratically to the file radius. Furthermore, a smaller confinement leads to an increase in pressure and shear stress on the wall.

For biofilms, which are known to exhibit viscoelastic behavior, the oscillatory component may only cause elastic, reversible deformation, and the steady component may be therefore be important for its removal by causing viscous deformation. The steady component of the flow can be increased by increasing the oscillation amplitude and frequency, and by using a smaller file (Equation 6.11). For thin files, the steady

component of the shear stress may actually be of the same order of magnitude as, or even higher than, the oscillatory component. The file radius may therefore allow for control over the relative magnitudes of the steady and the oscillatory component of the flow.

It is also of interest to discuss the influence of the viscosity on the acoustic streaming induced by endodontic files. The oscillation amplitude of the file is assumed to be unchanged (or the damping is corrected for). The oscillatory component of the acoustic streaming is then also unchanged, as the oscillatory component is governed by potential flow and viscosity does not play a role. The thickness of the inner and outer boundary layer around the file will change, but according to Equation 6.11 the resulting jet velocity is independent of viscosity, to a first approximation. Therefore a higher viscosity and unchanged oscillation amplitude should not change the velocities compared to low viscosity liquids; however the shear stress (Equation 6.15) can be increased, leading to a more efficient cleaning. However, a high viscosity can lead to non-linear terms in the governing equations that cannot be neglected any more and might influence the acoustic streaming velocities. More simulations and experiments are required to clarify this.

A recent article demonstrating an increase in cleaning efficacy of PUI at higher oscillation amplitudes [16] can be understood with the findings of this article, as a higher oscillation amplitude leads to higher velocities and therefore higher pressures and shear stresses. The flow pattern as observed experimentally and numerically in this study furthermore explains why the oscillation direction has been found to influence the cleaning efficacy of the PUI system [39].

Sonic devices for irrigation of the root canal have been shown to be much less effective than ultrasonic devices [44], which has been attributed to its single-antinode oscillation pattern, its amplitude being too large to fit in the root canal and its inability to generate cavitation. Based on the present theoretical analysis, a sonic device is unable to generate acoustic streaming, because both requirements 2 (boundary layer remains attached) and 3 (small amplitude of oscillation) for acoustic streaming to occur are not met. A typical sonic device makes use of a plastic tip with a diameter of 200  $\mu\text{m}$ , oscillating with an amplitude of 1 mm and a frequency around 175 Hz [44], therefore the oscillation amplitude cannot be considered small. Also, the vortex shedding frequency (Equation 6.1) is around 1 kHz, therefore flow separation will occur in the boundary layer. The absence of the steady component may limit the cleaning efficacy at remote locations or the removal of biofilms.

The oscillation pattern along the length of the endodontic file during ultrasonic oscillations has been shown to consist of approximately three wavelengths [29], the typical wavelength being approximately 5 mm. While this wavelength is much larger than the depth of measurement (100  $\mu\text{m}$ ) of the optical system employed in this study, the flow is likely to be three-dimensional instead of the two-dimensional approach of

this study. Especially since the measurements took place at the tip of the endodontic file, the third component can be the cause of the discrepancies between the measured velocities and the theoretical and numerical predictions. Furthermore, the limited number of particles that could be used in the measurements required averaging of the obtained velocities. Nevertheless, both the numerical model and the experiments suggest that the velocities predicted by Equation 6.11 and which are often used in the endodontic literature are overpredicted. The linear decrease of velocity in the secondary boundary layer as assumed in Equation 6.10 may lead to an overestimated jet velocity, as the velocity gradient towards the pole of the cylinder may actually be smaller. Another possibility is that higher order terms (beyond  $\varepsilon^2$ ) of the theoretical solution cannot be completely neglected, and the presence of a confinement, even when the confinement is large, may influence the jet formation as well. Figure 6.8 seems to confirm this, as the difference between the maximum velocities and the predicted velocities becomes larger for larger oscillation amplitudes. The difference in pressure and wall shear stress between theory and numerical simulation, and also with the bubble oscillation amplitude, can be explained by the finite size of the file instead of being a point source, and by geometrical effects.

The sinusoidal motion of the file as assumed here is actually a simplification of the motion of the file during operation inside an root canal. First, we assumed the oscillation to occur in a single direction only, whereas it has been reported that there is also a sideways component [28, 29]. This concurrent sideways motion can lead to a more complicated streaming pattern. Acoustic streaming is likely to remain induced, but, for example, the direction of jets may change, depending on the phase between the two directions of oscillation. Secondly, during a clinical procedure it is virtually impossible to avoid contact with the walls of the root canal, as demonstrated in a recent article [45]. Contact was observed to induce secondary oscillations on top of the 30 kHz driving frequency. Contact may lead to unsteady (transient) oscillations of the file, which could be more effective for cleaning because interference of frequencies may lead to temporary high velocities, while still inducing acoustic streaming. It has recently been demonstrated [46] that pulsed ultrasound, involving transient behavior at the start-up of each pulse, can actually increase the cleaning efficacy of PUI.

Cavitation was observed at the sharp edges of the cylinder with square cross-section. At those edges, large velocity gradients and corresponding pressure gradients can occur, which can induce cavitation from nuclei on the flow. The negative pressure necessary for cavitation can be estimated by requiring the oscillatory component of the pressure (equation ) to equal or exceed the ambient pressure ( $10^5$  Pa) plus the vapor pressure of the liquid ( $2 \cdot 10^3$  Pa) [47]. For typical endodontic files (oscillating unconstrained) and driving parameters, cavitation is likely to occur. The formation of cavitation bubbles violates acoustic streaming requirement 2, as the boundary layer doesn't remain attached to the file, which may hamper the formation of steady jets,

Nevertheless, the high-speed recordings still showed a steady flow, which presence is confirmed with a pilot experiment using a water-soluble dye. There may be an erroneous contribution to the velocity measurement because the tracer particles will have difficulty to follow the fast fluid flow around the collapsing bubbles cloud. Whether cavitation itself also contributes to cleaning cannot be answered from this study and is subject of ongoing work.

A file with a square cross-section was furthermore observed to lead to higher steady velocities, however more detailed analysis of oscillations of cylinders with a cross-section other than circular should be done, as is done by Kim & Troesch [48] for circular, square and rounded-square cross-sections. They have shown that acoustic streaming still occurs with cylinders of different cross-sections, although there are qualitative differences in boundary layers shape and location, and in the steady streaming. The good agreement between the two-dimensional CFD model and the theory and experiments described in this article allows for the use of the CFD model for the simulation of different file cross-sections. Also, for further insight into the coupling between file oscillation and induced streaming, the model will be extended to a two-way coupled three-dimensional model.

## 6.6 Conclusions

The theory of acoustic streaming appears to describe well the flow induced by an ultrasonically oscillating endodontic file. The presence of an oscillatory component, dominant near the file, and a steady component, further away from the file, has been confirmed using high-speed Particle Imaging Velocimetry and a Computational Fluid Dynamics model. Measurement of the pressure, both direct measurement and indirectly from *in-situ* bubble oscillations, also agree well with the theoretical and numerical predictions. The oscillatory component of both the pressure and shear stress is two or three orders of magnitude higher than its steady counterpart. Furthermore, the formation of steady jets is affected by the presence of a confinement; meanwhile the oscillatory velocities and associated pressure and shear stress are increased. Previous work considering only the steady component of the flow therefore underestimated the hydrodynamic effects induced by ultrasonic files. Future work should investigate the interaction of the acoustic streaming and induced cavitation with the actual material that needs to be removed (e.g., biofilm, dentin debris).

## References

- [1] M. Haapasalo, U. Endal, H. Zandi, and J. M. Coil, "Eradication of endodontic infection by instrumentation and irrigation solutions", *Endodontic Topics* **10**, 77–102 (2005).
- [2] P. Nair, "Pathogenesis of apical periodontitis and the causes of endodontic failures", *Critical Review of Oral Biology & Medicine* **15**, 348–381 (2004).
- [3] J. F. Siqueira, D. C. Lima, F. A. C. Magalhães, H. P. Lopes, and M. de Uzeda, "Mechanical reduction of the bacterial population in the root canal by three instrumentation techniques", *Journal of Endodontics* **25**, 332–335 (1999).
- [4] M. Richman, "The use of ultrasonics in root canal therapy and root resection", *Journal of Dental Medicine* **12**, 12–18 (1957).
- [5] R. N. Weller, J. M. Brady, and W. E. Bernier, "Efficacy of ultrasonic cleaning", *Journal of Endodontics* **6**, 740–743 (1980).
- [6] S. Lighthill, "Acoustic streaming", *Journal of Sound and Vibration* **61**, 391–418 (1978).
- [7] N. Riley, "Steady streaming", *Annual Review of Fluid Mechanics* **33**, 43–65 (2001).
- [8] A. D. Walmsley, "Ultrasound and root canal treatment: the need for scientific evaluation", *International Endodontic Journal* **20**, 105–111 (1987).
- [9] L. W. M. Van der Sluis, M. Versluis, M. K. Wu, and P. R. Wesselink, "Passive ultrasonic irrigation of the root canal: a review of the literature", *International Endodontic Journal* **40**, 415–426 (2007).
- [10] M. Ahmad, T. R. Pitt Ford, and L. A. Crum, "Ultrasonic debridement of root canals: acoustic streaming and its possible role", *Journal of Endodontics* **13**, 490–499 (1987).
- [11] M. Ahmad, T. R. Pitt Ford, L. A. Crum, and A. J. Walton, "Ultrasonic debridement of root canals: Acoustic cavitation and its relevance", *Journal of Endodontics* **14**, 486–493 (1988).
- [12] M. Ahmad, R. A. Roy, and A. G. Kamarudin, "Observations of acoustic streaming fields around an oscillating ultrasonic file", *Endodontics and Dental Traumatology* **8**, 189–194 (1992).
- [13] P. J. Lumley, A. D. Walmsley, and W. R. E. Laird, "Streaming patterns produced around endosonic files", *International Endodontic Journal* **24**, 290–297 (1991).
- [14] S. C. Lea, A. D. Walmsley, P. J. Lumley, and G. Landini, "A new insight into the oscillation characteristics of endosonic files used in dentistry", *Physics in Medicine and Biology* **49**, 2095–2102 (2004).
- [15] K. Gulabivala, Y.-L. Ng, M. Gilbertson, and I. Eames, "The fluid mechanics of root canal irrigation", *Physiological Measurements* **31**, R49–R84 (2010).
- [16] L.-M. Jiang, B. Verhaagen, M. Versluis, J. Langedijk, P. R. Wesselink, and L. W. M. Van der Sluis, "The influence of the ultrasonic intensity on the cleaning efficacy of passive ultrasonic irrigation", *Journal of Endodontics* **37**, 688–692 (2011), *see also Chapter 8 of this thesis*.
- [17] Lord Rayleigh, "On the circulation of air observed in Kundt's tubes and on some allied acoustical problems", *Philosophical Transactions of the Royal Society of London* **175**, 1–21 (1884).

- [18] H. Schlichting, *Boundary-layer theory*, 4th edition (McGraw-Hill) (1979).
- [19] W. L. Nyborg, "Acoustic streaming near a boundary", *The Journal of the Acoustical Society of America* **30**, 329–339 (1958).
- [20] W. P. Raney, J. C. Corelli, and P. J. Westervelt, "Acoustica streaming in the vicinity of a cylinder", *Journal of the Acoustical Society of America* **26**, 1006–1014 (1954).
- [21] J. Holtsmark, I. Johnsen, T. Sikkeland, and S. Skavlem, "Boundary layer flow near a cylindrical obstacle in an oscillating, incompressible fluid", *Journal of the Acoustical Society of America* **26**, 26–39 (1954).
- [22] N. Riley, "Oscillating viscous flows", *Mathematika* **12**, 161–175 (1965).
- [23] N. Riley, "The steady streaming induced by a vibrating cylinder", *Journal of Fluid Mechanics* **68** (1975).
- [24] J. T. Stuart, "Double boundary layers in oscillatory viscous flow", *Journal of Fluid Mechanics* **24**, 673–687 (1966).
- [25] P. W. Duck and F. T. Smith, "Steady streaming induced between oscillating cylinders", *Journal of Fluid Mechanics* **91**, 93–110 (1979).
- [26] E. W. Haddon and N. Riley, "The steady streaming induced between oscillating circular cylinders", *Quarterly Journal of Mechanics and Applied Mathematics* **32**, 265–282 (1979).
- [27] M. Ahmad, R. A. Roy, A. G. Kamarudin, and M. Safar, "The vibratory pattern of ultrasonic files driven piezoelectrically", *International Endodontic Journal* **26**, 120–124 (1993).
- [28] S. C. Lea, A. D. Walmsley, and P. J. Lumley, "Analyzing endosonic root canal file oscillations: an in vitro evaluation", *Journal of Endodontics* **36**, 880–883 (2010).
- [29] B. Verhaagen, S. C. Lea, L. W. M. van der Sluis, A. D. Walmsley, and M. Versluis, "Oscillation characteristics of endodontic files: numerical model and its validation", *IEEE - Transactions on Ultrasonics, Ferroelectrics and Frequency Control* accepted (2012), *see also Chapter 4 of this thesis*.
- [30] N. Riley, "Unsteady laminar boundary layers", *SIAM Review* **17**, 274–297 (1975).
- [31] B. J. Davidson and N. Riley, "Jets induced by oscillatory motion", *Journal of Fluid Mechanics* **53**, 287–303 (1972).
- [32] B. Verhaagen, C. Boutsoukis, G. L. Heijnen, L. W. M. Van der Sluis, and M. Versluis, "Role of the confinement of a root canal on jet impingement during endodontic irrigation", *Experiments in Fluids* accepted (2012), *see also Chapter 2 of this thesis*.
- [33] D. J. Phares, G. T. Smedley, and R. C. Flagan, "The inviscid impingement of a jet with arbitrary velocity profile", *Physics of Fluids* **12**, 2046–2055 (2000).
- [34] A. R. Williams and W. L. Nyborg, "Microsonation using a transversely oscillating capillary", *Ultrasonics* **8**, 36–38 (1970).
- [35] M. B. Glauert, "The wall jet", *Journal of Fluid Mechanics* **1**, 625–643 (1956).

- [36] M. P. Brenner, S. Hilgenfeldt, and D. Lohse, “Single-bubble sonoluminescence”, *Reviews of Modern Physics* **73**, 425–484 (2002).
- [37] T. Leighton, *The Acoustic Bubble* (Academic Press, London) (1994).
- [38] C. Boutsioukis, B. Verhaagen, M. Versluis, E. Kastrinakis, P. R. Wesselink, and L. W. M. van der Sluis, “Evaluation of irrigant flow in the root canal using different needle types by an unsteady computational fluid dynamics model”, *Journal of Endodontics* **36**, 875–879 (2010).
- [39] L.-M. Jiang, B. Verhaagen, M. Versluis, and L. W. M. Van der Sluis, “The influence of the oscillation direction of an ultrasonic file on the cleaning efficacy of passive ultrasonic irrigation”, *Journal of Endodontics* **36**, 1372–1376 (2010), *see also Chapter 7 of this thesis*.
- [40] L. W. M. Van der Sluis, M. P. J. M. Vogels, B. Verhaagen, R. G. Macedo, and P. R. Wesselink, “Study on the influence of refreshment/activation cycles and irrigants on mechanical cleaning efficiency during ultrasonic activation of the irrigant”, *Journal of Endodontics* **36**, 737–740 (2010).
- [41] M. Amato, I. Vanoni-Heineken, H. Hecker, and R. Weiger, “Curved versus straight root canals: the benefit of activated irrigation techniques on dentin debris removal”, *Oral Surgery, Oral Medicine, Oral Pathology, Oral Radiology and Endodontology* **111**, 529–534 (2011).
- [42] A. J. Harrison, P. Chivatxaranukl, P. Parashos, and H. H. Messer, “The effect of ultrasonically activated irrigation on reduction of enterococcus faecalis in experimentally infected root canals”, *International Endodontic Journal* **43**, 968–977 (2010).
- [43] A. Al-Jadaa, F. Paqué, T. Attin, and M. Zehnder, “Necrotic pulp tissue dissolution by passive ultrasonic irrigation in simulated accessory canals: Impact of canal location and angulation”, *International Endodontic Journal* **42**, 59–65 (2009).
- [44] L.-M. Jiang, B. Verhaagen, M. Versluis, and L. W. M. Van der Sluis, “Evaluation of a sonic device designed to activate irrigant in the root canal”, *Journal of Endodontics* **36**, 143–146 (2010), *see also Chapter 9 of this thesis*.
- [45] C. Boutsioukis, B. Verhaagen, A. D. Walmsley, L. W. M. Van der sluis, and M. Versluis, “On the occurrence of contact during pui”, (in progress) (2012), *see also Chapter 5 of this thesis*.
- [46] L.-M. Jiang, B. Verhaagen, M. Versluis, C. Zangrillo, D. Cuckovic, and L. W. M. Van der Sluis, “An evaluation of the effect of pulsed ultrasound on the cleaning efficacy of passive ultrasonic irrigation”, *Journal of Endodontics* **36**, 1887–1891 (2010), *see also Chapter 10 of this thesis*.
- [47] C. Brennen, *Cavitation and Bubble Dynamics* (Oxford University Press, Oxford) (1995).
- [48] S. K. Kim and A. W. Troesch, “Streaming flows generated by high-frequency small-amplitude oscillations of arbitrarily shaped cylinders”, *Physics of Fluids A* **1**, 975–985 (1989).

## Appendices

### 6.A Acoustic streaming along the file (coronal-to-apical direction)

The acoustic streaming induced by the oscillating endodontic file is not solely two-dimensional: there is also a flow along the length of the file, in coronal to apical direction (inside the root canal). Only the steady component of the flow is considered here, as we are concerned with irrigant transport.

#### 6.A.1 Experimental setup

The flow along the length of the file was measured using high-speed PIV, with an optical similar setup as described before. Here, the file was positioned in front of the camera in such a way that it was viewed from the side. The file was of the type ESI015 file, with circular cross-section, and was driven at 26.97 kHz with a customized hand piece (EMS, Nyon, Switzerland), driven with a 70 mW electrical signal generated by an arbitrary waveform generator (33220A, Agilent, Santa Clara, California, United States) and amplified with an audio amplifier (TA-FB740R, Sony, Tokyo, Japan). The file was held either inside a large water bath (dimensions  $75 \times 62 \times 117$  mm,  $\alpha = O(10^3)$ ) or at 1 mm from the apex of a silicon (Polydimethylsiloxane [PDMS], Sylgard 184, Dow-Corning, Midland, MI, USA) root canal model (size 45/.06,  $\alpha = 3$ ). With  $10\times$  magnification, only a 1 mm section of the file and optional root canal was visible, requiring each 1 mm section to be measured individually separately.

The high-speed camera recorded 100 frames at frame rates up to 32 kfps; PIV analyses was performed with ensemble averaging. The results therefore show the flow averaged over approx. 120 oscillations.

#### 6.A.2 Results

The flow patterns inside the water tank and inside the root canal are shown in Figures 6.13 and 6.14, respectively. The flow without confinement shows sideways streaming at the antinodes, with decreasing magnitude higher up the file (Figure 6.15). This is in good agreement with the reduction in oscillation amplitude (Figure 6.16), which, according to the acoustic streaming theory, is quadratically related to the steady flow velocity. There is a low-velocity inflow from below the tip toward the tip. The flow is not zero at the nodes: there appears to be a flow from antinodes in the  $-z$  direction (toward the tip), but not from antinodes in the  $+z$  direction (toward the file's attachment point), even though the oscillation amplitude and flow velocities increase in the  $+z$  direction. This could be due to the taper of the file, causing a flow in the  $-z$  direction.



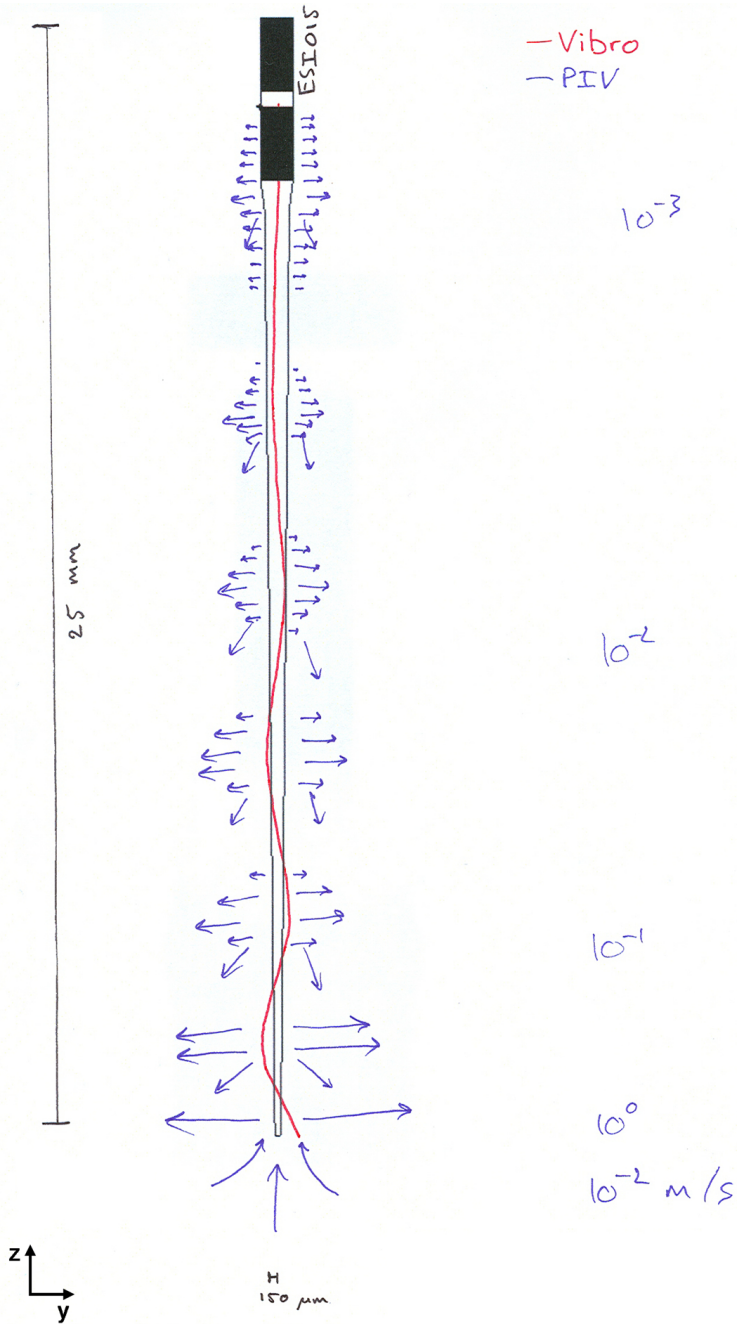


**Figure 6.13:** Sketch of the flow without the confinement of the root canal. Approximate velocities are given on the right; the oscillation pattern on the file is indicated in red (not to scale).

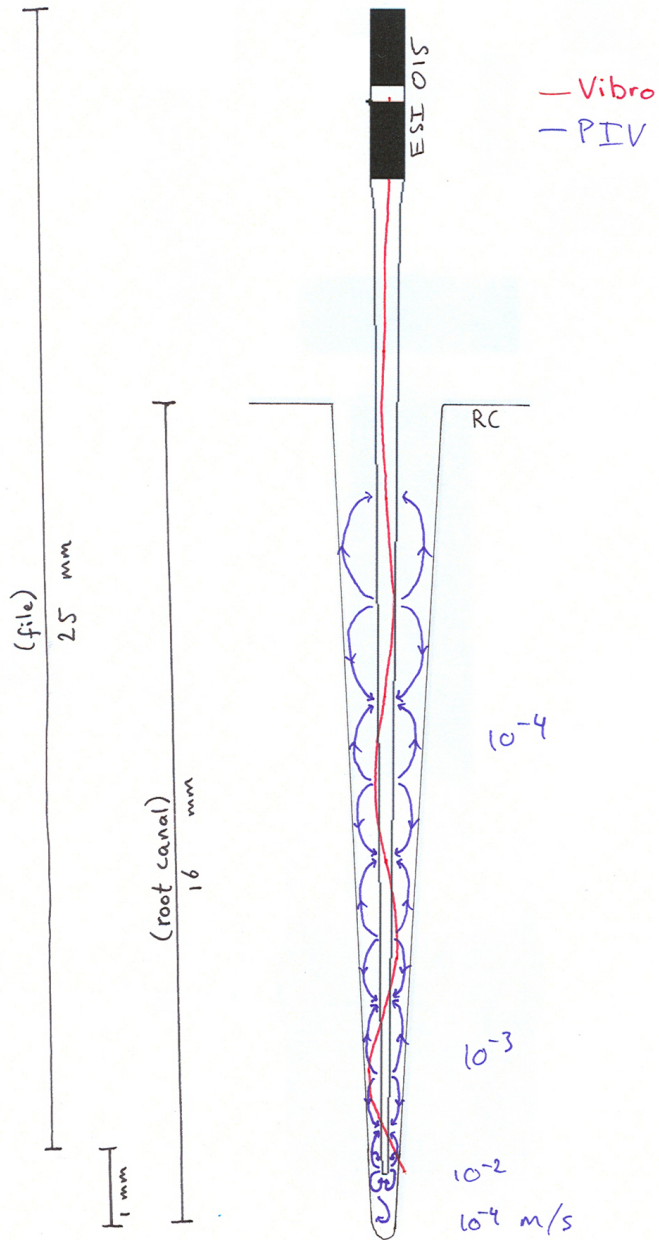


Figure 6.14: As in Figure 6.13, but now with the confinement of the root canal.

The flow pattern inside the root canal also shows sideways streaming at the antinodes, but the velocity magnitude is typically one order of magnitude smaller than without confinement (see Figure 6.15). The locations of low-velocity flow, associated with nodes on the file, appears to have been shifted compared to the unconfined case, due to two different driving frequencies. At the tip, there is a vortex visible, driving a second vortex near the apex. There is an inflow from below the tip toward the tip.

At each of the antinodes the flow is initially radially (toward the root canal wall) and then toward the nodes, both in the  $-z$  and  $+z$  direction, with no clear difference in magnitude between them. The flow velocities in the  $z$  direction are typically one order of magnitude lower than the radial velocities. The radial velocity magnitude decreases higher up the file, qualitatively in agreement with the reduction in oscillation amplitude, but the scaling with the file oscillation amplitude squared is not so clear here (Figure 6.16).

### 6.A.3 Discussion & Conclusion

The flow velocity inside the confinement decreases by approximately one order of magnitude, whereas the file oscillation amplitude and characteristics should remain largely unaffected [29]. Considering the acoustic streaming described above, this decrease in flow velocity could be attributed to the fact that the steady streaming (i.e., jet) needs some space to develop. On the other hand, the shift in distance between and location of the nodes of the file oscillation characteristics suggest that the file might be oscillating at a different frequency inside the confinement than outside the confinement, which is known to occur for this type of file ([29] and Chapter 4). A different driving frequency may result in a much lower oscillation amplitude and consequently a lower steady streaming velocity. The magnitude of the oscillation amplitude and induced velocity in the direction perpendicular to the current measurement plane was not assessed but could be significant for this different mode of oscillation.

The flow pattern that was measured here outside the root canal qualitatively matches the sketch by Lumley *et al.* (1991) [13]. However, the steady component of the acoustic streaming sketched by Ahmad *et al.* (1987) [10] shows primary streaming (small eddies) and secondary, larger-scale streaming, both qualitatively different from the streaming observed in the present study, even though the acoustic driving conditions were very similar. In fact, the streaming pattern by Ahmad *et al.* resembles closer our measurements inside the confinement of the root canal. Perhaps ambient acoustic conditions or different time scales (still photography vs. high-speed imaging in the present study) could explain these differences.

The flow velocity at the antinodes is quadratically related to the oscillation amplitude of the file, suggesting that the flow velocity and related shear stress are higher at antinodes near the tip at antinodes toward the attachment point. The flow near the

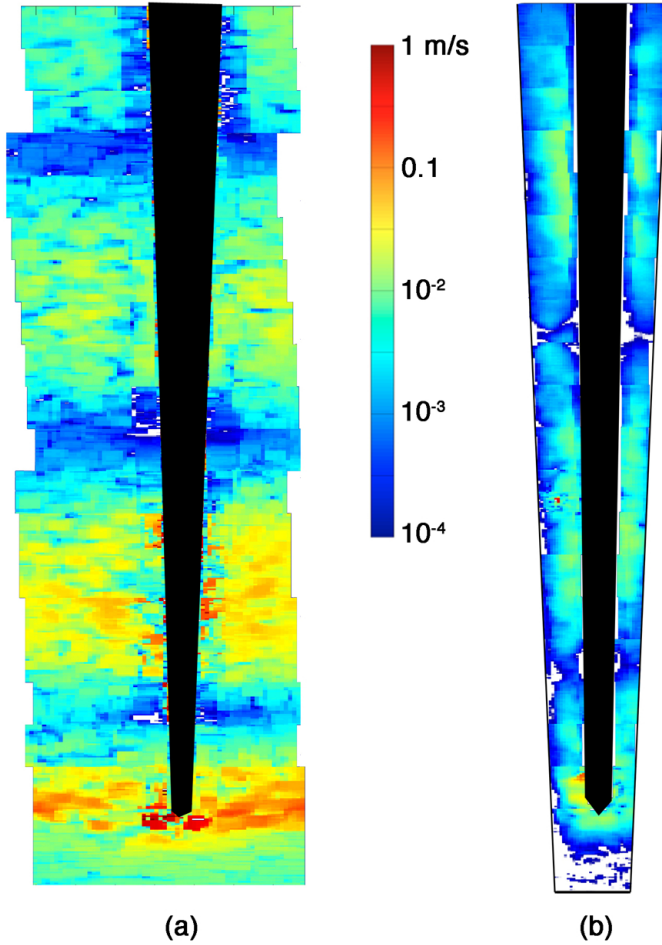


**Figure 6.15:** Velocity magnitudes of the steady component of the flow, without (a) and with (b) confinement of the root canal. Velocities are on a logarithmic scale.

nodes decrease toward zero, suggesting inefficient streaming around the nodes. Also the flow beyond the file insertion depth, toward the apex, decreases quickly with distance from the file (although in Chapter 11 it is shown that the flow can reach 3/4th of the distance to the apex, on a time scale of the order of seconds). This illustrates the need for up-and-down movement of the file during irrigation, or transient behavior (traveling waves) on the file (for example as induced by contact with the wall, see Chapter 5).

A three-dimensional Computational Fluid Dynamics model of PUI inside a root canal is currently under development by Christos Boutsoukis.

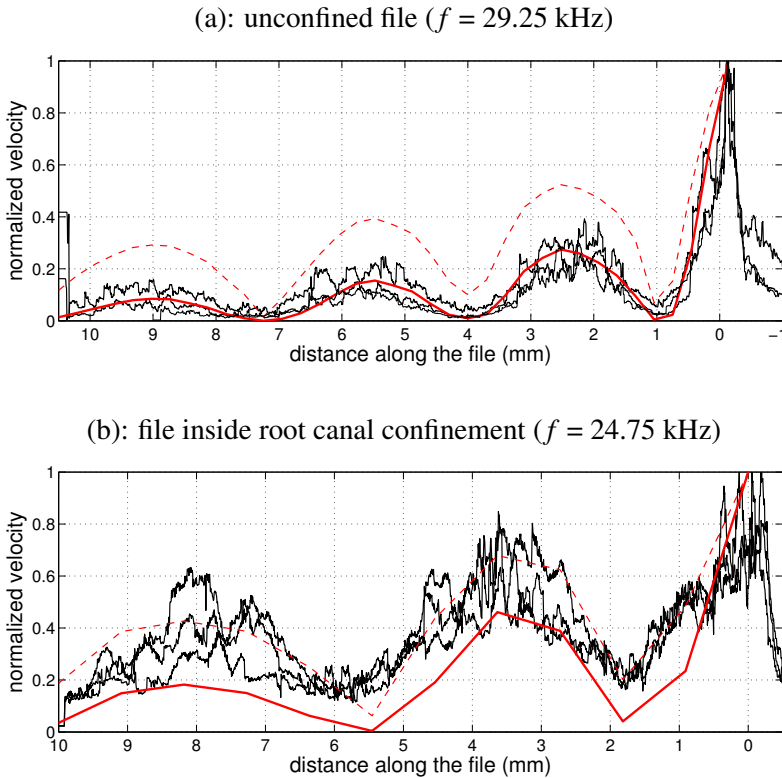


**Figure 6.16:** Normalized steady velocity magnitude along the length of the file, for three different driving powers (30, 50 and 70 mW, black lines), outside (a) and inside (b) the confinement of the root canal. The oscillation characteristic of the ESI015 file (dashed line), as measured with the vibrometer in Chapter 4, and its value squared (solid line) are plotted as well, in red.

## 6.B Supplementary material

*(Online at [http://stilton.tnw.utwente.nl/rootcanalcleaning/Gallery\\_of\\_Irrigant\\_Motion](http://stilton.tnw.utwente.nl/rootcanalcleaning/Gallery_of_Irrigant_Motion))*

Movie 1. High-speed visualization of acoustic streaming around an endodontic file. The black dots are tracer particles. Recording speed is 250 Kfps; the diameter of the file is 200  $\mu\text{m}$ .

Movie 2. Velocity vectors calculated by the CFD model, for a file oscillating inside a root canal.

Movie 3. Velocity vectors calculated by the CFD model, for a file oscillating near a flat wall.

Movie 4. Pressure magnitude as calculated by the CFD model, for a file oscillating inside a root canal.

Movie 5. Pressure magnitude as calculated by the CFD model, for a file oscillating near a flat wall.

Movie 6. High-speed visualization of a file oscillating near a flat wall. Cavitating bubbles can be observed on the file and on the wall. Recording speed is 250 Kfps; the distance between the file and the wall is 300  $\mu\text{m}$ .



# 7

## Influence of the oscillation direction of an ultrasonic file on the cleaning efficacy of passive ultrasonic irrigation \* †

**Abstract:** The oscillatory direction of an ultrasonically driven file was investigated in this chapter. Each of 20 *ex vivo* root canal models with a standard groove in the apical portion of one canal wall filled with dentin debris received PUI repeatedly, either with file oscillation toward the groove or with file oscillation perpendicular to the groove. Afterwards, the amount of dentin debris in the groove was evaluated. Oscillation of the ultrasonically driven file toward the groove was found to be more effective in removing dentin debris from the groove than oscillation perpendicular to the groove, which can be related to the observation from high-speed visualizations that there is a high-velocity jet from the file tip in a single direction following the file oscillation and a relatively slow inflow in the perpendicular direction.

---

\*Published as: L-M. Jiang, B. Verhaagen, M. Versluis and L.W.M. van der Sluis. “Influence of the Oscillation Direction of an Ultrasonic File on the Cleaning Efficacy of Passive Ultrasonic Irrigation”, *Journal of Endodontics* **36**(8), pp. 1372-1376 (2010)

†The high-speed imaging and its analysis in this chapter is part of the present thesis. The dentin debris removal experiments are due to Lei-Meng Jiang.



## 7.1 Introduction

Because instruments used for root canal preparation can merely touch a small part of the canal, mechanical preparation by instruments obviously does not suffice for the debridement of the complex root canal system [1, 2]. Irrigation has therefore been gaining increasing attention to improve the cleanliness of root canal systems after root canal instrumentation. Passive ultrasonic irrigation (PUI) has been suggested to be used to disinfect the areas beyond instruments by acoustically activating the irrigant [3–5]. Acoustic streaming has been shown to be useful in cleaning the root canal system [6].

Ultrasonically powered handpieces are normally attached with an oscillating instrument and operated at a certain frequency domain of 20–40 kHz. Previous *in vitro* investigations have shown that oscillation of the file perpendicular to the dentin surface had a greater influence on dentin removal than an oscillation parallel to the surface [7, 8], indicating that the energy was distributed non-uniformly around the oscillating file. Lumley *et al.* [9] have demonstrated a 3-dimensional streaming pattern around the ultrasonically activated files, while streaming occurred mainly in front of and behind the file parallel to the handpiece. In another study, Lumley *et al.* [10] found that a file oscillation directed toward oval recesses left less debris than a perpendicular oscillation. Despite these previous studies, a detailed description and understanding of the oscillation characteristics of ultrasonically driven files are still missing. The aims of this study were therefore (1) to investigate whether the orientation of the ultrasonically activated file had an influence on the increase of dentin debris removal from artificially made grooves simulating uninstrumented canal extensions in standardized root canals and (2) to investigate the streaming pattern around an ultrasonically oscillating file by using visualization techniques.

## 7.2 Materials and Methods

### 7.2.1 Dentin debris removal model

Straight roots from 20 extracted human maxillary canines were decapitated to obtain uniform root sections of 15 mm. The roots were embedded in self-curing resin (GC Ostron 100; GC Europe, Leuven, Belgium) and then bisected longitudinally through the canal in mesiodistal direction with a saw microtome (Leica Microsystems SP1600, Wetzlar, Germany). The surfaces of both halves were ground successively with 240-, P400-, and 600-grit sandpaper, resulting in smooth surfaces on which only little of the original root canal lumen was left. Four holes were drilled in the resin part, and the two halves were reassembled by four self-tapping bolts through the holes (Fig. 7.1A). The root canal space of the model was ensured as a closed system.

New root canals were prepared by K-files #15/.02 (Dentsply Maillefer, Ballaigues,

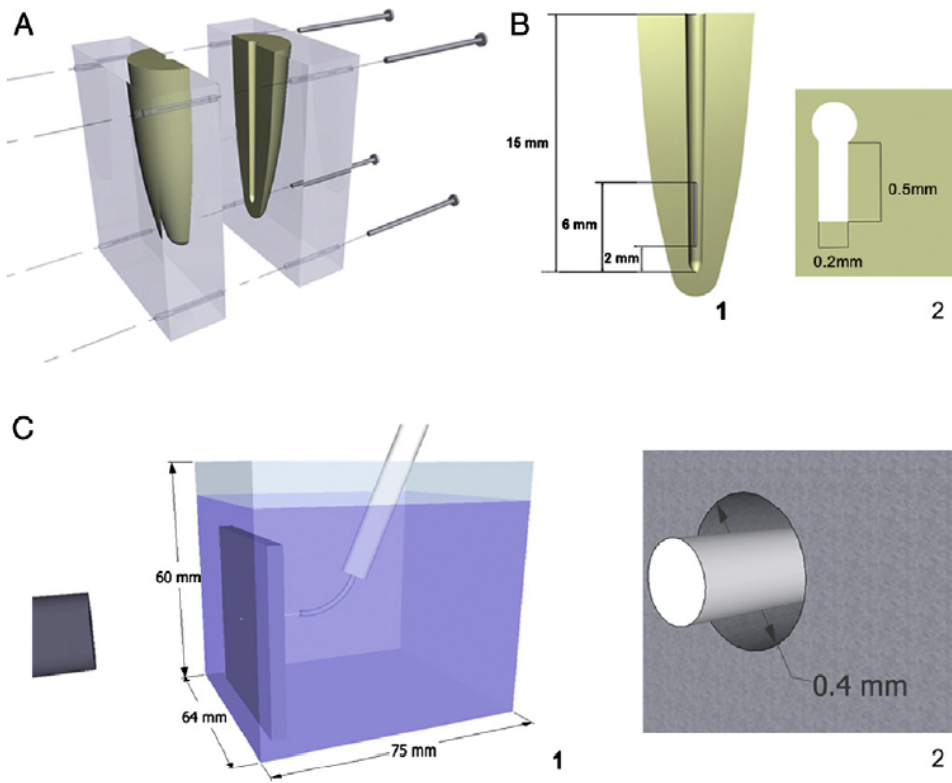


**Figure 7.1:** (A) Schematic representations of the standardized root canal model, its groove (B1) and cross section (B2). (C1) Drawing of the optical setup, showing the file inserted into the hole in the aluminum plate (details in C2), which is in turn inserted into a large water tank. The camera is positioned on the left, looking toward the hole.

Switzerland) and HERO 642 (MicroMega, Besancon, France) nickel-titanium rotary instruments to a working length (WL) of 15 mm, ISO size 30 and taper 0.06, resulting in standardized root canals. During preparation, the canals were rinsed with 1 mL of 2% NaOCl after each file, delivered by a 10-mL syringe (Terumo, Leuven, Belgium) and a 30-gauge needle (Navitip; Ultradent, South Jordan, UT).

A standard groove of 4 mm in length, 0.5 mm deep, and 0.2 mm wide, situated at 2-6 mm from WL [11], was cut in the wall of one half of each root canal with a customized ultrasonic tip (Fig.7.1B). A periodontal probe with an adapted 0.2-mm-wide tip was used to verify the dimension of each groove during and after preparation. The dimension of the groove is comparable to an apical oval root canal [12]. Each groove was filled with dentin debris, which was mixed with 2% NaOCl for 5 minutes, to simulate a situation in which dentin debris accumulates in uninstrumented canal extensions [11]. This model was introduced to standardize the root canal space and the amount of dentin debris present in the root canal before the irrigation procedure to increase the reliability of the dentin debris removal evaluation. The methodology is sensitive, and the data are reproducible [13, 14]. A pilot study has shown that a single model could be reused up to at least eight times without any visible defect on the surface of the canal wall. Therefore, the 20 models were used repeatedly in the 3 experimental groups, which are shown in Table 7.1.

### 7.2.2 Irrigation procedure

Specimens in all the experimental groups were rinsed with 2 mL irrigant (2% NaOCl) by using 10-mL syringes with 30-gauge needles placed 1 mm from WL. Then the irrigant was passively activated by an ultrasonic file for 10 seconds, with the oscillation perpendicular to the groove (group 1; Fig. 7.2C1) or toward the groove (group 2; Fig. 7.2C2). The ultrasonic activation was performed with a stainless steel #20/.00 file (IrriSafe; Acteon, Merignac, France) driven by an ultrasonic device (Suprasson PMax Newtron; Acteon) at power setting “blue 4”. Every attempt was made to keep the file centered in the canal to minimize contact with the canal walls to do passive ultrasonic activation. Group 3 acted as the control group, in which the ultrasonic file was inserted but not activated. All the experimental specimens received 2 mL irrigant, which was delivered again by a syringe as final flush.

### 7.2.3 Image evaluation and statistical analyses

Before and after each irrigation procedure, the root halves were separated, and the grooves were viewed through a stereomicroscope (Stemi SV6; Carl Zeiss, Goettingen, Germany) by using a cold light source (KL 2500 LCD; Carl Zeiss). Controls verified that no debris had fallen out of the groove during the assembly or disassembly process. Pictures were taken with a digital camera (Axio Cam; Carl Zeiss).

The debris left in the groove after irrigation was scored independently by three calibrated dentists by using the following score system: 0, the groove is empty; 1, less than half of the groove is filled with debris; 2, more than half of the groove is filled with debris; and 3, the complete groove is filled with debris [11, 14]. The percentage of interagreement should be more than 95%; if this percentage was lower than 95%, a consensus had to be reached.

The differences in debris scores between the groups were analyzed by means of the Kruskal-Wallis test and the Mann-Whitney test. The level of significance was set at  $\alpha = 0.05$ .

### 7.2.4 High-speed imaging experiments

An optical setup was constructed to visualize the oscillation of the same ultrasonically driven file used in the ex vivo study. To simulate the confinement of apical section of the root canal, a 1-mm-thick aluminum plate with a hole ( $\phi = 0.4$  mm) and a 4-mm-thick plate with a hole ( $\phi = 0.4$  mm) plus a groove with the same dimensions as the ex vivo model were used. The plate was positioned in a water tank (dimensions,  $75 \times 64 \times 60$  mm), and the ultrasonic file was centered in the hole (Fig. 7.1C). Tracer particles (hollow glass spheres,  $\phi = 11$   $\mu\text{m}$ ,  $\rho = 1.1 \cdot 10^3$   $\text{kg/m}^3$ ; SpheriCel; Potters Industries, South Yorkshire, UK) were added to the water for flow visualization.

The flow around the oscillating file was imaged through a microscope (BX-FM; Olympus, Tokyo, Japan) with a magnification of 1.25–20 $\times$ . Illumination was performed in bright-field by a continuous wave light source (ILP-1; Olympus, Tokyo, Japan). Recordings were made with a high-speed camera (HPV-1; Shimadzu Corp, Kyoto, Japan) at a frame rate of 125,000 frames per second, starting 2 seconds after initiation of file oscillation to be able to avoid transient file motion at startup. Recordings were analyzed by using a Particle Image Velocimetry (PIV) code developed in-house.

## 7.3 Results

The results of the ex vivo experiments are presented in Table 7.1. There is a statistically significant difference between each of the experimental groups ( $P < .0001$ ). When the irrigant was activated, significantly more dentin debris was removed than in the control group (no activation). Oscillation of the file toward the groove had a significantly greater influence on dentin debris removal than oscillation perpendicular to the groove ( $P = .002$ ).

The time-averaged flow pattern caused by an oscillating file in a large water tank is shown in Fig. 7.2A. The steady part of the flow depicted here consists of two “jets” in the direction of oscillation of the file. There is an inflow toward the file from

Group (N = 20)	Orientation of file oscillation	Irrigant	Intensity	Total duration (sec)	Score			
					0	1	2	3
1	Perpendicular to the groove	NaOCl	Blue 4	10	10 (50%)	9 (45%)	1 (5%)	0 (0%)
2	Toward the groove	NaOCl	Blue 4	10	19 (95%)	1 (5%)	0 (0%)	0 (0%)
3 (control)	N/A	NaOCL	0	10	0 (0%)	0 (%)	0 (0%)	20 (100%)

Score 0, the groove is empty; score 1, less than half of the groove is filled with debris; score 2, more than half of the groove is filled with debris; score 3, the complete groove is filled with debris.

**Table 7.1:** Experimental groups and the number of specimens at each score rank after irrigation procedure

the direction perpendicular to the oscillation direction. We observe an unsteady flow that is located within a distance of approximately 1 diameter of the file. Fig. 7.2B1 shows a close-up of the instantaneous flow pattern, while the file is moving in the direction indicated by the white arrow. In Fig. 7.2B2 we show the instantaneous flow pattern when the confinement of the root canal is included; Fig. 7.2C1 and C2 show the average flow pattern when the groove is also included (Movies 1 and 2). Flow velocities in the groove when the file oscillation is toward the groove are 3-5 times higher than when the file is oscillating perpendicular to the groove.

## 7.4 Discussion

The results showed that debris was reduced significantly more by PUI when the file oscillation was directed toward the groove than when the file oscillation was perpendicular to the groove, indicating that the oscillation direction of the ultrasonic file has a great influence.

The ultrasonically driven file oscillates mainly in the direction equal to the axis of the handpiece and a minor transverse vibration at right angles to the main one [9]. Lumley *et al.* [10] have shown more effective cleaning of an oval extension in the root canal when the oscillation of the file is directed toward the oval extension. They proposed two explanations: (1) the streaming forces are more intense toward the oval recess, and (2) the file was less likely to be constrained when it oscillated toward the recess. However, in the study by Lumley *et al.*, the ultrasonic file was used for root canal instrumentation; in other words, the file was intentionally in contact with the root canal wall. Therefore, the file was unable to vibrate freely; acoustic microstreaming would consequently be less intense, although it would not stop completely [15]. It could be hypothesized that when oscillating toward the groove, the file could vibrate somewhat more freely, despite intentional contact with the root canal wall, resulting in more intense streaming forces toward the groove.

PUI was performed in the current study, and the experimental setup was such that contact of the file with the root canal wall was prevented for both oscillation directions. Moreover, the oscillation amplitude of the file is approximately 28 mm

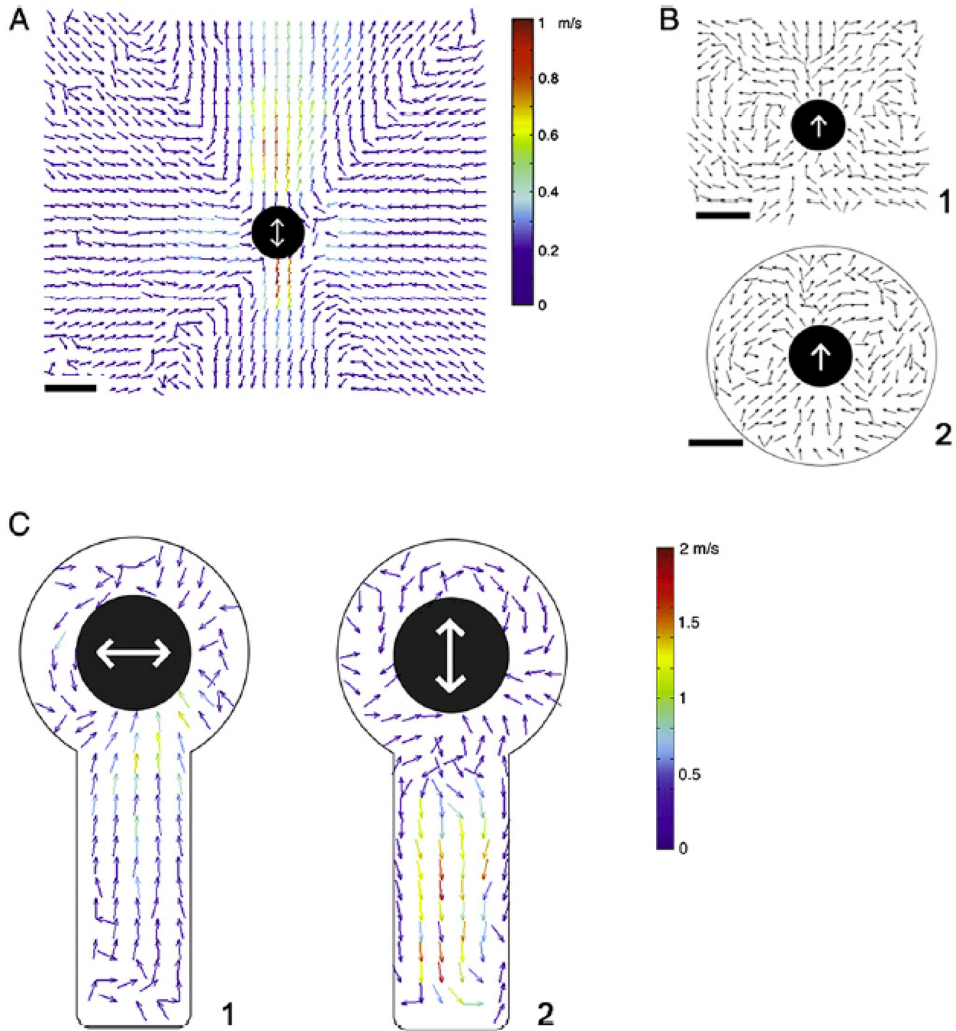


**Figure 7.2:** Direction (solid arrows) and magnitude (colors) of the flow caused by an ultrasonically oscillating file. White arrows in the black circles indicate the direction of oscillation. (A) Steady part of the flow when oscillating in a large water tank, averaged over 100 frames (0.8 ms). (B1) Unsteady part of the flow, single frame only; (B2) unsteady part of the flow in the confinement of a root canal, single frame only. (C) Sketch of the cross section of the root canal indicating the direction of oscillation with respect to the groove and the flow around the oscillating file; (C1) oscillation perpendicular to the groove (Movie 1), (C2) oscillation toward the groove (Movie 2). (Black bar is 0.2 mm.)

according to the manufacturer, which is smaller than the dimension of the root canal in the current study; thus, the file could vibrate freely whether its orientation was toward or perpendicular to the groove. Therefore, the only explanation for the different efficiency by the two ways of irrigation should be the difference in streaming of the irrigant around the oscillating file, consisting of both the streaming orientation and strength.

This streaming has been visualized with high-speed imaging. The results showed a high-velocity jet from the file tip in one dimension and a slow inflow in the perpendicular direction, which could well explain the consequences for the cleaning efficacy. Streaming has been held responsible for cleaning [6], in which the direction and the velocity of the flow might be the key factors.

The flow pattern as shown in Fig. 7.2A and B1 is qualitatively similar to the flow as described theoretically by Riley [16] and Stuart [17] and confirmed experimentally by Bertelsen [18]. The flow pattern with confinement, as shown in Fig. 7.2B2, is qualitatively similar to the flow as described theoretically by Duck & Smith [19]. All authors reported a boundary layer close to the oscillating object, which consisted of an oscillatory and a steady component. Outside this boundary layer, only the steady component remains, visible as jets in Fig. 7.2A and C2. In Fig. 7.2B1 and B2 it can be observed that the boundary layer is approximately 0.3 mm thick; therefore, in the apical area (when the groove is still filled with debris) the flow is dominated by the oscillatory component, which causes a shear stress circumferentially. In addition to the shear stress, it is expected that there is a push-pull mechanism by which removal of debris in the oscillation direction will be enhanced. This push-pull effect is induced by the oscillation of the file.

Once (the entrance of) the groove is starting to be emptied by removal of debris, there will be space available for the jet (steady streaming component) to form when the file is oscillating toward the groove. Shear stresses developed by this jet can enhance the removal of the debris in the groove. When the file oscillates perpendicular to the groove, the jet has no space to develop; therefore, the flow is again dominated by the oscillatory component and its push-pull effect. The fluid in the groove will contribute to the inflow toward the file; however, flow velocities inside the groove are smaller than when the file oscillates toward the groove and are unlikely to contribute much to the removal of debris from the groove.

In the studies by Riley [16], Stuart [17], Bertelsen [18], and Duck & Smith [19], a cylindrical file was considered, whereas the Irrisafe file used in this study has a square cross section, twisted along the length of the file. This difference in cross section might explain the increased divergence of the measured jet compared with the theoretical solution by Duck and Smith. Experiments performed by Kim & Troesch [20] and Tatsuno [21] by using square cylinders showed a flow pattern more similar to the flow pattern observed in this study.

The *ex vivo* dentin debris removal model used in this study is a closed system. The 2 halves of the root embedded in the resin matched perfectly and were fixed by the 4 bolts well to prevent any irrigant flow apically or laterally (Fig. 7.1A). Because the apical fluid movement mechanisms can be quite different between a closed and an open system [22], it is better to use a closed system like the model used in this study, which is more clinically relevant.

## References

- [1] O. Peters, K. Schönenberger, and A. Laib, "Effects of four Ni-Ti preparation techniques on root canal geometry assessed by micro computed tomography", *International Endodontic Journal* **34**, 221–230 (2001).
- [2] M.-K. Wu, L. Van Der Sluis, and P. Wesselink, "The capability of two hand instrumentation techniques to remove the inner layer of dentine in oval canals", *International Endodontic Journal* **36**, 218–224 (2003).
- [3] R. Sabins, J. Johnson, and J. Hellstein, "A comparison of the cleaning efficacy of short-term sonic and ultrasonic passive irrigation after hand instrumentation in molar root canals", *Journal of Endodontics* **29**, 674–678 (2003).
- [4] A. Burlinson, J. Nusstein, A. Reader, and M. Beck, "The in vivo evaluation of hand/rotary/ultrasound instrumentation in necrotic, human mandibular molars", *Journal of Endodontics* **33**, 782–787 (2007).
- [5] L. van der Sluis, M. Versluis, M. Wu, and P. Wesselink, "Passive ultrasonic irrigation of the root canal: a review of the literature", *International Endodontic Journal* **40**, 415–426 (2007).
- [6] M. Ahmad, T. Pitt Ford, and L. Crum, "Ultrasonic debridement of root canals: Acoustic streaming and its possible role", *Journal of Endodontics* **13**, 490–499 (1987).
- [7] P. Briggs, K. Gulabivala, C. Stock, and D. Setchell, "Dentine-removing characteristics of an ultrasonically energized k-file.", *International Endodontic Journal* **22**, 259–268 (1989).
- [8] K. Gulabivala, P. Briggs, and D. Setchell, "A comparison of the dentine-removing characteristics of two endosonic units.", *International Endodontic Journal* **26**, 26–36 (1993).
- [9] P. Lumley, A. Walmsley, and W. Laird, "Streaming patterns produced around endosonic files.", *International Endodontic Journal* **24**, 290–297 (1991).
- [10] P. Lumley, A. Walmsley, R. Walton, and J. Rippin, "Cleaning of oval canals using ultrasonic or sonic instrumentation", *Journal of Endodontics* **19**, 453–457 (1993).
- [11] S.-J. Lee, M.-K. Wu, and P. Wesselink, "The effectiveness of syringe irrigation and ultrasonics to remove debris from simulated irregularities within prepared root canal walls", *International Endodontic Journal* **37**, 672–678 (2004).
- [12] M. Wu, A. R'Oris, D. Barkis, and P. Wesselink, "Prevalence and extent of long oval canals in the apical third.", *Oral Surgery, Oral Medicine, Oral Pathology, Oral Radiology, and Endodontics* **89**, 739–743 (2000).



- [13] L. van der Sluis, M. Wu, and P. Wesselink, "The evaluation of removal of calcium hydroxide paste from an artificial standardized groove in the apical root canal using different irrigation methodologies", *International Endodontic Journal* **40**, 52–57 (2007).
- [14] L.-M. Jiang, B. Verhaagen, M. Versluis, and L. van der Sluis, "Evaluation of a sonic device designed to activate irrigant in the root canal", *Journal of Endodontics* **36**, 143–146 (2010), *See also chapter 9 of this thesis.*
- [15] S.-J. Lee, M.-K. Wu, and P. Wesselink, "The efficacy of ultrasonic irrigation to remove artificially placed dentine debris from different-sized simulated plastic root canals", *International Endodontic Journal* **37**, 607–612 (2004).
- [16] N. Riley, "Unsteady laminar boundary layers", *SIAM Review* **17** (1975).
- [17] J. Stuart, "Double boundary layers in oscillatory viscous flow", *J. Fluid Mech.* **24**, 673–687 (1966).
- [18] A. F. Bertelsen, "Experimental investigation of high-reynolds number steady streaming generated by oscillating cylinders", *Journal of Fluid Mechanics* **64**, 589–597 (1974).
- [19] P. Duck and F. Smith, "Steady streaming induced between oscillating cylinders", *J Fluid Mech* **91**, 93–110 (1979).
- [20] S. Kim and A. Troesch, "Streaming flows generated by high-frequency small-amplitude oscillations of arbitrarily shaped cylinders", *Physics of Fluids A* **1**, 975–985 (1989).
- [21] M. Tatsuno, "Circulatory streaming in the vicinity of an oscillating square cylinder", *Journal of the Physical Society of Japan* **36**, 1185–1191 (1974).
- [22] F. Tay, L.-S. Gu, G. Schoeffel, C. Wimmer, L. Susin, K. Zhang, S. Arun, J. Kim, S. Looney, and D. Pashley, "Effect of vapor lock on root canal debridement by using a side-vented needle for positive-pressure irrigant delivery", *Journal of Endodontics* **36**, 745–750 (2010).

## Appendices

### 7.A Supplementary material

*(Online at [http://stilton.tnw.utwente.nl/rootcanalcleaning/Gallery\\_of\\_Irrigant\\_Motion](http://stilton.tnw.utwente.nl/rootcanalcleaning/Gallery_of_Irrigant_Motion))*

Movie 1. High-speed visualization of the tip of a file oscillating inside a root canal confinement, perpendicular to the groove. The black dots are tracer particles. Recording speed is 125 Kfps.

Movie 2. High-speed visualization of the tip of a file oscillating inside a root canal confinement, now parallel to the groove. The black dots are tracer particles. Recording speed is 125 Kfps.

# 8

## The influence of the ultrasonic intensity on the cleaning efficacy of passive ultrasonic irrigation \* †

**Abstract:** In this chapter we evaluate the effect of the ultrasonic intensity on PUI to remove dentin debris from artificial depressions in one root canal wall, and whether there is any lateral effect beyond the ultrasonic tip. Each of 15 *in vitro* root canal models with four standard depressions in the apical part of one canal wall were filled with dentin debris and received PUI repeatedly, with different ultrasound intensities. The removal of dentin debris in the depressions was categorized as clean or not clean. The oscillation amplitude of the ultrasonic file at each intensity was recorded *in vitro* using time-resolved high-speed imaging. The results show that the highest intensity exhibited significantly better cleaning than all the other intensities; no significant difference was found between the four levels of the depressions within any of the four groups. High-speed imaging showed that the amplitude of the oscillating file increased as the intensity went up, which leads to a higher velocity of the irrigant around the file.

---

\*Published as: L-M. Jiang, B. Verhaagen, M. Versluis, J. Langedijk, P.R. Wesselink and L.W.M. van der Sluis. "The Influence of the Ultrasonic Intensity on the Cleaning Efficacy of Passive Ultrasonic Irrigation", *Journal of Endodontics* 37(5), pp. 688-692 (2011)

†The high-speed imaging and its analysis in this chapter is part of the present thesis. The dentin debris removal experiments are due to Lei-Meng Jiang.

## 8.1 Introduction

The improvement of currently available irrigation protocols to disinfect the inaccessible regions of the root canal space and the uninstrumented canal surfaces is important [1] because of insufficient debridement by instrumentation alone [2, 3]. An ultrasonically oscillating file transmits energy, causing acoustic microstreaming, which results in mixing of the irrigant, enabling it to reach those inaccessible regions and enhancing shear stress on the root canal surfaces at a distance from the file [4–7].

The apical third of the root canal system is particularly difficult to clean because of the typically challenging complexity of the root canal morphology [8, 9], making irrigant delivery and activation less effective [10]. Lee *et al.* [11] studied the efficiency of ultrasonic irrigation using root canal models with grooves and depressions in the apical portion of the root canal wall to simulate root canal irregularities. These studies indicated that the depressions in the root canal wall were more difficult to clean than the grooves [11, 12] and also revealed a lateral effect of the acoustic streaming around the file. Because an ultrasonic file does not always extend to the full length of the root canal and the cleaning of the apical area close to the apex could be critical [13], information about the cleaning in front of the tip could be valuable.

The intensity of ultrasonic activation, adjusted by the power setting on the ultrasonic device, influences the energy transmission from the ultrasonically oscillating file to the irrigant. Previous research showed that an increasing intensity did not always result in a linear increase of the displacement amplitude of the oscillating file [14, 15]. Because those observations investigated the oscillation of the file in free air, a direct relationship with acoustic microstreaming around and in front of the file could not be established. A full understanding of the effect of intensity on the cleaning efficacy of passive ultrasonic irrigation (PUI) through microstreaming is still lacking.

The aims of this study were (1) to measure the displacement amplitude of the oscillating file under different ultrasonic intensities by using high-speed imaging, (2) to evaluate the effect of ultrasonic intensity on the cleaning efficacy of PUI, and (3) to investigate the lateral effect beyond the file tip.

## 8.2 Materials and Methods

### 8.2.1 Dentin debris removal model

Straight roots from 15 extracted human maxillary canines were decoronated to obtain uniform root sections of 15 mm following the protocol described previously [16, 17]. Briefly, the roots were embedded in resin and bisected longitudinally. The surfaces of both halves were then ground to leave only a little of the original root canal lumen. Four depressions were drilled in the resin part, and the two halves were reassembled

by four self-tapping bolts through the depressions. All the models were checked to see if there was any leakage of liquid or gas apically or laterally before experiments. If there was any, rubber dam caulk would be applied to ensure that the root canal modeled a closed system.

Standardized root canals were established by K-flexofiles #15/.02 (Dentsply Maillefer, Ballaigues, Switzerland) and GT (Dentsply, Maillefer) nickel-titanium rotary instruments to a working length (WL) of 15 mm, an ISO size of 30, and a taper of 0.06. The final apical enlargement was performed with the Mtwo (VDW, Munich, Germany) nickeltitanium rotary instrument #35/.04. During instrumentation, the canals were rinsed with 1 mL 2% NaOCl after each file delivered by a 10-mL syringe (Terumo, Leuven, Belgium) and a 30-G needle (Navitip; Ultradent, South Jordan, UT).

With the help of a microscope and a round bur (H71.104.003; Komet, Lemgo, Germany) attached to a drilling machine, four standard depressions ( $\phi = 0.3$  mm) located at 0.5, 2, 4, and 6 mm from the WL were drilled in the wall of one half of each root canal (Fig. 8.1). Each depression was filled with dentin debris, which was mixed with 2% NaOCl for 5 minutes to simulate a situation in which dentin debris accumulates in uninstrumented canal extensions [11]. This model was introduced to standardize the root canal space and the amount of dentin debris present in the root canal before the irrigation procedure to increase the reliability of the dentin debris removal evaluation. The methodology is sensitive, and the data are reproducible [18]. The 15 models were used repeatedly in the four experimental groups, which are shown in Table 8.1.

### 8.2.2 Irrigation procedure

Specimens in all the experimental groups were rinsed with 2 mL irrigant (2% NaOCl) using 10-mL syringes with 30-G needles (Navitip) placed 1 mm from the WL, and the flow rate was approximately 5 mL/min. Then, PUI was performed with a stainless steel #25/.00 file (Irrisafe; Acteon, Merignac, France) driven by an ultrasonic device (Suprasson PMax; Satelec Acteon, Merignac, France) for 10 seconds with the in-plane oscillation direction toward the depressions. The device has four ultrasound intensity ranges indicated by the following colors: green, yellow, blue, and red. These colors correspond to an ultrasound intensity range, from the weakest to the strongest; each is adjustable with 10 levels. The following intensity settings were used in this study: blue 4 (group 1), yellow 4 (group 2), and green 4 (group 3). Every attempt was made to keep the file centered in the canal to minimize contact with the canal walls because any contact with the canal wall could dampen the oscillatory motion of the file. Group 4 acted as the control group; in this group, the ultrasonic file was inserted but not activated. All the experimental specimens received 2 mL irrigant, which was delivered with a syringe as the final flush.

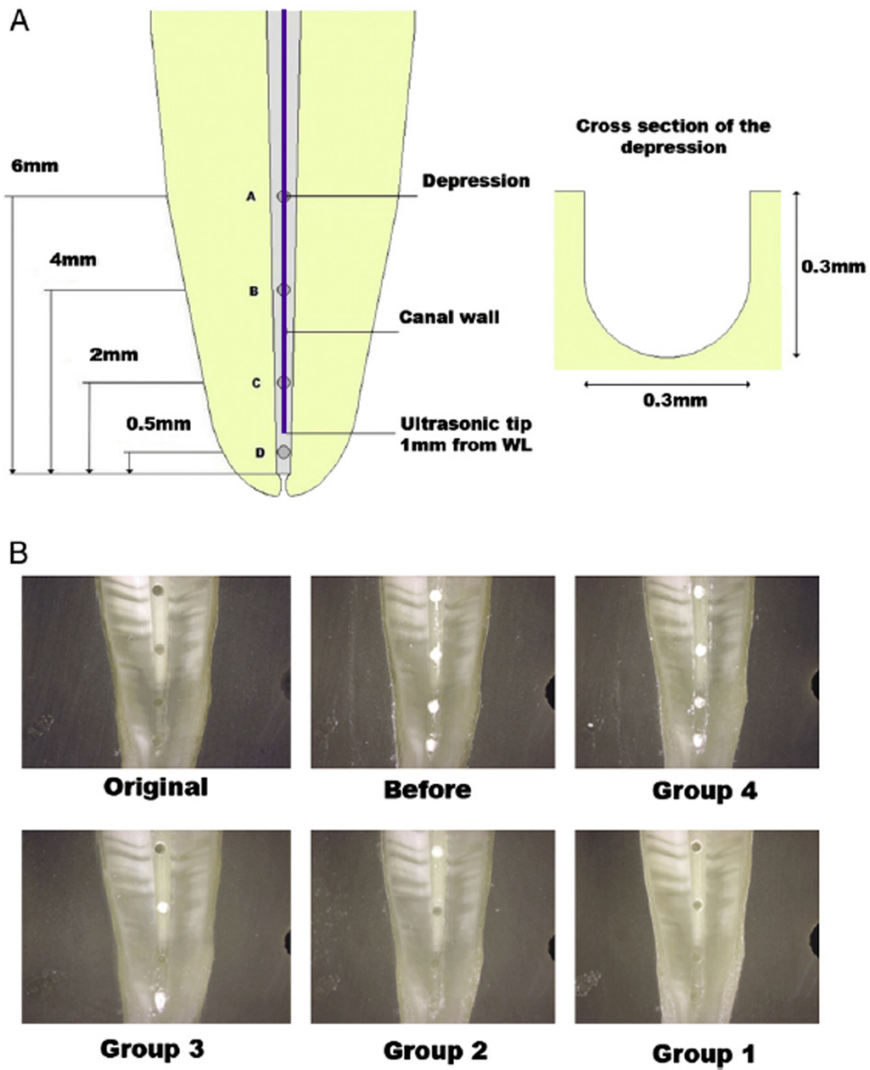


**Figure 8.1:** Schematic drawings of the root canal wall with depressions (A) and their typical images (B) before and after different irrigation procedures (group 4: needle irrigation, group 3: PUI green 4, group 2: PUI yellow 4, and group 1: PUI blue 4). The ultrasonic tip was positioned 1 mm from the WL during irrigation procedures.

### 8.2.3 Image evaluation and statistical analyses

Before and after each irrigation procedure, the root halves were separated, and the depressions were viewed through a stereomicroscope (Stemi SV6; Carl Zeiss, Göttingen, Germany) using a cold light source (KL 2500 LCD, Carl Zeiss). Pictures were taken with a digital camera (Axio Cam, Carl Zeiss). The sequence of all the pictures was randomized, and two calibrated examiners were blind to the group assignment.

The debris removal from each depression after irrigation was scored independently by two calibrated dentists. The samples were graded as “clean” if the depression was without any debris left or “not clean” if the depression was not completely clean. The percentage of interagreement should be more than 95%; if this percentage was lower than 95%, a consensus had to be reached.

The differences in debris removal between the depressions within each group and between the groups were analyzed using chi-square analysis. The level of significance was set at  $\alpha = 0.05$ .

### 8.2.4 High-speed imaging experiments

High-speed imaging was used to record the oscillation amplitude of the ultrasonic file at each intensity, both inside a large water-filled tank and inside a transparent, silicon model of a root canal with an apical size of 30 and a taper of 6%. The silicon model was made by casting poly-dimethyl-siloxane (Sylgard 184, Silicone Elastomer Kit; Dow-Corning, Coventry, UK) around a D-size hand spreader (Dentsply). Recordings were made with a high-speed camera (HPV-1; Shimadzu Corp, Kyoto, Japan) at a frame rate of 250,000 frames per second. A microscope with 20 $\times$  magnification (BX-FM; Olympus, Tokyo, Japan) was used for magnification. The Irrisafe #25/.00 file was fitted in front of the microscope and illuminated in bright-field mode by a continuous-wave light source (ILP-1, Olympus). By tracking the tip of the file in each of the recordings, the displacement amplitude was determined.

## 8.3 Results

At each depression level, dentin debris removal was significantly different between the experimental groups. The number of completely clean samples in each group and the P values when compared between groups are shown in Table 8.1. The value of kappa is statistically significantly different from 0, and its value of 0.828 suggests that the evaluators' scorings are mostly similar, with some exceptions.

If the number of completely clean depressions at all four levels were combined, all the ultrasonically activated groups removed more dentin debris than the nonactivated group (group 4) ( $P < .05$ ); group 1, with the highest intensity, exhibited significantly better cleaning efficacy than all the other groups. No significant difference was

Group ( <i>N</i> = 15)	Intensity	No. of clean samples	<i>P</i> value		
			Yellow 4	Green 4	Syringe
0.5 mm from the WL					
1	Blue 4	12	.028	.001	<.001
2	Yellow 4	6	–	.240	.034
3	Green 4	3	–	–	.291
4	Syringe (control)	1	–	–	–
2 mm from WL					
1	Blue 4	14	.034	.001	<.001
2	Yellow 4	9	–	.150	.028
3	Green 4	5	–	–	.417
4	Syringe (control)	3	–	–	–
4 mm from WL					
1	Blue 4	12	.128	.028	<.001
2	Yellow 4	8	–	.472	.006
3	Green 4	6	–	–	.034
4	Syringe (control)	1	–	–	–
6 mm from WL					
1	Blue 4	13	.001	.009	<.001
2	Yellow 4	4	–	.446	.035
3	Green 4	6	–	–	.007
4	Syringe (control)	0	–	–	–

Intensities were decreased from group 1 to group 3 (blue 4 > yellow 4 > green 4); – suggests that the data are not applicable or are duplicates.

**Table 8.1:** *The number of completely clean depressions after the irrigation procedure in each experimental group and the P value between groups*

seen between the other two groups with lower intensities. There was no significant difference between the four levels of the depressions within any of the four groups.

From the high-speed recordings, the displacement amplitude at each intensity was determined (Fig. 8.2). Increasing the intensity resulted in a linear increase in oscillation amplitude although there is some overlap between color codes. The confinement of the root canal caused a reduction in the oscillation amplitude of approximately 40%.

In the large water tank, cavitation was observed on the file tip for the intensities above blue 5 (Movie 1). Inside the confinement of the root canal, this threshold was green 5 (Movie 2). The bubble grows in the wake of the file when it moves from one maximum of displacement to the other and collapses when the file reaches the other maximum displacement.

## 8.4 Discussion

The model with depressions on the root canal wall used in this study was a modification of a previous one [11]. The modifications and advantages of the current model are three-fold. First, because the natural root canal varies considerably, the removal of the original root canal space allowed for the establishment of standardized root canals. Second, it is easy to assemble or disassemble the model, facilitating the root canal treatment procedure in vitro within the enclosed system and the evaluation of the interested area before and after the irrigation. Finally, the cleaning of the extra depression located at 0.5 mm from the WL could give an indication of the cleaning

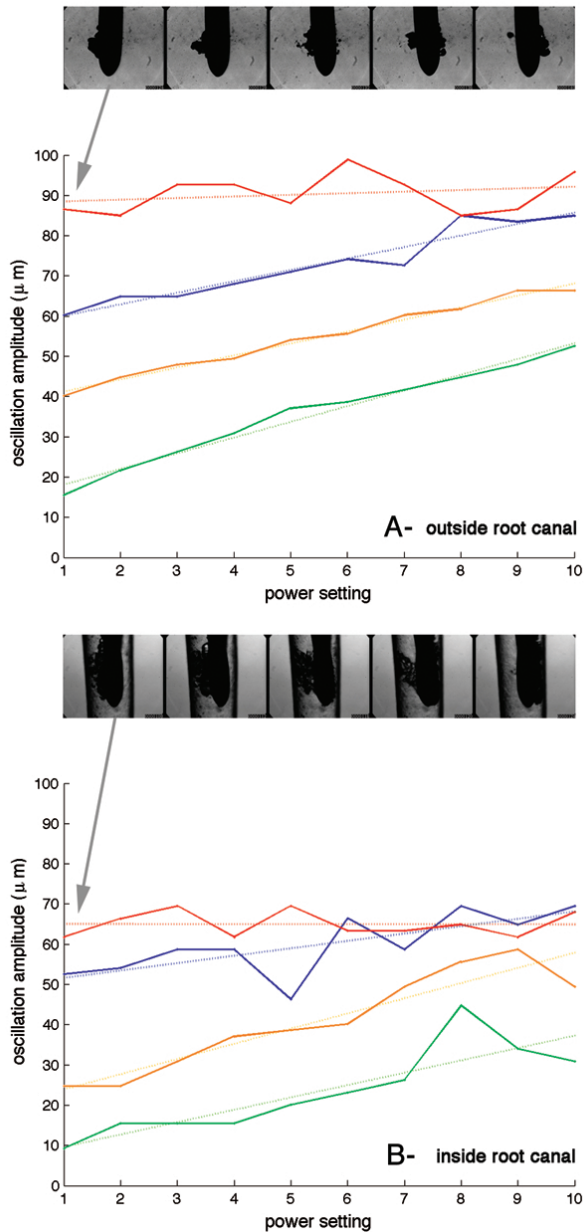


**Figure 8.2:** Oscillation amplitude of the ultrasonically oscillating file at various amplitudes; the colors of the lines match the colored intensities on the ultrasonic device, with 10 steps within each color. Five consecutive frames (4 microseconds between frames) are displayed to show the cavitation in the wake of the file during one half of an oscillation at intensity red 5. (A) The file was fitted inside a large water tank; (B) the file was fitted inside a size 30, taper 6% root canal model.



efficacy in front of the ultrasonically oscillating file tip.

It has been suggested that the velocity of the acoustic streaming occurring around oscillating files is directly influenced by factors such as the intensity of the generator and location on the file (7). Our study clearly showed that the cleaning efficacy was enhanced when the ultrasonic intensity rose, especially at the highest intensity used here, blue 4. In preliminary tests, we used root canal models with grooves under different intensity as well. This setup also showed that a higher intensity produced a better cleaning efficacy (data not shown). A higher intensity gives a higher amplitude of oscillation of the file (Fig. 2), which, in turn, results in higher velocities of the tip according to the following theoretic prediction given by Ahmad *et al.* [7]:

$$v = \frac{\omega \varepsilon_0^2}{a} \quad (8.1)$$

where  $v$  is the flow velocity (in meters per second),  $\omega$  is  $2\pi$  times the driving frequency (in Hertz),  $\varepsilon_0$  is the oscillation amplitude (in meters), and  $a$  the radius of the tip (in meters).

For intensities above the threshold where cavitation was observed, the deviation of the amplitude from the linear fit increases. This can partly be attributed to the fact that the tip of the file could not be observed any more because of cavitation bubbles. However, it is also possible that the cavitation bubbles affected the oscillation of the file because of the forces involved in bubble growth and collapse.

In our previous studies [16, 17] on evaluating the efficacy of PUI, a similar experimental model with a groove located at 2 to 6 mm from the WL was used and the ultrasonic tip was placed 1 mm from the WL, indicating that the file tip was apical to the groove (filled with dentin debris). Therefore, those studies did not provide any information about the cleaning efficacy in front of the ultrasonically oscillating tip. From the results of this study, it can be concluded that PUI has an effect in front of the oscillating file that is similar to the more coronally located areas in the apical root canal. Burluson *et al.* [19] reported that ultrasonically activated irrigation improved the canal and isthmus cleanliness in the apical region. The ultrasonically activated needle was placed coronally to the region they investigated, indicating an effect in front of the needle, which was confirmed by our findings. However, their ultrasonically activated needle was a needle through which the irrigant flowed into the root canal activated by ultrasound at the same time. Therefore, the flow pattern of the irrigant is different from that in our study, but the effect in front of the needle may be similar.

Ahmad *et al.* [7] suggested that the cleaning efficiency would be different alongside the ultrasonically oscillating file because the acoustic streaming would be more intense at the apical section of the file. Although the result of the current study showed no differences between the four levels of the depressions within any of the

experimental groups, it is not contradictory to Ahmads findings because the four depressions observed were located only in the apical portion.

One may argue if the effect in front of the ultrasonically oscillating file will cause extrusion of the irrigant. This was not the aim of this study and needs future study by using suitable models, because the root canal models in the present study have a closed, solid foramen. However, because the oscillation direction of the file is lateral and not longitudinal, extrusion of irrigant through the apical foramen is not expected.

## References

- [1] J. Gomes-Filho, K. Aurélio, M. Costa, and P. Bernabé, "Comparison of the biocompatibility of different root canal irrigants", *Journal of Applied Oral Science* **16**, 137–144 (2008).
- [2] O. Peters, K. Schönenberger, and A. Laib, "Effects of four ni-ti preparation techniques on root canal geometry assessed by micro computed tomography", *International Endodontic Journal* **34**, 221–230 (2001).
- [3] M.-K. Wu, L. Van Der Sluis, and P. Wesselink, "The capability of two hand instrumentation techniques to remove the inner layer of dentine in oval canals", *International Endodontic Journal* **36**, 218–224 (2003).
- [4] A. Al-Jadaa, F. Paqué, T. Attin, and M. Zehnder, "Necrotic pulp tissue dissolution by passive ultrasonic irrigation in simulated accessory canals: Impact of canal location and angulation", *International Endodontic Journal* **42**, 59–65 (2009).
- [5] A. Al-Jadaa, F. Paqué, T. Attin, and M. Zehnder, "Acoustic hypochlorite activation in simulated curved canals", *Journal of Endodontics* **35**, 1408–1411 (2009).
- [6] C. De Gregorio, R. Estevez, R. Cisneros, C. Heilborn, and N. Cohenca, "Effect of edta, sonic, and ultrasonic activation on the penetration of sodium hypochlorite into simulated lateral canals: an in vitro study", *Journal of Endodontics* **35**, 891–895 (2009).
- [7] M. Ahmad, T. Pitt Ford, and L. Crum, "Ultrasonic debridement of root canals: An insight into the mechanisms involved", *Journal of Endodontics* **13**, 93–101 (1987).
- [8] F. Pineda and Y. Kuttler, "Mesiodistal and buccolingual roentgenographic investigation of 7,275 root canals", *Oral Surgery, Oral Medicine, Oral Pathology* **33**, 101–110 (1972).
- [9] F. Vertucci, "Root canal anatomy of the human permanent teeth", *Oral Surgery Oral Medicine and Oral Pathology* **58**, 589–599 (1984).
- [10] F. Foschi, C. Nucci, L. Montebugnoli, S. Marchionni, L. Breschi, V. Malagnino, and C. Prati, "Sem evaluation of canal wall dentine following use of mtwo and protaper niti rotary instruments", *International Endodontic Journal* **37**, 832–839 (2004).
- [11] S.-J. Lee, M.-K. Wu, and P. Wesselink, "The effectiveness of syringe irrigation and ultrasonics to remove debris from simulated irregularities within prepared root canal walls", *International Endodontic Journal* **37**, 672–678 (2004).

- [12] S.-J. Lee, M.-K. Wu, and P. Wesselink, “The efficacy of ultrasonic irrigation to remove artificially placed dentine debris from different-sized simulated plastic root canals”, *International Endodontic Journal* **37**, 607–612 (2004).
- [13] P. Nair, S. Henry, V. Cano, and J. Vera, “Microbial status of apical root canal system of human mandibular first molars with primary apical periodontitis after ”one-visit” endodontic treatment”, *Oral Surgery, Oral Medicine, Oral Pathology, Oral Radiology and Endodontology* **99**, 231–252 (2005).
- [14] A. Walmsley and A. Williams, “Effects of constraint on the oscillatory pattern of endosonic files”, *Journal of Endodontics* **15**, 189–194 (1989).
- [15] S. Lea, A. Walmsley, P. Lumley, and G. Landini, “A new insight into the oscillation characteristics of endosonic files used dentistry”, *Physics in Medicine and Biology* **49**, 2095–2102 (2004).
- [16] L.-M. Jiang, B. Verhaagen, M. Versluis, and L. Van Der Sluis, “Influence of the oscillation direction of an ultrasonic file on the cleaning efficacy of passive ultrasonic irrigation”, *Journal of Endodontics* **36**, 1372–1376 (2010), *See also chapter 7 of this thesis*.
- [17] L.-M. Jiang, B. Verhaagen, M. Versluis, and L. van der Sluis, “Evaluation of a sonic device designed to activate irrigant in the root canal”, *Journal of Endodontics* **36**, 143–146 (2010), *See also chapter 9 of this thesis*.
- [18] L. van der Sluis, M.-K. Wu, and P. Wesselink, “The evaluation of removal of calcium hydroxide paste from an artificial standardized groove in the apical root canal using different irrigation methodologies”, *International Endodontic Journal* **40**, 52–57 (2007).
- [19] A. Burleson, J. Nusstein, A. Reader, and M. Beck, “The in vivo evaluation of hand/rotary/ultrasound instrumentation in necrotic, human mandibular molars”, *Journal of Endodontics* **33**, 782–787 (2007).

## Appendices

### 8.A Supplementary material

(Online at [http://stilton.tnw.utwente.nl/rootcanalcleaning/Gallery\\_of\\_Irrigant\\_Motion](http://stilton.tnw.utwente.nl/rootcanalcleaning/Gallery_of_Irrigant_Motion))

Movie 1. High-speed visualization of the tip of a file oscillating unconfined; cavitation can be observed on the tip of the file. Recording speed is 250 Kfps.

Movie 2. High-speed visualization of the tip of a file oscillating in the confinement of a silicon root canal model; cavitation can be observed between the tip of the file and the wall of the root canal. Recording speed is 250 Kfps.

# 9

## Evaluation of a sonic device designed to activate irrigant in the root canal \* †

**Abstract:** This chapter is concerned with the difference in the removal of dentin debris from a groove in the root canal by sonic or ultrasonic activation of the irrigant. The physical mechanisms of sonic activation were investigated using high-speed visualization of the oscillations of the sonic tip, both inside and outside the confinement of the root canal. Without irrigant activation, the grooves were still full of dentin debris. From the ultrasonic activated group, 89% of the canals were completely free of dentin debris, whereas from the sonic group, only 5.5% – 6.7% were. The oscillation amplitude of the sonically driven tips was observed to be  $1.2 \pm 0.1$  mm, resulting in much wall contact and no cavitation of the irrigant, thereby limiting its cleaning efficacy compared to ultrasonic activation.

---

\*Published as: L-M. Jiang, B. Verhaagen, M. Versluis and L.W.M. van der Sluis, “Evaluation of a Sonic Device Designed to Activate Irrigant in the Root Canal”, *Journal of Endodontics* **36**(1), pp. 143-146 (2010)

†The high-speed imaging and its analysis in this chapter is part of the present thesis. The dentin debris removal experiments are due to Lei-Meng Jiang.

## 9.1 Introduction

Irrigation of the root canal space is a fundamental aspect of root canal treatment. Techniques for acoustic and hydrodynamic activation of the irrigant have been developed [1–3], because needle irrigation is not effective in the apical part of the root canal [4, 5].

It has been shown that acoustic streaming and cavitation contribute to the cleaning efficiency of root canal irrigation [2, 3, 6]. Acoustic streaming can be defined as a rapid movement of fluid in a circular or vortex-like motion around a vibrating file [7]. Cavitation can be defined as the creation of vapor bubbles or the expansion, contraction, and/or distortion of preexisting bubbles (so-called cavitation nuclei) in a liquid; the process is coupled to acoustic energy [8]. Studies have shown that passive sonic activation of irrigant is inferior to its counterpart in ultrasonic [9, 10]. However, the details concerning those mechanisms have not been clarified.

The EndoActivator system (Advanced Endodontics, Santa Barbara, CA), a sonic device, has recently been developed for root canal irrigation. Special polymer tips can be driven sonically at 3 different frequencies to activate the irrigant. No data are currently available to support its use.

The aims of this study were (1) to determine the removal of dentin debris from the root canal by sonic or ultrasonic activation of the irrigant and (2) to evaluate the physical mechanisms of sonic activation by visualizing the oscillation amplitude of EndoActivator tips.

## 9.2 Materials and Methods

### 9.2.1 High-speed Imaging Experiments

An optical set-up was constructed to visualize the effect of sonic activation in a glass model of the root canal containing water. The canal was 10 mm in length, with an apical diameter of 0.30 mm and a taper of approximately 0.06. Imaging was performed by using a high-speed camera (Shimadzu Corp, Kyoto, Japan) at a frame rate of 4000 frames per second. From these recordings the oscillation amplitude of the tip was measured by using a calibrated reference grid (Edmund Optics, Barrington, NJ).

A microscope with 1.25–20 $\times$  magnification was used (BX-FM; Olympus, Tokyo, Japan) for magnification. The root canal was illuminated in bright-field by a continuous wave light source (ILP-1; Olympus).

### 9.2.2 Dentin Debris Removal Model

Straight roots from 18 extracted human maxillary canines were decoronated to obtain uniform root sections of 15 mm. The roots were embedded in self-curing resin

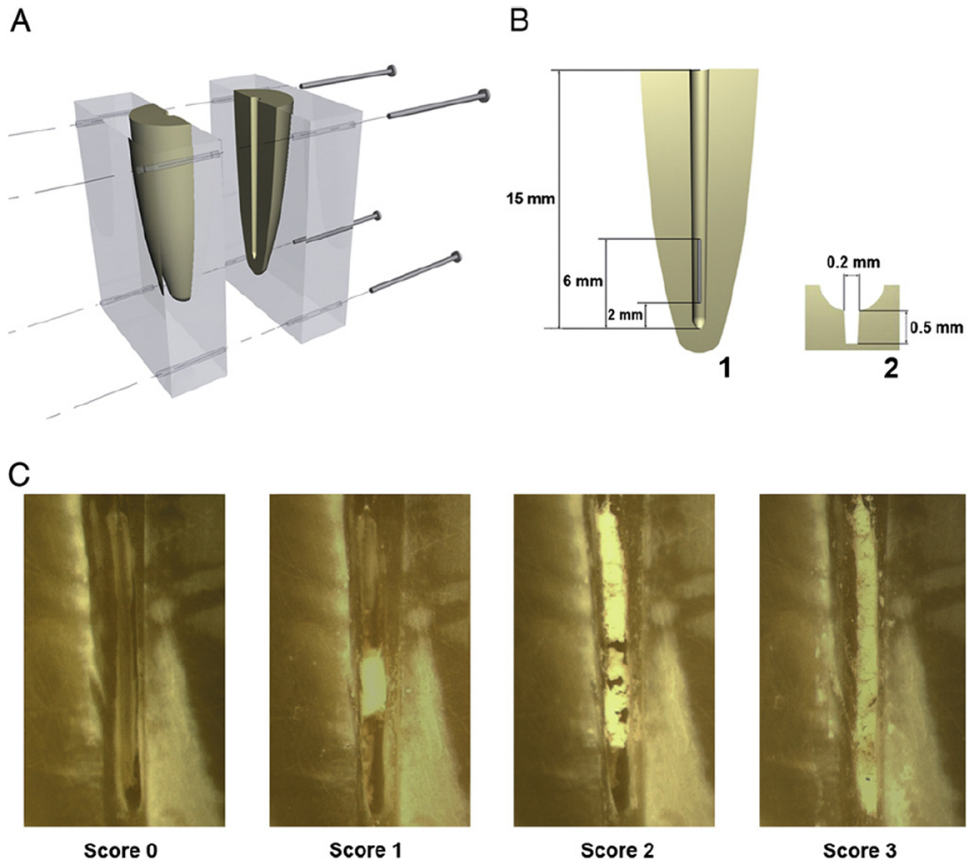


**Figure 9.1:** (A) Schematic representations of the standardized root canal model, its groove (B-1) and cross section (B-2). (C) Examples of the different score scales.

(GC Ostron 100; GC Europe, Leuven, Belgium) and then bisected longitudinally through the canal in mesiodistal direction with a saw microtome (Leica Microsystems SP1600, Wetzlar, Germany). The surfaces of both halves were ground successively with 240-, P400-, and 600-grit sandpaper, resulting in smooth surfaces on which only little of the original root canal lumen was left. Four holes were drilled in the resin part, and the two halves could be reassembled by four self-tapping bolts through the holes (Fig. 9.1A).

New root canals were prepared by K-files #15/.02 (Dentsply Maillefer, Ballaigues, Switzerland) and HERO 642 (MicroMega, Besancon, France) nickel-titanium rotary instruments to a working length (WL) of 15 mm, ISO size 30, and taper 0.06, resulting in standardized root canals. During preparation, the canals were rinsed with

1 mL of 2% NaOCl after each file and delivered by a 10-mL syringe (Terumo, Leuven, Belgium) and a 30-gauge needle (Navitip; Ultradent, South Jordan, UT).

A standard groove of 4 mm in length, 0.5 mm deep, and 0.2 mm wide, situated at 26 mm from WL [11] (Fig. 9.1B-1, B-2), was cut in the wall of one half of each root canal with a customized ultrasonic tip. A periodontal probe with an adapted 0.2-mm-wide tip was used to verify the dimension of each groove during and after preparation. The dimension of the groove is comparable to an apical oval root canal [12]. Each groove was filled with dentin debris, which was mixed with 2% NaOCl for 5 minutes, to simulate a situation in which dentin debris accumulates in uninstrumented canal extensions [11]. This model was introduced to standardize the root canal space and the amount of dentin debris present in the root canal before the irrigation procedure, to increase the reliability of the dentin debris removal evaluation. The methodology is sensitive, and the data are reproducible [13]. A pilot study has shown that a single model could be reused up to at least 8 times without any visible defect on the surface of the canal wall. Therefore, the 18 models were used repeatedly in the 6 experimental groups, which are the ultrasonic activated group, sonic activated groups by different frequencies or tips or irrigants, and control group (Table 9.1).

### 9.2.3 Irrigation Procedure

Specimens in all the experimental groups were rinsed with 2 mL irrigant (2%NaOCl or water) by using 10-mL syringes with 30-gauge needles placed 1 mm from WL. Then the residue of irrigant was passively activated for 20 seconds sonically or ultrasonically. In group 6, the sonic tip was inserted but not activated. Passive activation meant that every attempt was made to keep the file centered in the canal to minimize contact with the canal walls. This sequence was repeated twice, resulting in a total irrigation volume of 6 mL and a total irrigation time of 1 minute.

The ultrasonic activation was performed with a stainless steel #20/.00 file (Irrisafe; Satelec Acteon, Merignac, France) energized by a piezoelectronic unit (Suprason PMax; Satelec Acteon) at power setting “blue 4”. The sonic activation was performed with the EndoActivator system.

### 9.2.4 Image Evaluation and Statistical Analyses

Before and after each irrigation procedure, the root halves were separated, and the grooves were viewed through a stereomicroscope (Stemi SV6; Carl Zeiss, Göttingen, Germany) by using a cold light source (KL 2500 LCD; Carl Zeiss). Controls verified that no debris had fallen out of the groove during the assembly or disassembly process. Pictures were taken with a digital camera (Axio Cam; Carl Zeiss) and saved as ZVI files on a computer.

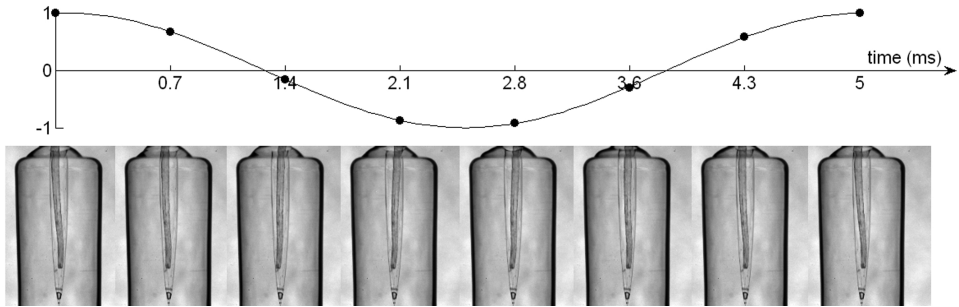


**Figure 9.2:** Oscillation of the file inside the root canal during 1 oscillation at mode 3 (190 Hz), recorded with a high-speed camera at 4000 frames per second; dots on the graph indicate at which time during the oscillation the frames were recorded.

The debris left in the groove after irrigation was scored independently and blindly by 3 calibrated dentists with the following score system: 0, the groove is empty; 1, less than half of the groove is filled with debris; 2, more than half of the groove is filled with debris; 3, the complete groove is filled with debris [11] (Fig. 9.1C). The percentage of inter-agreement should be more than 95%. If this percentage was lower than 95%, a consensus had to be reached.

The differences in debris scores between the groups were analyzed by means of the Kruskal-Wallis test and the Mann-Whitney test. The level of significance was set at  $\alpha = 0.05$ .

### 9.3 Results

The oscillation amplitude of the sonic tips in free air and in water was, respectively,  $1.1 \pm 0.1$  mm and  $0.6 \pm 0.1$  mm at the attachment point and  $3.1 \pm 0.1$  mm and  $1.2 \pm 0.1$  mm at the free end. The sonic tip showed only one node (at the attachment point) and one anti-node (at the free end) during oscillation, confirming an earlier study [14]. The actual frequencies of the sonic device turned out to be different from the frequencies listed in the sales brochure. Mode 1 was  $160 \pm 5$  Hz instead of 33 Hz (2000 cycles per minute [CPM]), mode 2 was  $175 \pm 5$  Hz instead of 100 Hz (6000 CPM), and mode 3 was  $190 \pm 5$  Hz instead of 166 Hz (10,000 CPM). The high-speed imaging experiments showed a lot of wall contact of the sonic tips during activation (Fig. 9.2), and no cavitation was observed (Movie 1).

The three investigators differed in scoring 6 of the 108 specimens; agreement was reached after discussion. After irrigation, the number and the percentage of samples at each score rank are presented in Table 9.1. There was a statistically significant difference between the experimental groups ( $P < .0001$ ). When the irrigant



Group (n = 18)	Activation system	Frequency (Hz)	Size/taper	Irrigant	Score			
					0	1	2	3
1	Ultrasonic	30,000	#20/.00	NaOCl	16 (90%)	1 (5%)	1 (5%)	0 (0%)
2	Sonic	190	#15/.02	NaOCl	3 (17%)	4 (22%)	9 (50%)	2 (11%)
3	Sonic	190	#25/.04	NaOCl	3 (17%)	6 (33%)	0 (0%)	9 (50%)
4	Sonic	160	#15/.02	NaOCl	1 (5%)	2 (11%)	12 (67%)	3 (17%)
5	Sonic	190	#15/.02	Water	0 (0%)	5 (28%)	12 (67%)	1 (5%)
6 (control)	No activation	0	#15/.02	NaOCl	0 (0%)	0 (0%)	0 (0%)	18 (100%)

Score 0, the groove is empty; score 1, less than half of the groove is filled with debris; score 2, more than half of the groove is filled with debris; score 3, the complete groove is filled with debris.

**Table 9.1:** Experimental groups and number of specimens ( $N=18$ ) at each score rank after irrigation procedure.

was activated, significantly more dentin debris was removed than control group; ultrasonic activation was significantly more efficient than sonic activation ( $P = .0001$ ). There was no significant difference between the sonic activation groups. From the ultrasonic activated group, 89% of the canals were completely free of dentin debris, whereas from the sonic group, 5.5% – 6.7% were.

## 9.4 Discussion

The results indicate that activation of the irrigant enhances the removal of dentin debris from the apical root canal. Because the ultrasonic file or sonic tips could not physically disturb the dentin debris in the groove, it can be concluded that the activated irrigant removed the dentin debris from the groove.

The fact that ultrasonic activation removed significantly more dentin debris than the sonic activation confirms the study of Sabins *et al.* [10]. A possible explanation is that the driving frequency of ultrasound (30 kHz) is higher than that of the sonic device (160-190 Hz). In principle, a higher frequency results in a higher flow velocity [15]. In addition, the flow velocity also increases, with increase in the oscillation amplitude of the tip for a certain frequency [15]. However, the oscillation amplitude of the sonically activated tip in water is approximately 1 mm while the diameter of the apical root canal is smaller than 0.5 mm, which implies extensive wall contact between the tip and the root canal wall. This inhibits free oscillation of the sonic tip, reducing the efficient streaming of the irrigant [15] and consequently the activation of the irrigant. This is confirmed both by the outcome of dentin debris removal and by the visualization experiment in which wall contact was observed (Fig. 9.2).

The difference between the lowest (160 Hz) and the highest (190 Hz) oscillation frequency of EndoActivator as we have tested is small, implying only small differences in streaming between frequency settings. That explained why there was no significant difference between the two frequency settings of the sonic activation.

It was also observed that no cavitation seemed to take place either on the sonic tip itself or on the wall of the glass model of the root canal. This can be related to the

velocity of the sonic tip, which was below the threshold needed for cavitation. Such a cavitation threshold can be determined by estimating the pressure required. If the pressure falls below the vapor pressure by a magnitude of the tensile strength, then rupture of the fluid can occur (cavitation). The tensile strength of pure water is very high, and therefore cavitation is often unobtainable. In many practical situations, however, there are microscopic voids containing gas on the interface between a solid surface (contaminant particles, cracks in the container) and the fluid. These nucleation sites have a much lower tensile strength and therefore make cavitation possible at much lower pressures. To get cavitation, the pressure decrease  $\Delta P$  must exceed the ambient pressure (1 atm or  $10^5$  Pa) plus the vapor pressure of the fluid (2000 Pa) [16]. In first approximation the velocity  $u$  leading to an onset of cavitation can be obtained from the Bernoulli equation:

$$\frac{1}{2}\rho u^2 = \Delta P \quad (9.1)$$

Roughly speaking then, the left-hand term of equation 9.1 should be larger than  $10^5$  Pa. By using  $\rho = 1000 \text{ kg/m}^3$  for water, the threshold velocity  $u$  is approximately 14 m/s. A sinusoidal oscillation at a frequency of 190 Hz and with an oscillation amplitude of 1.2 mm gives a velocity of only 1.4 m/s. An ultrasonic file, typically driven at 30 kHz and an amplitude of  $75 \mu\text{m}$ , reaches velocities above this threshold and can therefore generate cavitation, as previously observed by Ahmad *et al.* [15].

There are 3 types of EndoActivator tips currently available, #15/.02, #25/.04, and #35/.04. A different dimension of the tip applied in the same size root canal might produce different oscillations and irrigant flow, which could influence the effectiveness of the instruments. The size of the standardized model used in this study was #30/.06, which is clinically relevant. Therefore we tested the #15/.02 and #25/.04 tips. The #35/.04 tip should be tested with larger size and tapered root canal, so we did not include it. The results showed that there was no difference between the two types of sonic tips in amplitude, oscillatory pattern, or wall contact. The irrigant flow and streaming pattern of the irrigant were therefore equal, resulting in the same effectiveness of the irrigation.

There was no significant difference between NaOCl and water as irrigant when it was sonically activated. Because the fluidic properties of water and NaOCl are comparable [17], no differences in acoustic streaming between them were to be expected.

## References

- [1] R. Weller, J. Brady, and W. Bernier, "Efficacy of ultrasonic cleaning", *Journal of Endodontics* **6**, 740–743 (1980).
- [2] P. Lumley, A. Walmsley, and W. Laird, "Streaming patterns produced around endosonic files.", *International Endodontic Journal* **24**, 290–297 (1991).

- [3] A. Lussi, U. Nussbächer, and J. Grosrey, "A novel noninstrumented technique for cleansing the root canal system", *Journal of Endodontics* **19**, 549–553 (1993).
- [4] E. Rosenfeld, G. James, and B. Burch, "Vital pulp tissue response to sodium hypochlorite", *Journal of Endodontics* **4**, 140–146 (1978).
- [5] A. Burlison, J. Nusstein, A. Reader, and M. Beck, "The in vivo evaluation of hand/rotary/ultrasound instrumentation in necrotic, human mandibular molars", *Journal of Endodontics* **33**, 782–787 (2007).
- [6] R. Roy, M. Ahmad, and L. Crum, "Physical mechanisms governing the hydrodynamic response of an oscillating ultrasonic file.", *International Endodontic Journal* **27**, 197–207 (1994).
- [7] A. Walmsley, "Ultrasound and root canal treatment: the need for scientific evaluation.", *International Endodontic Journal* **20**, 105–111 (1987).
- [8] T. Leighton, *The Acoustic Bubble* (Academic Press, London) (1994).
- [9] S. Jensen, T. Walker, J. Hutter, and B. Nicoll, "Comparison of the cleaning efficacy of passive sonic activation and passive ultrasonic activation after hand instrumentation in molar root canals", *Journal of Endodontics* **25**, 735–738 (1999).
- [10] R. Sabins, J. Johnson, and J. Hellstein, "A comparison of the cleaning efficacy of short-term sonic and ultrasonic passive irrigation after hand instrumentation in molar root canals", *Journal of Endodontics* **29**, 674–678 (2003).
- [11] S.-J. Lee, M.-K. Wu, and P. Wesselink, "The effectiveness of syringe irrigation and ultrasonics to remove debris from simulated irregularities within prepared root canal walls", *International Endodontic Journal* **37**, 672–678 (2004).
- [12] M. Wu, A. R'Oris, D. Barkis, and P. Wesselink, "Prevalence and extent of long oval canals in the apical third.", *Oral surgery, oral medicine, oral pathology, oral radiology, and endodontics* **89**, 739–743 (2000).
- [13] L. W. M. Van der Sluis, M. K. Wu, and P. Wesselink, "The evaluation of removal of calcium hydroxide paste from an artificial standardized groove in the apical root canal using different irrigation methodologies", *International Endodontic Journal* **40**, 52–57 (2007).
- [14] A. Walmsley, P. Lumley, and W. Laird, "Oscillatory pattern of sonically powered endodontic files.", *International Endodontic Journal* **22**, 125–132 (1989).
- [15] M. Ahmad, T. Pitt Ford, L. Crum, and A. Walton, "Ultrasonic debridement of root canals: Acoustic cavitation and its relevance", *Journal of Endodontics* **14**, 486–493 (1988).
- [16] C. Brennen, *Cavitation and Bubble Dynamics* (Oxford University Press, Oxford) (1995).
- [17] D. Guerisoli, R. Silva, and J. Pecora, "Evaluation of some physico-chemical properties of different concentrations of sodium hypochlorite solutions", *Brazilian Endodontic Journal* **3**, 21–23 (1998).

## Appendices

### 9.A Supplementary material

*(Online at [http://stilton.tnw.utwente.nl/rootcanalcleaning/Gallery\\_of\\_Irrigant\\_Motion](http://stilton.tnw.utwente.nl/rootcanalcleaning/Gallery_of_Irrigant_Motion))*

Movie 1. High-speed visualization of the sonic device oscillating inside a glass root canal model. Recording speed is 4 Kfps.



# 10

## An evaluation of the effect of pulsed ultrasound on the cleaning efficacy of passive ultrasonic irrigation \* †

**Abstract:** Multiple activations of the irrigant by using pulsed ultrasound may enhance the removal of dentin debris from an extracted tooth model because of repeated acceleration of the irrigant. Each of 20 *in vitro* root canal models with a standard groove in the apical portion of one canal wall filled with dentin debris received PUI repeatedly, either without pulsation (group1) or with pulsation (duty cycle of 100%, 88%, 50%, or 13%). After each irrigation procedure, the amount of dentin debris in the groove was evaluated by taking photographs of the groove and scoring. The irrigation procedures were also visualized *in vitro* using high-speed imaging performed in glass root canal models. A 50% duty cycle showed a significant decrease in dentin debris removal; duty cycles of 13% and 88% showed no difference compared with continuous oscillation. The *in vitro* visualization showed increased streaming and cavitation during the start-up phase of each pulse.

---

\*Published as: L-M. Jiang, B. Verhaagen, M. Versluis, C. Zangrillo, D. Cuckovic and L.W.M. van der Sluis, "An Evaluation of the Effect of Pulsed Ultrasound on the Cleaning Efficacy of Passive Ultrasonic Irrigation", *Journal of Endodontics* **36**(11), pp. 1887-1891 (2010)

†The high-speed imaging and its analysis in this chapter is part of the present thesis. The dentin debris removal experiments are due to Lei-Meng Jiang.

## 10.1 Introduction

After the completion of a standard root canal preparation, the debridement of the root canal is, however, by far complete, leaving large untouched areas that may harbor tissue or dentin debris, microbes, and their byproducts [1–7]. The root canal system has better access for cleaning by an irrigant after finishing the instrumentation, and irrigation has a better possibility for cleaning the space beyond the prepared canal [8]. Therefore, a final rinse after the completion of the preparation is an essential part of root canal debridement.

It has been realized in recent years that irrigation dynamics play an important role in the cleaning process [9–11]. The use of a file in conjunction with an (ultra)sonic device that activates the irrigant has been proposed for the final rinsing step to enhance the cleaning of the root canal through streaming and cavitation [12–15].

Laser-activated irrigation has been shown to be more effective in removing dentine debris from the apical part of the root canal than passive ultrasonic irrigation (PUI) [16]. This improvement in cleaning efficacy may be associated with the fact that the irrigant becomes accelerated at every laser pulse [16]. Similarly, the acoustic streaming of the irrigant introduced by the ultrasonic activation may also be enhanced by repeated activations after introducing ultrasound pulsations into the system. Each activation causes an acceleration of the irrigant, and the governing fluid physics laws link acceleration to force. In addition, pulsed ultrasound has a direct effect on acoustic cavitation in a liquid [17–19]. Therefore, this study looks into the enhancement of the cleaning efficacy of PUI by pulsed ultrasound under the hypothesis that PUI with pulsation is more effective than without pulsation within 10 seconds.

## 10.2 Materials and Methods

### 10.2.1 Dentin debris removal model

Straight roots from 20 extracted human maxillary canines were decoronated to obtain uniform root sections of 15 mm. The roots were embedded in self-curing resin (GC Ostron 100; GC Europe, Leuven, Belgium) and then bisected longitudinally through the canal in mesiodistal direction with a saw microtome (Leica Microsystems SP1600, Wetzlar, Germany). The surfaces of both halves were ground successively with 240-, P400- and 600-grit sandpaper, resulting in smooth surfaces on which only little of the original root canal lumen was left. Four holes were drilled in the resin part, and the two halves were reassembled by four self-tapping bolts through the holes [9]. All the models were checked for any leakage of liquid or gas apically or laterally before experiments; if there was any, rubber dam caulk was applied to ensure the root canal space of the model was a closed system.

New root canals were prepared by K-files #15/02 (Dentsply Maillefer, Ballaigues, Switzerland) and HERO 642 (MicroMega, Besancon, France) nickel-titanium rotary instruments to a working length of 15 mm, ISO size 30, and taper of 0.06, resulting in standardized root canals. During preparation, the canals were rinsed with 1 mL of 2% NaOCl after each file delivered by a 10-mL syringe (Terumo, Leuven, Belgium) and a 30-G needle (Navitip; Ultradent, South Jordan, UT).

A standard groove of 4 mm in length, 0.5-mm deep, and 0.2-mm wide situated at 2 to 6 mm from the working length [20], was cut in the wall of one half of each root canal with a customized ultrasonic tip. A periodontal probe with an adapted 0.2-mm wide tip was used to verify the dimension of each groove during and after preparation. The dimension of the groove is comparable to an apical oval root canal [21]. Each groove was filled with dentin debris, which was mixed with 2% NaOCl for 5 minutes, to simulate a situation in which dentin debris accumulates in uninstrumented canal extensions [20]. This model was introduced to standardize the root canal space and the amount of dentin debris present in the root canal before the irrigation procedure to increase the reliability of the dentin debris removal evaluation. The methodology has been shown to be sensitive, and the data are reproducible [22]. A pilot study has shown that a single model could be reused at least 8 times without any visible defect on the surface of the canal wall. Therefore the 20 models were used repeatedly in the five experimental groups which are shown in Table 10.1.

### 10.2.2 Irrigation procedure

Specimens in all the experimental groups were rinsed with 2 mL of irrigant (2% NaOCl) using 10-mL syringes with 30-G needles (Navitip) placed 1 mm from the working length, and the flow rate was approximately 5 mL/min. Then, the irrigant was activated by an ultrasonic file #20/00 (IrriSafe; Acteon, Merignac, France) for 10 seconds without (group 1) or with (groups 2-4) pulsed ultrasound (Table 10.1). All the experimental specimens received 2 mL of irrigant, which was delivered again by a syringe as the final flush.

Every attempt was made to keep the file centered in the canal to minimize contact with the canal walls (passive activation). The file was driven at power setting yellow 4 by a piezoelectronic unit (Suprasson PMax; Satelec Acteon, Merignac, France) of which the footswitch was replaced by a customized pulse generator to be able to oscillate the file with pulsation.

### 10.2.3 Image evaluation and statistical analyses

Before and after each irrigation procedure, the root halves were separated, and the grooves were viewed through a stereomicroscope (Stemi SV6; Carl Zeiss, Göttingen, Germany) using a cold light source (KL 2500 LCD, Carl Zeiss). Controls verified that



no debris had fallen out of the groove during the assembly or disassembly process. Pictures were taken with a digital camera (Axio Cam, Carl Zeiss). The sequence of all the pictures was randomized, and two calibrated examiners were blind to the group assignment.

The debris left in the groove after irrigation was scored independently by the two calibrated dentists using the following score system: 0: the groove is empty, 1: less than half of the groove is filled with debris, 2: more than half of the groove is filled with debris, and 3: the complete groove is filled with debris (20). The percentage of inter-agreement should be more than 95%; if this percentage was lower than 95%, a consensus had to be reached. The differences in debris scores between the groups were analyzed by means of the Kruskal-Wallis test and the Mann-Whitney U test. The level of significance was set at  $\alpha = 0.05$ .

### 10.2.4 High-speed imaging experiments



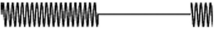


An optical setup was constructed in order to visualize the effect of pulsed ultrasonic activation in the two glass models of the root canal. Both models contain straight root canals of length 10 mm, an apical diameter of 0.30 mm, and a taper of approximately 0.06. One model had no side canals; the Irrisafe file (#20/.00) was positioned at 3 mm from the apex. The other model had one side canal with a diameter of 0.2 mm located at 2.0 mm from the apex; the Irrisafe file was positioned at 1 mm from the apex. The file was driven in both models under the same conditions as the *in vitro* experiments. The root canals were filled with 5% NaOCl, to which small hollow glass spheres (mean diameter, 11  $\mu\text{m}$ ; Spherichel, Potters Industries, South Yorkshire, UK) were added in order to track the fluid movement.

A zoom microscope with 1.25 $\times$  to 20 $\times$  magnification was used (BX-FM; Olympus, Tokyo, Japan) for magnification. The root canal was illuminated in bright field by a continuous-wave light source (ILP-1, Olympus). Imaging was performed using a high-speed camera (HPV-1; Shimadzu Corp, Kyoto, Japan) at a frame rate of 25,000 frames per second.

The amount of activity due to an oscillating file is determined from the recordings for each pulsation scheme. Movement of the particles in the fluid, file movement, or cavitation bubbles causes one frame to be different from the previous frame of the recording, and this difference in pixel values is taken as the activity of each frame.

## 10.3 Results

The two investigators differed in scoring seven specimens; agreement was reached after discussion ( $\kappa = 0.898$ ). The number and the percentage of samples at each score rank in different groups after the irrigation procedures are presented in Table

Group (N = 20)	Pulse intervals	Schematic representation (1 second)	Duty cycle (%) <sup>*</sup>	Score <sup>†</sup>			
				0 (%)	1 (%)	2 (%)	3 (%)
1	None		100	8 (40)	11 (55)	1 (5)	0 (0)
2	730 ms on/100 ms off		88	9 (45)	8 (40)	2 (10)	1 (5)
3	400 ms on/400 ms off		50	15 (75)	5 (25)	0 (0)	0 (0)
4	100 ms on/670 ms off		13	11 (55)	5 (25)	4 (20)	0 (0)
5 (control)	None		0	0 (0)	0 (0)	0 (0)	20 (100)

<sup>\*</sup>Duty cycle = length of the pulse divided by the total time of one cycle.

<sup>†</sup>Score 0, the groove is empty; score 1, less than half of the groove is filled with debris; score 2, more than half of the groove is filled with debris; score 3, the complete groove is filled with debris.

**Table 10.1:** Experimental groups and the number of specimens at each score rank after the irrigation procedure

10.1. Significant difference was only found between group 1 and group 3 ( $p = 0.023$ ). Activation of the irrigant with pulsed ultrasound with a duty cycle of 50% is more effective to remove apical dentin debris than that in the group without pulsed ultrasound.

The visualization recordings of the file oscillation and the streaming showed three different phases during one activation cycle. There was a start-up phase in the first 50 milliseconds, a steady phase during the remainder of the pulse, and a stopping phase of 20 milliseconds after the pulse had ended. The general timeline of events during each pulsation is shown in Figure 10.1-top. Figure 10.1-bottom shows the activity at a certain distance from the apex.

During the start-up phase, the amplitude of the file oscillation was large compared with its final, steady oscillation amplitude and, consequently, produced more streaming around the file than in the steady phase. The disturbance caused by the file that started its oscillation took approximately 10 milliseconds to reach remote areas like the apex and side canals. However, the penetration of the irrigant into the side canal was limited to approximately 0.5 mm from its entrance (Fig. 10.2).

Cavitation was also observed close to the tip of the file during the start-up phase, mostly generated at 0.5 mm from the tip. These bubbles occasionally split off and were transported to other locations in the root canal. Stable cavitation bubbles with a diameter of approximately 100  $\mu\text{m}$  have been observed up to 0.4 mm into the side canal where they tended to oscillate along with the file during the steady phase, thereby increasing the local streaming significantly.

During the steady phase, the file oscillations are not at a constant amplitude, except for an occasional unsteady motion, possibly because the file is not perfectly

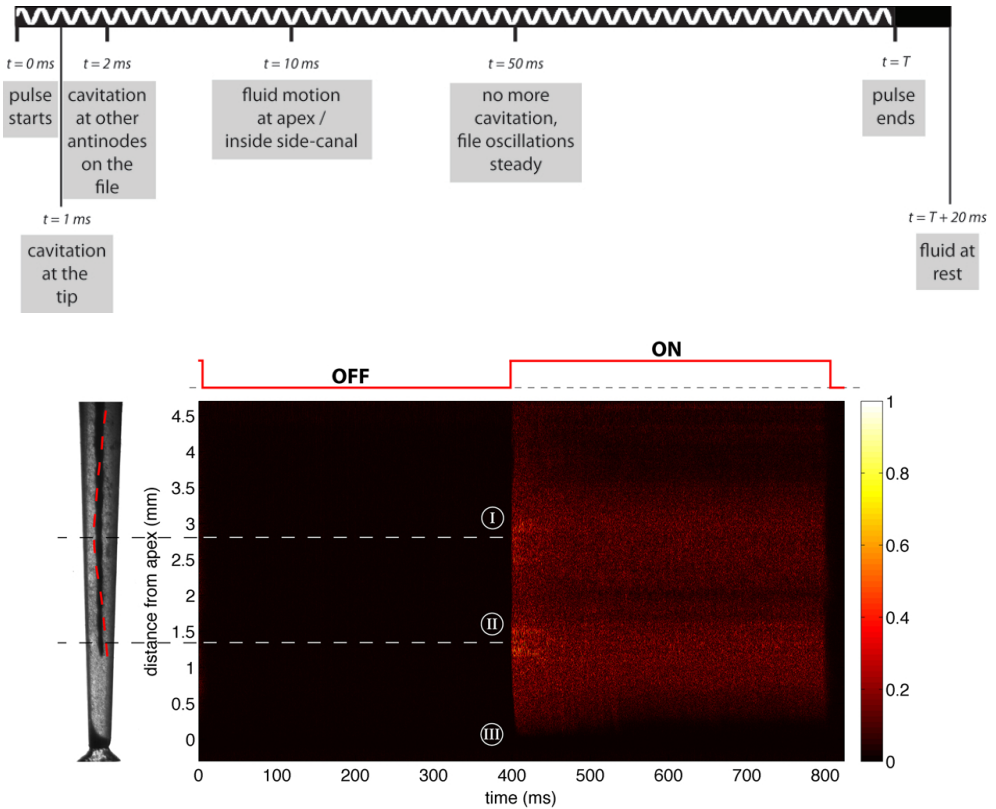


**Figure 10.1:** (top) Timeline of activities during one pulse of duration  $T$ . (bottom) Activity as observed on the recording of pulsation with a duty cycle of 50%. The off and on period of the pulse is indicated on top of the graph. On the left is a picture of the file inside the root canal with its oscillation pattern indicated with a red dotted line. Color indicates the amount of activity (arbitrary units). At the antinodes of the file, locations (I) and (II), there is high activity during the first 50 milliseconds related to the transient motion of the file and cavitation. It takes approximately 10 milliseconds for the fluid to reach or activity to start at the apex or location (III). This activity disappears within 100 milliseconds.

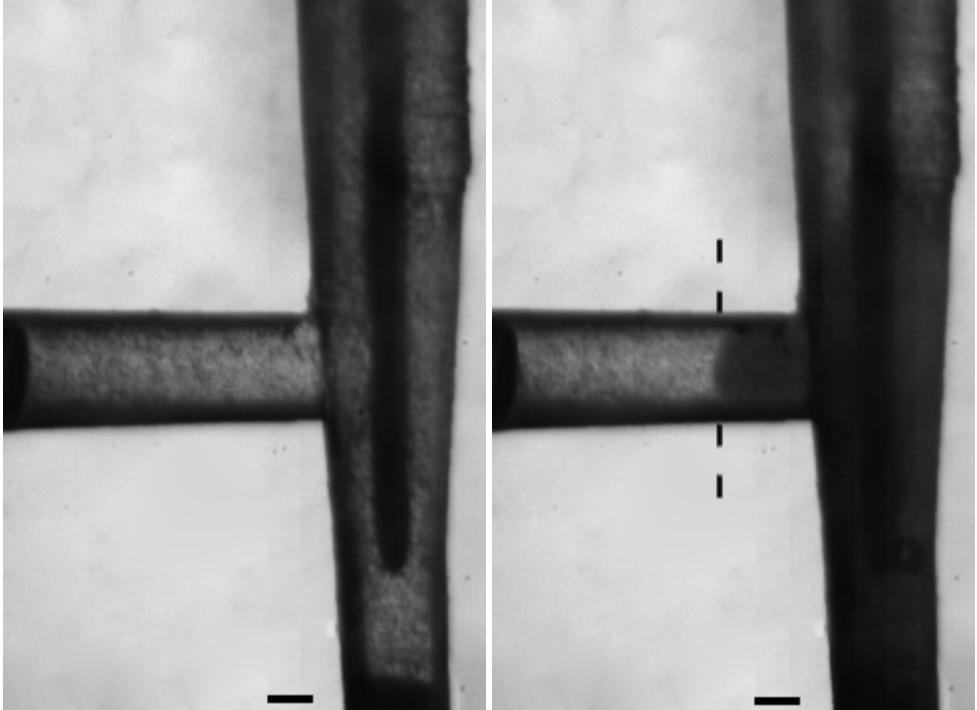


**Figure 10.2:** *The root canal model with a side canal showing the file (dark black shape) inside the main canal and the side canal. The left panel shows the root canal before activation, with only a few particles (black dots) floating around. The right panel shows the root canal after irrigation where the particles have been stirred up, resulting in dark areas. The dashed line shows the extension of irrigant penetration into the side canal. The black bar is 100  $\mu\text{m}$ .*

straight. Streaming close to the apex and side canals was very slow and barely observable at a frame rate of 25,000 frames per second. No cavitation was observed at the tip of the file. In the stopping phase, the fluid slowly came to a standstill in approximately 20 milliseconds.

## 10.4 Discussion

In this study, the ultrasound device was switched on and off repeatedly. The visualization experiments showed that the on period (activation) is composed of three phases: the start-up phase, the steady phase, and the stopping phase; the OFF period is a rest phase. During the first 50 milliseconds, there is more activity at the file tip than after 50 milliseconds; therefore, this time period is called the “start-up phase”. Afterwards, the oscillation and the streaming become stable, which is called the “steady phase”. The two phases produce different flow patterns of the irrigant, defined as “unsteady streaming” and “steady streaming” accordingly. All phases would have their own or combined influence on the efficacy of the irrigant to remove dentin debris from the root canal because of the mechanical effect by the streaming and the chemical effect.

According to the results of the visualization experiments, there are three interesting phenomena taking place. The oscillation of the file shows transient behavior because of the start-up of the file motion. This leads to increased amplitude of the ultrasonic file tip, which in turn causes an increase of the irrigant velocity (unsteady streaming) around the oscillating file. The unsteady streaming contributed majorly to the penetration of irrigant into (a small part of) the side canal. Therefore, it could be assumed that the irrigant would possibly penetrate into the groove of the *in vitro* model as well. Cavitation was observed behind the tip of the file, whereas no cavitation was observed during the steady oscillation of the file, suggesting that the generation of cavitation was related to the increase of amplitude during the start-up phase. Because there were 12 more start-up phases in group 3 (50% duty cycle) than in group 1 (100% duty cycle), this could explain why the former removed the dentin debris more efficiently from the groove.

However, all the pulsation groups (groups 2, 3, and 4) have the same number of pulsations or start-up phases, indicating that the steady streaming and the rest phase should be considered in order to explain the difference between these groups. For example, in group 4, there is no oscillation for 87% of the irrigation time, but the cleaning efficacy was still the same as the continuous mode or 100% duty cycle. This suggests that the extra activity during the “start-up phase” could compensate for the reduced duty cycle. This finding was a confirmation of an earlier pilot experiment with the same methodology ( $n = 12$ , 0.1 seconds on/0.9 seconds off).

Even more interesting is the result of group 2 (88% duty cycle); there are as many start-ups but longer streaming than in group 3 (50% duty cycle). However,

the cleaning efficacy of group 2 is no better than group 3. This finding was also a confirmation of an earlier pilot experiment with the same methodology (n = 12, 0.9 seconds on/0.1 seconds off). This suggests that also the rest phase plays an important role.

The duration of the start-up and steady phases could possibly influence the generation and dissolving of bubbles in the irrigant [18] and potential chemical effects [23] as well. As observed in the visualization experiment, stable bubbles oscillating along with the file oscillation increased the local streaming significantly. However, these bubbles typically are generated by cavitation on so-called cavitation nuclei [24], and these nuclei might dissolve during the rest phase. It is possible that a duty cycle of 50% is optimal for the reoccurrence of cavitation, again suggesting that the rest time of a pulsation scheme is also important.

Although the fluidic properties are similar between water and NaOCl [23], the mechanical removal of dentin debris was better with NaOCl than water-activated ultrasonically [22], suggesting that chemical effects also play a role in dentin debris removal. The duration of the activation and the rest phase could influence the chemical effects involved, which can hardly be observed by video recordings. Further studies are needed to elucidate these typical chemical aspects.

The dentin debris removal model used in this study is a closed system. The two halves of the root embedded in the resin matched perfectly and were fixed with four bolts to prevent any irrigant or gas escaping apically and laterally. Because the apical fluid movement mechanisms can be quite different between a closed and an open system [25], it is better to use a closed system like the model used in this study, which is more clinically relevant.

The straight canals are not very commonly encountered. However, the aim of this study was to discern between the effects of the different pulsation patterns of ultrasound on the cleansing of the apical root canal. For this purpose, the model appeared adequate because of the standardization of the research procedure. Further research is needed to elucidate the effect of different root canal curvatures on the application of ultrasonic activation of the irrigant.

## References

- [1] J. Gutiérrez and J. García, "Microscopic and macroscopic investigation on results of mechanical preparation of root canals", *Oral Surgery, Oral Medicine, Oral Pathology* **25**, 108–116 (1968).
- [2] C. Haga, "Microscopic measurements of root canal preparations following instrumentation.", *Journal of the British Endodontic Society* **2**, 41–46 (1968).
- [3] R. Walton, "Histologic evaluation of different methods of enlarging the pulp canal space", *Journal of Endodontics* **2**, 304–311 (1976).
- [4] M.-K. Wu, L. Van Der Sluis, and P. Wesselink, "The capability of two hand instrumentation

- techniques to remove the inner layer of dentine in oval canals”, *International Endodontic Journal* **36**, 218–224 (2003).
- [5] M.-K. Wu and P. Wesselink, “A primary observation on the preparation and obturation of oval canals”, *International Endodontic Journal* **34**, 137–141 (2001).
- [6] E. Schäfer and K. Zapke, “A comparative scanning electron microscopic investigation of the efficacy of manual and automated instrumentation of root canals”, *Journal of Endodontics* **26**, 660–664 (2000).
- [7] B. Tan and H. Messer, “The quality of apical canal preparation using hand and rotary instruments with specific criteria for enlargement based on initial apical file size.”, *Journal of Endodontics* **28**, 658–664 (2002).
- [8] K. Gulabivala, B. Patel, G. Evans, and Y. Ng, “Effects of mechanical and chemical procedures on root canal surfaces”, *Endodontic Topics* **10**, 103–122 (2005).
- [9] L.-M. Jiang, B. Verhaagen, M. Versluis, and L. van der Sluis, “Evaluation of a sonic device designed to activate irrigant in the root canal”, *Journal of Endodontics* **36**, 143–146 (2010), *See also chapter 9 of this thesis.*
- [10] C. Boutsioukis, T. Lambrianidis, E. Kastrinakis, and P. Bekiaroglou, “Measurement of pressure and flow rates during irrigation of a root canal ex vivo with three endodontic needles”, *International Endodontic Journal* **40**, 504–513 (2007).
- [11] C. Boutsioukis, T. Lambrianidis, and E. Kastrinakis, “Irrigant flow within a prepared root canal using various flow rates: A computational fluid dynamics study”, *International Endodontic Journal* **42**, 144–155 (2009).
- [12] R. Sabins, J. Johnson, and J. Hellstein, “A comparison of the cleaning efficacy of short-term sonic and ultrasonic passive irrigation after hand instrumentation in molar root canals”, *Journal of Endodontics* **29**, 674–678 (2003).
- [13] A. Burlison, J. Nusstein, A. Reader, and M. Beck, “The in vivo evaluation of hand/rotary/ultrasound instrumentation in necrotic, human mandibular molars”, *Journal of Endodontics* **33**, 782–787 (2007).
- [14] M. Ahmad, T. Pitt Ford, and L. Crum, “Ultrasonic debridement of root canals: Acoustic streaming and its possible role”, *Journal of Endodontics* **13**, 490–499 (1987).
- [15] L. Van Der Sluis, M. Versluis, M. Wu, and P. Wesselink, “Passive ultrasonic irrigation of the root canal: A review of the literature”, *International Endodontic Journal* **40**, 415–426 (2007).
- [16] S. De Groot, B. Verhaagen, M. Versluis, M.-K. Wu, P. Wesselink, and L. Van Der Sluis, “Laser-activated irrigation within root canals: Cleaning efficacy and flow visualization”, *International Endodontic Journal* **42**, 1077–1083 (2009), *See also chapter 13 of this thesis.*
- [17] A. Henglein, R. Ulrich, and J. Lilie, “Luminescence and chemical action by pulsed ultrasound”, *Journal of the American Chemical Society* **111**, 1974–1979 (1989).
- [18] J. Lee, M. Ashokkumar, S. Kentish, and F. Grieser, “Determination of the size distribution of sonoluminescence bubbles in a pulsed acoustic field”, *Journal of the American Chemical Society* **127**, 16810–16811 (2005).

- [19] A. Brotchie, F. Grieser, and M. Ashokkumar, "Effect of power and frequency on bubble-size distributions in acoustic cavitation", *Physical Review Letters* **102** (2009).
- [20] S.-J. Lee, M.-K. Wu, and P. Wesselink, "The effectiveness of syringe irrigation and ultrasonics to remove debris from simulated irregularities within prepared root canal walls", *International Endodontic Journal* **37**, 672–678 (2004).
- [21] M. Wu, A. R'oris, D. Barkis, and P. Wesselink, "Prevalence and extent of long oval canals in the apical third.", *Oral surgery, oral medicine, oral pathology, oral radiology, and endodontics* **89**, 739–743 (2000).
- [22] L. Van Der Sluis, M. Wu, and P. Wesselink, "The evaluation of removal of calcium hydroxide paste from an artificial standardized groove in the apical root canal using different irrigation methodologies", *International Endodontic Journal* **40**, 52–57 (2007).
- [23] L. van der Sluis, M. Vogels, B. Verhaagen, R. Macedo, and P. Wesselink, "Study on the influence of refreshment/activation cycles and irrigants on mechanical cleaning efficiency during ultrasonic activation of the irrigant", *Journal of Endodontics* **36**, 737–740 (2010).
- [24] M. Brenner, S. Hilgenfeldt, and D. Lohse, "Single-bubble sonoluminescence", *Reviews of Modern Physics* **74**, 425–484 (2002).
- [25] F. Tay, L.-S. Gu, G. Schoeffel, C. Wimmer, L. Susin, K. Zhang, S. Arun, J. Kim, S. Looney, and D. Pashley, "Effect of vapor lock on root canal debridement by using a side-vented needle for positive-pressure irrigant delivery", *Journal of Endodontics* **36**, 745–750 (2010).







# Irrigant flow beyond the insertion depth of an ultrasonically oscillating file in straight and curved root canals: visualization and cleaning efficacy \* †

**Abstract:** The influence of the insertion depth of an ultrasonically oscillating file on the flow toward the apex of a straight or curved root canal is investigated in this chapter. An extracted tooth model with artificial debris-filled depressions in one canal wall at 0.5, 2, 4, and 6 mm from the working length was used. Dye penetration and high-speed recordings of the flow in straight and curved canals showed the static and dynamic behavior of the flow during ultrasonic activation. The overall cleaning efficacy decreased with increasing distance between the file and the apex, with the depressions next to the file and within 3 mm in front of the file being the cleanest. The flow observed from the visualization experiments matched this distance, suggesting a direct relation between flow and cleaning. The observed flow depth increased with increasing power setting; the curvature of the root canal had no influence on the flow depth. High-speed imaging showed a start-up phase with deeper fluid activation than in the steady phase afterward.

---

\*Published as: M. Malki, B. Verhaagen, L-M. Jiang, W. Nehme, A. Naaman, M. Versluis, P.R. Wes-selink, L.W.M. van der Sluis, "Irrigant flow beyond the insertion depth of an ultrasonically oscillating file in straight and curved root canals: visualization and cleaning efficacy", *Journal of Endodontics* 38(5), pp. 657-661 (2012)

†The high-speed imaging and dye penetration experiments and their analysis in this chapter are part of the present thesis. The dentin debris removal experiments are due to Maher Malki.

## 11.1 Introduction

One of the primary goals of endodontic treatment is to heal apical periodontitis, which can be achieved by removing pulp tissue and microorganisms from the root canal system before placing a root canal filling [1]. The complex nature of the root canal anatomy, which consists of the lumen of the main root canal(s) and accessory canals, canal ramifications, apical deltas, fins, and transverse anastomoses, makes complete debridement with mechanical instrumentation alone a goal impossible to achieve [2, 3]. Therefore, irrigation with a suitable disinfectant is an essential part of a root canal treatment [4].

The apical root canal seems to be the most difficult part to clean because of its complex anatomy [5]. The small dimension and complex canal structure could hinder an effective flow of the irrigant [6]. Specifically, root canals often have a curvature [7], which has recently been shown to reduce the cleaning efficacy of several irrigation techniques [8, 9]. Apart from the mechanical effect of removing matter (like dentin debris produced by root canal instrumentation), an effective flow is needed for an adequate refreshment of the sodium hypochlorite solution [10]. Unfortunately, the mechanical effect of needle irrigation is limited in the apical root canal [5, 6]. This is also true for the refreshment of the irrigant, which is shown to be limited to 1.5 mm beyond the needle tip [11]. Agitation techniques could improve the apical cleaning efficacy, mechanically and chemically, by enhancing the irrigation dynamics [12].

Ultrasonic-activated irrigation is one of the possibilities to agitate a sodium hypochlorite solution in the root canal [13]. It has been shown that dentin debris, pulp tissue, and biofilm can be removed from the root canal wall by the shear stress produced by acoustic streaming of the irrigant [14, 15]. Furthermore, irrigant penetration in the apical lateral canals has been shown in an *in vitro* model [16]. A recent study showed that dentin debris could be removed from the root canal wall 0.5 mm beyond the file tip, which was positively related to the ultrasonic intensity used [17]. However, it is not known how far this effect extends and how the curvature of a root canal influences this depth. Therefore, the purposes of this study were to evaluate the influence of the insertion depth of an ultrasonically oscillating file on the ability to remove dentin debris from simulated canal irregularities in an extracted tooth model of a straight root canal and its influence on the flow of irrigant in both straight and curved canals at two different ultrasonic power settings.

## 11.2 Materials and Methods

### 11.2.1 Dentin Debris Removal Model

Straight roots from 15 extracted human maxillary canines were decoronated to obtain uniform root sections of 15 mm following a previously described protocol [17].

Briefly, the roots were embedded in self-curing resin (GC Ostron 100; GC Europe, Leuven, Belgium) and then bisected longitudinally through the canal in a mesiodistal direction. The surfaces of both halves were then grounded with sandpaper, resulting in smooth surfaces that leave only little of the original root canal lumen. Four holes were drilled in the resin part, and the two halves were reassembled by four self-tapping bolts through the holes. All the models were checked for leakage of liquid or gas apically or laterally before experiments; if there was any, rubber dam caulk would be applied to ensure that the root canal model was an entirely closed system.

Standardized root canals were established by K-Flexofiles #15/.02 (Dentsply Maillefer, Ballaigues, Switzerland) and GT (Dentsply Maillefer) nickel-titanium rotary instruments to a working length (WL) of 15 mm, ISO size 30, and taper 0.06. Preparation was done with the final apical enlargement by the Mtwo (VDW, Munich, Germany) nickel-titanium rotary instrument #35/.04. During instrumentation, the canals were rinsed with 1 mL of 2% NaOCl after each file insertion delivered with a 30G needle (Navitip, Ultradent, South Jordan, UT).

With the help of a microscope and a round bur (H71.104.003; Komet, Lemgo Germany) attached to a drilling machine, four standard depressions ( $\phi = 0.3$  mm), located at 0.5, 2, 4, and 6 mm from the WL were drilled in the wall of one half of each root canal [17]. Each depression was filled with dentin debris, which was mixed with 2% NaOCl for 5 minutes to achieve a wet sand-like consistency in order to simulate a situation in which dentin debris accumulates in uninstrumented canal irregularities during root canal preparation [17].

### 11.2.2 Irrigation Procedure

Specimens in all experimental groups were rinsed with 2 mL of irrigant (2% NaOCl) using 10-mL syringes with 30-G needles (Navitip) placed 1 mm from the WL, and the flow rate was approximately 5 mL/min. Then, ultrasonic-activated irrigation was performed with a 21-mm, stainless-steel, noncutting wire (#20, taper 00) (IrriSafe; Acteon, Merignac, France) driven by a piezoelectronic unit (Suprasson PMax, Acteon) at power setting of Blue 5 (frequency approximately 30 kHz and file tip displacement amplitude approximately 30 mm according to the manufacturer) for 10 seconds with the oscillation toward the depressions. The file was marked with a permanent black marker and inserted at different positions from the WL, namely 1 mm from the WL (group 1,  $n = 15$ ), 2 mm from the WL (group 2,  $n = 15$ ), 3 mm from the WL (group 3,  $n = 15$ ), 4 mm from the WL (group 4,  $n = 15$ ), and 5 mm from the WL (group 5,  $n = 15$ ). Group 6 acted as the control group, in which the ultrasonic file was inserted until 1 mm from the WL but was not activated by ultrasound. All the experimental specimens received 2 mL of irrigant, which was delivered again by a syringe as a final flush after the activation by ultrasound. After the irrigation, the canals were carefully dried with paper points.

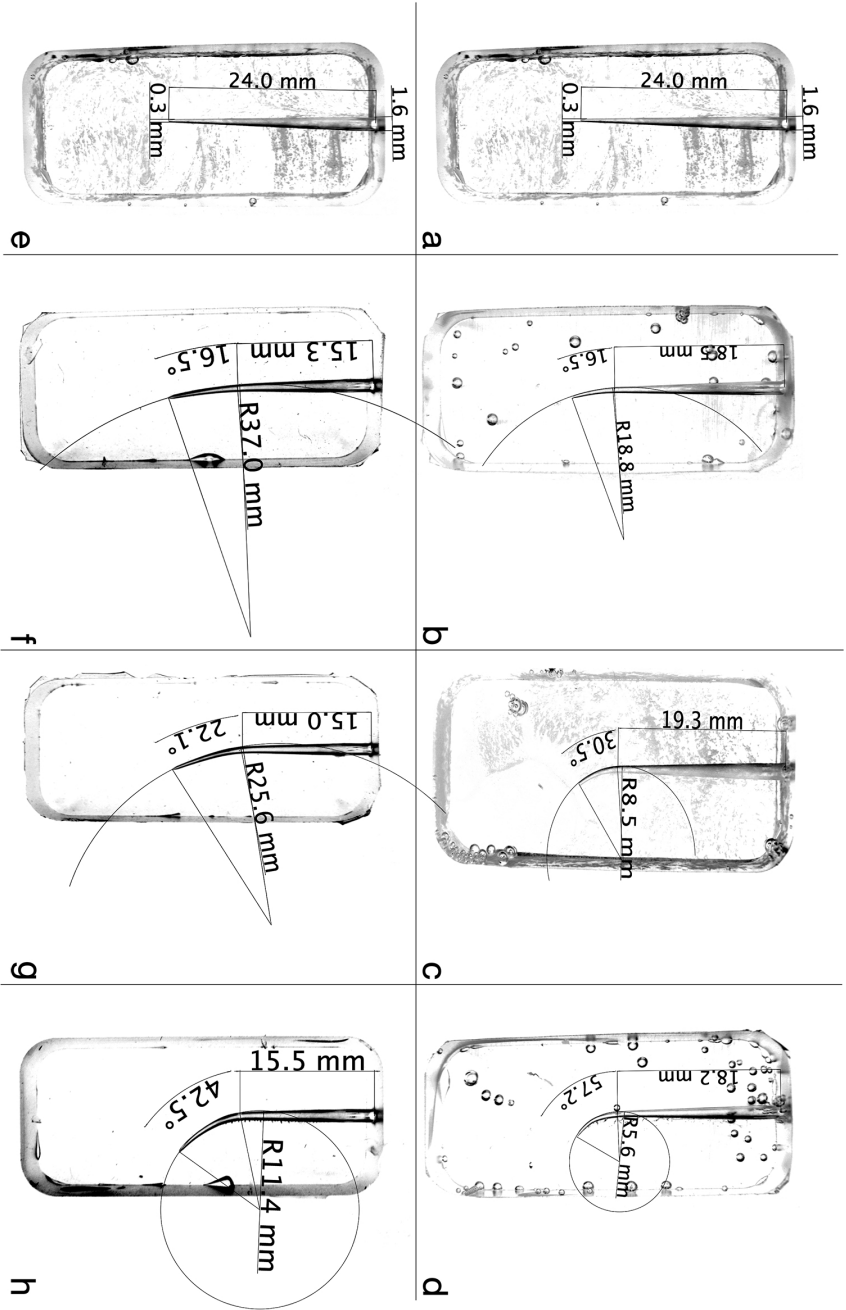


**Figure 11.1:** An overview of the curved transparent root canal models. The curvature is varied from (A and E) none to (B and F) moderate, (C and G) fair, and (D and H) severe; the curvature starts at 4 mm (A – D,  $L^* = 0.20$ ) or 8 mm (E – H,  $L^* = 0.35$ ) from the apex.

### 11.2.3 Image Evaluation and Statistical Analyses

Before and after each irrigation procedure, the root halves were separated, and the depressions were viewed through a stereomicroscope (Stemi SV6; Carl Zeiss, Göttingen, Germany) using a cold light source (KL 2500 LCD, Carl Zeiss) [17]. Controls verified that no debris had fallen out of the groove during the assembly or disassembly process. Pictures were taken with a digital camera (Axio Cam, Carl Zeiss). The sequence of all the pictures was randomized. The debris removal from each depression after irrigation was scored independently and blindly by two calibrated dentists. The samples were graded as clean if the depression is completely clean or not clean if the depression is not completely clean.

The percentage of interagreement should be more than 95%; if this percentage was lower than 95%, a consensus had to be reached. The differences in debris removal between the depressions within each group and between the groups were analyzed by chi-square analysis. The level of significance was set at  $\alpha=0.05$ .

### 11.2.4 Dye Penetration Experiments

The depth of flow was measured statically by injecting a dye mixture (Rood, Jo-La, Bharco Foods, Baambrugge, The Netherlands; fluidic properties similar to those of water) at the coronal opening of a transparent root canal and letting it distribute by the flow generated by the ultrasonically oscillating file. Transparent root canal models were created by solidifying polydimethylsiloxane (Sylgard 184; Dow-Corning, Midland, MI) around a D-size hand spreader, leaving a root canal of size 35/.06. These silicone models have a better optical access than prefabricated acrylic blocks and allow for manufacturing of root canals with a specific curvature by prebending the spreader with an EndoBender (Sybron Endo, Orange, CA) to create moderate, fair, or severe curvatures starting at 4 or 8 mm from the tip of the spreader (WL). The exact curvatures were determined afterwards by analyzing photos of the root canal models on the computer. A circle was drawn over the curvature, from which the radius  $R$  and the angle  $\alpha$  were obtained. From these two values, the relative arc length  $L_{arc}^*$  was calculated as follows:

$$L_{arc} = 2\pi R \frac{\alpha}{360} \quad (11.1)$$

$$L_{arc}^* = \frac{L_{arc}}{L + L_{arc}} \quad (11.2)$$

For the curvature starting at 4 mm,  $L_{arc}^* = 0.20 \pm 0.02$  and for the curvature starting at 8 mm,  $L_{arc}^* = 0.35 \pm 0.02$ . Figure 11.1 shows the root canal models, including analysis of their curvature.

A K10/25 file was inserted to 4 or 8 mm from the apex by hand and operated for 10 seconds. Measurements were performed at three power settings of the ultrasonic

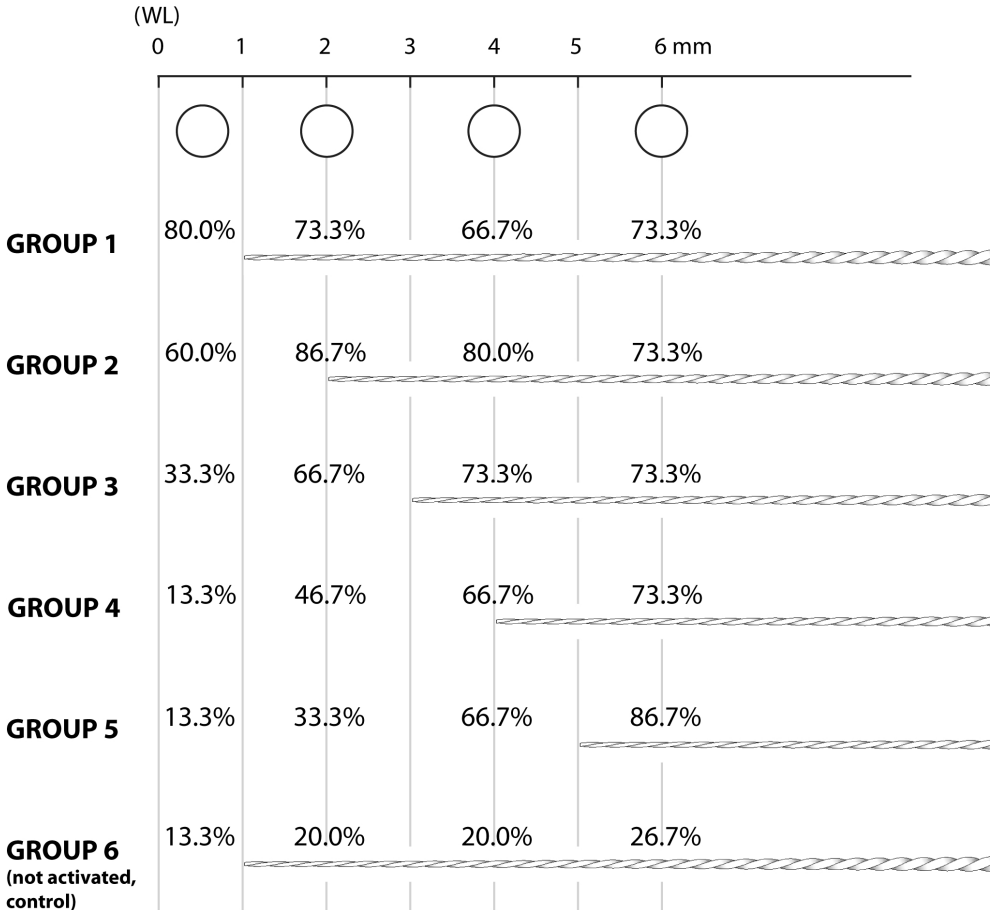


**Figure 11.2:** The percentage of completely clean depressions after the irrigation procedure in each experimental group.

device (Suprasson P-Max Newtron; Acteon Satelec, Bordeaux, France): Yellow 5, Blue 5, and Red 5 (in order of increasing power [17]). Each measurement was performed twice. Immediately afterward, a picture was taken of the root canal with a digital camera (D5100; Nikon, Tokyo, Japan) for analysis of the depth of dye penetration.

### 11.2.5 High-speed Imaging

The depth of flow was measured dynamically with the use of a high-speed camera (SA2; Photron, Tokyo, Japan), recording at 2,000 frames per second to record the movement of microparticles inside a transparent root canal model [14]. The same

models as in the dye penetration study were used. The K10/25 file was inserted to 4 or 8 mm from the apex and centered laterally in the canal. The root canal was then filled with water, to which hollow glass spheres with a diameter of 10  $\mu\text{m}$  were added as tracer particles. The root canal was fitted in front of a microscope (BX-FM; Olympus, Tokyo, Japan) with  $2.5\times$  magnification; light was provided in the bright-field mode using a continuous cold-light source (ILP-1, Olympus).

Measurements were performed at the three power settings also used in the dye penetration experiments. Analysis of the recordings was performed by subtracting consecutive frames in the recordings; a movement of the microparticles resulting from the induced flow leads to a change between the two image frames and therefore gives an indication of the image areas in which flow was present.

### 11.3 Results

The results are presented in Figure 11.2. The ultrasonically activated groups removed more dentin debris than the nonactivated control group ( $P < .0001$ ). Groups 1 and 2, with the file positioned 1 and 2 mm from the WL, exhibited significantly better cleaning efficacy than the other groups followed by group 3, which removed significantly more debris than groups 4 and 5. There was no significant difference between the four levels of the depression in groups 1 and 2 in contrast to groups 3, 4, and 5. Cleaning was observed up to 3 mm apically from the file tip with no significant difference between 0.5 and 2 mm from the tip. The  $\kappa$ -value was 0.85.

The dynamic behavior of the flow during the first 200 milliseconds after start-up is shown in Figure 11.3 in which the relative amount of flow is plotted as a function of depth and time. The graph shows a start-up phase with deeper fluid activation than in the steady phase afterward. The final state (flow depth beyond the file tip) for each power setting and curvature, as obtained with the dye penetration experiments, is shown in Figure 11.4. For power setting Yellow 5, the flow depth is typically slightly more than half of the distance to the apex; increasing the power setting increased the flow depth. At Blue 5 and an insertion depth of 4 mm from the apex of a straight canal, the flow depth was approximately 3 mm, which is in agreement with the cleaned areas in the extracted tooth experiments. The curvature did not have a significant influence on the flow depth.

### 11.4 Discussion

In ultrasonically activated irrigation, the irrigant is activated corresponding to a characteristic pattern of nodes and antinodes along the oscillating file [18]. The induced acoustic streaming leads to jets of irrigant that are directed toward the root canal wall [17]. These jets are responsible for the removal of dentin debris from artificial holes



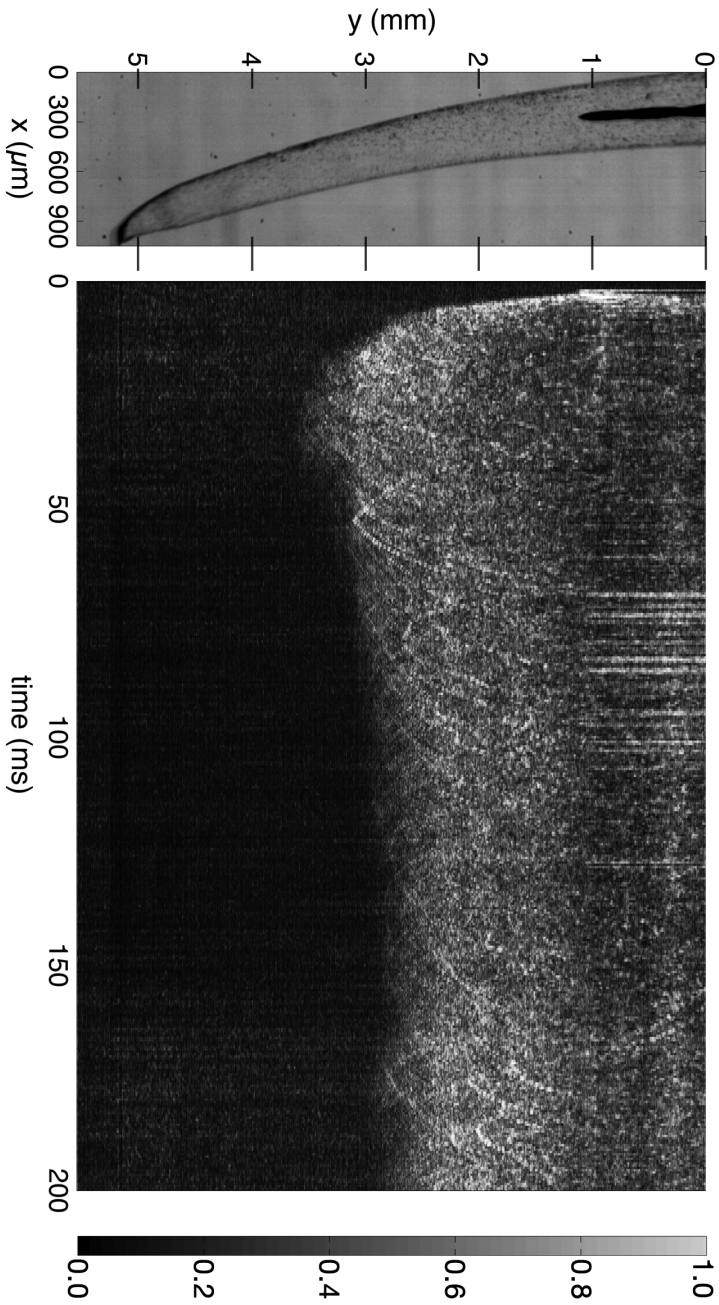


**Figure 11.3:** The flow depth as a function of time for the first 200 milliseconds after the start of the file oscillation. The left panel shows the initial state (note the different scales on the  $x$ - and  $y$ -axes), and the right panel shows the flow depth ( $y$ -axis, same scale as the left panel) over time ( $x$ -axis). Colors represent change between frames, representing flow. The power setting is Yellow 5; the distance from the file tip to the apex is 4 mm (moderate curvature).

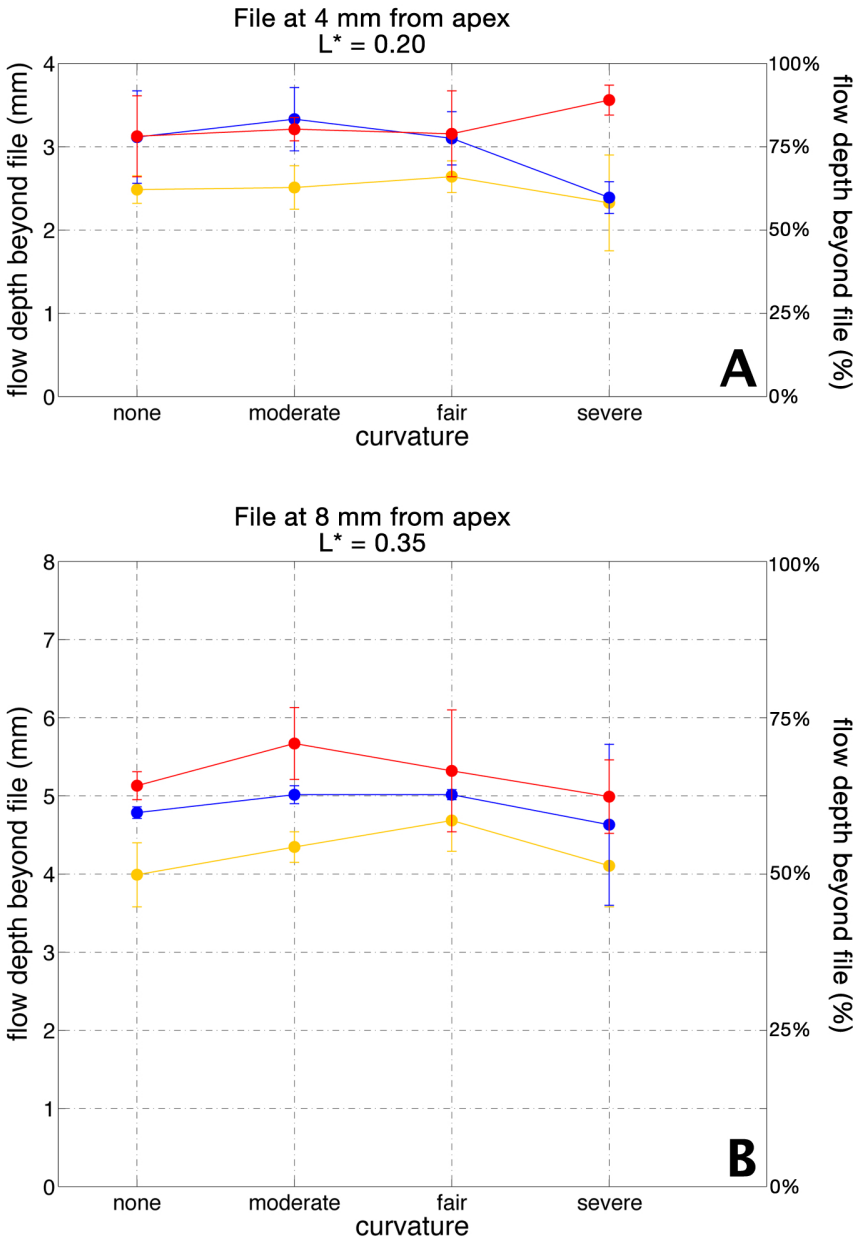


**Figure 11.4:** The flow depth beyond the file as a function of curvature and power setting (represented by line color, with red > blue > yellow). The y-axis labels show the flow depth beyond the file in millimeters (left) and in the percentage of the distance between the file tip and the apex (right).  $L^*$  is the relative size of the curvature, which is also the relative distance from the apex where the file was positioned.

in the root canal wall (lateral cleaning effect of the ultrasonically oscillating file) [14]. This cleaning effect can be observed from the coronal to the apical part of the root canal [17, 19]. Previous work reported a cleaning effect even 0.5 mm beyond the file tip that increased with the increasing intensity of the ultrasonic power [17].

In this chapter, we showed that in straight canals this cleaning effect extends until 3 mm in front of the file tip (power setting Blue 5, distance file tip-apex 4 mm) and that the cleaning effect decreases with the distance of the file tip to the depression filled with dentin debris (Fig. 11.2). We observed by visual methods that the flow depth of the irrigant is also 3 mm (at the same power setting and distance file tip apex), suggesting a direct relation between flow and cleaning. Therefore, the transparent root canal model gives some insight into the irrigant dynamics responsible for cleaning. However, the exact relation between flow and cleaning efficacy needs further studying because the more complex geometry (including the artificial depressions) of the root canal in the extracted teeth will affect the flow compared with the smooth transparent root canal model. There could also be a difference in the reflection of ultrasound by the silicon (transparent) root canal model walls compared with dentinal walls; however, the high-speed imaging showed no deformation of the silicone walls. Therefore, it was assumed that the silicone walls acted as solid walls for the fluid flow.

For needle irrigation, only severe root canal curvatures influence the cleaning efficacy [20]. However, in ultrasonically activated irrigation, the irrigant penetration is only influenced by the ultrasonic intensity [17] and the distance file tip apex if the file is placed without constraint in a curved root canal (just before the curve). The observation that the curvature does not influence the flow depth (Fig. 11.4) suggests that the microstreaming occurs typically on a much smaller scale than the curvature. Therefore, the apical extent of cleaning in curved canals will be comparable to the apical extent of cleaning in straight canals. It also suggests that the origin of the limitation in reaching the apex in a curved canal is not of a fluid dynamic nature but is rather related to geometric aspects, such as the location and length of the curvature. There is a difficulty in bringing the file tip close to the apex, which requires (pre)-bending of the file and/or implies much forced contact with the root canal wall, which may alter the file oscillation significantly, reduce the efficacy of the irrigant streaming, and increase the risk on file fracture. This is typically the case in the study of Amato *et al.* [8] in which the curvature was at 7 mm from the apex and the file was placed 1 mm short of the WL. In the study of Rödiger *et al.* [19], apart from the curvature and the placement of the file 2 mm from the WL, a cutting K-file instead of a noncutting file and the activation time (two times 1 minute) could have resulted in the production of dentin debris and could explain why they did not find a significant difference between (ultra)sonic activation of the irrigant or no activation [19]. The ultrasonic intensity for both studies was low.

In this chapter, we have considered the influence of the curvature of the root canal on the flow. It is known that for needle irrigation the size and taper of the root canal have an influence on the irrigant flow [6, 21]. For ultrasonic activation of an irrigant, an increasing taper positively influences the removal of dentin debris from the root canal when the irrigant is applied continuously in the pulp chamber [22]. However, in this study, the irrigant was delivered in the root canal by a syringe and then activated by an ultrasonically oscillating file. If we only evaluate the individual depressions, it is interesting to notice that the cleaning efficacy from these depressions is very similar, but the dimension of the root canal actually changed from apical to the coronal and from 0.39 mm (1 mm from the WL) to 0.60 mm (5 mm from the WL). According to this result, we could conclude that within this range, the dimension of the root canal did not influence the efficacy of dentin debris removal of the ultrasonic activation of the irrigant, which was delivered by a syringe in the root canal.

The conclusion we can draw from the current study is that the ultrasonically oscillating file could remove dentin debris from the root canal wall up to 3 mm in front of the file tip, coinciding with the observed flow. Furthermore, the root canal curvature had no influence on the irrigant flow.

## References

- [1] J. F. Siqueira and I. N. Rôças, “Clinical implications and microbiology of bacterial persistence after treatment procedures”, *Journal of Endodontics* **34**, 1291–1301 (2008).
- [2] N. A. Baker, P. D. Eleazer, and R. E. Averbach, “Scanning electron microscopic study of the efficacy of various irrigating solutions”, *Journal of Endodontics* **1**, 127–135 (1975).
- [3] J. F. Siqueira, D. C. Lima, F. A. C. Magalhães, H. P. Lopes, and M. de Uzeda, “Mechanical reduction of the bacterial population in the root canal by three instrumentation techniques”, *Journal of Endodontics* **25**, 332–335 (1999).
- [4] K. Gulabivala, B. Patel, G. Evans, and Y.-L. Ng, “Effects of mechanical and chemical procedures on root canal surfaces”, *Endodontic Topics* **10**, 103–122 (2005).
- [5] P. N. R. Nair, S. Henry, V. Cano, and J. Vera, “Microbial status of apical root canal system of human mandibular first molars with primary apical periodontitis after ‘one visit’ endodontic treatment”, *Oral Surgery, Oral Medicine, Oral Pathology, Oral Radiology and Endodontics* **99**, 231–252 (2005).
- [6] C. Boutsioukis, C. Gogos, B. Verhaagen, M. Versluis, E. Kastrinakis, and L. W. M. van der Sluis, “The effect of apical preparation size on irrigant flow in root canals evaluated using an unsteady computational fluid dynamics model”, *International Endodontic Journal* **43**, 874–881 (2010).
- [7] C. Cunningham and E. Senia, “A 3-dimensional study of canal curvatures in the mesial roots of mandibular molars”, *Journal of Endodontics* **18**, 294–300 (1992).
- [8] M. Amato, I. Vanoni-Heineken, H. Hecker, and R. Weiger, “Curved versus straight root canals: the benefit of activated irrigation techniques on dentin debris removal”, *Oral Surgery, Oral Medicine, Oral Pathology, Oral Radiology and Endodontics* **111**, 529–534 (2011).

- [9] T. Rödiger, S. Döllmann, F. Konietschke, S. Drebenstedt, and Hülsmann, “Effectiveness of different irrigant agitation techniques on debris and smear layer removal in curved canals: a scanning electron microscopy study”, *Journal of Endodontics* **36**, 1983–1987 (2010).
- [10] M. Haapasalo, U. Endal, H. Zandi, and J. M. Coil, “Eradication of endodontic infection by instrumentation and irrigation solutions”, *Endodontic Topics* **10**, 77–102 (2005).
- [11] C. Boutsoukias, B. Verhaagen, M. Versluis, E. Kastrinakis, P. R. Wesselink, and L. W. M. van der Sluis, “Evaluation of irrigant flow in the root canal using different needle types by an unsteady computational fluid dynamics model”, *Journal of Endodontics* **36**, 875–879 (2010).
- [12] L. S. Gu, J. R. Kim, J. Ling, K. K. Choi, D. H. Pashley, and F. R. Tay, “Review of contemporary irrigation and agitation techniques and devices”, *Journal of Endodontics* **35**, 791–804 (2009).
- [13] S. J. Lee, M. K. Wu, and P. R. Wesselink, “The effectiveness of syringe irrigation and ultrasonics to remove debris from simulated irregularities within prepared root canal walls”, *International Endodontic Journal* **37**, 672–678 (2004).
- [14] L.-M. Jiang, B. Verhaagen, M. Versluis, and L. W. M. van der Sluis, “The influence of the orientation of an ultrasonic file on the cleaning efficacy of ultrasonic activated irrigation”, *Journal of Endodontics* **36**, 1372–1376 (2010), *See also chapter 9 of this thesis*.
- [15] A. Burleson, J. Nusstein, A. Reader, and M. Beck, “The in vivo evaluation of hand/rotary/ultrasound instrumentation in necrotic human mandibular molars”, *Journal of Endodontics* **33**, 782–787 (2007).
- [16] C. de Gregorio, R. Estevez, R. Cisneros, C. Heilborn, and N. Cohenca, “Effect of edta, sonic and ultrasonic activation on the penetration of sodium hypochlorite into simulated lateral canals: an in vitro study”, *Journal of Endodontics* **35**, 891–895 (2009).
- [17] L.-M. Jiang, B. Verhaagen, M. Versluis, J. Langedijk, P. R. Wesselink, and L. W. M. van der Sluis, “The influence of the ultrasonic intensity on the cleaning efficacy of passive ultrasonic irrigation”, *Journal of Endodontics* **37**, 688–692 (2011), *See also chapter 8 of this thesis*.
- [18] M. Ahmad, T. R. Pitt Ford, and L. A. Crum, “Ultrasonic debridement of root canals: an insight into the mechanisms involved”, *Journal of Endodontics* **13**, 93–101 (1987).
- [19] T. Rödiger, M. Bozkurt, and M. Hülsmann, “Comparison of the vibrating system with syringe and passive ultrasonic irrigation in removing debris from simulated root canal irregularities”, *Journal of Endodontics* **36**, 1410–1413 (2010).
- [20] D. Nguy and C. Sedgley, “The influence of canal curvature on the mechanical efficacy of root canal irrigation in vitro using real-time imaging of bioluminescent bacteria”, *Journal of Endodontics* **32**, 1077–1080 (2006).
- [21] C. Boutsoukias, C. Gogos, B. Verhaagen, M. Versluis, E. Kastrinakis, and L. W. M. van der Sluis, “The effect of root canal taper on the irrigant flow: evaluation using an unsteady computational fluid dynamics model”, *International Endodontic Journal* **43**, 909–916 (2010).
- [22] L. W. M. van der Sluis, M. K. Wu, and P. R. Wesselink, “The efficacy of ultrasonic irrigation to remove artificially placed dentine debris from human root canals prepared using instruments of varying taper”, *International Endodontic Journal* **38**, 764–768 (2005).

# 12

## Sonochemical and high-speed optical characterization of cavitation generated by an ultrasonically oscillating dental file in root canal models \*

**Abstract:** Cavitation has been associated with Passive Ultrasonic Irrigation, but the nature and characteristics of the cavitating bubbles was not yet fully elucidated. Using sensitive equipment, the sonoluminescence (SL) and sonochemiluminescence (SCL) around these files have been measured, showing that cavitation occurs even at a very low power setting. Luminol photography and high-speed visualizations provided information on the spatial and temporal distribution of the cavitation bubbles. A large bubble cloud was observed at the tip of the files, but this was found not to contribute to SCL. Rather, smaller, individual bubbles observed at antinodes of the oscillating file with a smaller amplitude were leading to SCL. Confinements of the size of bovine and human root canals increased the amount of SL and SCL. However, the root canal models also showed the occurrence of air entrainment, resulting in the generation of stable bubbles and droplets near the air-liquid interface and eventual loss of liquid.

---

\*To be submitted to *Ultrasonics Sonochemistry* as: R.G. Macedo, B. Verhaagen, D. Fernandez Rivas, J.G.E. Gardeniers, L.W.M. van der Sluis, P.R. Wesselink and M. Versluis, "Sonochemical and high-speed optical characterization of cavitation generated by an ultrasonically oscillating dental file in root canal models"

## 12.1 Introduction

Ultrasound is regularly used in dentistry in a wide range of therapeutic applications, such as the cleaning and disinfection of the inner and outer surface of a tooth (root canal therapy and root scaling, respectively) [1]. Ultrasonic agitation of disinfecting solutions in the root canal, called Passive Ultrasonic Irrigation (PUI) [2], has been shown to improve the chemical and mechanical efficiency of root canal cleaning procedures [2, 3] and organic tissue dissolution during endodontic therapy [4]. PUI uses an endodontic file, driven at 30 kHz, that has been shown to induce acoustic microstreaming and cavitation, which are claimed as the working mechanisms of ultrasonic agitation [5–7].

The occurrence and use of cavitation during PUI has been discussed frequently over the past two decades. Cavitation has been demonstrated to occur around ultrasonically oscillating endodontic instruments in an unbounded medium [7–13]. Inside the root canal, Ahmad *et al.* [9] argued that cavitation is unlikely to occur, because due to space restrictions the amplitude of oscillation of the endodontic file cannot be high enough to produce cavitation. On the other hand, in a recent article [14] cavitation was shown to occur around the tip of an ultrasonically oscillating file, even within the confinement of a root canal, although only at high driving powers that are not commonly used clinically. Cavitation was also suspected to be causing the enhancement of sonochemical reactions around dental scalers [7]. There is, however, still no clear data on the number, size, location and nature of cavitating bubbles during PUI or on how the confinement of the root canal affects cavitation.

In non-pure liquids, cavitation is usually generated from nuclei, which are small pockets of air on hydrophobic dirt particles or walls. Bubbles can grow when the applied pressure difference is higher than the ambient pressure minus the vapor pressure of the liquid. For water, the ambient pressure is 100 kPa; the vapor pressure is approximately 2 kPa [15, 16]. This pressure difference needs to be generated by the oscillating endodontic file. Low pressures are expected near the trailing edge of the file, where the fluid velocities equals zero; the file itself moves with a velocity  $U = 2\pi fA$  (with  $f$  the oscillation frequency and  $A$  the amplitude of oscillation). The velocity gradient gives rise to a pressure gradient, according to the Navier-Stokes equation that governs the flow dynamics [17]. The velocity and pressure gradients around an endodontic file are similar to those that arise near ship propellers, pumps and homogenizers, where hydrodynamic cavitation is known to occur and lead to damage to the metal surfaces. This type of cavitation is generally referred to as edge or tip cavitation [11, 18–20].

Near an endodontic file, the velocity gradient can be estimated by assuming that the flow velocity around the file is equal to the oscillation velocity of the file  $U$ . The potential for cavitation to be generated is then characterized by the cavitation number  $\sigma$  [15]:

$$\sigma = \frac{P_{\text{ambient}} - P_{\text{vapor}}}{\frac{1}{2}\rho U^2} \quad (12.1)$$

where  $\rho$  is the density of the liquid. Under the condition that nuclei with radii larger than a critical radius are available, cavitation can occur when  $\sigma < 1$ , for which the velocity needs to exceed 15 m/s [15]. The typical frequency of oscillation for endodontic devices is 30 kHz, resulting in a threshold oscillation amplitude of approximately 80  $\mu\text{m}$ , which is a value that endodontic devices are able to attain at high power setting [21, 22].

A distinction can be made between transient cavitation, involving a violent collapse of a bubble, and stable cavitation, which involves more gentle radial oscillations [15]. Typically, transient cavitation is involved in sonochemistry (chemistry induced by sonication) [23–25] and surface modifications (cleaning, erosion) [26], whereas stable cavitation can lead to local enhancement of streaming and mixing [27, 28].

It is also known that cavitating bubbles can emit light [29] (*sonoluminescence*, SL) [30–33]. For SL to occur, the pressure and temperature conditions inside the collapsing bubble have to satisfy the conditions for ionization and subsequent light emission [34]. If a chemiluminescent molecule is present, its reaction with  $\text{OH}\cdot$  radicals also yields light emission, a process known as *sonochemiluminescence* (SCL) [35, 36]. For this, the conditions inside a bubble have to allow for the dissociation of water molecules, leading to  $\text{OH}\cdot$  radicals in this case:



Cavitating bubbles can generate SL or SCL, or both; the population of SL and SCL active bubbles are not exactly the same and strongly overlap [37–39]. The light emissions are generally faint, although SCL signals can be several orders of magnitude more intense than SL [37]. Dark conditions and the use of sensitive photo-multipliers are generally needed in order to detect SL or SCL, which then provide a measure of the amount of SL or SCL producing cavitation bubbles. Long exposure photography can be used as well, to obtain information on the spatial distribution of cavitating bubbles that produce the SCL [40]. Temporal information on the cavitating bubbles can be obtained with a passive acoustic detector [41, 42], however here we will use high-speed imaging, in order to obtain information on both spatial and temporal scales, and on the nature and onset of cavitation around the oscillating endodontic file.

The aims of this study were to quantify and to visualize the occurrence of cavitation around endodontic files. Using sensitive sonochemical methods for detecting SL and SCL, the occurrence of cavitation at various power settings is investigated, as well as the influence of the confinement on the occurrence of cavitation. Using a range of file types, the influence of different cross-sectional shapes, diameters and lengths of files on SL and SCL are studied. The SL and SCL measurements can



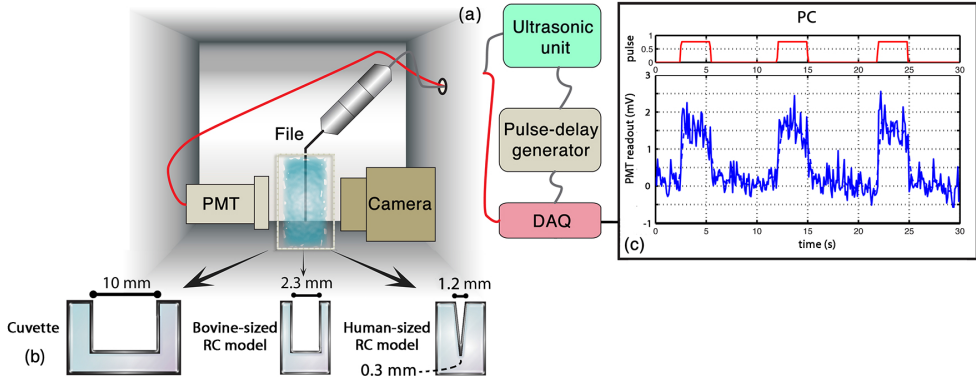


**Figure 12.1:** Sketch of the experimental setup, not to scale. The light-tight box and the equipment it contains is depicted on the right (a), with the models sketched below (b). An example of the SL signal recorded on the PC is shown on the left (c).










provide information on the nature and characteristics of the bubbles. Long-exposure SCL photography and high-speed imaging provide additional visual support on the location and behavior of cavitating bubbles at different operation and confinement conditions.

## 12.2 Materials & Methods

### 12.2.1 Ultrasound setup

A light-tight box with dimension  $1.2 \times 1.0 \times 0.5$  m was constructed (see Figure 12.1); dark conditions inside were verified with long-exposure photography. Inside the box, an endodontic file was positioned in a  $1.0 \times 1.0 \times 4.0$  cm cuvette (Plastibrand, Brand, Wertheim, Germany) or in an in-house manufactured glass root canal (RC) of bovine or human dimensions, submerged and fixed inside the cuvette. The bovine-sized model was a cylindrical closed-end tube of diameter 2.3 mm and a length of 29 mm. The human-sized model was a cone of apical diameter 0.3 mm, a taper of 6% and a length of 20 mm. The two root canal models allowed for the investigation of the influence of confinement on the occurrence of cavitation. The transmission coefficient of light through these glass models was measured and corrected for.

Table 12.1 gives an overview of the various files that have been tested; Figure 12.2 shows a picture of an endodontic file and the different cross-sections. The first number in the file name indicates the diameter (times  $10 \mu\text{m}$ ), the second number indicates the length (in mm). The K-files (Satelec Acteon, Merignac, France) have a square cross-section, the IrriSafe (IS) files (Satelec Acteon) have a square cross-section with rounded edges (with a radius of curvature of approximately  $0.25 \times$  file

File type	K10/21 <sup>a,c</sup>	K10/25 <sup>a,d</sup>	K15/25 <sup>d,f</sup>	K15/25P <sup>f,x</sup>	K25/21 <sup>c,e</sup>	K30/21 <sup>c</sup>	IS25/21 <sup>b,e</sup>	IS25/25 <sup>b,g</sup>	ET25L <sup>g</sup>
<b>Cross-sectional shape</b>									
<b>Sonoluminescence</b>									
<b>Cuvette</b>	×	×	×	×	×	×	×	×	×
<b>Sonoluminescence</b>									
<b>Cuvette</b>	×	×	-	-	×	-	×	×	-
<b>Bovine-sized RC model</b>	-	-	-	-	×	-	×	×	-
<b>Human-sized RC model</b>	-	-	-	-	×	-	×	×	-
<b>Calorimetry</b>									
<b>Cuvette</b>	×	×	×	×	×	×	×	×	×
<b>Bovine-sized RC model</b>	-	-	-	-	×	-	×	×	-
<b>Human-sized RC model</b>	-	-	-	-	×	-	×	×	-

**Table 12.1:** Overview of the file types and measurements on them (×), (a) and (b) allow for comparison of length (21 to 25 mm), (c) and (d) for comparison of diameter (0.10 to 0.25 and 0.30 mm [#10 to #25 and #30]), (e) and (f) for comparison of cross-section (square to Irrisafe), and (g) also for comparison of cross-section (Irrisafe to circular). (x) is polished to the same cross-section as Irrisafe files.

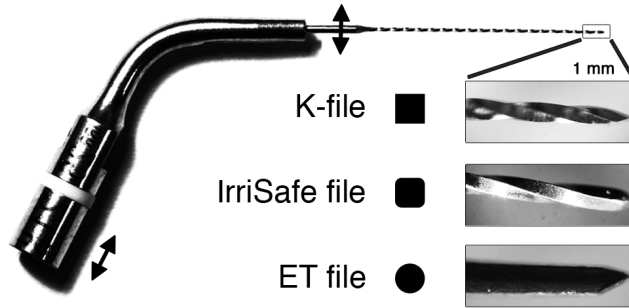


**Figure 12.2:** Picture of an endodontic file and the three different cross-sections. The vibration direction is indicated with arrows.

radius), and the ET25L (Satelec Acteon) has a circular cross-section [43]. One K-file (K15/25) was polished by the manufacturer to the same cross-section as IrriSafe files, in order to compare directly the influence of cross-section.

All files were driven with a commercial endodontic ultrasound device (P-Max, Satelec Acteon, Merignac, France). The power settings on that device range (from low to high) from ‘Green’ via ‘Yellow’ and ‘Blue’ to ‘Red’, each with 10 steps. A previous study showed that the oscillation amplitude increased with power settings, with overlap between ‘10’ and ‘1’ in consecutive power settings [14]. In the sonochemical experiments, the power setting was either increased (three measurements) or decreased (three measurements) between consecutive experiments, in order to investigate the presence of hysteresis. Each measurement group was measured three times; for each measurement a new file and fresh irrigant was used. Files that were suspected to have fractured (exhibited through a sudden drop in SL/SCL signal) were also replaced.

The ultrasound device was switched on and off in cycles with a period of 10 seconds, consisting of 3 seconds ON and 7 seconds OFF (duty cycle of 30%). The rest phase in between pulses should allow the fluid to return to its initial state with respect to its temperature and gas content. These pulses were generated with a pulse-delay generator (TGP110, TTI, Huntingdon, UK).

### 12.2.2 Sonoluminescence and Sonochemiluminescence

For sonoluminescence (SL), the cuvette and root canal models were filled with MilliQ air-saturated water. A photomultiplier tube (PMT; R508, Hamamatsu Photonics, Hamamatsu, Japan) was placed next to the cuvette. The PMT received an electrical voltage of 1.6 kV from a DC power supply (6516A, Hewlett-Packard, Palo Alto, CA, USA). Its output was recorded at a rate of 300 kHz with a high-speed data acquisition device (DAQ; USB-6356, National Instruments, Austin, TX, USA), which was

also recording the pulses. Calibration showed a linear response of the PMT up to an output voltage of 1 V, above which saturation occurs. Typical pulse and PMT signals are shown in Figure 12.1c. The PMT signal was filtered with a running average with Gaussian weighing over 11 samples; the average value during each pulse was used as final SL or SCL value.

For sonochemiluminescence (SCL), air-saturated aqueous luminol (0.1 mM luminol [Merck] in 0.1 M NaOH [Merck]) solution was used, of which more details can be found elsewhere [37]. The same PMT equipment as for SL was used to measure the SCL signal. Simultaneously, photos near the file were taken with a CCD photo-camera (D300, Nikon, Tokyo, Japan) and 50 mm, f/1.8 lens (Nikon) with an aperture of 1.8. The camera exposure was set at 30 seconds, with highest ISO value (Hi1.0) and automatic white balance. A photo was taken in ambient light before the SCL photos were taken, to identify the location of the cuvette or root canal model walls. The sum of the pixel intensity value intensity in a region-of-interest or along the file was calculated from the blue channel of the RGB photos, for quantitative analysis of the luminol photos. The intensity of the blue channel along two files was compared to the oscillation pattern of those files, as simulated with a previously described and validated one-dimensional model for endodontic files oscillating in air [43].

The reliability of the PMT measurements was tested using interclass correlation coefficient among three measurements of SCL of an ET25L file in three consecutive days. Each measurement was repeated six times. A coefficient score of 0.994 for single measurements with  $p < 0.001$  was found, assuring a high reliability and repeatability.

An estimate of the chemical activity of the OH $\cdot$  radicals produced by transient cavitation as compared to those dissolved in a NaOCl solution was made by a fast injection of luminol into the cuvette, filled with a 10% NaOCl solution (Sodium Hypochlorite, Sigma-Aldrich, St. Louis, MO, USA). The PMT response was recorded using the equipment described above. The luminol was injected at a flow rate of 1 mL/min through a 27G needle, driven by a syringe pump (NE1010, New Era Pump Systems, Wantagh, NY, USA).

### 12.2.3 Statistical analysis

Students *t*-tests for independent samples were performed to assess differences in SCL between files with different lengths (21 vs. 25 mm) and cross-sections (Square (K) vs. Square with round edges (Irrisafe) vs. Circular (ET)). ANOVA tests were used to assess the influence of diameter (size 10 vs. 25 vs. 30) in SCL and of the confinement (cuvette vs. bovine sized RC model vs. human sized RC model) in SL. For all tests,  $p$ -values  $< 0.05$  were considered statistically significant.

### 12.2.4 Calorimetry

The acoustic power density radiated by three files was measured inside the cuvette and the two root canal models. A 0.2 mm diameter T-type thermocouple with digital read-out (HI 93552R; HANNA Instruments, Woonsocket, RI, USA), sampling every 2 seconds, was fixed inside the cuvette or, in the case of the root canal models, glued inside a side channel of diameter 1.5 mm located at 2 mm from the apex of the root canal.

The files were driven for 1 minute by the same commercial endodontic device at power setting ‘Blue 1’ or ‘Red 10’. The acoustic power density  $W_{ac}$  (W/L) was determined from the temperature increase  $\Delta T$  measured during  $\Delta t$ :

$$W_{ac} = \frac{\rho c_p \Delta T}{\Delta t} \quad (12.3)$$

with  $\rho$  the density of the liquid and  $c_p$  its specific heat.

### 12.2.5 High-speed visualization

The generation of cavitation bubbles was visualized using a high-speed camera (HPV-1, Shimadzu Corp., Kyoto, Japan), recording at a frame rate of 1 million frames per second. The camera was attached to a microscope (BX-FM, Olympus, Tokyo, Japan) providing  $20\times$  magnification, resulting in a resolution of  $3 \mu\text{m}/\text{pixel}$ . Illumination was provided in bright-field mode using a continuous wave light source (ILP-1, Olympus). The file of interest was positioned parallel or perpendicular to the image plane, such that a side-view of (a section of) the file or its cross-section was visible and in focus. The file itself was submerged in a large water tank ( $75\times 62\times 117$  mm) filled with tapwater. For one set of experiments, degassed water, luminol or NaOCl (10%, Sigma-Aldrich, St. Louis, MO, USA) was used instead of tapwater.

The files were driven at power settings ‘Blue 5’ or ‘Red 5’ using the commercial endodontic ultrasound device (P-Max, Satelec Acteon).

In one additional experiment a dentin disc was placed at a distance of approximately  $200 \mu\text{m}$  from a K15/25 file, in order to investigate the influence of the presence of a wall on the cavitation. The dentin discs (diameter 5 mm, thickness 1.5 mm) were prepared from freshly prepared bovine incisors using a trephine [44].

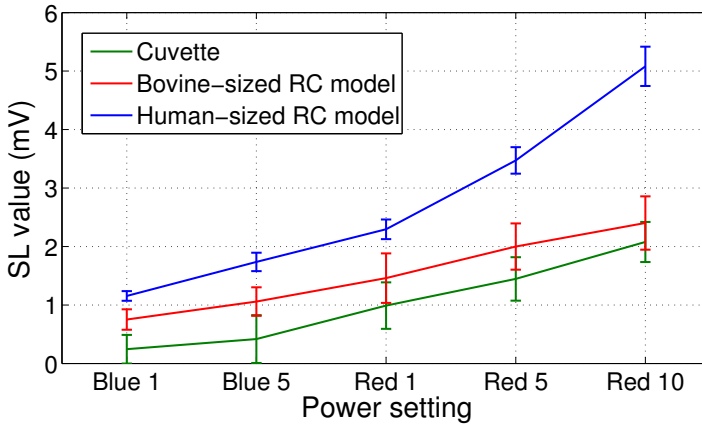


**Figure 12.3:** Average and standard deviation of the SL signal for an IS25/21 file inside different confinements (colors).

## 12.3 Results

### 12.3.1 Sonochemical characterization

#### SL measurements

During each pulse of ultrasound (3 seconds), there was an increase in PMT signal for the SL measurements, rising within 1 second, and falling off to the noise level within 1 second after the pulse ended (see Figure 12.1c for an example). As a general trend, the higher the power, the higher the signal output of the PMT. Below a power setting of ‘Blue 1’ no increase in PMT signal above the noise level could be detected.

The SL signal for one example file (IS25/21) inside the cuvette and bovine- and human-sized root canal models is plotted in Figure 12.3, showing that a smaller confinement (human- versus bovine-sized root canal mode, versus cuvette) increases the SL signal. This trend was observed for all files ( $p < 0.001$ ).

#### SCL measurements

The signal for SCL during each pulse was similar to that of SL, but approximately 3 orders of magnitude higher. Therefore, already at the low power setting of ‘Green 5’ (below the power settings plotted in Figures 12.3 and 12.4) a SCL signal could be observed for several files. The SCL signal as a function of power setting for various files oscillating inside the cuvette, is plotted in Figure 12.4, where the average and standard deviation of the 18 measurements are used. For all files there was an increase in SCL signal for increasing power setting. The SCL signal ranged 5 decades and is highly dependent on the file type. The IrriSafe files both resulted

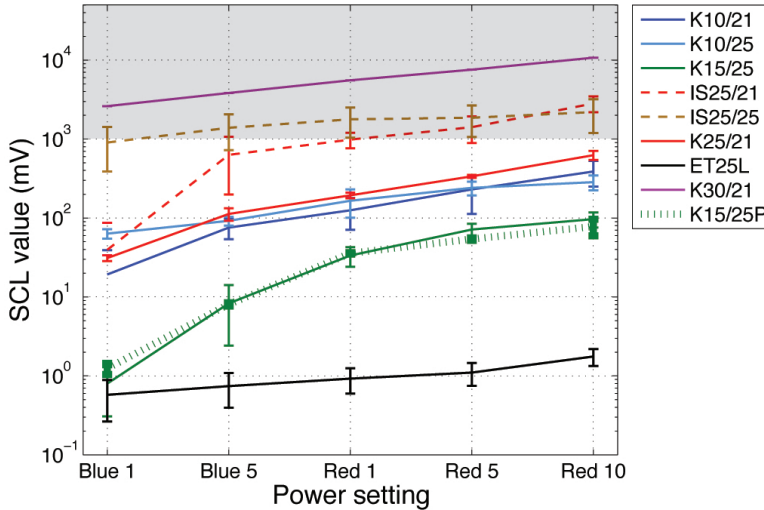


**Figure 12.4:** Average and standard deviation of the SCL signal measured with the PMT for nine different files, with varying length, diameter and cross-section, oscillating inside the cuvette. The shaded area above 1V represents saturated PMT response and therefore underestimated results.

in a SCL value higher than the K-files of similar dimensions ( $p = 0.001$ ). Files with a larger diameter generally also resulted in a higher SCL values ( $p < 0.001$ ). The ET25L, with a circular cross-section, resulted in significantly lower SCL values ( $p < 0.001$ ). The polished K15/25 file showed no differences with the unpolished K15/25 file ( $p = 0.567$ ).

There is no clear correlation between the amount of cavitation observed and the oscillation amplitude of the file tip as measured in a recent study [43], see Figure 12.5. This suggests that not only the oscillation amplitude (as a function of power) but also the file diameter and cross-section have an influence on the generation of cavitation, and further discussion is provided in the remainder of this work.

The injection of luminol into a NaOCl solution showed a rapid increase of the SCL signal, rising within one second to a value of 60 V, where it is fully saturated.

### Comparison of SL and SCL measurements

In Figure 12.6 the SL and SCL results for all files have been normalized to the maximum value of the K30/21 file. Both methods show that the K30/21 file generates most cavitation, followed by the two IrriSafe files. For SL, the ratio between files is different than for SCL, which can be attributed to the generation of bubbles that are either more light-producing or more chemically active [37, 38, 45]. Also, for SCL of several files the PMT was saturated, affecting the relative amplitudes, although the

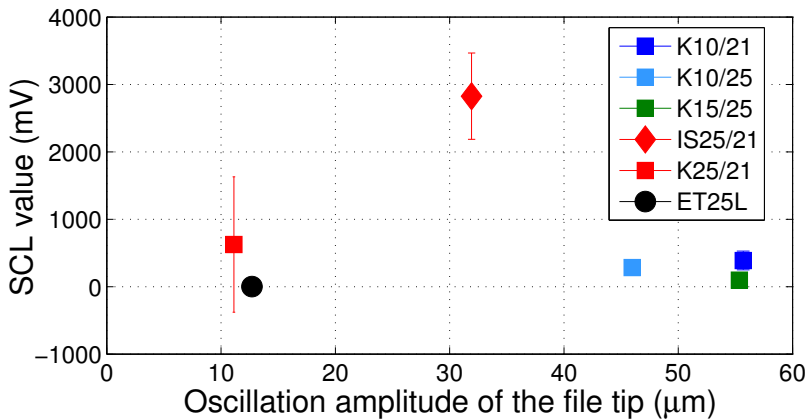


**Figure 12.5:** Average and standard deviation of the SCL signal for six files, plotted versus its oscillation amplitude as determined in a previous study [43].

ordinal scale should not be affected. The increase in cavitation with increasing power setting is also apparent from these plots.

The differences in SL and SCL values between increasing and decreasing the power for consecutive experiments were non-significant. Therefore hysteresis was ruled out, justifying combining the data in the increasing and decreasing power direction for the analysis of the SL and SCL measurements. Also, it can be concluded that the possible changes in temperature and gas content are not enough to alter the overall cavitation features.

### Luminol photography

Overlaying the blue luminol photos with the ambient light photos of the confinements showed a blue area (luminol photo signal) between the file and the wall (see Figure 12.7), especially at the higher power settings. In the cuvette there is a large area of luminol photo signal along the file, with brighter areas along the file that can be related to a distribution of nodes and antinodes along the file, see Figure 12.8. The bright areas are separated by a few millimeters, which is consistent with the distance between the antinodes on an oscillating file in air. The locations of the maxima in the luminol photos and the oscillation patterns do not match exactly, because the oscillation pattern is obtained from a simulation for files oscillating in air [43]; in water or luminol, the wavelength will increase, which will result in a better match of the maxima in the luminol photo intensity with the antinodes. Nevertheless, the areas of higher luminol photo intensity can be associated with the location of the antinodes away from the tip of the file and not with the tip of the file itself. Toward and beyond the tip of the file, the luminol photo intensity decreases.



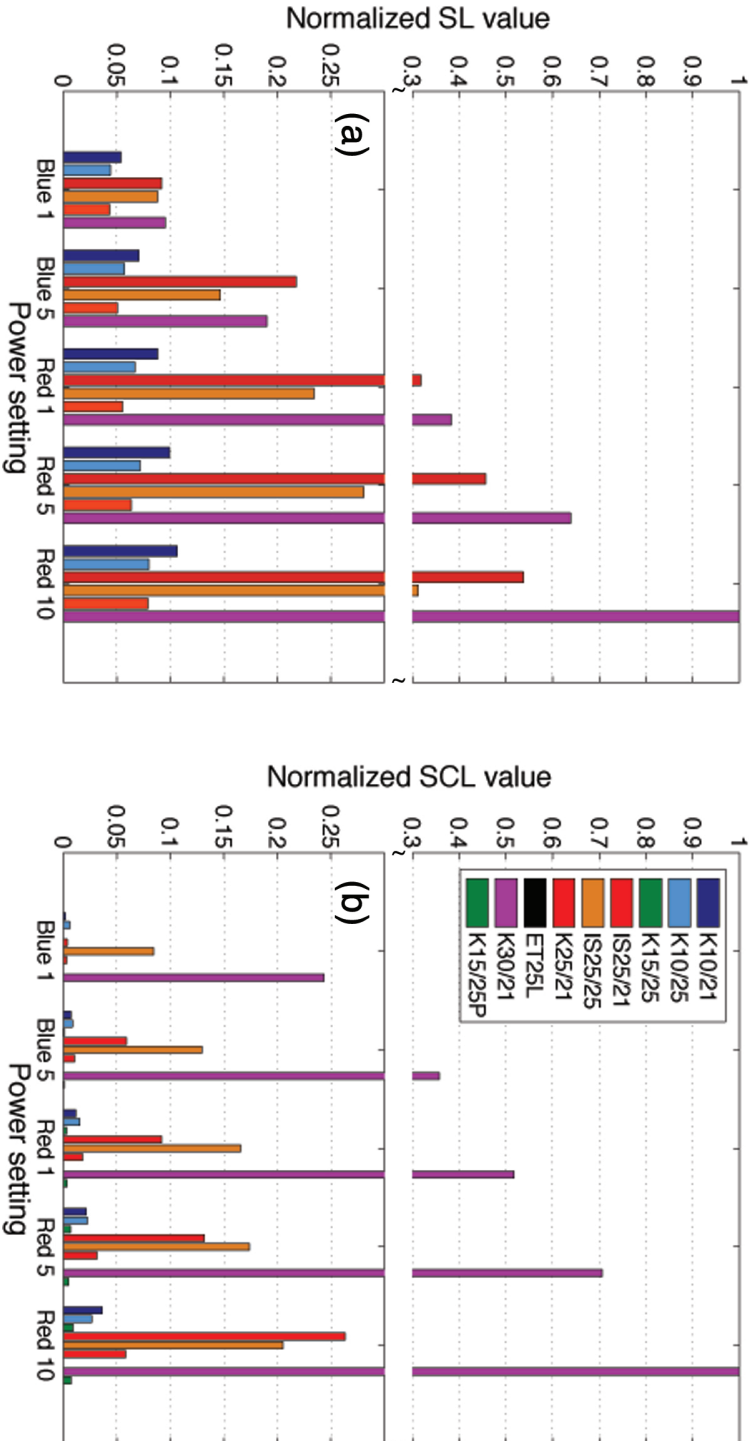


Figure 12.6: SL (a) vs. SCL (b) for various files. Note the double y-axis scaling.

In the confinement of the bovine- and human-sized root canal models, the luminol photo intensity was observed to be uniformly distributed between the file and the wall. The luminol photo signal was also observed beyond the file tip toward the apex of the confinement.

A quantitative analysis of the luminol photos showed an increase of intensity with increasing power (Figure 12.9b). These trends were similar to the SL and SCL results (Figure 12.9a). However, the luminol photos have a resolution of 2 decades whereas the SCL data spanned more than 5 decades, making the luminol photography method less sensitive than the SL and SCL methods.

### Calorimetry

Sonication of the water inside the cuvette showed a linear increase in temperature within the measurement time of 1 minute, see Figure 12.10a. The IS25/25 file driven at the high power setting was found to have the highest slope ( $0.08^{\circ}\text{C}/\text{sec}$ ) and a maximum temperature increase of  $4.9^{\circ}\text{C}$ , with the slope and temperature increase at low power setting being approximately half of those values. The K25/21 and IS25/21 file at the high power both had a slope of  $0.02^{\circ}\text{C}/\text{sec}$ .

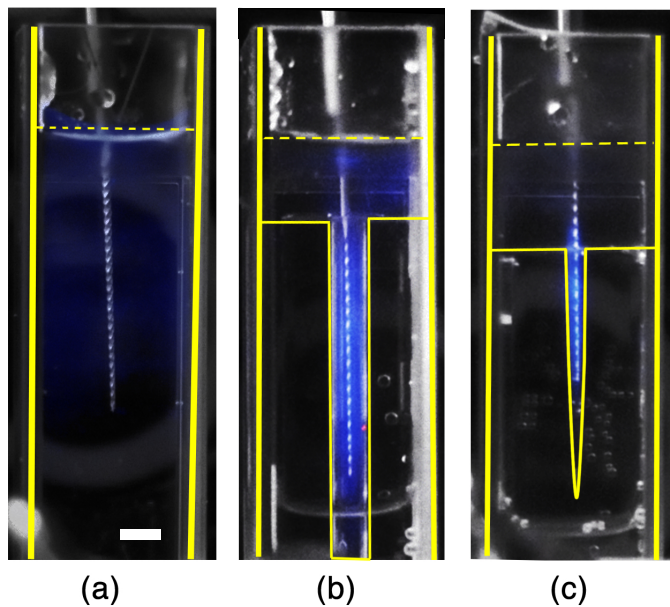


**Figure 12.7:** Overlay of luminol photos (blue) with ambient light photos, showing the spatial distribution of luminol inside the cuvette (a) and bovine-sized (b) and human-sized (c) root canal models. The confinements have been outlined with solid yellow lines; the luminol-air interface is indicated with a dashed yellow line. The white bar in (a) is 2.5 mm wide.

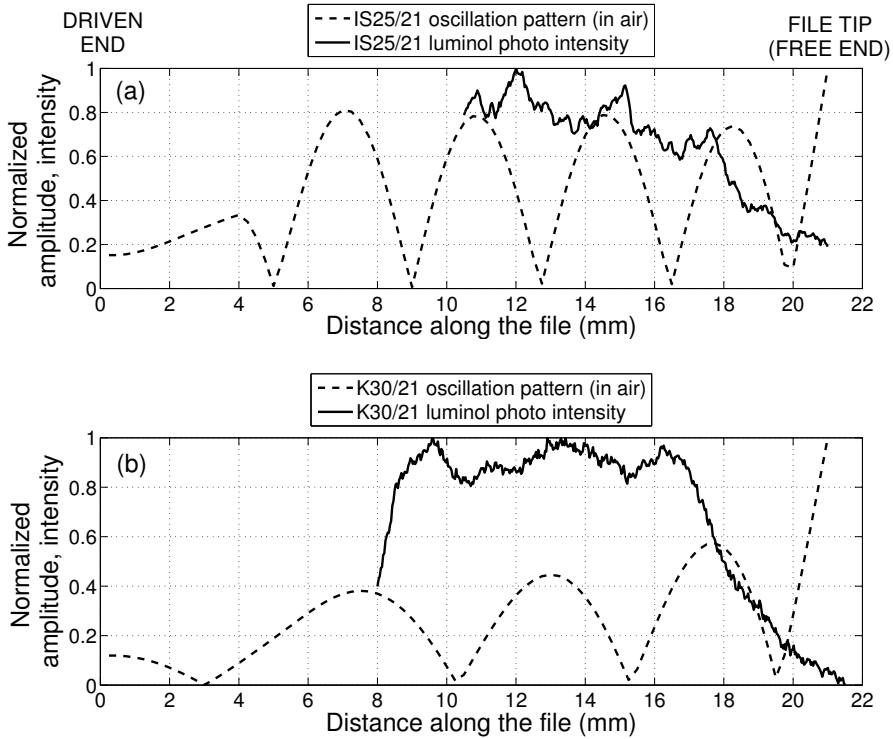


**Figure 12.8:** Comparison of the normalized intensity in the luminol photos of two files with the oscillation characteristics of those files. The oscillation characteristics are obtained from a previously described simulation [43] of the files oscillating in air. In water, the wavelength has been reported to increase, which will improve the match of the maxima in the luminol photo intensity with the antinodes.

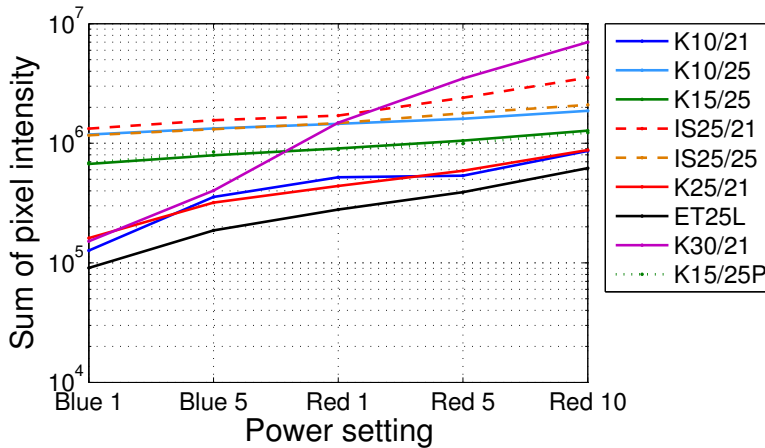


**Figure 12.9:** Luminol intensity for 5 power settings and 9 files, to be compared to Figure 12.4. The photo intensity ranges only three decades, whereas the PMT signal spans 6 decades.

Inside the bovine- and human-sized root canal models (Figure 12.10b and 12.10c, respectively), the temperature increased by 12 and 14°C, respectively, within 1 minute. The slopes were not linear but showed an initial fast rise in temperature, followed by a smaller slope. This change in slope could be due to heat conduction by the glass confinements that starts to play a role after a few seconds.

Table 12.2 shows the acoustic power density as calculated from Figure 12.10a-c and Equation 12.3, assuming a linear temperature increase over time. The acoustic power density is on the order of 0.1-1 W/L. The confinement of the bovine-sized root canal model increased the acoustic power density by a factor of 2.5 to 6, depending on the file. An even smaller confinement, of the size of a human root canal, increased the acoustic power density by another factor of 1.2 to 2.8. In all confinements, the IS25/25 file had the highest acoustic power density, followed by the K25/21 and IS25/21 files.

**Table 12.2:** Acoustic power density (W/L) for three different files and three confinements calculated using Equation 12.3. The files were driven at power setting ‘Red 10’. The standard deviation is 0.07 W/L.

$W_{ac}$ (W/L)	IS25/25	K25/21	IS25/21
Cuvette	0.34	0.07	0.08
Bovine-sized RC model	0.86	0.32	0.48
Human-sized RC model	0.99	0.86	1.35

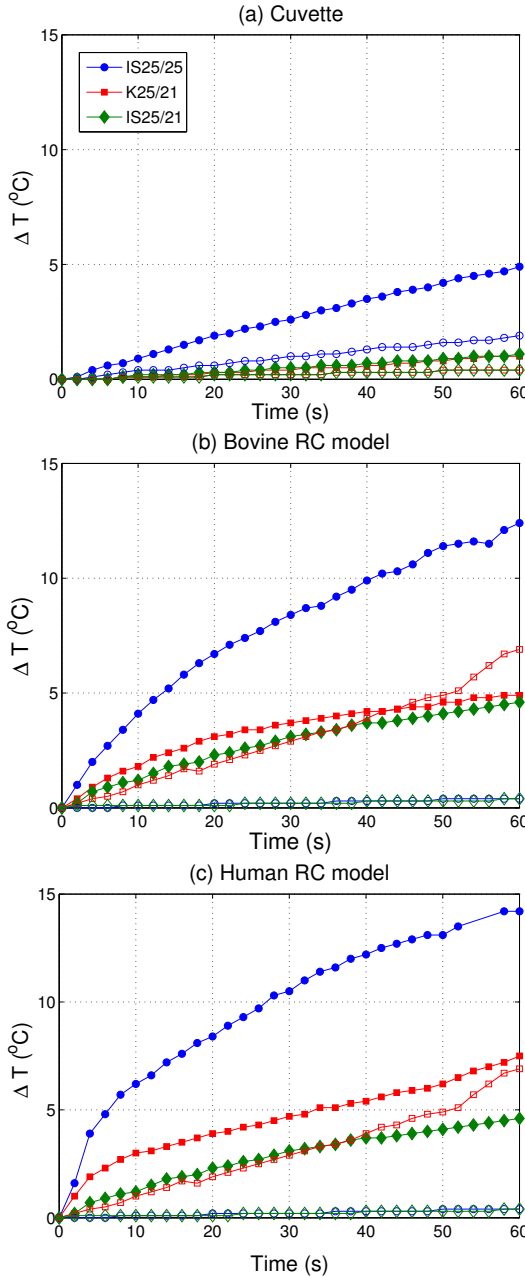


**Figure 12.10:** Plot of temperature increase versus ultrasound insonification time, for three files (colors), inside the cuvette (a) or bovine-sized (b) or human-sized (c) root canal (RC) model. Low and high power are indicated with open and closed symbols, respectively. The values are averages of 3 measurements. The standard deviations are not indicated for clarity but are at most  $1^{\circ}\text{C}$ .

### 12.3.2 High-speed visualization

High-speed recordings provided confirmation of the occurrence of cavitation, dominantly at the tip of the file where a large cloud of bubbles was formed with a size on the order of the file diameter. At subsequent antinodes along the file, single, smaller cavitation bubbles were observed (diameter on the order of  $10\ \mu\text{m}$ ), see Figure 12.11 and Supplementary Movie 1. The generation of the large bubble cloud at the tip of the file can be observed in more detail in the recordings of the cross-section of the file, see Figure 12.12 and Supplementary Movie 2.

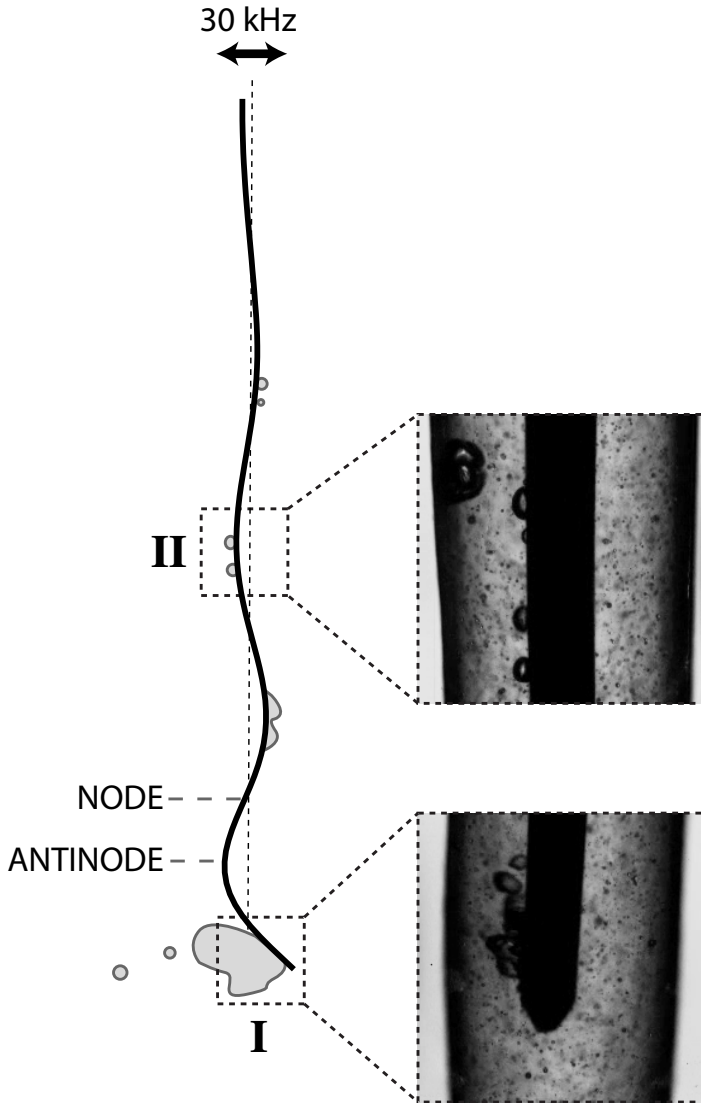
The orientation of the square cross-section was observed to have a large influence on the cavitation formed at the file edges. When the in-focus tip of the file oscillated along the diagonal of the cross-section ('diamond'), cavitation was observed at the edges of the cross-section. However, when the in-focus tip of the file had one side in the direction of oscillation ('square'), the cavitation cloud was observed to form out-of-focus, i.e. at a part of the file with diamond orientation. The distance between square and diamond orientation along the length of the file is  $0.25\ \text{mm}$  [43], whereas the focal depth of the microscope optics is around  $0.10\ \text{mm}$ .

The bubble cloud was observed to start growing in front of the moving file already during the deceleration of the file, i.e. before reaching its maximum displacement. This can be attributed to a phase difference between file oscillation velocity and induced pressure, as predicted in a previous study [22].

The bubble cloud was observed to grow and collapse twice per period in the wake of the oscillating file. Small bubbles with a diameter less than  $5\ \mu\text{m}$  were observed to split off from the bubble cloud and obtain a steady velocity of approximately  $1\ \text{m/s}$  away from the file. These bubbles could be observed for at least  $3\ \text{ms}$  before becoming invisible, which could be due to the bubbles dissolving or the stream of bubbles diverging, thereby moving out of focus. The generated bubbles were therefore likely to be of the stable cavitation type, which was further confirmed by their tendency to flow along a glass wall placed nearby rather than collapse onto it.

Degassing the tap water before oscillating the file resulted in a reduction (to almost zero) in the size of the bubble cloud and the number of bubbles split off (see Figure 12.13), which is as expected since there is less gas and nuclei available to nucleate bubbles. Oscillating the file in a luminol solution appears not to affect the size of the bubble cloud compared to tap water. When using a NaOCl solution, on the other hand, a large increase in size of the bubble cloud was observed and also resulted in larger bubbles being shed off, which is a typical effect of a salty solution that is described in literature [46, 47].

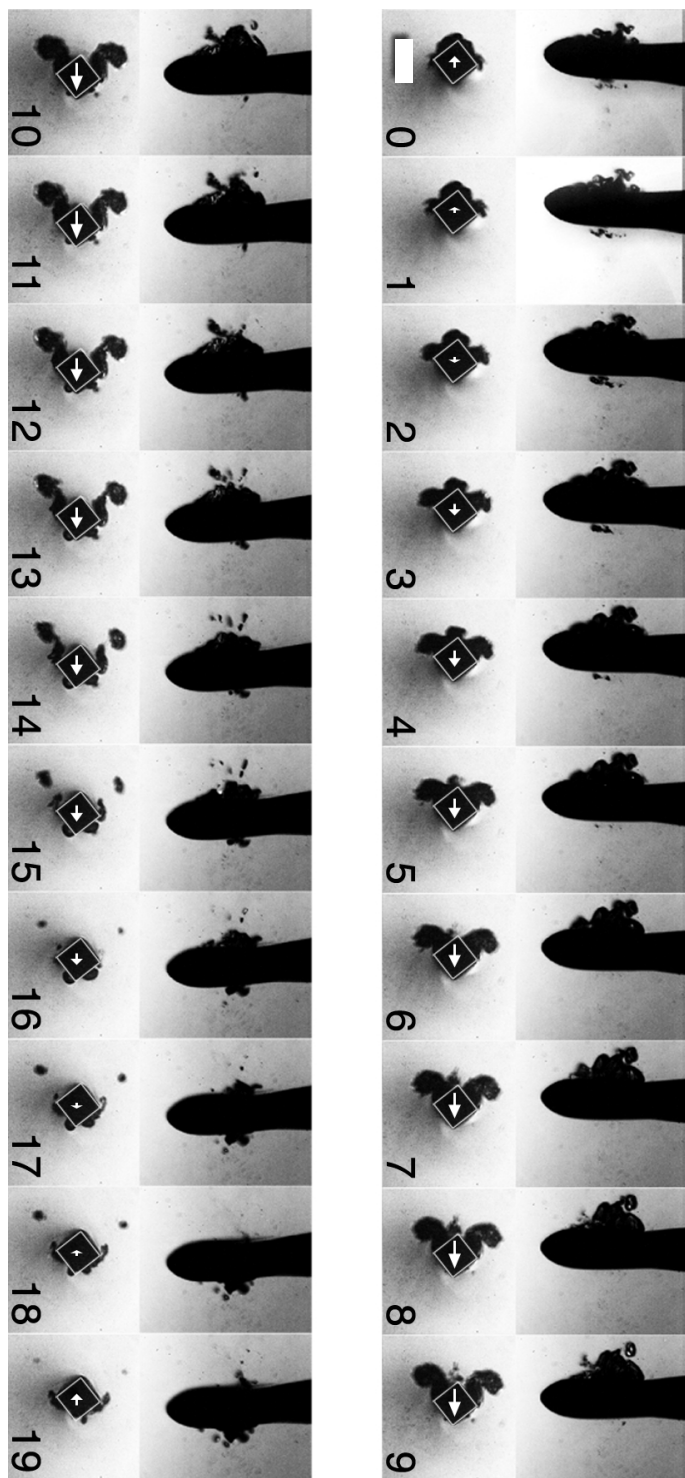
A dentine wall placed within  $200\ \mu\text{m}$  of the oscillating file did not reduce or increase the amount of cavitation occurring close to the file, see Figure 12.14. However, more interesting was the observation that the bubble cloud tended to collapse onto the file rather than the wall, independent of the distance between the file and



**Figure 12.11:** Sketch of the occurrence of cavitation along the length of an oscillating file, based on Supplementary Movie 1. At the tip of the file (I), a large cavitation bubble cloud is formed; at other antinodes (II), only small, single bubbles are observed. Still images are taken from Supplementary Movie 1, where the file is oscillating inside the confinement of a root canal model.

## 12.3. RESULTS

**Figure 12.12:** Cavitation at the tip as visualized from the side (upper rows) and head-on (lower rows), during one half of an oscillation cycle. The white arrows indicate the direction in which the file moves; their length represents velocity magnitude. The numbers indicate time in microseconds. The white bar is 200  $\mu\text{m}$ . See also Supplementary Movie 2 for the cross-sectional view.





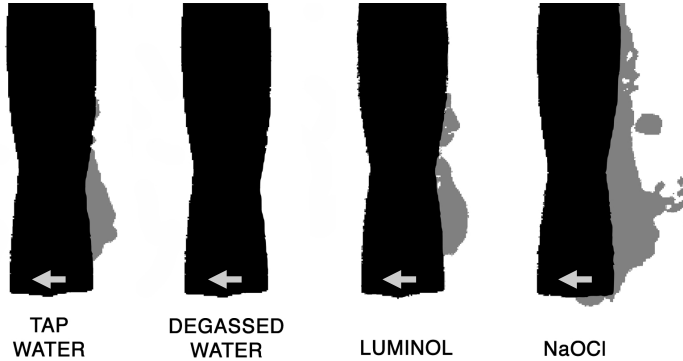


**Figure 12.13:** Representative images of the cavitation cloud (grey) on the tip of a K-file (black), in different liquids. The arrows indicate that the motion of the file is to the left. The diameter of the file at the tip is  $150\ \mu\text{m}$ .

the wall. Cavitating bubbles were only incidentally observed on the dentine wall. Similar observations were made for the file oscillating inside the confinement of the root canal (see Supplementary Movie 1), where cavitation on the glass wall was only observed in a limited number of cases. However, the roughness (potential bubble nucleation sites) of the wall of a real root canal is much larger than that of the glass models employed here, therefore more cavitation is expected inside a real tooth.

The water-air interface at the coronal part of the root canal was observed to be unstable when certain files and insertion depths were used, see Figure 12.15 and Supplementary Movie 3. This instability can be related to an antinode of the oscillating file coinciding with the air-water interface. Droplets were observed to split off from the unstable interface, leading to a reduction of the amount of fluid present in the root canal, as also reported in a previous study [3]. The instability of the interface also led to air entrainment, resulting in large and stable bubbles (more than  $100\ \mu\text{m}$  in diameter) in the root canal liquid volume. Such stable bubbles could oscillate together with the ultrasonic file and exhibit surface oscillations, which can locally increase the streaming significantly, even at remote locations such as inside a side channel of the root canal (see Supplementary Movie 4).

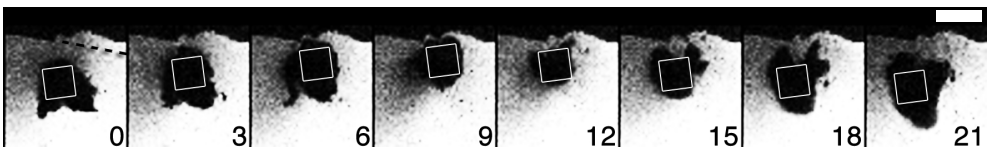


**Figure 12.14:** File next to a dentin wall, showing no collapse of the bubble cloud on the wall. The dashed line in the first panel indicates the original extend of the wall, showing the damage done by the file itself. Numbers indicate time (in  $\mu\text{s}$ ); the white bar is  $200\ \mu\text{m}$ .

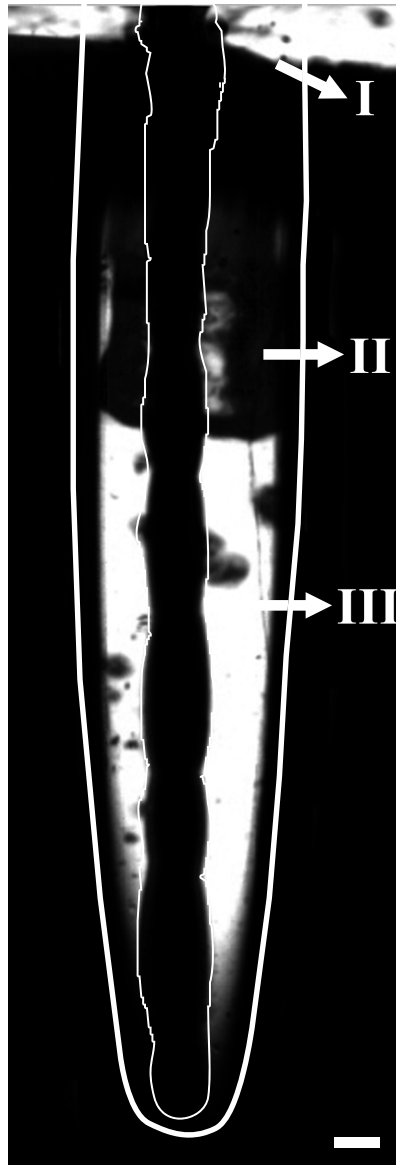


**Figure 12.15:** Air entrainment due to an oscillating file (outlined in white) inside a glass root canal model (thick white line). An antinode of the oscillating file leads to instabilities at the air-irrigant interface (I), resulting in the generation of a spray of droplets of irrigant. After some time, this loss of irrigant results in a large volume fraction of the root canal being occupied by air rather than irrigant (II). Stable bubbles can split off from this air pocket (III). The white bar is 200  $\mu\text{m}$ .

## 12.4 Discussion

The sonochemical and visualization measurements have shown that cavitation can take place around endodontic files, even inside the confinement of a root canal model. The amount of cavitation varied between the file types; the averaged SCL signals spanned 5 decades. Due to the multiple parameters covered by the selection of files (file length, diameter and cross-section), a general trend is not easy to extract. One result is that the polishing of the square cross-section of the IrriSafe files did not affect the SL and SCL signals. A larger diameter did increase the SL and SCL signals, which can be explained by a larger amount of fluid that has to be displaced by a thicker file, leading to larger velocity and pressure gradients. The observation that cavitation could already be measured for very low power setting ('Green 5'), where the oscillation velocity of the file is below the 15 m/s cavitation threshold limit as derived in the introduction, suggests that the fluid flows around the edges of the file with a velocity higher than the oscillation velocity of the file.

This low power setting is one that is actually used in clinic. The high power settings that were required for detection with SL and visualization methods [14] are not used frequently in the clinic for PUI and therefore less relevant.

Changing the file length, diameter or cross-section of the file was shown previously to have a large and not straightforward influence on the file oscillation characteristics [43]. However, no clear relation between SCL value and the predicted oscillation amplitude at the tip of the various files was found (Figure 12.5), in spite of our finding and that of a previous study [12] that a higher amplitude (power setting) for a single file does increase the SCL value. This leads to the hypothesis that the cavitation cloud observed at the tip of the file does not induce a measurable amount of SCL, but that it is rather the smaller bubbles that were observed at the other antinodes that contribute to the SCL emission. This hypothesis is supported by the observation that the IrriSafe files generated a higher SCL signal. The IrriSafe files have a lower tip oscillation amplitude than K-files of similar dimension, but all antinodes on the IrriSafe files have approximately the same amplitude due to the absence of a taper on these files, leading to a preference for more and smaller bubbles all along the file rather than a large bubble cloud at the tip. The K-files typically have a high amplitude at the tip, leading to the formation of the cavitation bubble cloud, but the amplitude of consecutive antinodes decreases rapidly and seems not to generate any cavitation. The luminol photos also support this hypothesis, as generally near the tip of the files the intensity of the blue channel of the photos decreased. It should also be considered that there may be bubbles present with a size smaller than the optical resolution, which nevertheless could contribute to the SL and SCL signals.

The different nature of the large bubble cloud and the small individual bubbles can be explained in the following way. Bubble clouds as the one observed at the file tip are known to affect the sound field in a way that a lower intensity is experienced

by bubbles inside the cloud due to acoustic shielding. As a consequence, the energy focusing effect of each individual bubble collapse and the active bubble population are reduced, leading to less SCL intensity when compared to the single bubbles induced at locations along the file with lower amplitude [48, 49]. It is expected that these spherical bubbles collapse more symmetrically and efficiently and are therefore contributing the most to radical production. Cavitating bubbles in bubble clouds furthermore have a smaller expansion maximum radius [50], which also affects the SL and SCL [49].

Considering the file oscillation amplitude in terms of acoustic power, similar results are reported in the literature. It has been found that higher power can be detrimental to  $\text{OH}\cdot$  radical formation [25, 37]. The reason for this is that a population of smaller and more spherical bubbles is proportionally larger at low power, as the growing and collapsing bubbles do not affect each other yet, contrary to high power. Furthermore, numerical simulations on  $\text{OH}\cdot$  production rate suggest that a decrease of SCL takes place if, due to a high pressure, the bubble temperature inside an air bubble is too high and  $\text{OH}\cdot$  is consumed by oxidizing nitrogen inside the bubble [51]. The bubble temperature can also increase as a result of bubble-bubble interaction with smaller bubbles [52].

As mentioned in the Introduction, cavitating bubbles can generate SL or SCL, or both; the population of SL and SCL active bubbles are not exactly the same and strongly overlap [37–39]. In this chapter we have localized the bubbles that are SCL active using both high-speed imaging and long-exposure luminol photography. Unfortunately, equipment for long-exposure SL photography, as used elsewhere [37, 53], was not available. Whereas we hypothesized that the smaller bubbles observed will be more SCL active than the larger ones, we cannot provide similar evidence for the situation of SL emission.

The calorimetry measurements have shown that during one minute, the temperature of the liquid increases with 1–15°C (Figure 12.10). According to literature [54], a drastic decrease in SL in water takes place as temperature increases from 15 to 70°C. As the temperature increases in the liquid, the gas concentration decreases, making the number of nucleated bubbles decrease. Also the ratio of vapor to gas increases as the solubility of gas decreases, which diminishes SL. Furthermore, the bubble can become saturated by vapor and, in the final stage of the adiabatical collapse, can arrest the compression phase, decreasing the SL intensity. There are several other parameters and reactions taking place inside the bubble (which depend on frequency as well) that are beyond the scope of this study but are reported elsewhere [51, 54–57]. In this study, however, the ultrasound is pulsed with 3 second pulses and 7 second rest intervals, thereby limiting such temperature effects. Pulsation is furthermore reported to have beneficial sonochemical effects, for example when the pulse length is tuned to the dissolution time of the generated bubbles [58].

The reaction between NaOCl and luminol resulted in a SCL value that was much higher than the highest value of SCL produced for all of the files. As saturation of the PMT was likely, the ratio of OH<sup>•</sup> production by cavitation to that dissolved in the NaOCl solution could not be determined. Nevertheless the enhancement by OH<sup>•</sup> production by cavitation to the chemical cleaning effect of NaOCl is probably small.

The observation that the areas of high intensity in the luminol photos are not limited to the vicinity of the file but are actually spread out between the file and the wall, suggests that the reaction between the luminol and the radicals produced by cavitation does not always take place in the vicinity of the file. Cavitation can also take place at crevices in the circumferential wall and tiny bubbles that have split off from the bubble cloud (possibly smaller than the optical resolution of 3  $\mu\text{m}/\text{pixel}$ ). Such interpretation has been observed and numerically modeled in a recent article [59]. Inside the root canal confinements the acoustic field may be such that even beyond the file tip cavitation of small bubbles can occur. These small bubbles do not lose their sphericity and are therefore very SCL active compared to the larger bubbles observed.

A smaller confinement was found to lead to an increase in the SL and SCL signals. This could be attributed to the increase in acoustic power density emitted within these confined geometries, due to the presence of the root canal walls [60], but also to the increase in pressures as predicted in a previous study [22]. It should be noted that the human-sized root canal model has a conical shape rather than a cylindrical shape, which could affect the SL and SCL signals because of the decreasing space around the file toward its tip. It should be also noted that the cuvette might not be considered an ‘unconfined’ case, as the sides of the cuvette are only 50 times larger than the typical diameter of a file.

In the present study, the files were positioned in the center of the root canal during the sonochemical characterization experiments, which however is difficult inside the small human-sized root canal model. A recent study [61] has indicated that, during clinical use of passive ultrasonic irrigation, contact with a wall cannot be avoided, which introduces a secondary, audible frequency on top of the 30 kHz oscillation. These two frequencies can lead to constructive or destructive interference, resulting in occasionally higher or lower velocities, with an associated probability of cavitation occurrence (see Supplementary Movie 5).

The bubble cloud at the file tip tended to collapse on the file itself, not on a nearby wall, where removal of biofilms and smear layer is required. Erosion and cleaning of a solid hard wall takes place by jetting of collapsing bubbles and shock waves induced upon collapse [26, 62, 63]. However, bubbles collapsing near a soft wall may generate a jet away from the wall, thereby pulling the soft material off the wall [64]. Therefore if the file is close to the wall when the bubble collapses, this cavitation cloud may enhance the cleaning of root canals, without causing erosion

damage to the dentin wall.

The reported observation during clinical use of PUI that droplets are generated outside of the root canal cavity [65], suggests that the instability of the irrigant-air interface and resulting air entrainment as shown here, does indeed take place. Air entrainment was also often observed for the glass models employed in this study when not submerged in the cuvette, leading to a root canal filled with large air bubbles. Air entrainment results in loss of irrigant, in the extreme case preventing generation of acoustic streaming [22], for which a fluid is required. The stable bubbles entrained, however, could itself enhance the cleaning of the root canal system. Also the SL emission may increase, as suggested in different studies, where the gas uptake by the liquid at higher powers resulted in an increased SL value [66]. The free surface oscillation itself has previously been reported to negatively affect SCL values [37, 67].

The SL and SCL methods of cavitation detection used in this chapter were more sensitive than the method using the luminol photos (Figure 12.9). Therefore, previous studies using luminol photography [7, 13] probably underestimated the occurrence of cavitation, which is present already for lower power settings as this study shows. Nevertheless, the luminol photos are useful in obtaining information on the spatial distribution of cavitation (for instance Figure 12.8), which cannot be obtained from the SL and SCL PMT measurements. Other dosimetry methods have been reported in the literature, e.g. terephthalic acid (TA) ([68]). However, a pilot study showed that the concentration range that was generated with our ultrasound equipment was below the sensitivity level of the TA method. Another dosimetry method reported recently [69], using tert-butyl nitrite (t-BuONO), is a more promising method and has been proven to be applicable *ex vivo* up to the volume of bovine root canals. A comparison with the present methodology remains to be performed. In future work, additional temporal detail and insight into the oscillatory or transient nature of the cavitation can be obtained using passive acoustic detection.

The high-speed imaging performed in the present study can provide additional information on the occurrence of cavitation in a small region-of-interest during a short time span, whereas the luminol photos show a large region-of-interest time-averaged over several seconds. The combination of these three techniques is then a good approach for an integral characterization of endodontic files and equipment. This article has shown that such characterization of cavitation in passive ultrasonic irrigation is relevant because cavitation occurs and may contribute to mechanical and chemical cleaning.

## 12.5 Conclusion

The generation of cavitation in different root canal models, generated by the oscillation of several endodontic files, was demonstrated even at low power settings by

means of sonochemical (SL and SCL) and optical techniques. This methodology of testing endodontic devices was found to be sensitive and is a useful method in the characterization of existing or new endodontic files and devices.

The amount of cavitation varied between the files; the averaged SCL signals spanned 5 decades. Due to the multiple parameters covered by the selection of files (file length, diameter and cross-section), a general trend is not easy to extract. Generally speaking, a larger diameter increased the cavitation activity. The confinement of a bovine and a human root canal was mimicked and showed an increase of cavitation activity by an increase in the number and size of the bubbles, and an increase in the SL and SCL values.

High-speed recordings showed that a cloud of cavitation bubbles, generated at the sharp edges of a file with a square cross-section, only collapsed on the file itself and not on a nearby wall. This bubble cloud did not contribute to SCL, but may help the root canal cleaning by pulling on material on a nearby wall. At antinodes with smaller amplitude, small individual bubbles were observed and suspected to contribute to the major part of the SL and SCL values.

Air entrainment in the liquid volume leading to stable cavitation bubbles was also demonstrated.

## Acknowledgements

The authors would like to thank Sib Jan Boorsma and Gert-Wim Bruggert for constructing the light-tight box and Cock Harteveld at COPS (University of Twente) for the loan of the PMT equipment. We furthermore acknowledge Roy Kooijman of TCO (University of Twente) for manufacturing the glass root canal models, Michel Hoogenkamp at ACTA for the dentin discs, and Francis Dieras at Satelec Acteon and Olivier Breguet at FKG for polishing the files to the specific cross-section.

## References

- [1] A. D. Walmsley, "Applications of ultrasound in dentistry", *Ultrasound in Medicine and Biology* **14**, 7–14 (1988).
- [2] L. W. M. Van der Sluis, M. Versluis, M. K. Wu, and P. R. Wesselink, "Passive ultrasonic irrigation of the root canal: a review of the literature", *International Endodontic Journal* **40**, 415–426 (2007).
- [3] R. G. Macedo, P. R. Wesselink, F. Zaccheo, D. Fanali, and L. W. M. Van der Sluis, "Reaction rate of NaOCl in contact with bovine dentine: effect of activation, exposure time, concentration and pH", *International Endodontic Journal* **43**, 1108–1115 (2010).
- [4] W. R. Moorer and P. R. Wesselink, "Factors promoting the tissue dissolving capability of sodium hypochlorite", *International Endodontic Journal* **15**, 187–196 (1982).

- [5] L.-M. Jiang, B. Verhaagen, M. Versluis, and L. W. M. Van der Sluis, “The influence of the oscillation direction of an ultrasonic file on the cleaning efficacy of passive ultrasonic irrigation”, *Journal of Endodontics* **36**, 1372–1376 (2010), *see also Chapter 7 of this thesis*.
- [6] M. Ahmad, T. Pitt Ford, and L. Crum, “Ultrasonic debridement of root canals: An insight into the mechanisms involved”, *Journal of Endodontics* **13**, 93–101 (1987).
- [7] T. Joyce Tiong and G. J. Price, “Ultrasound promoted reaction of rhodamine B with sodium hypochlorite using sonochemical and dental ultrasonic instruments”, *Ultrasonics Sonochemistry* **19**, 358–364 (2012).
- [8] A. D. Walmsley, “Ultrasound and root canal treatment: the need for scientific evaluation”, *International Endodontic Journal* **20**, 105–111 (1987).
- [9] M. Ahmad, T. R. Pitt Ford, L. A. Crum, and A. J. Walton, “Ultrasonic debridement of root canals: Acoustic cavitation and its relevance”, *Journal of Endodontics* **14**, 486–493 (1988).
- [10] W. R. E. Laird and A. D. Walmsley, “Ultrasound in dentistry. part 1 - biophysical interactions”, *Journal of Dentistry* **19**, 14–17 (1991).
- [11] R. A. Roy, M. Ahmad, and L. A. Crum, “Physical mechanisms governing the hydrodynamic response of an oscillating ultrasonic file”, *International Endodontic Journal* **27**, 197–207 (1994).
- [12] S. C. Lea, G. J. Price, and A. D. Walmsley, “A study to determine whether cavitation occurs around dental ultrasonic scaling instruments”, *Ultrasonics Sonochemistry* **12**, 233–236 (2003).
- [13] B. Felver, D. V. King, S. C. Lea, G. J. Price, and A. D. Walmsley, “Cavitation occurrence around ultrasonic dental scalers”, *Ultrasonics Sonochemistry* **16**, 692–697 (2009).
- [14] L.-M. Jiang, B. Verhaagen, M. Versluis, J. Langedijk, P. R. Wesselink, and L. W. M. Van der Sluis, “The influence of the ultrasonic intensity on the cleaning efficacy of passive ultrasonic irrigation”, *Journal of Endodontics* **37**, 688–692 (2011), *see also Chapter 8 of this thesis*.
- [15] C. E. Brennen, *Cavitation and bubble dynamics* (Oxford University Press) (1995).
- [16] L.-M. Jiang, B. Verhaagen, M. Versluis, and L. W. M. Van der Sluis, “Evaluation of a sonic device designed to activate irrigant in the root canal”, *Journal of Endodontics* **36**, 143–146 (2010), *see also Chapter 9 of this thesis*.
- [17] P. Kundu and I. Cohen, *Fluid mechanics*, 3rd edition (Elsevier Academic Press, San Diego, CA, USA) (2004).
- [18] R. E. A. Arndt, V. H. Araki, and H. Higuchi, “Some observations of tip-vortex cavitation”, *Journal of Fluid Mechanics* **229**, 269–289 (1991).
- [19] F. Hegedüs, C. Hös, Z. Pandula, and L. Kullmann, “Measurement of the cavitating vortex shedding behind rectangular obstacles”, in *25th IAHR Symposium on Hydraulic Machinery and Systems. IOP Conference Series: Earth and Environmental Science*, volume 12, 012066 (2010).
- [20] W. Wienken, J. Stiller, and A. Keller, “A method to predict cavitation inception using large-eddy simulation and its application to the flow past a square cylinder”, *Journal of Fluids Engineering* **218**, 316–325 (2006).



- [21] S. C. Lea, A. D. Walmsley, and P. J. Lumley, "Analyzing endosonic root canal file oscillations: an in vitro evaluation", *Journal of Endodontics* **36**, 880–883 (2010).
- [22] B. Verhaagen, C. Boutsoukis, L. W. M. Van der Sluis, and M. Versluis, "Acoustic streaming induced by ultrasonically oscillating endodontic files", *Physics of Fluids (to be submitted)* (2012), *see also Chapter 6 of this thesis*.
- [23] K. Suslick, S. Doktycz, and E. Flint, "On the origin of sonoluminescence and sonochemistry", *Ultrasonics* **28**, 280–290 (1990).
- [24] M. Ashokkumar and T. J. Mason, *Sonochemistry* (John Wiley & Sons, Inc.) (2000).
- [25] D. Fernandez Rivas, A. Prosperetti, A. G. Zijlstra, D. Lohse, and H. J. G. E. Gardeniers, "Efficient sonochemistry through microbubbles generated with micromachined surfaces", *Angewandte Chemie International Edition* **49**, 9699–9701 (2010).
- [26] D. Fernandez Rivas, B. Verhaagen, J. Seddon, A. G. Zijlstra, L.-M. Jiang, L. W. M. Van der Sluis, A. Prosperetti, M. Versluis, D. Lohse, and H. J. G. E. Gardeniers, "Localized removal of layers of metal, polymer or biomaterial by cavitating microbubbles", *Biomicrofluidics* **6**, 034114 (2012), *see also Chapter 16 of this thesis*.
- [27] P. Marmottant, M. Versluis, N. De Jong, S. Hilgenfeldt, and D. Lohse, "High-speed imaging of an ultrasound-driven bubble in contact with a wall: "narcissus" effect and resolved acoustic streaming.", *Experiments in Fluids* **41**, 147–153 (2006).
- [28] R. H. Liu, J. Yang, M. Z. Pindera, M. Athavale, and P. Grodzinski, "Bubble-induced acoustic micromixing", *Lab Chip* **2**, 151–157 (2002).
- [29] E. N. Harvey, "Sonoluminescence and sonic chemiluminescence", *Journal of the American Chemical Society* **61**, 2392–2398 (1939).
- [30] F. Young, "Sonoluminescence from water containing dissolved gases", *The Journal of the Acoustical Society of America* **60**, 100 (1976).
- [31] K. Suslick, N. Eddingsaas, D. Flannigan, S. Hopkins, and H. Xu, "Extreme Conditions during Multibubble Cavitation: Sonoluminescence as a Spectroscopic Probe", *Ultrasonics Sonochemistry* **18**, 842–846 (2011).
- [32] D. Lohse, "Sonoluminescence-Cavitation hots up", *Nature* **434**, 33–34 (2005).
- [33] C. Ohl, T. Kurz, R. Geisler, O. Lindau, and W. Lauterborn, "Bubble dynamics, shock waves and sonoluminescence", *Philosophical Transactions of the Royal Society of London. Series A: Mathematical, Physical and Engineering Sciences* **357**, 269–294 (1999).
- [34] S. Hilgenfeldt, S. Grossmann, and D. Lohse, "A simple explanation of light emission in sonoluminescence", *Nature* **398**, 402–405 (1999).
- [35] S. Hatanaka, H. Mitome, K. Yasui, and S. Hayashi, "Single-bubble sonochemiluminescence in aqueous luminol solutions", *Journal of the American Chemical Society* **124**, 10250–10251 (2002).
- [36] P. Kanthale, M. Ashokkumar, and F. Grieser, "Sonoluminescence, sonochemistry (h<sub>2</sub>o<sub>2</sub> yield) and bubble dynamics: Frequency and power effects", *Ultrasonics Sonochemistry* **15**, 143 – 150 (2008).

- [37] D. Fernandez Rivas, M. Ashokkumar, T. Leong, K. Yasui, T. Tuziuti, S. Kentish, D. Lohse, and H. J. Gardeniers, "Sonoluminescence and sonochemiluminescence from a microreactor", *Ultrasonics Sonochemistry* **19**, 1252–1259 (2012).
- [38] A. Brotchie, F. Grieser, and M. Ashokkumar, "Effect of power and frequency on bubble-size distributions in acoustic cavitation", *Physical Review Letters* **102**, 84302 (2009).
- [39] J. Lee, M. Ashokkumar, S. Kentish, and F. Grieser, "Determination of the size distribution of sonoluminescence bubbles in a pulsed acoustic field", *Journal of the American Chemical Society* **127**, 16810–16811 (2005).
- [40] H. N. McMurray and B. P. Wilson, "Mechanistic and spatial study of ultrasonically induced luminol chemiluminescence", *The Journal of Physical Chemistry A* **103**, 3955–3962 (1999).
- [41] R. O. Cleveland, O. A. Sapozhnikov, M. R. Bailey, and L. A. Crum, "A dual passive cavitation detector for localized detection of lithotripsy-induced cavitation in vitro", *Journal of the Acoustical Society of America* **107**, 1745–1758 (2000).
- [42] C. C. Coussios, C. H. Farny, G. ter Haar, and R. A. Roy, "Role of acoustic cavitation in the delivery and monitoring of cancer treatment by high-intensity focused ultrasound (hifu)", *International Journal of Hyperthermia* **23**, 105–120 (2007).
- [43] B. Verhaagen, S. C. Lea, L. W. M. van der Sluis, A. D. Walmsley, and M. Versluis, "Oscillation characteristics of endodontic files: numerical model and its validation", *IEEE - Transactions on Ultrasonics, Ferroelectrics and Frequency Control* **accepted** (2012), *see also Chapter 4 of this thesis*.
- [44] D. M. Deng and J. M. Ten Cate, "Demineralization of dentin by streptococcus mutans biofilms grown in the constant depth film fermentor", *Caries Research* **38**, 54–61 (2004).
- [45] S. Labouret and J. Frohly, "Bubble size distribution estimation via void rate dissipation in gas saturated liquid. application to ultrasonic cavitation bubble fields", *The European Physical Journal Applied Physics* **19**, 39–54 (2002).
- [46] L. W. M. Van der Sluis, M. P. J. M. Vogels, B. Verhaagen, R. G. Macedo, and P. R. Wesselink, "Study on the influence of refreshment/activation cycles and irrigants on mechanical cleaning efficiency during ultrasonic activation of the irrigant", *Journal of Endodontics* **36**, 737–740 (2010).
- [47] M. Wall, M. Ashokkumar, R. Tronson, and F. Grieser, "Multibubble sonoluminescence in aqueous salt solutions", *Ultrasonics Sonochemistry* **6**, 7–14 (1999).
- [48] Z. Zeravcic, D. Lohse, and W. van Saarloos, "Collective oscillations in bubble clouds", *Journal of Fluid Mechanics* **680**, 114–149 (2011).
- [49] S. Hatanaka, K. Yasui, T. Kozuka, T. Tuziuti, and H. Mitome, "Influence of bubble clustering on multibubble sonoluminescence", *Ultrasonics* **40**, 655–660 (2002).
- [50] K. Yasui, Y. Iida, T. Tuziuti, T. Kozuka, and A. Towata, "Strongly interacting bubbles under an ultrasonic horn", *Physical Review E* **77**, 016609 (2008).
- [51] K. Yasui, T. Tuziuti, and Y. Iida, "Optimum bubble temperature for the sonochemical production of oxidants", *Ultrasonics* **42**, 579–584 (2004).

- [52] K. Yasui, A. Towata, T. Tuziuti, T. Kozuka, and K. Kato, "Effect of static pressure on acoustic energy radiated by cavitation bubbles in viscous liquids under ultrasound", *The Journal of the Acoustical Society of America* **130**, 3233–3242 (2011).
- [53] M. Ashokkumar, J. Lee, Y. Iida, K. Yasui, T. Kozuka, T. Tuziuti, and A. Towata, "Spatial distribution of acoustic cavitation bubbles at different ultrasound frequencies", *ChemPhysChem* **11**, 1680–1684 (2010).
- [54] Y. Didenko, D. Nastich, S. Pugach, Y. Polovinka, and V. Kvochka, "The effect of bulk solution temperature on the intensity and spectra of water sonoluminescence", *Ultrasonics* **32**, 71 – 76 (1994).
- [55] D. Flannigan and K. Suslick, "Plasma formation and temperature measurement during single-bubble cavitation", *Nature* **434**, 52–55 (2005).
- [56] E. Flint and K. Suslick, "The temperature of cavitation", *Science* **253**, 1397 (1991).
- [57] K. Okitsu, T. Suzuki, N. Takenaka, H. Bandow, R. Nishimura, and Y. Maeda, "Acoustic multibubble cavitation in water: A new aspect of the effect of a rare gas atmosphere on bubble temperature and its relevance to sonochemistry", *The Journal of Physical Chemistry B* **110**, 20081–20084 (2006).
- [58] C. Dekerkcheer, K. Bartik, J.-P. Lecomte, and J. Reisse, "Pulsed sonochemistry", *The Journal of Physical Chemistry A* **102**, 9177–9182 (1998).
- [59] D. Fernandez Rivas, L. Stricker, A. G. Zijlstra, H. J. G. E. Gardeniers, D. Lohse, and A. Prosperetti, "Ultrasound nucleated bubbles and their sonochemical radical production", *Ultrasonics Sonochemistry* **accepted** (2012).
- [60] Y. Iida, K. Yasui, T. Tuziuti, Sivakumar, and Y. Endo, "Ultrasonic cavitation in microspace", *Chemical Communications* 2280–2281 (2004).
- [61] C. Boutsioukis, B. Verhaagen, A. D. Walmsley, M. Versluis, and L. W. M. Van der Sluis, "Occurrence of contact during passive ultrasonic irrigation", *International Endodontic Journal* **to be submitted** (2012), *see also Chapter 5 of this thesis*.
- [62] D. Krefting, R. Mettin, and W. Lauterborn, "High-speed observation of acoustic cavitation erosion in multibubble systems", *Ultrasonics sonochemistry* **11**, 119–123 (2004).
- [63] T. J. C. Terwisga, P. A. Fitzsimmons, L. Ziru, and E. J. Foeth, "Cavitation erosion - a review of physical mechanisms and erosion risk models", in *Proceedings of the 7th International Symposium on Cavitation CAV2009*, 1–13 (2009).
- [64] E.-A. Brujan, K. Nahen, P. Schmidt, and A. Vogel, "Dynamics of laser-induced cavitation bubbles near an elastic boundary", *Journal of Fluid Mechanics* **433**, 251–281 (2001).
- [65] *Personal communication with several endodontists*.
- [66] A. Henglein, R. Ulrich, and J. Lilie, "Luminescence and chemical action by pulsed ultrasound", *J. Am. Chem. Soc.* **111**, 1974–1979 (1989).
- [67] T. Tuziuti, K. Yasui, T. Kozuka, and A. Towata, "Influence of liquid-surface vibration on sonochemiluminescence intensity", *The Journal of Physical Chemistry A* **114**, 7321–7325 (2010).

- [68] S. L. Lea, G. J. Price, and A. D. Walmsley, "A study to determine whether cavitation occurs around dental ultrasonic scaling instruments", *Ultrasonics Sonochemistry* **12**, 233–236 (2005).
- [69] R. G. Macedo, S. I. Nikitenko, B. Verhaagen, D. Fernandez Rivas, J. G. E. Gardeniers, M. Versluis, and L. W. M. Van der Sluis, "Sonochemical dosimetry with iso-butyl nitrite and its potential application in dental research", *Ultrasonics Sonochemistry* **(to be submitted)** (2012).

## 12.A Supplementary material

(Online at [http://stilton.tnw.utwente.nl/rootcanalcleaning/Gallery\\_of\\_Irrigant\\_Motion](http://stilton.tnw.utwente.nl/rootcanalcleaning/Gallery_of_Irrigant_Motion))

Movie 1 - Cavitation along the file Composition of 15 high-speed recordings of a file (oscillating shape in the center) oscillating inside a glass root canal model (walls). The sinusoidal oscillation pattern of the file can be seen. A cloud of cavitation bubbles can be observed at the tip of the file; smaller cavitation bubbles occur at other antinodes. Recording speed is 500 Kfps; the diameter of the file is 200  $\mu\text{m}$ .

Movie 2 - Cavitation around a square cross-section High-speed recording of the generation of a cavitation cloud around a file with a square cross-section, viewed toward the tip of the file. Recording speed is 1 Mfps; the cross-section has sides of 200  $\mu\text{m}$ .

Movie 3 - Air entrainment High-speed recording of the instability of the air-irrigant interface at the coronal opening of the root canal. Once the instability has developed, droplets can be observed to split off. After some time, the irrigant loss is significant, leading to air entrainment in the root canal. The final frame shows the state after 1 second. Recording speed is 10 Kfps; the file diameter is 200  $\mu\text{m}$ .

Movie 4 - Stable bubble oscillations Stable oscillations of a bubble trapped in a side channel. These bubbles were generated by air entrainment during a preceding experiment. The bubble oscillates optimally if its resonance frequency matches the frequency of the oscillating file, for which the bubble radius should be 100  $\mu\text{m}$ . Recording speed is 10 Kfps, the file diameter is 200  $\mu\text{m}$ .

Movie 5 - Contact with a wall Oscillation of a file inside a cylindrical confinement, as viewed toward the tip. The file was put in contact with the wall on purpose, leading to a secondary frequency of the file oscillation. Beating of these two frequencies leads occasionally to a high velocity moving the file away from the wall, during which cavitation at the file tip can be observed. Recording speed is 125 Kfps; the diameter of the confinement is 600  $\mu\text{m}$ .



## **Part III**

# **Laser-Activated Irrigation**



# 13

## Laser-activated irrigation within root canals: cleaning efficacy and flow visualization \* †

**Abstract:** The dentin debris removal efficiency of laser-activated irrigation is evaluated here with the groove model, together with a visualization *in vitro* of the fluid dynamics during the activation of the irrigant by an Er:YAG laser, using high-speed imaging at a relevant timescale. Laser-activated irrigation was significantly more effective in removing dentine debris from the apical part of the root canal than passive ultrasonic irrigation or hand irrigation when the irrigant was activated for 20 seconds. The high-speed recordings suggest that streaming, caused by the collapse of the laser-induced cavitation bubble, is the main cleaning mechanism of LAI. Shockwaves, generated upon bubble collapse, generated cavitation as well.

---

\*Published as: S.D. de Groot, B. Verhaagen, M. Versluis, M.-K. Wu, P.R. Wesselink and L.W.M. van der Sluis, "Laser-activated irrigation within root canals: cleaning efficacy and flow visualization", *International Endodontic Journal* **42**, pp. 1077-1083 (2009)

†The high-speed imaging and theoretical analysis in this chapter are part of the present thesis. The dentin debris removal experiments are due to Sjoerd de Groot.



## 13.1 Introduction

An important procedure during root canal treatment is the irrigation of the root canal. Needle irrigation is the standard procedure but unfortunately, needle irrigation is not effective in the apical part of the root canal [1–4] and in isthmuses or oval extensions [5, 6]. Therefore, acoustic and hydrodynamic activation of the irrigant have been developed [7–9], which have been shown to contribute to the cleaning efficiency [8–10]. The physical mechanisms underlying these cleaning procedures, however, are not well-understood [11].

Laser-activated irrigation (LAI) has been introduced as a powerful method for root canal irrigation [12–14]. The laser radiation produces transient cavitation in the liquid through optical breakdown by strong absorption of the laser energy [12]. LAI can result in smear layer removal from the root canal wall, but also cause extrusion of irrigant through the apex [13, 14]. However, the removal of dentine debris from the root canal by LAI has not yet been studied. Furthermore, Blanken & Verdaasdonk [12] suggested repeating their visualization experiment with a single high-speed camera recording, visualizing a single pulse, to improve the understanding of the cavitation process.

The purpose of this study was to evaluate *ex vivo* the removal of artificially placed dentine debris in standardized root canals by needle irrigation, passive ultrasonic irrigation (PUI) and LAI. LAI was also visualized *in vitro* using high-speed imaging at a timescale relevant to the cleaning process ( $\mu$ s). The resulting flow is theoretically described using a fluid-dynamical model.

## 13.2 Materials and methods

### 13.2.1 Dentine debris removal

Maxillary canines with straight root canals were decoronated; the length of the remaining root was 15 mm for all teeth. The roots were then embedded in self-curing acrylic resin (Ostron 100, GC Tokyo, Japan) and then split longitudinally through the canal in mesio-distal direction. To remove the imprint of the root canal, both halves were ground with sand paper and fixed with four screws (see Figure 13.1a). Then, the root canals were prepared by K-files hand instruments (Dentsply Maillefer, Ballaigues, Switzerland) and mechanically driven Race NiTi instruments (FKG Dentaire, La Chaux-de-Fonds, Switzerland), to a length of 15 mm, size 35 and 0.06 taper resulting in a standardized root canal. To verify the standardization of the models, the canal diameter of six randomly chosen models was measured at 2, 6 and 10 mm from the apical end of the canal, using a KS100 Imaging system 3.0 (Carl Zeiss Vision GmbH, Halbermoos, Germany). At 2 mm, the average canal diameter was found to be  $0.47 \pm 0.02$  mm (diameter of the Race NiTi instrument: 0.47 mm); at 6 mm the

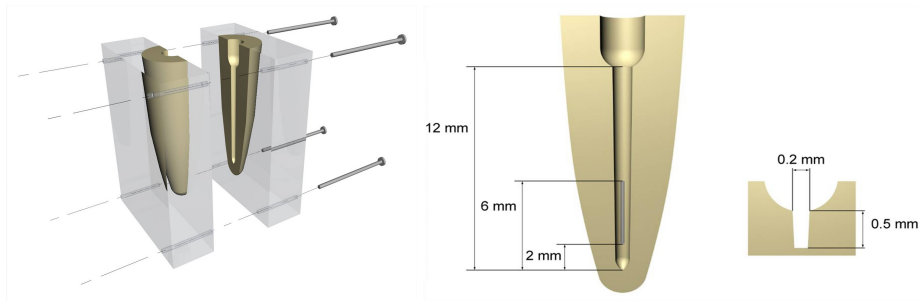


**Figure 13.1:** Schematic representations of the standardized root canal model (a), its groove (b), and its cross section (c).

average canal diameter was  $0.71 \pm 0.02$  (0.71) and at 10 mm the diameter was  $0.94 \pm 0.02$  (0.95). These measured values demonstrate that the root canals were indeed uniform and standardized.

The coronal 3 mm of the canal was enlarged by a no. 23 round bur (Dentsply Maillefer) with a diameter of 2.3 mm, simulating a pulp chamber. A standard groove of 4 mm in length, 0.5 mm deep and 0.2 mm wide, situated at 26 mm from working length (see Figure 13.1b,c), was cut in the wall of one-half of each root canal with an ultrasonically driven tip (P5 Booster, Satelec, Acteongroup, Merignac, France). The dimension of the groove was comparable with that of an oval extension of a root canal. Each groove was filled with dentine debris mixed with 2% NaOCl to simulate a situation in which dentine debris accumulates in uninstrumented canal extensions (Lee et al. 2004). This model was introduced to standardize the root canal anatomy and the amount of dentine debris present in the root canal before the irrigation procedure, in order to increase the reliability of dentine debris removal evaluation. The methodology is sensitive and the data are reproducible [15].

Three irrigation protocols were tested. In all groups, the needle, wire and fibre were inserted 1 mm short of the working length and were moved slowly up and down 4 mm in the apical half of the root canal; the activation time was 20 seconds, the total irrigation time was 50 s and the total irrigant volume was 4 mL. In group 1 ( $n = 20$ ) needle irrigation with 4 mL of 2% NaOCl solution was performed with a 10 mL syringe and a 30 gauge needle (Navitip, Ultradent, South Jordan, UT, USA). In group 2 ( $n = 20$ ), the 2% NaOCl solution was activated by ultrasound using PUI. A stainless steel noncutting wire (size 20) (Irrisafe, Satelec, Acteongroup) was used, driven by an ultrasonic device (Suprasson Pmax Newtron, Satelec, Acteongroup) at power setting blue 4 (frequency 30 KHz, displacement amplitude ca.  $30 \mu\text{m}$  according to the manufacturer). Subsequently the canal was flushed with 2 mL of 2% NaOCl solution using a 10 mL syringe and a 30 gauge needle. In group 3 ( $n = 20$ ), the 2%

NaOCl solution was activated by laser radiation (KEY2 laser, KaVo Dental GmbH, Biberach, Germany) from an optical fibre laser tip with outer diameter 280  $\mu\text{m}$  and length 30 mm (type Gr. 30 28, Kavo Dental GmbH). Calibration by the manufacturer showed that the optical fibre has a reduction factor of 0.36, which results in a fluence of 146  $\text{mJ}/\text{mm}^2$  for a laser pulse energy setting of 100 mJ. The Er:YAG laser emits at a wavelength of 2.94  $\mu\text{m}$  which coincides with the major absorption band of water [16]. A pilot study demonstrated that the optimal settings for dentine debris removal from the root canal are a low power setting of 80 mJ per pulse and a pulse repetition frequency of 15 Hz. Finally, the canal was flushed with 2 mL of 2% NaOCl solution using a 10 mL syringe and a 30 gauge needle.

After irrigation the root canals were dried with paper points. Subsequently, the two halves were separated and the amount of debris in the groove was evaluated. Before and after the irrigation, a digital image was taken of the groove, using a Photomakroskop M400 microscope with a digital camera (Wild, Heerbrugg, Switzerland) at 40 $\times$  magnification. The quantity of dentine debris in the groove before and after irrigation was scored double blind and independently by three dentists using the following scores: score 0: the groove is empty, score 1: less than half of the groove is filled with dentine debris; score 2: more than half of the groove is filled with dentine debris; score 3: the groove is completely filled with dentine debris. The differences in dentine debris scores between the different groups were analysed by means of the Kruskal-Wallis and Mann-Whitney tests (level of significance  $\alpha = 0.05$ ).

### 13.2.2 High-speed imaging experiments

An optical setup was constructed in order to visualize the effect of the Er:YAG laser radiation in an artificial root canal containing water or NaOCl. Optical recordings were made at a pulse repetition rate of the Er:YAG laser of 1 Hz and a pulse energy between 80 and 250 mJ per pulse. The laser fibre tip was inserted up to 1 mm from the apical end of a glass root canal model. The canal was 12 mm in length with an apical diameter of 0.35 mm and taper 0.06. Imaging was performed using a high-speed camera (FastCam APXRS, Photron, Tokyo, Japan), recording at a frame rate of 14 000 frames per second, attached to a microscope with 12 $\times$  magnification (SZX12, Olympus, Tokyo, Japan). The root canal model was illuminated in bright-field by a continuous wave light source (ILP-1, Olympus).

## 13.3 Results

### 13.3.1 Dentine debris removal

The debris scores before and after irrigation are presented in table 13.1. The difference between the groups was statistically significant (Kruskal-Wallis test,  $P < 0.0001$ ).

The debris score in group 3 was significantly lower than group 2 ( $P = 0.002$ ) and group 1 ( $P < 0.0001$ ), and the score in group 2 was significantly lower than group 1 ( $P < 0.0001$ ).

### 13.3.2 High-speed imaging experiments

The high-speed recordings of the laser activity inside the artificial (glass) canal showed that irrigant was vapourized by the laser pulse energy and that a large vapour bubble was created at the fibre tip, similar to that observed previously [17]. The bubble grew with a velocity of the order of 1 m/s during the pulse duration (see Figure 13.2 and Movies 1 and 2); a higher energy laser pulse corresponded to a longer growth time of the bubble. When the laser pulse ended, the bubble collapsed with a velocity of the order of 1 m/s. Upon collapse, a shockwave was generated [18], whose negative-pressure tail caused secondary cavitation in the root canal with a relatively large bubble near the collapse site (which was usually at the apex). The cavitation bubble then collapsed again and this cycle repeated for a number of times, until it was damped out within a few milliseconds (6 ms at 250 mJ per pulse). Smaller bubbles with a typical diameter of 10  $\mu\text{m}$  remain buoyant for a longer time (even up to the next pulse), also at the apical end of the root canal.

The laser-induced bubble grew predominantly in the coronal direction, as there was a confinement at the apex. The depth reached by this bubble depended on the position of the fibre and the laser energy, but never fully extended to the apex. It was observed that when a small bubble was present at the apex, it grew during the collapse phase of the laser-induced bubble and collapsed and renucleated in anti-phase with the laser-induced bubble (figure 13.2a (indicated with the no. 4 in panel *p*), whereas in Figure 13.2b this bubble was not present).

It was observed that the laser-induced bubble grew larger when NaOCl was used as an irrigant solution. Consequently, it had a longer collapse time as compared with having water as an irrigant. It was also found that a higher amount of smaller bubbles were present after laser activation when using NaOCl as the irrigant solution.

Because of the impulsive growth of the laser-induced bubble the fluid was pushed outward at the free surface at the coronal part (see Figure 13.3 and Movie 3). For a laser energy exceeding 120 mJ per pulse it was observed that some fluid was ejected from the root canal, leaving less irrigant in the root canal.

## 13.4 Discussion

The results of the *ex vivo* experiments demonstrate that within the time frame of 20 seconds, LAI is more effective in removing dentine debris from an artificial groove in the apical part of the root canal than ultrasonically activated or syringe irrigation.

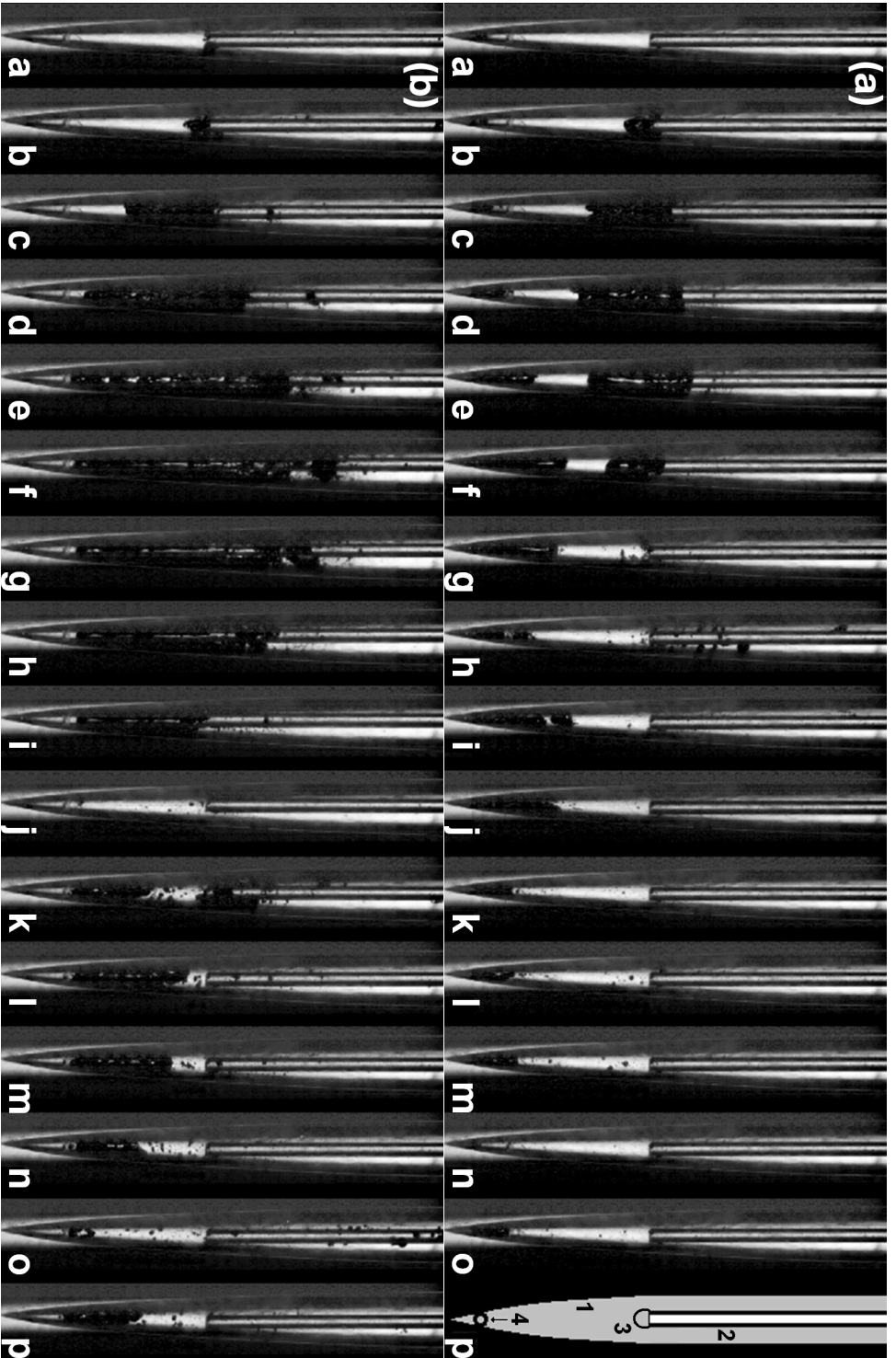


**Figure 13.2:** (Movies 1 and 2) Visualization of the laser-generated vapor bubble. The laser energy was 60 mJ per pulse in (a) and 250 mJ per pulse in (b). Image sequence is from left to right. The interframe time is 140  $\mu$ s. Panel p in (a) shows a sketch of the setup, with 1) the root canal model, 2) the laser fiber tip (outer diameter 280  $\mu$ m), 3) the laser-induced cavitation bubble, and 4) a stable cavitation bubble at the apex.

Score:	0 n (%)	1 n (%)	2 n (%)	3 n (%)
Needle irrigation	0	0	4 (20%)	16 (80%)
Ultrasonic irrigation	6 (30%)	8 (40%)	6 (30%)	0
Laser-activated irrigation	16 (80%)	4 (20%)	0	0

**Table 13.1:** Dentine debris score in the groove after the irrigation procedures per group (no. cases and percentage of total; 20 cases in total for each irrigation procedure). Scoring system: 0: the groove is empty; 1: less than half of the groove is filled with debris; 2: more than half of the groove is filled with debris; 3: the complete groove is filled with debris.

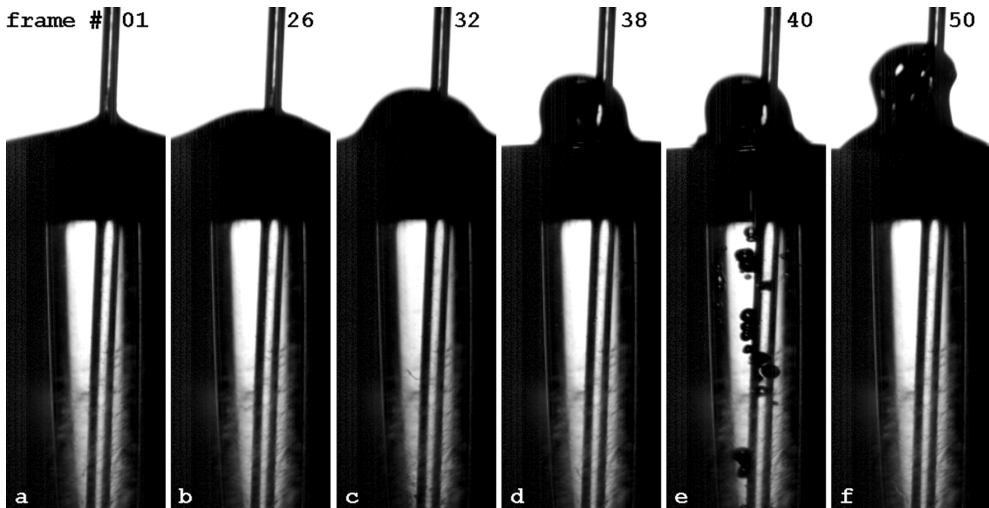


**Figure 13.3:** (Movie 3) Pinch-off at the free surface at the coronal part of the glass root canal model. Secondary cavitation bubbles are formed (in e) upon passage of a shockwave generated by the vapor bubble inertial collapse at the laser fiber tip. The frame rate is 14,000 frames/second.

The high-speed recordings have shown that vaporization of the irrigant causes a large bubble to grow, which then collapses and renucleates a few times. During this process, secondary cavitation bubbles are formed. The fluid flow associated with such an inertial collapse, combined with acoustic streaming resulting from the oscillations of smaller bubbles, could explain the cleaning efficacy of LAI; however, a more detailed study is required to elucidate the principal cleaning mechanism. The secondary cavitation bubbles can also assist in the cleaning of the root canal wall, as they are excited by the bubble collapse of the consecutive laser pulse. As the flow does not penetrate all the way into the apex, a trapped bubble in the apex (most likely a remainder of previous laser pulses) could assist in the cleaning of the apical part of the root canal.

The irrigant flow in the root canal due to the collapsing laser-induced bubble can be modeled by a flow in concentric annuli for heights above the insertion depth of the fibre. For the typical flow velocity of 1 m/s (value obtained from the high-speed recordings by measuring the bubble wall displacement between consecutive frames), the Reynolds number  $Re = \frac{Ud\rho}{\mu}$  (with  $U$  the flow velocity,  $d$  the distance between the cylinders,  $\rho$  the density of the liquid and  $\mu$  the dynamic viscosity) for a flow in annuli is of the order of 300. According to Rothfus *et al.* [19], the transition to turbulence occurs over the range 2100-3700, therefore the flow in this problem is treated as laminar flow.

Rothfus *et al.* [19] also give the laminar flow velocity distribution for flow in concentric annuli:

$$u(r) = 2u_{av} \frac{r_1^2 - r^2 + \left( \frac{r_2^2 - r_1^2}{\ln\left(\frac{r_2}{r_1}\right)} \right) \ln\left(\frac{r}{r_1}\right)}{r_2^2 + r_1^2 - 2r_m^2} \quad (13.1)$$

where  $r_m$  is the radius of maximum velocity, given by:

$$r_m = \sqrt{\frac{r_2^2 - r_1^2}{2 \ln\left(\frac{r_2}{r_1}\right)}} \quad (13.2)$$

Using  $\tau = -\mu \frac{\partial u}{\partial r}$  the shear stress for laminar flow in annuli is given by:

$$\tau(r) = -2\mu u_{av} \frac{\left( \frac{r_2^2 - r_1^2}{r} \right) - 2r \ln\left(\frac{r_2}{r_1}\right)}{(r_2^2 + r_1^2) \ln\left(\frac{r_2}{r_1}\right) - r_2^2 + r_1^2} \quad (13.3)$$

Using standard values for density  $\rho = 1000 \text{ kg/m}^3$  and dynamic viscosity  $\mu = 1 \cdot 10^{-3} \text{ m}^2/\text{s}$ , and a measured average velocity  $u_{av} = 5 \text{ m/s}$  and cylinder radii  $r_1 = 140 \text{ }\mu\text{m}$  (inner) and  $r_2 = 300 \text{ }\mu\text{m}$  (outer), the shear stress on the inner wall is  $496 \text{ N/m}^2$

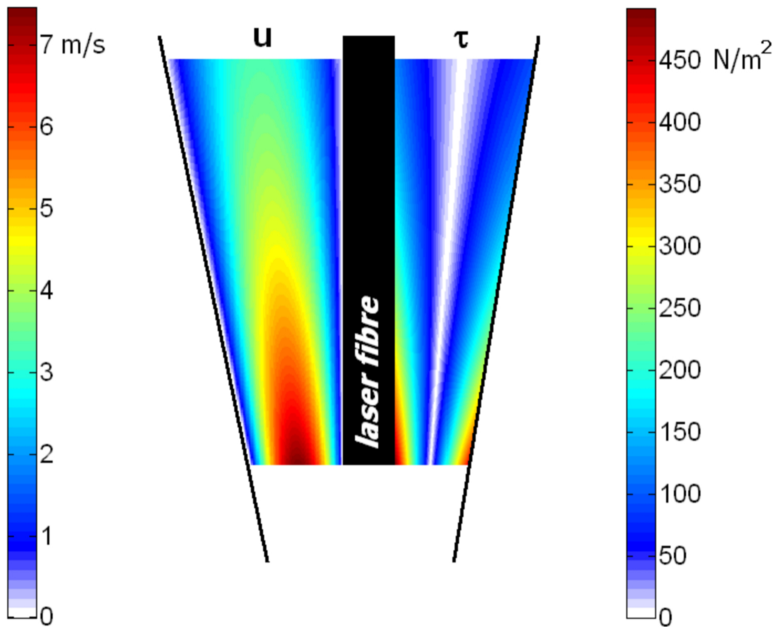


**Figure 13.4:** Average velocity profile (left) and shear stress distribution (right) between two concentric cylinders of which the outer cylinder represents the tapered root canal wall. The average velocity at the laser fiber tip is set at 5 m/s. The region below the laser fiber tip is intentionally left blank, as details of the streaming pattern in the apical part are missing and are part of a future study.



and on the outer wall  $436 \text{ N/m}^2$ . These values are one order of magnitude lower than the shear stress generated by a laser-induced cavitation bubble of radius  $0.75 \text{ mm}$  next to a single wall, which is reported to generate a shear stress of up to  $3.5 \cdot 10^3 \text{ N/m}^2$  [20]. No quantitative data on the adhesion strength of dental intracanal biofilms to dentine or its failure shear stress is available in the literature.

Figure 13.4 shows the velocity profile calculated with the theory described above in a tapered canal with a cylinder inserted, assuming an average velocity of  $5 \text{ m/s}$  at the fibre tip (taken from experiment). The profile on the left of the inner cylinder is the velocity profile; the profile on the right is the shear stress distribution. The plot clearly shows that on the inner cylinder (the laser fibre) the shear stress is higher than on the outer cylinder (the root canal wall).

The root canal diameter increases with height, therefore the average velocity decreases with height. This results in the shear stress being highest next to the tip of the laser fibre. LAI is therefore expected to be most effective in the region close to the fibre tip, with decreasing efficiency away from the tip.

Using a 27G needle and a volume flow rate of  $0.30 \text{ mL/s}$  [21] it follows that the typical fluid velocity in needle irrigation is of the order of  $1 \text{ m/s}$  at the needle orifice, which is the same order of magnitude as the flow velocities developed with LAI. Likewise for PUI with  $u = \frac{\omega e_0^2}{a}$  ( $\omega = 2\pi f =$  oscillation frequency,  $e_0 =$  oscillation amplitude and  $a =$  file radius [22]) a typical fluid velocity of the order of  $1 \text{ m/s}$  was found. One possible explanation for the improvement in cleaning efficacy with LAI is the impulsive nature of the laser-generated bubble dynamics. Because of the pulsations the fluid becomes accelerated at every pulse and the acceleration gives rise to inertial forces, whereas a steady streaming as in needle irrigation and PUI only exerts viscous stress. This would also explain why the irrigation duration is an important factor and why a high pulse repetition rate of the laser is more efficient than a lower one, as found in the pilot-study.

Previous studies have shown side-effects caused by the use of these types of lasers in the root canal. Carbonization of the root canal and cracks were observed when laser tips were used in the root canal [23]. Kimura *et al.* [24] have shown a temperature increase of the root canal wall of  $3\text{-}6 \text{ }^\circ\text{C}$ . The current study did not monitor these side effects, because the aim of this study was clarification of the fluid mechanical working mechanisms.

## 13.5 Conclusion

Laser-activated irrigation was more effective in removing the artificially placed dentine debris from the root canal than needle irrigation or PUI when the irrigant was activated for 20 seconds.

## References

- [1] Z. Ram, "Effectiveness of root canal irrigation", *Oral Surgery, Oral Medicine, Oral Pathology* **44**, 306–312 (1977).
- [2] R. Salzgeber and J. Brilliant, "An in vivo evaluation of the penetration of an irrigating solution in root canals", *Journal of Endodontics* **3**, 394–398 (1977).
- [3] M. Abou-Rass and F. Patonai Jr., "The effects of decreasing surface tension on the flow of irrigating solutions in narrow root canals", *Oral Surgery, Oral Medicine, Oral Pathology* **53**, 524–526 (1982).
- [4] A. Druttman and C. Stock, "An in vitro comparison of ultrasonic and conventional methods of irrigant replacement.", *International Endodontic Journal* **22**, 174–178 (1989).
- [5] S.-J. Lee, M.-K. Wu, and P. Wesselink, "The efficacy of ultrasonic irrigation to remove artificially placed dentine debris from different-sized simulated plastic root canals", *International Endodontic Journal* **37**, 607–612 (2004).
- [6] A. Burlinson, J. Nusstein, A. Reader, and M. Beck, "The in vivo evaluation of hand/rotary/ultrasound instrumentation in necrotic, human mandibular molars", *Journal of Endodontics* **33**, 782–787 (2007).
- [7] R. Weller, J. Brady, and W. Bernier, "Efficacy of ultrasonic cleaning", *Journal of Endodontics* **6**, 740–743 (1980).
- [8] P. Lumley, A. Walmsley, and W. Laird, "Streaming patterns produced around endosonic files.", *International Endodontic Journal* **24**, 290–297 (1991).
- [9] A. Lussi, U. Nussbächer, and J. Grosrey, "A novel noninstrumented technique for cleansing the root canal system", *Journal of Endodontics* **19**, 549–553 (1993).
- [10] R. Roy, M. Ahmad, and L. Crum, "Physical mechanisms governing the hydrodynamic response of an oscillating ultrasonic file", *International Endodontic Journal* **27**, 197–207 (1994).
- [11] L. W. M. Van der Sluis, M.-K. Wu, M. Versluis, and P. Wesselink, "Passive ultrasonic irrigation of the root canal: a review of the literature", *International Endodontic Journal* **40**, 415–426 (2007).
- [12] J. Blanken and R. Verdaasdonk, "Cavitation as a working mechanism of the Er,Cr:YSGG laser in endodontics: a visualization study", *J Oral Laser Appl* **7**, 97–106 (2007).
- [13] R. George and L. Walsh, "Apical extrusion of root canal irrigants when using Er:YAG and Er,Cr:YSGG lasers with optical fibers: An in vitro dye study", *Journal of Endodontics* **34**, 706–708 (2008).
- [14] R. George, I. Meyers, and L. Walsh, "Laser activation of endodontic irrigants with improved conical laser fiber tips for removing smear layer in the apical third of the root canal", *Journal of Endodontics* **34**, 1524–1527 (2008).
- [15] L. W. M. Van der Sluis, M.-K. Wu, and P. Wesselink, "The evaluation of removal of Ca(OH)<sub>2</sub> from an artificial standardized groove in the apical root canal using different irrigation methodologies.", *International Endodontic Journal* **40**, 52–57 (2007).

- [16] C. W. Robertson and D. Williams, "Lambert absorption coefficients of water in the infrared", *Journal of the Optical Society of America* **61**, 1316–1320 (1971).
- [17] W. Lauterborn, "High-speed photography of laser-induced breakdown in liquids", *Applied Physics Letters* **21**, 27–29 (1972).
- [18] J. Holzfuss, M. Rüggeberg, and A. Billo, "Shock wave emissions of a sonoluminescing bubble", *Physical Review Letters* **81**, 5434–5437 (1998).
- [19] R. Rothfus, C. Monrad, and V. Senecal, "Velocity distribution and friction factor in smooth concentric annuli", *Industrial & Engineering Chemistry* **42**, 2511–2520 (1950).
- [20] R. Dijkink and C.-D. Ohl, "Measurement of cavitation induced wall shear stress", *Applied Physics Letters* **93** (2008).
- [21] C. Boutsioukis, T. Lambrianidis, E. Kastrinakis, and P. Bekiaroglou, "Measurement of pressure and flow rates during irrigation of a root canal ex vivo with three endodontic needles", *International Endodontic Journal* **40**, 504–513 (2007).
- [22] M. Ahmad, T. Pitt Ford, L. Crum, and A. Walton, "Ultrasonic debridement of root canals: Acoustic cavitation and its relevance", *Journal of Endodontics* **14**, 486–493 (1988).
- [23] E. Matsuoka, J. Jayawardene, and K. Matsumoto, "A morphological study on root canal preparation using Erbium,Chromium:YSGG laser", *JOLA* **1**, 17–22 (2005).
- [24] Y. Kimura, K. Yonaga, K. Yokoyama, J. Kinoshita, Y. Ogata, and K. Matsumoto, "Root surface temperature increase during Er:YAG laser irradiation of root canals", *Journal of Endodontics* **28**, 76–78 (2002).

## Appendices

### 13.A Supplementary material

*(Online at [http://stilton.tnw.utwente.nl/rootcanalcleaning/Gallery\\_of\\_Irrigant\\_Motion](http://stilton.tnw.utwente.nl/rootcanalcleaning/Gallery_of_Irrigant_Motion))*

Movie 1. Visualization at the apex of the root canal, laser intensity 60 mJ/pulse.

Movie 2. Visualization at the apex of the root canal, laser intensity 250 mJ/pulse.

Movie 3. Visualization at the corona of the root canal, laser intensity 250 mJ/pulse.

## **Part IV**

# **Cleaning efficacy**



# 14

## Irrigant transport into dental microchannels \*

**Abstract** Sodium hypochlorite (NaOCl) has been shown to be an effective antimicrobial agent during root canal treatment. However, the root canal is a complex system geometrically and it is not known how far the NaOCl can penetrate into the side channels of the root canal and into the dentinal tubules (diameter of a few micrometer), to reach bacteria residing up to hundreds of micrometers inside them. A numerical study was performed to assess the penetration rate of NaOCl into the side channels and tubules, considering both diffusion and convection. The model was validated experimentally using a fluorescent dye. Convection was studied separately using a Computational Fluid Dynamics model, validated with Particle Imaging Velocimetry experiments. Both diffusion and convection were found to be slow on the time scale of an irrigation procedure. Convection contributed within two channel diameters, requiring more than 10 minutes for a significant concentration of NaOCl to reach the far end of a tubule. Diffusion was enhanced when the concentration at the side channel entrance was kept constant, which suggests that frequent irrigant replenishment and/or irrigant activation during a root canal treatment are beneficial. Alternative methods should be considered to improve irrigant penetration into side channels and tubules.

---

\*To be submitted to *Physics in Medicine and Biology* as: B. Verhaagen, C. Boutsoukis, C.P. Sleutel, L.W.M. van der Sluis and M. Versluis, "Irrigant transport into dental microchannels"

## 14.1 Introduction

The root canal of a tooth is a geometrically complex system, consisting not only of the main root canal, but also secondary, accessory and lateral channels, with a diameter between 20 and 300  $\mu\text{m}$ , which can also be interconnected [1, 2]; see the sketch in Figure 14.1. These ramifications occur in more than 25% of the root canals, most frequently in the apical area of the main root canal [1]. They can harbor microorganisms and tissue remnants that, in order to heal the tooth and prevent a reinflammation, needs to be removed during a root canal treatment [3].

Microorganisms can also reside within dentinal tubules, which are even smaller microchannels (diameter 0.5-3.2  $\mu\text{m}$ ) that run through the dentin wall of the root canal [4]. In an infected root canal system, microorganisms can invade the tubules even to their full length [5–8]. Microorganisms inside the tubules are largely protected from both host defense and local antimicrobial treatment [8, 9]. Although there is no consensus on the possible clinical effect of these microbes on root canal treatment outcome [10], it seems reasonable to undertake efforts against them.

Sodium hypochlorite (NaOCl) is currently regarded as the preferred irrigant for root canal irrigation because of its wide-spectrum antimicrobial activity [11, 12] and tissue dissolving capabilities [13]. Hypochlorous acid (HOCl) and the hypochlorous ion ( $\text{OCl}^-$ ) are considered the essential antimicrobial components of a NaOCl solution [11]. However, they are rapidly inactivated when in contact with the organic material [13, 14] present in the root canal ramifications. Fresh irrigant is therefore delivered intermittently by irrigation throughout the root canal treatment session.

The flow (convection) that is generated by irrigant delivery techniques is dominantly in the longitudinal direction of the root canal, flowing between the delivery needle and the root canal wall [15–18]. This flow is known to cause mixing of the irrigant in the main channel and shear stress on the biofilm on the root canal wall [16, 18], but it is not yet known whether it can create irrigant flow into the side channels and tubules. If convection is not able to deliver the irrigant, then NaOCl has to be distributed through diffusion, induced by the concentration gradient of NaOCl (or its components) between the fresh irrigant in the main channel and liquid filling the side channel or tubule. However, diffusion is typically slow, whereas on the other hand efficient convection inside microchannels is generally difficult to achieve [19]. Clinically it has been confirmed that the contents of lateral canals, isthmuses and oval extensions remain relatively unaffected by instruments and irrigants using needle irrigation [20, 21].

Previous studies [22, 23] evaluated irrigant penetration into dentinal tubules indirectly by studying the antimicrobial effect of irrigants inside infected tubules. However, critical factors such as time of exposure to the irrigant were not standardized. Recently, irrigant diffusion into dentinal tubules was investigated *ex vivo* at a small number of time steps [24]. Apart from these, no data are available on the convection

or diffusion rate of the irrigant into the tubules during a certain time interval. Such knowledge would help determining the necessary irrigant refreshment rate during clinical procedures.

The aim of the present study was to investigate the time-dependent transport of sodium hypochlorite by convection and diffusion into both side channels and tubules, in order to give a prediction for the time scales necessary for transport into the full length of those side channels and tubules. Also the relative contribution of convection and diffusion is investigated, and how these can be influenced using the flow applied in the root canal. Numerical simulations for convection and diffusion are validated for the side channels, both experimentally and through comparison with theoretical predictions.

### 14.1.1 Side channel/tubule geometry and irrigant properties

Figure 14.1 shows a sketch of the root canal system, including side channels and tubules and the flow from a needle during irrigation. Side channel and tubules are discussed separately throughout this article, however, except for the diameter, their physical properties are assumed equal. The side channel or tubule is assumed to be a straight, unbranched cylinder of length  $L = 1$  mm long and a diameter in the range  $d = 0.5\text{-}100 \mu\text{m}$  [1, 25]; their cross-section is more or less circular, however for comparison to theory and experiment also rectangular cross-sections are considered. The side channels and tubules have an orifice open to the main root canal and a closed end on the cemental side, and are assumed to be filled with dentinal fluid with fluidic properties similar to water [26, 27], without any organic material or microbes. The main root canal is assumed to be filled or being filled with irrigant, a 2.5% NaOCl solution, having similar fluidic properties as water [28, 29] and  $\text{pH} = 11$ , at which value the equilibrium has shifted entirely towards  $\text{OCl}^-$  [30].

## 14.2 Convection-diffusion equation

The time-dependent transport of the irrigant through convection and diffusion in one dimension is described by Fick's second law [31]:

$$\frac{\partial C(x,t)}{\partial t} = D \frac{\partial^2 C(x,t)}{\partial x^2} - U(x) \frac{\partial C(x,t)}{\partial x} \quad (14.1)$$

The term on the left hand side describes the rate of change in concentration  $C(x,t)$  over time  $t$ ; the first term on the right is the spatial diffusion with diffusion coefficient  $D$  and distance  $x$  from the side channel entrance; the second term is the convection, with  $U(x)$  the local, steady velocity. The one-dimensional version of Ficks law was used because the large aspect ratio  $\beta$  (length to diameter) of the side channel or tubule is at least 10.



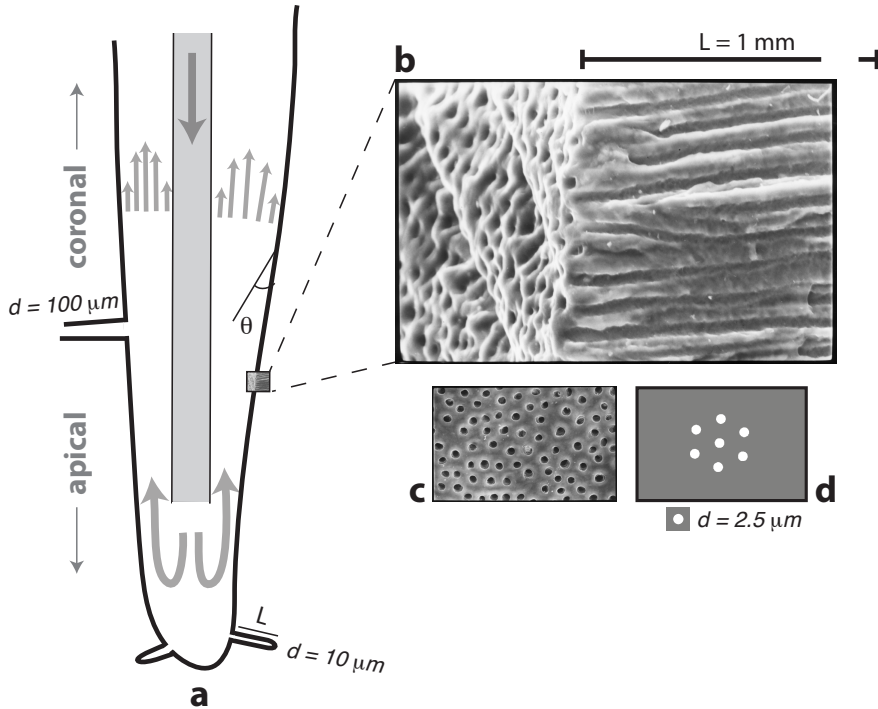


**Figure 14.1:** Schematic drawing of the root canal system with side channels and tubules. In (a) the apical third of the root canal is drawn, with the flow pattern from a needle during irrigation and the angle of impingement  $\theta$  indicated. (b) is a SEM image showing a cross-section of the wall of the root canal with tubules present. (c) shows a SEM image of the tubules faced from the front, and (d) shows the corresponding arrangement of tubules as used in the CFD simulation for convection. SEM images are courtesy of L. Vasiliadis (Dept. Endodontology, Dental School, Aristotle University of Thessaloniki). Naming conventions for the direction towards the tip (apical) and the crown of the tooth (coronal) are indicated.

The concentration at  $x = 0$  is assumed to be either (a) increasing over time up to  $C_0$  (inflow into the root canal, similar to the experiments), (b) fixed at  $C_0$  (corresponding to continuous, optimal flushing of the root canal), or (c)  $C_0$  only at  $t=0$  and decreasing over time due to the irrigant transport (corresponding to a single delivery of irrigant in the root canal):

$$C(x = 0, t) = C_0(t) \quad (14.2a)$$

$$C(x = 0, t) = C_0 \quad (14.2b)$$

$$C(x = 0, t) = C_0 - \sum C(x, t) \quad (14.2c)$$

At  $x = L$ , the side canal is assumed to be closed (Neumann boundary condition):

$$\frac{\partial C(x = L, t)}{\partial x} = 0 \quad (14.3)$$

There is an analytical solution to Equation 14.1 for the case of a constant concentration at  $x = 0$  [31]:

$$C(x, t) = C_0 \operatorname{erfc} \left( \frac{x}{2\sqrt{D_e t}} \right) + C_0 \operatorname{erfc} \left( \frac{x + 2L}{2\sqrt{D_e t}} \right) \quad (14.4)$$

where the closed end of the side channel at  $x = L$  is included by adding a mirror source at  $x = 2L$ . The diffusion coefficient  $D_e$  is the diffusion constant  $D$  plus a correction for the presence of convection [32, 33]:

$$D_e = D(1 + \kappa Pe^2). \quad (14.5)$$

The Peclet number  $Pe = Ud/D$  is the ratio of convection to diffusion, characterized by the local velocity  $U(x)$ .  $\kappa$  is a geometrical constant that can be calculated explicitly for a cylindrical or rectangular microchannel ( $\frac{1}{48}$  and  $\frac{1}{26.25}$ , respectively) [34, 35].

When the the concentration at the entrance of the side channel is increasing over time, or for more complex velocity distributions, Equation 14.1 has to be solved numerically, which will be demonstrated in Section 14.4. The velocity distribution will be determined in the following section.

### 14.3 Convection into side channels and tubules

The flow inside the side channels and tubules is driven by the flow in the root canal, induced during irrigation of the root canal [36] (see Figure 14.1). This resembles a lid- or shear-driven cavity, which is a well-studied problem in the literature [37] and is known to lead to a cascade of counterrotating vortices [38], with a rapidly decreasing velocity. This vortex structure is notoriously ineffective in flushing out, or delivering irrigant, deep into the cavity.

The vortex structure inside the side channel is governed by a complex stream function  $\psi$ , of which the velocity decreases exponentially with distance  $x$  into the side channel:

$$\psi \propto e^{-\frac{\lambda|x|}{d}} \quad (14.6)$$

The size and strength of the vortices can be obtained from the eigenvalue  $\lambda$  of the stream function [37], which is solely determined from the geometry of the side channel. The size of the vortices is given by  $\pi 2R/\text{Im}(\lambda)$ ; the exponential decay in magnitude of the velocity in the successive vortices is calculated from  $-\pi \text{Re}(\lambda)/\text{Im}(\lambda)$ .

For a three-dimensional side channel with circular cross-section, the eigenvalue is  $2.59+1.12i$  [37] which gives an vortex size of  $2.79d$  and a velocity decrease of  $\frac{1}{1386}$ . A cavity with a rectangular cross-section (of width  $w$  and height  $h$ ) has a higher decrease in velocity than one with a circular cross-section, due to the presence of corners that increases damping. For a channel with rectangular cross-section, the eigenvalue is  $4.28+1.80i$  [39], resulting in an vortex size of  $1.74d_h$  and a velocity decrease between consecutive vortices of  $\frac{1}{1707}$ . The hydraulic diameter of the rectangular cross-section is used as relevant dimension for scaling:

$$d_h = \frac{2wh}{w+h} \quad (14.7)$$

For the remainder of this chapter, when discussing side channels with a rectangular cross-section, it is understood that ‘diameter’ refers to the hydraulic diameter.

The number of vortices that is formed inside the side channel depends on the aspect ratio of length to diameter  $\beta$ . For shear driven, two-dimensional cavity flow it has been shown that the spacing of vortices is identical to the Moffatt vortices [40], for  $\beta \geq 4$ . When  $\beta$  is smaller than 4, as is the case for very wide side channels, there may be just one or two vortices, or simply an inflow into the side channel with the same direction as the driving flow, for which the exponential decay in velocity magnitude cannot be predicted with the eigenvalue method. The value for  $\beta$  at which the transition from inflow to vortex structure occurs may be different in a three-dimensional system [37].

It is assumed that the flow rate through the main channel only influences the initial velocity of the vortices but does not affect the velocity decrease or the eddie spacing, as long as Stokes flow is still applicable. For Stokes flow, inertia doesn’t play a role, and the Reynolds number at the side channel entrance is smaller than 1:

$$Re = \frac{\rho U d}{\mu} < 1 \quad (14.8)$$

where  $\rho$  and  $\mu$  are the density and the viscosity of the liquid, respectively.

### 14.3.1 Numerical setup

Computational Fluid Dynamics (CFD) is employed to investigate the convection inside three-dimensional tubules and side channels of the root canal.

#### Circular tubules

The flow in a transverse section of a root canal (apical size 0.45 mm, 6% taper), lying between 4 and 5 mm from the apex, with a needle (external diameter 320  $\mu\text{m}$ ) centered within the root canal [16] was modeled in one CFD model. Seven dentinal tubules were simulated as microchannels with a circular cross-section with a diameter of 2.5  $\mu\text{m}$ . The tubules were arranged in a hexagonal pattern with a distance of 8.5  $\mu\text{m}$  between them (Figure 14.1d), corresponding to a density of approximately 8,190 tubules per  $\text{mm}^2$  [25]. The tubules were assumed to be filled with water. The pre-processor software Gambit 2.4 (Fluent Inc., Lebanon, NH, USA) was used to build the 3-D geometry and the hexahedral mesh of approximately 360,000 cells (mean cell volume  $9 \cdot 10^{-7} \text{ mm}^3$ ), which was verified to provide grid-independent results. A no-slip boundary condition was imposed on all walls; atmospheric pressure was imposed on the coronal side of the root canal section.

Two different cases were studied regarding flow velocity and angle  $\theta$  of impingement (indicated in Figure 14.1) of the flow on the root canal wall. Case A ( $\theta = 0^\circ$ ) corresponds to a flow parallel to the wall and perpendicular to the tubules. In case B, the effect of a flow under an impingement angle  $\theta = 45^\circ$  was studied. This simulates the effect of angulation of the tubule or flow not parallel to the root canal wall, for example induced by a side-vented needle [16]. A fully developed parabolic velocity profile with an average velocity of 5 m/s was imposed, consistent with a clinically realistic irrigant flow rate of 15.6 mL/min through a 30G flat needle [36].

Only convection was studied with the CFD model. The commercial CFD software FLUENT 6.3 (Fluent Inc.) was used to set up and solve the steady-state problem using a finite volume approach, and to analyze the results. Additional details on the CFD model of flow in a root canal can be found in previous studies [16, 41].

#### Square side-channels

A second CFD model simulated side channels with a rectangular cross-section and a diameter of 16 - 57  $\mu\text{m}$ , similar to the experimental setup described below. The model consisted of a main channel (simulating the root canal lumen) with a cross-section of  $500 \times 168 \mu\text{m}$  and length 1.4 mm and a side channel (simulating closed apical extensions, isthmuses or tubules) originating on one side of the root canal at a distance of 1.2 mm down the main channel. The side channel had a height of 39  $\mu\text{m}$  and length 1 mm; its width was varied from 10 to 100  $\mu\text{m}$  ( $\beta = 100$  to 10,

width ( $\mu\text{m}$ )	hydraulic diameter ( $\mu\text{m}$ )	$\beta$
10	16	100
40	40	25
100	57	10

**Table 14.1:** Width, hydraulic diameter and length-to-diameter ratio  $\beta$  for the three side channels that were investigated. The length is 1 mm for all channels.

respectively). This geometry was built and solved in COMSOL Multiphysics v4.2a (COMSOL AB, Stockholm, Sweden).

The root canal and the side channel were assumed to be filled with water with initially zero velocity. The inflow on one side of the root canal had a flat profile, which was observed to develop into a parabolic profile within an entrance length of 0.3 mm. The average velocity of the inflow was calculated from the flow rate (between 0.01 and 3.2 mL/min) using the cross-sectional area of the root canal. The other end of the root canal (beyond the side channel) was imposed to be an outlet (atmospheric pressure). No-slip was imposed on the walls of the microchannels.

The mesh of the whole domain consisted of approximately 80,000 tetrahedral cells (mean cell volume of  $1.8 \cdot 10^{-15} \text{ m}^3$ ), with a higher mesh density near the boundaries and inside the side channel to resolve the small-scale flows expected there. A grid-independency check was performed to ensure the accuracy of the mesh.

The tolerance for the solved variables was set to  $10^{-6}$ , which ensured that the flow in at least half of the side channel length could be resolved. As the flow velocity decreases rapidly, resolving the flow further on in the side channel required even smaller tolerances, leading to increasing computational costs.

The flow velocities were evaluated on a horizontal plane at a height  $z = 20 \mu\text{m}$ .

### 14.3.2 Experimental setup for validation

Only rectangular microchannels could be manufactured for the experimental validation of convection. The mold for a microfluidic device containing a main channel and several side channels (Figure 14.2) was manufactured using soft lithography techniques. The microfluidic device itself was produced in silicon (Polydimethylsiloxane, Sylgard 184, Dow-Corning, Midland, Michigan, United States) and bonded onto a glass microscope slide after plasma cleaning.

The side channels had a width  $w$  of 10, 40 or 100  $\mu\text{m}$  and a height  $h$  of 39.4  $\mu\text{m}$ , with corresponding hydraulic diameters of 16, 40 and 57  $\mu\text{m}$  and  $\beta = 100$ , 25 and 10, respectively. The side channels were closed at the remote end at a length  $L$  of 1 mm and were situated at one corner of the main channel, which had a height of  $h_m = 168 \mu\text{m}$  and a width of  $w_m = 500 \mu\text{m}$ . The spacing between side channels along

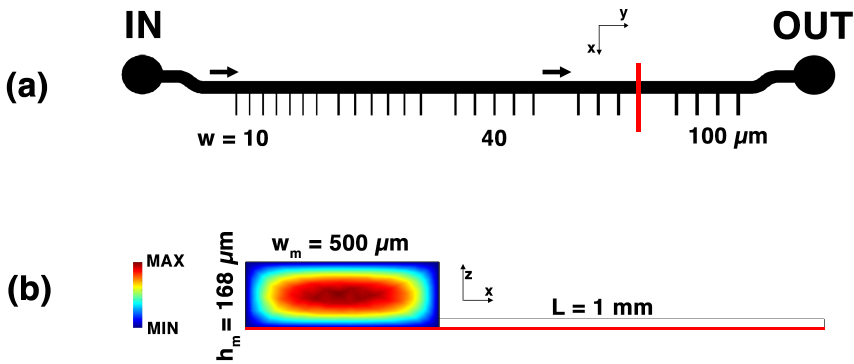


**Figure 14.2:** (a) Drawing of the microfluidic device with a main channel (dimensions  $w_m \times h_m$ ) and side channels of varying width  $w$ . In the cross-section (red line, (b)), the position of the side channels in the corner of the main channel is indicated, showing that the entrance velocity (colors, from simulation) of the side channel is much lower than the average velocity in the main channel.

the main channel was at least 5 times the side channel width, assuming that then at each side channel the flow is unaffected by the previous side channel.

The velocity at the entrance of a side channel can be estimated from the velocity profile in the corner of the main channel. An approximation for the velocity profile in the main channel is given by [42] (see also Figure 14.2b):

$$u(x, z) = U \left( \frac{m+1}{m} \right) \left( \frac{n+1}{n} \right) \left( 1 - \left( \frac{2x}{w_m} \right)^m \right) \left( 1 - \left( \frac{2z}{2h_m} \right)^n \right) \quad (14.9)$$

The factors  $m$  and  $n$  depend on the ratio of  $2h_m/w_m$ ; for  $2h_m/w_m < 2/3$ ,  $n = 2$  and  $m = 1.54 \cdot w_m/(2h_m)$ . With a flow rate of 1 mL/min, the average velocity  $U = Q/A = 0.20 \text{ m/s}$ . Assuming that the side channel does not affect the velocity profile, the driving velocity for the side channel can be evaluated from the flow inside the main channel, at a distance from the wall of  $\frac{1}{10}$  times the longest side of the rectangular cross-section (empirical assumption). For a side channel width of 10 or 40, or 100  $\mu\text{m}$ , the velocity at a distance of  $\frac{1}{10} \cdot d$  from the wall is  $10^{-2.5}$  or  $10^{-1.8} \text{ m/s}$ , respectively.

Demi water was pumped through the microfluidic device by a syringe pump (PHD 22/2000, Harvard Apparatus, Holliston, MA, USA) at flow rates in the range 0.1 - 1 mL/min. Polymer microspheres (mean diameter of 0.2 or 2  $\mu\text{m}$  and density of  $1.05 \cdot 10^3 \text{ kg/m}^3$ ; Red Fluorescent Polymer Microspheres, Duke Scientific Corp., Palo Alto, CA, USA) were added to the water as tracer particles. Their displacement was imaged through a microscope (BX-FM; Olympus, Tokyo, Japan) with a magnification of 10-100 $\times$ , having a focal depth of 47.5-7.6  $\mu\text{m}$ , respectively. Volume

illumination was performed in bright-field by a continuous-wave light source (ILP-1; Olympus). Recordings were made with a high-speed camera (SA1.1, Photron, Tokyo, Japan) at frame rates between 50 and 500 frames per second, and were analyzed by using a micro-Particle Image Velocimetry ( $\mu$ PIV) code developed in-house, employing ensemble averaging over at least 50 frames of the recordings.

### 14.3.3 Results

#### Convection into circular tubules: simulations.

Cases A and B resulted in a similar flow pattern inside the tubules, where a cascade of up to four counter-rotating vortices was formed, driven by the flow in the main channel (Figure 14.3). For both impingement angles  $\theta$ , the irrigant velocity dropped more than three orders of magnitude between the vortices (Figure 14.4, yellow line), which had a size of approximately  $7 \mu\text{m} = 2.8$  times the diameter. After four vortices, the velocity had decreased to the highest level of accuracy of the CFD model and no more vortices could be identified. The numerical result for the velocity decrease agreed well with the theoretically predicted slope based on the eigenvalues.

For flow impinging under an angle of  $45^\circ$  (case B), the CFD model predicted a flow similar to case A, but with velocities one order of magnitude higher. The vortex size was still  $7 \mu\text{m}$  and the decay factor between vortices was three orders of magnitude.

No difference was observed between each of the seven tubules or in the velocity profile close to the tubules, implying that the presence of the tubules, at least for this density, did not affect the velocity profile in the main canal or the conditions in adjacent tubules.

#### Convection into rectangular side channels: simulations and experiments.

Both the CFD simulation and the PIV measurements of rectangular side channels showed counterrotating vortices for the narrow channels ( $\beta = 25$  or  $100$ ) and inflow-only into the microchannel for a channel width of  $100 \mu\text{m}$  ( $\beta = 10$ ). In the simulations, up to five vortices could be identified for these narrow channels, at which point the velocity magnitude had decreased to the level of accuracy of the CFD model. Experimentally, only one or two counterrotating vortices could be observed for  $\beta = 25$  or  $100$ , before Brownian motion of the tracer particles at  $10^{-6}$  m/s became dominant, which was not present in the CFD model. The size of the first vortex and the location of the vortex center correspond very well with the simulation (Figure 14.5). The size of the vortices for  $\beta = 25$  or  $100$  in the simulations correspond well with the theoretical prediction of 1.74 times the hydraulic diameter, within the accuracy of the numerical grid.

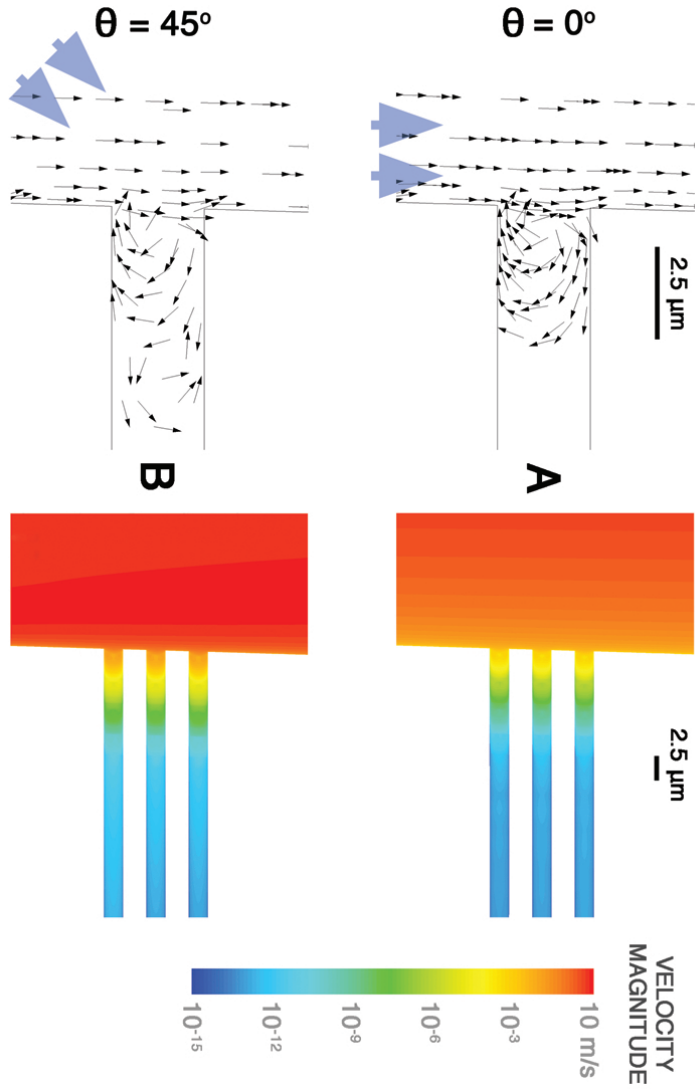


**Figure 14.3:** Flow pattern (left) and velocity magnitude (right, logarithmic scale) of the convection inside the tubules as obtained from the CFD model. The impingement angles  $\theta$  of the flow in the main root canal are indicated with blue arrows. Close to the tubule orifices, the flow is always parallel the wall.



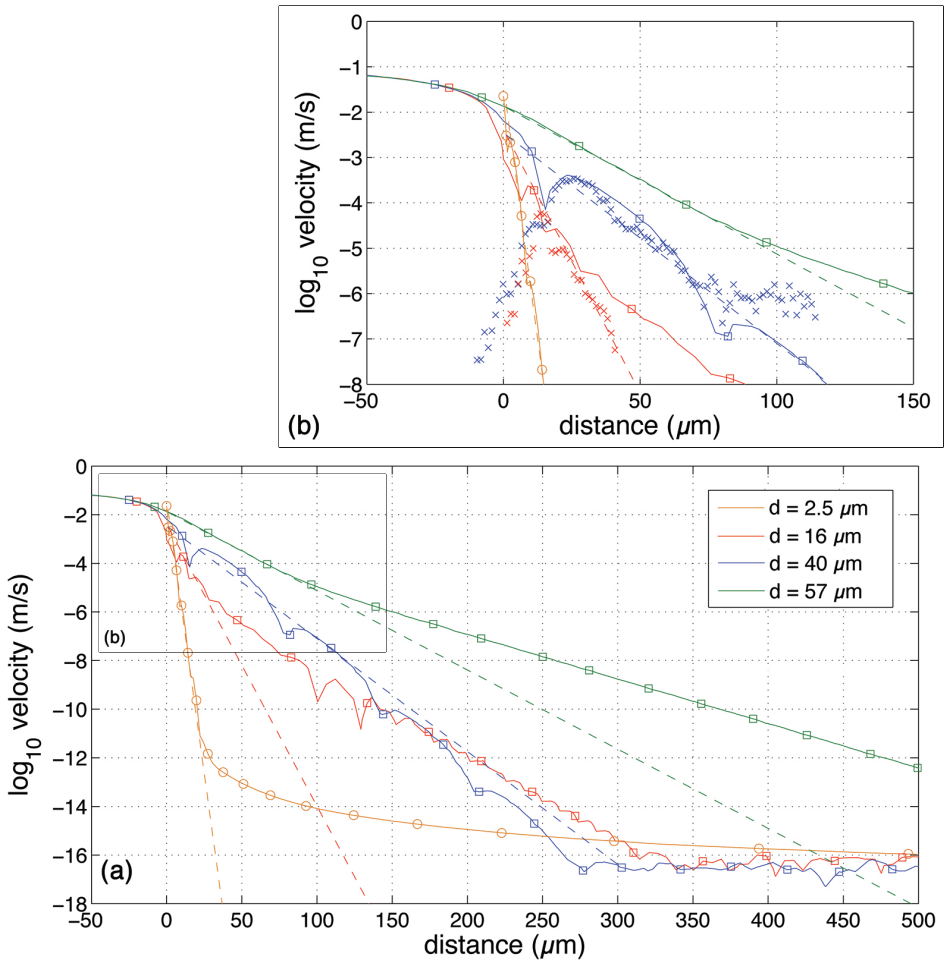


**Figure 14.4:** Velocity in the center of the side channel versus distance in the side channel, including results from both numerical models (solid lines) and experiments (crosses, inset (b) only), for circular ( $\circ$ ) and rectangular ( $\square$ ) cross-sections with (hydraulic) diameter  $d$ . The dashed lines show theoretical predictions based on the diameter (circular cross-section) or hydraulic diameter (rectangular cross-section), with an initial velocity obtained from the flow in the main channel at a distance of  $h/10$  from the wall.

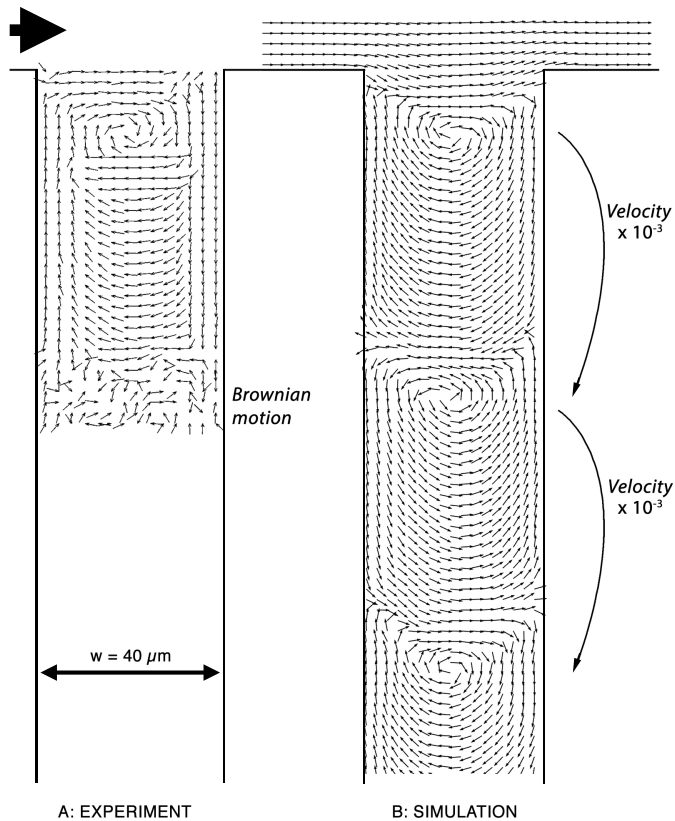


**Figure 14.5:** Velocity vectors inside a side channel of width  $w = 40 \mu\text{m}$ , driven by a flow from left to right. One vortex can be identified in the experimental result (A), whereas a cascade of vortices is visible in the numerical prediction (B).

The velocities along the longitudinal axis in the center of the side channel are plotted in Figure 14.4, together with the theoretical result based on the hydraulic diameter of the side channel. There is a good agreement between numerical result and theoretical prediction close to the channel entrance, although further inside the channel the velocity appears to decrease with a different slope than theoretically predicted. The velocity magnitude obtained from the experiments also matches the numerical prediction for the velocity along the length of a side channel well, for both  $w = 40 \mu\text{m}$  and  $10 \mu\text{m}$  (Figure 14.4). Velocities above  $10^{-3}$  m/s were too high to be measured with the PIV setup; velocities below  $10^{-6}$  m/s are dominated by Brownian motion.

## 14.4 Convection-diffusion into side channels and tubules

### 14.4.1 Convection and diffusion regimes

Convection was shown to decrease rapidly with the distance into a side channel; diffusion may therefore play an important role in the transport of irrigant. Using Equation 14.5 an estimate can be made of the regions where convection or diffusion is dominant. The convection is approximated by a one-dimensional velocity distribution along the side channel by only considering the velocity in the center of the side channel in the three-dimensional numerical model.

Equations 14.4 and 14.5 suggest that convection attributes only to irrigant transport when  $Pe > \sqrt{\kappa^{-1}}$ , assuming constant concentration at the entrance of the microchannel. Figure 14.6 shows the convection and diffusion dominated regions along the length of a side channel or tubule, for rectangular and circular channels of various widths, and for NaOCl and for a fluorescent dye with diffusion coefficient  $D = 0.4 \cdot 10^{-9} \text{ m}^2/\text{s}$ . The diffusion coefficient of  $\text{OCl}^-$  was estimated to be  $D = 1.5 \cdot 10^{-9} \text{ m}^2/\text{s}$  [43], independent of the concentration. HOCl is expected to have a diffusion coefficient similar to that of  $\text{OCl}^-$ .

The convection region is limited to approximately two times the side channel diameter. For tubules with a diameter of  $2.5 \mu\text{m}$ , this means that only the first  $5 \mu\text{m}$  is governed by convection, and the remaining 99.5% of the tubule length by diffusion. For the circular side channels a slightly larger region is governed by convection than for the rectangular side channels, due to the absence of damping in the corners. Due to the higher diffusion coefficient of NaOCl than that of the fluorescent dye, diffusion dominates in a larger region.

### 14.4.2 Numerical model of transport of NaOCl and fluorescent dye

The transport of irrigant and the contribution of convection and diffusion was studied in more detail by solving the convection-diffusion equation (Equation 14.1) numerically, using a fully explicit discretization on a one-dimensional grid. A spatial resolution of  $1 \mu\text{m}$  and temporal resolution of  $0.25 \text{ ms}$  was used. The tubule or side channel was assumed to be closed at the far end ( $x = L$ ). The velocity along the side channel is calculated from the eigenvalues and entrance velocities as discussed in Section 14.3. The numerical model included  $150 \mu\text{m}$  of the main channel, where the concentration of NaOCl was assumed to either increase, to be constant, or to be allowed to decrease over time. The latter condition is based on experimental observations and is approximated with an error function that approaches unity within an empirical time interval  $T$ :

$$C_0(t) = C_0 \text{erf}(t/T). \quad (14.10)$$

with  $T \approx 30/Q$  and  $Q$  the flow rate in mL/min.

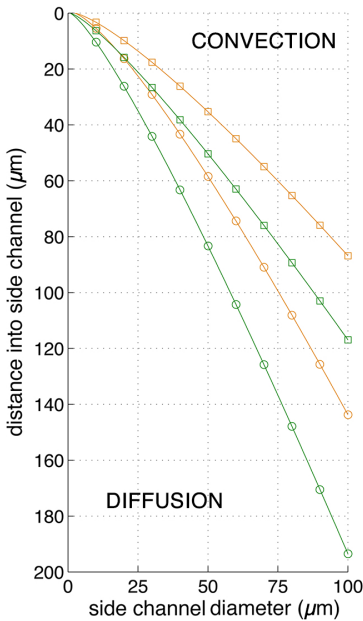


**Figure 14.6:** Convection and diffusion dominated regimes along the length of a side channel for NaOCl (orange) or the fluorescent dye (green), as a function of channel width (or diameter) with circular (○) or rectangular (□) cross-section.

Simulations are performed for the transport of a model irrigant, being a fluorescent dye with a diffusion coefficient of  $0.4 \cdot 10^{-9} \text{ m}^2/\text{s}$ , into a rectangular side channel with a diameter of  $57 \text{ } \mu\text{m}$  ( $w = 100 \text{ } \mu\text{m}$ ,  $\beta = 10$ ), at a flow rate of 0.10, 0.30 and 0.80 mL/min, which could be experimentally verified. In addition, the transport of NaOCl (with a diffusion coefficient of  $1.5 \cdot 10^{-9} \text{ m}^2/\text{s}$ ) into a circular tubule of diameter  $2.5 \text{ } \mu\text{m}$  is simulated, for one flow rate.

Both diffusion-only and diffusion-convection were calculated, to study the effect of convection on irrigant transport.

### 14.4.3 Experimental setup for dye transport validation

Using the same microfluidic device as described in Section 14.3, the transport of a fluorescent dye was measured using fluorescence microscopy. A mercury light source (U-LH100HG, Olympus) was used in dark-field mode to excite the fluorescent dye (Alexa Fluor 488, Invitrogen, Carlsbad, CA, USA) in the range 455-495 nm; the emitted light in the range 505-555 nm was filtered using a FITC filter set and dichroic mirror (Semrock, Lake Forrest, IL, USA). A photcamera (D300, Canon, Tokyo, Japan) captured the images at a rate of 1 frame per second, using a shutter time of 1/30, ISO 1000 and white balance at 5000K.

The fluorescent dye was dissolved at a concentration of  $1.7 \text{ } \mu\text{g}/\text{mL}$  and was pumped through the microfluidic device by a syringe pump (PHD 22/2000, Harvard

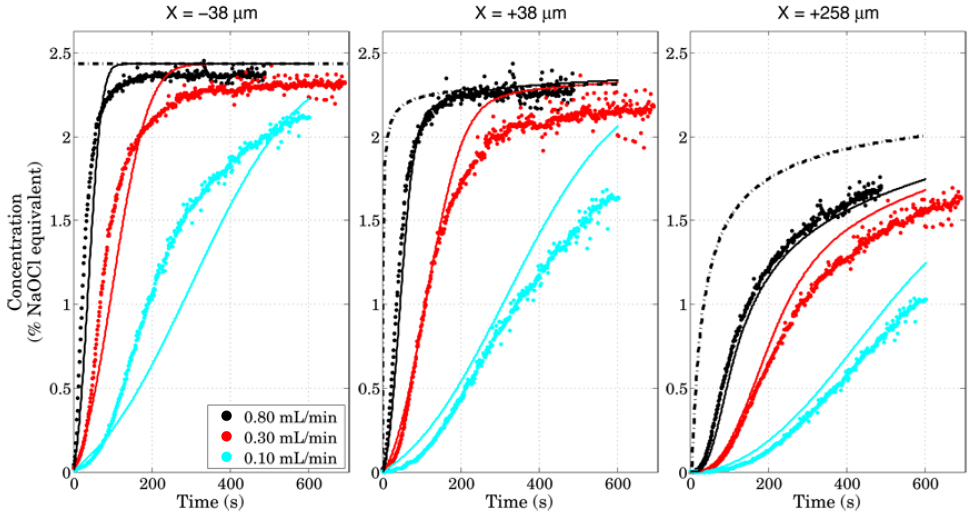


**Figure 14.7:** Irrigant (or dye) concentration at three locations in the side channel for three flow rates (colors). The dots are experimental data, the solid lines are numerical results for dye into side channels with a rectangular cross-section and a diameter of  $d = 57 \mu\text{m}$ . The dashed black line is the theoretical solution for a flow rate of  $0.80 \text{ mL/min}$ .

Apparatus) at a flow rate of  $0.10$ ,  $0.30$  or  $0.80 \text{ mL/min}$ . Calibration was performed using dilutions of the fluorescent dye, and corrected for the intensity profile of the light source and optical aberrations due to the microfluidic device.

The recordings were analyzed by evaluating the image intensity over time at three locations, one being near the entrance of the side channel ( $x = -38 \mu\text{m}$ ) and two inside the side channel ( $x = +38$  and  $+258 \mu\text{m}$ ). At these locations, the intensity was averaged over an area of  $55 \times 55 \mu\text{m}$ , normalized and converted to concentration.

## 14.4.4 Results

### Concentration evaluated at three locations

The concentration of fluorescent dye at three locations in the rectangular side channel as a function of time is plotted in Figure 14.7. Near the entrance ( $x = -38 \mu\text{m}$ ) the rate of increase is of the order of minutes, depending on the flow rate. The concentration at locations inside the side channel ( $x = +38$  or  $+258 \mu\text{m}$ ) increases at a much lower rate, and at  $x = +258 \mu\text{m}$  it takes more than 5 minutes to obtain only half the initial concentration, for a flow rate of  $0.30 \text{ mL/min}$ .

The experimentally measured concentration of fluorescent dye at the three locations show trends for the concentration increase that agree very well with the numer-

ical prediction (Figure 14.7). The concentrations at the side channel entrance ( $x = -38 \mu\text{m}$ ) do not match the concentration increase function that was assumed for the numerical model, nevertheless the evolution of the concentration at  $x = +38$  and  $+258 \mu\text{m}$  resembles the numerical prediction very well.

The theoretical result based on Equation 14.4 (dashed line) shows a similar trend in concentration increase, but at a higher rate, as the theoretical solution is based on a fixed concentration at the side channel entrance.

The numerical calculation of NaOCl transport into a cylindrical tubule with diameter  $2.5 \mu\text{m}$ , shows that NaOCl is transported at a higher rate, even though the convection is less than for large channels with a rectangular cross-section (Figure 14.4). This suggests again that diffusion dominates and that the higher diffusion coefficient of NaOCl compared to the fluorescent dye is important.

### Concentration evaluated at five time points

Figure 14.8 shows the result of the numerical transport model for diffusion and convection of NaOCl, at five specific times. The inflow conditions (a), the irrigant diffusion coefficient (b) and the side channel cross-sectional shape (c) and diameter (d) are all varied.

The three different conditions for the concentration at the channel entrance (Equation 14.2a-c) lead to distinct evolutions of the concentration distribution. When a finite amount of NaOCl is placed at the tubule entrance, the irrigant is observed to spread out quickly, and as this leads to a smaller concentration gradient the diffusion slows down. After 10 minutes, the concentration has leveled out to a concentration of 16% of the concentration at the channel entrance. Convection leads to only a limited increase in penetration rate, although the increase is slightly higher for the side channel than for the tubule, due to larger eddies and therefore a slower decrease of velocity. Overall, the transport rate of NaOCl is very similar for both the tubules and the side channel, as in both channels there is diffusion of NaOCl, and convection only contributes within two diameters from the channel entrance.

Keeping the concentration  $C_0$  at the tubule entrance constant enhances the penetration of irrigant significantly, leading to a 5.4 times higher concentration at the far end of the tubule after 10 minutes, which then has increased to a value of 86% of the initial concentration. Similar to a finite amount of irrigant, the concentration gradient decreases and the diffusion slows down.

An increase of entrance concentration over time shows only a small difference in concentration distribution compared to a constant entrance concentration, suggesting that the increase in concentration at the entrance is quick compared to the total simulated time.

The numerical solution is found to match the analytical solution (Equation 14.4)

for a constant entrance concentration very well (not shown); at 10 seconds the difference between analytical and numerical solution is less than 1%.

Figure 14.8 shows repeatedly that diffusion is the dominant transport mechanism. In (b) the diffusion coefficient is increased 4 times, leading to a significant increase in the amount of NaOCl transported compared to the fluorescent dye. Furthermore, neglecting convection (a, dashed line) or changing the convection by changing the cross-sectional shape (c) or diameter (d) of the side channel lead only to very small changes in the irrigant distribution along the side channel or tubule.

## 14.5 Discussion

The flow generated by a needle during root canal irrigation was found to induce a cascade of vortices inside side channels or tubules in the dentin wall, with velocities that are rapidly decreasing. Convection dominates the transport of antimicrobial irrigant only within approximately two times the diameter into a side channel or a tubule. Especially for the narrow tubules, where the convection-dominated region stops within  $5 \mu\text{m}$ , irrigant transport will have to take place through diffusion, which has been shown to be slow, requiring many minutes for irrigant to diffuse into the side channels.

According to Fick's Law (Equation 14.1), the rate of irrigant diffusion is dependent on the concentration gradient, which, however, decreases as the irrigant is diffused. Continuous refreshment of the irrigant in the vicinity of the tubule orifice enhanced the diffusion rate into the tubule considerably. During a root canal treatment it would therefore be beneficial to ensure regular refreshment and/or stirring of the irrigant by an activation technique such as Passive Ultrasonic Activation [44]. Recently, a system has been introduced which combines both refreshment and stirring [45].

A flow impinging under an angle onto the side channel or tubule could increase the convective transport into the microchannel; for the tubule it was shown that the flow velocity inside the tubule increased by one order of magnitude. However, a one-order-of-magnitude increase in velocities still would not result in a useful increase in irrigant transport, as the rapid velocity decrease in the side channel was shown to be independent of the impingement angle. This is in agreement with theory [37], as the size of the vortices only depends on the cavity diameter, not on the inflow velocity, and the decay factor is a constant.

The use of the CFD model for the study of convection into tubules and side channels was validated by comparing the vortex size and velocity decrease between the CFD model results and the theoretical predictions, and by comparing the velocities measured with PIV for a side channel with rectangular cross-section, which were all found to agree well. The one-dimensional numerical model for irrigant transport

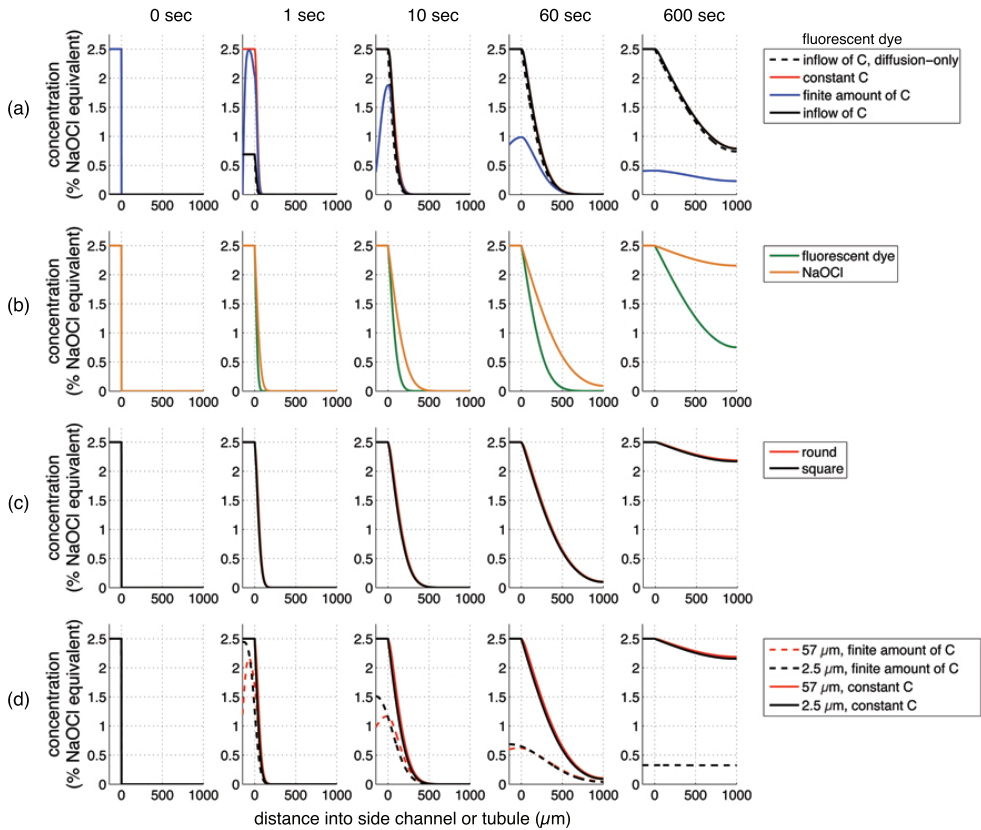


**Figure 14.8:** Irrigant distribution along a side channel or tubule, at five times, as calculated by the numerical transport model. Transport of (constant concentration) NaOCl into a square side channel of diameter  $57\ \mu\text{m}$  is assumed, unless noted otherwise in the legend. In (a) the inflow conditions for the irrigant concentration  $C$  are varied (solid black line corresponds to figure 14.7), in (b) the irrigant (i.e. diffusion constant), in (c) the cross-sectional shape, and in (d) the diameter and also the concentration condition at the entrance.



based on Fick's law also agreed very well with measurements inside a side channel with rectangular cross-section. However, these validation experiments could only be performed on side channels with a rectangular cross-section, having a width of at least  $10\ \mu\text{m}$  and made out of silicon. This leaves an uncertainty on whether the results for a cylindrical tubule with a diameter of  $2.5\ \mu\text{m}$  are valid. Experimentally, however, microchannels of the size of a tubule are very difficult to fabricate and measuring convection and dye transport in them is a challenge for future work.

The results presented here are for ideal conditions, as in reality, side channels and tubules exhibit a rich variety of geometrical properties, including tapering, curvature (S-shape) and non-smooth walls. Furthermore, we assumed that there was no consumption of irrigant due to a reaction, implying a 'best case' scenario for irrigant transport. This becomes clear when comparing our results to those of Zou *et al.* [24], who measured the transport of NaOCl into tubules *ex vivo* after 2, 5 or 20 minutes of immersion. Whereas in our model the irrigant concentration at 1 mm from the tubule entrance reached 86% of the initial concentration after 10 minutes, Zou *et al.* found a penetration depth (discoloring) of only  $300\ \mu\text{m}$  after 20 minutes, dependent on temperature and concentration of the irrigant. Most of the penetration took place within the first two minutes, with rapid decrease in penetration rate afterwards. Reaction with biomaterial inside the tubules and a complex geometry (branching) of the tubules are possible explanations for the limited irrigant penetration found by Zou *et al.*, as their models were subject to biological variation.

OCl<sup>-</sup> is rapidly consumed while reacting with microbes and other organic material present inside the tubules and around the tubule orifice [13, 14], which leads to a decrease in concentration of OCl<sup>-</sup> and consequently their diffusion rate. The amount of organic material itself decreases too, because of its reaction with OCl<sup>-</sup>. The rate at which consumption takes place depends on the concentration, the pH and the temperature of the OCl<sup>-</sup> and the organic material, but most importantly on the composition of the organic material and area of surface contact [13]. Unfortunately, data on the reaction rate is not available; therefore consumption was neglected here.

Even under the ideal conditions assumed in this study, irrigant penetration was found to be slow. Therefore other techniques should be considered to improve irrigant flow into the side channels and the tubules through improved convection (e.g., irrigant activation techniques like passive ultrasonic irrigation [44], or cavitation-based pumping [46]) and diffusion (e.g., higher concentration or temperature [24], or electrokinetics [47]).

## 14.6 Conclusions

The numerical models and experimental measurements show that convection of irrigant into a side channel or tubule during root canal irrigation is limited to twice the

diameter of the microchannel. Especially for tubules, having a diameter of only a few micrometer, most of the irrigant transport takes place through diffusion, which is slow. Simulations predict that diffusion needs more than 10 minutes to raise the concentration at the far end of a tubule to 86%, when the irrigant concentration at the entrance of the tubule is maintained at a constant value. A finite amount of concentration at the channel entrance is even less effective in delivering irrigant. Alternative methods should therefore be considered to improve irrigant penetration into side channels and tubules.

The numerical results show good agreement with experimental measurements of the flow and the irrigant transport. However, the side channels and tubules are much simplified compared to the real root canal geometry. Future numerical work should include more complex channel shapes, and also include reaction in the diffusion-convection equation.

## Acknowledgement

The authors are grateful to Prof. L. Lefferts for valuable discussions; Assoc. Prof. L. Vasiliadis is acknowledged for the SEM images of the tubules.

## References

- [1] Q. D. De Deus and B. Horizonte, "Frequency, location, and direction of the lateral, secondary, and accessory canals", *Journal of Endodontics* **1**, 361–366 (1975).
- [2] M. Venturi, R. Di Lenarda, C. Prati, and L. Breschi, "An in vitro model to investigate filling of lateral canals", *Journal of Endodontics* **31**, 877–881 (2005).
- [3] P. Nair, "Pathogenesis of apical periodontitis and the causes of endodontic failures", *Critical Review Of Oral Biology & Medicine* **15**, 348–381 (2004).
- [4] D. H. Pashley, S. M. Thompson, and F. P. Stewart, "Dentin permeability: Effects of temperature on hydraulic conductance", *Journal of Dental Research* **62**, 956–959 (1983).
- [5] M. Haapasalo and D. Orstavik, "In vitro infection and disinfection of dentinal tubules", *Journal of Dental Research* **66**, 1375–1379 (1987).
- [6] D. Orstavik and M. Haapasalo, "Disinfection by endodontic irrigants and dressings of experimentally infected dentinal tubules", *Endodontics and Dental Traumatology* **6**, 142–149 (1990).
- [7] F. Perez, T. Rochd, J. P. Lodter, P. Calas, and G. Michel, "In vitro study of the penetration of three bacterial strains into root dentine", *Oral Surgery, Oral Medicine, Oral Pathology* **76**, 97–103 (1993).
- [8] A. R. Vieira, J. F. Siqueira Jr, D. Ricucci, and W. S. Lopes, "Dentinal tubule infection as the cause of recurrent disease and late endodontic treatment failure", *Journal of Endodontics* **38**, 250–254 (2012).

- [9] L. B. Peters, P. R. Wesselink, J. F. Buijs, and A. J. Van Winkelhoff, "Viable bacteria in root dentinal tubules of teeth with apical periodontitis", *Journal of Endodontics* **27**, 76–81 (2001).
- [10] L. B. Peters, P. R. Wesselink, and W. R. Moorer, "The fate and the role of bacteria left in root dentinal tubules", *International Endodontic Journal* **28**, 95–99 (1995).
- [11] M. Haapasalo, U. Endal, H. Zandi, and J. M. Coil, "Eradication of endodontic infection by instrumentation and irrigation solutions", *Endodontic Topics* **10**, 77–102 (2005).
- [12] M. Zehnder, "Root canal irrigants", *Journal of Endodontics* **32**, 389–398 (2006).
- [13] W. R. Moorer and P. R. Wesselink, "Factors promoting the tissue dissolving capability of sodium hypochlorite", *International Endodontic Journal* **15**, 187–96 (1982).
- [14] H. K. Haapasalo, E. K. Siren, T. M. Waltimo, D. Orstavik, and M. P. Haapasalo, "Inactivation of local root canal medicaments by dentine: an in vitro study", *International Endodontic Journal* **33**, 126–131 (2000).
- [15] Y. D. Hsieh, C. H. Gau, S. F. Kung Wu, E. C. Shen, P. W. Hsu, and E. Fu, "Dynamic recording of irrigating fluid distribution in root canals using thermal image analysis", *International Endodontic Journal* **40**, 11–17 (2007).
- [16] C. Boutsoukis, B. Verhaagen, M. Versluis, E. Kastrinakis, P. R. Wesselink, and L. W. M. van der Sluis, "Evaluation of irrigant flow in the root canal using different needle types by an unsteady computational fluid dynamics model", *Journal of Endodontics* **36**, 875–879 (2010).
- [17] Y. Shen, Y. Gao, W. Qian, N. D. Ruse, X. Zhou, H. Wu, and M. Haapasalo, "Three-dimensional numeric simulation of root canal irrigant flow with different irrigation needles", *Journal of Endodontics* **36**, 884–889 (2010).
- [18] B. Verhaagen, C. Boutsoukis, G. L. Heijnen, L. W. M. Van der Sluis, and M. Versluis, "Role of the confinement of a root canal on jet impingement during endodontic irrigation", *Experiments in Fluids* **submitted** (2012).
- [19] T. M. Squires and S. R. Quake, "Microfluidics: Fluid physics at the nanoliter scale", *Reviews of Modern Physics* **77**, 977–1026 (2005).
- [20] A. Burlison, J. Nusstein, A. Reader, and M. Beck, "The in vivo evaluation of hand/rotary/ultrasound instrumentation in necrotic, human mandibular molars", *Journal of Endodontics* **33**, 782–787 (2007).
- [21] D. Ricucci and J. F. Siqueira Jr, "Fate of the tissue in lateral canals and apical ramifications in response to pathologic conditions and treatment procedures", *Journal of Endodontics* **36**, 1–15 (2010).
- [22] E. Berutti, R. Marini, and A. Angeretti, "Penetration ability of different irrigants into dentinal tubules", *Journal of Endodontics* **23**, 725–727 (1997).
- [23] A. J. Harrison, P. Chivatxaranukl, P. Parashos, and H. H. Messer, "The effect of ultrasonically activated irrigation on reduction of enterococcus faecalis in experimentally infected root canals", *International Endodontic Journal* **43**, 968–977 (2010).
- [24] L. Zou, Y. Shen, W. Li, and M. Haapasalo, "Penetration of sodium hypochlorite into dentin", *Journal of Endodontics* **36**, 793–796 (2010).

- [25] P. J. Carrigan, D. R. Morse, M. L. Furst, and I. H. Sinai, "A scanning electron microscopic evaluation of human dentinal tubules according to age and location", *Journal of Endodontics* **10**, 359–363 (1984).
- [26] C. T. Coffey, M. J. Ingram, and A. M. Bjorndal, "Analysis of human dentinal fluid", *Oral Surgery* **30**, 835–837 (1970).
- [27] G. Berggren and M. Brännström, "The rate of flow in dentinal tubules due to capillary attraction", *Journal of Dental Research* **44**, 408–415 (1965).
- [28] D. M. Z. Guerisoli, R. Silva, and J. D. Pecora, "Evaluation of some physico-chemical properties of different concentrations of sodium hypochlorite solutions", *Brazilian Endodontic Journal* **3**, 21–3 (1998).
- [29] L. W. M. van der Sluis, M. Voogels, B. Verhaagen, M. Versluis, and P. Wesselink, "An evaluation of the effect of different irrigants on the cleaning efficacy of ultrasonic root canal irrigation", *Journal of Endodontics* **36**, 737–740 (2010).
- [30] G. McDonnell and D. Russell, "Antiseptics and disinfectants: Activity, action, and resistance", *Clinical Microbiology Reviews* **12**, 147–179 (1999).
- [31] J. Crank, *The mathematics of diffusion*, 2nd edition (Clarendon Press, Oxford) (1975).
- [32] G. I. Taylor, "Conditions under which dispersion of a solute in a stream of solvent can be used to measure molecular diffusion", *Proceedings of the Royal Society of London. Series A, Mathematical and Physical Sciences* **225**, 473–477 (1954).
- [33] A. R. Aris, "On the dispersion of a solute in a fluid flowing through a tube", *Proceedings of the Royal Society of London. Series A, Mathematical and Physical Sciences* **235**, 67–77 (1956).
- [34] A. Ajdar, N. Bontoux, and H. A. Stone, "Hydrodynamic dispersion in shallow microchannels: the effect of cross-sectional shape", *Analytical Chemistry* **78**, 387–392 (2006).
- [35] N. Bontoux, A. Pépin, Y. Chen, A. Ajdari, and H. A. Stone, "Experimental characterization of hydrodynamic dispersion in shallow microchannels", *Lab on a Chip* **6**, 930–935 (2006).
- [36] C. Boutsioukis, T. Lambrianidis, and E. Kastrinakis, "Irrigant flow within a prepared root canal using various flow rates: a computational fluid dynamics study.", *International Endodontic Journal* **42**, 144–55 (2009).
- [37] P. N. Shankar and M. D. Deshpande, "Fluid mechanics in the driven cavity", *Annual Review of Fluid Mechanics* **32**, 93–136 (2000).
- [38] H. K. Moffatt, "Viscous and resistive eddies near a sharp corner", *Journal of Fluid Mechanics* **18**, 1–18 (1964).
- [39] K. N. Lakshmisha Santanu De and K. Nagendra, "Simulation of laminar flow in a three-dimensional lid-driven cavity by lattice boltzmann method", *International Journal of Numerical Methods for Heat and Fluid Flow* **19**, 790–815 (2009).
- [40] J. J. L. Higdon, "Stokes flow in arbitrary two-dimensional domains: shear flow over ridges and cavities", *Journal of Fluid Mechanics* **159**, 195–226 (1985).

- [41] C. Boutsoukis, B. Verhaagen, M. Versluis, E. Kastrinakis, and L. W. M. van der Sluis, “Irrigant flow in the root canal: experimental validation of a computational fluid dynamics model using high-speed imaging”, *International Endodontic Journal* **43**, 393–403 (2010).
- [42] D. B. Holmes and J. R. Vermeulen, “Velocity profiles in ducts with rectangular cross sections”, *Chemical Engineering Society* **23**, 717–722 (1968).
- [43] B. E. Poling, J. M. Prausnitz, and J. P. O’Connell, *The properties of gases and liquids*, 5th edition (McGraw-Hill, New York) (2001).
- [44] L. W. M. Van der Sluis, M. Versluis, M. K. Wu, and P. R. Wesselink, “Passive ultrasonic irrigation of the root canal: a review of the literature”, *International Endodontic Journal* **40**, 415–426 (2007).
- [45] R. Gutarts, J. Nusstein, A. Reader, and M. Becks, “In vivo debridement efficacy of ultrasonic irrigation following hand-rotary instrumentation in human mandibular molars”, *Journal of Endodontics* **31**, 166–170 (2005).
- [46] A. Shrestha, S.-W. Fong, B.-C. Khoo, and A. Kishen, “Delivery of antibacterial nanoparticles into dentinal tubules using high-intensity focused ultrasound”, *Journal of Endodontics* **35**, 1028–33 (2009).
- [47] C. Zhao and C. Yang, “Advances in electrokinetics and their applications in micro/nano fluidics”, *Microfluidics and Nanofluidics* **in press** (2012).

# 15

## Removal of a hydrogel with Passive Ultrasonic Irrigation

**Abstract** In this chapter, a hydrogel is shown to exhibit viscoelastic behavior similar to a biofilm. The hydrogel is subjected to acoustic streaming induced by an ultrasonically oscillating endodontic file. Visualizations of the interaction between the acoustic streaming and the hydrogel suggest that the steady component of the flow is dominant for viscous deformation of the hydrogel, while the oscillatory component of the flow induces an elastic deformation. Interestingly, a traveling stable cavitation bubble was found to be highly efficient in removing the hydrogel from the substrate. Stable bubbles were formed near the hydrogel during its reaction with NaOCl, although the size of the bubbles formed is not optimal for maximum oscillation amplitude in combination with the employed 30 kHz ultrasound.

## 15.1 Introduction

A biofilm is an agglomeration of bacteria, which produce a slime (the extracellular polymeric substance, or EPS) that protects the bacteria from mechanical attacks [1]. The EPS makes the biofilm a viscoelastic fluid, causing the biofilm to exhibit elastic behavior at low stress and viscous flow behavior at high stress [2], thereby protecting the contained bacteria. At stresses exceeding the cohesive strength of the biofilm, parts of the biofilm may detach (mechanical failure of the biofilm, a process called sloughing [3–5]) from the bulk biofilm and reattach at a different location where the mechanical and chemical conditions are more favorable [6].

Bacteria occur in a wide variety of systems, where they may be beneficial, e.g. for chemical conversions [7]. However, in many occurrences, e.g. inside root canals [8], their presence has a negative influence on the performance of a system. Generally biofilms therefore need to be removed, and many cleaning strategies have been developed to deal with biofilms, which can broadly be separated into chemical and mechanical attacks. However, biofilms have been around for more than 3 billion years and have found many ways for coping with removal attempts, both mechanically and chemically [6], and it has been realized that complete sterilization of a system is impossible. Cleaning strategies should therefore be based on restraining the negative influence of biofilms to a minimum.

One specific example that lies at the base of the present study is the cleaning of root canals during an endodontic treatment, when bacteria have caused an inflammation of the tooth tip [8] and the body's immune system cannot remove its source within the root canal. During the root canal treatment, an antimicrobial fluid is injected into the root canal using a needle and syringe [9]. However, it has been found that this procedure is not able to remove all bacteria from the geometrically complex root canal system, resulting in an estimated total of 40% of the treatments to be unsuccessful [10]. Nowadays new techniques are available to agitate the fluid in order to induce a stress on the biofilm on the root canal walls and to mix the antimicrobial fluid. One such technique is Passive Ultrasonic Irrigation, which makes use of a thin miniature file (diameter 200  $\mu\text{m}$ , taper 2%, length 25 mm) which is driven at 30 kHz in order to induce acoustic streaming and possibly cavitation [11]. The acoustic streaming is known to consist of an oscillating component and a steady component [12], which both could contribute to the removal of the biofilm. However, it remains to be shown how the two components affect a biofilm and what the role of cavitation is.

In order to evaluate the cleaning efficacy of the acoustic streaming, the exact mechanical properties of real biofilms need to be known, which are generally difficult to assess, for a number of reasons. Firstly, a biofilm cultured in the lab is significantly different from those encountered in real-life systems, because the composition is widely varying (for example, in one root canal more than 400 bacterial species have

been found [13]) and their cohesive and adhesive strength is dependent on the conditions (e.g. shear stress) under which the biofilm has grown. Typical values found in literature give a Young's modulus of the order of  $10^2$  Pa and a cohesive shear strength of  $10^1$  Pa [3, 6, 14–16]. Secondly, measurement of the mechanical properties should take place on a short time scale (within minutes), because the biofilm is a living organism and will adapt to its environment.

In order to investigate the fluid-biofilm interaction without those difficulties, we present here a hydrogel with viscoelastic properties, which can be made very repeatable and with specific mechanical properties. This hydrogel is used as a substitute for a biofilm [17], in order to investigate the cleaning mechanisms of ultrasonic root canal irrigation.

## 15.2 Materials & Methods

### 15.2.1 Hydrogel preparation

A hydrogel was made using 1.0 g of gelatine (Merck, Whitehouse Station, NJ, USA) and 0.02 g hyaluronan (Sodium hyaluronate 95%, Fisher, Waltham, MA, USA) in 45 mL of warm tap water [18]. Gelatine is a protein that mimicks bacteria; the addition of hyaluronan, a carbohydrate, creates an EPS-like material, as the hyaluronan binds many water molecules. 0.1 g of water-based food dye (KTC, Wednesbury, UK) and 0.2 g of hollow glass spheres (average diameter of  $10\ \mu\text{m}$ , density  $1100\ \text{kg/m}^3$ ; Spherichel, Potters Industries, South Yorkshire, UK) was added to make the biofilm better visible. This mixture was stirred and degassed with a centrifuge before it was allowed to cool down to room temperature. The final density of the hydrogel was  $1.07(\pm 0.07) \cdot 10^3\ \text{kg/m}^3$ .

At room temperature the mixture becomes a stiff gel, however, just before that happened the hydrogel was placed on a glass substrate ( $24 \times 24 \times 0.1\text{mm}$ ; Menzel gläser, Braunschweig, Germany) and allowed to dry for approximately 10 minutes. During the drying stage the hydrogel is binding to the glass substrate; cooling down of the gel stiffened the gel.

The glass substrate was prepared by placing two layers of Scotch tape (3M, St. Paul, MN, USA) on two edges of the glass substrate with a distance of approximately 1 mm between them. A drop of hydrogel was smeared out over the tape, which was removed after 5 minutes of drying, leaving a 1 mm wide and  $100\ \mu\text{m}$  high line of hydrogel on the glass substrate.

### 15.2.2 Irrigation protocol

The glass substrate was transferred to a water bath (dimensions  $75 \times 62 \times 117\ \text{mm}$ ) filled with demi-water, where it was fixed horizontally with a clamp which could be



translated with a translation stage (9067M, New Focus, San Jose, CA, USA). A 22G needle (inner diameter of 0.4 mm; Terumo, Leuven, Belgium) or an ultrasonically oscillating file (Irrisafe size 25/21, Satelec Acteon, Merignac, France) was positioned at a specific distance above the biofilm and could also be translated with another translation stage (same type), to vary the distance between the hydrogel and the needle or the file.

The flow through the needle was driven at flow rates up to 1 mL/min, using a syringe pump (NE-1010, New Era Pump Systems, Wantagh, NY, USA) and a 10 mL syringe (Plastipak, Becton-Dickinson, Oxford, UK). For each imaging measurement the pump was switched on, allowed to obtain maximum flow rate and stopped before commencing the next measurement. Alternatively, the needle was placed far away from the glass substrate and allowed to obtain a steady flow rate, and then lowered toward the hydrogel in steps of 100  $\mu\text{m}$ .

The ultrasonically oscillating file was driven by a commercial endodontic device (P-Max, Satelec) at various power settings.

### 15.2.3 Imaging and analysis

The water bath was placed in front of a microscope (BX-FM, Olympus, Tokyo, Japan) with 1.25-20 $\times$  magnification; the microscope was positioned horizontally in order to image the hydrogel from the side. Illumination was provided in bright-field mode using a continuous cold-light source (ILP-1, Olympus). A CCD-camera (LM156, Lumenera, Ottawa, ON, Canada) attached to the microscope recorded the behavior of the hydrogel at frame rates up to 28 fps.

Both positive and negative flow rates of the flow through the needle were used. From the deformation induced by the flow with positive flow rate, the Young's modulus of the hydrogel can be determined. Tracking the glass particles inside the hydrogel results in a strain  $\Delta y$  depending on the stress exerted by the flow from the needle. The stress on the hydrogel is roughly estimated from the stagnation pressure  $P_+$ , obtained from the Bernoulli equation:

$$P_+ = \frac{1}{2}\rho u_+^2 \quad (15.1)$$

thereby neglecting the complex two-way coupling of the flow with the hydrogel. The average flow velocity  $u_+ = Q/A$  can be calculated from the flow rate  $Q$  and the area  $A = \pi R^2$  of the needle orifice with radius  $R$ . The Young's modulus is then calculated from the stagnation pressure and the compression of the hydrogel  $\Delta y/Y_0$ :

$$E = \frac{P}{\Delta y/Y_0} \quad (15.2)$$

The flow with negative flow rate causes a negative pressure (suction) around the needle orifice. The magnitude of the pressure  $P_-$  is again difficult to determine due

to the two-way coupling between the flow and the hydrogel, but its order of magnitude can be estimated from the Bernoulli equation (equation 15.1), considering the flow going into the needle or the flow in-between the needle and the glass substrate (separated by a distance  $h$ ). The average velocity  $u_- = Q_-/A$ , where  $A$  can be the needle orifice area ( $A = \pi R^2$ ) or the influx area below the needle ( $A = 2\pi R h$ ).

For high-speed imaging of the behavior of the hydrogel, the low-speed camera was replaced by a high-speed CCD camera (HPV-1, Shimadzu Corp., Kyoto, Japan), recording at frame rates up to 250,000 fps. The other components of the setup were the same as for the low-speed imaging.

### 15.2.4 Chemical cleaning

The time scale of chemical removal of the hydrogel was assessed by submerging a 2D hydrogel into bleach and observing its removal. The hydrogel was placed inside a chamber of height 150  $\mu\text{m}$ , length 20 mm and width 3 mm, created by fixing a cover glass (20 $\times$ 20mm) on top of a microscope slide using double-sided tape with thickness 150  $\mu\text{m}$ . The hydrogel inside the chamber was only accessible from two sides. The glass slide was then immersed in a tank (dimension 45  $\times$  25  $\times$  30 mm) filled with 30 mL of a 5% NaOCl solution (Sodium Hypochlorite, Sigma-Aldrich, St. Louis, MO, USA) and recording of the process was started to observe the removal rate of the hydrogel. For the recording the same equipment was used as for the low-speed imaging, but now with a recording speed of 14 fps. This measurement was done three times; another recording was made while an ultrasonically oscillating file (same as before) was oscillating at a distance of 500  $\mu\text{m}$  from the entrance of the hydrogel chamber, at an angle of 45° with respect to the chamber. As a control experiment the plate was submerged in a tank containing demi-water.

Analysis of the reaction rate was done by tracking the interface between the hydrogel and the bleach during a recording, which was moving into the chamber. The resulting change in the interface location versus time was filtered with a running average filter over 10 samples with Gaussian weighing, and recalculated to volume.

## 15.3 Results

### 15.3.1 Viscoelastic properties of the hydrogel

A positive flow rate from the needle positioned at 300  $\mu\text{m}$  from the hydrogel-covered glass substrate resulted in elastic deformation of the hydrogel for flow rates below 0.05 mL/min (stagnation pressure 20 mPa); the hydrogel relaxed elastically to its original shape after switching off the flow. For flow rates above 0.05 mL/min, the hydrogel started to show viscous behavior by flowing away from the stagnation point of the needle flow; switching off the flow resulted in a net displacement of the particles

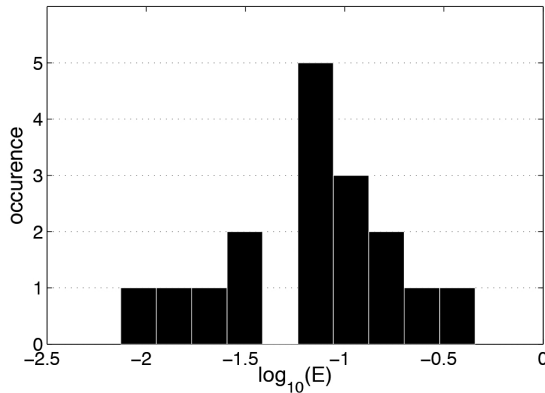


**Figure 15.1:** Measured values of the Young modulus of the hydrogel and their occurrence.

in the hydrogel with respect to their initial position. Viscoelastic behavior is therefore apparent. Flow rates higher than 0.20 mL/min (stagnation pressure 300 mPa) resulted in plastic deformation by permanent disruption (failure), and in the end removal, of the hydrogel.

From the recordings, 17 particles were selected which appeared in the center of the flow from the needle, based on their location and whether or not the particle was in focus. For these particles the maximum displacement was recorded, with which the Young's modulus was calculated. The resulting values and their occurrences are plotted in figure 15.1, showing that the Young's modulus has a magnitude of the order of  $10^{-1}$  Pa. The spread in the result is due to the particles not being exactly in the center of the flow from the needle, and the hydrogel properties may have varied.

The viscoelastic behavior was also visible when the needle approached the hydrogel while having a constant, positive flow rate (supplementary movie 1). Figure 15.2 shows the displacement two particles entrapped in the hydrogel. When the needle was positioned far away these particles do not move. However, when the needle is approaching within a distance of 600  $\mu\text{m}$  the particles start to displace, following elastic behavior. When the needle is held at a distance of 450  $\mu\text{m}$  or less, the particles are still displacing, even though there is no change in the flow, suggesting viscous behavior.

Suction through the needle (supplementary movie 2) caused deformation of the hydrogel at low flow rates; for flow rates above 0.2 mL/min, sloughing was observed. During sloughing, the hydrogel was stretched and was observed to flow (viscoelastic behavior) toward the needle orifice, until a part of the hydrogel detached, after which the hydrogel retracted elastically and remained stationary or started another cycle of sloughing, depending on the suction pressure. Continuous sloughing removed the

hydrogen part by part, also the parts attached to the glass substrate. For flow rates above 0.5 mL/min, the hydrogel was completely removed; for lower flow rates parts of the hydrogel could remain. Figure 15.3 shows the trajectory of five particles during sloughing. The retraction after sloughing (after approximately 4 and 17 seconds) can be observed as a indication of elastic behavior; the overall displacement after sloughing or when the flow was stopped suggests viscous behavior.

The fluidic pressure toward the needle orifice needed for sloughing and detachment to occur was of the order of  $10^{-1}$  Pa.

### 15.3.2 Ultrasonic irrigation

The flow induced by an ultrasonically oscillating file at a distance of  $100\ \mu\text{m}$  from the hydrogel was observed to always remove the hydrogel, except at the lowest power setting ('Green 1'). By approaching the hydrogel during file oscillation, the hydrogel was observed to deform, similar to the flow from a needle at low flow rate, suggesting that the steady component of the flow was causing the removal of the hydrogel. At

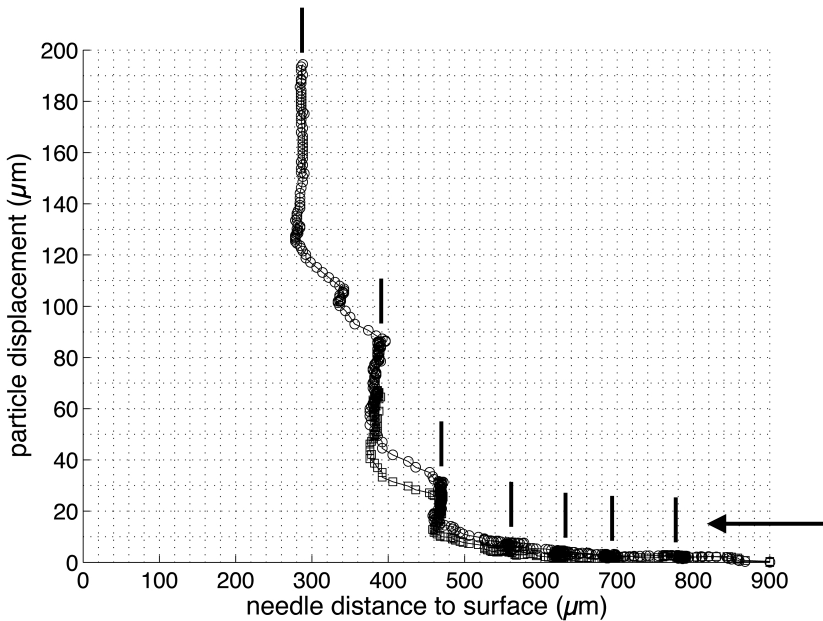


**Figure 15.2:** Displacement of two particles ( $\circ$  and  $\square$ ) in the hydrogel due to the flow from a needle that is approaching the hydrogel. The black arrow indicates the direction of approaching; each data point is one point in time ( $\Delta t = 35\ \text{ms}$ ). The vertical black lines indicate locations where the needle has been hold still for approximately 1 second. Flow rate: 0.05 mL/min.

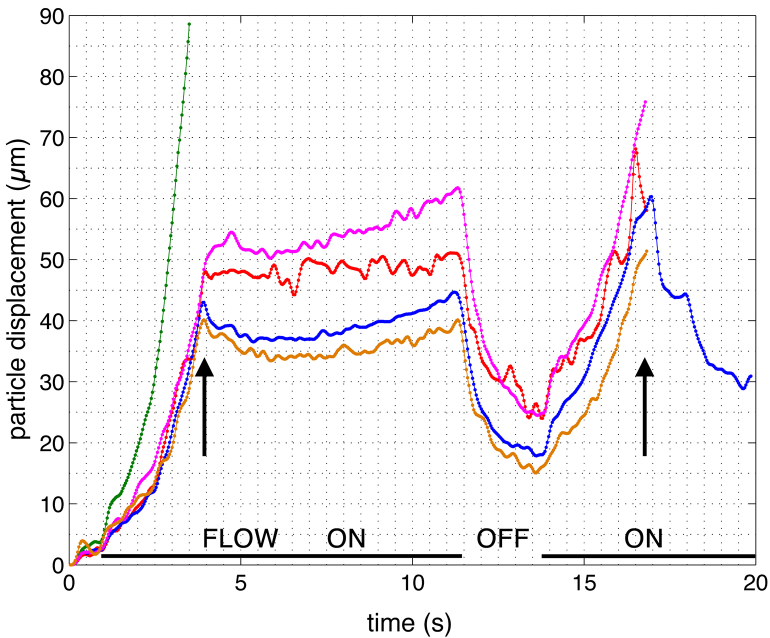
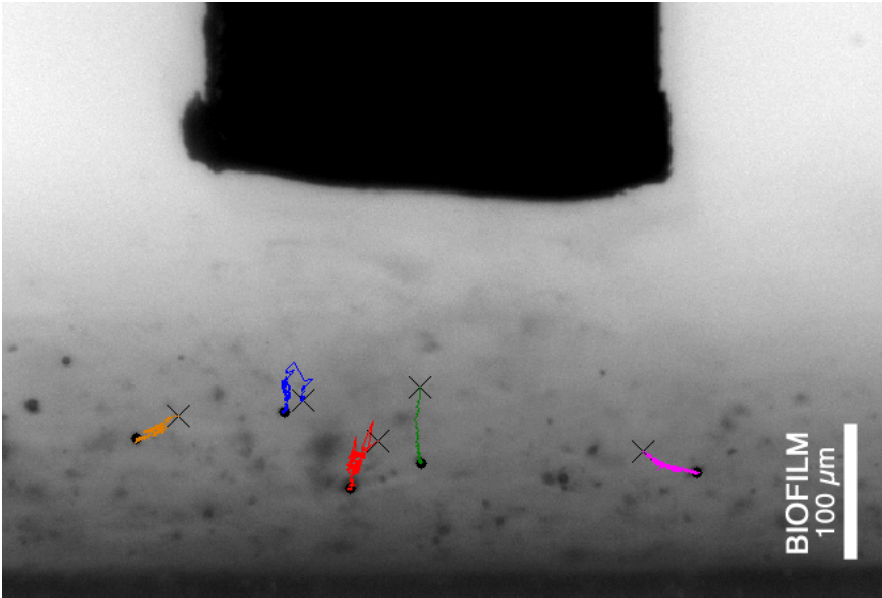


**Figure 15.3:** Displacement of five particles in the hydrogel due to suction flow from a needle. The top figure shows the particle trajectories, the bottom picture shows the corresponding displacement as a function of time. The first black arrow indicates the moment of sloughing of the green particle, the second black arrow indicated the moment of sloughing for the purple particle. The crosses are the final positions of the particles. The flow rate was 0.45 mL/min.

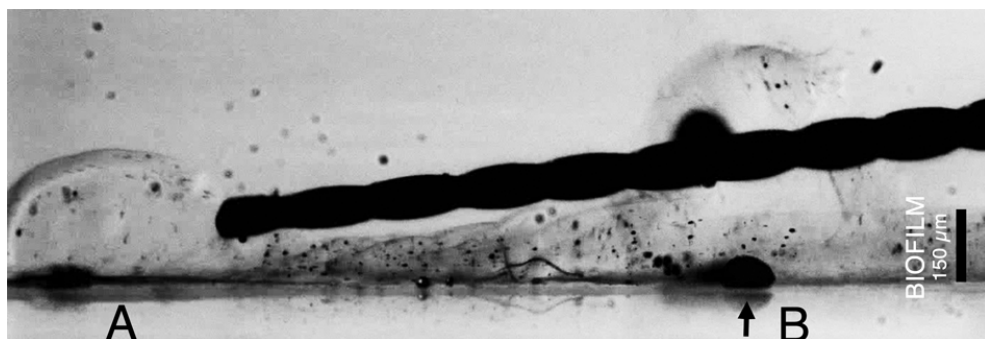


**Figure 15.4:** (*Movie 1*) Removal of the hydrogel with an ultrasonically oscillating file. The removal at location A is very similar to that caused by the flow from a needle and is due to the steady part of the acoustic streaming; the removal at location B is due to the bubble indicated with the arrow. The scale bar on the right shows the initial height of the hydrogel ( $150\ \mu\text{m}$ ).

small distances between the file and the hydrogel, the biofilm flowed away.

High-speed imaging at the time scale of file oscillations confirmed that at large distances between oscillating file and the hydrogel the hydrogel did not oscillate but only flows away. The hydrogel removal took place on a much larger time scale (order of  $100\ \text{ms}$ ) than the period of oscillation ( $33\ \mu\text{s}$ ) of the file. Only when the file was placed within  $100\ \mu\text{m}$  of the surface of the hydrogel, the hydrogel was observed to oscillate. However, these oscillations appeared to be elastic; no net displacement was observed due to the oscillatory motion. Furthermore, when looking along the file, the areas affected most were those associated with the antinodes of the oscillation pattern on the file.

Transient cavitation was observed in the high-speed images, as a cloud of bubbles was formed at the trailing edge of the tip of the oscillation file. However, this bubble cloud appeared to collapse back onto the file and not toward the biofilm, thereby not contributing to its removal. Occasionally, with low-speed imaging, a stable cavitation bubble was observed near or under the hydrogel (figure 15.4 and supplementary material movie 3). This bubble was very efficient in removing the hydrogel locally, where the streaming induced by the file was not enough to remove the hydrogel.

### 15.3.3 Reaction rate of the hydrogel with NaOCl

Within seconds after submerging the 2D hydrogel into NaOCl, bubbles started to appear within the hydrogel near its interface with the NaOCl (figure 15.5 and supplementary movie 4). These bubbles typically grew within 10 seconds to an average radius of  $30\ \mu\text{m}$ , before detaching from the hydrogel and floating upward. The parti-

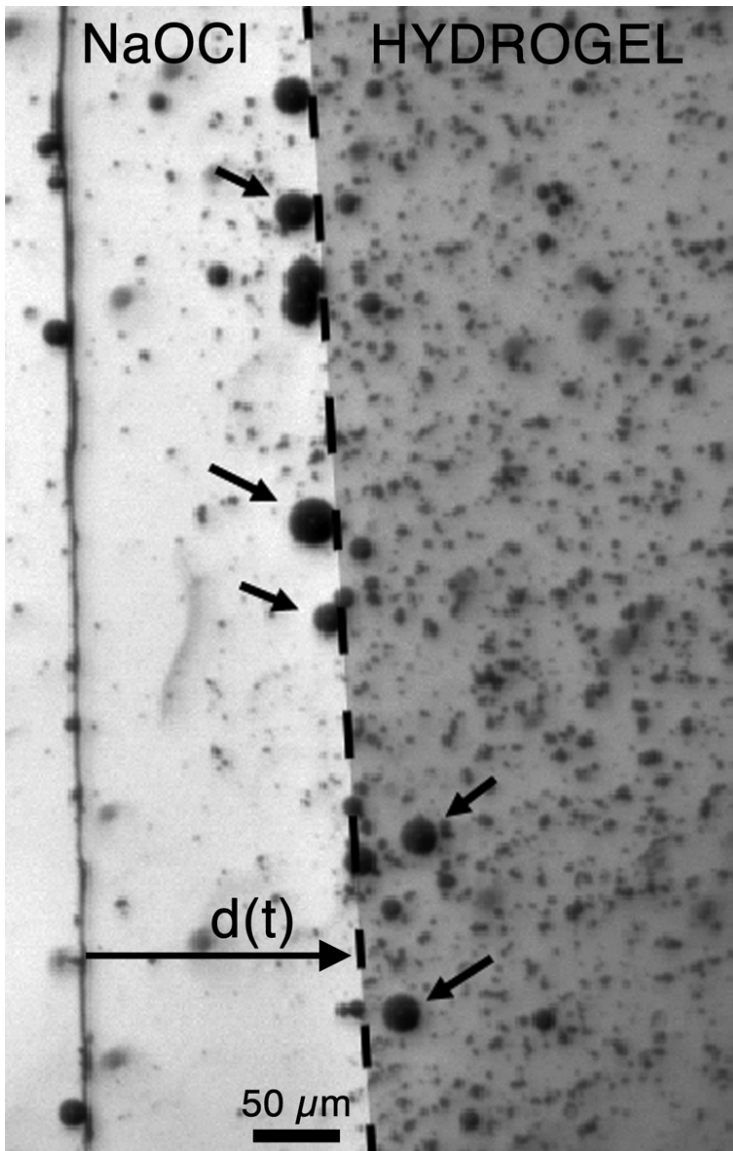


**Figure 15.5:** Image of the reaction interface (dashed line) between hydrogel and NaOCl. The hydrogel (on the right) is colored gray to aid the eye; the particles embedded in the hydrogel are also visible. Some of the generated bubbles are indicated with a black arrow; these bubbles grow within the hydrogel near the surface and detach when they have grown large enough. From these images the displacement of the interface  $d(t)$  is obtained. The vertical line to the left is the edge of the hydrogel chamber, indicating the initial position of the interface. This image is taken at  $t = 45$  seconds.

cles embedded in the hydrogel were observed to flow upward as well, suggesting that the generated bubbles take part of the hydrogel with them. The interface advanced over time at a speed of ca.  $10 \mu\text{m/s}$  (figure 15.6), from which the average reaction rate was calculated to be  $4.1 \cdot 10^{-6} \pm 1.0 \cdot 10^{-6} \text{ mL/s}$ . When the hydrogel was immersed in water, no bubbles were formed and the interface did not displace.

The presence of an oscillating file did not enhance the reaction rate significantly ( $3.83 \cdot 10^{-6} \text{ mL/s}$ ), suggesting that the mixing by ultrasonic irrigation was not beneficial and there was already enough NaOCl available to not slow down its reaction with the hydrogel.

## 15.4 Discussion

### 15.4.1 Mechanical properties of the hydrogel

The hydrogel used in this study was found to have viscoelastic behavior similar to biofilms. The Young's modulus of the hydrogel used in this study was found to

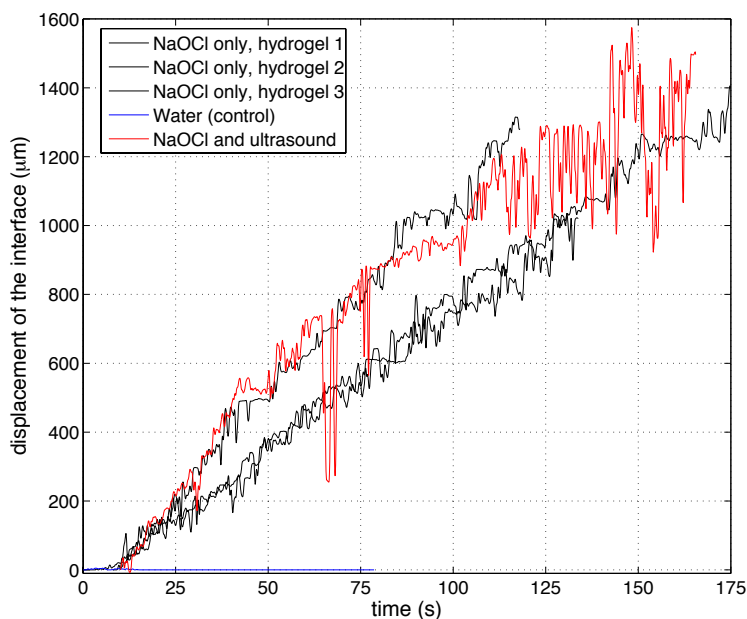


**Figure 15.6:** Interface displacement during the reaction of NaOCl with a 2D hydrogel layer (black) and in the presence of ultrasonic irrigation (red). The blue line shows the reaction rate when water was used instead of NaOCl.



be of the order of  $10^{-1}$  Pa; the cohesive and adhesive strengths were also of the order of  $10^{-1}$  Pa. Literature on the mechanical properties of real biofilms reports a Young's modulus of  $10^1$ - $10^3$  Pa [3, 6, 14–16]; three orders of magnitude higher than found for the present hydrogel. The cohesive shear strength is reported to be of the order of  $10^1$  Pa [15, 19] - two orders of magnitude higher than this hydrogel. The hydrogel could therefore be considered a soft, loosely attached biofilm. Changing the concentration of the ingredients of the hydrogel or varying the drying time or cross-linking with glutaraldehyde could result in a stiffer hydrogel. The attachment of the hydrogel to glass is, however, difficult to control [20], but is important since real biofilms are stratified, with a stronger, well adhering layer at its base [21].

Methods using a direct applied force, like tensile and compression tests or indenters coupled to force transducers [22], should be applied to get more exact values for the mechanical properties of hydrogels and biofilms. Hydrodynamic techniques always suffer from the complex interplay between the flow and the soft material, making it difficult to calculate the exact stress applied.

The advantage of the hydrogel used in this study over a biofilm is the fact that it can be made reproducibly. However, making the hydrogel reproducibly requires good control over component concentrations, temperature and drying time. In addition, swelling of the hydrogel was observed after several minutes during the visualization experiments, which affects its mechanical properties.

### 15.4.2 Cleaning mechanism of PUI

The recordings of the ultrasonically oscillating file and the hydrogel made clear that the steady component of the flow dominates in removing the hydrogel by applying a shear stress that has been calculated previously [12] to be able to attain values in the viscous domain of the viscoelastic behavior.

The shear stress due to the oscillating component of the flow only causes oscillatory elastic deformation of the hydrogel. While repeated elastic deformation could lead to hydrogel material fatigue over time [6], no plastic deformation appears to be caused by the oscillatory component.

For biofilms, being stiffer than the hydrogel, it is expected that the oscillating component of the stress is too small to cause sloughing or viscous deformation and the steady component is likely mainly responsible for the cleaning.

### 15.4.3 Cavitation

The time and length scales (gradients) associated with the exerted stress are important with regard to the behavior of a viscoelastic material. Cavitation bubbles, both transient and stable, typically exhibit large velocities and accelerations on a small time

scale, making them efficient in plastically deforming a hydrogel or biofilm (Chapter 16).

The observation that a stable cavitation bubble enhanced the hydrogel removal locally during ultrasonic irrigation, suggests that the addition of microbubbles could be beneficial for the removal of a hydrogel or biofilm in real-life applications. The oscillation velocity of these bubbles can be much higher than the oscillations induced by the ultrasound itself, and also typically occurs on a smaller scale [23]. The radius  $R_{bubble}$  (in mm) of such bubbles would have to match the driving frequency  $f$  (in kHz) of the ultrasound in order to have maximum oscillations of these bubbles [24]:

$$R_{bubble} = \frac{3.3}{f}. \quad (15.3)$$

The bubbles that were formed during the reaction between NaOCl and the hydrogel in the present experiments had a smaller average radius (30  $\mu\text{m}$ ) than the optimal radius (100  $\mu\text{m}$  at 30 kHz). The final size of the bubbles will depend on how quickly they can detach from the hydrogel and on the amount of gas produced, which in turn depends on the molecules in the hydrogel or biofilm. Therefore a biofilm, having a higher viscoelasticity and richer molecular composition than the present hydrogel, could very well generate bubbles that match the currently used frequency of 30 kHz. Bubbles are also known to attain the optimal radius under ultrasound irradiation through a process called *rectified diffusion* [25]. Alternatively, the bubbles could be driven to oscillate while they are still growing, i.e. at an earlier stage, which would require higher ultrasound frequencies. Bubbles that have grown to a size of 10  $\mu\text{m}$  would require a driving frequency of 330 kHz.

No literature has been found on the type of gas that is formed (and make up the bubbles) during the reaction between NaOCl and proteins. However, the smell that developed during the reaction resembled a 'swimming pool', which is known to be caused by (mono-, di- and tri-) chloramines ( $\text{NH}_2\text{Cl}$ ) formed during the reaction between HOCl and  $\text{NH}_3$  (ammonia in sweat and urine) [26, 27]. The NaOCl itself did not smell strongly. Nitrogen is also present in the proteins making up the gelatin, therefore chloramine gas is a good candidate for the gas type making up the bubbles.

Endodontic files have been demonstrated to generate transient cavitation under certain conditions (Chapter 12). While we have shown here that the transient cavitation bubbles do not tend to collapse toward the hydrogel, the production of radicals due to transient cavitation was found to be significant compared to the radicals in NaOCl, suggesting that transient cavitation at endodontic files may be capable of enhancing biofilm removal through sonochemical reactions within the root canal. Also, small, stable bubbles have been observed to split off during the transient cavitation near endodontic files. Furthermore, air may be entrained at the entrance of the root canal during Passive Ultrasonic Irrigation (see Chapter 12), contributing to the presence of stable bubbles inside the root canal.

## 15.5 Conclusions

A gelatin-based hydrogel showed viscoelastic behavior and is therefore a promising substitute for a biofilm when studying flow-biofilm interaction. However, in its current composition the hydrogel appears to be softer and weaker attached than a typical biofilm.

Imaging of the biofilm under mechanical or chemical strain showed that the main cleaning mechanism of passive ultrasonic irrigation appears to be the steady component of the induced acoustic streaming, possibly aided by stable cavitation bubbles, removing the hydrogel within one second. The oscillatory component of the flow and transient cavitation were not observed to contribute to biofilm removal. A chemical reaction with NaOCl showed slow disintegration (nanoliters per second) of the hydrogel, during which gas bubbles are formed. A higher ultrasound frequency could possibly make those stable bubbles enhance biofilm removal.

## 15.6 Acknowledgement

The author would like to thank prof. J.F.J. Engbersen for valuable suggestions regarding the composition of the hydrogel.

## References

- [1] H.-C. Flemming, T. R. Neu, and D. J. Wozniak, "The eps matrix: The "house of biofilm cells"", *Journal of Bacteriology* **189**, 7945–7947 (2007).
- [2] V. Körstgens, H.-C. Flemming, J. Wingender, and W. Borchard, "Uniaxial compression measurement device for investigation of the mechanical stability of biofilms", *Journal of Microbiological Methods* **46**, 9–17 (2001).
- [3] C. Picioreanu, M. Van Loosdrecht, and J. Heijnen, "Two-dimensional model of biofilm detachment caused by internal stress from liquid flow", *Biotechnology and Bioengineering* **72**, 205–218 (2001).
- [4] P. Stoodley, Z. Lewandowski, J. D. Boyle, and H. M. Lappin-Scott, "Structural deformation of bacterial biofilms caused by short-term fluctuations in fluid shear: An in situ investigation of biofilm rheology", *Biotechnology and Bioengineering* **65**, 83–92 (1999).
- [5] P. Stoodley, S. Wilson, R. Cargo, C. Piscitelli, and C. J. Rupp, "Detachment and other dynamic processes in bacterial biofilms", in *Surfaces in Biomaterials 2001 Symposium Proceedings*, 189–192 (Surfaces in Biomaterials Foundation, Minneapolis, USA) (2001).
- [6] H.-C. Flemming, J. Wingender, and U. Szewzyk, *Biofilm highlights*, Springer Series on Biofilms, 1st edition (Springer, Berlin, Heidelberg, Germany) (2011).
- [7] B. Van der Zaan, J. De Weerst, H. Rijnaarts, W. M. De Vos, H. Smidt, and J. Gerritse, "Degradation of 1,2-dichloroethane by microbial communities from river sediment at various redox conditions", *Water Research* **43**, 3207–3216 (2009).

- [8] P. Nair, "Pathogenesis of apical periodontitis and the causes of endodontic failures", *Critical Review of Oral Biology & Medicine* **15** (2004).
- [9] C. Boutsoukis, B. Verhaagen, M. Versluis, E. Kastrinakis, P. R. Wesselink, and L. W. M. van der Sluis, "Evaluation of irrigant flow in the root canal using different needle types by an unsteady computational fluid dynamics model", *Journal of Endodontics* **36**, 875–879 (2010).
- [10] M. J. De Cleen, A. H. Schuurs, P. R. Wesselink, and M. K. Wu, "Periapical status and prevalence of endodontic treatment in an adult dutch population", *International Endodontic Journal* **26**, 112–119 (1993).
- [11] L. W. M. Van der Sluis, M. Versluis, M. K. Wu, and P. R. Wesselink, "Passive ultrasonic irrigation of the root canal: a review of the literature", *International Endodontic Journal* **40**, 415–426 (2007).
- [12] B. Verhaagen, C. Boutsoukis, L. W. M. Van der Sluis, and M. Versluis, "Acoustic streaming induced by ultrasonically oscillating endodontic files", (to be) submitted to *Physics in Fluids* (2012), *see also Chapter 6 of this thesis*.
- [13] L. E. Chavez de Paz, "Redefining the persistent infection in root canals: possible role of biofilm communities", *Journal of Endodontics* **33**, 652–62 (2007).
- [14] S. Bayouhd, A. Othmane, L. Mora, and H. Ben Ouada, "Assessing bacterial adhesion using dlvo and xdlvo theories and the jet impingement technique", *Colloids and Surfaces B: Biointerfaces* **73**, 1–9 (2009).
- [15] W. M. Dunne Jr., "Bacterial adhesion: Seen any good biofilms lately?", *Clinical Microbiology Reviews* **15**, 155–166 (2002).
- [16] P. C. Y. Lau, J. R. Dutcher, T. J. Beveridge, and J. S. Lam, "Absolute quantitation of bacterial biofilm adhesion and viscoelasticity by microbead force spectroscopy", *Biophysical Journal* **96**, 2935–2948 (2009).
- [17] C. Mayer, R. Moritz, C. Kirschner, W. Borchard, R. Maibaum, J. Wingender, and H.-C. Flemming, "The role of intermolecular interactions: studies on model systems for bacterial biofilm", *International Journal of Biological Macromolecules* **26**, 3–16 (1999).
- [18] A. N. Jataru-Cadinoiu, M. Popa, S. Curteanu, and C. A. Peptu, "Covalent and ionic co-cross-linking - an original way to prepare chitosan–gelatin hydrogels for biomedical applications", *Journal of Biomedical Materials Research A* **98A**, 342–350 (2011).
- [19] Y. H. An and R. J. Friedman, *Handbook of bacterial adhesion*, 1st edition (Humana Press, Totowa, NJ, USA) (2000).
- [20] G. Sagvolden, I. Giaever, and J. Feder, "Characteristic protein adhesion forces on glass and polystyrene substrates by atomic force microscopy", *Langmuir* **14**, 5984–5987 (1998).
- [21] A. Rochex, A. Massé, R. Escudie, J. J. Godon, and N. Bernet, "Influence of abrasion on biofilm detachment: evidence for stratification of the biofilm", *Journal of Industrial Microbiology and Biotechnology* **36**, 467–470 (2009).
- [22] A. W. Cense, "A spray based method for biofilm removal", Ph.D. thesis, Technical University of Eindhoven (2005).

- [23] P. Marmottant, M. Versluis, N. De Jong, S. Hilgenfeldt, and D. Lohse, "High-speed imaging of an ultrasound-driven bubble in contact with a wall: "narcissus" effect and resolved acoustic streaming.", *Experiments in FLuids* **41**, 147–153 (2006).
- [24] C. E. Brennen, *Cavitation and bubble dynamics* (Oxford University Press) (1995).
- [25] M. P. Brenner, S. Hilgenfeldt, and D. Lohse, "Single-bubble sonoluminescence", *Reviews of Modern Physics* **73**, 425–484 (2002).
- [26] J. C. Bailar and A. F. Trotman-Dickenson, *Comprehensive inorganic chemistry*, 1st edition (Pergamon Press Ltd., Oxford, UK) (1973).
- [27] German Chemical Society, ed., *Gmelins handbuch der anorganische chemie*, chapter Chlor, 8th edition (Verlag Chemie GmbH) (1969).

## Appendices

### 15.A Supplementary material

(Online at [http://stilton.tnw.utwente.nl/rootcanalcleaning/Gallery\\_of\\_Irrigant\\_Motion](http://stilton.tnw.utwente.nl/rootcanalcleaning/Gallery_of_Irrigant_Motion))

Movie 1. Real-time visualization of the deformation of a hydrogel (dotted structure) due to a jet of water from a needle. The needle is approaching the hydrogel in steps of 100  $\mu\text{m}$ ; the flow rate is constant at 0.05 mL/min. Both elastic and viscous behavior can be observed. Scale: the outer diameter of the needle is 720  $\mu\text{m}$  (22G).

Movie 2. Real-time visualization of the deformation of a hydrogel (dotted structure) due to suction from a needle at a flow rate of 0.45 mL/min. Sloughing behavior can be observed. Scale: the outer diameter of the needle is 720  $\mu\text{m}$  (22G).

Movie 3. Real-time visualization of the removal of a hydrogel from a glass surface by PUI. A K-file is positioned at a large distance away from the hydrogel; an elastic deformation of the hydrogel near the file tip can be observed. Towards the end of the movie, a stable cavitation bubble can be observed to aid in the removal of the hydrogel. Recording speed is 15 fps; the hydrogel is initially 150  $\mu\text{m}$  thick.

Movie 4. Real-time visualization of the reaction between NaOCl (left) and the hydrogel squeezed between two plates (right, dotted structure; the solid line is the border of the plates). Bubbles can be observed to grow near the reaction interface; those reaching (on average) a radius of 30  $\mu\text{m}$  float upward (gravity is pointing downward). Bubbles generated elsewhere can also be observed to pass by, out of focus.

# 16

## Localized removal of layers of metal, polymer or biomaterial by ultrasound cavitation microbubbles \*

**Abstract** We present an ultrasonic device with the ability to locally remove deposited layers from a glass slide in a controlled and rapid manner. The cleaning takes place as the result of cavitating bubbles near the deposited layers and not due to acoustic streaming. The bubbles are ejected from air-filled cavities micromachined in a silicon surface, which, when vibrated ultrasonically at a frequency of 200 kHz, generate a stream of bubbles that travel to the layer deposited on an opposing glass slide. Depending on the pressure amplitude, the bubble clouds ejected from the micropits attain different shapes as a result of complex bubble interaction forces, leading to distinct shapes of the cleaned areas. We have determined the removal rates for several inorganic and organic materials and obtained an improved efficiency in cleaning when compared to conventional cleaning equipment. We also provide values of the force the bubbles are able to exert on an AFM tip.

---

\*Published as: D. Fernandez Rivas, B. Verhaagen, J. Seddon, A.G. Zijlstra, L.-M. Jiang, L.W.M. van der Sluis, M. Versluis, D. Lohse and Han J.G.E. Gardeniers. "Localized removal of layers of metal, polymer or biomaterial by ultrasound cavitation microbubbles", *Biomicrofluidics* **6**, 034114 (2012)

## 16.1 Introduction

Bubbles have been under analysis at least since the Greek times [1], and play an important role in physics, chemistry, medicine, and technology. The generation of bubbles by acoustic cavitation has been studied for many years, however without special measures there is little control over its occurrence and their behavior can at first sight be surprising and puzzling [2]. Whether or not cavitation due to pressure oscillations will occur, depends not only on the acoustic field, but also on physical properties and conditions such as the amount of gas in the liquid and the presence of nucleation sites. Once these are controlled, one can achieve fully controllable cavitation, in excellent agreement with the theoretical predictions [3].

Cavitation has found use in several applications, based either on its chemical or mechanical effects [4–7]. In water solutions exposed to ultrasound, for example, an enhancement of chemical reactions can be achieved. Short lived radicals form at the breakdown of water molecules, due to the high pressures and temperatures in the collapsing bubble's interior [8–10].

The use of acoustics in microfluidics and specially in bio-applications has received considerable attention in the last decade [11–13]. Acoustic cavitation can produce surface modifications, including damage, through high-speed liquids jets and shockwaves generated upon the asymmetric collapse of cavitation bubbles near a surface [14–16]. These mechanical effects have been considered by many as negative, as it may give rise to significant erosion and abrasion, for example demonstrated by the cavitation damage on ship propellers [2] and artificial heart valves [17, 18]. However, in specific cases the mechanical effect of cavitation has been shown to be useful for practical applications, for example for cell disruption and drug uptake [19, 20], or mixing and particle size reduction [21]. besides several other biological effects [15, 22]. Also in electronics, cavitation has been useful for the modification of surfaces (roughening, cleaning and gold plating, among others), using liquids as benign as water. The undesired use of hazardous substances, high temperature and long process times can be avoided or reduced by the use of cavitation [23]. The use of ultrasound has therefore been considered as a “green solution” for the above mentioned applications, given the reduction in power usage and chemicals.

Nevertheless, practical uses of cavitation are in general limited because of a lack of control over the location and amount of cavitation. Under the irradiation of ultrasound to a liquid, bubbles originate from nuclei at random locations. Quantification of cavitation effects (erosion and cleaning particularly) is very difficult due to its random occurrence and also due to different materials and equipment used in different laboratories and industrial equipment [4, 24]. This situation has prevented the upscaling and extended usage of desirable effects of cavitation such as localized cleaning or surface modifications [25]. Control over cavitation location requires special measures as, for example, the use of a laser [19], by seeding the liquid with particles

and irradiating with a shockwave [26], or from gas-filled crevices in smooth surfaces exposed to shockwaves [27], or continuous ultrasonic irradiation [28].

Here we show the generation of cavitation in various liquids for fast removal (order of tenths of seconds) of several deposited materials from a glass substrate with millimetric control, based on well-defined cavitation nucleation sites [28]. This article will start with the description of the experimental setup for the localized generation of cavitation, as well as the methods for characterization of unwanted cavitation erosion on the underlying substrate. Next, a short description of the various materials that have been investigated for removal by cavitation is given. Additionally, to obtain information on the force generated by a bubble, a measurement of the magnitude of the forces that the bubbles exert on an AFM tip is provided. The measured material removal rates will be presented and discussed; determination of the adhesion strength of the different materials is described in the appendices.

## 16.2 Experimental setup

### 16.2.1 Materials to be removed

The cleaning of surfaces is a process that is required in a wide variety of applications, with an equally wide range of materials that need to be removed from the given surface. Each of these materials and surfaces have their specific mechanical and chemical properties that provide different adhesion strengths between both. Here we list some typical materials to be removed, which are all studied in this work.

#### 1. Solid hard materials

The solid hard materials used in this study are Gold (Au), Platinum (Pt), Chromium (Cr) and Titanium (Ti), both categorized as metals, and Olin and AZ96, which can be categorized as organic materials, and are commonly used as photoresists in microfabrication of semiconductors and microelectromechanical systems (MEMS).

#### 2. Soft biomaterials

Contrary to the solid hard materials, soft biological materials may deform (visco)elastically before cohesive or adhesive failure takes place [29, 30]. Elastic materials typically display significant strain when subjected to a stress, and relax back to the initial shape and position when the stress is removed. Only when the stress exceeds the material's yield stress and enters the plastic domain of the soft material, cohesive failure will take place. Viscoelastic materials, however, exhibit viscous behavior when the stress exceeds the yield stress; the material will flow away and there will be a net displacement when



the stress is removed [31, 32]. One of the most commonly encountered viscoelastic materials is the biofilm, which can often be found in pipes, on medical implants and inside and on teeth, where it often has a negative influence on efficiency or health [30, 33]. The biofilm is a structure of bacteria enclosed by a self-produced extracellular matrix [34, 35]. This matrix provides the viscoelastic properties of the biofilm, which protects the embedded bacteria from high stresses.

### 3. Cells

Another biological material of great importance nowadays is a cancer cell. The study of the reaction of a cell to different environmental conditions with minimal interference in their habitat is still a problem. Cavitation has been used to address this issue [22, 36], while it also is able to porate cells for drug uptake due to shear forces [19].

## 16.2.2 Material removal experiments

### Ultrasonic cavitation setup

The continuous and localized generation of cavitating bubbles has been accomplished by ultrasonically vibrating a silicon surface containing micropits [28]. When pouring liquid over the silicon substrate, individual gas bubbles were entrapped in the pits; vibrating the surface ultrasonically resulted not only in acoustic streaming from the oscillating surface, but for large enough pressures also in pinch-off of gas bubbles from the micropits, as detailed elsewhere [37].

The silicon substrate with micropits was placed in a cavitation cell container made of glass with 25 mm outer diameter, 15 mm inner diameter and 6 mm depth, matching one quarter of the wavelength at the operation frequency of  $200 \pm 5$  kHz. A piezo element (PZ27, Ferroperm) of thickness 6 mm and diameter 25 mm was glued to the cell bottom. A sketch of the cavitation cell is given in Figure 16.1. For each experiment, the cell was filled with fresh ultra-pure water (milliQ, milliPore). Also, ethanol, bleach and acetone were investigated given their extensive use in general and ultrasonic cleaning applications. Additionally, a cell cultivation liquid medium was used.

The micropits were etched under clean room conditions on double-side polished silicon wafers by means of a plasma dry-etching machine (Adixen AMS 100 SE, Alcatel). The wafer was then diced in square chips with a side of 10 mm. The edge of these substrates have a step of  $58 \mu\text{m}$  with four notches radially and equally spaced (see Figure 16.2).

Each pit had a diameter of  $30 \mu\text{m}$  and a depth of approximately  $10 \mu\text{m}$ ; multiple pits were arranged in four different configurations: single pits, two pits separated by

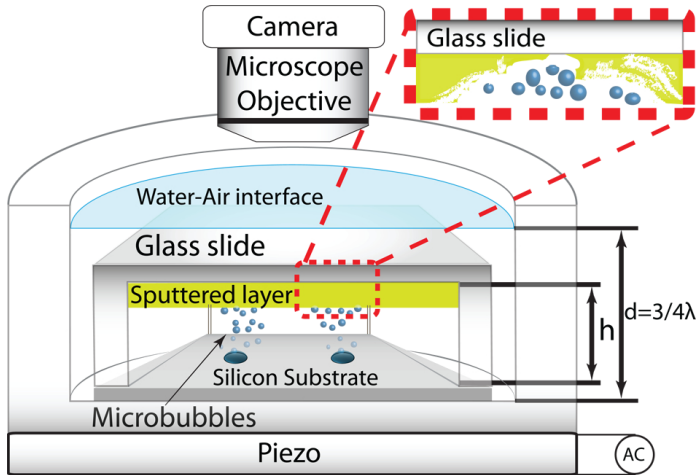


**Figure 16.1:** Schematic representation of the experimental setup. The gap between the glass slide and the silicon substrate  $h = 100 \mu\text{m}$ . The water column height is 5 mm.

a distance of 1 mm, three pits arranged at the corners of an equilateral triangle with a side of 1 mm, and four pits at the corners of a 1 mm side square.

The piezo element was driven by a sinusoidal signal generated by an arbitrary waveform generator (33120A, Hewlett Packard) and amplified by means of an audio amplifier (TA-FB740R QS, Sony). The voltage, current and power to the piezo element were monitored with a power meter (HM8115-2, Hameg). The duration of the experiments was short enough (typically less than 5 minutes) so that the temperature increased no more than approximately  $5^\circ\text{C}$  (measured with a T-type thermocouple with digital read-out; HI 93552R, HANNA Instruments).

Two different power settings were used with all pit arrangements: Low (0.182 W) and High (0.629 W). The corresponding approximate acoustic pressure amplitudes were measured to be 225 kPa and 350 kPa, with error values provided by the manufacturer as 20%. These pressures were measured using a needle hydrophone (HNR-500, Onda) positioned  $65 \mu\text{m}$  above the center of the chip.

### Imaging setup

The occurrence of cavitation and the removal of the deposited materials was imaged through the air-water interface with a CCD camera (LM165M, Lumenera Corp., Ottawa, ON, Canada), recording at a frame rate of 15 fps and an exposure time of  $10 \mu\text{s}$ . For the removal of metal layers, a color high-speed camera (SA2, Photron, San Diego, CA, USA) was used, recording at frame rates between 60 and 2000 frames per second and an exposure time of  $30 \mu\text{s}$ . The cameras were attached to a microscope (BX-FM, Olympus, Tokyo, Japan) with  $10\times$  magnification, with a focal depth

Table 16.1: Overview of material properties and removal characteristics

Material	Layer thickness ( $\mu\text{m}$ )	Contact angle ( $^\circ$ ) Advancing, Receding	Removal by... (Y/N/Partial) Bubbles, Scratch	Removal rate ( $\text{mm}^2/\text{s}$ )	Adhesion <sup>d</sup>
Glass	-	$79.9 \pm 1.3, 41.0 \pm 1.7$	- <sup>d</sup>	- <sup>e</sup>	- <sup>e</sup>
<i>Solid materials</i>					
Gold	$45 \cdot 10^{-3}$ <sup>b</sup>	$86.9 \pm 0.5, 72.7 \pm 0.6$	Y, Y	0.01	$2260 \pm 50$ N/m
Platinum	$36 \cdot 10^{-3}$ <sup>b</sup>	$87.0 \pm 0.3, 73.7 \pm 0.9$	Y, Y	0.001	$4400 \pm 150$ N/m
Chromium	$45 \cdot 10^{-3}$ <sup>b</sup>	$75.7 \pm 0.6, 42.5 \pm 1.5$	N, N	- <sup>e</sup>	- <sup>c</sup>
Titanium	$15 \cdot 10^{-3}$ <sup>b</sup>	$73.6 \pm 0.8, 45.8 \pm 2.4$	N, N	- <sup>e</sup>	- <sup>c</sup>
<i>Organic materials</i>					
Olin	$3.5 - 5.2$ <sup>b</sup>	- <sup>c</sup>	N, P	- <sup>e</sup>	- <sup>c</sup>
AZ96	$2.0$ <sup>b</sup>	- <sup>c</sup>	N, P	- <sup>e</sup>	- <sup>c</sup>
<i>Biomaterials</i>					
Biofilm	20	- <sup>c</sup>	Y, - <sup>c</sup>	0.1	$10^{-1}$ N/m <sup>2</sup>
Hydrogel	100	- <sup>c</sup>	Y, - <sup>c</sup>	0.1	- <sup>c</sup>
Cells	- <sup>c</sup>	- <sup>c</sup>	Y, - <sup>c</sup>	- <sup>c</sup>	- <sup>c</sup>

<sup>a</sup>Solid materials: N/m, measured with AFM; Viscoelastic materials: N/m<sup>2</sup>, measured with hydrodynamic technique

<sup>b</sup>Thickness determined with a Profile measurement device (Veeco Dekak 8)

<sup>c</sup>These values could not be measured

<sup>d</sup>No glass erosion took place as a result of bubble cavitation activity for less than 30 min

<sup>e</sup>Not applicable

of approximately 10  $\mu\text{m}$  [38]. Illumination was provided through the microscope in dark-field mode by a continuous cold-light source (ILP-1, Olympus).

The recordings of surface layer removal were analyzed using MatLab (The Mathworks, Natick, MA, USA), by converting each frame to black and white and determining the cleaned area. The size of each pixel was determined using a calibration grid with markers of well-defined size.

### Layer deposition

The glass slides on which materials of interest were deposited were made of fused silica wafers. A circular chamber of 8 mm diameter and a depth of 158  $\mu\text{m}$  and four protruding notches that match the notches in the silicon substrate (described before) were etched on one face of each glass slide section. The wafer was then diced in chips with a side of 10 mm. In this way when placing the glass slide on top of the silicon substrate a microchamber of 100  $\mu\text{m}$  height was formed (see Figure 16.2). Each material type that was investigated required a different deposition procedure, which is now outlined.

**Solid hard materials** A single wafer sputter coater (home-made system available in MESA+ Nanolab) for deposition of metallic layers was used to deposit gold, platinum, chromium and titanium. To deposit organic materials (photoresists Olin 35 and AZ96), hexamethyldisilazane (HMDS) was first spin-coated as a primer to provide chemical bond of the photoresists and strong adhesion to the glass slide on a single wafer spin-coater (Primus coater WB21).

**Biomaterials** The biofilm model used here was described recently for use in endodontics [39]. In brief, round glass coverslips attached to a customized stainless steel lid were suspended in a medium inoculated with bacteria. In this model, biofilm attachment and growth is an active process against gravity. Microbiology Cells of *E. faecalis* V583 and *P. aeruginosa* HG 1776, both clinical isolates, were grown and maintained as pure cultures on blood agar plates. *E. faecalis* was cultured under anaerobic conditions (80%  $\text{N}_2$ , 10%  $\text{H}_2$  and 10%  $\text{CO}_2$ ) whilst *P. aeruginosa* was cultured in air, both at 37 °C. Growth medium for overnight cultures of biofilms was BHI broth containing 0.5 BHI, 50 mmol/L 1,4-piperazinediethanesulfonic acid, buffer, 5% saccharose and 1 mmol/L  $\text{Ca}^{2+}$ . Phosphate-buffered saline was used to wash during refreshment of the medium. *E. faecalis* and *P. aeruginosa* were inoculated in wells with additional  $\text{Ca}^{2+}$  in the broth of a 24-well multiwell plate. Round glass coverslips, diameter 12 mm and thickness 140  $\mu\text{m}$ , mounted on a custom-made stainless steel lid, were suspended in the broth. In this experiment, biofilms grown for 96 hours were used. The broth was refreshed daily. Inoculation of bacteria and the biofilm growth took place at 37 °C in air. The average biofilm thickness was estimated to be 20  $\mu\text{m}$ , with some bacteria colonies up to 50  $\mu\text{m}$ .

A biofilm was mimicked with a hydrogel, created by dissolving 1 g gelatin (Merck,

Whitehouse Station, NJ, USA), 0.02 g hyaluronan (Sodium hyaluronate 95%, Fisher, Waltham, MA, USA) and 0.1 g red food color (KTC, Wednesbury, UK) in 45 mL warm water[40]. Hollow glass spheres with a mean diameter of 10  $\mu\text{m}$  (Spherichel, Potters Industries, South Yorkshire, UK) were added as tracer particles. The final density of the hydrogel was  $1.07(\pm 0.07) \cdot 10^3 \text{ kg/m}^3$ . This hydrogel was cooled down to room temperature before depositing on a glass slide with raised edges of approximately 100  $\mu\text{m}$  height. The glass slide was then left to cool down for 7 or 15 minutes, during which the hydrogel dries and attaches to the glass, before the ultrasound and imaging was applied.

MCF-7 human breast carcinoma cells were cultured on the same glass slides; its adhesion resistance when exposed to the cavitation bubbles from the triangular array of micropits was investigated in the cavitation setup. The culture medium was made of Dulbecco's Modified Eagle Medium (DMEM, Gibco), L-Glutamate, fetal bovine serum (FBS), Antibiotics (Penicillin and Streptomycin) and Fungicide.

Table 16.1 gives an overview of the various deposited materials and their properties.

### 16.2.3 Cavitation damage

The glass substrate onto which the gold was deposited, was inspected for erosion damage using a scanning electron microscope (SEM, HR-SEM 1550, Zeiss). After the gold was removed by cavitation, the glass substrates were exposed to cavitation for another 1, 5, 10, 15 or 30 minutes before SEM images were taken.

### 16.2.4 AFM up-thrust measurements of cavitation cloud force

An Atomic Force Microscope (AFM, Agilent 5100) in non-contact tapping mode was used to measure the up-thrust force from the bubble cloud. A silicon  $n^+$  flat disc tip cantilever (Nanosensors PL2-NCLR-10, spring constant of 48 N/m and resonant frequency 190 kHz in air and 73 kHz in water) with a diameter of ca. 1.8  $\mu\text{m}$  and tip height of ca. 12  $\mu\text{m}$  was used. The cantilever was withdrawn 100  $\mu\text{m}$  from a single-pit substrate surface to mimic the separation between the micropits and 'to-be-cleaned' surfaces in the previous measurements. Both low and high ultrasonic powers were used, although for the high power the resulting signal was clipping. The cantilever approached from a distance of 1 mm in a line passing over the bubble clouds. As it happens in the experiments with the glass slides and deposited layers, the bubbles traveled to the cantilever and collapsed against it. Unfortunately, the cantilever was destroyed during the second pass at this force, so the measurements were stopped.

## 16.3 Results

### 16.3.1 Cavitation occurrence, in the absence of deposited materials

Switching on the ultrasound leads to a continuous generation of microbubbles with a size range of 2-17  $\mu\text{m}$ , determined from the video recordings and shown in Figure 16.8 (see also Fernandez *et al.* (2012) [41]). Bubbles smaller than 2  $\mu\text{m}$  could not be visualized due to the resolution of the camera. Varying the pressure amplitude (power) and the different arrangements of pits resulted in different bubble patterns, as a result of the complex interplay of primary and secondary *Bjerknes forces*, microstreaming and also the inertial forces acting on the moving microbubbles in the close vicinity of the glass slide. The bubbles were observed to travel towards the glass slide on top of them where they come in focus of the optical setup. This upward motion is a result of the effect of secondary Bjerknes forces, which makes bubbles close to a hard surface “feel” the presence of their image bubble as an attraction force, driving the bubbles closer to the wall.

Increasing the power resulted in an increase in the number of ejected bubbles around the pits, forming a bubble cloud or cluster. At high power, with more than one pit, the bubble clusters are attracted to each other and at a given power level (between 0.182 and 0.629 W), the bubbles start to travel towards the geometrical center of the pit array [28, 41] (see Figure 16.7 left column). These bubble cluster configurations are reversible, although there is hysteresis in the amplitude necessary to return to the separated clouds, which is lower than needed for making the bubbles travel to the geometrical center of the pit configuration.

### 16.3.2 Removal of deposited materials by cavitation

#### Observations

Compared to the experiments with and without glass slide, a clear difference can be observed in terms of stabilizing the free water-air interface oscillation when the glass slide is not present. When the glass slide is placed, the traveling and standing wave components change dramatically, contributing to complex effects of bubble cavitation conditions (measured for example through the occurrence of sonochemical reactions) [42].

The opaque materials deposited on the glass slide, when placed on top of the cavitation cell, did not allow for optical visualization of the cavitation bubbles. However, taking as a representative example the case of deposited gold, when switching on the ultrasound at low power (0.182 W), we see that almost instantly (within 2 seconds) a small opening appears in the gold layer right on top of where the pits are located (Movie 1). If the power is kept constant the removed gold layer area increases slowly over time. For the case of one pit, increasing the power makes the removed

area increase until a maximum area is reached (approximately  $0.03 \text{ mm}^2$ ). Increasing the power for the two, three and four pit geometries, for which situation the bubbles travel to the geometrical center as described above, an area corresponding to the area of the bubble trajectories is removed. Therefore, for two pits a linearly extended area is typically observed. Accordingly, we find a triangular shape for the three pits and a distorted rectangular shape for the case of four pits; see Figure 16.2 and Figure 16.7, right column. For Au and Pt we observed a similar surface removal behavior.

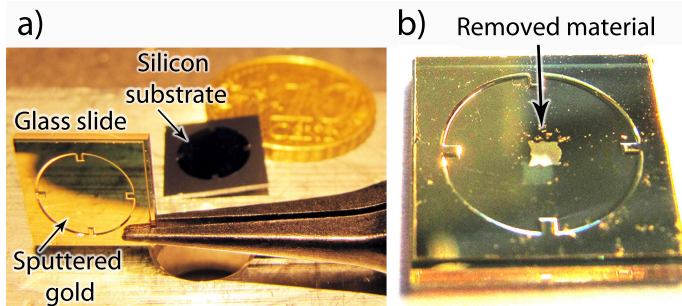


**Figure 16.2:** a) A black tweezer holds a gold sputtered glass slide prior to exposure to cavitating bubbles; in the background a silicon substrate is shown. b) A zoomed view of the same glass slide after exposure to cavitating bubbles from four pits in the cavitation cell described in this paper. The glass slide has sides of 10 mm.

For the cases of deposited Cr, Ti and the organic materials, there was no surface removal with the same initial conditions as for Au and Pt. Manually creating a scratch in the layer close to the geometrical center allowed for confirming the presence of the bubbles in the scratched areas, but no material was removed from Cr and Ti layers. After scratching of the photoresist materials the bubbles were able to detach a few pieces of photoresist material only occasionally (Figure 16.3 and Movie 2). The removed pieces of (all) layers could sometimes be trapped by the oscillating bubbles for a relative long period of time (at least more than 30 seconds if no conditions changed).

When the ultrasound is switched off abruptly, the pits may be expected to be filled with water and perhaps, if a bubble is still inside any of the pits, are unable to nucleate more bubbles, deactivating the acoustic bubble generation. If ultrasound is turned on again therefore no cavitation from the micropits takes place. This is why this procedure allows for studying the effect of acoustic streaming alone on material removal. We could not observe removal of any material in the situations where no bubbles were present, allowing us to conclude that the forces associated to streaming alone were not sufficient to remove any of the tested materials. The quantification of streaming from the air-filled pits could not be assessed with the current setup.

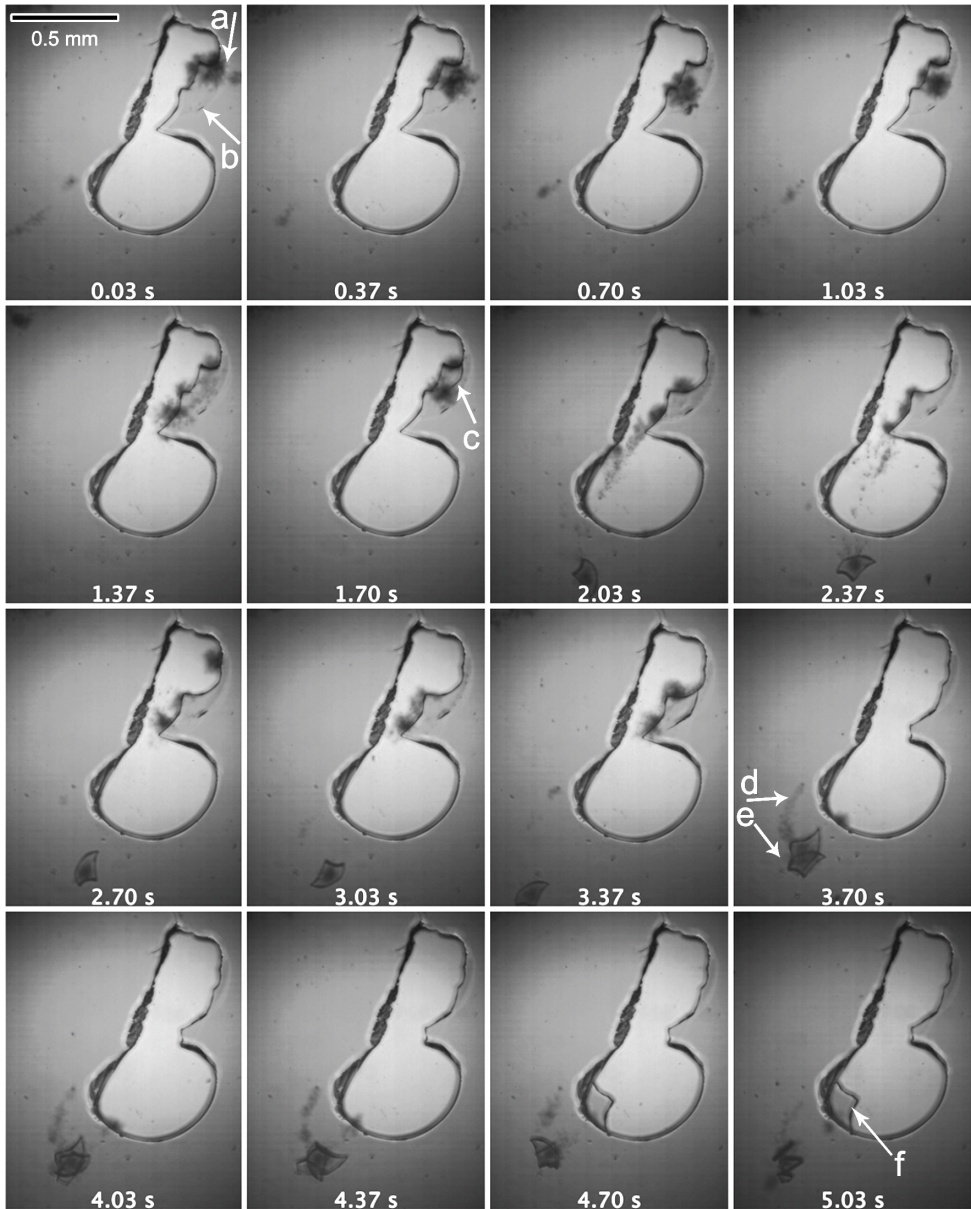


**Figure 16.3:** (Movie 2) Montage of a time series of frames recorded for the case of AZ96 photoresist. The center part of each frame shows a portion of manually removed AZ96. Arrow a points out a cloud of bubbles as a darker region cavitating close to a crack in the AZ96 layer (arrow b). Arrow c shows how the crack grew within about 1 second. After 1.7 s, the bubbles (arrow d) “trapped” a small portion of AZ96 as indicated by arrow e. Eventually, after approximately 4.7s, the small portion gets stuck in the border line of removed material. The pits do not appear in these pictures since they are out of the field of view.



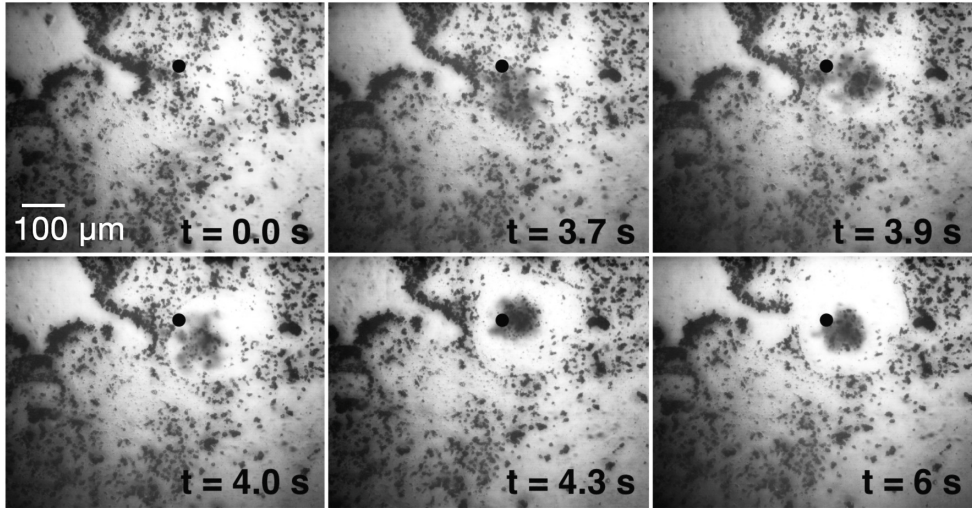


**Figure 16.4:** (Movie 3) Stills from a recording of a biofilm being removed by bubbles. The gray area with black dots is the area covered by biofilm, the location of the pit is indicated with a large black dot. The bubbles can be identified as the blurred dark region around the pit.

The biofilm that was grown on a glass substrate was initially visible as a gray area containing dark clusters of bacteria (Figure 16.4 and Movie 3). Due to transparency of the biofilm the bubble cloud below the biofilm-covered substrate was visible when the ultrasound was turned on. The biofilm was then removed quickly when the bubble cloud was attracted by the biofilm-covered substrate. No biofilm was removed by the streaming or by bubble clusters when not attracted to the glass surface.

A similar behavior was observed for the hydrogel. The hydrogel appeared softer and attached with weaker force than the biofilm, both after 7 and 15 minutes of drying, but neither was removed by the acoustic streaming alone.

The distance between the hydrogel or biofilm and the micropits was less well-defined than for the metal and hard organic deposited layers, due to the non-uniform thickness of these layers and flexible (softer) nature. Therefore the bubbles were less likely to travel toward these layers, which resulted in slow or no increase in removed area after initial removal.

The MCF-7 cells grown on the glass substrate were also removed when the bubbles were present, leaving the outlier cells attached, as can be seen in Figure 16.5. The liquid cultivation media produced bubbles similar to those in water. The contour of the removed area resembles again the shape of the bubble cloud for the three pits configuration.

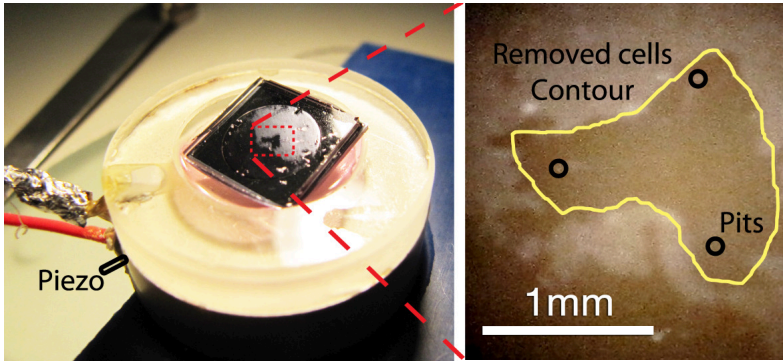


**Figure 16.5:** Cavitation cell and experimental results after removing MCF-7 cells fixed to a glass slide. The liquid cultivation media's pinkish color is visible inside the cavitation cell glued to the piezo.

### Removal rates

The area in which gold has been removed by the bubbles originated from a single pit, after approximately 1 minute, is of the order of  $0.1 \text{ mm}^2$ ; for 4 pits this area increases by one order of magnitude to  $1 \text{ mm}^2$ , see figure 16.6. The rate of removal during the initial growth of the removed area is of the order of  $0.1 \text{ mm}^2/\text{s}$ ; this reduces by one order of magnitude to  $0.01 \text{ mm}^2/\text{s}$  during steady growth. For platinum, once a scratch had been made, the steady removal rate is of the order of  $0.001 \text{ mm}^2/\text{s}$ .

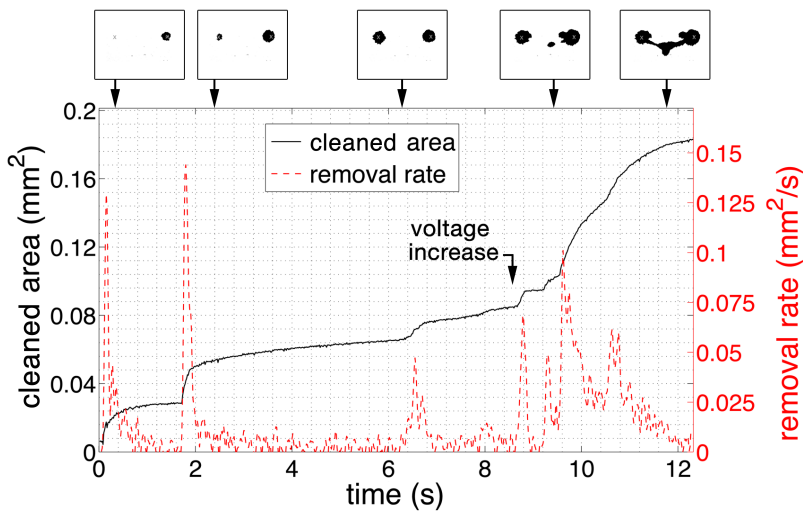


**Figure 16.6:** Size of cleaned area and its derivative (i.e., removal rate) extracted from video measurements

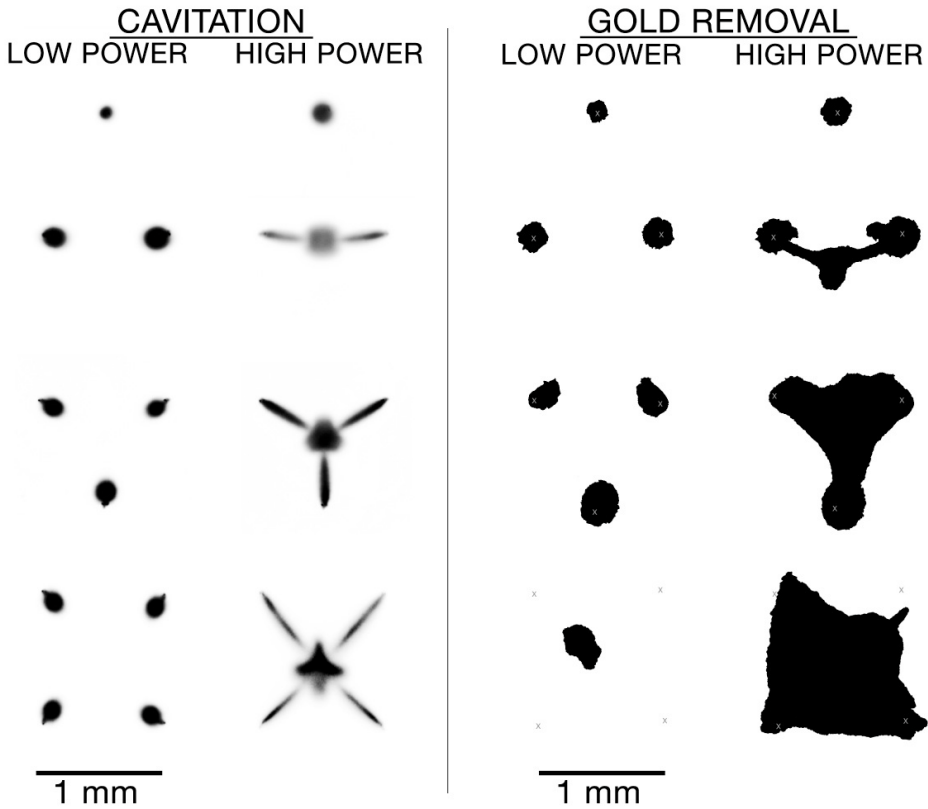


**Figure 16.7:** From top to bottom and left to right, the cases for 1 to 4 pits at low and high power. Left: Bright field illumination (inverted color) showing bubble patterns with slow speed imaging. Right: Contour shape of cleaned area in gold (black) due to bubble cavitation.

The removal of the hydrogel and the biofilm were recorded at lower imaging speeds, providing less detailed information on the removal rates. However, estimates for the removal rate of the hydrogel give a value similar to that of gold, being of the order of  $0.01 \text{ mm}^2/\text{s}$ , with initial removal rates up to  $0.1 \text{ mm}^2/\text{s}$ . The initial rate of removal of the biofilm was estimated to be  $0.1 \text{ mm}^2/\text{s}$  as well, with only minor increase in removed area after the initial removal.

The cleaning effect of bubbles is restricted locally by how close the pits and the nucleated bubbles are from the surface to be cleaned. The bubbles cannot travel farther than a given distance away from the pits, or nearby other bubbles. This is due to the required conditions for continuous cavitation such as available gas content and negative pressure values provided by the oscillating pressure field.

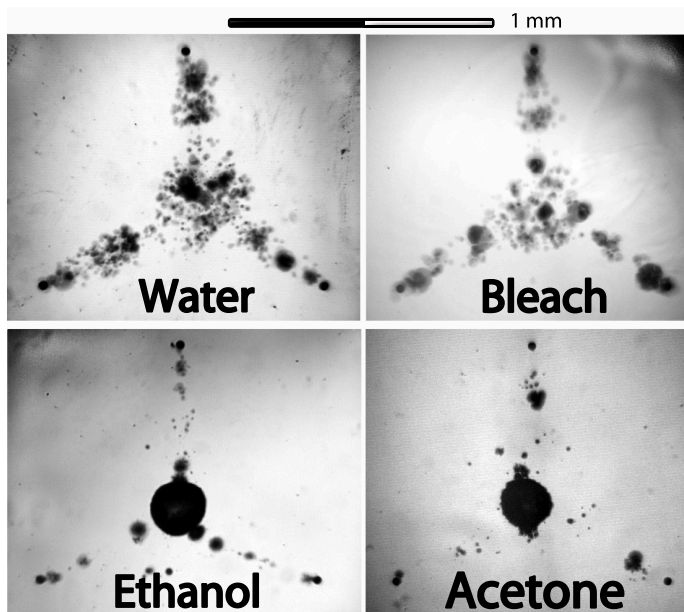


**Figure 16.8:** Bubble pattern for four different liquids tested (no glass slide on top). The bubbles generated are clearly different for each substance but qualitatively similar between water and bleach and between ethanol and acetone.

### 16.3.3 Different liquids

Bubbles were observed to be generated in all five liquids investigated. Individual images are shown in Figure 16.8. For water and bleach the bubble shapes are similar, with an apparent higher number of bubbles than for ethanol and acetone. For these two organic liquids we can see smaller bubbles ejected from the pits and a larger bubble growing at the midpoint that, upon reaching a given size, floats away. The experiments with MCF-7 cells were carried out with the same liquid cultivation media showing similar bubble cavitation as in water (see Figure 16.5). We expect similar removal effects for these liquids as for water, but it was not within the scope of this paper to address this topic further.

### 16.3.4 Cavitation erosion

After the maximum period of 30 minutes of ultrasound exposure, no erosion was visible on the glass surface, as investigated by SEM analysis. This shows a different effect than the erosion observed on Si surfaces in our previous studies [41]. The reasons for this are that Si has a crystalline atomic structure and is brittle whereas glass is amorphous and does not exhibit the same mechanical properties. Additionally, the erosion we observed on Si surfaces was on the substrates from which the bubbles

were generated, whereas here the bubbles have travelled a considerable distance (150  $\mu\text{m}$  from its nucleation sites) to the glass surface, and the acoustic conditions have changed considerably.

### 16.3.5 Bubble cloud forces

The AFM measurements showed that the force was intermittent, with an average deflection of the cantilever of ca. 500 nm, which corresponds to a force of 20  $\mu\text{N}$ . Using the tip area of the cantilever, the pressure exerted by the bubble cloud can be estimated to be of the order of 50 atm.

The force measurements in both directions of sweep were symmetric, which is especially important for the direction that runs along the length of the cantilever, across the tip, and into free water (where there are no bubbles present). The sweep force had a plateau maximum attributed to the cantilever being directly above the pit, plus slightly to either side but with the bubble streams redirecting to the tip. The value of the force given is the average of the maxima of both the lateral and long ways sweeps, which agree with each other to within error, which thus represents the bubbles hitting the end of the cantilever.

The sweeps pass over the end of the cantilever so we assume that the force measurements can be interpreted in the usual sense in AFM measurements. That the sweep along the length of the cantilever and into free space appears symmetric, represents the fact that the cantilever's "lever" is more than double the distance away from the surface.

Finally, in terms of incorrectly interpreting interference from bubbles as deflection, the laser spot is wholly and exclusively on the back side of the lever (we do not see interference with the bare substrate from an overlapping spot, as an example of the standard control measure). The chip is much wider than the probe's 2  $\mu\text{m}$  end and all bubbles direct towards the end and terminate there for the cases when we use the force measurement. Also, the temporal resolution limit is given by the resonant frequency (190 kHz in air and 73 kHz in water), which is lower than the piezo frequency (200 kHz), so we measure only averages of impacts and not individual events.

## 16.4 Discussion

### 16.4.1 Cleaning action of bubbles

With the micropits employed in this chapter it was shown that metal thin layers (Au and Pt), biomaterials (biofilm, cells and hydrogel) and organic materials (photoresists) could be removed in a certain local area, defined by the bubble cloud from the micropits. Surprisingly, the removal rates were similar for the metal and the viscoelastic layers, while they all have entirely different mechanical and adhesive prop-

erties. This suggests that the bubbles can exert enough mechanical force to remove all of these materials, but that the amount of material that each bubble can remove during one cycle is limited. The deposited material will have to be removed piece by piece, cycle after cycle as a result of several bubbles (clusters) cavitating close to a layer (see Figure 16.5). As more material gets removed, the bubbles have to travel a larger distance from their origin (pit or geometrical center of the pits array), but are becoming less likely to do so, consequently slowing down the removal rate.

When acoustic cavitation bubbles are in contact with hydrophobic surfaces, it could be expected that no cushion layer of liquid exists that would dampen the liquid jet impact as a result of bubble collapse (the hydrophobic or -philic properties of surfaces and adhesion forces among them have been reported elsewhere) [43–45]. Accordingly, the hydrophobicity of the deposited material might have an influence on the material removal, as for bubbles it is easier to collapse towards a hydrophobic wall. As reported elsewhere, the hydrophobic force is uniquely determined by the contact angle [46]. Interestingly, water on Au and on Pt, both removed by the cavitating bubbles, has a much higher (receding) contact angle than on the other metals (see Appendix 16.D and Table 16.1 for contact angle measurement details and results), suggesting that the bubbles could reach those two metals more easily than the other metals. It is not known how much this effect contributes to the cleaning effect.

The fact that microbubbles were generated in ethanol, acetone, bleach, and cell cultivation medium as well as in water suggests that the cleaning with the help of microbubbles can be enhanced for chemical cleaning processes. AZ96 and Olin are commonly removed by acetone; bleach is used routinely in biological/medical applications like dentistry to kill bacteria. According to the results of this study, cavitation could mechanically enhance the chemical removal.

We focused on water since is the “greenest” solvent normally used in cleaning applications but other liquids may be used with similar effects. Another important fact related to our experiment is the small volumes needed to remove the desired substrates. This becomes important when considering cleaning applications with less green solvents (e.g. acetone, toluene, etc.).

To address the influence of the radicals produced by the cavitating microbubbles [28] on the removal of deposited metal materials, all the metals were exposed to hydrogen peroxide (Sigma-Aldrich 30% as provided). For Au there was no reaction observed at least for the first 5 minutes, after which occasionally some small regions presented small detachment areas (ca. 1 mm<sup>2</sup>). For Pt there was some chemical activity observed (bubbling and gas formation) that led to detachment of virtually the complete layer in a couple of seconds. For Cr and Ti, there was no reaction within the observation time of 10 minutes. This allows us to conclude that if there is any contribution of chemical radicals (e.g. H<sup>•</sup> or OH<sup>•</sup>) to the removal rates it will be minimal under the conditions attained with cavitation bubbles nucleated from the

pits.

The acoustic microbubble generation from the micro pits can be sustained for at least several hours if the temperature is kept constant and gas loss is prevented. This means that the loss of gas associated to the microbubble generation does not deactivate the pits, evidencing a process of rectified gas diffusion into the pits. More details on the bubble behavior can be found elsewhere [28, 41].

We observed stable cavitation from the pits with the glass slide placed on top for at least 30 min. However, normally the removed layer areas did not increase much more after the first 3 min if no change in the ultrasound conditions or moving of the glass slide took place.

Additionally, the low operation power compared with conventional ultrasonic cleaning devices (one order of magnitude lower in our case) and the control over the areas to be removed, makes the present cleaning device useful in several applications. Furthermore, the amount of erosion damage of the glass substrate was found to be low.

## 16.4.2 Detachment kinetics

### Solid hard materials

The detachment of material layers by cavitating bubbles can occur due to material defects, at which the bubbles can perform further detachment. Once a crack is formed, detachment could proceed by peeling and tearing mechanisms due to bubble jetting, and presumably also due to shock waves generated at cavitation bubble collapses and reflections from the hard surfaces. The contribution of streaming can be ruled out based on the above reported observations that there is no cleaning for streaming only (without bubbles). Note that the removal of a thin film may follow a different timeline than traditional cavitation erosion in bulk materials, as the material properties of the bulk and a layer of the same material might be different [47]. To explain the differences in cleaned area and removal rates between the various metals we have to consider their different adhesion characteristics.

For the *metals*, a first estimation can be obtained by considering the formation of metal oxides on the surface of the metals. Even though the films are sputtered under Argon conditions, the thickness of all layers is small enough to allow metal oxides to form on the surface. It is known that thin films of oxygen active metals have a higher adhesion to glass than films of noble metals[48] because of molecular electrostatic bonds between the metal oxides and glass [49].

The likeliness of a metal to form an oxide layer can be obtained from its affinity of oxygen, which is directly related to the (negative) heat of oxide formation of the metal. Au and Pt (heats of oxide formation of 79.5 kJ/mol and -134 kJ/mol for  $\text{Au}_2\text{O}_3$  and  $\text{PtO}_2$ , respectively) do not oxidize easily since these are noble metals,

and are therefore expected to have a lower adhesion to glass than Cr and Ti (heats of oxide formation of -1130 kJ/mol and -912.1 kJ/mol for Cr<sub>2</sub>O<sub>3</sub> and TiO<sub>2</sub> respectively) [50, 51].

The bonding of photoresists (AZ96 and Olin) to glass is strengthened by the strong chemical bond provided by the HDMS priming step. For that reason, only where defects in the layer existed, the bubbles were able to remove material.

The exact value for the adhesion for these solids is difficult to obtain, as the ways and experimental techniques to quantify it are still controversial [52]. At the root of this problem lies the fact that the individual surfaces to be bonded (metal/inorganic layers and glass surface in our case) have different properties when bonded than when separated. Many factors can affect a bond, such as impurities, roughness, defects or inhomogeneity on any of both substances, actions of the environmental and mechanical stresses.

Therefore, instead of theoretically predicting the adhesion of the solids of which the layer and substrate are made off, it is more relevant to attempt to measure the actual deposited materials' adhesion with a given experimental system or technique. There are many adhesion measurement techniques described in the literature, including nucleation methods (based on deposition, only able to give basic adhesion values) and mechanical methods (direct pull-off, moment or topple, ultracentrifugal, ultrasonic, adhesive tape peel, scratch, abrasion, laser spallation, etc.) [47]. However, the values provided by one technique or given apparatus might not coincide with another technique or with values given in the literature for similar systems. Comparison with the literature should therefore be treated with care, and it is advisable to perform adhesion tests in each individual system [50].

In order to get a qualitative comparison for the adhesion of the solid hard materials used in this study, we have performed our own scratch tests on the solid hard materials, using an AFM and standard Scotch tape test. The details can be found in Appendices 16.A and 16.B, respectively; the relative adhesion strength of these materials can be summarized as follows: Au < Pt < Olin and Az96 < Ti and Cr.

As another qualitative comparison, and more relevant to ultrasonic cleaning, the removal of the solid hard materials was investigated in a commercial ultrasound bath (Appendix 16.C), showing non-localized removal of Au and Pt under maximum ultrasound conditions, or no removal after 10 minutes. Taking as an example the case of Au, our technique provided better localized and faster layer removal (compare Figures 16.2 and 16.11).

### Soft biomaterials

*Biofilms* are known to be able to adhere strongly to a substrate. The initial state of biofilm formation is the adhesion of planktonic bacteria to a substrate, after which the biofilm structure is developed. The bacteria themselves adhere to a substrate



due to a multitude of forces, based on both physicochemical and molecular/cellular interactions [53, 54]. During its mature state, the biofilm has also been found to increase its adherence through the production of functional amyloids, among others [30].

Literature reports a wide range of viscoelastic and adhesive properties of encountered biofilms, as these properties depend on the ecology of the biofilm and also on the conditions under which the biofilm has been grown [29, 30, 54–56]. Furthermore, the properties of the substrate itself are important, for example the surface roughness and hydrophobicity [30, 54].

A *hydrogel* can have better defined viscoelastic properties, as there is more control over its production, and can be used as a substitute for a biofilm when studying the mechanical behavior of biofilms [57]. However, a hydrogel is not grown but deposited onto the glass slide and therefore its attachment to a substrate is expected to be generally weaker than for a biofilm, relying only on physicochemical interactions between glass and hydrogel proteins [58].

The elastic modulus and adhesion of the hydrogel were estimated using a hydrodynamic technique, of which the details and results are given in Appendix 16.E. The hydrogel was observed to have a weaker attachment to the substrate than the typical values for a biofilm, which is in agreement with our handling observations. However, considering the observation that the hydrogel did show viscoelastic behavior, it can be considered a soft biofilm. The mechanical properties of the hydrogel can be further tuned by changing its composition and through cross-linking.

The viscoelastic materials were not removed by the acoustic streaming alone, whereas the cavitation cloud could remove them locally within a few seconds. An explanation for this different behavior could be the timescales at which both components react. The pressure magnitude and fluctuations associated with acoustic streaming could be still in the elastic regime of the viscoelastic behavior; the pressure associated with transient bubble dynamics, however, can locally have a high magnitude and fast fluctuation, causing deformations in the viscous regime, and possibly even in the plastic regime.

Many of the MCF-7 cells grown on the glass slide had been detached due to the induced cavitation cloud. However, optical visualization does not give any information on the cells around the area that was cleaned. Those cells might have been lysed through sonoporation, as has been demonstrated by Ohl *et al.* [59]. Their method of dead-live staining could provide the information on the viability of the remaining cells.

## 16.5 Conclusions

Localized generation of cavitation from micropits was shown to be able to remove deposited thin metal and organic films and biomaterials on a millimetric scale in less than 1 minute. The shape and extent of the cleaned area is related to the number of micropits; the rate of removal was of the order of  $0.1 \text{ mm}^2/\text{s}$ . Basic adhesion tests provided some insight into the likeliness of a material to be removed.

The low operation power and small volumes of liquid required, together with the limited cavitation erosion damage, make the cleaning device presented here a “green” solution for localized cleaning in many applications.

## 16.6 Acknowledgments

The authors acknowledge S. Schlautmann from the MCS group, University of Twente for his support in the microfabrication processes, H.A. Visser from the CTW group, University of Twente for lending surface adhesion equipment and R. de Ruiter from the PCF group, University of Twente, for assistance in the contact angle measurements. The cells were provided and cultured by A. Sridhar and S. le Gac from the BIOS group, University of Twente.

## References

- [1] A. Prosperetti, “Bubbles”, *Physics of Fluids* **16**, 1852–1865 (2004).
- [2] D. Lohse, “Bubble puzzles”, *Physics Today* **56**, 36–41 (2003).
- [3] B. M. Borkent, S. Gekle, A. Prosperetti, and D. Lohse, “Nucleation threshold and deactivation mechanisms of nanoscopic cavitation nuclei”, *Phys. Fluids* **21** (2009).
- [4] S. Barnett, G. Ter Haar, M. Ziskin, W. Nyborg, K. Maeda, and J. Bang, “Current status of research on biophysical effects of ultrasound”, *Ultrasound in Medicine and Biology* **20**, 205–218 (1994).
- [5] M. Ashokkumar and T. J. Mason, *Sonochemistry* (John Wiley & Sons, Inc.) (2000).
- [6] J. H. Bang and K. S. Suslick, “Applications of ultrasound to the synthesis of nanostructured materials”, *Advanced Materials* **22**, 1039–1059 (2010).
- [7] G. Cravotto and P. Cintas, “Harnessing mechanochemical effects with ultrasound-induced reactions”, *Chem. Sci.* **3**, 295–307 (2012).
- [8] M. P. Brenner, S. Hilgenfeldt, and D. Lohse, “Single-bubble sonoluminescence”, *Reviews of Modern Physics* **74**, 425–484 (2002).
- [9] Y. T. Didenko and K. S. Suslick, “The energy efficiency of formation of photons, radicals and ions during single-bubble cavitation”, *Nature* **418**, 394–397 (2002).
- [10] D. Lohse, “Sonoluminescence-Cavitation hots up”, *Nature* **434**, 33–34 (2005).

- [11] L. Y. Yeo and J. R. Friend, "Ultrafast microfluidics using surface acoustic waves", *Biomicrofluidics* **3**, 012002 (2009).
- [12] P. Marmottant and S. Hilgenfeldt, "Controlled vesicle deformation and lysis by single oscillating bubbles", *Nature* **423**, 153–156 (2003).
- [13] R. Karshafian, P. D. Bevan, R. Williams, S. Samac, and P. N. Burns, "Sonoporation by ultrasound-activated microbubble contrast agents: Effect of acoustic exposure parameters on cell membrane permeability and cell viability", *Ultrasound in Medicine & Biology* **35**, 847 – 860 (2009).
- [14] S. Ohl, E. Klaseboer, and B. Khoo, "The dynamics of a non-equilibrium bubble near biomaterials", *Physics in Medicine and Biology* **54**, 6313–6336 (2009).
- [15] C. Ohl, M. Arora, R. Iking, N. De Jong, M. Versluis, M. Delius, and D. Lohse, "Sonoporation from jetting cavitation bubbles", *Biophysical Journal* **91**, 4285–4295 (2006).
- [16] C. Ohl, T. Kurz, R. Geisler, O. Lindau, and W. Lauterborn, "Bubble dynamics, shock waves and sonoluminescence", *Philosophical Transactions of the Royal Society A: Mathematical, Physical and Engineering Sciences* **357**, 269–294 (1999).
- [17] H. Lee, A. Homma, E. Tatsumi, and Y. Taenaka, "Observation of cavitation pits on mechanical heart valve surfaces in an artificial heart used in in vitro testing", *Journal of Artificial Organs* **13**, 17–23 (2010).
- [18] E.-A. Brujan, "Cardiovascular cavitation", *Medical Engineering and Physics* **31**, 742–751 (2009).
- [19] R. Dijkink, S. Le Gac, E. Nijhuis, A. Van den Berg, A. Vermes, A. Poot, and C.-D. Ohl, "Controlled cavitation-cell interaction: trans-membrane transport and viability studies", *Physics in Medicine and Biology* **53**, 375 (2008).
- [20] C.-D. Ohl and B. Wolfrum, "Detachment and sonoporation of adherent hela-cells by shock wave-induced cavitation", *Biochimica et Biophysica Acta - General Subjects* **1624**, 131–138 (2003).
- [21] T. Mason, A. Cobley, J. Graves, and D. Morgan, "New evidence for the inverse dependence of mechanical and chemical effects on the frequency of ultrasound", *Ultrasonics Sonochemistry* **18**, 226 – 230 (2011).
- [22] P. Riesz and T. Kondo, "Free radical formation induced by ultrasound and its biological implications", *Free Radical Biology and Medicine* **13**, 247–270 (1992).
- [23] A. Cobley, L. Edgar, M. Goosey, R. Kellner, and T. Mason, "Initial studies into the use of ultrasound to reduce process temperatures and chemical usage in the pcb desmear process", *Circuit World* **37**, 15–23 (2011).
- [24] T. Okada, Y. Iwai, S. Hattori, and N. Tanimura, "Relation between impact load and the damage produced by cavitation bubble collapse", *Wear* **184**, 231–239 (1995).
- [25] P. Gogate and A. Pandit, "Sonochemical reactors: Scale up aspects", *Ultrasonics Sonochemistry* **11**, 105–117 (2004).
- [26] M. Arora, C. Ohl, and D. Lohse, "Effect of nuclei concentration on cavitation cluster dynamics", *The Journal of the Acoustical Society of America* **121**, 3432–3436 (2007).

- [27] N. Bremond, M. Arora, C.-D. Ohl, and D. Lohse, “Controlled multibubble surface cavitation”, *Phys. Rev. Lett.* **96**, 224501 (2006).
- [28] D. Fernandez Rivas, A. Prosperetti, A. G. Zijlstra, D. Lohse, and H. J. G. E. Gardeniers, “Efficient sonochemistry through microbubbles generated with micromachined surfaces”, *Angewandte Chemie International Edition* **49**, 9699–9701 (2010).
- [29] C. Picioreanu, M. Van Loosdrecht, and J. Heijnen, “Two-dimensional model of biofilm detachment caused by internal stress from liquid flow”, *Biotechnology and Bioengineering* **72**, 205–218 (2001).
- [30] H.-C. Flemming, J. Wingender, and U. Szewzyk, *Biofilm highlights*, Springer Series on Biofilms, 1st edition (Springer-Verlag, Berlin Heidelberg) (2011).
- [31] P. Stoodley, Z. Lewandowski, J. D. Boyle, and H. M. Lappin-Scott, “Structural deformation of bacterial biofilms caused by short-term fluctuations in fluid shear: An in situ investigation of biofilm rheology”, *Biotechnology and Bioengineering* **65**, 83–92 (1999).
- [32] P. Stoodley, S. Wilson, R. Cargo, C. Piscitelli, and C. J. Rupp, “Detachment and other dynamic processes in bacterial biofilms”, in *Surfaces in Biomaterials 2001 Symposium Proceedings*, 189–192 (Surfaces in Biomaterials Foundation, Minneapolis, USA) (2001).
- [33] S. Seltzer, I. B. Bender, J. Smith, I. Freedman, and H. Nazimov, “Endodontic failures—an analysis based on clinical, roentgenographic, and histologic findings”, *Oral Surgery, Oral Medicine and Oral Pathology* **23**, 500–516 (1967).
- [34] H.-C. Flemming, T. R. Neu, and D. J. Wozniak, “The eps matrix: The “house of biofilm cells””, *Journal of Bacteriology* **189**, 7945–7947 (2007).
- [35] I. Portenier, T. Waltimo, D. Orstavik, and M. Haapasalo, “The susceptibility of starved, stationary phase, and growing cells of enterococcus faecalis to endodontic medicaments”, *Journal of Endodontics* **31**, 380–386 (2005).
- [36] L. Kuznetsova and W. Coakley, “Applications of ultrasound streaming and radiation force in biosensors”, *Biosensors and Bioelectronics* **22** (2007).
- [37] A. Zijlstra, “Acoustic surface cavitation”, Ph.D. thesis, University of Twente (2011).
- [38] C. D. Meinhart, S. T. Wereley, and M. H. B. Gray, “Volume illumination for two-dimensional particle image velocimetry”, *Measurement Science and Technology* **11**, 809–814 (2000).
- [39] S. V. Van der Waal, L. W. M. Van der Sluis, R. A. Özok, R. A. M. Exterkate, P. R. Wesselink, and J. J. De Soet, “The effects of hyperosmosis or high pH on a dual-species biofilm of pseudomonas aeruginosa and enterococcus faecalis: an in vitro study”, *International Endodontic Journal* **44**, 1110–7 (2011).
- [40] A. N. Jataru-Cadinoiu, M. Popa, S. Curteanu, and C. A. Peptu, “Covalent and ionic co-cross-linking - an original way to prepare chitosan–gelatin hydrogels for biomedical applications”, *Journal of Biomedical Materials Research A* **98A**, 342–350 (2011).
- [41] D. Fernandez Rivas, L. Stricker, A. G. Zijlstra, H. J. G. E. Gardeniers, D. Lohse, and A. Prosperetti, “Ultrasound nucleated microbubbles and their sonochemical radical production”, *Ultrasonic Sonochemistry* **under review** (2012).

- [42] D. Fernandez Rivas, M. Ashokkumar, T. Leong, K. Yasui, T. Tuziuti, S. Kentish, D. Lohse, and H. J. G. E. Gardeniers, "Sonoluminescence and sonochemiluminescence from a microreactor", *Ultrasonic Sonochemistry* **in press** (2012).
- [43] J. Israelachvili and R. Pashley, "Measurement of the hydrophobic interaction between two hydrophobic surfaces in aqueous electrolyte solutions", *Journal of Colloid And Interface Science* **98**, 500–514 (1984).
- [44] A. Freitas and M. Sharma, "Effect of surface hydrophobicity on the hydrodynamic detachment of particles from surfaces", *Langmuir* **15**, 2466–2476 (1999).
- [45] R. Vos, M. Lux, K. Xu, W. Fyen, C. Kenens, T. Conard, P. Mertens, M. Heyns, Z. Hatcher, and M. Hoffman, "Removal of submicrometer particles from silicon wafer surfaces using hf-based cleaning mixtures", *Journal of The Electrochemical Society* **148**, G683–G691 (2001).
- [46] R.-H. Yoon, D. Flinn, and Y. Rabinovich, "Hydrophobic interactions between dissimilar surfaces", *Journal of Colloid and Interface Science* **185**, 363–370 (1997).
- [47] K. Mittal, *Adhesion measurement: Recent progress, unsolved problems, and prospects*, 5–16, in [60] (1976).
- [48] P. Benjamin and C. Weaver, "Adhesion of metal films to glass", *Proceedings of the Royal Society of London. Series A. Mathematical and Physical Sciences* **254**, 177–183 (1960).
- [49] D. E. Riemer, "High-adhesion thick-film gold without glass of metal-oxide power additives.", *IEEE transactions on components, hybrids, and manufacturing technology* **CHMT-8**, 474–480 (1985).
- [50] J. Dini, *Electrodeposition: the materials science of coatings and substrates* (William Andrew) (1993).
- [51] R. Weast, ed., *CRC Handbook of Chemistry and Physics*, 52 edition (CRC PRESS) (1971).
- [52] J. Minford, *Durability evaluation of adhesive bonded structures*, chapter 9, 239–284 (Plenum Press) (1991).
- [53] Y. H. An and R. J. Friedman, *Handbook of bacterial adhesion*, 1st edition (Humana Press, Totowa, NJ, USA) (2000).
- [54] W. M. Dunne Jr., "Bacterial adhesion: Seen any good biofilms lately?", *Clinical Microbiology Reviews* **15**, 155–166 (2002).
- [55] S. Bayouduh, A. Othmane, L. Mora, and H. Ben Ouada, "Assessing bacterial adhesion using dlvo and xdlvo theories and the jet impingement technique", *Colloids and Surfaces B: Biointerfaces* **73**, 1–9 (2009).
- [56] P. C. Y. Lau, J. R. Dutcher, T. J. Beveridge, and J. S. Lam, "Absolute quantitation of bacterial biofilm adhesion and viscoelasticity by microbead force spectroscopy", *Biophysical Journal* **96**, 2935–2948 (2009).
- [57] C. Mayer, R. Moritz, C. Kirschner, W. Borchard, R. Maibaum, J. Wingender, and H.-C. Flemming, "The role of intermolecular interactions: studies on model systems for bacterial biofilm", *International Journal of Biological Macromolecules* **26**, 3–16 (1999).

- [58] G. Sagvolden, I. Giaever, and J. Feder, "Characteristic protein adhesion forces on glass and polystyrene substrates by atomic force microscopy", *Langmuir* **14**, 5984–5987 (1998).
- [59] C.-D. Ohl, M. Arora, R. Iking, N. De Jong, M. Versluis, M. Delius, and D. Lohse, "Sonoporation from jetting cavitation bubbles", *Biophysical Journal* **91**, 4285–4295 (2006).
- [60] K. Mittal, ed., *Adhesion measurement of thin films, thick films, and bulk coatings : a symposium presented at ASTM headquarters, American Society for Testing and Materials* (Philadelphia : American Society for Testing and Materials) (1976).
- [61] J. Vossen, *Measurement of Film-substrate bond strength by laser spallation*, 122–131, in Mittal [60] (1976).

## 16.A AFM scratch test for the adhesion of solid hard materials

### 16.A.1 Experimental setup

The adhesion of Au and Pt was determined by scratching these deposited layers using the same AFM as before, but with a different spherical cap tip (Micromasch NSC35, spring constant of 14 N/m, resonant frequency 315 kHz) in contact mode. For these measurements, the surface was scanned continuously over a  $20\mu\text{m} \times 20\mu\text{m}$  areas with the contact force increased gradually every  $5\mu\text{m}$ . Once the metal layer began to tear, the cantilever was lifted and moved elsewhere on the substrate, before the process was repeated. Several repeated measurements were carried out.

### 16.A.2 Results

Only gold and platinum could be removed with this AFM scratch test. The required removal forces were found to be  $22.6 \pm 0.5\mu\text{N}$  (Au) and  $44.0 \pm 1.5\mu\text{N}$  (Pt), which, using a removal width of  $R = 10\text{ nm}$ , correspond to peeling strengths of  $2260 \pm 50\mu\text{N/m}$  (Au) and  $4400 \pm 150\mu\text{N/m}$  (Pt).

The gold and platinum layers delaminated differently to each other (Figure 16.9). For the gold layer, once the metal had been compromised it continued to delaminate from the glass substrate even if the contact force was reduced to less than  $0.5\mu\text{N}$ . However, the platinum delaminated in a stick-slip, patchy fashion, in any case, so lowering the contact force by only a few percent led to no further damage. Even at a constant force of  $44.0 \pm 1.5\mu\text{N}$ , the scratch was intermittent. The scratch widths were increased to  $90\mu\text{m}$  for platinum to better see the effect.

The required forces and peeling strengths for metal removal given above were measured on defect-free areas of the surface. It is interesting to note that the surfaces peeled at much lower applied forces if the AFM probe collided with an optically-sized ( $\sim 10\mu\text{m}$ ) asperity. For the gold, the required force and peeling strength were

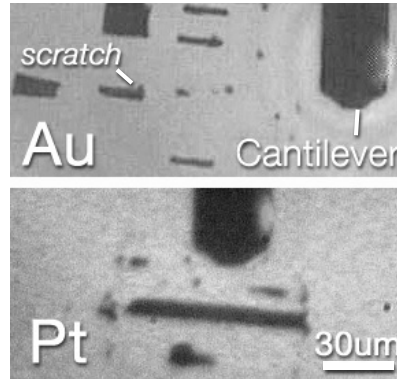


**Figure 16.9:** The top image is for the gold sample and several scratch lines can be seen. Each one is  $20\ \mu\text{m}$  wide. The lower image is for the platinum sample. As a guide to the eye, the AFM probe mount is  $30\ \mu\text{m}$  wide.

dramatically reduced to approx.  $2.1\ \mu\text{N}$  and  $210\ \text{N/m}$ , respectively, whilst those for platinum were reduced to approx.  $20\ \mu\text{N}$  and  $2000\ \text{N/m}$ .

## 16.B Macroscopic scratch test for the adhesion of solid hard materials

### 16.B.1 Experimental setup

A hardness tester kit (SP0010, Thermimport Quality Control) and a cross-cut adhesion tester kit (CC2000 SP1690, Thermimport Quality Control) were used to analyze the adhesion strength of the solid hard materials. The hardness tester kit consisted of a Tungsten-Carbide tip with 1 mm diameter and a spring with 0-300 g load capacity and can be used to measure the wear (by scratching) or fail resistance of coatings, plastics, etc. The cross-cut adhesion tester kit is based on ISO 2409 Standards and provides a semiquantitative measurement of adhesion. First, perpendicular cuts with parallel blades were performed through the layers, touching the glass slide; afterwards a dedicated adhesive tape is attached and, when detached, it can remove weakly adhered patches of each layer. According to the amount of removed material, a classification of surface adhesion quality is given with a score between 0 and 5; 0 being the stronger attached where none of the squares is detached after peeling off the tape.

### 16.B.2 Results

The hardness tester is a simple semi-quantitative test for surface hardness in which all materials layers were scratched with 1 g (minimum setting that could be used).

The scratch test of the different solid hard materials used showed a marked difference between the metal and organic layers (Figure 16.10). When scratching the

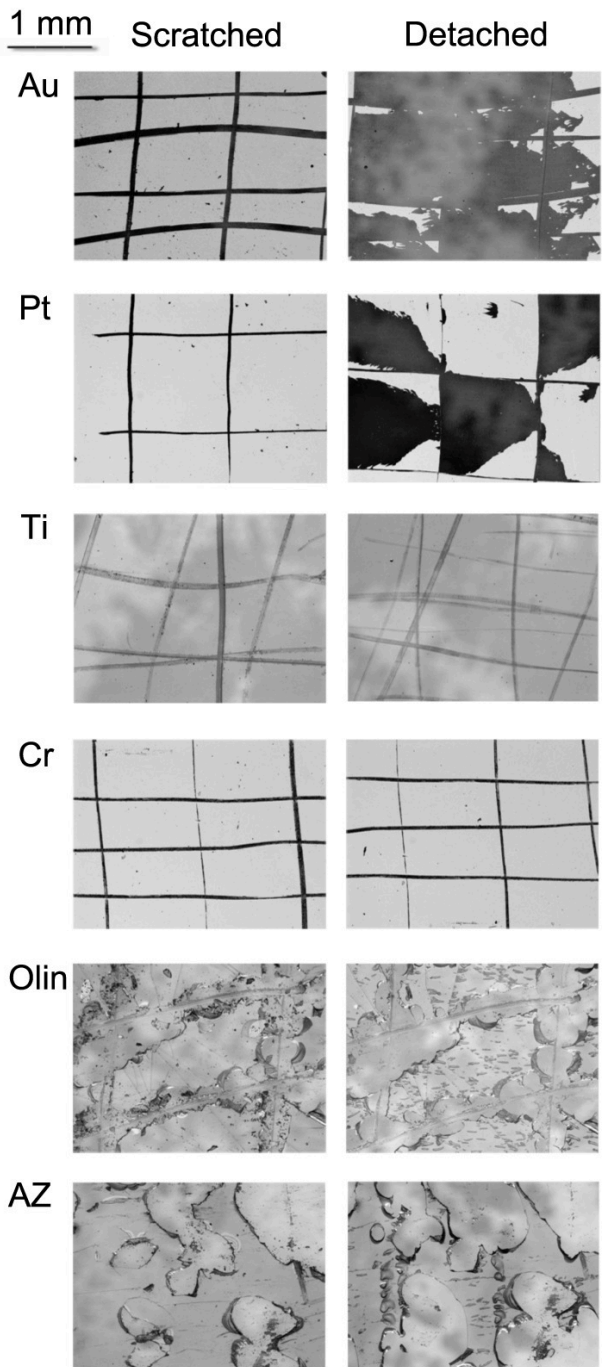


**Figure 16.10:** The left column shows the various deposited layers after the cuts are performed. The right side shows the same region after peeling off the adhesive tape.



organic layers (thicker and more brittle) we observed small parts detaching and it was not possible to cut well defined squares as in the case of the metals.

Au and Pt were the weakest attached materials falling in the 5-and-4 and 4-and-3 category respectively. For Au layers we observed that the layer flaked in large ribbons and along the edges where most squares were removed (more than 35 % of the total area). For Pt we saw that most squares were partially or totally removed (more than 15 % of the total area). For Cr and Ti we classified it as 1-and-0 as we observed very small flakes of the coating at the intersections of the cuts and no square could be removed (less than 5% of the area removed).

For AZ and Olin we found that some chunks were removed in a way that could be cataloged 2-and-1, but the squares were not neatly formed as these brittle layers cracked; see Figure 16.10.

Summarizing, the qualitative adhesion of the solid hard materials can be arranged, in order of weakest to strongest, as: Au < Pt < Olin and Az96 < Ti and Cr.

This qualitative quantification is consistent with values provided in the literature using other techniques. For example, for the metals, a laser spallation technique was used to find a direct correlation between the bond strength on silicon oxide substrates with the free energy of oxide formation of the arriving metal vapor for both evaporated and sputtered metals [61]. The energies at which the films detached were: Au (25 J/cm<sup>2</sup>), Cr (75 J/cm<sup>2</sup>) and Ti (125 J/cm<sup>2</sup>), showing the same relative adhesion strength as found in the present study.

## **16.C Ultrasonic bath test for the adhesion of solid hard materials and comparison with current setup**

### **16.C.1 Experimental setup**

A commercial ultrasonic bath (VWR) operating at 20 kHz was used to test the adhesion strength of the layers with a conventional ultrasonic apparatus and a comparison of the removal capabilities for each deposited sample was performed.

### **16.C.2 Results**

With the ultrasonic bath, no material was removed after 10 minutes of sonication. All samples were individually placed in a conventional configuration of a glass beaker of 200 mL (Schott) glued to a microscope glass slide (see Figure 16.11 Test A).

As an extreme test we placed each sample facing down, directly against the bottom surface of the ultrasonic bath. For Au and Pt we observed surface removal without localization and for Cr or Ti we saw no removal at all (see Figure 16.11 Test B).

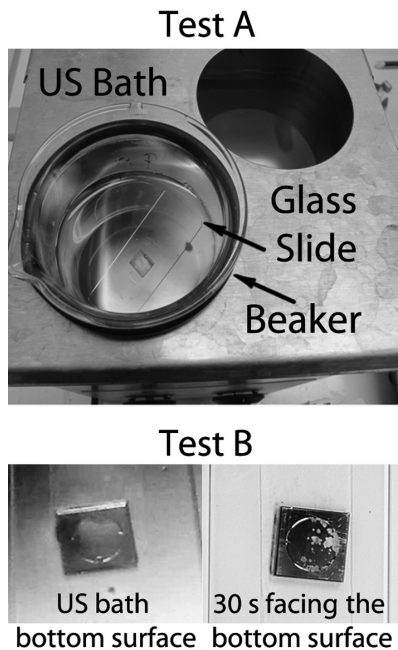


**Figure 16.11:** *Experimental conditions provided to test adhesion strength for all layers; in this case for Gold deposited on a glass substrate. Test A shows how the glass substrate was glued to a glass slide and inserted in a glass beaker filled with water as normally cleaning US baths are used. After 10 min no material was removed in any case. Test B shows the extreme conditions used to be able to remove material (only Au and Ti) but no localization of the removed material.*

## 16.D Contact angle measurement of solid hard materials

### 16.D.1 Experimental setup

The advancing and receding contact angles of a sessile drop of tapwater on the gold-, platinum-, chromium- and titanium-coated glass chips in air was determined using a commercial contact angle goniometer (OCA30, Dataphysics, Filderstadt, Germany). The advancing and receding contact angles were determined automatically thrice by the contact angle goniometer during volume change of a drop of volume  $10 \mu\text{L}$  at a rate of  $0.25 \mu\text{L/s}$ . The non-clean conditions in the ultrasound setup were mimicked by using tap water and by not cleaning the chips before contact angle measurement.

### 16.D.2 Results

The results are included in Table 16.1. Au and Pt were found to have a larger receding contact angle than the other solid hard materials.

## 16.E Hydrodynamic characterization of the viscoelastic properties of the the hydrogel

### 16.E.1 Experimental setup

The properties of the hydrogel used in this study have been measured by determining the strain induced by the stress exerted by the flow from a needle. More details on the characterization can be found in Chapter 15.

When the flow through the needle is driven with a positive pressure, a jet is created, which has a stagnation pressure  $P$  of  $P = \frac{1}{2}\rho u^2$ , where  $\rho$  is the density of the liquid (water:  $1000 \text{ kg/m}^3$ ) and  $u = Q/A$  is the average velocity, estimated from the flow rate  $Q$  and the needle orifice  $A$ . The setup consisted of a 22G needle (Terumo, Leuven, Belgium; internal diameter of  $0.413 \text{ mm}$ ) positioned at a distance of  $300 \mu\text{m}$  above the hydrogel-covered surface, through which a flow with flow rates in the range  $0.01 - 1 \text{ mL/min}$  were created by a syringe pump (NE1010, New Era Pump Systems, Wantagh, NY, USA). By recording (LM165 camera, Lumenera) the displacement of particles embedded in the hydrogel that appeared to be near the stagnation region of the jet, the Young modulus of the hydrogel can be estimated.

Using the same needle but with a negative pressure, a pulling force is exerted on the hydrogel. Parts of the hydrogel detach (sloughing) from the bulk hydrogel when the suction pressure exceeds the cohesive and adhesive forces of the hydrogel. The suction pressure can be estimated roughly from the Bernoulli pressure along the streamlines of the flow toward the needle orifice.

### 16.E.2 Results

The hydrogel, when subjected to stagnation pressure from a jet generated with a needle, displayed elastic behavior for flow rates higher than  $0.01 \text{ mL/min}$ , and additional viscous behavior for flow rates higher than  $0.1 \text{ mL/min}$ . By tracking the displacement of embedded particles in the elastic regime, the Young modulus of the hydrogel was estimated to be of the order of  $10^{-1} \text{ Pa}$ . When using a negative pressure (suction) through the needle, sloughing was observed to occur for flow rates above  $0.2 \text{ mL/min}$ , from which the adhesive and cohesive strengths are estimated to be of the order of  $10^{-1} \text{ Pa}$ .

The mechanical properties of the biofilm could not be determined, because its limited thickness prohibited proper recording of its deformation and the other tests used for the organic materials and metals are not applicable. However, overall the biofilm appeared to be stiffer and better attached to the substrate than the hydrogel was. This agrees with the typical range of values of the Young's modulus and cohesive and adhesive strengths for biofilms given in literature [29–32, 54–56], which are typically two or three order of magnitude higher than those measured for the

hydrogel.

## 16.F Supplementary material

*(Online at [http://stilton.tnw.utwente.nl/rootcanalcleaning/Gallery\\_of\\_Irrigant\\_Motion](http://stilton.tnw.utwente.nl/rootcanalcleaning/Gallery_of_Irrigant_Motion))*

Movie 1. Removal of a deposited layer of gold by cavitating microbubbles, originating from two pits. After increasing the power (at  $t \approx 8$  seconds), the bubble clouds start to move toward each other and remove an area in-between the two pits. Recording speed is 50 fps.

Movie 2. Removal of a deposited layer of photoresist (AZ96). Recording speed is 50 fps.

Movie 3. Removal of a deposited layer of biofilm (black dots). Recording speed is 50 fps.



**Part V**

**Backmatter**



# 17

## General discussion and outlook



## 17.1 Irrigation of the root canal

Irrigation of the root canal during endodontic treatment is crucial in cleaning the root canal system of bacteria, dentin debris and the smear layer. This thesis has described the fluid dynamics and working mechanisms of some of the techniques available for irrigant delivery and activation and how the confinement of the root canal affects the fluid dynamics. Using the Damköhler number, an estimate of the efficacy of irrigant refreshment during needle irrigation compared to its reaction time has been made. Furthermore, the capability of various irrigant activation systems to remove dentin debris from artificial grooves in the root canal wall has been evaluated. The results of those experiments show a clear improvement in cleaning efficacy when using Passive Ultrasonic Irrigation (PUI) or Laser-Activated Irrigation (LAI), even though the shear stress induced by those systems is of the same order as that of needle irrigation. The shear stress is therefore probably not the most relevant parameter; rather, the oscillatory or impulsive nature of the activation systems and the associated micromixing appear to be relevant for cleaning.

However, these *in vitro* studies are still a simplification of the complex *in vivo* clinical situation, as, for example, we did not yet evaluate smear layer or biofilm removal from a root canal, or take into account the full complexity of the root canal system (discussed below). A first clinical study on the improvement in treatment outcome when using PUI as compared to needle irrigation alone is currently being done with a randomized controlled trial, in a collaboration between the Academic Center for Dentistry in Amsterdam and the Beijing University School and Hospital of Stomatology in China. Interpretation of those *in vivo* results, however, will have to be done carefully, in order to properly relate the clinical findings to the working mechanisms of the irrigation systems as observed in this thesis.

## 17.2 The complexity of the root canal system

In the Introduction and Chapters 11 and 14 it was pointed out that the root canal system is geometrically very complex, possibly including curvatures in multiple directions, side channels and isthmuses and the apical delta, and tubules. Those locations are largely untouched during the instrumentation step of a root canal treatment but are excellent hiding places for bacteria [1]. The visualization experiments reported throughout this thesis, however, have been made with a straight, unbranched root canal with smooth walls. Only in Chapters 11 and 14, curvature, side channels and tubules have been investigated in an attempt at mimicking the root canal complexity. While simplifying the root canal geometry was necessary for understanding the fluid dynamics of root canal irrigation, future work should investigate the influence of these complexities in more detail, e.g. with real teeth made transparent [2].

The influence of a certain feature of the complex root canal on the flow arguably only needs to be considered when the specific feature has a length scale similar to a typical length scale of the flow. The tubules were observed not to affect the flow over them (Chapter 14), but real root canals have a much higher roughness that might affect the streaming near the tubules' entrance, which can have a significant effect on the flow into the tubules. The curvature of the root canal did not change the irrigant penetration depth significantly (Chapter 11), as the microstreaming in PUI takes place on a smaller scale than the curvature. However, side channels do have a size comparable to the microstreaming and could therefore have an effect on the flow in the main root canal and the side channels. Resolving this flow requires solving the two-way coupling between the applied flow and the flow inside the side channel.

The glass root canal models used in Chapters 9 and 13 have a hardness and acoustic properties similar to dentin, but it proved difficult to manufacture root canals of specific dimensions and geometry in glass. PDMS, used in many of the other chapters, can be made in any shape for which an appropriate mold is available. However, PDMS is much softer than glass and virtually transparent for ultrasound (see the Discussion section of Chapter 4), thereby affecting the acoustics inside the root canal. Nevertheless, standing waves in the root canal are not expected since the wavelength of ultrasound at 30 kHz in water is of the order of 5 cm.

The reaction of the irrigant with biomaterial during convection and diffusion in the root canal system has also not been taken into account, even though it determines (Damköhler number) how adequate the convection is in delivering fresh irrigant in all locations of the root canal system. The experiments with an extracted tooth model reported in some of the chapters of this thesis, only evaluates the removal of debris from grooves in the root canal wall; a model including a realistic biofilm and/or a smear layer could yield additional information valuable for investigating the effectiveness of an irrigation system. Creating biofilms, and studying their reaction with irrigants, is a hot topic in endodontics [3–5], but also a challenging one, as biofilms are difficult to grow in a controlled way in order to perform laboratory tests on them.

### 17.2.1 Vapor lock

Entrapment of a large air bubble in the apical part of the root canal, also termed vapor lock, has been reported during needle irrigation of root canals, *ex vivo* [6–8] and *in vivo* [8, 9]. This bubble could obstruct irrigant penetration. Air entrapment has already been demonstrated and studied in top-filled conical capillaries in 1989 [10–12], but it was also shown that this air bubble disappears after a relatively long time as fluid can get to the apex of the conical capillary via a thin liquid film between the air bubble and the capillary wall [13]. A recent experimental and CFD study that we have performed [14] has shown that this entrapped air bubble can also easily be removed with flow from a needle inserted into the conical capillary.

### 17.3 High-speed visualizations of irrigant flow

High-speed imaging was a valuable tool in many of the chapters of this thesis, providing a visual understanding of the flow and its cleaning efficacy in the main root canal lumen as well as in curved canals and side channels. Because of the high velocities and small length scales involved in the irrigation systems, high-speed imaging is an indispensable tool for understanding the dynamics of these systems. Each of these systems has its own characteristic time scale and associated frame rate, ranging from 1 fps (side channels, Chapter 14) to 1 million fps (cavitation and acoustic streaming during PUI, Chapters 6 and 12).

Combined with Particle Imaging Velocimetry (PIV), high-speed imaging is a powerful tool for both qualitative and quantitative analysis of the flow. The current  $\mu$ PIV setup is suitable for analysis of the flow in a single plane, although a large range of velocities and dark areas near the root canal wall sometimes provide difficulties for proper analysis of the flow. An extension to three-dimensional velocity measurements would be very useful considering the essentially three-dimensional flow inside the root canal confinement. 3D-PIV in microfluidics is not easy to setup, but may be possible by estimating the out-of-focus component of consecutive 2D slices [15, 16].

Due to the size of the root canal the flow scale is larger than common for microfluidics, yet smaller than macrofluidics. Rather, the sub-millimeter size of the root canal suggests ‘millifluidics’. There are some differences with typical microfluidic flow characteristics, as the Reynolds number can easily reach orders of  $10^2$  to  $10^3$ . Furthermore, the relatively small magnification of 1.25-20 $\times$ , necessary to have a proper field of view, leads to a focal depth of the order of 100  $\mu\text{m}$ , which is one quarter of the diameter of the root canal. For PIV this means that many particles are in focus and the PIV results are volume-averages instead of from a thin plane.

A fluorescent dye can be a good model compound for the transport of irrigant by convection and diffusion, but still requires a translation to irrigants like NaOCl. The latter cannot be detected with conventional optical techniques; simultaneous measurement of velocity and concentrate would therefore require more advanced techniques (e.g. [17]).

### 17.4 Outlook

The experiments with the hydrogel in Chapter 15 revealed that the steady component of the acoustic streaming induced by an ultrasonically oscillating file is the main cleaning mechanism of removal, although at short distances from the wall the file cannot induce the steady jets. However, the acoustic streaming seemed to be primarily effective at the tip of the file and not at other locations along the file. Also, the

effectiveness of PUI is highly dependent on direction and distance between the file and a wall. PUI, therefore, could use improvements in order increase the cleaning efficacy. A new file design can be based on the acoustic streaming and associated pressures that are generated, the risk of damaging the wall through cutting, and the risk on file fracture. Design parameters are the cross-sectional shape, the diameter and the twisting of the file and the oscillation characteristics. Several tools developed during this project, like the one-dimensional numerical model and vibrometer system, the cavitation quantification setup and the numerical model for acoustic streaming, can aid in evaluating new file designs. It is also worthy to mention the newest file designs, which have a flow through the needle during ultrasonic oscillation. This combination of needle irrigation and passive ultrasonic irrigation, named Continuous Ultrasonic Irrigation (CUI), could enhance the irrigant refreshment compared to PUI.

While cavitation was found to be very efficient in removing biofilm from a substrate (Chapter 16), its use during PUI was found to be limited (Chapter 12). On the other hand, the observation that a stable bubble, oscillating together with the file, could significantly enhance hydrogel removal at all locations along the file suggests the use of stable microbubbles to enhance the removal of biofilms. A further advantage of using oscillating bubbles is the fact that their activity is much less restricted to a specific direction or distance with respect to the oscillating file than the streaming itself, suggesting an effectiveness even in remote locations inside the root canal.

Those microbubbles can be added to the irrigant that is injected into the root canal during a root canal treatment. However, the flow from a needle during irrigant injection as obtained in Part I was shown in Chapter 14 to have difficulties in penetrating into remote locations like the side channels. Generating the bubbles on-site could overcome this problem, and in Chapter 15 it was shown that the reaction between NaOCl and proteins can provide these bubbles at the interface of hydrogel/biofilm and irrigant. The use of ultrasonic frequencies higher than the currently employed 30 kHz could be beneficial to match the resonance frequency of bubbles at an earlier stage of their growth and therefore faster disrupt the biofilm/hydrogel. Ideally, this would result in the development of a non-contact system, with ultrasound applied from outside the tooth, similar to the non-instrumentation technique already described in 1993 by Lussi *et al.* [18], but which never made it to the market.

The hydrogel employed in Chapter 15 is promising as a substitute for biofilm. Besides the production of bubbles during the reaction with NaOCl, the hydrogel showed viscoelastic behavior, although its estimated properties suggested that it was a very soft biofilm. However, these properties can be changed through the concentrations of the components of the hydrogel and by cross-linking with glutaraldehyde. Its attachment to a substrate, however, is difficult to control. Nevertheless, with a proper protocol, a they can be made reproducibly and could therefore be a good substitute to study the mechanical behavior of biofilms, until the use of real biofilms is feasible.

In this thesis I have shown the fluid dynamics involved in root canal irrigation, which I think is both interesting and important for the most important step for the success of a root canal treatments. Future work should focus on the interaction of the fluid with biofilms, both mechanically and chemically. Because of the rich, dynamical behavior of biofilms, studying that interaction would be an even more complex, multidisciplinary, but above all also a very interesting subject.

## References

- [1] P. Nair, "Pathogenesis of apical periodontitis and the causes of endodontic failures", *Critical Review of Oral Biology & Medicine* **15** (2004).
- [2] M. Tagger, "Clearing of teeth for study and demonstration of pulp", *Journal of Dental Education* **40**, 172–174 (1976).
- [3] Y. Shen, S. Stojicic, W. Qian, I. Olsen, and M. Haapasalo, "The synergistic antimicrobial effect by mechanical agitation and two chlorhexidine preparations on biofilm bacteria", *Journal of Endodontics* **36**, 100–104 (2010).
- [4] M. T. Arias-Moliz, C. M. Ferrer-Luque, M. P. González-Rodríguez, M. J. Valderrama, and P. Baca, "Eradication of enterococcus faecalis biofilms by cetrimide and chlorhexidine", *Journal of Endodontics* **36**, 87–90 (2010).
- [5] L. E. Chávez de Paz, G. Bergenholtz, and G. Svensäter, "The effects of antimicrobials on endodontic biofilm bacteria", *Journal of Endodontics* **36**, 70–77 (2010).
- [6] F. R. Tay, L.-s. Gu, G. J. Schoeffel, C. Wimmer, L. Susin, K. Zhang, S. N. Arun, J. Kim, S. W. Looney, and D. H. Pashley, "Effect of vapor lock on root canal debridement by using a side-vented needle for positive-pressure irrigant delivery", *Journal of Endodontics* **36**, 745–750 (2010).
- [7] C. De Gregorio, R. Estevez, R. Cisneros, C. Heilborn, and N. Cohenca, "Effect of edta, sonic, and ultrasonic activation on the penetration of sodium hypochlorite into simulated lateral canals: An in vitro study", *Journal of Endodontics* **35**, 891–895 (2009).
- [8] J. Vera, A. Arias, and M. Romero, "Dynamic movement of intracanal gas bubbles during cleaning and shaping procedures: The effect of maintaining apical patency on their presence in the middle and cervical thirds of human root canals - an in vivo study", *Journal of Endodontics* **38**, 200–203 (2012).
- [9] J. Vera, A. Arias, and M. Romero, "Effect of maintaining apical patency on irrigant penetration into the apical third of root canals when using passive ultrasonic irrigation: An in vivo study", *Journal of Endodontics* **37**, 1276–1278 (2011).
- [10] G. I. Dovgyallo, N. P. Migun, and P. P. Prokhorenko, "The complete filling of dead-end conical capillaries with liquid", *Journal of Engineering Physics and Thermophysics* **56**, 395–397 (1989).
- [11] N. P. Migoun and M. A. Azouni, "Filling of one-side-closed capillaries immersed in liquids", *J Colloid Interf Sci* **181**, 337–340 (1996).

- [12] N. P. Migun and A. I. Shnip, "Model of film flow in a dead-end conic capillary", *Journal of Engineering Physics and Thermophysics* **75**, 1422–1428 (2002).
- [13] A. V. Pesse, G. R. Warrier, and V. K. Dhir, "An experimental study of the gas entrapment process in closed-end microchannels", *International Journal of Heat and Mass Transfer* **48**, 5150–5165 (2005).
- [14] C. Boutsioukis, E. Kastrinakis, B. Verhaagen, M. Versluis, and L. W. M. Van der Sluis, "Apical vapor lock in root canals ex vivo: a combined experimental and computational fluid dynamics approach", *International Endodontic Journal* **in progress** (2013).
- [15] M. S. Pommer, A. R. Kiehl, G. Soni, N. S. Dakessian, and C. D. Meinhart, "A 3d-3c micro-piv method", in *Proceedings of the 2nd IEEE International Conference on Nano/Micro Engineered and Molecular Systems* (Bangkok, Thailand) (2007).
- [16] C. Poelma, J. M. Mari, N. Foin, M.-X. Tang, R. Krams, C. G. Caro, P. D. Weinberg, and J. Westerweel, "3D Flow reconstruction using ultrasound PIV", *Experiments in Fluids* **50**, 777–785 (2011).
- [17] M. Wellhausen, G. Rinke, and H. Wackerbarth, "Combined measurement of concentration distribution and velocity field of two components in a micromixing process", *Microfluidics & Nanofluidics* **12**, 917–926 (2012).
- [18] A. Lussi, U. Nussbächer, and J. Grosrey, "A novel noninstrumented technique for cleansing the root canal system", *Journal of Endodontics* **19**, 549–553 (1993).



# Summary

This thesis investigates the fluid dynamics involved with root canal irrigation, starting with the most commonly used technique for irrigation, i.e. by a needle and syringe, in Part I, which is still the most commonly used technique for irrigation. High-speed Particle Imaging Velocimetry (PIV) recordings and a Computational Fluid Dynamics (CFD) model have revealed the flow pattern and velocity magnitudes for needles with an open end or a side outlet, which was modeled as an axisymmetric or a non-axisymmetric microjet, respectively. There is good agreement between CFD and experiment, validating the use of the CFD model for investigating the fluid flow during irrigation. The axisymmetric jet is found to be stable and agrees well with the theoretical prediction for this type of jet, however, a confinement causes instabilities to the jet. The confinement of the root canal has a pronounced influence on the flow, both for the axisymmetric and the non-axisymmetric jet, by reducing the velocity in the jets by one order of magnitude. The confinement also increases the pressure at the apex, which was measured locally with a miniature pressure sensor positioned there. The non-axisymmetric jet inside the confinement shows a cascade of eddies with decreasing velocity, which, according to the calculated Damköhler numbers, does not provide adequate irrigant refreshment at the apex with respect to the reaction time of the irrigant with a biofilm.

The fluid refreshment inadequacy confirmed the need for irrigant activation techniques. Part II discusses Passive Ultrasonic Irrigation (PUI), which makes use of an ultrasonically (30 kHz) oscillating file that exhibits a pattern of nodes and antinodes and which activates the flow in the root canal. The oscillation characteristics of various endodontic files have been analyzed with a one-dimensional numerical model, which agreed well with vibrometer measurements, when the geometrical and material properties of the file were accurately known. The model can also make predictions for the location where file fracture is likely to occur. Contact with a wall was observed to lead to a secondary, audible oscillation frequency, superimposed on the 30 kHz oscillation, and also induces traveling waves. As the 30 kHz oscillation was not severely affected, contact with a wall should not lead to a significant reduction in induced streaming, and PUI can still be called *passive*. Experiments performed by 30 endodontists on an *in vitro* root canal model showed that contact with the wall



nearly always takes place, but the actual time of contact is short, due to the secondary frequency. With more space around the file (larger root canal or longer distance to the apex), the amount of contact decreased.

The oscillating endodontic file was shown to induce acoustic streaming. The presence of an oscillatory component, dominant near the file, and a steady component, further away from the file, has been confirmed using high-speed Particle Imaging Velocimetry and a two-dimensional Computational Fluid Dynamics model. Measurement of the pressure, both direct measurement and indirectly from bubble oscillations, also agreed well with the theoretical and numerical predictions. The oscillatory component of both the pressure and the shear stress is two or three orders of magnitude higher than its steady counterpart and cannot therefore be neglected, as was done in previous studies. Furthermore, the formation of steady jets is affected by the presence of a confinement; meanwhile the oscillatory velocity and associated pressure and shear stress are increased. The cleaning efficacy of the induced flow was evaluated in an extracted tooth model, measuring the removal of dentin debris from an artificial groove or hole in the wall, representing an area that is difficult to clean. Oscillating the file in the direction of the groove or hole, or increasing the oscillation amplitude, enhanced the cleaning efficacy significantly. Pulsed activation of the file was also beneficial for the cleaning efficacy, but only under a well-defined pulsation scheme. Beyond the tip of the file, towards the apex of the root canal, only half of the area could be cleaned, both in straight and curved root canals. A device operating at sonic frequencies was not effective for cleaning, possibly due to the amplitude being too large and the streaming being not effective at such frequencies. All these findings of debris removal were supported by high-speed visualizations.

Finally, sonochemical measurements and visualizations of cavitation occurring during Passive Ultrasonic Irrigation are reported. Transient cavitation is generated by most of the files, in the form of a large bubble cloud at the file tip and smaller bubbles at subsequent antinodes. High-speed visualizations showed that the bubble cloud collapsed predominantly on the file itself and not on the wall, but its collapse can pull material off a neighboring wall. Sonoluminescence and sonochemoluminescence was observed, not in the bubble cloud, but rather in the small single bubbles at subsequent antinodes. The confinement of the root canal increased the amount of cavitation, which was also predicted by the theory of acoustic streaming. At the air-water interface at the coronal part of the root canal, air entrainment lead to the entrapment of stable cavitation bubbles in the root canal.

Another activation technique, Laser Activated Irrigation (LAI), was investigated in Part III. Laser-activated irrigation was significantly more effective in removing dentin debris from the apical part of the root canal than passive ultrasonic irrigation or hand irrigation when the irrigant was activated for 20 seconds. The high-speed

recordings suggest that streaming, caused by the collapse of the laser-induced cavitation bubble, is the main cleaning mechanism of LAI. Shockwaves, generated upon bubble collapse, generated additional cavitation bubbles.

In the last part of this thesis, Part IV, the cleaning by the induced streaming and cavitation was investigated. The penetration of irrigant into side canals, and specifically tubules, through diffusion and convection was observed to be slow, with convection only dominant in a region within two times the channel diameter from the entrance. Irrigant transport through diffusion, however, is very slow, requiring many minutes for the irrigant to penetrate the full length of a side channel.

The removal of a biofilm from a substrate by the acoustic streaming from an ultrasonically oscillating file was evaluated by mimicking the viscoelastic behavior of a biofilm with a hydrogel and visualizing its behavior. The oscillatory component of the acoustic streaming appeared to cause only elastic deformation, whereas the steady component induced viscous deformation and therefore the actual cleaning. The removal of the hydrogel was assisted by a stable microbubble, driven at resonance. Stable bubbles were also generated during the reaction of the hydrogel with bleach, however these bubbles were too small to be driven in resonance with the driving acoustic field to enhance the cleaning. Furthermore, the time scale of the chemical reaction was much larger than that of the removal by acoustic streaming or cavitation. Finally, with a novel system employing micromachined pits driven at 200 kHz, cleaning was demonstrated within seconds for biofilm, hydrogel, cells and even deposited metals like gold and platinum due to cavitation was demonstrated, showing the potential of using cavitation bubbles for cleaning.



# Samenvatting

Dit proefschrift beschrijft de vloeistofdynamica van irrigatie van het wortelkanaal. De meestgebruikte methode voor irrigatie is die met een naald en een spuit, waarvan de vloeistofdynamica is beschreven in Deel 1. Experimenten met hogesnelheids-Particle Imaging Velocimetry en numerieke simulaties met een Computational Fluid Dynamics code hebben laten zien hoe, en hoe snel, de irrigatievloeistof uit een naald met een open uiteinde of een opening aan de zijkant door het apicale gedeelte van het wortelkanaal stroomt. De experimentele en numerieke resultaten komen goed met elkaar overeen, wat vertrouwen geeft in de simulaties. De resultaten voor de axisymmetrische stroming uit de naald met open uiteinde komen ook goed overeen met theoretische voorspellingen, hoewel de nabijheid van de wortelkanaalwand zorgt voor instabiliteiten in de vloeistofstraal. De omsluiting van het wortelkanaal zorgt ook voor een afname van de snelheid van de vloeistof met een factor tien. Bovendien hebben metingen met een mini-druksensor laten zien dat de druk bij de punt van het wortelkanaal dan toeneemt. Voor optimale en veilige irrigatie van het wortelkanaal zijn zowel een lage druk als een goede verversing vereist. De verversing van de irrigatievloeistof is gemeten aan de hand van het Damköhler getal, dat laat zien dat de naald met open uiteinde wel voor genoeg verversing van de irrigatievloeistof zorgt, maar de wervelingen die een naald met zijopening veroorzaakt, niet.

Vanwege de slechte verversing van de irrigatievloeistof in het (hoofd)wortelkanaal met de naald met zijopening, en ook die in de zijkanalen van het wortelkanaal - zelfs met de naald met open einde -, is het nodig de vloeistof te activeren. Deel 2 van dit proefschrift gaat over een dergelijke techniek, namelijk Passive Ultrasonic Irrigation (PUI), waarin een dunne vijl door middel van ultrasone trillingen (30 kHz) de vloeistof in beweging brengt. Het patroon van knopen en buiken dat op de vijl ontstaat is gemeten met behulp van een vibrometer, en ook gesimuleerd in een eendimensionaal model. De resultaten van die twee methoden voor een tiental endodontische vijlen komen goed overeen, zolang tenminste de materiaaleigenschappen en de geometrie in detail bekend zijn. Het numerieke model lijkt ook geschikt te zijn om de breekpunten van vijlen te voorspellen, en om te voorspellen wat er gebeurt als de vijl in contact komt met een wand tijdens zijn oscillaties. Na contact bleek de vijl zich van de wand af en vervolgens weer terug te bewegen, met een frequentie die in

het hoorbare gebied ligt. Bovendien treden er lopende golven op de vijl op. Ondertussen blijf de vijl even hard trillen met een frequentie van 30 kHz. Contact zorgt dus niet per se voor demping van de oscillaties of van de geïnduceerde stroming. De vraag hoeveel contact er daadwerkelijk optreedt tijdens een wortelkanaalirrigatie met PUI is beantwoord met behulp van 30 endodontologen die in een *in-vitro* wortelkanaalmodel PUI hebben uitgevoerd. Ze bleken altijd contact te maken, maar de duur van de contact is maar kort, vanwege de hierboven beschreven beweging van de wand af. Meer ruimte rondom de vijl (zoals in een groter wortelkanaal) verminderde de hoeveelheid contact dat de tandartsen maakten.

De oscillerende vijl veroorzaakt akoestische stromingen die worden gekenmerkt door zowel een oscillerend als een continu veld dat beide bijdraagt aan de schoonmaakefficiëntie van PUI. De theoretische voorspellingen voor deze akoestische stromingen en bijbehorende drukken zijn experimenteel bevestigd met behulp van hogesnelheids-Particle Imaging Velocimetry en lokale drukmetingen en numeriek met een twee-dimensionaal Computational Fluid Dynamics model. Het oscillerende gedeelte van de druk en de afschuifspanning op een vlakke wand is twee tot drie orde-groottes groter dan het continue gedeelte van de stroming, en in een wortelkanaal wordt dit verschil nog groter omdat het continue gedeelte van de stroming wordt beïnvloed door de krappe ruimte. Het oscillerende gedeelte moet dus in acht genomen worden, terwijl het in eerdere studies is verwaarloosd. Aan de andere kant is het continue veld juist weer belangrijk voor het mengen en verversen van de irrigatievloeistof.

De efficiëntie van PUI is gemeten met behulp van een geprepareerd wortelkanaal waarin handmatig dentinegruis is aangebracht in een holte in de wortelkanaalwand. Verwijdering van dit gruis verbeterde als de vijl in de richting van de holte oscilleerde en ook als de oscillatieamplitude toenam. Een gepulseerd trillende vijl zorgde ook voor een hogere schoonmaakefficiëntie, maar alleen bij een specifiek aan/uit schema. Visualisaties van het gebied tussen de vijl en de wortelkanaalpunt lieten zien dat slechts de helft van die ruimte werd schoongemaakt, zowel in rechte als in kromme kanalen. Een commercieel apparaat dat plastic vijlen laat trillen op sonische frequenties (100 Hz) bleek helemaal niet effectief in het verwijderen van het gruis, wat te wijten is aan een te grote amplitude en de afwezigheid van akoestische stromingen. Alle bevindingen met het wortelkanaalmodel met dentinegruis zijn bevestigd aan de hand van hogesnelheidsopnamen.

De oscillerende vijl kan ook cavitatiebellen opwekken, die vervolgens ook kunnen bijdragen aan het schoonmaken van het wortelkanaal. De locatie, grootte en chemische activiteit van deze bellen is onderzocht met behulp van visualisaties en licht-gevoelige apparatuur. Bijna alle typen vijlen blijken wel cavitatiebellen op te wekken, voornamelijk aan de punt van de vijl, waar een wolk van bellen ontstaat.

Verder van de punt van de vijl worden kleinere, individuele belletjes gevormd, en het zijn juist deze bellen die sonochemisch actief lijken te zijn. De visualisaties lieten zien dat de bellenwolk bij de vijlpunt voornamelijk op de vijl zelf implodeert en niet op een dichtbij zijnde wand. De begrenzing van het wortelkanaal zorgt voor een toename in cavitatie, zoals ook was verwacht op basis van de berekende drukken. Daarnaast kunnen bij het grensvlak van water en lucht bovenaan in het wortelkanaal luchtbellen ingesloten worden. Deze stabiele bellen kunnen vervolgens samen met het ultrageluid bijdragen aan het schoonmaken van de wortelkanaal.

Deel 3 van dit proefschrift gaat over een hele andere techniek om de irrigatievloeistof te activeren, namelijk met behulp van een laser. Metingen met het wortelkanaalmodel met dentinegruis lieten zien dat een laser veel effectiever is dan de ultrasoon trillende vijl, binnen een tijdspanne van 20 seconden. Dit kan worden verklaard aan de hand van hogesnelheidsopnamen, waarop te zien is dat aan de punt van de laserfiber een grote bel wordt gevormd, die vervolgens met hoge snelheid implodeert en schokgolven veroorzaakt, met nog meer cavitatiebellen tot gevolg.

In het laatste deel (4) van dit proefschrift is gekeken naar de mechanismen die ten grondslag liggen aan het schoonmaken van een wortelkanaal met behulp van vloeistofstroming en cavitatiebellen. Een van de gebieden die moeilijk schoon te maken is, zijn de tubules. Dit zijn zijkanaaltjes in de wortelkanaalwand met een diameter van enkele micrometers en een lengte van enkele millimeter. Hier blijkt een stroming nauwelijks verder te komen dan twee maal de diameter van de tubulus, en de irrigatievloeistof zal zich door middel van diffusie moeten verplaatsen om zo de dieperliggende bacteriën in die kanalen te bereiken. Diffusie is echter zo langzaam dat het vele minuten duurt om het eind van de tubulus te bereiken.

Het verwijderen van een biofilm (een laag bacteriën) van een oppervlak is onderzocht door de viscoelastische eigenschappen van biofilms na te bootsen met een hydrogel. De interactie van de biofilm met de akoestische stroming rondom een ultrasoon trillende vijl is vervolgens gefilmd. Het oscillerende veld van de stroming blijkt alleen elastische deformatie te veroorzaken, en het is het continue deel dat de biofilm daadwerkelijk verwijdert, eventueel geholpen door een stabiel oscillerende bel in de directe nabijheid. Dat soort bellen worden door de biofilm zelf al geproduceerd tijdens zijn reactie met bleekmiddel (een veelgebruikte irrigatievloeistof), alleen zijn die bellen te klein om resonant te trillen met de 30 kHz frequentie van de vijl. De chemische reactie zelf was veel langzamer dan de verwijdering door de vloeistofstroming en oscillerende bellen. Een nieuw systeem, waarin bellen gevormd worden uit enkele speciaal gefabriceerde microscopisch kleine gaatjes en geactiveerd met ultrageluid met een frequentie van 200 kHz, liet veelbelovende resultaten zien voor wat betreft het verwijderen van de biofilm, van cellen en ook van metalen zoals goud en platina.



# List of publications and presentations

## Publications

- [1] B. Verhaagen, C. Boutsoukis, G. L. Heijnen, L. W. M. Van der Sluis, and M. Versluis, "Role of the confinement of a root canal on jet impingement during endodontic irrigation," *Experiments in Fluids*, 2012. accepted.
- [2] D. Fernandez Rivas, B. Verhaagen, J. Seddon, A. G. Zijlstra, L.-M. Jiang, L. W. M. Van der Sluis, A. Prosperetti, M. Versluis, D. Lohse, and H. J. G. E. Gardeniers, "Localized removal of layers of metal, polymer or biomaterial by ultrasound cavitation microbubbles," *Biomicrofluidics*, vol. 6, p. 034114, 2012.
- [3] B. Verhaagen, S. C. Lea, L. W. M. van der Sluis, A. D. Walmsley, and M. Versluis, "Oscillation characteristics of endodontic files: numerical model and its validation," *IEEE - Transactions on Ultrasonics, Ferroelectrics and Frequency Control*, 2012. accepted.
- [4] M. Malki, B. Verhaagen, L.-M. Jiang, W. Nehme, A. Naaman, M. Versluis, P. R. Wesselink, and L. W. M. van der Sluis, "Irrigant flow beyond the insertion depth of an ultrasonically oscillating file in straight and curved root canals: Visualization and cleaning efficacy," *Journal of Endodontics*, vol. 38, no. 5, pp. 657–661, 2012.
- [5] L.-M. Jiang, B. Verhaagen, M. Versluis, J. Langedijk, P. R. Wesselink, and L. W. M. Van der Sluis, "The influence of the ultrasonic intensity on the cleaning efficacy of passive ultrasonic irrigation," *Journal of Endodontics*, vol. 37, no. 5, pp. 688–692, 2011.
- [6] L.-M. Jiang, B. Verhaagen, M. Versluis, C. Zangrillo, D. Cuckovic, and L. W. M. Van der Sluis, "An evaluation of the effect of pulsed ultrasound on the cleaning efficacy of passive ultrasonic irrigation," *Journal of Endodontics*, vol. 36, no. 11, pp. 1887–1891, 2010.
- [7] C. Boutsoukis, C. Gogos, B. Verhaagen, M. Versluis, E. Kastrinakis, and L. W. M. Van der Sluis, "The effect of root canal taper on the irrigant flow:



- evaluation by an unsteady computational fluid dynamics model,” *International Endodontic Journal*, vol. 43, no. 10, pp. 909–916, 2010.
- [8] C. Boutsoukis, C. Gogos, B. Verhaagen, M. Versluis, E. Kastrinakis, and L. W. M. Van der Sluis, “The effect of apical preparation size on the irrigant flow in the root canal: evaluation by an unsteady computational fluid dynamics model,” *International Endodontic Journal*, vol. 43, no. 10, pp. 874–881, 2010.
- [9] C. Boutsoukis, B. Verhaagen, M. Versluis, E. Kastrinakis, C. Gogos, and L. W. M. Van der Sluis, “The effect of needle depth on irrigant flow in the root canal: evaluation by an unsteady computational fluid dynamics model,” *Journal of Endodontics*, vol. 36, no. 10, pp. 1664–1668, 2010.
- [10] C. Boutsoukis, B. Verhaagen, M. Versluis, E. Kastrinakis, and L. W. M. Van der Sluis, “Irrigant flow in the root canal: experimental validation of an unsteady computational fluid dynamics model using high-speed imaging,” *International Endodontic Journal*, vol. 43, no. 5, pp. 393–403, 2010.
- [11] L.-M. Jiang, B. Verhaagen, M. Versluis, and L. W. M. Van der Sluis, “The influence of the oscillation direction of an ultrasonic file on the cleaning efficacy of passive ultrasonic irrigation,” *Journal of Endodontics*, vol. 36, no. 8, pp. 1372–1376, 2010.
- [12] C. Boutsoukis, B. Verhaagen, M. Versluis, E. Kastrinakis, P. R. Wesselink, and L. W. M. Van der Sluis, “Evaluation of irrigant flow in the root canal using different needle types by an unsteady computational fluid dynamics model,” *Journal of Endodontics*, vol. 36, no. 5, pp. 875–879, 2010.
- [13] L. W. M. Van der Sluis, M. P. J. M. Vogels, B. Verhaagen, R. Macedo, and P. R. Wesselink, “Study on the influence of refreshment/activation cycles and irrigants on mechanical cleaning efficiency during ultrasonic activation of the irrigant,” *Journal of Endodontics*, vol. 36, no. 4, pp. 737–740, 2010.
- [14] L.-M. Jiang, B. Verhaagen, M. Versluis, and L. W. M. Van der Sluis, “Evaluation of a sonic device designed to activate irrigant in the root canal,” *Journal of Endodontics*, vol. 36, no. 1, pp. 143–146, 2010.
- [15] S. D. De Groot, B. Verhaagen, M. Versluis, M.-K. Wu, P. R. Wesselink, and L. W. M. Van der Sluis, “Laser-activated irrigation within root canals: Cleaning efficacy and flow visualization,” *International Endodontic Journal*, vol. 42, no. 12, pp. 1077–1183, 2010.
- [16] C. Chlon, C. Gudon, B. Verhaagen, W. T. Shi, C. S. Hall, J. Lub, and M. R. Böhmer, “Effect of molecular weight, crystallinity, and hydrophobicity on the

acoustic activation of polymer-shelled ultrasound contrast agents,” *Biomacromolecules*, vol. 10, no. 5, pp. 1025–1031, 2009.

- [17] B. Verhaagen, “Ultrasonic cleaning of root canals - a fluid mechanical view,” Master’s thesis, University of Twente, 2008.

## Presentations

1. **Acoustical Society of America** 17/05/2012  
Hong Kong  
‘Ultrasonic cleaning of root canals’
2. **Physics@FOM** 17/01/2012  
Eindhoven, The Netherlands  
‘Ultrasonic cleaning of root canals’ (*poster*)
3. **Burgersdag 2012** 12/01/2012  
Veldhoven, The Netherlands  
‘Ultrasonic cleaning of root canals’ (*poster*)
4. **American Physics Society, Division of Fluid Dynamics autumn meeting** 20/11/2011  
Baltimore, MD, USA  
‘Ultrasonic cleaning of root canals’
5. **Physics@FOM** 19/01/2011  
Veldhoven, The Netherlands  
‘Ultrasonic cleaning of root canals’
6. **International Conference on Acoustics** 26/08/2010  
Sydney, Australia  
‘Ultrasonic cleaning of root canals’
7. **Seminar at University of Queensland, Dental School** 15/08/2010  
Brisbane, Australia  
‘Cavitation in dentistry’

8. **IFEA 8<sup>th</sup> World Endodontic Conference** 08/10/2010  
Athens, Greece  
Irrigant penetration into dentinal tubules (*poster*)
9. **MicroNanoConference** 17/11/2010  
University of Twente, Enschede, The Netherlands  
Ultrasonic cleaning of root canals (*poster*)
10. **JMBC Burgersdag** 13/01/2010  
Enschede, The Netherlands  
'Fluid dynamics at the dentist - Cleaning root canals with ultrasound'
11. **Conference European Society of Endodontists (ESE)** 26/09/2009  
Edinburgh, UK  
'High-speed visualization of irrigant flow'
12. **Meeting Nederlandse Vereniging voor Endodontisten (NVVE)** 09/05/2009  
Amsterdam, The Netherlands  
'Vloeistofdynamische aspecten van irrigeren' (*invited*)
13. **Conference American Association of Endodontists (AAE)** 01/05/2009  
Orlando, FL, USA  
'Fluid dynamic aspects of laser-activated irrigation'
14. **Soft Matter meeting '08** 08/10/2008  
University of Twente, Enschede, The Netherlands  
'Ultrasonic cleaning of root canals'

# Dankwoord

Dit is inmiddels een erg dik proefschrift geworden. Al het werk dat hierin beschreven is had ik nooit alleen kunnen doen maar is het gevolg van het werken in een hele prettige onderzoeksgroep en samenwerking met vele mensen, voor wie ik dan ook graag nog twee extra pagina's wil toevoegen.

Allereerst mijn directe begeleider, Michel Versluis. Je hebt me erg vrij gelaten tijdens mijn onderzoek, waardoor ik goed heb kunnen leren zelfstandig een onderzoeksproject uit te voeren en zelf de richting te bepalen, alhoewel dat niet altijd even makkelijk was. Gelukkig heb je me ook vaak advies gegeven, over het ontwerp en de interpretatie van experimenten en theorie, plus de altijd handige reistips. Hartelijk bedankt voor je begeleiding in de afgelopen jaren!

Toen ik met dit project begon, wist ik nog helemaal niets van tandheelkunde en endodontologie. Gelukkig was Luc van der Sluis altijd bereid om de tandheelkundige kant uit te leggen en de natuurkundige kant te bediscussiëren. Luc, ik heb met veel plezier met je samen mogen werken en bedankt voor alle hulp en begeleiding en plezier tijdens de conferenties. En het spijt me dat ik je veelvoud aan ideeën niet allemaal heb kunnen uitvoeren en onderzoeken.

Ik wil ook graag mijn promotor Detlef Lohse bedanken dat ik dit onderzoek in zijn vakgroep heb mogen doen, een plek dat onder zijn leiding een geweldige plek is om te werken, met goede faciliteiten en mensen.

Daarnaast wil ik STW graag bedanken voor de financiële ondersteuning.

The dental aspect of this project was also covered by the other members of the 'Endo Dreamteam': Lei-meng Jiang, Ricardo Macedo and Christos Boutsoukis. I very much enjoyed working with all of you on the various projects and I learned a lot from you. I think our combination of backgrounds and perspectives have resulted in some beautiful articles. It was always a pleasure to visit you at ACTA or AUTH or join you at conference trips and get introduced into the dental world.

Ook de samenwerking binnen de 'schoonmaakploeg', Aaldert Zijlstra en David Fernandez Rivas, was erg prettig. 'Bubblemaster' David, vooral het afgelopen jaar hebben we veel samen gewerkt en als we in ons tempo blijven doorgaan volgen er vast nog vele leuke bellen-artikelen. En dan komen we ook vast wel een keer aan een jamsessie toe...

I would like to thank Simon Lea, Jonathan Robinson and Damien Walmsley from

the Dental School in Birmingham for allowing me to visit them and do measurements with their vibrometry system, and for taking me for lunch and drinks at the memorable 'The Bull'.

Het kantoor waarin ik werkte werd wel eens 'het stille kantoor' genoemd, wat voor ons eigenlijk gewoon lekker werkte. En hulp was altijd beschikbaar wanneer nodig, waarvoor ik Ivo, Rajaram en Ceyda dan ook dankbaar ben. Als zij er eens niet waren, was hulp gelukkig altijd ergens anders in de groep wel te vinden, zeker met zo'n grote, gevarieerde, goede en ook gezellige groep als POF is. Natuurlijk is de sociale kant ook erg belangrijk, en de dagelijkse koffie pauze 's ochtends, de POF United voetbalwedstrijden en de groepsborrels waren dan ook altijd erg gezellig.

Van de POF-leden wil ik verder in het bijzonder Gert-Wim en Martin bedanken voor het technisch mogelijk maken van allerlei sub-millimeter grootte onderdelen van mijn opstelling en het oplossen van allerlei problemen, waarvoor jullie altijd weer een ingenieuze oplossing vonden. Bas evenzo bedankt, voor het oplossen van computervraagstukken en voor het voor de zoveelste keer repareren van dezelfde versterker. En Joanita, hartelijk bedankt voor het regelen van allerlei administratieve taken. Zonder jullie duurt een PhD onderzoek zeker twee keer zo lang. Daarnaast wil ik ook Gerrit graag bedanken voor je hulp met allerlei (theoretische) vraagstukken.

In de afgelopen vier jaar heb ik twee masterstudenten begeleid, Lammert Heijnen en Pascal Sleutel, wiens werk heeft bijgedragen aan twee artikelen. Lammert en Pascal: jullie begeleiden was niet alleen nuttig voor die artikelen, maar ook voor mij - ik heb veel van jullie kunnen leren, qua begeleiden, uitleggen en in het lab werken. Daarnaast heb ik vele 'Experimental Techniques in Physics of Fluids' studenten voor me in het lab mogen laten werken: Joost Weijs & Tess Homan (2008), Raymond Coenders & Pieter Palsma (2009), Chiel Grijzen & Carla Kloeze (2010) en Jolien Hessels & Sanne Slegers (2011). Jullie verkennende onderzoeken zijn allemaal nuttig gebleken voor latere experimenten, bedankt dus!

Tenslotte wil ik nog iedereen bedanken die me de afgelopen jaren hebben gesteund, waaronder mijn familie en vrienden en iedereen die bij verjaardagen, zodra mijn onderzoek aan bod kwam, zijn/haar tandartservaringen kwijt wilde.

De laatste woorden zijn voor Roos. Toen ik aan mijn PhD begon was ik nog alleen. Nu, vier jaar later, ben ik getrouwd met de leukste en liefste vrouw die ik ken. Samen met jou voel ik me veel zelfverzekerder en gelukkiger en de basis die we samen hebben is onmisbaar voor mij voor de toekomst. Ik hou van je.

## About the author

Bram Verhaagen was born on August 6, 1985, in Hengelo (Ov) and grew up in Borne. He attended high school ‘CSG Het Noordik’ in Almelo at the level ‘Atheneum’. After finishing high school in 2003 he went on to study Applied Physics at the University of Twente (UT) in Enschede. During his bachelor studies, he stayed for 6 months at the Kungliga Tekniska Högskolan in Stockholm (Sweden) to take courses on Management and Intellectual Property Rights, as part of the ‘minor’ phase of the Bachelor program. Extracurricular activities involved writing for the popular scientific magazine ‘Focus’ by student association Arago, for which he also was editor-in-chief.

After graduating in the Physics of Fluids group of the UT with a bachelor thesis on the breaking of confined kidney stones with shockwaves, Bram continued with a masters program in the Physics of Fluids track. As an optional ‘course’ he was offered to perform preliminary high-speed visualizations of root canal irrigation with ultrasound and laser, and this project suited him so well that it also became his master project. But before graduating, he did a three-month internship at Philips Research NA in Briarcliff (NY, USA) on drug release from microcapsules using ultrasound. And because of a fruitful internship, he was offered to return to Philips at Briarcliff for another three months after his graduation in July 2008.

The next four years, up to the presentation of this thesis, were a continuation of the master project on the cleaning of root canals, in close collaboration with research groups in Amsterdam, Greece and the United Kingdom. Together with many conferences world-wide this fueled his interest for traveling. Following his PhD graduation, he will work for another year on product development by applying the results of his research to novel commercial root canal cleaning devices.

Bram also enjoys photography. Furthermore, he has over 20 years experience in playing the piano, and since recently also guitar and *cajon*. He married Roos in 2012 and they currently live in Borne.







